Proceedings of the National Conference on

Current Issues in Cosmology, Astrophysics and High Energy Physics (CICAHEP)

Dibrugarh, India, November 2 - 5, 2015

Volume 01

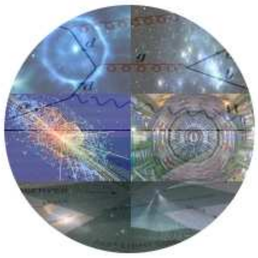

Proceedings of the National Conference on

Current Issues in Cosmology, Astrophysics and High Energy Physics (CICAHEP)

Dibrugarh, India, November 2 – 5, 2015

Volume 01

Organized by the

Department of Physics, Dibrugarh University

Rajabheta, Dibrugarh 786004, Assam, India

Supported by

Science and Engineering Research Board (SERB)
Department of Science and Technology, Government of India

Tata Institute of Fundamental Research (TIFR), Mumbai

Inter-University Centre for Astronomy and Astrophysics (IUCAA), Pune

Board of Research in Nuclear Sciences (BRNS)
Department of Atomic Energy, Government of India

Indian National Science Academy (INSA), New Delhi

Editor

Umananda Dev Goswami
Department of Physics
Dibrugarh University
Dibrugarh 786004, Assam, India

Committees

National Organizing Committee

Prof. B. S. Acharya, TIFR, Mumbai (Chair)
Prof. Sunanda Banerjee, SINP, Kolkata
Prof. A. K. Buragohain, VC, Dibrugarh University (Advisor)
Dr. Bipul Bhuyan, IIT, Guwahati
Prof. K. Boruah, Gauhati University, Guwahati
Dr. V. R. Chitnis, TIFR, Mumbai
Prof. D. K. Choudhury, Gauhati University, Guwahati
Prof. H. L. Duorah, Gauhati University, Guwahati
Dr. U. D. Goswami, Dibrugarh University, Dibrugarh (Convenor)
Prof. Ajit K. Kembhavi, Formar Director, IUCAA, Pune
Prof. Pankaj S. Joshi, TIFR, Mumbai
Prof. Sayan Kar, IIT, Kharagpur
Dr. P. Poulose, IIT, Guwahati
Prof. A. R. Rao, TIFR, Mumbai
Prof. M. Sami, Director, CTP, JMI, New Delhi
Prof. Asoke K. Sen, Assam University, Silchar
Prof. N. N. Singh, Manipur University, Imphal
Prof. Tarun Souradeep, IUCAA, Pune
Prof. P. Sreekumar, Director, IIA, Bangalore

Local Organizing Committee

Prof. M. N. Dutta, Registrar, Dibrugarh University
Prof. A. N. Phukan, Dibrugarh University
Prof. P. K. Bhuyan, Dibrugarh University
Dr. P. K. Saikia, Dibrugarh University
Dr. K. Bhuyan, Dibrugarh University
Dr. P. Dutta, Dibrugarh University
Mr. B. R. Kalita, Dibrugarh University
Mr. G. S. Das, Dibrugarh University
Dr. B. Kalita, Dibrugarh University
Dr. B. Pathak, Dibrugarh University
Dr. P. J. Phukan, Dibrugarh University
Dr. N. Dutta, Dibrugarh University
Dr. C. Duorah, Dibrugarh University
Mrs. R. Devi, Dibrugarh University
Mr. S. Acharjee, Dibrugarh University
Dr. U. D. Goswami, Dibrugarh University (Convenor)

Supporting Members

Dr. A. T. T. Mostako, Dibrugarh University
Mr. Pankaj Borthakur, Dibrugarh University
Mr. Diganta Bora, Dibrugarh University
Mr. Gunadeep Chetia, Dibrugarh University
Mr. Karunakar Borah, Dibrugarh University
Mr. Rakteem Borthakur, Dibrugarh University
Mr. Mriganka Boruah, Dibrugarh University
Mr. Pranjal Rajkhowa, Dibrugarh University
Mr. Achyut Kumar Phukan, Dibrugarh University
Sheikh Rustam Ali, Dibrugarh University
Mr. Ramani Gogoi, Dibrugarh University
Mr. Naba Gogoi, Dibrugarh University

Invited Delegates

Prof. J. V. Narlikar, IUCAA, Pune (Keynote Speaker)
Prof. B. S. Acharya, TIFR, Mumbai (Session Chair)
Prof. Kajari Mazumdar, TIFR, Mumbai (Plenary Speaker, Session Chair)
Prof. Pankaj S. Joshi, TIFR, Mumbai (Plenary Speaker, Session Chair)
Prof. Naba K. Mondal, TIFR, Mumbai (Plenary Speaker)
Prof. Narayan Banerjee, IISER, Kolkata (Plenary Speaker)
Prof. Raj Gandhi, HRI, Allahabad (Plenary Speaker)
Prof. K. P. Singh, TIFR, Mumbai (Plenary Speaker)
Prof. Tarun Souradeep, IUCAA, Pune (Plenary Speaker, Session Chair)
Prof. A. K. Ray, TIFR, Mumbai (Plenary Speaker, Session Chair)
Prof. Sayan Kar, IIT, Kharagpur (Session Chair)
Dr. V. R. Chitnis, TIFR, Mumbai (Plenary Speaker, Session Chair)
Dr. K. K. Yadav, BARC, Mumbai (Plenary Speaker)
Prof. Shrihari Gopalakrishna, IMSC, Chennai (Plenary Speaker)
Dr. A. K. Pandey, ARIES, Nainital (Plenary Speaker, Session Chair)
Dr. Koushik Dutta, SINP, Kolkata (Plenary Speaker)
Prof. N. N. Singh, Manipur University, Imphal (Plenary Speaker, Rapporteur, Session Chair)
Prof. K. Boruah, Gauhati University, Guwahati (Session Chair)
Prof. Madhurjya P. Bora, Gauhati University, Guwahati (Rapporteur)
Dr. Bipul Bhuyan, IIT, Guwahati (Plenary Speaker, Session Chair)
Dr. P. S. Joarder, Bose Institute, Kolkata (Session Chair)
Dr. U. Alam, ISI, Kolkata (Rapporteur)
Dr. H. Nandan, GKV, Haridwar, Uttarakhand (Rapporteur)
Dr. S. Somorendro Singh, University of Delhi (Rapporteur)

Areas with Codes

General Relativity and Cosmology:	**COS**
Classical General Relativity:	**1**
Quantum Gravity:	**2**
Standard Cosmology:	**3**
String Inspired Cosmology:	**4**
Dark Energy:	**5**
Dark Matter:	**6**
Alternative Gravity Theories:	**7**
Inflation and Early Universe Cosmology:	**8**
Other:	**9**
Astrophysics & Astronomy:	**A&A**
X-Ray Astronomy:	**1**
Infrared Astronomy:	**2**
Optical Astronomy:	**3**
Solar Astrophysics:	**4**
High energy Astrophysics (Neutron Stars, Magnetars, Black Holes, Gravitational Collapse):	**5**
Gravitational Waves and Gravitational Wave Astronomy:	**6**
Other:	**7**
High Energy Physics:	**HEP**
Particle Physics - Theory:	**1**
Particle Physics - Experiment:	**2**
Particle Physics-Phenomenology:	**3**
Physics Beyond Standard Model:	**4**
String Theory:	**5**
Gamma-Ray Astronomy:	**6**
Cosmic Ray Physics:	**7**
Other:	**8**

Preface

Organizing Conferences in different emerging areas of research is one of the important academic activities of an university or a research institution, which provide a lucid opportunity to new generation of researchers as well as the established researchers to exchange their views with a wide section of co-workers and peers in a lively environment of interaction and then to prepare their future course of action. In this sense, the **National Conference on Current Issues in Cosmology, Astrophysics and High Energy Physics (CICAHEP)**, organized by the Department of Physics, Dibrugarh University during November 2 – 5, 2015 was one of the finest national conferences organized. It is heartening to note that the participants represented almost all regions of India, especially so, as it was held in the remote far-east region of the country, which is not easily accessible. Eminent speakers were drawn from leading institutions across India like, Tata Institute of Fundamental Research (TIFR), Mumbai; Inter-University Centre for Astronomy and Astrophysics (IUCAA), Pune; Bhabha Atomic Research Centre (BARC), Mumbai; Harish-Chandra Research Institute (HRI), Allahabad; Institute of Mathematical Sciences (IMSC), Chennai; Saha Institute of Nuclear Physics (SINP), Kolkata; Aryabhatta Research Institute of Observational Sciences (ARIES), Nainital; Indian Institute of Science Education and Research (IISER), Kolkata; Physical Research Laboratory (PRL), Ahmedabad; Bose Institute, Kolkata; Indian Statistical Institute (ISI), Kolkata; Indian Institute of Technology, Kharagpur; and Indian Institute of Technology, Guwahati. Moreover, the internationally acclaimed theoretical astrophysicist and cosmologist Professor J. V. Narlikar graced this event as the keynote speaker. At this moment, I take opportunity to thank Professor Narlikar for taking pains in travelling a very long distance from Pune to Dibrugarh, inspite of his advanced age, and inspiring a new generation of researchers through his excellent talk. With the active support of the Vice-Chancellor Professor Alak K. Buragohain this conference provided a lively atmosphere for exchange of ideas and forging collaborations. I'm quite sure that all participants have benefited and carried something positive from this conference to their respective destinations.

Publication of conference proceedings is an important task of the organizing committee for the event to be more productive because, this will carry the presentations of participants to wider audience and then give cascading effect for the growth of knowledge. However, in the process of publication of the proceedings of a conference, lots of efforts and patience are required from the end organizer, in particular from the editor(s). I hope this proceedings will be able to reach a wide class of researchers of the concerned areas and will be able to fulfill their partial requirements. Finally, as the Chairperson of the National Organizing Committee (NOC) of this event I would like to thank all members of the NOC, Local Organizing Committee, all participants and all other associated individuals for making the event memorable and a very successful one.

June, 2016

B. S. Acharya
Chair, NOC, CICAHEP 2015 &
Professor, TIFR, Mumbai-400005.

A note from the Convenor cum Editor

The main motivations for organizing this event (CICAHEP 2015) was to make an awareness among the budding researchers of the North-Eastern part of our country about the importance and appeals of research works in the fascinating and challenging research fields of Cosmology, Astrophysics and High Energy Physics as well as to provide an effective platform for interactions with experts to those who are already in these fields of research from this North-Eastern region. As Cosmology, Astrophysics and High Energy Physics are most inter-related and inter-dependent branches of physics research in modern times of inter-disciplinary research, another motivation of this conference is to provide an effective interaction platform for researchers in these areas. This was the first national conference organized by the Dibrugarh University in such wide areas of emerging physics research and I feel that it served my purpose partially for what it was organized as mentioned. There were 24 invited delegates and 70 other participants in this conference from all over India. The keynote address of the conference was delivered by the internationally acclaimed Cosmologists and Astrophysicist Professor Jayant Vishnu Narlikar, Emeritus Professor, IUCAA, Pune on **Some Conceptual Problems in Cosmology**. In his address, Professor Narlikar highlighted many prospective areas for future research in the Cosmology and related fields. Another 14 eminent scientists of national and international repute had delivered plenary talks on various emerging issues in this conference. These scientists include, Professor Naba K. Mondal, Project Director, India-based Neutrino Observatory and Senior Professor, TIFR, Mumbai; Professor Narayan Banerjee, Indian Institute of Science Education and Research (IISER), Kolkata; Professor Pankaj S. Joshi, TIFR, Mumbai; Dr. K. K. Yadav, Bhabha Atomic Research Centre (BARC), Mumbai; Dr. Varsha R. Chitnis, TIFR, Mumbai; Dr. Bipul Bhuyan, IIT, Guwahati; Professor Kajari Mazumdar, TIFR, Mumbai; Professor Raj Gandhi, Harish-Chandra Research Institute (HRI), Allahabad; Professor A. K. Ray, TIFR, Mumbai; Professor K. P. Singh, TIFR, Mumbai; Professor Tarun Souradeep, IUCAA, Pune; Dr. Anil K. Pandey, Aryabhatta Research Institute of Observational Sciences (ARIES), Nainital; Professor Shrihari Gopalakrishna, Institute of Mathematical Sciences (IMSC), Chennai; and Dr. Koushik Dutta, Saha Institute of Nuclear Physics (SINP), Kolkata. A special lecture on Nobel Prize in Physics, 2015 was delivered by Professor N. N. Singh, Manipur University, Imphal.

The number of contributory papers in the conference were 64. Among them, 41 were presented as contributory talks and the rest were presented as the posters. In the cosmology section there were 22 papers (14 oral presentations and 8 poster presentations), in the Astrophysics section there were 11 papers (8 oral presentations and 3 poster presentations) and in the High Energy Physics section there were 31 papers (19 oral presentations and 12 poster presentations).

Various sessions of this conference were chaired by most of plenary speakers and some other eminent scientists of national and international repute or well-know personality in the fields. They include, Professor B. S. Acharya, TIFR, Mumbai (who is also the Chairperson, CICAHEP, 2015); Professor Sayan Kar, IIT, Kharagpur; Prof. K. Boruah, Gauhati University, Guwahati; and Dr. P. S. Joarder, Bose Institute, Kolkata.

Rapporteuring on various contributory papers in the conference were done by Professor N. N. Singh, Manipur University, Imphal (on High Energy Physics Section); Professor Madhurjya P Bora, Gauhati University, Guwahati (on Astronomy and Astrophysics Section), Dr. H. Nandan, Gurukula Kangri Vishwavidyalaya, Haridwar (on Cosmology Section); Dr. U. Alam, Indian Statistical Institute (ISI), Kolkata (on Cosmology Section); and Dr. S. Somorendro Singh, Delhi University, Delhi (on High Energy Physics Section).

However, for this proceedings we have received only 43 papers including the keynote address and 3 plenary papers ($\sim$ 54% of total presentations). Out of this, two contributory papers could not be included in the proceedings due to extreme plagiarism in one paper and lack of physics value in another paper. Moreover, no rapporteur papers in the proceedings could be published due to some technical difficulties. So, this proceedings contains only 41 papers: 37 contributory and 4 invited papers. I hope that this proceedings will be helpful to those for whom it is intended.

This conference was the outcome of the helps and painstaking efforts of many individuals, as well as the financial supports of different institutions and organizations, without which it would not have been possible for us to successfully complete the same. At this moment I should show my gratitude to all of them. In this context, I take this opportunity to extend my sincere gratitude to our Vice-Chancellor Professor Alak K. Buragohain for his generous helps including a substantial financial contribution and for his kind opulence supports in different aspects in organizing this event.

I am extremely grateful to Professor B. S. Acharya and Dr. Varsha R. Chitnis of Tata Institute of Fundamental Research (TIFR), Mumbai for all sort of helps in organizing this event. In spite of his very busy schedule, Professor Acharya, who is a leading High Energy Physicists of our country, had agreed to chair the National Organizing Committee (NOC) of this conference and guided me to make the event a successful one. Dr. Chitnis, who is a well known Gamma-Ray Astrophysicist of our country, took the initiative and did many paper works with Professor Acharya to provide a good amount of financial sanction from TIFR to this conference. My many thanks are due also to the TIFR authority for a financial sanction to organize the event.

Also I am very much thankful to Professor Ajit K. Kembhavi, Former Director, Inter-University Centre for Astronomy and Astrophysics (IUCAA), Pune for his kind financial support from IUCAA and his valuable advice to make the event a successful one. At this moment, I would like to extend my sincere thanks to all members of the NOC for their consent to be a part of the event as well as for other academic helps in this connection. In passing, I would also like to thank Science and Engineering Research Broad (SERB), Government of India; Board of Research in Nuclear Sciences (BRNS), Government of India; and Indian National Science Academy, New Delhi for their financial supports to us.

The most cheerful beginning of the event was that Professor J. V. Narlikar had graced the event as the Keynote Speaker at the cost of his invaluable time. I am deeply grateful to him for the same. In the same sense, I am grateful to all other invited delegates who had agreed to help us at different capacities in the event in expense of their indispensable moments. I am equally grateful to all other participants, for their contributions and their keen interests in the conference.

It is also my duty to gratefully acknowledge the helps and supports of the Register of our University, Professor M. K. Dutta; all my colleagues from our Department; a large pool of our student volunteers, especially Rakteem Borthakur, Mriganka Boruah and Pranjal Rajkhowa; members of the Finance and Administrative Divisions of our University; staffs members of our University Guest House and all other persons whose names I could not mention here, in making the event a very successful one. Thank you all again.

June, 2016 — Umananda Dev Goswami
Dibrugarh, India

Contributors

B. S. Acharya, Department of High Energy Physics, Tata Institute of fundamental Research, Homi Bhabha Road, Mumbai-400005, India

Debika Banerjee, Department of Physics, National Institute of Technology, Durgapur-713209, West Bengal, India

Narayan Banerjee, Indian Institute of Science Education and Research, Kolkata; Mohanpur campus, West Bengal-741246, India

D. K. Banik, Department of Physics, Dibrugarh University, Dibrugarh-786004, Assam, India

S. K. Banik, Department of Physics, Dibrugarh University, Dibrugarh-786004, Assam, India

Arunava Bhadra, High Energy and Cosmic Ray Research Centre, University of North Bengal, Siliguri-734013, India

Himali Bhatt, Astrophysical Sciences Division, Bhabha Atomic Research Centre, Mumbai-400085, Maharashtra, India

N. Bhatt, Astrophysical Sciences Division, Bhabha Atomic Research Centre, Mumbai-400085, Maharashtra, India

Palak Bhatt, Department of Physics, Sardar Patel University, Vallabh Vidyanagar, Gujarat-388120, India

S. Bhattacharyya, Astrophysical Sciences Division, Bhabha Atomic Research Centre, Mumbai-400085, Maharashtra, India

K. Bhuyan, Department of Physics, Dibrugarh University, Dibrugarh-786004, Assam, India

D. Bisht, Department of Physics, DSB Campus, Kumaun University, Nainital-263002, Uttarakhand, India

Anindya Biswas, Department of Physics, Ranaghat College, Ranaghat, West Bengal-741201, India

Debasish Borah, Department of Physics, Indian Institute of Technology, Guwahati-781039, Assam, India

Neelakshi Niti Kachari Borah, Department of Physics, Gauhati University, Guwahati-781014, Assam, India

Ashit Kumar Chakraborty, Society for Cosmological Research, Kolkata-700026, West Bengal, India

Tanmoy Chakraborty, Formerly Department of Mechanical Engineering, NITK Surathkal, Mangaluru-575025, Karnataka, India

H. C. Chandola, Centre of Advanced Study, Department of Physics, D.S.B. Campus, Kumaun University, Nainital-263001, India

Varsha Chitnis, Department of High Energy Physics, Tata Institute of Fundamental Research, Homi Bhabha Road, Mumbai-400005, India

D. K. Choudhury, Department of Physics, Gauhati University, Guwahati-781014, Assam, India; Physics Academy of North-East, Guwahati-781014, Assam, India

G. S. Das, Department of Physics, Dibrugarh University, Dibrugarh-786004, Assam, India

Tapashi Das, Department of Physics, Gauhati University, Guwahati-781014, Assam, India

Chandan Duarah, Department of Physics, Dibrugarh University, Dibrugarh-786004, Assam, India

Anuj Kumar Dubey, Department of Physics, Assam University, Silchar-788011, Assam, India

A. K. Durgapal, Department of Physics, DSB Campus, Kumaun University, Nainital-263002, Uttarakhand, India

K. Dutta, Department of Physics, Gauhati University, Guwahati-781014, Assam, India

Sunandan Gangopadhyay, Department of Physics, West Bengal State University, Barasat, North 24 Paraganas, West Bengal, India

Shubrangshu Ghosh, Centre for Astroparticle Physics and Space Science, Bose Institute, Block EN , Sector V, Salt Lake-700091, Kolkata, India

Deepanjali Goswami, Department of Physics, Indian Institute of Technology, Guwahati-781039, Assam, India

U. D. Goswami, Department of Physics, Dibrugarh University, Dibrugarh-786004, Assam, India

P. Hazarika, Department of Physics, Dibrugarh University, Dibrugarh-786004, Assam, India

Ng. Ibohal, Department of Mathematics, Manipur University, Imphal - 795003, Manipur, India

Ngangbam Ishwarchandra, Department of Physics, Manipur University, Imphal - 795003, Manipur, India

Reju Sam John, Department of Physics, Pondicherry Engineering College and Visiting Scholar, IUCAA, Pune

K. Kalita, Department of Physics, Gauhati University, Guwahati-781014, Assam, India

Harish Kumar, Department of Physics, Pondicherry Engineering College, Pondicherry

Priyanka Kumar, Department of Physics, Cotton College, Guwahati-781001, Assam, India

Jugal Lahkar, Department of Physics, Gauhati University, Guwahati-781014, Assam, India

Shiyuan Li, School of Physics, Shandong University, Jinan-250100, China

Luxmi Machahari, Department of Physics, Gauhati University, Guwahati-781014, Assam, India

H. Nandan, Department of Physics, Gurukula Kangri Vishwavidayalaya, Haridwar-249404, Uttarakhand, India

Jayant V. Narlikar, Inter-University Centre for Astronomy and Astrophysics Ganeshkhind, Pune-411007, India

Pranavi Pachipula, Formerly Department of ECE, Sri Venkateswara College of Engineering for Women, JNTUA, Tirupati-517507, Andhra Pradesh, India

Smruti Patel, Department of Physics, Sardar Patel University, Vallabh Vidyanagar, Gujarat-388120, India

Mahadev Patgiri, Department of Physics, Cotton College, Guwahati-781001, Assam, India

S. D. Pathak, School of Physics, Shandong University, Jinan-250100, China

Surajit Paul, Department of Physics, University of Pune and Associate faculty IUCAA, Pune

Poulose Poulose, Department of Physics, Indian Institute of Technology, Guwahati-781039, Assam, India

Garima Punetha, Centre of Advanced Study, Department of Physics, D.S.B. Campus, Kumaun University, Nainital-263001, India

K. D. Purohit, Department of Physics, Hemwati Nandan Bahuguna Garhwal University, Srinagar Garhwal, Uttarakhand-246174, India

Debobrata Rajak, Department of Physics, Indian Institute of Technology Hyderabad, Yeddumailaram-502205, Telangana, India

Anirban Saha, Department of Physics, West Bengal State University,Barasat, North 24 Paraganas, West Bengal, India

P. K. Sahariah, Department of Physics, Cotton College, Guwahati-781001, Assam, India

Sukadev Sahoo, Department of Physics, National Institute of Technology, Durgapur-713209, West Bengal, India

Baishali Saikia, Department of Physics, Gauhati University, Guwahati-781014, Assam, India

S. Somorendro Singh, Department of Physics & Astronomy, University of Delhi, Delhi-110007, India

Tamal Sarkar, University Science Instrumentation Centre, University of North Bengal, Siliguri-734013, India

A. K. Sen, Department of Physics, Assam University, Silchar-788011, Assam, India

Rajibul Shaikh, Centre for Theoretical Studies, Indian Institute of Technology Kharagpur, Kharagpur-721302, West Bengal, India

Ashok K. Singal, Astronomy and Astrophysics Division, Physical Research Laboratory, Navrangpura, Ahmedabad-380 009, Gujarat, India

B. B. Singh, Department of High Energy Physics, Tata Institute of fundamental Research, Homi Bhabha Road, Mumbai-400005, India

K. K. Singh, Astrophysical Sciences Division, Bhabha Atomic Research Centre, Mumbai-400085, Maharashtra, India

K. P. Singh, Department of Astronomy & Astrophysics, Tata Institute of Fundamental Research, Homi Bhabha Road, Mumbai-400005, India

K. Sashikanta Singh, Department of Physics, Gauhati University, Guwahati-781014, Assam, India

N. Nimai Singh, Department of Physics, Manipur University, Canchipur, Imphal-795003, Manipur, India

A. K. Tickoo, Astrophysical Sciences Division, Bhabha Atomic Research Centre, Mumbai-400085, Maharashtra, India

Rashmi Uniyal, Department of Physics, Gurukula Kangri Vishwavidayalaya, Haridwar-249404, Uttarakhand, India

M. M. Verma, Department of Physics, University of Lucknow, Lucknow-226007, Uttar Pradesh, India

P. C. Vinodkumar, Department of Physics, Sardar Patel University, Vallabh Vidyanagar, Gujarat-388120, India

B. K. Yadav, Department of Physics, University of Lucknow, Lucknow-226007, Uttar Pradesh, India

R. K. S. Yadav, Aryabhatta Research Institute of Observational Sciences, Manora peak, Nainital-263002, Uttarakhand, India

Contents

Part I
Invited Talks

Some conceptual problems in cosmology

Jayant V. Narlikar

Inter-University Centre for Astronomy and Astrophysics Ganeshkhind, Pune-411007, India

jvn@iucaa.ernet.in

1. Introduction

Today the standard model for cosmology is one in which the universe was born with an enormous explosion in a state of high energy, in which it had infinite density and temperature. In fact no physically meaningful description is available for that initial state. Nevertheless most cosmologists like to work on the very early universe with huge extrapolations of physics known and verified today and of the astronomical data observed today. Not surprisingly such an approach leads to serious conceptual difficulties.

In this opening lecture I will highlight some of these issues. Given the limited time for this talk I will confine myself to two basic problems: dark matter and dark energy.

2. Dark matter

What is the meaning of 'dark' or 'unseen' matter? In the old days there was the adage: "Seeing in believing". This implied that only the evidence that you can see with your eyes can be trusted. The science of astronomy evolved through the process of 'observing' with naked eye, and later with telescope. Even when Galileo used his new invention, the telescope for the first time, several viewers were uncomfortable with the findings made with its help, as they showed many more aspects of the universe, than were visible to the naked eye. Thus doubts were expressed about the reality of craters on the Moon, the spots on the Sun, and Jupiters satellites when seen by Galileo's telescope.

Galileo's telescope, and others that followed his pioneering instruments monopolized viewing to the form of light that our eyes are sensitive to. By the end of the nineteenth century, physicists were aware that light can come in other forms too with wavelengths vastly different from those which give the visible light. Twentieth century gradually brought those other forms of light to the service of astronomy and 'seeing' now means using any of the different forms of light for observing.

It is against this background that we now describe the difficulty associated with dark or unseen matter. It means the matter that cannot be seen but whose existence can nevertheless be inferred by indirect observations. The historical example of the discovery of planet Neptune, shows that the existence of the planet was inferred by noticing its perturbing effect on the motion of planet Uranus. Thus the existence of the new planet *could be deduced* even before it was seen in the conventional way. And the interaction that played a crucial role in the episode was the gravitational interaction. In modern times, gravitational interaction plays a similar role in revealing the existence of matter that could not otherwise be seen by using any form of light. It is this type of matter that is labelled *dark matter*. How does it get detected?

An analogy from the field of economics is worth recalling in this context. Think of a country which has two economic systems in force. The first is the official (visible) one based on declared incomes and expenses; one which is on the records of the Internal Revenue Department. The second, parallel economy is run by the so-called black money, based on incomes and expenditures not reported to the taxman.

Now, even though the black money is not declared or recorded, experts can make a shrewd estimate of its extent. This is estimated by its visible impact on the country's economy. The construction activity, election campaign expenses, massive entertainment events, etc. are the dynamical effects of black money. Thus the economic activity generated by it gives the clue to the amount of black money in circulation.

Dark matter in astronomy is like black money in economics. Although not directly observed, its gravitational influence on the visible matter in its neighbourhood can give astronomers good estimates of its total amount. Perhaps the most dramatic example of this type is the *black hole*. A black hole is a highly compact object whose gravitational pull is so strong that not even light can leave its surface. A very massive star may shrink under its own gravity and become a black hole when its surface gravity has grown powerful enough to pull back its own radiation. A black hole can therefore never be seen. Yet its gravitational influence will help to reveal its presence in space. For example consider a star having a planet going round it. If the star shrinks and shrinks and becomes a black hole, it will be invisible. Yet the planet will continue to feel its gravitational attraction and will keep orbiting round it. So if we see a planet going round and round but no star that is visibly controlling its movement, then we conclude that the planet is going round a black hole. By observing details of the planetary motion, theoreticians can tell where the black hole is located and what is its mass.

2.1 Evidence for dark matter

We will now come to cosmological evidence for dark matter, mainly from two different types of systems: spiral galaxies and clusters of galaxies.

2.1.1 *Rotations of spiral galaxies*

Our Milky Way belongs to the class of *spiral* galaxies. As the name implies, a spiral galaxy has two or more arms winding outwards like the spring of a classical wind-up clock. The arms are the regions where stars are concentrated. The gaps between arms are relatively less populated with stars, although they may carry gas and dust. The typical picture of a spiral galaxy also indicates that there is no sharp boundary to the galaxy...it sort of merges into darkness as one goes farther and farther from the more populated central region.

Astronomers believed (and justifiably so!) that the darkness engulfing the galaxy in the outward parts is indicative of its gradual but definitive approach towards a boundary. Thus they assumed that beyond some specified perimeter, there is no mass belonging to the galaxy. Certainly there are no shining stars, nor are there any indications of gas or absorbing dust either beyond the assumed boundary. With the advent of radio astronomy, however, astronomers discovered that there are small or large clouds of neutral hydrogen gas in circulation round the typical spiral galaxy. These clouds are located far and near, extending well beyond the assumed boundary of the galaxy.

In the 1960s and 70s radio astronomers were able to measure speeds of such clouds and relate them to the galaxy around which they might be moving. We may use here the analogy of the planets moving round the Sun in our own planetary system. We know from measurements of speeds of these planets that *the farther they are from the Sun the slower they orbit*. For example, Mercury, the nearest planet, has an orbiting speed around 48 kilometres per second, whereas for the most distant planet Pluto (now designated as a dwarf planet) the speed is less than a mere 5 kilometres per second. Theoretically this result can be understood with the help of Newtons laws of motion and gravitation. Applying the same laws, astronomers expected the clouds farther and farther away from the galaxy to have smaller and smaller rotational speeds.

They were in for a surprise. The speeds did not seem to be dropping off; rather they stayed constant over a very long range. The figure 1 below shows results for a typical spiral galaxy. As the rotation curve showed a constant speed over a long distance, it came to be known as 'flat rotation curve'.

To resolve this mysterious behaviour, let us go back to the solar system example. There the speed drops off because we know that the planets are moving under the attraction of the Sun and this attraction drops off as one moves away from the centre of attraction. There is a definitive formula which tells us how the rotational speed of a planet should drop off with distance from the Sun. The speeds of all planets from Mercury to Pluto check out OK on this formula. Indeed this was the classic discovery of Johannes Kepler in the early seventeenth century for which Newtons law of gravitation provided the mathematical explanation. But the same law applied to the neutral hydrogen clouds attracted by the galaxy, does not seem to be working. Why not? Even the more sophisticated Einsteins theory of gravity fares no better.

2.1.2 *The need for dark matter*

Whenever there is a conflict between a well established law and observations, two possible courses of action suggest themselves:

1. Re-examining the observations in case something crucial is missed out...

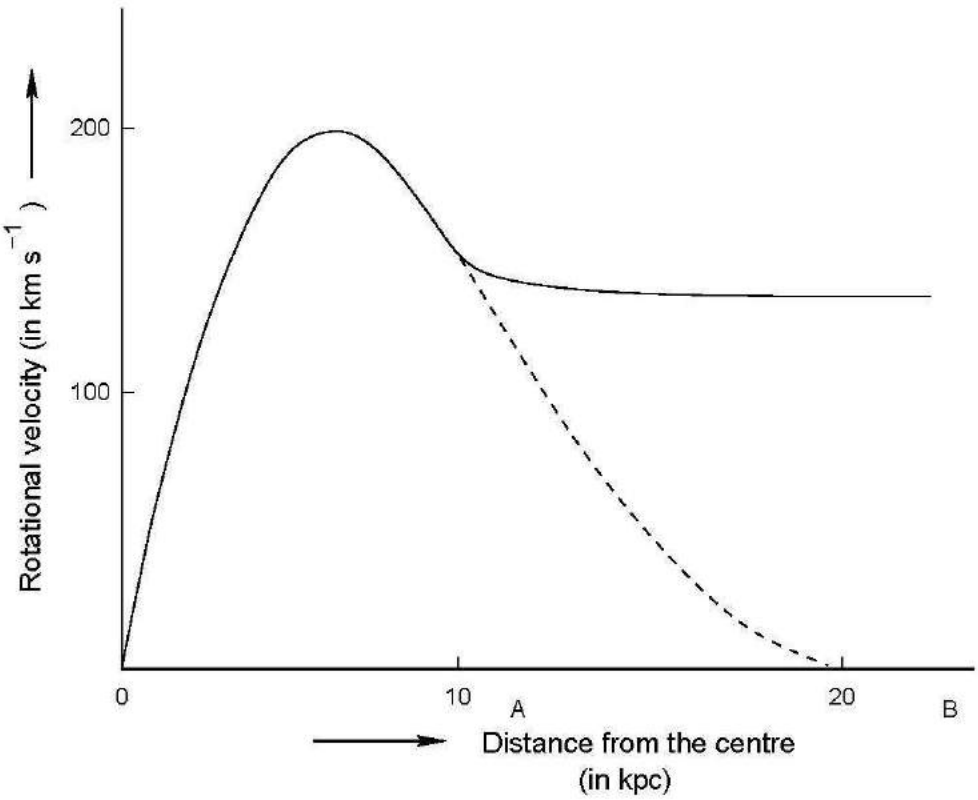

Figure 1. Flat rotation curve of a typical spiral galaxy.

2. Change the law for something deeper and more subtle.

What the majority of physicists and astrophysicists would like to follow is the first alternative. This involves admitting that our observations of galaxies are incomplete and that there is invisible matter present which extends *well beyond* the visible part of the galaxy. In terms of distances, we can argue for our own Milky Way like this. The visible matter made of stars, dust and gas may extend over a disc of radius 15 kiloparsecs. However, the dark matter is expected to be present well beyond this radius. It is because of this extra matter that the gravitational influence of the galaxy extends much farther, and so the rotation speeds of neutral hydrogen clouds extend without attenuation out to distances of 50 kiloparsecs or beyond.

What would the dark matter be made of ? Black holes? Since these are very efficient in holding back light, this alternative suggests itself. We could have black holes formed from remnants of massive stars that stopped shining after their nuclear fuel stocks were spent up. A second possibility could be planet-like objects that are not self-luminous. Any object with mass not exceeding around the tenth of a solar mass cannot shine on its own because its core temperature is not high enough to ignite a nuclear reactor. Such objects are called *Brown Dwarfs* and these would not be seen by normal telescopes. These are examples of 'conventional' types of dark matter. Given the hypothesis that dark matter exists, these are the options one may think of in the first instance. Indeed, till early 1980s these were the main options before the cosmologists.

However, today cosmologists favour other more esoteric options, which are lumped together under a class called *Non-Baryonic Dark Matter* (NBDM). These options are, by definition, made of particles that do not form parts of atomic nuclei. Atomic nuclei contain neutrons and protons which are called baryons and almost all matter we see in the universe consists of these as well as light particles like electrons and neutrinos. Thus masses of black holes or brown dwarfs are mainly made up of baryons. As yet there have been no particles so far discovered by high energy physicists that could be classified as NBDM. In the 1980s the possibility that neutrinos may have a fair amount of mass (corresponding to an energy of up to about 30 electron volt) had raised the option that dark matter may be accounted for by neutrinos. However, those options have now fallen by the wayside. Although neutrinos may have mass, it would still be far too small to explain the dark matter in galaxies. We will return to this issue of what the dark matter is made of later, after we have described the second line of evidence for dark matter on an even grander scale.

2.1.3 *Clusters of galaxies*

In Figure 2, we show a photograph of a typical cluster of galaxies. A typical cluster contains several hundred galaxies and they all apparently move randomly within the cluster. These random motions are of the order of 250-500 kilometres per second. *These motions are over and above those arising from the expansion of the universe*. Thus a typical cluster takes part in the overall expansion process, and additionally has galaxies moving within it at random speeds.

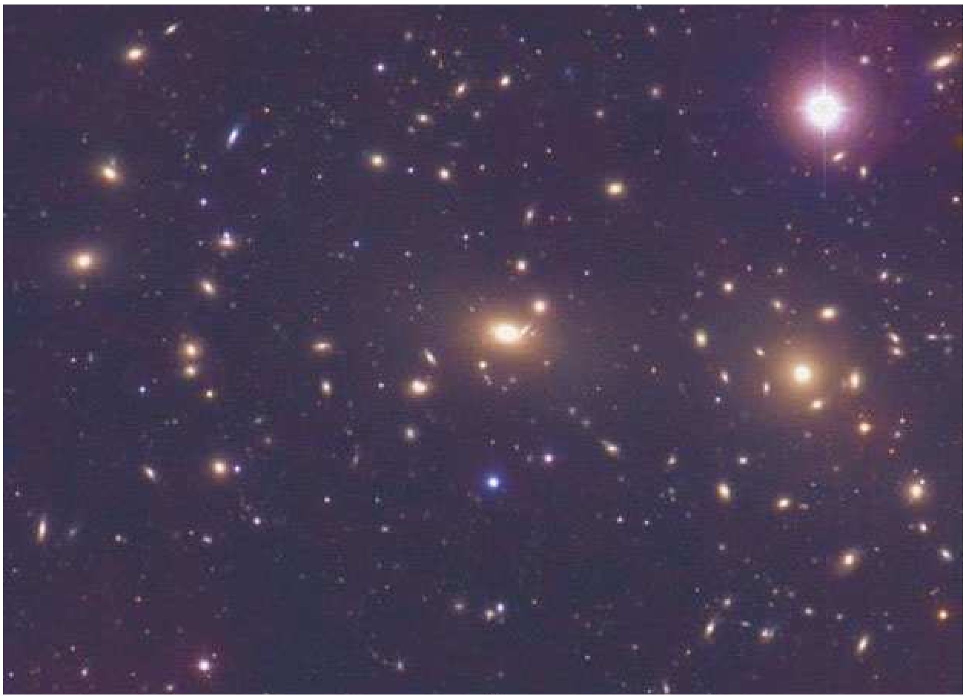

Figure 2. A typical cluster of galaxies.

If we assume a cluster is an isolated dynamical system of many bodies which have been moving under one-anothers gravitational attraction for a long enough time to settle down to some steady state, then we can deduce a simple result from Newtons laws of motion and gravitation. It is that the energy of motion, the so-called kinetic energy of all moving galaxies is comparable in magnitude to their total gravitational potential energy. This is known as the *virial theorem*. So if we estimate the two energies for clusters, we can verify if the virial theorem does apply to them.

For most clusters it does not. The energy residing in motion of the visible galaxy is much higher than the energy residing in gravitational attraction. The discrepancy is large enough to make one think. One possible conclusion can be that the clusters have not yet had time to settle down and so the virial theorem does not apply to them. This could happen if the cluster is expanding or contracting all round. The Armenian astrophysicist Viktor Ambartsumian had concluded back in the early 1960s that the clusters are expanding, having been created in an explosion. Based on his assessment of the data, Ambartsumian concluded that the clusters are examples of explosive creation of matter.

The majority view, however, is different. The view is that the clusters have indeed settled down to an equilibrium state and the reason we have a deficiency of gravitational energy is because we are not able to see all the matter present in the cluster. Suppose there is a lot of dark matter within the cluster which is not moving fast. Such matter will not contribute much kinetic energy, but would give rise to large gravitational energy by virtue of its mass. This is why we notice a deficiency of gravitational energy.

This argument has therefore suggested to the theoreticians that they can add as much dark mass as they need to make up the energy deficiency. The amount of dark matter to be added this way far exceeds the visible matter. Whereas in the case of rotation curves of spiral galaxies the ratio of dark to visible matter may be around 3 to 1 or so, in the case of the clusters the ratio may go up to 10:1 or even more.

2.1.4 *What is dark matter made of?*

So, now we come back to the question posed earlier...what is such dark matter made of? Even though it is not seen, we can argue for the options like black holes or brown dwarfs. However, there are problems with these options. First one has to argue for a physical scenario that led to so much of matter being in this form. This may or may not be a very difficult problem...with sufficient ingenuity, the theoretician may come up with a plausible scenario. But cosmologists who adhere to the big bang model, object to this possibility.

The big bang theorists would be worried if so much dark matter existed in these relatively normal forms. For these forms are all made of baryonic dark matter (BDM). If there were so much of BDM around, a difficulty arises with the big bang scenario of how light nuclei, especially deuterium were made. In the process of primordial nucleosynthesis first proposed by George Gamow, and later worked on by several other astrophysicists, one crucial conclusion was that if the density of baryons exceeded a critical limit, *practically no primordial deuterium would be made*. And it also became clear that if we begin to allow all or most of dark matter in clusters and galaxies to be baryonic, that critical limit would certainly be exceeded. Thus no deuterium would be formed.

In fact, a difficulty of even greater magnitude awaited the big bang theorist when he resorted to the inflationary scenario. It is believed that the phase transition leading to a break down of symmetry at the time of the end of epoch of grand unification, the universe had an inflationary phase. The outcome was that the universe had a flat geometry with a density

$$\rho = 3H^2/8\pi G$$

which far exceeded the deuterium limit. Thus, if the inflation did happen, it would leave the universe with a density very close to the critical density. If all this matter were normal baryonic matter, its density would be 25-30 times higher than the limit tolerated by deuterium synthesis process. We shall use the density parameter Ω to denote the ratio of the actual density to the flat density mentioned above.

So the conventional big bang theory runs into a serious problem. If it allows inflation, it runs foul of deuterium production in the primordial nucleosynthesis. It also ends up with far more dark matter than the evidence from galaxies and clusters suggests. This latter difficulty can be resolved by supposing that there exists dark matter not only inside clusters but also in the space between them. However, the first problem was more serious. To find a way out therefore, big bang cosmologists have supposed that the bulk of dark matter in or out of the clusters is *non-baryonic*. The non-baryonic dark matter (NBDM) is an esoteric option which has to be adopted because there is *no other alternative for survival of the big bang nucleosynthesis scenario*. An alternative name given to such a NBDM particle is ”weakly interacting massive particle” or a WIMP!

Why do we call NBDM esoteric? Because there has, as yet, been no laboratory demonstration of it. Nor has it been detected in any astronomical scenario. Rather, the theoretical possibilities for such matter come from the as yet untested theories of very high energy particles. Man made accelerators do not reach these kinds of energies. So what we are effectively asked to accept is that bulk of the matter in the universe is of this strange kind, far exceeding the normal kind of matter that astronomers are familiar with.

3. Dark energy

We recall that in the early stages of cosmology, Einstein had introduced the cosmological force of repulsion in his equations, to obtain the mathematical model of a static universe. Later when he discovered that observations favoured an expanding universe and that his original equations did yield expanding models, he more or less abandoned this extra force.

Cosmologists have since had a love-hate relationship with the cosmological force. Whenever they feel that their models are threatened by new observations they invoke the force, perhaps with reluctance, only to abandon it if later it is discovered that the observations were not threatening after all. The intensity of this force is typified by a constant often denoted by λ or Λ. Thus the force of repulsion between two masses separated by distance r is simply λr. The constant in todays universe is very small and this indicates that the force of repulsion implied by it is very small on the terrestrial, stellar or galactic scale. However, on the scale of the universe as a whole, it is significant. A positive λ means the force is of repulsion and on a large scale it makes the universe accelerate. Is the universe really accelerating?

Extensive work on this question was done by Allan Sandage in the 1960s and 1970s, and the results of his studies of distant galaxies indicated that the universe is *decelerating*, that is, its rate of expansion is slowing down. At the time, the Friedmann models without the λ-term indicated the same conclusion and so were in favour. The only model that stood apart was the steady state model that implied that the universe is accelerating. Later this test fell into disuse as it was realized that there were several imponderables, including observational errors that made any definitive conclusion impossible. Indeed, summarizing the overall cosmological data in the 1986 Symposium on cosmology at Beijing, Malcolm Longair concluded that the data did not require a nonzero cosmological constant.

However, the test was revived in the 1990s when it became possible to make dedicated studies of exploding stars, called *supernovae* lying in distant galaxies. A particular class of supernovae, called Type Ia supernovae seemed to have the property that they provided a standard candle for measuring galactic distances. Let us first try to understand what this statement means.

The Type Ia supernova typically, represents a highly compact star blowing up as it loses its internal equilibrium. The intensity of the star shoots up after the explosion and it reaches a peak in luminosity within a few days.

The important thing to note is that the supernova becomes very bright and may outshine the entire galaxy in which it is housed, but for a few days. The peak luminosity therefore makes it easy to spot a supernova even if it is located in a very distant galaxy. And, it seems that the maximum brightness attained by the star is more or less the same from one Type Ia supernova to another. So we can use the method of measuring distances of astronomical objects to estimate the distances of galaxies in which the supernovae are located. The fainter the supernova the further away it is, as per the rule that farther candles look dimmer. The fact that the peak intensity for all Type Ia supernovae is the same is called the 'standard candle hypothesis'.

A 'Supernova Cosmology Watch' programme was set up to observe and record any such sudden eruptions in galaxies with redshifts ranging up to around 1-1.5. These redshifts are higher than those of galaxies used by Sandage in his earlier studies...those went up to around 0.5. Thus we are in principle able to sample a more remote part of the universe with the help of supernovae.

The method is then to look at supernovae at different distances and see how their redshifts change with distance. Redshifts are obtained by studying the spectra of galaxies, while distances are estimated by using the standard candle of Type Ia supernovae. Broadly we expect that if the universe is decelerating the distances will increase with redshift more slowly than if the universe were accelerating.

If the observers hoped to find a confirmation of the earlier results that the universe is decelerating, they were in for disappointment. The distances as estimated from supernova standard candle seemed to increase faster with redshift than allowed by any decelerating model. Rather the indications were that *the universe seems to be accelerating!*

At this stage it would have been fair on the part of observers to have acknowledged that the conclusion in favour of an accelerating universe had been predicted by the much-maligned steady state universe. Even though in the 1990s, the steady state universe was no longer in serious contention, a note of this historical fact should have been made. However, the result was simply announced as favouring the standard big bang model with a non-zero cosmological constant.

That this was a volt-face on the part of the big bang establishment can be seen from the fact that as late as 1997, the general belief was that there is no cosmological constant and that the universe is decelerating. While changing the model so significantly from what had been previously in vogue, it should have been admitted that such a change was being forced on the theory by observations. That the present approach has no predictive value is seen from the circumstance that todays observers ask the following question: *What value of the cosmological constant will give a good fit to what is observed?*

Like good salesmen for inflationary hypothesis, the cosmologists announced this finding as confirming the inflationary paradigm by arguing that the results bore support for the conclusion that the universe is flat, i.e., with $\Omega = 1$. What was not emphasized was the result that the data gave the best fit for the value $\Omega = 1.3$.

According to current wisdom, the density parameter Ω these days is made up of three components: (1) visible (baryonic) matter, (2) cold dark matter (CDM) and (3) dark energy. Of these we have already elaborated upon the first two. The third component is related to Λ the magnitude of the cosmological constant. After studying the supernova results and also the fluctuations of the microwave background, cosmologists have come to the conclusion that the contribution to Ω from these three components can be quantified quite precisely as follows: (1) The contribution of baryonic matter is 4%, (2) the contribution of NBDM is 23% and (3) the contribution of dark energy is 73%.

If these precise values are to be believed, then cosmologists are telling us that the most familiar form of matter and energy that astronomers see, occupies only 4% of all matter-energy in the universe. The remaining 96% is made of the esoteric dark matter while the lions share is taken up by dark energy, which is still more esoteric. The ironical aspect of these conclusions is that the major components in the above distribution have not been found so far.

This situation will remind those who have read Hans Andersen stories, of the emperor who was offered new clothes that only non-sinners could see! For those who have not read the story *The emperor's new clothes* here is a synopsis of the same.

4. The emperor's new clothes

An emperor was fond of trying new dresses and spent a fortune on various fashion designs. One day a couple of dressmakers from a far away land came to his court promising clothes made of such fine variety that only the virtuous and the righteous could see them: those who lived a sinful life would not be able to see them. The emperor was pleased by this offer and accorded them liberal funds and facilities to make a royal dress. Taking considerable time over the process the tailors returned carrying their handiwork.

The king sent an emissary, a minister, to examine the dress. When the packet was opened, the minister could see nothing in it. However, recalling the makers' admonition that only the righteous and virtuous could see them he felt that if he admitted to seeing nothing, he would be branded a sinner and dismissed from his job. So he reported to the Emperor praising the dress in glowing terms. Thus the Emperor was all eager to try on the new clothes himself and parade in them through the main street of his capital.

When he came to try them on, the Emperor too could see no dress; but as the tailors went through elaborate motions of placing it on his body, commenting on how well it looked on His Majesty, he too felt that admitting seeing nothing, would lead to his forsaking his kingdom as not being virtuous and righteous. So he got ready to join the procession followed by his courtiers who were all praise for the new suit, since none wanted to be fired from his job.

As the procession went through the town people gathered on the street to applaud. Although they saw their emperor naked, they too dared not say so for fear of being branded sinners. Finally, it was left to a simple child, who had no personal stake in the matter to come out with the fact when he asked his mother: "Why is the Emperor not wearing anything?" That was when everybody realized that the emperor and his court had been taken for a ride!

Modern cosmology, has brought us to a similar situation when we ask: just how much matter and energy are present in our universe? And, how much of it we can see and how much we *cannot see*?

5. Concluding remarks

To end this account, we summarize it as follows. It is clear that the important observations of flat rotation curves of galaxies opened up the pandoras box of dark matter. The evidence for dark matter is certainly there if one continues to have faith in the laws of Newton and Einstein. However, how much dark matter is really warranted? If one is not prejudiced by belief in inflation then one need not have $\Omega = 1$. One can manage with much less matter.

Can it all be baryonic as our experience of the rest of astronomy would have us believe? If you are not committed to the notion of primordial nucleosynthesis, then the answer is ”yes”. But if one is firmly wedded to the view that inflation did take place and that light nuclei were made in a primordial nucleosynthetic process, then one is driven to postulating that a lot of dark matter is esoteric, non-baryonic.

Coming to dark energy, the major argument in favour of it rests on inflation and the observations of distant supernovae. But there too the chain of reasoning may have glitches. Are we sure that the standard candle hypothesis is valid? If there is significant variation in the peak intensity of light from Type Ia supernovae, then the distance measurement on which the test rests is not so reliable. When we infer the distance of a supernova from its observed faintness, we ignore the presence of any absorbing intergalactic dust. Our knowledge of intergalactic medium is still very primitive, and by ignoring intergalactic dust in estimating distances, we may be committing the same error that galactic astronomers committed more than a century ago when they were estimating stellar distances without knowledge of interstellar dust. Intergalactic dust will make a supernova look dimmer than in the absence of dust and so if we ignore the effect of dust absorption, we will be overestimating the distance of a supernova and this error will grow further away the supernova is. So instead of the cosmological constant causing an accelerated universe in which all distances get enhanced, it may be the absorption by dust that makes high redshift supernovae look dimmer.

Even if we discount the dust alternative and stick with the accelerating universe, we find that data do not really fit the simple model in which a constant Λ accelerates the universe. One needs a variable Λ thus making the hypothesis messier. For, more recent evidence apparently points to acceleration over a limited period. Thus theoreticians are getting lost in more and more complex models of dark energy, which have no predictive power.

Perhaps we should leave the last say with the Pythagoreans, the learned followers of the Greek mathematician philosopher Pythagoras more than two millennia ago who hypothesized that the Earth goes round *not the Sun*, but round a ’Central Fire’. When quizzed about why we don’t see the central fire, they further hypothesized that another body, which they called *Counter Earth* lies between the central fire and us, So the skeptics began to ask: Why don’t we see the Counter Earth? To this query their answer was that Greece was on the other side with respect to the Counter Earth and so we cannot see it. However, this defence also collapsed as people could ’go to the other side’ and see that there was no central fire and no counter earth.

Cosmology may eventually acquire its own unprejudiced interpreters of the universe.

Restoration of unitarity in anisotropic quantum cosmology

Narayan Banerjee

Indian Institute of Science Education and Research, Kolkata; Mohanpur campus, West Bengal-741246, India

narayan@iiserkol.ac.in

It is generally believed that the solution of Wheeler-DeWitt equation for any anisotropic cosmological model is non-unitary and hence does not conserve probability. This remains a pathology in standard quantum cosmology. We show that this behaviour is not actually pathological and can be removed by a proper ordering of operators.

1. Inroduction

As gravity does not have any universally accepted quantum theory, cosmology provides an arena where quantum principles are applied to a gravitational system. When the universe was small, smaller than Planck length, classical gravity would not work and a quantum picture is indeed required. This also provides a possibility that a quantum picture might resolve the initial singularity. The relevant action for gravity is given as

$$\mathcal{A} = \int_M d^4x\sqrt{-g}\,R + 2\int_{\partial M} d^3x\sqrt{h}\,h_{ab}\,K^{ab} + \int_M d^4x\sqrt{-g}\,L_m, \tag{1}$$

where h_{ab} is the induced metric over spatial hypersurface, ∂M is the boundary of the four dimensional manifold M, K^{ab} is the extrinsic curvature and L_m represents the matter Lagrangian. The units are so chosen that $c = 16\pi G = \hbar = 1$.

In order to have a tractable problem, one often works in a minisuperspace, where a particular metric from amongst all possible metrics is chosen using symmetry and thus the degrees of freedom is reduced to a finite number. Einstein-Hilbert action is written in terms of the metric, and the metric for the space-section, h_{ij} and the matter degrees of freedom are the relevant variables. Then the procedure is standard, the conjugate momenta are defined, the Hamiltonian is formed, the coordinates and momenta are promoted to operators, using canonical quantization, and the Schrodinger equation, in this case known as the Wheeler-DeWitt equation, is written with the relevant constraint. Replace the momenta by the corresponding operators, e.g., if Π_{ij} is the momentum conjugate to the dynamical variable h_{ij}, then

$$[h_{ij}, \Pi^{ij}] = \imath.$$

Hamiltonian constraint in this case is given by $\rightarrow H = 0$. Wheeler-DeWitt equation can now be written as

$$H\Psi = 0.$$

1.1 Problems with quantum cosmology

There are many problems in quantum cosmology, such as *problem of interpretation*, *problem of the identification of a time parameter*, and many others. One of these many others is that the anisotropic models are believed to be nonunitary! This leads to a non-conservation of probability. The observed universe, however, is isotropic, so this problem might have been ignored. But, this isotropy is not a theoretical requirement. So this nonunitary leads to an inconsistency in the quantization scheme. The motivation of the present talk is to show that the alleged nonunitary can actually be removed.

It is interesting to note that in the absence of a properly oriented scalar time parameter, this nonconservation of probability is often obscure. The cosmic time t does not serve the purpose, as it is a coordinate and not a scalar parameter. So we start with a choice of a time parameter.

If we work with a model with a fluid, the evolution of a fluid in the model comes to the rescue. The action with a fluid can be written as

$$\mathcal{A} = \int_M d^4x\sqrt{-g}\,R + 2\int_{\partial M} d^3x\sqrt{h}\,h_{ab}\,K^{ab} + \int_M d^4x\sqrt{-g}\;P, \tag{2}$$

where P is the pressure due to the perfect fluid. We now take a break and consider the fluid. The velocity vector of a perfect fluid can be written in terms of thermodynamic quantities as [1, 2]

$$u_\nu = \frac{1}{h}(\epsilon_{,\nu} + \theta S_{,\nu}),$$

where h, S, ϵ and θ are the velocity potentials having their own evolution equations. The first two of the quantities are specific enthalpy and the specific entropy respectively while the other two do not have specific physical significance. Two more potentials, connected with vorticity, are dropped as we shall not consider any example of a metric with a vorticity. u^μ is normalized as $u^\nu u_\nu = 1$. Only two are actually used, namely, ϵ and S, as ϵ and h are related by $u^\mu \epsilon_{,\mu} = -h$, while θ can be settled using the normalization of u^μ.

1.2 Problem with anisotropic models

It is quite widely believed that anisotropic models are nonunitary [3]. An explicit example was given by Alvarenga *et al* in the case of a Bianchi I model [4]:

$$ds^2 = n^2dt^2 - \left[e^{(\beta_0+\beta_+ +\sqrt{3}\beta_-)}dx^2 + e^{(\beta_0+\beta_+ -\sqrt{3}\beta_-)}dy^2 + e^{(\beta_0-2\beta_+)}dz^2\right], \tag{3}$$

the Wheeler-DeWitt equation

$$\left(\frac{\partial^2}{\partial\beta_0^2} - \frac{\partial^2}{\partial\beta_+^2} - \frac{\partial^2}{\partial\beta_-^2}\right)\phi = 24E\phi e^{3(1-\alpha)\beta_0}, \tag{4}$$

indeed yields a non-unitary evolution!

The reason for the alleged nonunitary is not really known, but normally the hyperbolicity in the Hamiltonian is held as the culprit. But we shall see that this is not quite right. An improper operator ordering, rather, might hold the key. For Bianchi V, it was shown that with an operator ordering, probability conservation holds good for large "time" [5]. Naturally this is not enough, as nonunitarity is a mathematical property, and a model is either unitary or not, there is hardly any scope for minimizing that! But the hint is obvious, an ordering of operators may do the trick. With this clue, it was shown quite clearly that unitarity can in fact be restored in a Bianchi I model with a clever operator ordering [6]. It was also shown by the same authors that with a suitable transformation of variables at the classical level, the ordering may not at all be required. This takes care of the objection that why the chosen ordering is sacred. More examples were later found in Bianchi V and IX [7] and Kantowski-Sachs models [8].

In the present talk, I shall take up the example of a Bianchi III metric, which, like the Kantowski-Sachs model, has a varying spatial curvature, and is thus more general.

2. Bianchi III cosmology

The Bianchi type III model is given by the metric

$$ds^2 = n^2dt^2 - e^{2\sqrt{3}\beta_+}dr^2 - e^{-2\sqrt{3}(\beta_+ + \beta_-)}\left[d\theta^2 + \sinh^2(\theta)\,d\phi^2\right]. \tag{5}$$

Lapse function n, β_+ and β_- are functions of time t. Bianchi III metric in this form is similar to the Kantowski-Sachs cosmology where the hyperbolic coefficient of $d\phi^2$ is replaced by a sinusoidal function. Given the action, the Hamiltonian for the gravity sector can be written as

$$H_g = \frac{n}{24}e^{\sqrt{3}(\beta_+ + 2\beta_-)}\left[-p_{\beta_-}^2 + p_{\beta_+}^2 + 48e^{-2\sqrt{3}\beta_-}\right], \tag{6}$$

where p_i's are the momenta, canonically conjugate to β_i's. We effect the set of canonical transformations,

$$
\begin{gathered}
T = -p_S \exp(-S) p_\epsilon^{-\alpha-1}, \\
p_T = p_\epsilon^{\alpha+1} \exp(S), \\
\epsilon' = \epsilon + (\alpha+1)\,\tfrac{p_S}{p_\epsilon}, \\
p'_\epsilon = p_\epsilon,
\end{gathered}
$$

and write the Hamiltonian for the fluid sector as

$$
H_f = n e^{\alpha\sqrt{3}(\beta_+ + 2\beta_-)} p_T. \tag{7}
$$

The net (super) Hamiltonian is given by $H = H_g + H_f$. A variation with respect to n yields the Hamiltonian constraint,

$$
e^{\sqrt{3}(1-\alpha)(\beta_+ + 2\beta_-)} \left\{ -p_{\beta_-}^2 + p_{\beta_+}^2 + 48 e^{-2\sqrt{3}\beta_-} \right\} + 24 p_T = 0.
$$

We now promote the dynamical variables to operators, $p_i \mapsto -\imath\hbar\partial_{\beta_i}$ for $i = 0, +, -$, and $p_T \mapsto -\imath\hbar\partial_T$. This mapping is equivalent to postulating the fundamental commutation relations

$$
[\beta_i, p_j] = \imath\hbar\delta_{ij}\mathbf{I}.
$$

With the Hamiltonian constraint $H = 0$, the Wheeler-DeWitt equation becomes

$$
H\psi = 0.
$$

Some points to note here are (i) the Poisson brackets $\{\epsilon', p'_\epsilon\} = 1$ and $\{T, p_T\} = 1$ are satisfied and other Poisson brackets $\rightarrow 0$. This ensure the canonical structure with the new variables. Also note that $\frac{dT}{dt} > 0$, meaning T has the same sign as the cosmic time ! And, is a monotonically increasing function.

2.1 General perfect fluid: $\alpha \neq 1$

In this case we propose following operator ordering

$$
[-e^{\frac{\sqrt{3}}{2}(1-\alpha)(\beta_+ + 4\beta_-)} \frac{\partial}{\partial\beta_+} e^{\frac{\sqrt{3}}{2}(1-\alpha)\beta_+} \frac{\partial}{\partial\beta_+}
$$

$$
+ e^{\sqrt{3}(1-\alpha)(\beta_+ + \beta_-)} \frac{\partial}{\partial\beta_-} e^{\sqrt{3}(1-\alpha)\beta_-} \frac{\partial}{\partial\beta_+}
$$

$$
+ 48 e^{-2\sqrt{3}\beta_-} e^{\sqrt{3}(1-\alpha)(\beta_+ + 2\beta_-)}]\Psi
$$

$$
= 24\imath \frac{\partial\Psi}{\partial T},
$$

and effect a transformation of variables as

$$
\chi_+ \equiv e^{-\frac{\sqrt{3}}{2}(1-\alpha)\beta_+} \;\&\; \chi_- \equiv e^{-\sqrt{3}(1-\alpha)\beta_-}
$$

,

and use separability ansatz $\Psi = \phi(\chi_+, \chi_-) e^{-\imath ET}$ so that

$$
H_g\phi = -\frac{1}{\chi_-^2}\frac{\partial^2\phi}{\partial\chi_+^2} + \frac{1}{\chi_+^2}\frac{\partial^2\phi}{\partial\chi_-^2} + 48\chi_-^{\frac{2\alpha}{1-\alpha}}\chi_+^{-2}\phi = 24E\phi. \tag{8}
$$

Unitarity restored:

Now it is easy to see that one can use Neumann's theorem which states that

"A symmetric operator $\hat{A}$ defined on domain $\mathcal{D}$ has equal deficiency index, if there exists a norm preserving anti-unitary conjugation map $C : \mathcal{D} \to \mathcal{D}$ such that $[\hat{A}, C] = 0$, which, in turn, shows that $\hat{A}$ admits self-adjoint extension".

H_g satisfies the conditions !! (Here C is the map which takes ϕ to ϕ^*). So, the Hamiltonian admits self-adjoint extension i.e., a unitary evolution. The same analysis in fact holds for a Kantowski-Sachs model as well.

Rationale behind the operator ordering:

The kinetic term $\frac{\partial^2\phi}{\partial\chi_\pm^2}$ multiplied with $\chi_\mp^2$. Hence, the condition for H_g being symmetric is same as the condition for a standard Laplacian to be symmetric, and we have the following condition

$$\left[\phi\frac{\partial\phi^*}{\partial\chi_\pm} - \phi^*\frac{\partial\phi}{\partial\chi_\pm}\right]_0^\infty = 0.$$

Once it is guaranteed to be a symmetric operator, the self-adjoint extension is obvious following Neumann's theorem. The particular operator ordering is a sufficient condition for making H_g symmetric, but, however, it is not a necessary one.

2.2 A specific example: Stiff fluid ($P = \rho$)

For a stiff fluid the Wheeler-DeWitt equation with the above operator ordering takes the form

$$\left\{\frac{\partial^2}{\partial\beta_-^2} - \frac{\partial^2}{\partial\beta_+^2} + 48e^{-2\sqrt{3}\beta_-}\right\}\Psi = 24\imath\frac{\partial\Psi}{\partial T}.$$

With a separation of variables, $\Psi = \phi(\beta_-)\psi(\beta_+)e^{-\imath ET}$, this equation gives,

$$\left\{\frac{\partial^2}{\partial\beta_-^2} + 3k_+^2 + 48e^{-2\sqrt{3}\beta_-}\right\}\phi = 24E\phi,$$

$$\left[\frac{\partial^2}{\partial\beta_+^2} + 3k_+^2\right]\psi = 0.$$

With $||\psi|| \equiv \int_{-\infty}^{\infty} d\beta_+\psi\psi^*$, the solution is unitary; the norm for the β_+ sector is time independent and finite (by explicit construction of wavepacket). The equation for the β_- sector can be recast in the standard self-adjoint form (using the variable $\chi \equiv e^{-\sqrt{3}\beta_-}$),

$$\frac{d}{d\chi}\left(\chi\frac{d\phi}{d\chi}\right) + \left(16\chi - \frac{8E - k_+^2}{\chi}\right)\phi = 0,$$

with inner product given by $\langle\phi_1|\phi_2\rangle \equiv \int_0^\infty d\chi\, \chi\, \phi_1^*(\chi)\phi_2(\chi)$. This Hamiltonian for β_- sector is self-adjoint as well, ensuring a unitary time evolution.

We have now sufficiently proved that the alleged onounitarity is actually an unwarranted threat in the standard Wheeler-DeWitt quantization scheme of cosmological models. Now the question is that if one has to pay some price for the self-adjoint extension of the Hamiltonian. One important finding is that the anisotropy, given by the equation

$$\sigma^2 = \frac{1}{12}\left[(\frac{\dot{g_{11}}}{g_{11}} - \frac{\dot{g_{22}}}{g_{22}})^2 + (\frac{\dot{g_{22}}}{g_{22}} - \frac{\dot{g_{33}}}{g_{33}})^2 + (\frac{\dot{g_{33}}}{g_{33}} - \frac{\dot{g_{11}}}{g_{11}})^2\right],$$

is indeed a nonzero object [9]. However, the scale invariance is lost! But this is a more generic problem in the self-adjoint extensions, and not specific to cosmology. It now remains to be seen what other symmetry might be lost in this.

3. Summary

We can summarized our above discussions into following important points:

- The threat of nonconservation of probablity is not real!
- Anisotropic models with constant spatial curvature (Bianchi I, V, IX) as well as varying spatial curvature (Bianchi III, KS), on proper operator ordering, show unitary evolution.
- In fact, thanks to Neumann's theorem, as all the Bianchi models and KS, possess a symmetric Hamiltonian, a self-adjoint extension is always possible.
- The unitarity is restored, not at the cost of anisotropy.

References

[1] B.F. Schutz, Phys. Rev. D, **4**, 3559 (1971).
[2] V.G. Lapchinskii and V.A. Rubakov, Theor. Math. Phys. **33**, 1076 (1977).
[3] N. Pinto-Neto and J.C. Fabris, Class. Quantum Grav. **30**, 143001 (2013).
[4] F.G. Alvarenga, A.B. Batista, J.C. Fabris, N.A. Lemos and S.V. B. Goncales, GRG **35**, 1639 (2003).
[5] B. Majumder and N. Banerjee, Gen. Relativ. Gravit., **45**, 1 (2013).
[6] S. Pal and N. Banerjee, Phys.Rev. D, **90**, 104001 (2014).
[7] S. Pal and N. Banerjee, Phys. Rev. D, **91** 044042 (2015).
[8] S. Pal and N. Banerjee, Class. Quantum Grav., **32**, 205005 (2015).
[9] S. Pal, Class. Quantum Grav., **33**, 045007 (2016).

Very High Energy Gamma Ray Astronomy using HAGAR Telescope System

Varsha Chitnis (for HAGAR collaboration)

Department of High Energy Physics, Tata Institute of Fundamental Research, Homi Bhabha Road, Mumbai-400005, India

vchitnis@tifr.res.in

Very High Energy gamma ray astronomy is passing through a very exciting phase at present. This, comparatively new branch of astronomy has emerged as a major astronomical discipline during last decade, with the detection of more than 170 objects belonging to diverse astronomical classes. In this talk, a brief review of the field will be given. India has a long tradition of research in this area. At present 7-element High Altitude Gamma Ray (HAGAR) telescope system is operational in Ladakh region of Himalayas. This telescope system, the first phase of 4-Institute collaboration, Himalayan Gamma Ray Observatory (HiGRO), has been observing various astronomical sources since 2008 and has successfully detected VHE gamma ray emission from extragalactic objects like Mrk 421, Mrk 501 as well as galactic sources including Crab nebula/pulsar. Details of HAGAR telescope system will be given and some of the recent results as well as future plans will be discussed.

1. Introduction

Very High Energy or VHE gamma ray astronomy covering the energy range of few 10's of GeV - few 10's of TeV is one of the youngest branches of astronomy. It has evolved into a mature branch of astronomy during last decade, with the detection of more than 170 astronomical sources belonging to diverse classes. In the next section of this paper, brief review of the field is given. This is followed by description of HAGAR telescope system operational in Ladakh region of Himalayas for last few years and some of the recent resulted from HAGAR and future plans.

2. Physics motivation for VHE gamma ray astronomy

Gamma rays provide one of the best windows to study nonthermal universe. Cosmic rays with energies extending upto 10^{20} eV, following powerlaw distribution, form one nonthermal component. Even after more than 100 years since discovery, origin and acceleration of cosmic rays is unresolved mystery. Supernova remnants (SNRs) are thought to be the sites for lower energy cosmic rays upto 10^{15} eV i.e. upto the knee region of cosmic ray spectrum. Higher energy cosmic rays probably originate from Active Galactic Nuclei or AGNs. Acceleration of charged particles to very high energies produces gamma rays through various processes. So study of VHE gamma ray emission from these sources will shed some light on cosmic ray origin. This study will also give insight into emission regions and emission processes in these objects.

There are some other research areas which can be explored through study of VHE gamma ray emission. It is possible to study physics beyond standard model through searches for dark matter. WIMPs or weakly interacting massive particles are popular candidates for dark matter. Annihilation of WIMPs is expected to produce detectable signal in VHE gamma ray range. Likely candidate sites are galactic halo, galactic centre, dwarf galaxies or galaxy clusters.

There is also possibility to check for Lorentz invariance through study of rapid time variations in VHE emission from distant objects. Also it is possible to get indirect estimation of Extragalactic Background Light (EBL) through study of VHE emission from AGNs. This has implications about star formation history of the Universe.

VHE gamma ray emission has been detected from 175 sources so far [1]. These include variety of galactic and extragalactic objects. Amongst galactic sources prominent classes are supernova remnants (13 shell type SNRs and 10 with molecular clouds detected so far), pulsar wind nebulae or PWN (35), pulsars (2) and binaries (5). Amongst extragalactic sources these are predominantly AGNs (61), radio galaxies (4), starburst galaxies (2), massive star clusters (4) etc. Examples from some of the categories are discussed below.

2.1 Supernova remnants

Massive stars end their life through supernova explosions. This explosion blows off outer layers of star forming supernova remnant. Supernova remnants are thought to be the sites for acceleration of cosmic rays and possible mechanism is diffusive shock acceleration. VHE gamma ray emission from supernova remnants extending beyond few 10's of TeV provide indication of possible cosmic ray acceleration. VHE emission is detected from 13 shell type supernova remnants and 10 supernova remnants with molecular clouds. One example is supernova remnant RXJ1713.7-3946 detected by HESS with spectrum extending upto 100 TeV with slope of -2, which is consistent with shock acceleration scenario [2]. This is still not considered as conclusive evidence as these gamma rays could originate from neutral pion decay from proton proton interaction or by Compton scattering of VHE electrons with cosmic microwave background radiation. Present data is not able to distinguish between these two scenarios. Multiwaveband morphological studies with better angular resolution and spatially resolved spectral measurements are needed to settle this issue.

2.2 Pulsar wind nebulae (plerions)

In many cases supernova explosion results in rapidly rotating neutron star which is called pulsar. Quite often supernova remnants show bright core within the shell, powered by pulsar wind consisting of electrons and positrons. VHE gamma ray emission is detected from 35 PWN so far. One typical example is Crab nebula with nonthermal emission extending over 21 decades of frequencies. Spectral energy distribution (SED) of Crab nebula in gamma ray band is explained in terms of Synchrotron Self-Compton (SSC) model [3]. According to this model, relativistic electrons emit Synchrotron photons which are Compton upscattered to gamma ray energies by same population of electrons. Even though Crab nebula is a well studied object, there are several aspects which are not yet understood. For example, there were rapid high energy gamma ray flares with rise time of few hours seen by AGILE and Fermi-LAT, which are not yet fully understood [4].

2.3 Gamma ray pulsars

Pulsars are highly magnetized rapidly rotating neutrons stars where rotation axis is misaligned with magnetic field axis. As neutron star spins, the beam of radiation sweeps through our line of sight and we see pulsations. Pulsations are seen in various wavebands. Emission mechanism for gamma rays was thought to be curvature radiation produced when high energy charged particle moves along curved magnetic field, resulting in exponentially cutoff powerlaw spectrum. Exact shape of the spectrum depends on the place from where gamma ray emission originated. There are various models about the emission region like polar cap, outer gap and slot-gap etc.

VHE gamma ray pulsations were detected from Crab pulsar at a period of 33 ms initially by MAGIC telescope at energies above 25 GeV and later by VERITAS at energies above 100 GeV, upto 400 GeV [5]. Earlier gamma ray spectrum detected by Fermi-LAT was fitted with a exponential cutoff powerlaw consistent with curvature radiation. However, detection of pulsations at energies above 100 GeV cannot be explained by curvature radiation. Entire gamma ray spectrum is fitted with a broken power law and inverse Compton scattering is one likely mechanism. Also possibility of two mechanisms one dominant at lower gamma ray energies below the spectral break and second one dominant above the break is being discussed. Very recently MAGIC has detected pulsations from Crab pulsar all the way upto 1.5 TeV [6], further strengthening these interpretations.

Only other pulsar detected at VHE energies is Vela pulsar. This was detected by second phase of HESS, 28 m diameter telescope, i.e. the largest VHE gamma ray telescope in the world. Pulsations are seen clearly at a period of 89 ms at energies above 30 GeV [7].

2.4 TeV binaries

TeV binaries are composed of a massive star and a compact object and emit variable, modulated VHE emission. Five binaries are detected at VHE energies. One example is LSI+61° 303, where emission was found to show modulation of 26.5 days which is orbital period of the system. Companion star is Be star with circumstellar disk and nature of compact object, whether it is neutron star or black hole is not clear. VHE emission is mainly seen in the orbital phases of 0.4–0.7 [8]. There are two types of models proposed to explain this emission. According to microquasar model, compact object is powered by mass accretion from companion star producing collimated jets. These jets boost energy of stellar photons to VHE gamma rays. According to binary pulsar scenario, pulsar winds are powered by rotation of neutron star and interaction of pulsar wind with companion star outflow produces VHE gamma rays [9]. It is not yet clear which model is correct. Multiwaveband studies are expected to provide the clue.

2.5 Active Galactic Nuclei

AGNs are the distant galaxies with bright nuclei, powered by supermassive black hole at the centre accreting matter from host galaxy. VHE gamma ray emission is detected from 61 Blazar classs AGNs including BL Lacs and FSRQs. Blazars are characterised by variability in all wavebands on various time scales ranging from minutes to years, with wide flux variations. These objects have jets pointed towards us, so we see Doppler boosted emission from jets. SEDs of these objects are characterised by two broad peaks or humps and depending on location of these peaks, Blazars are classified as Low-frequency peaked Blazars (LBL), Intermediate-frequency peaked Blazars (IBL) and High-frequency peaked Blazars (HBL). Most of the Blazars detected at VHE energies are HBL type. HBLs show first peak in SED at X-ray energies and second one at TeV energies. First peak is generally attributed to Synchrotron emission from energetic electrons, whereas origin of second peak is not clear. According to various proposed theories this emission could be originating from leptonic beam or hadronic beam in jets. One popular leptonic model is SSC model which readily explains good correlation seen between X-ray and gamma ray flares from several TeV Blazars. However, sometimes orphan TeV flares are also seen from some Blazars which not accompanied by corresponding increase at X-ray energies. These are inconsistent with SSC model and explained using other leptonic models like external Compton (EC) or hadronic models or lepto-hadronic models. EC model is similar to SSC but here photons for Compton upscattering come from elsewhere, from outside the jet, possibly from accretion disk, torus or BLR. This model is used quite often to explain gamma ray emission from LBLs and FSRQs. Amongst hadronic models there are proton synchrotron, proton induced cascades due to interaction of protons with ambient matter or photon fields. There is a particular interest in hadronic models from the point of view of explaining cosmic ray origin.

One important characteristic of Blazars is their time variability. This variability is seen in all wavebands including gamma ray band. One example is spectacular flare detected by HESS experiment from PKS2155-304, where flux increased as high as 15 Crab units with rise time of 173 s [10]. Another interesting flare was detected from Mkn 501 by MAGIC experiment lasting for about half an hour showing significant lag between photons of different energies in TeV band. Time delay of about 4 minutes was seen between lowest and highest energies in this case [11]. Using these kind of time lags, it is possible to constrain quantum gravity models. Using this particular flare, lower limits on quantum gravity parameter were derived. Another important information obtained from variability time scale is the size of the emission region.

One more important aspect of these studies is estimation of Extragalactic Background Light or EBL. EBL is isotropic diffuse radiation of UV, optical and IR photons. It is sum of starlight emitted by galaxies through the history of the Universe. EBL shows two humped spectral energy distribution. First hump in UV-optical corresponds to starlight and second hump corresponds to UV/optical light absorbed by dust and re-radiated in the infrared. Direct measurements of EBL are extremely difficult due to strong foreground contamination by galactic and zodiacal light. Various theoretical models are available, but these are poorly constrained. VHE gamma rays from distant AGNs interact with EBL photons producing electron positron pair resulting in distortion and attenuation of intrinsic spectrum. Attenuation depends on energy as well as distance of the source, generating gamma ray horizon. Distortion caused in VHE spectrum of Blazars by EBL can be used for estimation of EBL itself. One such attempt of evaluation of EBL was done using data from two Blazars at redshifts of 0.186 and 0.165 obtained from HESS experiment [12]. Upper limit on EBL derived from these measurements indicated that Universe is transparent than expected. This work was later extended using sample from seven Blazars and EBL was estimated over the wavelength range of 0.3-10 μm [13]. As more data becomes available these estimates will get revised further.

3. HAGAR Telescope System

3.1 Atmospheric Cherenkov Technique

Gamma rays from astronomical sources can not penetrate Earth's atmosphere and hence are detected using satellite based detectors. At energies above 100 GeV, due to rapidly falling flux from astronomical sources, it is not possible to use satellite based detectors very efficiently because of requirement for very large detector areas. On the other hand, VHE gamma rays are detected far more efficiently using ground based atmospheric Cherenkov technique. Gamma rays are detected indirectly in this technique. Gamma ray interacts at the top of the atmosphere, through various processes generates shower of charged particles in the atmosphere, these charged particles then cause atmosphere to emit bluish Cherenkov light (see Fig.1). This light is detected using telescope consisting of mirror/reflector and one or more photomultiplier tubes or PMTs at focus. This light comes as a flash lasting for a few ns and is spread over a circular region with radius of about 100 m at observation level. There are two variants of atmospheric Cherenkov technique, angular imaging and wavefront sampling. In imaging technique, there is a large reflector with cluster of PMTs at the focus. Images of air showers are recorded in this technique. On the other hand, in wavefront sampling technique, there is a distributed array of small size telescopes sampling Cherenkov light across the Cherenkov pool. In this technique, arrival time of Cherenkov shower front and Cherenkov photon density are recorded at various locations in Cherenkov pool. Arrival time information gives the direction of shower axis and Cherenkov photon density is a measure of primary energy. HAGAR telescope system is based on this technique.

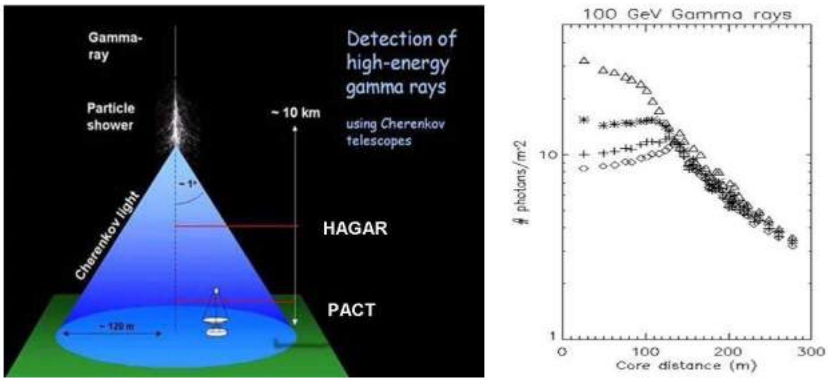

Figure 1. Left panel : Atmospheric Cherenkov technique, Right panel: Variation of Cherenkov photon density with core distance for simulated showers initiated by 100 GeV gamma rays for various altitudes (diamond : sea level, plus sign : 1 km, asterisk : 2.2 kms and triangle : 4.5 kms altitude)

3.2 HiGRO collaboration experiments

Tata Institute of Fundamental Research (TIFR) entered the field of VHE gamma ray astronomy in 1969. Initial activities were at Ooty and were shifted to Pachmarhi in Madhya Pradesh in 1980s. Bhabha Atomic Research Centre (BARC) also started activities in this field in 1980s. Recently TIFR was operating Pachmarhi Array of Cherenkov Telescopes and BARC has been operating TACTIC at Mt. Abu. Both these experiments are at an altitude of about 1 km and have low energy thresholds in the neighbourhood of about 1 TeV. There is a strong physics motivation for lowering energy thresholds of atmospheric Cherenkov telescopes. For example, detection of distant AGNs or GRBs and detection of pulsed component in pulsars is possible only with instruments with thresholds around 100 GeV or less. There are two ways of reducing energy threshold. First alternative is to use large mirrors, which is expensive. Second cost effective alternative is to install telescope at high altitude location. As one goes to high altitude location, Cherenkov photon density in the cone increases. Also atmospheric attenuation of Cherenkov photons is lower at high altitude locations. Because of these two factors, there is a significant increase in Cherenkov photon density near shower core at high altitude location. This is seen clearly from Fig.1 (right panel), where variation of Cherenkov photon density from simulated showers initiated by 100 GeV gamma rays is plotted as a function of distance from shower axis (or core distance) for four different altitudes from sea level to 4.5 kms altitude. Cherenkov photon density near shower core is factor of 4-5 higher at 4.5 kms altitude than that at sea level. As a result, there is a significant reduction in energy threshold of atmospheric Cherenkov telescope installed at high altitude location.

Himalayan Gamma Ray Observatory (HiGRO) collaboration was formed with the motivation of setting up atmospheric Cherenkov telescopes at high altitude location in Himalayas. This is a collaboration between four institutes : TIFR, IIA (Indian Institute of Astrophysics), BARC and SINP (Saha Institute of Nuclear Physics). There is also some participation from Dibrugarh University in this collaboration. HiGRO experiments are located at a place called Hanle in Ladakh region of Himalayas. This is the place where IIA has set up Indian Astronomical Observatory (IAO). Altitude of the base camp of IAO is 4.3 kms. Ladakh is a high altitude cold desert with hardly any rainfall and very little snowfall with clear sky almost throughout the year. Hanle is easily accessible by road from Leh throughout the year at a distance of about 250 kms. HAGAR is the first phase of HiGRO and MACE, described in the paper [14], is the second phase.

3.3 HAGAR : instrument details

HAGAR or High Altitude Gamma Ray Telescope system is an array of seven telescopes deployed in the form of a hexagon (see Fig.2). Spacing between the telescopes is 50 m. Each telescope consists of seven para-axially mounted parabolic mirrors, each of diameter 0.9 m. At the focus of each mirror UV sensitive PMT from Photonis with make XP2268B is mounted. Field of view of HAGAR is 3 deg FWHM. Pulses from PMTs are brought to the control room through coaxial cables.

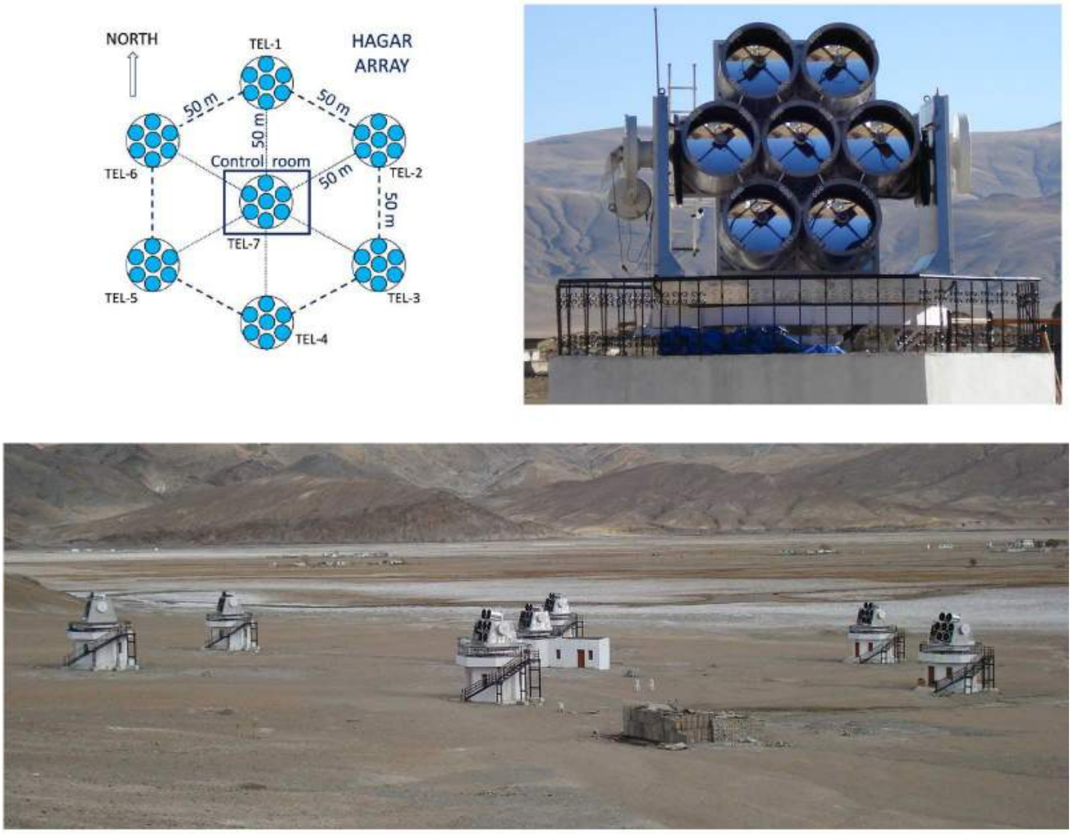

Figure 2. Top left : Layout for HAGAR, Top right : One of the telescopes from HAGAR, Bottom : HAGAR array of 7 telescopes

Installation of HAGAR began at Hanle in 2005 and was completed in 2008. Fig.2 shows the photograph of entire array with closer view of one of the telescopes. Tracking system of HAGAR is based on alt-azimuth design. Maximum zenith angle coverage is upto 85 deg. Steady state pointing accuracy of servo is ± 10 arc-sec. Maximum slew rate is 30 deg/minute. Average pointing accuracy of a mirror is estimated to be 12.5 arc-minutes [15].

High voltages of individual PMTs of HAGAR are controlled using CAEN controller. In control room pulses from individual PMTs are added to form seven telescope pulses. Data acquisition system is CAMAC based and interrupt driven. Trigger is generated when at least 4 telescope pulses out of 7 cross the discriminator threshold in coincidence window of 60 ns. Data recorded for each event includes relative arrival time of shower front at each mirror accurate to 0.25 ns as given by TDCs, pulse height or charge at each telescope recorded using 12 bit ADC and absolute arrival time of event accurate to μs as given by Real Time Clock (RTC) module synchronised with GPS. In addition to this telescope pulse profiles are also recorded in 1 ns bins using waveform digitizer. Further details for HAGAR are given in [16].

3.4 Performance parameters for HAGAR

Extensive simulations were carried out to understand performance of HAGAR. Since atmospheric Cherenkov experiments cannot be directly calibrated, their performance can be understood only through simulations. These simulations consist of two parts. First part is the simulation of extensive air showers initiated by gamma rays and various species of cosmic rays. CORSIKA package is used for this purpose [17]. Packages GHEISHA and VENUS were used respectively for simulating low and high energy hadronic interactions whereas EGS4 was used for electron-photon interactions. US standard atmospheric profile was used. Showers initiated by gamma rays, protons, alpha particles and electrons were simulated. Impact parameter range was varied over 0-300 m, viewcone range of 0-4 deg was used for cosmic ray showers. HAGAR geometry and geomagnetic field at Hanle was taken into consideration. Mirror reflectivity was set to 80% and quantum efficiency curve for PMT was used. Typically few million showers were generated for each species. This sample was then passed through detector simulation program which takes into account various parameters specific to HAGAR system like PMT and cable response, trigger criteria etc. Further details of these simulations are given in [18].

Cosmic ray trigger rate estimated from these simulations is 13 Hz which agrees with the observed trigger rate. Energy threshold given as the peak of the differential rate curve is estimated to be about 208 GeV for 4 fold trigger condition. Expected gamma ray rate from Crab like sources is 6.3 counts per minute. Sensitivity corresponds to detection at the level of 1.2 $\sigma/\sqrt{hour}$ for Crab like sources. In other words, Crab nebula can be detected at a significance level of 5 sigma in 17 hours.

3.5 HAGAR observations and results

Regular observational runs with HAGAR commenced in September 2008. During last seven years more than 4000 hours of data were collected in the form of observational and various calibration runs. Observations of astronomical sources are typically carried out in ON-OFF pairs of duration about an hour each. Several galactic and extragalactic sources were observed in last seven years. Amongst galactic sources, the longest coverage is for Crab nebula/pulsar (about 320 hours) followed by Geminga pulsar (about 200 hours), whereas amongst extragalactic sources, longest coverage is for Mkn 421 (about 260 hours) followed by Mkn 501 (about 185 hours) and 1ES2344+514 (about 145 hours).

In data analysis, initially selection cuts based on data quality, stability of rates etc. are applied to data constituting ON-OFF pair. Then for each event, arrival direction of shower is determined. For this purpose, relative arrival times of shower front at various telescopes are fitted with a plane front. Normal to this front gives direction of shower axis. Then space angle, i.e angle between shower axis direction and pointing direction of the telescope is calculated. Space angle distributions generated for ON-OFF pairs are then compared and normalized and gamma ray signal is estimated as excess events in signal region. Some of the prominent results from HAGAR are given below.

3.5.1 *Crab nebula*

Crab nebula is a very well studied object discussed earlier. It is a bright and steady source considered as a standard candle. With HAGAR we had very long coverage for this source. After applying data quality cuts, 103 hours of data were left which were analysed further. Seasonwise count rates from Crab nebula for six years data are shown in Fig.3. Flux is estimated to be $(2.01\pm0.11) \times 10^{-10}$ ph/cm^2/s for the threshold of 234 GeV, which is consistent with the measurements from other experiments like Whipple and MAGIC (see Fig.3) [19].

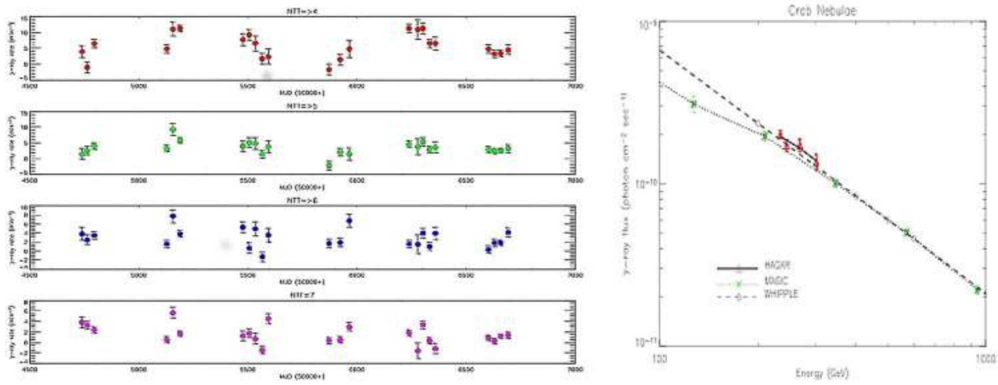

Figure 3. Left : Seasonal light curve of Crab nebula from HAGAR spanning six years of data. Different panels correspond to different trigger conditions, at least 4, 5, 6 and 7 telescopes triggering, from top to bottom. Right : Flux measurements from HAGAR as a function of energy shown by red triangles. Dotted and dashed lines correspond to spectral measurements from MAGIC and Whipple respectively.

3.5.2 *Crab and other pulsars*

Search for pulsations was carried out in Crab data collected by HAGAR. Data stretch of about 140 hours was used for this purpose. Using absolute arrival time of each event recorded with μs accuracy and using known ephemeris of pulsar with period of 33 ms, phase was calculated for each event and phasogram was generated which is shown in Fig.4. Excess is seen clearly at phases marked P1 and P2. These are the phases at which excess is seen by Fermi-LAT and other experiments. This type of excess is not seen in the background data validating the result. Significance of this excess is estimated. So there is indication of pulsations from Crab at significance level of 3.6σ [20]. Attempts are being made to improve the significance by adding more data and also by refining the cuts applied in analysis. Some more pulsars including Geminga, PSR J0357+3206, PSR J0633+0632 and PSR J2055+2539 were observed with HAGAR. There is no statistically significant detection of pulsations from any of these pulsars and upper limits on pulsed flux are estimated.

3.5.3 *Mkn 421*

Amongst extragalactic sources, we had longest coverage for Mkn 421. This is a nearby Blazar (z=0.031) of HBL type. VHE gamma ray emission was discovered by Whipple from this source in 1992. This was the first blazar to be detected at VHE gamma ray energies. It is known to show frequent flaring behaviour. One large flare from this source appeared in February 2010, which was seen by VERITAS, HESS and HAGAR. Results from HAGAR data collected during February-April 2010 are shown in Fig.5. This figure shows seasonwise count rates from HAGAR for estimated energy threshold of 250 GeV. In February, from 8 hours of data, source was detected at the significance level of 12.7σ. Mean count rate was 13.4 counts per minute and rate decreased in subsequent seasons. Fig.6 shows lightcurve from HAGAR along with the X-ray light curve from ASM onboard RXTE. Similar pattern is seen in both the cases. HAGAR detected maximum flux on the night of 17th February and flux level was about 6-7 crab units. Average flux in February was 3 crab units and it decreased to one crab unit in March and April.

Fig.6 shows multiwaveband data for February 2010 flare. These data were obtained from following instruments,

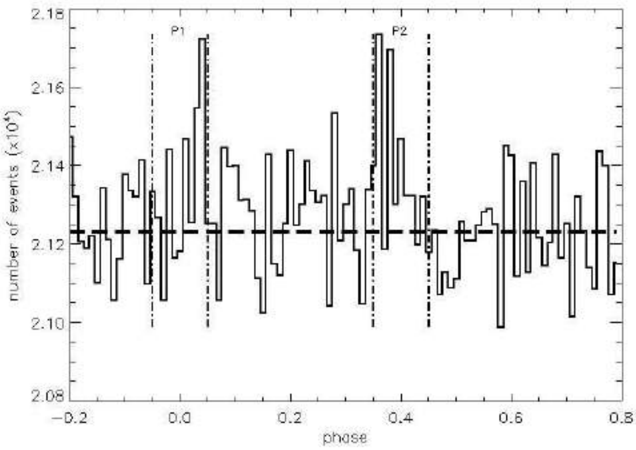

Figure 4. Phasogram of Crab pulsar from HAGAR. Excess is seen at phases marked by P1 and P2.

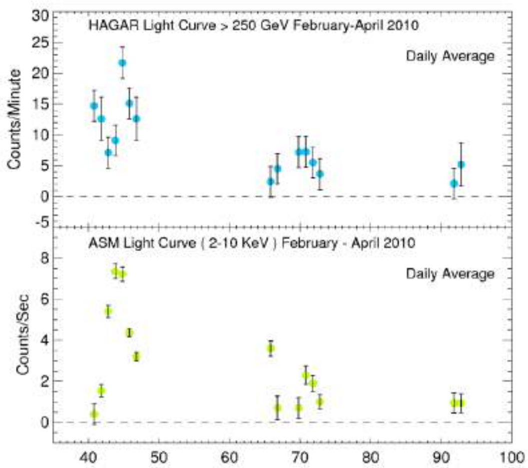

Figure 5. Light curve of Mkn 421 from HAGAR during February-April 2010 (top panel) and corresponding X-ray light curve from ASM onboard RXTE.

radio data from OVRO, optical data from SPOL, X-ray data from Swift and RXTE, high energy gamma ray data from Fermi-LAT and VHE data from HAGAR. Multiwaveband light curves for February 2010 are shown with panels arranged in the order of increasing energy from top to bottom. Flare peaking around 16-17th February is seen in most of the wavebands.

Evolution of Mkn 421 SED was studied during this flaring episode. For this purpose, multiwaveband light curve was divided into four states, pre-flare (13-15 February), moderate flare (16 February), TeV flare (17 February) and post flare (18-19 February) state. SEDs were generated for these four states and fitted with Synchrotron Self Compton model. One zone SSC model developed by Krawczynski et al. [21] was used for this purpose. SED during TeV flare state is shown in Fig.6 along with the one zone SSC fit. For all the states one zone SSC model seems to fit data well. Model parameters for all four states are listed in Table 1. We tried to explain this flaring episode in terms of passing shock and details are given in [22].

Work on longterm data of Mkn 421 covering seven years (2009-2015) is underway. Lightcurve from HAGAR data is shown in Fig.7. Multiwaveband light curves and SEDs are being studied [23].

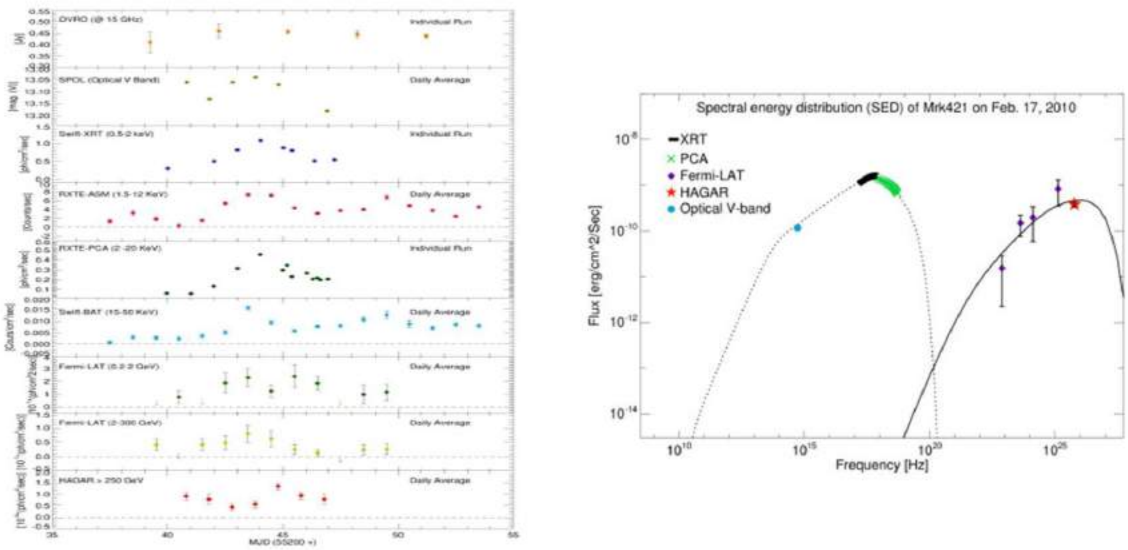

Figure 6. Left panel : Multiwaveband light curve of Mkn 421 during February 2010, Right panel : Multiwaveband SED of Mkn 421 during flare detected by HAGAR on 17th February 2010.

Table 1. Parameters for single zone SSC fit to Mkn 421 SEDs.

State	Magnetic field (G)	Doppler factor δ	log E_{min} (eV)	log E_{max} (eV)	log E_{break} (eV)	p1	p2	U_e $[10^{-3}]$ (erg/cc)	$\eta = U_e/U_B$
State1	0.026	19.5	9.6	12.1	11.3	2.4	4.3	0.9	33.46
State2	0.029	22.0	8.0	12.1	11.4	2.2	3.9	1.4	41.83
State3	0.029	21.0	9.4	12.1	11.45	2.2	4.1	1.0	29.88
State4	0.028	21.0	9.1	12.1	11.45	2.3	4.1	8.5	27.24

3.5.4 *Mkn 501*

Another Blazar observed extensively with HAGAR is Mkn 501. This is again nearby Blazar (z=0.034) of HBL type, discovered by Wipple in 1996. It is a highly variable source. Data collected by HAGAR in years 2010 and 2011 are analysed. Source was detected 5σ significance level during April-May 2011 with flux level of 1.5 crab units. Multiwaveband light curve is generated and SEDs are fitted with SSC model. These SEDs could not be fitted with one zone SSC model. So additional zone was introduced and two zone SSC model was found to give satisfactory fit as shown in Fig.8. According to this model, there are two emission zones, inner and outer one. Radius of inner zone corresponds to variability time scale of 7 hours and outer zone to 48 hours. Further details are given in [24].

3.5.5 *Other Blazars*

We have observed some more blazars using HAGAR including 1ES1426+428, 1ES1218+304 and 3C454.3. First two Blazars are detected by MAGIC experiment, but at much lower flux level compared to Mkn 421 and Mkn 501. HAGAR sensitivity being inferior to VERITAS and MAGIC, these Blazars were not detected with HAGAR with good statistical significance. 3C454.3 is not detected by any VHE experiment probably because of its high redshift (z=0.859). It was observed by HAGAR during detection of flare by Fermi-LAT in year 2009. There is no statistically significant detection of gamma ray signal from HAGAR data and upper limits on flux were estimated for all these source. Details of these results are given in [25].

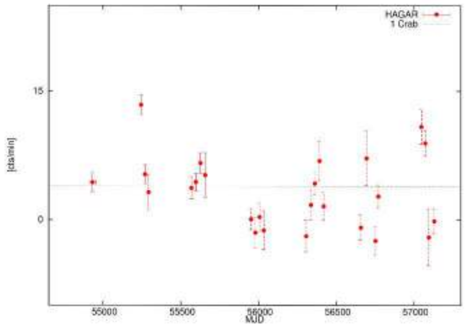

Figure 7. Lightcurve of Mkn 421 from HAGAR during 2009-2015.

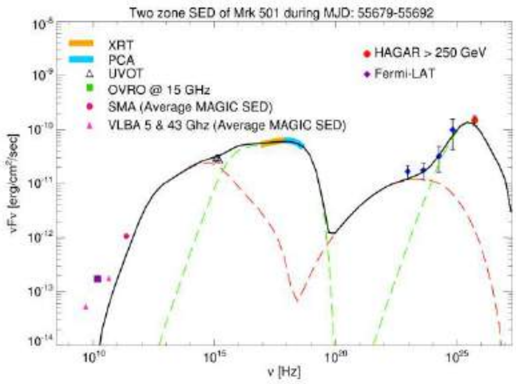

Figure 8. Multiwaveband SED of Mkn 501 fitted with two zone SSC model.

4. Future prospects

After successful installation and operation of HAGAR at Hanle, HiGRO collaboration is entering more ambitious second phase of experiments, i.e. MACE telescope. Installation of MACE is at advanced stage at Hanle and first light is expected by 2017 [14]. Also there are plans of participation in next generation observatory, Cherenkov Telescope Array, an international collaboration involving 1200 scientists/engineers from 31 countries [26, 27].

References

[1] http://tevcat.uchicago.edu/
[2] F. Aharonian et al., A&A **464**, 235 (2007).
[3] A. A. Abdo et al., ApJ **708**, 1254 (2010).
[4] R. Buehler et al., ApJ **749**, 26 (2012).
[5] E. Aliu et al., Science **334**, 69 (2011).
[6] S. Ansoldi et al., A&A **585**, A133 (2016).
[7] C. Stegman, for HESS collaboration, presentation at TeVPA-2014, June 2014, Amsterdam.
[8] J. Albert et al., Science **312**, 1771 (2006).
[9] I. F. Mirabel, Science **312**, 1759 (2006).
[10] F. Aharonian et al., ApJ **664**, L71 (2007).
[11] J. Albert et al., ApJ **669**, 862 (2007).
[12] F. Aharonian et al., Nature **440**, 1018 (2006).
[13] A. Abramowski et al., A&A **550**, A4 (2013).
[14] K. K. Yadav, these proceedings.
[15] K. S. Gothe et al., Experimental Astronomy **35**, 489 (2013).

[16] V. R. Chitnis et al., 32nd International Cosmic Ray Conference, Beijing, China, **9**, 166 (2011).
[17] D. Heck et al., Report FZKA6019, Forschungszentrum Karlsruhe GmbH, Karlsruhe (1998).
[18] L. Saha et al., Astroparticle Physics **42**, 33 (2013).
[19] B. B. Singh et al., paper presented at 33rd ASI meeting at NCRA-Pune during 17-20 February 2015.
[20] B. B. Singh et al., 32nd International Cosmic Ray Conference, Beijing, China, **7**, 87 (2011).
[21] H. Krawczynski et al., ApJ **601**, 151 (2004).
[22] A. Shukla et al., A&A **541**, id.A140 (2012).
[23] A. Sinha et al. To appear in A&A (2016).
[24] A. shukla et al., ApJ **798**, id.2 (2015).
[25] P. Hazarika et al., these proceedings.
[26] https://portal.cta-observatory.org/Pages/Home.aspx
[27] B. S. Acharya et al., Astroparticle Physics **43**, 3 (2013).

AstroSat: India's First Multi-wavelength Astronomy Satellite

K. P. Singh

Department of Astronomy & Astrophysics, Tata Institute of Fundamental Research, Homi Bhabha Road, Mumbai-400005, India

singh@tifr.res.in

AstroSat launched on September 28, 2015 is India's first Space Observatory. It is designed to observe the universe simultaneously in multi-wave bands spanning a very broad range of wavelengths in the visible, ultraviolet, and X-rays. All the scientific instruments on-board were made operational in a sequential manner starting on October 1st, 2015. The performance parameters of the various scientific instruments and some results from the first observations carried out after their commissioning are presented here.

1. Introduction

It has become increasingly clear over the past few decades that understanding the nature of cosmic objects and their emission processes in different wavelength regions requires observing them simultaneously in as many wave-bands as possible. This has, hitherto, been possible in only a very few space missions for various technical reasons as the requirements and environments vary. Multi-wave band observations are extremely important for understanding the physics of regions with strong gravity, e.g., accretion disks and columns around White Dwarfs as in Cataclysmic Variables, Neutron Star Binaries and galactic binaries with a few solar mass Black Holes as well as supermassive black-holes in extragalactic sources like active galactic nuclei (AGN). Such observations are also very important to unravel the physics of highly accelerated streams of particles in astronomical jets as seen in Blazars and mini-quasars. Strong Magnetic fields that are responsible for Cyclotron lines seen around accreting neutron stars, and physics of very hot coronal plasmas in active stars, supernova remnants and clusters of galaxies are other areas of research requiring simultaneous multi-wave observations.

AstroSat, weighing 1513 Kg, was launched from the Satish Dhawan Space Centre in Shriharikota (SHAR) by an augmented Polar Satellite Launch Vehicle (PSLV) on 28th September 2015 at 10 AM (IST) into a circular orbit 650 kms above Earth with an inclination of 6 degrees north. There are five principal instruments for observations onboard AstroSat. Four of these are co-aligned to within a few arc mins to look at the same source in the sky and observe it simultaneously in the wave-bands of visible, near ultra-violet (NUV), far ultra-violet (FUV), soft X-rays and hard X-rays. In addition there is Charge Particle Monitor (CPM) to monitor the charged particle background and is used for the safety of certain instruments and to screen the X-ray events. Fig.1 shows the complete Astrosat. The pointing towards a cosmic source is controlled by gyros and star sensors, while ensuring the safety of all the instruments. Three X-ray instruments together give an unprecedented large X-ray bandwidth, with hard X-ray sensitivity that is better than the previous NASA mission known as Rossi X-ray Timing Explorer (RXTE). The imaging capability in the NUV and FUV is better than in the older UV mission of NASA known as GALEX. The near Equatorial launch of the satellite ensures low background hard X-ray detectors. The main characteristics of the five instruments are briefly described below, followed by the first light results. For a more detailed description of all the instruments, the reader is referred to [1] and references therein. *At the time of this presentation, only the X-ray instruments had been switched on, therefore the first light results from only the X-ray payloads are given here. Subsequently the UVIT was switched on and is working perfectly.*

2. X-ray Instruments

2.1 Soft X-ray imaging Telescope (SXT)

SXT, based on the principle of grazing incidence, consists of a set of nested coaxial and con-focal shells of conical mirrors approximating paraboloidal and hyperboloidal shapes in Wolter I geometry. X-rays are incident on a conical mirror representing a paraboloidal (1α) surface. The reflected X-rays are further reflected by a second conical mirror representing a hyperboloid (α) surface which focuses the X-rays onto a charge coupled device (CCD). The conical surfaces made of aluminium foils have a smooth gold surface replicated on them giving a smoothness in the range of $7 - 10$ Angstroms (FWHM). The focal length of the telescope is 2 meters and the on-axis point spread function (PSF) in the focal plane has a FWHM of ~ 20. The CCD (CCD-22 with 600×600 pixels

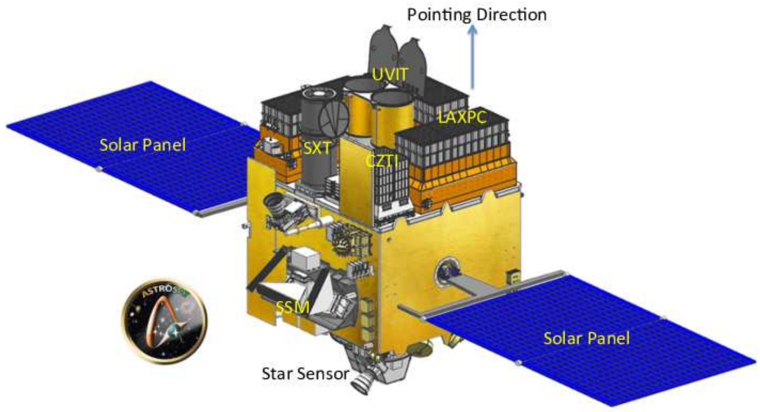

Figure 1. A 3D view of the fully assembled AstroSat showing the main instruments.

used in Swift XRT and XMM-Newton MOS) at the focus is housed in a Focal Plane Camera Assembly (FPCA). The FPCA built in collaboration with the University of Leicester, U.K., provides protection from energetic protons via a shield surrounding the CCD inside the FPCA. The CCD is cooled to 191^0K (-82^0C) by a thermo-electric cooler (TEC) and a radiator plate assembly. A very thin optical blocking filter is similar to the XMM-Newton thin filter is kept above the CCD. The CCD is illuminated permanently by four individual Fe^{55} radioactive calibration sources shining on the four corners (outside the field of view) of the CCD, and used for in-flight calibration at two principal line energies of $\sim$ 5.9 keV and 6.5 keV. There is a provision for reading the CCD using six data modes: "Photon Counting" (PC) mode, "Photon Counting Window" (PCW) mode, "Fast Windowed Photon Counting" (FW) mode, "Bias Map" (BM) mode, "Calibration" (Cal) mode and "House Keeping" (HK) mode. In the PC mode, data from the entire CCD will be collected but only those events that are above a specified threshold energy only will be transmitted. The PCW mode is similar to the PC mode, but the data are collected from one of the predefined smaller square windows on the CCD chosen by the user and uploaded by a tele-command. The readout time in the PC and PCW modes is $\sim$ 2.4 s. In the FW mode, a fixed window of 150$\times$150 pixels centred on the CCD will be used. The readout time of this mode will be approximately 278 ms. The Cal mode will be used to check the calibration of SXT using data from four corner windows of the CCD, with a small central window on the source. In the BM mode, the entire CCD frame will be sent without any threshold. The energy bandwidth of the SXT is $0.3 - 8$ keV. The effective area of the telescope, after taking into account the efficiency of the filter and the CCD, is $\sim$ 128 cm^2 at 1.5 keV, and $\sim$ 22 cm^2 at 6 keV. The field of view (fov) of the SXT is $\sim$ 40 arcmin (dia). The spectral resolution is $\sim$ 5-6% at 1.5 keV, and $\sim$ 2.5% at 6 keV. The SXT can detect sources as faint as $\sim 10^{-13}$ ergs cm^{-2} s^{-1} at 5σ in an exposure of $\sim$ 20000 s. SXT will be instrumental in doing X-ray spectroscopy and measuring the low energy absorption. With a psf of 2 arcmin, SXT is less susceptible to pile-up effects in the CCD and provides capability to observe bright sources in soft X-rays.

2.2 Large Area Xenon Proportional Counters (LAXPCs)

LAXPCs are 3 identical proportional counters each with its own independent front-end electronics, HV supply, and signal processing electronics. Each unit consists of 60 anode cells of size 3$\times$3$\times$100 cm^3 arranged in 5 layers providing a 15 cm deep X-ray detection volume filled with a mixture of 90% Xenon + 10% Methane at a pressure of 1520 torr. A Veto layer surrounds the main X-ray detection volume on 3 sides to reject events due to charged particles and interaction of high energy photons in the detector thus reducing the background. The alternate anode cells of each layer are linked together and operated in mutual anti-coincidence, and so are the outputs from different layers, to further reduce the non-cosmic X-ray background. An aluminised Mylar film of 50 microns thickness serves to seal the gas inside and act as the entrance window for X-rays into the detector. A gas purifier system will recycle the gas regularly in each LAXPC. The Mylar window is supported against the gas pressure by a honeycomb shaped collimator made of aluminium cells in a square geometry. The fov of the LAXPC is $1^o \times 1^o$ defined by a multilayer collimator of tin, copper and aluminium placed in a collimator housing and aligned with the openings in the aluminium collimator below. A 1 mm thick tin sheet coated with copper surrounds each LAXPC unit and shields from high energy X-rays entering the detector from the sidewalls. In normal mode of operation, LAXPC has two modes running simultaneously: (a) Broad Band Counting (BBC) that records the event rates in various energy bands in a selectable time bin (8 ms to 1024 ms; default value 64 ms), and (b) Event Mode Data that records the arrival time of each event with an accuracy of 10 micro sec, its energy and identity. The energy bandwidth for each LAXPC is $3 - 80$ keV, and the total effective are is 8000 cm^2 in the energy band of $5 - 20$ keV. The energy resolution is 12% at 22 keV. It has the best time resolution of all the instruments. LAXPC has no spatial resolution except when it is scanning mode where it can reach a resolution of $1{-}5$ arcmin. With its large area and low background it is expected to detect a 0.1 mCrab source in $\sim$ 1000 s at 3σ level.

2.3 Cadmium-Zinc-Telluride Imager (CZTI)

CZTI with a detection area of 976 cm^2 consists of 64 modules of CZT each of area 15.25 cm^2, arranged in four identical and independent quadrants. A passive collimator (fov = $4.6^o \times 4.6^o$ FWHM for energies ¡ 100 keV) helps in allowing nearly parallel X-rays to enter the detector. A Coded Aperture Mask (CAM) made of 0.5 mm thick Tantalum plate is of the same size as the detector is positioned above the collimator. CAM has a pre-determined pattern of open and closed squares/rectangles matching the size of the detector pixels. The patterns are based on 255-element pseudo-noise Hadamard Set Uniformly Redundant Arrays. Seven types of patterns, with some repeats, were placed in the form of a 4×4 matrix to generate the CAM for one quadrant. This same pattern is placed on other quadrants, rotated by 90^o, 180^o and 270^o respectively. At energies $>$ 100 keV the collimator slats and the coded mask become progressively transparent. For Gamma Ray Bursts, the instrument behaves like an all-sky open detector. The CZT detectors are operated at temperature of $\sim 0^o$C by passive cooling provided by a radiator plate. A Cesium Iodide (Tl) based scintillator detector (20 mm thickness) located just under the CZT detector modules and viewed by a photomultiplier tube is used for Veto ing background events. A radioactive (Am^{241}) calibration source module is mounted in a gap between the base of the collimator slats and the detector plane in each quadrant and illuminates the CZT detector with alpha-tagged 60 keV photons for calibration of the energy response. Each individual pixel is connected to a pre-amplifier, which is embedded in an Application Specific Integrated Circuit (ASIC). The X-ray detector has a detection efficiency of 95% within $10 - 120$ keV and an energy resolution ($\sim$ 8% at 100 keV). The processing electronics carries out reading, analysing, storing and/or transferring of detector data to the satellite via data formatter, and responding to tele-commands, just like all the other X-ray instruments. The CZTI can operate in 16 modes. It has the capability to measure polarisation in the $100 - 300$ keV region.

2.4 Scanning Sky Monitor (SSM)

SSM operating in $2.5 - 10$ keV bandwidth consists of three identical units of position sensitive gas-filled proportional counters with a coded-mask and associated electronics mounted on a rotating platform to scan the sky. Each unit scans the sky in one dimension over a fov of $\sim 22^o \times 100^o$. The effective area of SSM is 53 cm^2 at 5 keV (11 cm^2 at 2.5 keV). An aluminised Mylar window, 50 μm thick seals the gas and is supported by a collimator and coded mask. Six different coded mask patterns with 50% transparency, provide position resolution of $\sim$ 1 mm at 6 keV with corresponding angular resolution $\sim$12 arc min on the sky in the coding direction (2.5^o In a direction perpendicular to the coding direction). The energy resolution is $\sim$ 25% at 6 keV, and the 3σ detection sensitivity is $\sim$ 28 mCrab for 10 minutes integration. The time resolution is 1 ms.

3. Ultra-Violet Imaging Telescopes (UVIT)

The twin telescopes of UVIT image the sky simultaneously in three broad wavebands: FUV (130-180 nm), NUV (200-300 nm), and VIS (320-550 nm). The optics configuration is Ritchey-Chretian (R$-$C 2), with a hyperbolic primary (f/4.5) mirror with effective diameter of 375 mm and focal length of 4.750 m. The fov is $\sim$ 28 arc min (dia), and the spatial resolution (FWHM) is $<$ 1.8 arc sec for the FUV and NUV channels, and $\sim$ 2.2 arc sec for the VIS

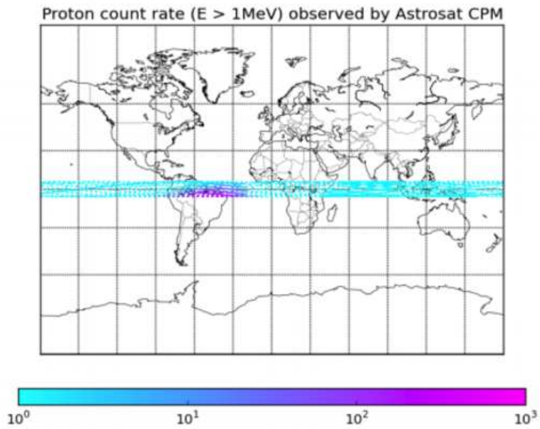

Figure 2. The map of SAA as measured by the CPM. Courtesy: the SSM team.

channel. Several filters are mounted in filter-wheels in front of detectors for selecting narrower wavelength bands. In the FUV and NUV channels, gratings are also provided for low-resolution ($\sim$ 100) slit-less spectroscopy. The detectors used in the focal planes are intensified CMOS type with an aperture of $\sim$ 40 mm (dia). The UV detectors are used in photon counting mode and the visible detector in integration mode. The entire array of 512$\times$512 pixels covering the entire fov or a part of it in a "window" mode can be read at rates up to 600 frames s^{-1}, depending on the area of the window. The effective areas as a function of the wavelengths have been estimated for all the filter and telescope combinations and varies from $8 - 50$ cm^2 depending on the combination used, The time resolution is 1.7 ms. The detection sensitivity is 20 mag in FUV in a 200 sec observation at 5σ level.

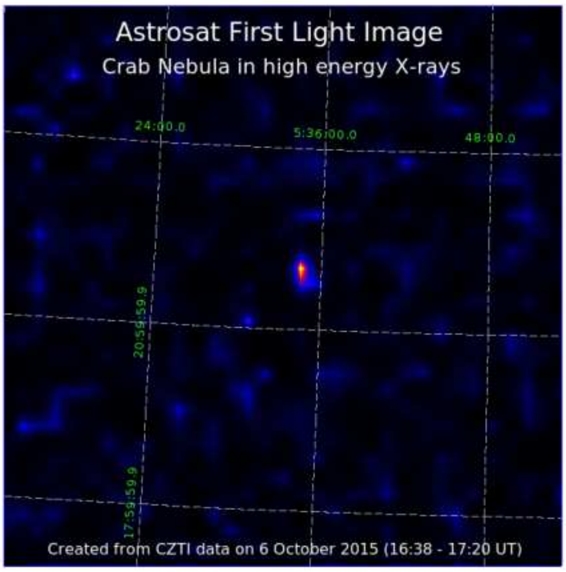

Figure 3. The first light image of the Crab with the CZTI (right). Courtesy: the CZTI team.

4. First light results from X-ray instruments

The first scientific instrument to be switched on was the CPM, and it resulted in the scan of the South Atlantic Anomaly giving a map of the high energy protons (Fig.2). The CZTI was switched on next and obtained an image of the Crab in hard X-rays, shown in Fig.3. This was followed by the operationalisation of the SSM (Fig.4), and

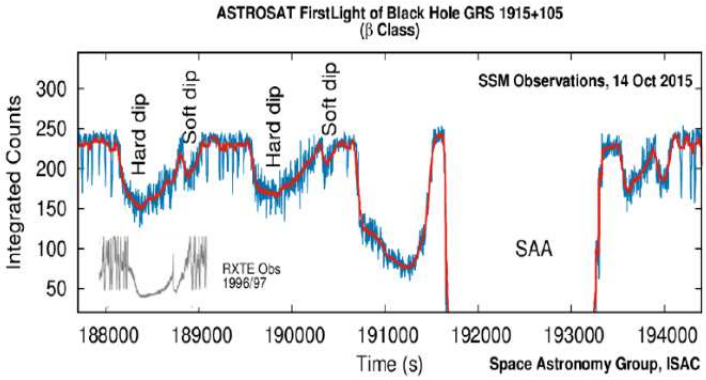

Figure 4. X-ray light curve of a black-hole X-ray binary GRS1915+105 seen with the SSM. Courtesy: the SSM team.

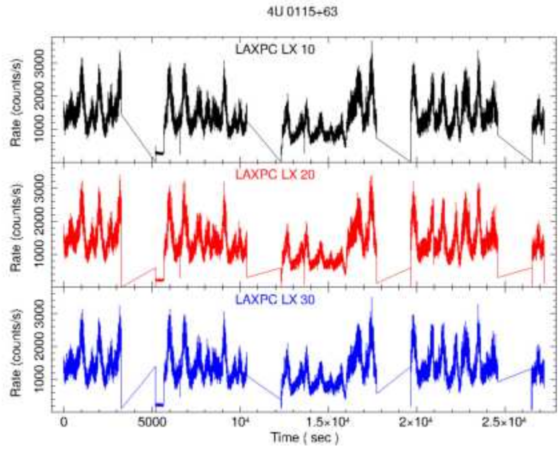

Figure 5. X-ray light curves, as seen with all the 3 units of LAXPC, from a High Mass X-ray Binary (4U0115+63) with a pulsating neutron star (high magnetic field) companion. Courtesy: the LAXPC team.

the three units of LAXPC (Fig.5). The SSM observation of GRS1915+105 shows that the comparison with an earlier observation with RXTE, is excellent. The LAXPC observation showed that all the 3 units are working equally well and are similar in their performance as per the design. LAXPC units also detected the 3.6 s pulsations from 4U0115+63. The camera door of the SXT was opened on October 26, 2015 and an X-ray images of a blazar (PKS2155-304) was recorded (Fig.6). The image and the number of counts recorded established that SXT has a point spread function of ~ 2 arc min (FWHM) and can reach the designed detection sensitivity. Detailed analysis of these and other similar observations and the characterisation of all the instruments will be completed during the Performance Verification phase of the satellite ending on March 31, 2016. This will be followed by 6 months of guaranteed time observations by the instrument teams, after which the satellite will be open to public for observations, based on the peer review process.

5. Acknowledgements

I thank the payload managers of all the instruments, viz., Profs. A. R. Rao (CPM & CZTI), J. S. Yadav (LAXPC), H. M. Antia (LAXPC), Dr. M. C. Ramadevi (SSM), and S.N. Tandon (UVIT) for providing details of their instruments and for sharing their results with me freely. I thank the current PI, Dr. S. Seetha, the earlier PI, Prof. P. C. Agrawal, and the Project Director, Sh. K. S. Sarma for steering the project to its completion and a successful launch. I thank the scientific, technical and laboratory staff in the Department of Astronomy and Astrophysics, TIFR, Mumbai, TIFR workshop, TIFR transport section, and all the project teams at ISAC, Bengaluru, VSSC,

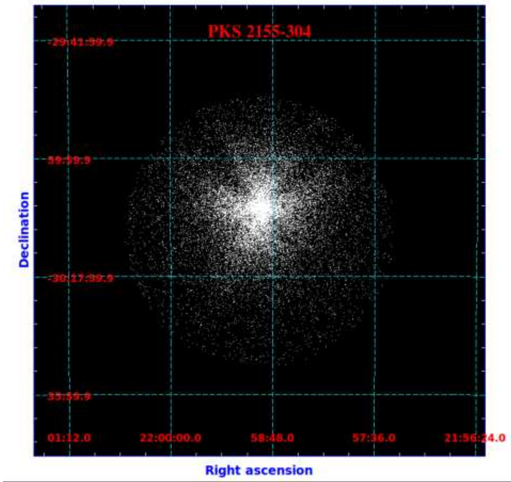

Figure 6. First light image of soft X-rays from a blazar, PKS2155-304, at a redshift of 0.116, with the SXT.

Trivandrum, SAC, Ahmedabad, the mission team at SHAR and at ISTRAC and ISSDC, Bengaluru, who worked tirelessly for AstroSat.

References

[1] KulinderPal Singh et al., SPIE, 9144-63 (2014).

Part II
General Relativity and Cosmology (PS1)

Gravitational redshift from rotating body having intense magnetic field

Anuj Kumar Dubey and A. K. Sen

Department of Physics, Assam University, Silchar-788011, Assam, India

Presenter: Anuj Kumar Dubey (*danuj67@gmail.com*); COS.1, Oral, CICAHEP15.14

It is well known fact that gravitational field can alter the space-time structure and gravitational redshift is its one example. Electromagnetic field can also alter the space-time similar to gravitational field. So electromagnetic field can give rise to an additional effect on gravitational redshift. There are many objects in nature, like neutron stars, magnetars etc which have high amount of rotation and magnetic field. In the present paper we will derive the expression of gravitational redshift from rotating body having intense magnetic field by using the action function of the electromagnetic fields.

1. Introduction

General relativity is not only relativistic theory of gravitation proposed by Einstein, but it is the simplest theory that is consistent with experimental data. Gravitational redshift of light is one of the predictions of general relativity and also provides evidence for the validity of the principle of equivalence. Any relativistic theory of gravitation consistent with the principle of equivalence will predict a redshift.

Gravitational redshift has been reported by most of the authors without consideration of rotation of a body. Neglecting the rotation, the geometry of space time can be described using the well-known spherically symmetric Schwarzschild's geometry and information on the ratio $\frac{M}{r}$ of a compact object can be obtained from the gravitational redshift, where M and r are mass and radius respectively. Thus the redshifted angular frequency ω' and the original angular frequency ω of a photon in Schwarzschild geometry are related by the relation (page 268, of Landau and Lifshitz [1]):

$$\omega^{'} = \frac{\omega}{\sqrt{g_{tt}}} = \frac{\omega}{\sqrt{1-\frac{r_g}{r}}}, \tag{1}$$

where $r_g = 2GM/c^2$ is the Schwarzschild radius.

Adams in 1925 has claimed first about the confirmation of the predicted gravitational redshift from the measurement of the apparent radial velocity of Sirius B [2]. Pound and Rebka in 1959 were the first to experimentally verify the gravitational redshift from nuclear - resonance [3]. Pound and Snider in 1965 had performed an improved version of the experiment of Pound and Rebka, to measure the effect of gravity, making use of Mossbauer - Effect [4]. Snider in 1972 has measured the redshift of the solar potassium absorption line at 7699 $\AA$ by using an atomic - beam resonance - scattering technique [5]. Krisher et al. in 1993 had measured the gravitational redshift of Sun [6]. Nunez and Nowakowski in 2010 had obtained an expression for gravitational redshift factor of rotating body by using small perturbations to the Schwarzschild's geometry [7]. Payandeh and Fathi in 2013 had obtained the gravitational redshift for a static spherically symmetric electrically charged object in Isotropic Reissner – Nordstrom Geometry [8]. Dubey and Sen in 2014 had obtained the expression for gravitational redshift from rotating body in Kerr Geometry. They also showed the rotation and the latitude dependence of gravitational redshift from a rotating body (such as pulsars) [9]. The expression of Gravitational Redshift Factor $\Re$ from rotating body in Kerr geometry was given as (Equation (69), Dubey and Sen [9])

$$\Re(\phi,\theta) = \sqrt{g_{tt} + g_{\phi\phi}(\frac{d\phi}{cdt})^2 + 2g_{t\phi}(\frac{d\phi}{cdt})}. \tag{2}$$

Dubey and Sen in 2015 had obtained the expression for gravitational redshift from charged rotating body in Kerr - Newman Geometry. They showed that gravitational redshift increases as the electrostatic and magnetostatic charges increase, for a fixed value of latitude at which light ray has been emitted. Gravitational redshift increases from pole to equatorial region (maximum at equator), for a given set of values for electrostatic and magnetostatic charge [10].

With this background in the present paper we will derive the expression of gravitational redshift from rotating body having intense magnetic field by using the action function of the electromagnetic fields.

2. Geometry of rotatating body

When rotation is taken into consideration, the covariant form of metric tensor for Kerr family (Kerr (1963) [11], Newman et al. (1965) [12]) in terms of Boyer-Lindquist coordinates with signature (+,-,-,-) is expressed as

$$ds^2 = g_{tt}c^2dt^2 + g_{rr}dr^2 + g_{\theta\theta}d\theta^2 + g_{\phi\phi}d\phi^2 + 2g_{t\phi}cdtd\phi, \tag{3}$$

where g_{ij}s are non-zero components of Kerr family. If we consider the three parameters: mass M, rotation parameter a and electric charge Q and/or magnetic charge P, then it is easy to include charge in the non-zero components of g_{ij} of Kerr metric, simply by replacing r_gr with $r_gr - Q^2 - P^2$. Non-zero components of g_{ij} of Kerr-Newman metric are given as follows (page 261-262 of Carroll (2004) [13]):

$$g_{tt} = 1 - \frac{r_gr - Q^2 - P^2}{\rho^2}, \tag{4}$$

$$g_{rr} = -\frac{\rho^2}{\Delta}, \tag{5}$$

$$g_{\theta\theta} = -\rho^2, \tag{6}$$

$$g_{\phi\phi} = -[r^2 + a^2 + \frac{(r_gr - Q^2 - P^2)a^2sin^2\theta}{\rho^2}]sin^2\theta, \tag{7}$$

$$g_{t\phi} = \frac{asin^2\theta(r_gr - Q^2 - P^2)}{\rho^2} \tag{8}$$

with

$$\rho^2 = r^2 + a^2cos^2\theta \tag{9}$$

and

$$\Delta = r^2 + a^2 - r_gr + Q^2 + P^2, \tag{10}$$

where rotation parameter of the source $a = \frac{J}{Mc}$.

If we replace $r_gr - Q^2 - P^2$ by $r_gr - Q^2$ and further if we put rotation parameter of the source a equal to zero, then it reduces to Reissner - Nordstrom metric. Also if we replace $r_gr - Q^2 - P^2$ by r_gr then the Kerr-Newman metric reduces to Kerr metric and further if we put rotation parameter of the source a equal to zero then it reduces to Schwarzschild metric.

3. The action function of the electromagnetic fields

The action function S for the whole system, consisting of an electromagnetic field as well as the particles located in it, must consist of three parts given (page 71, of Landau and Lifshitz [1]) as

$$S = S_f + S_m + S_{mf}, \tag{11}$$

where S_m is that part of the action which depends only on the properties of the particles, that is, just the action of free particles. The quantity S_{mf} is that part of the action which depends on the interaction between the particles and the field. The quantity S_f is that part of the action which depends only on the properties of the field itself, that is, S_f is the action for a field in the absence of charges. Thus S_m, S_{mf} and S_f has the form as

$$S_m = -\sum mc\int ds, \tag{12}$$

$$S_{mf} = -\sum \frac{e}{c}\int A_k dx^k, \tag{13}$$

$$S_f = -\frac{1}{16\pi c}\int F_{ik}F^{ik}d\Gamma. \tag{14}$$

Using equations (12), (13) and (14), the action equation (11) for field and particle can be written as

$$S = -\sum mc \int ds - \sum \int \frac{e}{c} A_k dx^k - \frac{1}{16\pi c} \int F_{ik} F^{ik} d\Gamma, \tag{15}$$

where $d\Gamma = cdt\ dx\ dy\ dz$, is four dimensional volume element. The potential A_k is the potential at that point of space time at which the corresponding particle is located. The potential A_k and electromagnetic field tensor F_{ik}, refer to actual field, that is, the external field plus the field produced by particles themselves; A_k and F_{ik} depends on the positions and velocities of the charges.If we consider charges e to be distributed continuously in space. Then we can introduce the charge density ρ such that ρdV is the charge contained in the volume dV. We can also replace the sum over the charges by an integral over the whole volume.

We can define the current four-vector as

$$j^i = \rho \frac{dx^i}{dt}. \tag{16}$$

The space component of this vector form of the current density vector can be written as

$$\mathbf{j} = \rho \mathbf{v}, \tag{17}$$

where $\mathbf{v}$ is the velocity of the charge at given point. The time component of the current four-vector is $c\rho$. Thus j^i can be written as

$$j^i = (c\rho, \mathbf{j}). \tag{18}$$

Now using equation (16), we can rewrite the second term of the action (as given by equation (15)) as

$$-\sum \int \frac{e}{c} A_k dx^k = -\frac{1}{c} \int \rho \frac{dx^i}{dt} A_i dV dt = -\frac{1}{c^2} \int A_i j^i d\Gamma. \tag{19}$$

On substituting the value of $A_i j^i (= A_0 j^0 - \mathbf{A.J} = c\rho\Phi - \mathbf{A.J})$, the above equation (19) can be written as

$$-\frac{1}{c^2} \int A_i j^i d\Gamma = -\frac{1}{c^2} \int (\Phi c\rho) dV cdt + \frac{1}{c^2} \int \mathbf{A.J}\ dV\ cdt. \tag{20}$$

The energy stored in the magnetic field in S.I. system is given (page 94 of Scheck [14] and page 213-214 of Jackson [15]) as

$$\frac{1}{2c} \int \mathbf{A.J}\ dV = \frac{1}{2\mu_0} \int H^2 dV. \tag{21}$$

In Gaussian system the above equation (21) of magnetic energy can be written as

$$\frac{1}{2c} \int \mathbf{A.J}\ dV = \frac{1}{8\pi} \int H^2 dV. \tag{22}$$

From above equation (22), we can write,

$$\frac{1}{c^2} \int \mathbf{A.J}\ dV = \frac{1}{4\pi\ c} \int H^2 dV. \tag{23}$$

Using equation (23), we can write equation (20) as

$$-\sum \int \frac{e}{c} A_k dx^k = -\frac{1}{c^2} \int (\Phi c\rho) dV cdt + \frac{1}{c^2} \int \mathbf{A.J}\ dV\ cdt = -\frac{1}{c} \int \Phi \rho d\Gamma + \frac{1}{4\pi c} \int H^2 d\Gamma. \tag{24}$$

The above equation (24) is the second term of the action equation (as given by equation (15)). We have (page 73, of Landau and Lifshitz [1]),

$$F_{ik} F^{ik} = 2(H^2 - E^2) = \text{invariant}. \tag{25}$$

Now using the above equation (25), we can write the third term of the action (as given by equation (15)) as

$$-\frac{1}{16\pi\ c} \int F_{ik} F^{ik} d\Gamma = -\frac{1}{16\pi\ c} \int 2\ (H^2 - E^2) d\Gamma. \tag{26}$$

Using equations (24) and (25), the action equation (as given by equation (15)) can be rewritten as

$$S = -\sum mc \int ds - \frac{1}{c}\int \Phi\, \rho\, d\Gamma + \frac{1}{4\pi\, c}\int H^2\, d\Gamma - \frac{1}{8\pi\, c}\int (H^2 - E^2)\, d\Gamma. \tag{27}$$

After Simplification above equation (27) can we written as

$$S = -\sum mc \int ds - \frac{1}{c}\int \Phi\, \rho\, d\Gamma + \frac{1}{8\pi\, c}\int (H^2 + E^2)\, d\Gamma. \tag{28}$$

4. Gravitational redshift

Apsel in 1978 - 1979 had discussed, that the motion of a particle in a combination of gravitational, electrostatic and magnetostatic fields can be determined from a variation principle of the form $\delta \int d\tau = 0$. The field and motion equations are actually identical to Maxwell - Einstein theory. The theory predicted that even in a field free region of space, electro and magneto static potentials can alter the phase of wave function and the life time of charged particle [16, 17]. The space time is a Riemannian space with metric g_{ij}, it is natural to assume that law of motion for a particle in a combination of gravitational and electromagnetic fields ([16, 17]) as

$$\delta \int d\tau = 0, \tag{29}$$

where

$$d\tau = \frac{\sqrt{g_{ij}dx^i dx^j} + \frac{eA_i dx^i}{mc^2}}{c}. \tag{30}$$

The above equation (30) can be rewritten as

$$cd\tau = ds = \sqrt{g_{ij}dx^i dx^j} + \frac{eA_i dx^i}{mc^2}. \tag{31}$$

In case of rotating body, we can use the value of $ds^2 = g_{ij}dx^i dx^j$ for Kerr geometry as given by equation (3). From the analogy given by Apsel in equations (29-31) and using the equation of action (as given by equation (28)), we can write the modified action equation as

$$\tilde{S} = -\sum mc \int \sqrt{g_{tt}c^2dt^2 + g_{rr}dr^2 + g_{\theta\theta}d\theta^2 + g_{\phi\phi}d\phi^2 + 2g_{t\phi}cdtd\phi} - \frac{1}{c}\int \Phi\, \rho\, d\Gamma + \frac{1}{8\pi\, c}\int (H^2 + E^2)\, d\Gamma. \tag{32}$$

Finally, if we consider a rotating star having intense magnetic field (such as pulsars), then we can take an approximation $\Phi = 0$ and E = 0. Now earlier obtained equation of action (32) can be rewritten as

$$\tilde{S} = -\sum mc \int \sqrt{g_{tt}c^2dt^2 + g_{rr}dr^2 + g_{\theta\theta}d\theta^2 + g_{\phi\phi}d\phi^2 + 2g_{t\phi}cdtd\phi} + \frac{1}{8\pi c}\int H^2 d\Gamma. \tag{33}$$

From the above equation (33), we can write new form of $d\tilde{s} = c\, d\tilde{\tau}$ as

$$d\tilde{s} = \sqrt{g_{tt}c^2dt^2 + g_{rr}dr^2 + g_{\theta\theta}d\theta^2 + g_{\phi\phi}d\phi^2 + 2g_{t\phi}cdtd\phi} + \frac{H^2 dV cdt}{8\pi mc^2}. \tag{34}$$

For a sphere, the photon is emitted at a location on its surface where $dr = d\theta = 0$, when the sphere rotates. Now above equation (34) can be written as

$$c\, d\tilde{\tau} = cdt\left[\sqrt{g_{tt} + g_{\phi\phi}(\frac{d\phi}{cdt})^2 + 2g_{t\phi}(\frac{d\phi}{cdt})} + \frac{H^2 dV}{8\pi mc^2}\right] \tag{35}$$

which can be rewritten as

$$\frac{d\tilde{\tau}}{dt} = \sqrt{g_{tt} + g_{\phi\phi}(\frac{d\phi}{cdt})^2 + 2g_{t\phi}(\frac{d\phi}{cdt})} + \frac{H^2}{8\pi \varrho_m c^2}, \tag{36}$$

where, $\varrho_m = m/dV$ is the scalar mass density. $\tilde{\tau}$ and t are proper time and world time respectively. The quantity $\frac{d\phi}{cdt}$ is termed as angular velocity of frame dragging (as discussed in details [9, 10]). In General relativity, redshift Z and redshift factor $\Re$ are defined as [9, 10]

$$\frac{d\tilde{\tau}}{dt} = \frac{\omega_{ob}}{\omega_{em}} = \Re = \frac{1}{Z+1} = \frac{\lambda_{em}}{\lambda_{ob}}, \tag{37}$$

where ω and λ denote frequency and wavelength respectively. Emitter's and observer's frame of reference are indicated by subscripts *em* and *ob*. A redshift Z of zero corresponds to an un-shifted line, whereas $Z < 0$ indicates blue-shifted emission and $Z > 0$ red-shifted emission. A redshift factor $\Re$ of unity corresponds to an un-shifted line, whereas $\Re < 1$ indicates red-shifted emission and $\Re > 1$ blue-shifted emission.

From equation (36) and (37), we can write redshift factor $\Re$ as

$$\Re = \sqrt{g_{tt} + g_{\phi\phi}(\frac{d\phi}{cdt})^2 + 2g_{t\phi}(\frac{d\phi}{cdt})} + \frac{H^2}{8\pi\varrho_m c^2}. \tag{38}$$

The above expression (38) is the expression of gravitational redshift from rotating body having intense magnetic field. The first term of the expression is due to mass and rotation effect, which is gravitational redshift from rotating body and given as

$$\Re_{mass+rotation} = \sqrt{g_{tt} + g_{\phi\phi}(\frac{d\phi}{cdt})^2 + 2g_{t\phi}(\frac{d\phi}{cdt})}. \tag{39}$$

The second term is due to the presence of intense magnetic field in the rotating body, which is an additional magnetic redshift and given as

$$\Re_{mag}(H, \varrho_m) = \frac{H^2}{8\pi\varrho_m c^2}. \tag{40}$$

For a typical neutron star the value of magnetic field is $H \sim 10^{12}$ Gauss and density is $\varrho_m \sim 10^{15} - 10^{16}\ \frac{gm}{c^3}$ (page 293 of Straumann [18]). From equation (40), we can obtain an additional magnetic redshift by using the values of scalar mass density (ϱ_m) and magnetic field (H).

5. Conclusions

In the present work the expression of gravitational redshift from rotating body having intense magnetic field has been derived by using the action function of the electromagnetic fields. The first term of the derived expression is due to mass and rotation effect, which is gravitational redshift from rotating body. While the second term is due to the presence of intense magnetic field in the rotating body, which is an additional magnetic redshift. If we ignore the electric field E and magnetic field H contribution then we can obtain the corresponding expression for redshift factor $\Re$ in Kerr Geometry [9].

References

[1] L. D. Landau and E. M. Lifshitz, *The Classical Theory of Fields*, Vol. 2, 4th revised edition, Butterworth - Heinemann, Indian Reprint (2008).
[2] W. S. Adams, Observatory **48**, 337 (1925).
[3] R. V. Pound and G. V. Jr. Rebka, Phys. Rev. Lett. **3**, 9 (1959).
[4] R. V. Pound and J. L. Snider, Phys. Rev. **140**, 3B (1965).
[5] J. L. Snider, Phys. Rev. Lett. **28**, 13 (1972).
[6] T. P. Krisher, D. Morabito and J. D. Anderson, Phys. Rev. Lett. **70**, 2213 (1993).
[7] P. D. Nunez and M. Nowakowski, J. Astrophys. Astr. **31**, 105 (2010).
[8] F. Payandeh and M. Fathi, Int. J. Theor. Phys. **52 (9)**, 3313 (2013).
[9] A. K. Dubey and A. K. Sen, Int. J. Theor. Phys. **54 (7)**, 2398 (2014).
[10] A. K. Dubey and A. K. Sen, Astrophys Space Sci. **360 (29)**, (2015).
[11] R. P. Kerr, Phys. Rev. Lett. **11**, 237 (1963).
[12] E. T. Newman, E. Couch, K. Chinnapered, A. Exton, A. Prakash and R. Torrence, J. Math. Phys. **6**, 918 (1965).

[13] S. Carroll, *Space time and Geometry*, Vol. 1, Pearson / Addison-Wesley (2004).
[14] F. Scheck, *Classical Field Theory*, Springer - Verlag Berlin Heidelberg (2012).
[15] J. D. Jackson, *Classical Electrodynamics*, 3rd edition, John Wiley and Sons, Inc. (1925).
[16] D. Apsel, International Journal of Theoretical Physics **17**, 8 (1978).
[17] D. Apsel, Gernal Relativity and Gravitation **10**, 4 (1979).
[18] N. Straumann, *General Relativity with applications to Astrophysics*, Springer Verlag (1984).

Charged black hole in the presence of dark energy

Ngangbam Ishwarchandra[a] and Ng. Ibohal[b]

(a) Department of Physics, Manipur University, Imphal - 795003, Manipur, India

(b) Department of Mathematics, Manipur University, Imphal - 795003, Manipur, India

Presenter: Ng. Ibohal (*ngibohal@associates.iucaa.in*); COS.1, Oral, CICAHEP15.38

We discuss exact solutions of Einstein's field equations describing the charged Schwarzschild black hole in two different dark energy backgrounds. These are regarded as embedded solutions that the charged Schwarzschild black hole is embedded into the dark energy spaces producing charged Schwarzschild-dark energy black holes, as Reissner-Nordstrom-dark energy black holes. Here we consider the dark energy solutions having the equation of state parameter $w = -1/2$. It is found that the space-time geometry of solution is non-vacuum Petrov type D in the classification of space-times. We study the strong energy conditions for the energy-momentum tensors of the Reissner-Nordstrom-dark energy solution, which can be able to explain the different between the repulsive gravitational field for *dark energy* as well as the attractive gravitational field for *normal matter* like electromagnetic field. It is also shown that the metric tensor for the Reissner-Nordstrom-dark energy solution can be expressed in two different Kerr-Schild ansatze establishing the fact that the embedded dark energy solution is an exact solution of Einstein's field equations.

1. Introduction

The standard general relativistic interpretation of dark energy is based on the cosmological constant [1], which has the simplest model for a fluid with the equation of state parameter $w = p/\rho = -1$, $\rho = -p = \Lambda/K$ with $K = 8\pi G/c^4$ [2]. It turns out the cosmological constant to be the de Sitter solution with cosmological constant Λ representing a relativistic dark energy with the non-perfect fluid energy-momentum tensor $T_{ab} = 2\,\rho\,\ell_{(a}\,n_{b)} + 2\,p\,m_{(a}\bar{m}_{b)}$, whose trace is $T = 2(\rho - p)$ [3], different from the one, $T^{(\mathrm{pf})} = \rho - 3p$ of the perfect fluid energy-momentum tensor $T^{(\mathrm{pf})}_{ab} = (\rho^* + p)u_a\,u_b - p\,g_{ab}$. This suggests that a relativistic dark energy must have a line-element describing a space-time geometry having gravitational field in the form of energy-momentum tensor possessing a negative pressure with a minus sign in the equation of state parameter. It is also true that a vacuum space-time with $T_{ab} = 0$ cannot have negative pressure to determine the equation of state parameter value with minus sign. Hence, the cosmological constant in *vacuum* Einstein's field equations cannot describe the negative pressure to possess a minus sign in the equation of state parameter. The criteria of minus sign in the equation of state is to indicate the matter distribution in the space-time to be a *dark energy*, otherwise the plus sign in the equation of state is for the *normal matter*. According to the properties of de Sitter solution as relativistic dark energy, there is another relativistic dark energy solution admitting an energy-momentum tensor with the equation of state parameter $w = p/\rho = -1/2$, $\rho = 4m/Kr$, $p = -2m/Kr$, where m is a non-zero constant considered to be the mass of dark energy [4]. It is also to emphasize that the equation of state parameter $w = -1/2$ for the dark energy belongs to the range $-1 < w < 0$ focussed for the best fit with cosmological observations [5] and references there in. Here we shall refer this solution simply as dark energy solution without giving any extra prefix. It is also to note that the energy-momentum tensor with negative pressure for the de Sitter dark energy model violates the strong energy condition, showing the repulsive gravitational field of the matter, whereas the energy-momentum tensor of a normal matter field with positive pressure satisfies the strong energy condition, showing the attractive gravitational field of the matter.

In general relativity the Schwarzschild solution is regarded as a black hole in an asymptotically flat space. Its generalization is the Reissner-Nordstrom black hole. The Reissner-Nordstrom-de Sitter solution is the charged extension of the Schwarzschild-de Sitter solution which is interpreted as a black hole in an asymptotically de Sitter space with the cosmological constant Λ [6]. The Reissner-Nordstrom-de Sitter solution is also considered as an embedded black hole that the Reissner-Nordstrom solution is embedded into the de Sitter space to produce the Reissner-Nordstrom-de Sitter black hole [7]. Here we are looking for an exact solution to describe the Reissner-Nordstrom black hole in the dark energy with the parameter $w = p/\rho = -1/2$ as Reissner-Nordstrom-dark energy black hole. The embedded dark energy solution will be the generalization of Schwarzschild-dark energy black hole [8] .

Here we consider the dark energy solution possessing a non-perfect fluid energy-momentum tensor having an equation of state parameter $\omega = p/\rho = -1/2$ with negative pressure derived in [4]. For deriving the Reissner-Nordstrom-dark energy solution we adopt the mass function expressed in a power series expansion of the radial coordinate [9] as

$$\hat{M}(u,r) = \sum_{n=-\infty}^{+\infty} q_n(u)\, r^n, \tag{1}$$

where $q_n(u)$ are arbitrary functions of retarded time coordinate $u = t - r$. The mass function $\hat{M}(u,r)$ has a powerful role in generating new exact solutions of Einstein's field equations [10]. Wang and Wu [9] have utilized the mass function in deriving *non-rotating* embedded Vaidya solution into other spaces by choosing the function $q_n(u)$ corresponding to the index number n. Further utilizations of the mass function $\hat{M}(u,r)$ have been extended in rotating system and found the role of the number n in generating rotating embedded solutions of the field equations [10]. Here we shall consider the cases of the index number n as $n = 0, -1, 2$. That the value $n = 0$ corresponds to the Schwarzschild solution, $n = -1$ for the charge term and $n = 2$ for the dark energy solution possessing the equation of state parameter $\omega = -1/2$ [4]. These values of n will conveniently combine in order to obtain embedded charged Schwarzschild-dark energy black hole or Reissner-Nordstrom-dark energy black hole. The resulting solution will be an extension of the non-charged Schwarzschild-dark energy black hole discussed in [8], which is again a further extension of the work of [4] with the dark energy when $n = 2$. Here we recall conveniently that the Reissner-Nordstrom-de Sitter black hole is the combination of two solutions corresponding to the index number $n = 0, -1$ (Reissner-Nordstrom) and $n = 3$ (de Sitter), different from the Reissner-Nordstrom-dark energy solution (to be discussed here) with $n = 0, -1, 2$ in the power series expansion of mass function $\hat{M}(u,r)$.

2. Reissner-Nordstrom black hole in dark energy

In this section we shall show the derivation of an embedded Reissner-Nordstrom-dark energy solution to Einstein's field equations. This solution will describe charged Schwarzschild black hole in asymptotically dark energy background as the Reissner-Nordstrom-de Sitter black hole is regarded as a black hole in asymptotically de Sitter space [12]. For deriving an embedded Reissner-Nordstrom-dark energy solution, we choose the Wang-Wu function $q_n(u)$ in the expansion series of the mass function $\hat{M}(u,r)$ as

$$q_n(u) = \begin{cases} M, & \text{when } \ n = 0 \\ -e^2/2, & \text{when } \ n = -1 \\ m, & \text{when } \ n = 2 \\ 0, & \text{when } \ n \neq 0, -1, 2, \end{cases} \tag{2}$$

where M and e are constants. Then, the mass function takes the form

$$\hat{M}(u,r) = \sum_{n=-\infty}^{+\infty} q_n(u)\, r^n = M + r^2 m - \frac{e^2}{2r}. \tag{3}$$

Then using this mass function in general canonical metric in Eddington-Finkestein coordinate system (u, r, θ, ϕ),

$$ds^2 = \Big\{1 - \frac{2\hat{M}(u,r)}{r}\Big\} du^2 + 2du\, dr - r^2 d\Omega^2,$$

with $d\Omega^2 = d\theta^2 + \sin^2\theta\, d\phi^2$, we find a line element

$$ds^2 \;\; = \;\; \Big[1 - r^{-2}\Big\{2r(M + mr^2) - e^2\Big\}\Big]\, du^2 + 2du\, dr - r^2 d\Omega^2, \tag{4}$$

where m is a constant regarded as the mass of the dark energy; and M and e denote the mass and the charge of Reissner-Nordstrom black hole. The line-element will reduce to that of Schwarzschild black hole when $m = e = 0$ with singularity at $r = 2M$, and also it will be that of dark energy when $M = e = 0$ having singularity at $r = (2m)^{-1}$ [4]. The line-element (4) will have a singularity when $g_{uu} = 0$, which has three roots $r = r_i$, $i = 1, 2, 3$. The Reissner-Nordstrom solution has two roots $r = r_\pm$ for $g_{uu} = 0$ when $m = 0$. It is noted that the mass m should not be considered here to be zero for the existence of the dark energy.

The null tetrad components for metric line element are obtained as follows

$$\begin{aligned}
\ell_a &= \delta_a^1, \\
n_a &= \frac{1}{2}\Big[1 - \frac{1}{r^2}\Big\{2r(M+mr^2) - e^2\Big\}\Big]\,\delta_a^1 + \delta_a^2, \\
m_a &= -\frac{r}{\sqrt{2}}\left\{\delta_a^3 + i\sin\theta\,\delta_a^4\right\}
\end{aligned} \tag{5}$$

with the normalization conditions $\ell_a n^a = 1 = -m_a \bar{m}^a$ and other inner products being zero. The above stationary space-time (4) possesses an energy-momentum tensor describing the interaction of dark energy with the electromagnetic field as the source of gravitational field:

$$T_{ab} \;=\; 2\,\rho\,\ell_{(a}\,n_{b)} + 2\,p\,m_{(a}\bar{m}_{b)}, \tag{6}$$

where the quantities are found as

$$\begin{aligned}
\rho &= \frac{4}{Kr}m + \frac{e^2}{Kr^4}, \\
p &= -\frac{2}{Kr}m + \frac{e^2}{Kr^4}.
\end{aligned} \tag{7}$$

These ρ and p are the density and pressure respectively for dark energy interacting with the electromagnetic field. Here K denotes the universal constant $K = 8\pi G/c^4$. The equation (7) indicates that the contribution of the gravitational field to T_{ab} is measured by dark energy mass m and the electric charge e of Reissner-Nordstrom solution. The energy-momentum tensor (6) is calculated from Einstein's field equations $R_{ab} - (1/2)Rg_{ab} = -KT_{ab}$ of gravitational field for the space-time metric (4) as shown in the reference [4].

As in general relativity the physical properties of a space-time geometry are determined by the nature of the matter distribution in the space, it is convenient to express the energy-momentum tensor (6) in such a way that one must be able to understand it easily in order to study the physical properties of the embedded solution. Thus, the total energy-momentum tensor (EMT) for the solution (4) may, without loss of generality, be decomposed in the following form as:

$$T_{ab} = T_{ab}^{(\mathrm{e})} + T_{ab}^{(\mathrm{DE})}, \tag{8}$$

where the EMTs for the electromagnetic field $T_{ab}^{(\mathrm{e})}$ and the dark energy $T_{ab}^{(\mathrm{DE})}$ are respectively given as:

$$\begin{aligned}
T_{ab}^{(\mathrm{e})} &= 2\,\rho^{(\mathrm{e})}\ell_{(a}\,n_{b)} + 2\,p^{(\mathrm{e})}m_{(a}\bar{m}_{b)} \\
T_{ab}^{(\mathrm{DE})} &= 2\rho^{(\mathrm{DE})}\,\ell_{(a}\,n_{b)} + 2p^{(\mathrm{DE})}\,m_{(a}\bar{m}_{b)},
\end{aligned}$$

where the coefficients are as

$$\rho^{(\mathrm{e})} = p^{(\mathrm{e})} = \frac{1}{Kr^4}e^2, \tag{9}$$

$$\rho^{(\mathrm{DE})} = \frac{4}{Kr}m, \quad p^{(\mathrm{DE})} = -\frac{2}{Kr}m. \tag{10}$$

Thus, the equation of state parameters for the dark energy and the electromagnetic field are found as

$$\omega^{(\mathrm{DE})} = \frac{p^{(\mathrm{DE})}}{\rho^{(\mathrm{DE})}} = -\frac{1}{2} \tag{11}$$

$$\omega^{(\mathrm{e})} = \frac{p^{(\mathrm{e})}}{\rho^{(\mathrm{e})}} = 1. \tag{12}$$

These two equations show that the equation of state parameter for dark energy has a minus sign in (11), whereas the electromagnetic field (normal matter) has a plus sign (12) indicating the difference between dark energy and the normal matter.

The energy-momentum tensor (8) satisfies the energy conservation law [3] expressed in Newman-Penrose (NP) formalism [13]

$$T^{ab}{}_{;b} = T^{(\mathrm{e})ab}{}_{;b} + T^{(\mathrm{DE})ab}{}_{;b} = 0. \tag{13}$$

Here T^{ab} itself satisfies the conservation law. On the other hand, we also find that both $T^{(\mathrm{e})ab}$ and $T^{(\mathrm{DE})ab}$ are separately satisfied the same (vide [8]). The above equation (13) shows the fact that the metric of the line element (4) describing embedded Reissner-Nordstrom-dark energy is a solution of Einstein's field equations. We find the trace of the energy momentum tensor T_{ab} (6) as

$$T = 2(\rho - p) = \frac{12}{Kr}m. \tag{14}$$

Here we observe that $\rho - p$ must be always greater than zero for the existence of the dark energy in embedded Reissner-Nordstrom-dark energy solution (4) with $m \neq 0$, (if $\rho = p$ implies that m will vanish). It is found that the charge e does not appear in (14) showing the fact that the trace of the energy-momentum tensor for electromagnetic field always vanishes. The decomposition of energy-momentum tensor (8) indicates the interaction of electromagnetic field $T^{(\mathrm{e})}_{ab}$ with the dark energy $T^{(\mathrm{DE})}_{ab}$ in the Reissner-Nordstrom-dark energy space-time (4).

It is also convenient to write the energy-momentum tensor (6) in terms of time-like u_a $(u^a u_a = 1)$ and space-like v_a $(v^a v_a = -1)$ vector fields as

$$T_{ab} = (\rho + p)(u_a u_b - v_a v_b) - p g_{ab} \tag{15}$$

where $u_a = (1/\sqrt{2})(\ell_a + n_a)$ and $v_a = (1/\sqrt{2})(\ell_a - n_a)$. This is certainly different from the energy-momentum tensor of the perfect fluid $T^{(\mathrm{pf})}_{ab} = (\rho + p)u_a\, u_b - p\, g_{ab}$ with the trace $T^{(\mathrm{pf})} = \rho - 3p$. We observe from the energy densities and the pressures given in (9) and (10) that the energy-momentum tensors for dark energy and electromagnetic field obey the weak energy and the dominant energy conditions given in [8]. However, $T^{(\mathrm{DE})}_{ab}$ violates the strong energy condition

$$p^{(\mathrm{DE})} \geq 0, \quad \rho^{(\mathrm{DE})} + p^{(\mathrm{DE})} \geq 0 \tag{16}$$

due to the negative pressure (10), and implies that the gravitational force of the dark energy is repulsive which may cause the acceleration of the model, like the cosmological constant leads to the acceleration of the expansion of the Universe. But, the energy-momentum tensor for electromagnetic field $T^{(\mathrm{e})}_{ab}$ possessing the positive pressure (9) obeys the strong energy condition leading the attractive gravitational field

$$p^{(\mathrm{e})} \geq 0, \quad \rho^{(\mathrm{e})} + p^{(\mathrm{e})} \geq 0. \tag{17}$$

Here we establish the different between the repulsive gravitational field for *dark energy* as well as the attractive gravitational field for *normal matter* like electromagnetic field.

The non-vanishing tetrad components of Weyl tensor C^a_{bcd} of the embedded Reissner-Nordstrom-dark energy black hole (4) is found as

$$\psi_2 = \frac{1}{r^4}\Big\{ - rM + e^2 \Big\}. \tag{18}$$

The Weyl scalar ψ_2 indicates that the space-time of the embedded solution (4) is Petrov type D in the classification of space-times. The mass m of the dark energy does not appear in (18) which shows the intrinsic property of the conformally flatness of the dark energy, even embedded into the Reissner-Nordstrom black hole.

The Reissner-Nordstrom-dark energy metric can be expressed in Kerr-Schild ansatz on the dark energy background

$$g^{(\mathrm{RNDE})}_{ab} = g^{(\mathrm{DE})}_{ab} + 2Q(r)\ell_a \ell_b \tag{19}$$

where $Q(r) = -Mr^{-1} + e^2 r^{-2}/2$. Here, $g^{(\mathrm{DE})}_{ab}$ is the dark energy metric and ℓ_a is geodesic, shear free, expanding and zero twist null vector for both $g^{(\mathrm{DE})}_{ab}$ as well as $g^{(\mathrm{RNDE})}_{ab}$. The above Kerr-Schild form can also be recast on the Reissner-Nordstrom background as

$$g^{(\mathrm{RNDE})}_{ab} = g^{(\mathrm{RN})}_{ab} + 2\hat{Q}(r)\ell_a \ell_b \tag{20}$$

where $\hat{Q}(r) = -mr$. These two Kerr-Schild forms (19) and (20) show the fact that the Reissner-Nordstrom-dark energy space-time (4) with the mass m of the dark energy is a solution of Einstein's field equations. It is to emphasize the fact that the two metrics $g^{(\mathrm{RN})}_{ab}$ for Reissner-Nordstrom solution and $g^{(\mathrm{DE})}_{ab}$ for dark energy cannot be added in order to obtain $g^{(\mathrm{RNDE})}_{ab}$ as $g^{(\mathrm{RNDE})}_{ab} \neq \frac{1}{2}\Big\{ g^{(\mathrm{RN})}_{ab} + g^{(\mathrm{DE})}_{ab} \Big\}$. It is the fact that in general relativity two physically known solutions cannot be added to derive a new embedded solution.

3. Conclusion

In this paper we proposed an exact solution of Einstein's field equations describing the Reissner-Nordstrom black hole embedded into the dark energy space having negative pressure as Reissner-Nordstrom-dark energy black hole. This embedded solution is the straightforward generalization of Schwarzschild-dark energy solution [8]. Here we have followed the method of generating embedded solutions of Wang and Wu [9] by considering the power index n as $n = 0, -1$ and 2 in the derivation of the solution. Then we calculate all the NP quantities for the line element and find that the embedded space-time possesses an energy-momentum tensor of the electromagnetic field interacting with the dark energy having negative pressure. We have shown the difference between the dark energy and the normal matter (like electromagnetic field) that dark energy has the equation of state parameter with minus sign, whereas the normal matter has the parameter with plus sign. The energy-momentum tensor of the dark energy distribution in the embedded space-time (4) violates the strong energy condition leading to a repulsive gravitational force, whereas that of the electromagnetic field satisfies the strong energy condition producing attractive gravitation field. The metric tensor of Reissner-Nordstrom-dark energy solution is able to express in Kerr-Schild ansatze on different backgrounds (19) and (20) establishing the fact that the Reissner-Nordstrom-dark energy space-time (4) with the mass m of the dark energy is a solution of Einstein's field equations.

The decomposition (8) of energy-momentum tensor (6) indicates the interaction of electromagnetic field with the dark energy. This is one of the remarkable properties of the Reissner-Nordstrom-dark energy that two different matters of distinct physical properties are present in one energy-momentum tensor (6) as the source of gravitational field. It is also seen that the trace of T_{ab} is $T = 2(\rho - p) = 2(\rho^{(\mathrm{DE})} - p^{(\mathrm{DE})})$ which is different from that of perfect fluid $T^{(\mathrm{pf})} = \rho - 3p$. The energy-momentum tensor for the dark energy with negative pressure violates the strong energy condition while that for the electromagnetic field with positive pressure obeys the condition showing the difference between the dark energy and the normal matter (electromagnetic field). In fact the embedded solution (4) possessing a non-perfect fluid energy-momentum tensor may be an example of space-times which are enable to explain how the dark energy is different from the normal matter.

4. Acknowledgement

One of the authors (Ibohal) is thankful to the Inter-University Centre for Astronomy and Astrophysics (IUCAA), Pune for hospitalities during his visit.

References

[1] Durrer, R. and Maartens, R.: *Gen. Rel. Grav.*, **40**, 301–328 (2008).
[2] Padmanabhan, T.: *Gen. Rel. Grav.*, **40**, 529-564 (2008).
[3] Ibohal, N.: *Int. J. Mod. Phys. D*, **18**, 853–863 (2009).
[4] Ibohal, N., Ishwarchandra, N. and Singh, K. Y.: *Astrophys. Space Sci.*, **335**, 581–591 (2011).
[5] Caldwell, R. R., Dave, R. and Steinhardt, P. J.: *Phys. Rev. Lett.* **80**, 1582–1585 (1998).
[6] Gibbons, G. W. and Hawking, S. W.: *Phys. Rev. D*, **15**, 2738–2751 (1977).
[7] Cai, R. G., Ji ,J. Y. and Soh, K. S. *Class Quantum Grav.* **15**, 2783–2793 (1998).
[8] Ishwarchandra, N., Ibohal, N. and Singh, K. Y.: *Astrophys. Space Sci.*, **353**, 633–639 (2014).
[9] Wang, A. and Wu, Y.: *Gen. Rel. Grav.* **31,** 107–114 (1999).
[10] Ibohal, N.: *Gen. Rel. Grav.*, **37**, 19–51 (2005).
[11] Ibohal, N. and Dorendro, L.: *Int. J. Mod. Phys. D* **14**, 1373–1412 (2005), gr-qc/0412132.
[12] Patino, A. and Rago, H.: *Phys. Lett. A* **121**, 329–330 (1987).
[13] Newman, E. T. and Penrose, R.: *J. Math. Phys.*, **3**, 566–578 (1962).
[14] Bousso, R.: *Gen. Relativ. Gravit.* **40**, 607–637 (2008).
[15] Sahni, V.: *Lect, Notes Phys.* **653**, 141–180 (2004); astro-ph/0403324.
[16] Sahni, V. and Starobinsky, A.: *Int. J. Mod. Phys. D*, **15**, 2105–2132 (2006).

COW test of the weak equivalence principle: A low-energy window to look into the noncommutative structure of space-time?

Anirban Saha
Department of Physics, West Bengal State University,Barasat, North 24 Paraganas, West Bengal, India
anirban@iucaa.ernet.in; COS.2, Oral, CICAHEP15.50.2

We construct the quantum mechanical model of an experiment by Colella, Overhauser and Werner (COW), where gravitationally induced quantum-mechanical phase shift in the interference between coherently split and separated neutron de Broglie waves are studied to demonstrated the validity of WEP, assuming that the underlying space time has a granular structure, described by a canonical noncommutative algebra of coordinates x^{μ}. The time-space sector of the algebra is shown to add a mass-dependent contribution to the gravitational acceleration felt by neutron de Broglie waves measured the experiment. This makes time-space noncommutativity a potential candidate which can cause a false-positive signature of the violation of WEP even if the ratio of the inertial mass m_i and gravitational mass m_g is a universal constant. We therefore argue that the COW-type experiments can be used as a probe for the evidence of NC structure of space-time.

1. Introduction

At the Planck scale the space-time is thought to have a granular structure that can be described by a noncommutative (NC) geometry with space-time coordinates x^{μ} satisfying the algebra

$$[x^{\mu}, x^{\nu}] = i\Theta^{\mu\nu}, \tag{1}$$

where $\Theta^{\mu\nu}$ is a constant anti-symmetric tensor. This idea of such NC space-time has gained interest in the recent past when it was commonly realized that the low energy effective theory of D-brane in the background of NS-NS B field lives on noncommutative manifold [1, 2]. Further, in the brane world scenario [3], our space-time may be the world volume of a D-brane, and thus can be described by noncommutative geometry (1). From the physical perspective as well, it has long been suggested that in the Gedanken experiment of localizing events in a space-time with Planck scale resolution, a sharp localization induces an uncertainty in the space-time coordinates which can be naturally described by the noncommutative geometry (1) [4]. Although effects of such a NC structure of space-time may only appear near the string/Planckian scale, we hope that some low energy relics of such effects may exist and their phenomenology can be explored at the level of quantum mechanics (QM) [5, 6, 7, 8, 9, 10].

2. The WEP and its experimental background

The structure of space-time may be best revealed through gravitational interaction. In fact, the central idea of Einstein's general theory of relativity (GTR) is based on the interpretation of gravity as a property of space-time, i.e. its curvature. This interpretation relies upon the Weak Equivalence Principle (WEP) which has its experimental foundation in the universality of free fall (UFF) that demands the following: That the ratio $\frac{m_i}{m_g} = \alpha$ between the inertial mass m_i and gravitational mass m_g, both appearing in the classical equation of motion

$$\ddot{x} = \frac{m_g}{m_i} g = \frac{g}{\alpha} = g' \tag{2}$$

of a freely falling "point like" particle immersed in the nearly homogeneous local gravitational field $g = \frac{GM_E}{{R_E}^2}$ caused by Earth's mass M_E is a universally constant. Here we have ignored the nominal height from ground level h with respect to the Earth's radius R_E. The effect of the Earth's gravitational field g is the gravitational acceleration of the particle $\ddot{x} = g' = \frac{g}{\alpha}$ which, if α indeed is a universal constant and does not vary from one particle species to another, is same for all kind of material particles.

As it happens, most theoretical attempts to connect GTR to standard model allow for violation of the WEP [11]. Naturally, the WEP has a long and persistent history of various kinds of experimental tests. Motivation for this stems from desire to gain insight into some alternative/modified version of GTR. In experimental tests of WEP with macroscopic objects we look for species-dependent value of the gravitational acceleration g' caused by change in the value of α for different particle species. In the Eötvös-type experiments possible violations are parametrised by the Eötvös factor, defined as

$$\eta\left(A,B\right)=\frac{\delta g'\left(A,B\right)}{g'_{average}\left(A,B\right)}=2\frac{\ddot{x}\left(A\right)-\ddot{x}\left(B\right)}{\ddot{x}\left(A\right)+\ddot{x}\left(B\right)} \tag{3}$$

for two macroscopic test masses made of materials A and B. Currently the lowest bound is reached for the elements Beryllium and Titanium, using rotating torsion balances [12], $\eta\left(\mathrm{Be},\mathrm{Ti}\right) < 2.1\times10^{-13}$. Future tests like "MICRO-Satellite à traînée Compensée pour l'Observation du Principe d'Equivalence" (MICROSCOPE) [13], to be launched in 2016 aim at a lower bound of 10^{-15}. In the atomic/subatomic regime using improvements on the earlier Eötvös-type experiments, Dicke *et al* in 1961 concluded that neutrons and protons in nuclei experience the same gravitational acceleration g' within about $2\times10^{-9}g'$ [14] by comparing acceleration of PbC1 (neutron-proton ratio R = 1.45) and of Cu (R = 1.19). That a free neutron experiences the same g' it experiences within a nucleus was experimentally confirmed [15] in 1965 by measuring g' from the difference of fall of two well-collimated beams of high and low velocity neutrons while traversing a long evacuated horizontal flight path. A comparison of neutron scattering lengths, with measurement techniques both dependent[1] and independent[2] of gravity, also leads to a verification of the WEP [16] in 1976. However, these results, though obtained for free neutrons behaving as matter waves, are still a consequence of their classical parabolic path under gravity as required by the correspondence principle and hence no quantum features are involved.

The scenario changed during 1974 to 1979, when Colella, Overhauser and Werner (COW), in a series of experiments [17] demonstrated the validity of WEP using gravitationally induced quantum-mechanical phase shift in the interference between coherently split and separated neutron de Broglie waves at the 2 MW University of Michigan Reactor, the validity of equivalence principle in the so called "quantum limit" was claimed to have been examined. The verification was complimented in 1983 by repeating the experiment in an accelerated interferometer where gravitational effects are compensated [18]. This established that the Schrödinger equation in an accelerated frame predicts a phase shift which agrees with observation as assumed earlier by COW [19] for the validity of strong equivalence principle in the quantum limit. Since then, the WEP in the quantum domain has been verified, time and again, with ever increasing accuracy.

3. COW test and the NC space-time structure

Given the roll of WEP in attributing gravity as a property of the space-time, one may think of the COW experiments a test of the space-time property at the quantum level. Therefore, it will not be surprising if some trace of the granularity of the space-time structure that is believed to exist at the Plank scale resolution, manifest itself, even in the low energy regime where quantum mechanical tests of WEP are currently being performed. In this paper we therefore construct the quantum mechanical theory describing the COW experiment with the assumption that the underlying space-time that we live in has a NC structure described by the relation (1). Our motivation is to investigate if some manifestation of this NC geometry shows up in the observable results. Specifically, we work out the gravity-induced phase-shift which shows a leading order NC contribution. We shall argue that this NC term will lead to an apparent violation of WEP in COW-type test data. We also put forward a suggestion to trace this apparent violation of the WEP to its' NC origin if such COW-type experiments can be performed with different atomic/subatomic particles. That can serve as evidence of the NC structure of space-time.

4. Modeling the COW experiment in NC space-time

We start by discussing how to introduce the NC space-time structure in the system. Since in QM space and time could not be treated on an equal footing, we impose the geometry (1) at a field theoretic level and eventually reduce the theory to quantum mechanics[3]. This allows us to examine the effect of the whole sector of space-time

[1] Slow neutrons reflected from liquid mirrors after having fallen a hight.

[2] By transmission measurements on liquid prob.

[3] This is a reasonable starting point since single particle quantum mechanics can be viewed as the one-particle sector of quantum field theory in the very weakly coupled limit where the field equations are essentially obeyed by the Schrödinger wave function [6].

noncommutativity in an effective noncommutative quantum mechanical (NCQM) theory. Owing to the extreme smallness of the NC parameters the current/near future experiments can only hope to detect the first order NC effects. Since it has been demonstrated in various formulations of NC gravity [20] that the leading NC correction in the gravity sector is second order we can safely assume the Newtonian gravitational field g remains unaltered for all practical purpose.

The NC Schrödinger field theory describing cold neutron beams in Earth's gravitational field (along the x-axis) in a vertical xy $(i = 1, 2)$ plane is

$$\hat{S} = \int d^2xdt\ \hat{\psi}^\dagger \star \left[i\hbar\partial_0 + \frac{\hbar^2}{2m_i}\partial_i\partial_i - m_g g\hat{x} \right] \star \hat{\psi}. \tag{4}$$

Since there is no direct way to relate the physical observables to the NC operators in (4), we consider the NC fields $\hat{\psi}$ as functions in the deformed phase space where ordinary product is replaced by the star product [1, 6] which, for two fields $\hat{\phi}(x)$ and $\hat{\psi}(x)$, is given by

$$\hat{\phi}(x) \star \hat{\psi}(x) = \left(\hat{\phi} \star \hat{\psi}\right)(x) = e^{\frac{i}{2}\theta^{\alpha\beta}\partial_\alpha\partial^{'}_\beta}\hat{\phi}(x)\hat{\psi}(x^{'})\big|_{x^{'}=x}. \tag{5}$$

Due to the linear form of the gravitational potential in action (4), expanding the star product and expressing everything in terms of commutative variables only gives corrections to first order in the NC parameters and all the higher order terms vanish. This leads to an equivalent commutative description of the original NC model in terms of the non-canonical action

$$\hat{S} = \int d^2xdt\psi^\dagger \left[i\hbar\left(1 - \frac{\eta}{2\hbar}m_g g\right)\partial_t + \frac{\hbar^2}{2m_i}{\partial_i}^2 - m_g gx - \frac{i}{2}m_g g\theta\partial_y \right]\psi, \tag{6}$$

where NC effect is manifest by the presence of NC parameter $\Theta^{10} = \eta$ among time and spatial directions. The term with spatial NC parameter $\Theta^{12} = \theta$ and first derivative ∂_y can be absorbed in the ${\partial_y}^2$ and is therefore inconsequential. We use a physically irrelevant rescaling[4] of the fields $\psi \mapsto \tilde{\psi} = \sqrt{\left(1 - \frac{\eta}{2\hbar}m_g g\right)}\psi$ to recast this non-canonical form of action with a conventionally normalized kinetic term such that the fields evolves in a canonical manner. This leads to

$$\hat{S} = \int d^2xdt\ \tilde{\psi}^\dagger \quad \left[i\hbar\partial_t + \frac{\hbar^2}{2m_i\left(1 - \frac{\eta}{2\hbar}m_g g\right)}{\partial_i}^2 - \frac{m_g gx}{\left(1 - \frac{\eta m_g g}{2\hbar}\right)} \right]\tilde{\psi}. \tag{7}$$

Comparing with the standard Schrödinger action we can immediately read off the observed inertial mass as $\tilde{m}_i = 2m_i\left(1 - \frac{\eta}{2\hbar}m_g g\right)$. Assuming the NC effect to be very small the interaction can be written in terms of this observed inertial mass $\tilde{m}_i$ as

$$\frac{m_g gx}{\left(1 - \frac{\eta m_g g}{2\hbar}\right)} = \tilde{m}_i g'x\left(1 + \frac{\eta\tilde{m}_i g'}{\hbar}\right), \tag{8}$$

where we have used equation (2) to replace $m_g g$ with $m_i g'$ [5]. The final form of the canonical action reads

$$\hat{S} = \int d^2xdt\ \tilde{\psi}^\dagger \quad \left[i\hbar\partial_t + \frac{\hbar^2}{2\tilde{m}_i}{\partial_i}^2 - \tilde{m}_i g'x\left(1 + \frac{\eta\tilde{m}_i g'}{\hbar}\right) \right]\tilde{\psi} \tag{9}$$

leading to the equation of motion

$$i\hbar\partial_t\tilde{\psi} = -\left[\frac{\hbar^2}{2\tilde{m}_i}{\partial_i}^2 + \tilde{m}_i g'x\left(1 + \frac{\eta\tilde{m}_i g'}{\hbar}\right) \right]\tilde{\psi} \tag{10}$$

that can be considered at the level of quantum mechanics with $\tilde{\psi}$ interpreted as the Schrödinger wave function.

[4] Since the experimental setup is confined to a small region of space-time where the local gravitational field g is essentially constant, this rescaling amounts to multiplying the field variable by a constant.

[5] Note that replacing $m_g g$ with $m_i g'$ follows from the definition of gravitational acceleration g' for an individual particle, as in (2), and not from the assumption of WEP. WEP is required when we assume that such accelerations for two separate particle species are identical for same gravitational field g.

Equation (10) describes the NCQM of a freely falling neutron in earth's gravity in terms of commutative variables. Thus equation (10) will serve as the desired theoretical model of the COW test constructed in a NC space-time. Note that since we have successfully expressed the equation (10) in terms of the commutative variables completely, bringing out the NC effect explicitly as an additional term in the process, so the principles of ordinary quantum mechanics readily apply to the equation. In the next section we use this equation in context of the COW experiment to calculate the quantum mechanical phase-shift induced by gravity.

5. Analysis of the model: NC effect in the COW phase-shift

We can readily derive the Ehrenfest relations

$$\frac{d}{dt} < x > \;=\; \frac{< p >}{\tilde{m}_i}, \tag{11}$$

$$\frac{d^2}{dt^2} < x > \;=\; g'\left(1 + \frac{\eta \tilde{m}_i g'}{\hbar}\right) = \tilde{g}' \tag{12}$$

for the average velocity and acceleration of the neutrons. Thus, though representing an NC system, this Schrödinger equation (10) behaves similar to that in ordinary/commutative space. However, the two crucial differences with the commutative result are

1. the appearance of observed inertial mass of the neutron $\tilde{m}_i$ in the average momentum (11) and
2. the observed gravitational acceleration $\tilde{g}'$ in (12) experienced by a quantum mechanically behaving system, namely the neutron, is now mass-dependent due to the NC structure of space-time.

Note that contrary to the common expectation that Ehrenfest theorem will lead to results mimicking classical behaviour i.e. a quantum mechanical wave packet will move, on an average, along a classical particle trajectory subject to the applied potential [21], here we have a observable quantum mechanical effect that is not washed out by the averaging process and shows up as a deviation from the classical trajectory. That this effect is of NCQM origin is established by the explicit appearance of the ratio $\frac{\eta}{\hbar}$.

In a COW-type experimental setting the gravitational potential is much smaller than the total energy of the neutrons and we can calculate the gravity induced phase-shift from (10) by the semi-classical prescription of matter-wave interferometry [22, 23]

$$\Delta\varphi_{grav} = -\frac{1}{\hbar}\tilde{m}_i \tilde{g}' \left(l_1 \sin\phi\right) \Delta t, \tag{13}$$

where ϕ is the tilt angle between the plane containing the coherently splitted neutron beams and the horizontal plane, giving rise to an effective height $l_1 \sin\phi$ of one of the neutron beam paths with respect to the other. Since the effective potential is time-independent here we can use the paraxial approximation to compute

$$\Delta t = l_2 / \frac{d}{dt} < x > = \frac{l_2 \tilde{m}_i \lambda_0}{h}, \tag{14}$$

where $\lambda_0 = h/ < p >$ is the laboratory neutron de Broglie wavelength corresponding to the average neutron momentum $< p >$ in (11). Combining (13) and (14) we find

$$\Delta\varphi_{grav} = -\frac{A \sin\phi}{2\pi\hbar^2} \lambda_0 {\tilde{m}_i}^2 \tilde{g}', \tag{15}$$

where $A = l_1 l_2$ is the area enclosed by the interfering beams. This phase difference depends on the mass-dependent $\tilde{g}'$.

Comparing this theoretical prediction (15) with the experimentally measured gravity induced phase-shift one can obtain the *quantum mechanically observed* gravitational acceleration $\tilde{g}'\,(\mathrm{n})$ felt by a neutron. We intend to stress the quantum mechanical nature of the observation because phase-shift is a quantum phenomena and it is only in the quantum regime that any NC effect will be picked up. This data, when confronted with local classical gravitational acceleration g' measured with macroscopic bodies where no NC effect is possible, will exhibit a discrepancy given by

$$\frac{\delta g}{g_{\rm av}} = \frac{\tilde{g}'\left(\mathrm{n}\right) - g'}{g_{\rm av}} = \frac{g'\left(\mathrm{n}\right) - g'}{g_{\rm av}} + \frac{\eta \tilde{m}_i \left(g'\left(\mathrm{n}\right)\right)^2}{\hbar g_{\rm av}}. \tag{16}$$

Here $g'\left(\mathrm{n}\right) = \frac{g}{\alpha(\mathrm{n})}$ is the acceleration the neutron would feel due to Earth's gravitational field g if our space-time followed the ordinary Hisenberg algebra instead of the NC algebra (1). The first term signifies the violation of the WEP, if any, caused by the non-universality of α, i.e. $\alpha\left(\mathrm{n}\right) \neq \alpha$ (macroscopic) and the second term arise as an effect of the NC structure of space-time showing an apparent violation even if α in equation (2) is a universal constant. This sets a limitation on the accuracy to which WEP can be verified at the quantum limit by COW experiments on ultra-cold neutrons.

6. Conclusion

In principle the apparent violation due to NC effect should be identifiable if the COW-type experiments can be performed with different atomic/subatomic particle species. With the first term vanishing/negligible in equation (16), the discrepancy for different species will vary linearly with their masses and the slope $\frac{\eta g'}{\hbar}$ will give the absolute value of the NC parameter. Such a linear variation of discrepancy with particle mass, if indeed observed, will serve to establish the granular structure of the space-time we live in. Of course this holds only if any true violation due to non-universality of α occurs beyond the accuracy level where the NC effect starts affecting the data. In the best case scenario the COW-type experiments and its other variants such as atom-interferometer based on fountain of laser-cooled atoms [24], may open a low-energy "window" to reveal the noncommutative structure of space-time.

7. Acknowledgement

The author would like to thank Patrick Das Gupta for enlightening comments and also the financial support of DST SERB under Grant No. SR/FTP/PS-208/2012.

References

[1] N. Seiberg, E. Witten, [JHEP **09** (1999) 032]; A.A. Bichl*et al*, [hep-th/0102103]
[2] See for example, R.J. Szabo, Phys. Rept. **378** (2003) 207 and the referances therein.
[3] I. Antoniadis, N. Arkani-Hamed, S Dimopoulos, G. Dvali, Phys. Lett. **B 436** 257-263,1998.
[4] S. Doplicher, K. Fredenhagen and J. E. Roberts, Phys. Lett. **B 331** 39 (1994); S. Doplicher, K. Fredenhagen and J. E. Roberts, Commun. Math. Phys. 172, 187 (1995); D.V. Ahluwalia, Phys. Lett. **B 339** 301-303, 1994.
[5] M. Chaichian, M.M. Sheikh-Jabbari, and A. Tureanu, Phys. Rev. Lett. **86**, 2716 (2001).
[6] B. Chakraborty, S. Gangopadhyay, A. Saha, Phys. Rev. **D 70** 107707 (2004).
[7] A. Saha, S. Gangopadhyay, Phys. Lett.**B 681** 96 (2009).
[8] A. Saha, S. Gangopadhyay, S. Saha, Phys. Rev.**D 83** (2011) 025004.
[9] O. Bertolami, J. G. Rosa, C. M. L. de Aragao, P. Castorina, D. Zappala, Phys. Rev. **D 72** (2005) 025010.
[10] A. Saha, Eur. Phys. J.**C 51** 199 (2007).
[11] T. D. Lee and C. N. Yang, Phys. Rev. **98** 1501 (1955); Y. Fujii, Nature (London), Phys. Sci. 234, 5 (1971); P. Fayet, Phys. Lett. **B 171** 261 (1986); T. R. Taylor and G. Veneziano, Phys. Lett. **B 213** 450 (1988); T. Damour and A. M. Polyakov, Nucl. Phys. **B 423** 532 (1994); S. Dimopoulos and G. F. Giudice, Phys. Lett. **B 379** 105 (1996); T. Damour, Class. Quantum Grav. 13 A33 (1996).
[12] S. Schlamminger *et al*, Phys. Rev. Lett. **100** 041101 (2008).
[13] http://microscope.onera.fr/
[14] R. H. Dicke, Sci. Am. 205, 84 (1961); R. H. Dicke, in Relativity, Groups and Topology, edited by C. DeWitt and B. DeWitt (Gordon and Breach Science Publishers, Inc., New York, 1964).
[15] J. W. T. Dabbs, J. A. Harvey, D. Paya, and H. Horstmann, Phys. Rev. **139** B756 (1965).

[16] L. Koester, Phys. Rev. **D 14** 907 (1976).
[17] A. W. Overhauser and B.Colella, Phys. Rev. Lett. 33, 1237 (1974); R.Collela*et al*, Phys. Rev. Lett. 34, 1472 (1975); S. A. Werner *et al*, Phys. Rev. Lett. **42** 1103 (1979).
[18] U. Bonse and T. Wroblewski, Phys. Rev. Lett. **51** 1401, (1983).
[19] J.-L. Staudenmann and S. A. Werner, R. Colella and A.W. Overhouser, Phys. Rev. **A 21** 1419 (1983).
[20] P. Mukherjee, A. Saha, Phys. Rev. **D 74** (2006) 027702 and the references therein.
[21] J.J. Sakurai, *Modern Quantum Mechanics*, Addison Wesley, 2000.
[22] Paul R. Berman, *Atom Interferometry*, Academic Press, 1997.
[23] A. D. Cronin, J. Schmiedmayer and D. E. Pritchard, Rev. Mod. Phys. **81** 1051 (2009).
[24] A. Peters, K. Y. Chung and S. Chu, Nature **400** 849 (1999).

Dynamics of higher dimensional FRW cosmology in $R^p \exp(\lambda R)$ gravity

S. K. Banik, D. K. Banik and K. Bhuyan

Department of Physics, Dibrugarh University, Dibrugarh-786004, Assam, India

Presenter: S. K. Banik (*sebikabanik063@gmail.com*); COS.7, Oral, CICAHEP15.76

We study the cosmological dynamics for $R^p \exp(\lambda R)$ gravity theory in the Metric formalism, using dynamical systems approach. Considering higher dimensional FRW geometries in case of a perfect fluid which exerts same pressure in the normal and extra dimensions, we find the exact solutions, and study their behavior and stability for both in vacuum and matter cases. It is found that stable solutions exist corresponding to accelerated expansion at late times which can describe the inflationary era of the universe. We also study the evolution of the scale factors both in the normal and extra dimensions for different values of anisotropy parameter and the number of extra dimensions for such a scenario.

1. Introduction

$f(R)$ gravity theories have a long history. They can lead to a period of accelerated expansion of the early universe. More recently they are used in cosmology as an alternative to dark energy for explaining the observed late-time accelerated expansion of the universe. In these theories, the Hilbert-Einstein action of General Relativity (GR) is generalized by replacing the Ricci scalar R with a non-linear function $f(R)$ [1]. One of the conditions for viability of $f(R)$ is $f'(R) > 0$, $f''(R) > 0$. Many viable forms of $f(R)$ gravity theories are intensively studied in [1,2].

In earlier epochs, our universe was much smaller and the energy of the universe was typically high enough so that the present four dimensional spacetime could have been preceded by a higher dimensional one. The dynamics of the universe with the extra dimensions will be different as compared to the normal four dimensional one and hence such models could have been a promising mechanism to explain the late time accelerated expansion of the universe. In the recent years many important solutions of Einstein's equations dealing with higher dimensional model have been obtained [3,4]. However, the dynamics of higher dimensional models with $f(R)$ gravity have not been much explored using dynamical system analysis (DSA).

The main aim of this paper is to investigate the phase-space analysis of higher dimensional FRW geometries, in a universe governed by exponential gravity of the form $f(R) = R^p \exp(\lambda R)$, where the parameter λ is an arbitrary real number; considering the matter content as a perfect fluid. The major focus is on the late-time stable solutions. The kinematical quantities such as deceleration parameter, scale factor, shear scalar and matter energy density have also been studied. We examine how the dynamics of the universe evolves with different values of anisotropy parameter as well as the number of extra dimensions.

2. Field Equations

Here we consider the line element for $(1 + 3 + D)$-dimensional spacetime metric as [4]

$$ds^2 = -dt^2 + A^2(t)\delta_{ij}dx^i dx^j + B^2(t)\delta_{IJ}dX^I dX^J, \tag{1}$$

where i, j = 1, 2, 3 denote three normal spatial dimensions and $I, J = 4, 5, ..., (D + 3)$ represent D extra spatial dimensions. $n = D + 3$ represents total spatial dimensions. $A(t)$ and $B(t)$ denote the scale factors in normal dimensions and extra dimensions respectively.

The universe is assumed to be filled with distribution of matter described by energy momentum tensor of a perfect fluid:

$$T_{\mu\nu} = (\rho + P)u_\mu u_\nu - P g_{\mu\nu}, \tag{2}$$

where ρ is the energy density and P is the pressure and u_μ is the $(1 + 3 + D)$-dimensional velocity vector. The Friedmann's Field equation in $(1 + 3 + D)$ dimensions using the metric (1) can be written as

$$\frac{(n-1)}{2n}\Theta^2 - \sigma^2 + \Theta\frac{\dot{f}'}{f'} - \frac{1}{2f}(Rf' - f) - \frac{\rho}{f'} = 0 \tag{3}$$

where,

$$\Theta = n\frac{\dot{a}}{a} = 3\frac{\dot{A}}{A} + D\frac{\dot{B}}{B}, \qquad \sigma^2 = \frac{3D}{2n}\left(\frac{\dot{A}}{A} - \frac{\dot{B}}{B}\right)^2, \tag{4}$$

$$R = 6\frac{\ddot{A}}{A} + 2D\frac{\ddot{B}}{B} + 6\frac{\dot{A}^2}{A^2} + 6D\frac{\dot{A}\dot{B}}{AB} + D(D-1)\frac{\dot{B}^2}{B^2} = 2\dot{\Theta} + \frac{n+1}{n}\Theta^2 + 2\sigma^2 \tag{5}$$

where, Θ, σ and R represent the volume expansion scalar, the shear scalar [5] and the Ricci scalar respectively. $H = \frac{\dot{a}}{a}$ is the Hubble parameter and a is the average scale factor. The dot denotes derivative with respect to time. We may obtain the solutions for the scale factors directly from the Einstein equations as [4, 6]

$$A(t) = a(t)\exp(\Sigma_1 W(t)), \qquad B(t) = a(t)\exp(\Sigma_2 W(t)) \tag{6}$$

where, $W(t)$ is defined as

$$W(t) = \int \frac{dt}{a(t)^n} \tag{7}$$

and the constants Σ_1 and Σ_2 satisfy the relation

$$3\Sigma_1 + D\Sigma_2 = 0. \tag{8}$$

3. Dynamical System Approach

For the implementation of DSA, let us introduce the set of expansion normalized dimensionless variables as:

$$\Sigma = \frac{2n}{n-1}\frac{\sigma^2}{\Theta^2}, \qquad x = \frac{2n}{n-1}\frac{\dot{f}'}{f'\Theta}, \qquad y = \frac{n}{n-1}\frac{R}{\Theta^2}, \qquad z = \frac{n}{n-1}\frac{f}{f'\Theta^2}, \qquad \Omega = \frac{2n}{n-1}\frac{\rho}{f'\Theta^2}. \tag{9}$$

Using the constraint equation $1 - \Sigma + x - y + z - \Omega = 0$, we can investigate the reduced dynamical system in the variables (Σ, y, z, Ω).

The Friedmann equation (3) for $f(R) = R^p \exp(\lambda R)$ can be written as

$$\begin{aligned}
\frac{d\Sigma}{d\tau} &= (n-1)\Sigma\left[-2y + z - \Omega\right], \\
\frac{dy}{d\tau} &= \frac{(n-1)}{2}y\left[\frac{2(n+1)}{n-1} + 2\Sigma - 2y + \frac{(-1+\Sigma+y-z+\Omega)yz}{y^2 - pz^2}\right], \\
\frac{dz}{d\tau} &= \frac{(n-1)}{2}z\left[\frac{3n+1}{n-1} + \Sigma - 3y + z - \Omega + \frac{(-1+\Sigma+y-z+\Omega)y^2}{y^2 - pz^2}\right], \\
\frac{d\Omega}{d\tau} &= \frac{(n-1)}{2}\Omega\left[\frac{1+n(1-2w)}{n-1} + \Sigma - 3y + z - \Omega\right]
\end{aligned} \tag{10}$$

where, the new time variable τ is defined as $\tau = \ln a$.

4. Results

4.1 The vacuum case

For the vacuum case, $\Omega = 0$ $(\rho = 0)$ equation (10) becomes

$$\begin{aligned}
\frac{d\Sigma}{d\tau} &= (n-1)\Sigma\left[-2y + z\right], \\
\frac{dy}{d\tau} &= \frac{(n-1)}{2}y\left[\frac{2(n+1)}{n-1} + 2\Sigma - 2y + \frac{(-1+\Sigma+y-z)yz}{y^2 - pz^2}\right], \\
\frac{dz}{d\tau} &= \frac{(n-1)}{2}z\left[\frac{3n+1}{n-1} + \Sigma - 3y + z + \frac{(-1+\Sigma+y-z)y^2}{y^2 - pz^2}\right].
\end{aligned} \tag{11}$$

In order to find the fixed points we need to set equation (11) equal to zero. For obtaining the basic observable quantities, like deceleration parameter, scale factor and shear for a fixed point we use the formalism based on [7]. The first-order differential equations for Θ and σ in terms of the dynamical variables can be written as

$$\dot{\Theta} = -\left(\frac{n+1}{n-1} + \Sigma_i - y_i\right)\frac{(n-1)\Theta^2}{2n} = -(1+q_i)\frac{\Theta^2}{n}, \tag{12}$$

$$\frac{\dot{\sigma}}{\sigma} = -\frac{(n-1)}{2n}\left(\frac{n+1}{n-1} + \Sigma_i + y_i - z_i\right)\Theta, \tag{13}$$

where $q_i = \frac{n-1}{2}(1 + \Sigma_i - y_i)$ represents the deceleration parameter and $_i$ denotes the evaluation at an specific fixed point.

The fixed points A_v, D_v, E_v and L_v are found to represent power-law solution, while for the points B_v and C_v, we have $\dot{\Theta} = 0$, which implies such points correspond to de Sitter solutions. Only the points on L_v (except for the point at $\Sigma = 0$) have nonzero shear. The fixed points in vacuum case and their solutions i.e., deceleration parameter, scale factor and shear along with their stability are listed in Table 1. The fixed points B_v and C_v (when $n = 2p-1$) are non-hyperbolic with 2D stable manifold. Center manifold theorem is used for these two points, to find their stabilities, since only these two points have the probability to being a solution.

Table 1. Fixed points and their solutions for deceleration parameter, scale factor and shear associated with fixed points in vacuum case. We use the notation $y_* = \frac{p(2np-3n+2p-1)}{(n-1)(p-1)(2p-1)}$, $z_* = \frac{(2np-3n+2p-1)}{(n-1)(p-1)(2p-1)}$ and $\sigma_* = \sigma_0 a_0^{-\frac{1}{2}\left(n+1+\Sigma_*(n-1)\right)} t^{-1}$.

Points /Line	Fixed points (Σ, y, z)	Deceleration parameter (q)	Scale factor (a)	Shear (σ)	Existence	Stability
A_v	$(0,0,0)$	$\frac{n-1}{2}$	$a_0 t^{\frac{2}{n+1}}$	0	always	Non-hyperbolic with 2D unstable manifold
B_v	$\left(0, \frac{n+1}{n-1}, 0\right)$	-1	$a_0 e^{\frac{1}{n}\Theta_0 t}$	0	always	Non-hyperbolic with 2D stable manifold
C_v	$\left(0, \frac{n+1}{n-1}, \frac{2}{n-1}\right)$	-1	$a_0 e^{\frac{1}{n}\Theta_0 t}$	0	always	Non-hyperbolic with 2D stable manifold for $n = 2p-1$ Stable for $\frac{8(n+1)(2p-n-1)}{(n+1)^2-4p} > 0$ for $n \neq 2p-1$
D_v	$\left(0, 0, -\frac{3n+1}{n-1}\right)$	$\frac{n-1}{2}$	$a_0 t^{\frac{2}{n+1}}$	0	$p \neq 0$	Saddle with 2D stable manifold
E_v	$\left(0, y_*, z_*\right)$	$\frac{n-4p^2+4p-1}{2(p-1)(2p-1)}$	$a_0 t^{\frac{2(p-1)(2p-1)}{n-2p+1}}$	0	$p \neq 1, \frac{1}{2}$; $n \neq 2p-1$	Stable for $\frac{2np-3n+2p-1}{(p-1)} > 0$, $\frac{n-2p+1}{(p-1)(2p-1)} > 0$
L_v	$(\Sigma, 0, 0)$	$\frac{n-1}{2}(\Sigma+1)$	$a_0 t^{\frac{2}{n+1+\Sigma(n+1)}}$	σ_*	$\Sigma \geq 0$	Non-hyperbolic with 2D unstable manifold

4.2 The matter case

For matter case the equations of the system in terms of the four variables Σ, y, z and Ω are given by equation (10). In order to find the fixed points we need to set equation (10) equal to zero as done in vacuum case. These fixed points are listed in Table 2. We can find scale factor, shear and energy density for a fixed point in the matter case, using the first-order differential equations of Θ, σ and ρ which are given by

Table 2. Fixed points and their solutions for deceleration parameter, scale factor and shear associated with fixed points in matter case. We use the notation $y_* = \frac{p(2np-3n+2p-1)}{(n-1)(p-1)(2p-1)}$, $z_* = \frac{(2np-3n+2p-1)}{(n-1)(p-1)(2p-1)}$, $\sigma_* = \sigma_0 a_0^{-\frac{1}{2}\left(n+1+\Sigma_*(n-1)\right)} t^{-1}$, $\rho_{*1} = \rho_0 t^{-\frac{2n}{n+1}(1+w)}$ and $\rho_{*2} = \rho_0 e^{-(1+w)\Theta_0 t}$.

Points /Line	Fixed points (Σ, y, z)	Deceleration parameter (q)	Scale factor (a)	Shear (σ)	Energy density (ρ)	Existence
A_m	$(0,0,0,0)$	$\frac{n-1}{2}$	$a_0 t^{\frac{2}{n+1}}$	0	0	always
B_m	$\left(0, \frac{n+1}{n-1}, 0, 0\right)$	-1	$a_0 e^{\frac{1}{n}\Theta_0 t}$	0	0	always
C_m	$\left(0, \frac{n+1}{n-1}, \frac{2}{n-1}, 0\right)$	-1	$a_0 e^{\frac{1}{n}\Theta_0 t}$	0	0	always
D_m	$\left(0, 0, -\frac{3n+1}{n-1}, 0\right)$	$\frac{n-1}{2}$	$a_0 t^{\frac{2}{n+1}}$	0	0	$p \neq 0$
E_m	$\left(0, y_*, z_*, 0\right)$	$\frac{n-4p^2+4p-1}{2(p-1)(2p-1)}$	$a_0 t^{\frac{2(p-1)(2p-1)}{n-2p+1}}$	0	0	$p \neq 1, \frac{1}{2}$; $n \neq 2p-1$
F_m	$\left(0, 0, 0, \frac{1+n(1-2w)}{n-1}\right)$	$\frac{n-1}{2}$	$a_0 t^{\frac{2}{n+1}}$	0	ρ_{*1}	always
G_m	$\left(0, \frac{n+1}{n-1} 0, -\frac{2(1+n+nw)}{n-1}\right)$	-1	$a_0 e^{\frac{1}{n}\Theta_0 t}$	0	ρ_{*2}	always
L_m	$(\Sigma, 0, 0, 0)$	$\frac{n-1}{2}(\Sigma+1)$	$a_0 t^{\frac{2}{n+1+\Sigma_*(n+1)}}$	σ_*	0	$\Sigma \geq 0$

$$\dot{\Theta} = -\left(\frac{n+1}{n-1} + \Sigma_i - y_i\right)\frac{(n-1)\Theta^2}{2n} = -(1+q_i)\frac{\Theta^2}{n}, \tag{14}$$

$$\frac{\dot{\sigma}}{\sigma} = -\frac{(n-1)}{2n}\left(\frac{n+1}{n-1} + \Sigma_i + y_i - z_i + \Omega_i\right)\Theta. \tag{15}$$

$$\dot{\rho} = -(1+w)\rho\Theta \tag{16}$$

where, $w = \frac{P}{\rho}$ is the equation of state parameter.

The fixed points A_m, D_m, E_m, F_m and L_m are found to represent power-law solution, while for the points B_m, C_m and G_m, we have $\dot{\Theta} = 0$, which implies such points correspond to de Sitter solutions. Only the line of fixed points L_m is anisotropic. The fixed points A_m, B_m, C_m, D_m, E_m and the line of fixed points L_m correspond to vacuum solutions ($\rho = 0$). Therefore we find the energy density for the remaining two fixed points F_m and G_m.

4.3 Evolution of the scale factors both in normal and extra dimensions

In order to investigate how the dynamics of the universe evolves we plot the solution of scale factors $A(t)$ and $B(t)$ with respect to time for the anisotropic fixed point taking different values of anisotropy parameter Σ_1 and the number of extra dimensions D in Fig. 1 and Fig. 2. Fig. 1 shows that the expansion in scale factor $A(t)$ in the normal dimension varies too fast if we increase the value of anisotropy parameter Σ_1, which implies that shear helps in expansion. For the same Σ_1, the rate of expansion of scale factor $A(t)$ is reduced if the number of extra dimension D is increased. It indicates that increase in number of extra dimensions reduces the effect of shear and hence reduces expansion. In Fig. 2, the scale factor $B(t)$ in extra dimension flips its behavior from contracting to expanding phase if we decrease Σ_1, but it becomes constant asymptotically. These results are found to be consistent with the results in [4].

5. Conclusions

In vacuum case, we have found that stable de Sitter solutions are present corresponding to isotropic fixed points B_v and C_v, which can describe the accelerated of the present universe and also the inflationary era of earlier universe. Also E_v describes accelerated expansion when $\frac{4p^2-n-4p+1}{n-2p+1} > 0$ and $n > 2p-1$. The solutions associated with the isotropic fixed points A_v, D_v, E_v and line of anisotropic fixed points L_v correspond to decelerated expansion allowing structure formation, but they are not stable. These points are required to be unstable in order to obtain a cosmology evolving towards a dark energy era.

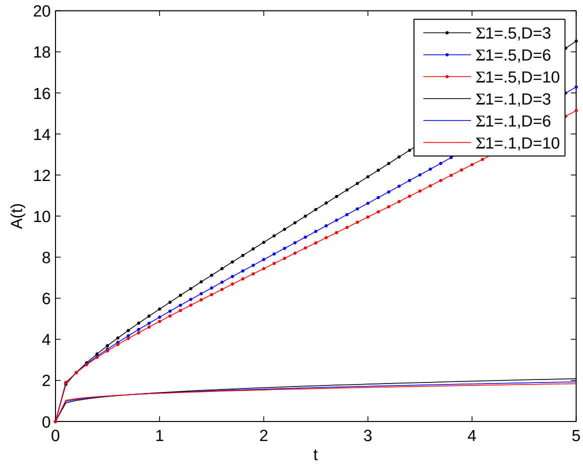

Figure 1. Evolution of scale factor $A(t)$ for different values of Σ_1 and D.

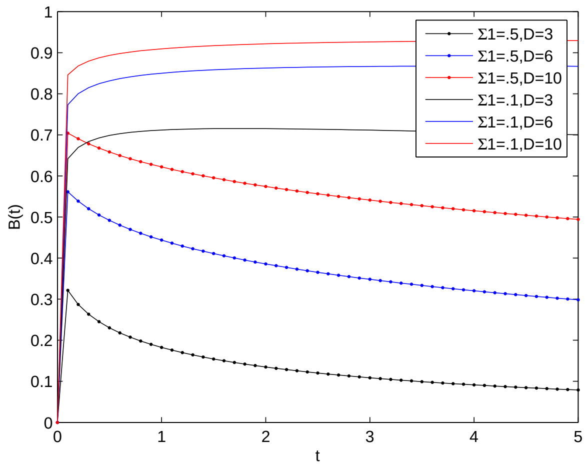

Figure 2. Evolution of scale factor $B(t)$ for different values of Σ_1 and D.

In matter case, the solutions related with the isotropic fixed points B_m, C_m and G_m represent de-Sitter expansions describing accelerated expansion. E_m represents power law solution, but it describes accelerated expansion for $\frac{4p^2-n-4p+1}{n-2p+1} > 0$ and $n > 2p - 1$. Thus, this cosmological model could describe both the inflationary era and the recent acceleration of the universe. The solutions related with the isotropic fixed points A_m, D_m, E_m and the line of anisotropic fixed points L_m corresponds to decelerated expansion of the universe.

Our study for the evolution of scale factors with different number of extra spatial dimensions D and different values of anisotropy parameter Σ_1 shows that shear helps in expansion in the normal spacetime, while increase in the number of extra dimension reduces the effect of shear. The scale factor $B(t)$ in extra dimension flips its behavior from contracting to expanding phase if we decrease Σ_1 but it becomes constant asymptotically.

References

[1] T. P. Sotiriou et al., Rev. Mod. Phy. **82**, 451 (2010); T. Clifton et al., Phys. Rep. **513**, 1 (2012); S. Nojiri et al., Phys. Rep. **505**, 59 (2011); A. D. Felice et al., Living Rev. Rel. **13**, 3 (2010).

[2] L. Amendola et al., Phys. Rev. D **75**, 083504 (2007); S. Carloni et al., Gen. Rel. Grav. **41**, 1757 (2009); G. Leon et al., J. Cosmology Astroparticle Phys. **05**, 032 (2014).
[3] I. Pahwa et al., J. Cosmology Astroparticle Phys. **09**, 015 (2011); K. D. Purohit et al., Int. J. Theor. Phys. **51**, 1329 (2012); Y. C. Huang et al., arXiv:1404.7676v1 [gr-qc] (2014).
[4] I. Pahwa et al., Astrophys. Space Sci. **360**, 58 (2015).
[5] A. Pradhan et al., Rom. Journ. Phys. **57**, 1222 (2012).
[6] D. L. Caceres et al., arXiv:1003.3491 [gr-qc] (2010).
[7] J. A. Leach et al., Class. Quant. Grav. **23**, 4915 (2006); N Chan, Dynamical Systems in Cosmology, Ph.D. Thesis, University College, London, (2012); S. K. Banik et al., Ind. J. Phys. **89**, 11 1213 (2015).

Dynamics of homogeneous, anisotropic Bianchi I cosmology in $f(R)$ gravity in Palatini formalism

D. K. Banik, S. K. Banik and K. Bhuyan

Department of Physics, Dibrugarh University, Dibrugarh-786004, Assam, India

Presenter: D. K. Banik (*debikabanik05@gmail.com*); COS.7, Poster, CICAHEP15.77

We perform a detailed analysis of the dynamics of homogeneous and anisotropic Bianchi I geometries in $f(R)$ gravity theory, formulated within the Palatini formalism, using dynamical systems approach. We find the exact solutions and study the behavior and stability of these solutions. The model based on this theory can produce a sequence of radiation-dominated, matter-dominated and de-Sitter periods. Solutions corresponding to radiation-dominated and matter-dominated are found to be unstable. Stable solutions exist corresponding to accelerated expansion at late times. We also found an anisotropic fixed point which shows the behaviour of shear in this scenario.

1. Introduction

There exist a huge observational evidence which confirmed that our universe is undergoing the late time accelerated expansion era. In order to explain this, different approaches have been adopted. One of such approach is the use of modified gravity models, where gravitational part of Einstein's General Relativity (GR) is changed to explain this acceleration of the present universe. $f(R)$ gravity models [1–4] are one of the simplest models among the various modified gravity models, in which the Lagrangian density in the Hilbert-Einstein action is written in terms of a nonlinear function of Ricci scalar R, which provides extra curvature terms in the field equations.

Depending on the variational principle applied to the action in order to get the field equations, we can have three versions of $f(R)$ gravities. The first one is the usual $f(R)$ gravity in metric formalism [1], in which the action is varied with respect to the metric only, while the connections are the Christoffel symbols, described in terms of the metric. The second one is the $f(R)$ gravity in Palatini formalism [1, 5–7], in which the metric and the connections are considered as independent variables and the action is varied with respect to both the variables, with the assumption that the matter action does not depend on the connection. There exists one more most general formalism known as metric-affine $f(R)$ gravity [1] in which we use the Palatini formalism but abandon the assumption that the matter action is independent of the affine connection.

For the best representation of the present universe, we use the Friedmann-Robertson-Walker (FRW) model [8–10] which is homogeneous and isotropic. However, it is believed that the early universe could have been inhomogeneous and anisotropic. Bianchi type models help us to understand the anisotropy present in the universe. In a recent paper [11] the cosmological dynamics of homogeneous and anisotropic Bianchi I geometries in case of $f(R) = \exp(\lambda R)$ gravity is analysed using the metric formalism.

It is difficult to find exact cosmological solutions in the study of Higher Order Theories of Gravity (HOTG) due to the high degree of non-linearity exhibited by these theories. In the study of cosmology, the use of dynamical systems approach (DSA) [12–14] has the advantage of giving a relatively simple method to find the solutions.

The main objective of this paper is to deal with the Bianchi I cosmological models based on the theories of the type $f(R) = R - \beta/R^n$ using DSA in Palatini formalism. Here we have performed a detailed analysis of the cosmological behaviour by determining all the equilibrium points and then by studying their stability and cosmological evolution.

2. $f(R)$ theories in Palatini formalism:

Let us consider the action for $f(R)$ theory of gravity [5] as follows

$$A = \int d^4x\sqrt{-g}\left[\frac{1}{2\kappa}f(R) + L_m + L_r\right] \tag{1}$$

where, $f(R)$ is a function of the Ricci scalar R, L_m and L_r represent the Lagrangians of the matter and radiation respectively, g is the determinant of metric tensor $g_{\mu\nu}$, $\kappa = 8\pi G$ and G is the gravitational constant. Here we consider Palatini variation of the action, which treats the metric and the affine connection as two independent variables. Varying the action (1) with respect to the metric $g_{\mu\nu}$, the field equation is obtained as [5]

$$f'(R_{\mu\nu}) - \frac{1}{2}f(R)g_{\mu\nu} = \kappa T_{\mu\nu} \tag{2}$$

where, prime denotes the derivatives with respect to R. The energy momentum tensor $T_{\mu\nu}$ is given by

$$T_{\mu\nu} = -\frac{2}{\sqrt{-g}}\frac{\delta(L_m + L_r)}{\delta g_{\mu\nu}}. \tag{3}$$

Varying the action (1) with respect to the connection $\Gamma_{\mu\nu}$, the field equation is obtained as

$$\nabla(\sqrt{-g}f'(R)g^{\mu\nu}) = 0. \tag{4}$$

3. $f(R)$ gravity in Bianchi I metric

The line element of the Bianchi I metric which is homogeneous and anisotropic is given by [11]

$$ds^2 = -dt^2 + A^2(t)dr^2 + B^2(t)[d\theta^2 + \theta^2 d\phi^2] \tag{5}$$

where, $A(t)$ and $B(t)$ are expansion scale factors. $0 \leq r \leq \infty, 0 \leq \theta \leq \pi$, $0 \leq \phi \leq 2\pi$ are the comoving coordinates and t is the cosmological time. For this metric, the generalised Friedmann field equation is

$$\frac{2}{3}f'\left[\theta + \frac{3}{2}\frac{\dot{f}'}{f'}\right]^2 - 2f'\sigma^2 - f = \kappa(\rho_m + \rho_r) \tag{6}$$

where, we have used the following parameters [11]

$$\theta = 3H = \frac{\dot{A}}{A} + 2\frac{\dot{B}}{B}, \qquad \sigma^2 = \frac{1}{3}\left[\frac{\dot{A}}{A} - \frac{\dot{B}}{B}\right]^2 \tag{7}$$

where, θ and σ^2 are the volume expansion scalar and the shear scalar respectively. The Hubble parameter H is defined as $H = \frac{\dot{a}}{a}$, where a is the scale factor and the dot represents the derivative with respect to time. ρ_m and ρ_r are the energy densities of matter and radiation, respectively, which satisfy the conservation equations, given by [5]

$$\dot{\rho}_m + \theta\rho_m = 0, \qquad \dot{\rho}_r + \frac{4}{3}\theta\rho_r = 0. \tag{8}$$

For local rotational symmetry (LRS), the trace free Gauss-Codazzi equation [15] for $f(R)$ gravity is given by

$$\dot{\sigma} = -\left[\theta + \frac{f''\dot{R}}{f'}\right]\sigma. \tag{9}$$

Taking trace of the equation (2) and considering that the trace of the radiative fluid vanishes, we obtain

$$f'R - 2f = -\kappa\rho_m. \tag{10}$$

Using equations (6) - (10), we obtain

$$\dot{R} = \kappa\frac{\theta\rho_m}{f''R - f'} = -\theta\frac{f'R - 2f}{f''R - f'}. \tag{11}$$

Using Eqs. (6) and (11) it can be shown that

$$\theta^2 = \frac{6\kappa(\rho_m + \rho_r) + 3(f'R - f) - 6f'\sigma^2}{2f'\xi} \tag{12}$$

where,

$$\xi = \left[1 - \frac{3}{2}\frac{f''(f'R - 2f)}{f'(f''R - 2f')}\right]^2. \tag{13}$$

4. Dynamical Systems Approach

Let us introduce the following dimensionless variables:

$$x = \frac{3}{2}\frac{(f'R - f)}{f'\xi\theta^2}, \qquad \Sigma = \frac{3\sigma^2}{\xi\theta^2}, \qquad \Omega_r = \frac{3\kappa\rho_r}{f'\xi\theta^2}, \qquad \Omega_m = \frac{3\kappa\rho_m}{f'\xi\theta^2}. \tag{14}$$

The constraint equation can be written as

$$1 = x + \Sigma + \Omega_r + \Omega_m. \tag{15}$$

Differentiating equation (12) and using equations (6) - (13), we find

$$2\frac{\dot\theta}{\theta^2} = 3H = -1 + x - \frac{1}{3}\Omega_r - \Sigma - \frac{f''\dot R}{f'\theta}\Sigma - \frac{f''\dot R}{f'\theta} - \frac{\dot\xi}{\xi\theta} + \frac{3}{2}\frac{f''R\dot R}{f'\xi\theta^3}. \tag{16}$$

Using the variables in equation (14) together with equations (15) and (16), the evolution equations can now be written as follows:

$$\frac{dx}{dN} = x\left[3 - 3x + 3\Sigma + 3C(R)(1-x) + 3D(R)\Sigma\right], \tag{17}$$

$$\frac{d\Sigma}{dN} = \Sigma\left[-3 - 3x + 3\Sigma - 3C(R) + 3D(R)(\Sigma - 1)\right], \tag{18}$$

$$\frac{d\Omega_r}{dN} = \Omega_r\left[-1 - 3x + 3\Sigma - 3C(R) + 3D(R)\Sigma\right] \tag{19}$$

where, $N \equiv \ln a$ and the variables $C(R)$ and $D(R)$ can be written as

$$C(R) = \frac{R\dot f'}{\theta(f'R - f)}, \qquad D(R) = \frac{f''\dot R}{\theta f'}. \tag{20}$$

The effective equation of state (EOS) w_{eff} and the deceleration parameter q are related to the volume expansion scalar θ by

$$\frac{\dot\theta}{\theta^2} = -\frac{1}{2}(1 + w_{eff}), \qquad \dot\theta = (1+q)\frac{\theta^2}{3}. \tag{21}$$

Now using equation (14) in equation (21), gives

$$w_{eff} = -x + \Sigma + \frac{1}{3}\Omega_r + \frac{f''\dot R}{f'\theta}\Sigma + \frac{f''\dot R}{f'\theta} + \frac{\dot\xi}{\xi\theta} - \frac{3}{2}\frac{f''R\dot R}{f'\xi\theta^3}, \tag{22}$$

$$q = -1 + \frac{3}{2}\left[-1 + x - \Sigma - \frac{1}{3}\Omega_r - \frac{f''\dot R}{f'\theta}\Sigma - \frac{f''\dot R}{f'\theta} - \frac{\dot\xi}{\xi\theta} + \frac{3}{2}\frac{f''R\dot R}{f'\xi\theta^3}\right]. \tag{23}$$

Using equations (22) and (23), we can find w_{eff} and q at any fixed point.

5. Cosmological dynamics for $f(R) = R - \beta/R^n$

In this case $C(R)$, $D(R)$ and R can be expressed as

$$C(R) = n\frac{R^{(1+n)} - (n+2)\beta}{R^{(1+n)} + n(n+2)\beta}, \tag{24}$$

$$D(R) = -\frac{[R^{(1+n)} - (n+2)\beta][n(n+2)\beta]}{[R^{(1+n)} + n(n+2)\beta][R^{(1+n)} + n\beta]}, \tag{25}$$

$$R^{(1+n)} = \beta\frac{3x + n(x - \Sigma - \Omega_r + 1) - \Sigma - \Omega_r + 1}{2x}. \tag{26}$$

The fixed points of a system are determined by setting equations (17) - (19) equal to zero. For this type of $f(R)$ the fixed points are given by

Table 1. Fixed points and solutions for equation of states, deceleration parameter, scale factor, shear and eigenvalues associated with the fixed points of $f(R) = R - \beta/R^n$.

Points	Ω_m	EOS (w_{eff})	Deceleration parameter (q)	Scale factor (a)	Shear (σ)	Eigenvalues $[\lambda_1, \lambda_2, \lambda_3,]$
P_{r1}	0	$\frac{1}{3}$	1	$a_0\|t\|^{\frac{1}{2}}$	0	$[4+3n, 1, -2]$
P_{r2}	0	$-\frac{2}{3} - \frac{1}{n}$	$-\frac{1}{2} - \frac{3}{2n}$	$a_0\|t\|^{\frac{2n}{n-3}}$	0	$\left[1, 1, \left(1+\frac{3}{n}\right)\right]$
P_m	1	0	$\frac{1}{2}$	$a_0\|t\|^{\frac{2}{3}}$	0	$[3(1+n), -1, -3]$
P_d	0	-1	-1	$a_0 e^{\frac{1}{3}\theta_0 t}$	0	$[-3, -4, -6]$
P_{s1}	0	1	2	$a_0\|t\|^{\frac{1}{3}}$	$\sigma_0 a_0^{-3}\|t\|^{\frac{2}{3}}$	$[3(2+n), 3, 2)]$
P_{s2}	0	$-1-\frac{2}{n}$	$-1-\frac{3}{n}$	$a_0\|t\|^{-\frac{n}{3}}$	$\sigma_0 a_0^{\frac{3}{n}}\|t\|^{\frac{2}{3}}$	$\left[-\frac{3}{n}, \frac{3}{n}, \left(-1-\frac{3}{n}\right)\right]$

Table 2. Fixed points and their stability for $f(R) = R - \beta/R^n$.

Range	P_{r1}	P_{r2}	P_m	P_d	P_{s1}	P_{s2}
$n < -3$	saddle with 2D stable manifold	unstable	stable	–	saddle with 2D unstable manifold	saddle with 2D unstable manifold
$n = -3$	saddle with 2D stable manifold	non-hyperbolic with 2D unstable manifold	stable	–	saddle with 2D unstable manifold	non-hyperbolic with 2D unstable manifold
$-3 < n < -2$	saddle with 2D stable manifold	saddle with 2D unstable manifold	stable	–	saddle with 2D unstable manifold	unstable
$n = -2$	saddle with 2D stable manifold	saddle with 2D unstable manifold	stable	–	non-hyperbolic with 2D unstable manifold	unstable
$-2 < n < -\frac{4}{3}$	saddle with 2D stable manifold	saddle with 2D unstable manifold	stable	stable	unstable	unstable
$n = -\frac{4}{3}$	non−hyperbolic saddle	saddle with 2D unstable manifold	stable	stable	unstable	unstable
$-\frac{4}{3} < n < -1$	saddle with 2D unstable manifold	saddle with 2D unstable manifold	stable	stable	unstable	unstable
$-1 < n < 0$	saddle with 2D unstable manifold	saddle with 2D unstable manifold	saddle with 2D unstable manifold	stable	unstable	unstable
$n > 0$	saddle with unstable manifold	unstable	saddle with 2D stable manifold	stable	unstable	stable

1. $P_r : (x, \Sigma, \Omega_r) = (0, 0, 1)$
   In this case the numerator and the denominator of equation (26) tend to zero. Therefore we split the analysis into following parts [5]:
   A. $P_{r1} : \beta/R^n \ll 1$
   B. $P_{r2} : \beta/R^n \gg 1$
2. $P_m : (x, \Sigma, \Omega_r) = (0, 0, 0)$
3. $P_m : (x, \Sigma, \Omega_r) = (1, 0, 0)$
4. $P_m : (x, \Sigma, \Omega_r) = (0, 1, 0)$
   In this case also the numerator and the denominator of equation (26) tend to zero; therefore we again split the analysis into following parts:
   A. $P_{s1} : \beta/R^n \ll 1$
   B. $P_{s2} : \beta/R^n \gg 1$

A summary of these fixed points and their associated solutions[13] are listed in Table 1. In order to find the stability of the fixed points we have to linearized the system of equations (17) - (19). The stability of the fixed points in this case are listed in Table 2.

6. Conclusion

In this paper, we have investigated the dynamics of the cosmological models based on the theories of the type $f(R) = R - \beta/R^n$ using DSA in Palatini formalism in case of homogeneous and anisotropic Bianchi I metric. For this model, we have found the exact solutions and study their behaviour and stability in terms of the values of the parameter n. It has been found that isotropic fixed point P_d associated with de-sitter expansion is stable for $n > -2$, which corresponds to accelerated expansion of the universe. The points P_{r1}, P_{r2} describing the radiation dominated era are found to be unstable for all values of n, while the point P_m describing the matter dominated era is also found to be unstable but for $n > -1$. The anisotropic fixed point P_{s1} is unstable for any values of n and the another anisotropic fixed point P_{s2} is unstable for $n < 0$, and shear evolves inversely with time corresponding to these two anisotropic fixed points.

References

[1] T. P. Sotiriou et al., Rev. Mod. Phys. **82**, 451 (2010).
[2] S. Capozziello et al., arXiv: 0909.4672 [gr-qc].
[3] S. Capozziello et al., Gen. Rel. Grav. **40**, 357 (2008).
[4] F. S. N. Lobo, arXiv: 0807.1640 [gr-qc].
[5] S. Fay et al., Phys. Rev. D **75**, 063509 (2007).
[6] D. N. Vollick, Phys. Rev. D **68**, 063510 (2003).
[7] E. E. Flanagan, Phys. Rev. Lett. **92**, 071101 (2004).
[8] S. Carloni et al., Class. Quant. Grav. **22**, 4839 (2005).
[9] M. Abdelwahab et al., Class. Quant. Grav. **25**, 135002 (2008).
[10] S. Carloni et al., Gen. Rel. Grav. **41**, 1757 (2009).
[11] S. K. Banik et al., Ind. J. Phys. **89 (11)**, 1213 (2015).
[12] N. Chan, *Dynamical Systems in Cosmology*, Ph.D. Thesis (University College, London) (2012).
[13] L. Perko, *Differential Equations and Dynamical Systems* (NewYork: Springer) (1996).
[14] S. Wiggins, *Introduction to Applied Nonlinear Dynamical Systems and Chaos* (New York: Springer) (2003).
[15] J. A. Leach et al., Class. Quant. Grav. **23**, 4915 (2006).

Explanation of the accelerated expansion of the universe and dark energy with irreversible thermodynamics*

Debobrata Rajak

Department of Physics, Indian Institute of Technology Hyderabad, Yeddumailaram-502205, Telangana, India

ph15mscst11009@iith.ac.in; *rajak.vishal@yahoo.in*; COS.5, COS.8, Poster, CICAHEP15.99

In this paper, by invoking the laws of irreversible thermodynamics the accelerated expansion of the universe is explained. It is shown that the entropy of the universe, at any particular instant of time, plays a significant role in the accelerated expansion of the universe. Considering the universe to be filled with a classical mono-atomic, homogeneous and isotropic gas under classical non-equilibrium situations, two generalized forces causing the expansion of the universe are arrived at. One of the two forces, the trivial force, has affinity to volume expansion and the non-trivial force has affinity to spatial expansion. The acceleration of the expansion of the universe is due to the spatial expansion caused by the non-trivial force and which in turn might account for the presence of the dark energy. It is shown in this paper that the non-trivial generalized force and the dark energy, providing the negative pressure for spatial expansion, can be explained with irreversible thermodynamics.

1. Introduction

Since the experimental validation of the accelerated expansion of the universe and the associated dimming of the Type Ia supernovae [1], there has been a plethora of theoretical constructions to explain the dynamics of the universe, each one with increasing number of complexities. There are candidates that explain this by assuming the existence of exotic matter with negative pressure, etc. [2, 3, 4, 5, 6].

The homogeneous and isotropic cosmological models based on FLRW metric, having proved to be remarkably successful. But with the introduction of data from WMAP and distant supernova together with the the data from supernovae and galaxy distributions and cosmic microwave background anisotropies lead to introduction of cosmological constant Λ or vacuum energy Ω_Λ [7, 8]. Along these there are other approaches like that of dark energy models which attempt to provide a dynamical explanation of the cosmological constant requiring fine-tuning [6]. Together with modifications on cosmological scales of the general theory of relativity, like that of $f(R)$ gravity theory which is plagued with instabilities in the metric formalism [9]. There are also in-homogeneous cosmological models based on spherically symmetric but in-homogeneous LTB metric [10].

The relation between the pressure P, volume V and the internal energy of an ideal gas is related as $PV = \frac{2}{3}U$. The relation like this, in general, leads to the study of thermodynamics systems of the form $PV = \omega U$, where ω is a constant and can be positive or negative. The accelerating expansion of the universe and the associated dimming of the Type Ia Supernovae is explained by assuming the existence of substances that exert negative pressure, with $\omega < -\frac{1}{3}$ [3, 11]. The cold dark matter candidates of cosmological models are described phenomenologically by $PV = \omega U$, where for $\omega = -1$ corresponds to positive cosmological constant and $\omega < -1$ corresponds to phantom dark energy characterised by null chemical potential [5].

In this article I'll deal only for $\omega = \frac{2}{3}$ which implies a universe filled with monoatomic ideal gas [4]. The normal statistical thermodynamic equations for energy density, entropy density and chemical potential of the universe remains the same as that of an monoatomic ideal gas [3, 4].

2. Entropy and the accelerated expansion of the universe

In nature reversible process are fictive. Rather all the process are irreversible in nature. This comes from the second law of thermodynamics. Which states that the entropy of any isolated system always increases for any process, or mathematically we have $dS \geq 0$ where S is the entropy of the system [12, 15]. Now the universe being an isolated system the entropy of the universes always increases. The Sauckur-Tetrode equation for entropy of a gas obtained

*Best poster presentation in the Cosmology section.

by following the Boltzmann statistic is given as

$$S = \frac{5Nk}{2} + Nk \ln \left[\frac{V(2\pi mkT)^{2/3}}{Nh^3} \right], \tag{1}$$

where $k = 1.381 \times 10^{-23} J/K$ is the Boltzmann constant, V is the volume, T is the temperature, N is the number of particles, m is the mass of the particles and $h = 6.626 \times 10^{-34} m^2 Kgs^{-1}$ [15]. A simple rearrangement of the above equation will yield the volume V of the gas as a function of entropy S given as

$$V = \exp \left[\frac{S}{Nk} - \frac{5}{2} - \ln \frac{(2\pi mkT)^{\frac{3}{2}}}{Nh^3} \right]. \tag{2}$$

Now, since at a given instant at some point of the universe some sort of irreversible process is always going on. As from the second law of thermodynamics it follows that for every single irreversible process the entropy of the universe increases. Due to which the entropy of the universe is a monotonic increasing function of time. The rate of change of entropy S' as $S' = \lim_{\Delta t \to 0} \frac{\Delta S}{\Delta t} = \frac{dS}{dt}$. Since entropy is a non-decreasing function of time hence $S' \geq 0$. On similar grounds we have the second derivative of entropy with respect to time defined as $S'' = \frac{d^2 S}{dt^2}$. From thermodynamics we have the second time derivative of entropy defined as the rate of entropy production and is negative as for any system to attain thermodynamic equilibrium has its entropy maximal. The rate of the expansion of the universe is calculated by differentiating equation (2) with respect to time:

$$V' = \frac{d}{dt} \exp \left[\frac{S}{Nk} - \frac{5}{2} - \ln \frac{(2\pi mkT)^{\frac{3}{2}}}{Nh^3} \right]. \tag{3}$$

Differentiating again gives the acceleration of expansion of the universe and is given as

$$\begin{aligned} V'' = &\left[\left(\frac{S}{Nk} \right)' - \left(\ln \frac{(2\pi mkT)^{\frac{3}{2}}}{Nh^3} \right)' \right]^2 \exp \left[\frac{S}{Nk} - \frac{5}{2} - \ln \frac{(2\pi mkT)^{\frac{3}{2}}}{Nh^3} \right] \\ &+ \left[\left(\frac{S}{Nk} \right)'' - \left(\ln \frac{(2\pi mkT)^{\frac{3}{2}}}{Nh^3} \right)'' \right] \exp \left[\frac{S}{Nk} - \frac{5}{2} - \ln \frac{(2\pi mkT)^{\frac{3}{2}}}{Nh^3} \right]. \end{aligned} \tag{4}$$

On analyzing equation (4) we find that the term, $\exp[\frac{S}{Nk} - \frac{5}{2} - \ln \frac{(2\pi mkT)^{\frac{3}{2}}}{Nh^3}]$ and the squared term, $[(\frac{S}{Nk})' - (\ln \frac{(2\pi mkT)^{\frac{3}{2}}}{Nh^3})']^2$ are always positive as the exponential of any term is always ≥ 0 and the square of any number is also positive. But the term $[(\frac{S}{Nk})'' - (\ln \frac{(2\pi mkT)^{\frac{3}{2}}}{Nh^3})'']$ is negative. Assuming that the term $(\ln \frac{(2\pi mkT)^{\frac{3}{2}}}{Nh^3})''$ is negligible compared to $(\frac{S}{Nk})''$ we have the the second term to be negative as the rate of decrease of entropy is negative.

Although we must have certain contributions due to the $(\ln \frac{(2\pi mkT)^{\frac{3}{2}}}{Nh^3})''$ as the universe was definitely hotter at the beginning than now and thus T' must exist and must be negative and T'' too is negative as the universe cooled rapidly at the beginning than now. Though we know the behavior of T but we don't know the behavior of N, h, k and m. As these might be different at different time of the universe.

3. Generalized force governing the dynamics of universe

In practice, we can consider the universe to be composite thermodynamic system, with identical and non-identical subsystems separated by permeable diathermal wall and non-rigid boundaries. In addition to this I'll consider non-equilibrium situations, where physical quantities like mass, temperature, pressure, etc. are a subject to change in both time and space and the flow of matter and the dynamic change of the various physical parameters of the subsystems are governed by the gradient of the parameters and their time dependence. In this non-equilibrium universe we have spatially homogeneous states, dividing the system into small cells.

To any irreversible thermodynamic process, one can in principle, associate two important types of parameters: one to describe the 'force' that drives the process and the other to describe the 'response' to the force [12, 14]. Again, from irreversible thermodynamics if the extensive parameters of two subsystems of a system are unconstrained then an equilibrium is reached when the affinity vanishes [12, 14, 15]

The universe itself works similar to a composite irreversible thermodynamic system. As in one part of the universe or the other we have some sort of irreversible process happening due to which the entropy of the universe is always increasing.

The processes in the universe being irreversible in nature we can, in principle, safely apply the laws of non-equilibrium thermodynamics. In non-equilibrium thermodynamics if an extensive parameter of two subsystems are unconstrained, an equilibrium is obtained when the affinity vanishes [12, 13, 14].

For a universe that is expanding at an accelerated rate we have the volume to be an extensive parameter that is unconstrained. Hence for an equilibrium to be reached we must have the affinity associated with volume to be zero. The affinity associated with the volume is mathematically defined as $A_v = (\frac{\partial S^0}{\partial V})_{V_0}$ which must be zero for a system to be in an equilibrium state [12]. But if A_v is non zero we have irreversible process taking place which takes the system, here the universe, to a state of equilibrium. A state of equilibrium is also defined as the state at which the entropy of the system, here the universe, is maximum. Thus we can say that the a generalized force that drives the universe can be written as A_v. Or that A_v is the force that causes the accelerated expansion of the universe.The response to the generalized force is defined as the rate of change of the extensive parameter $J_v = \frac{dV}{dt}$ [12, 13, 14].

3.1 Volume element of the expanding universe

The FLRW metric gives the volume element as [16]

$$d^3V = R^3(t)\frac{1}{\sqrt{1-ar^2}}r^2 dr \sin\theta d\theta d\phi. \tag{5}$$

The above metric can be written as

$$dV = dV(k(t,r,\theta,\phi),\tau) = k(t)\tau, \tag{6}$$

where $\tau = r^2 dr \sin\theta d\theta d\phi$ is the normal volume element and $k(t,r,\theta,\phi) = R^3(t)\frac{1}{\sqrt{1-ar^2}}$. Where k is the expansion factor and in general can be a function of both time and space. Signifying that the expansion can vary both spatially and temporally different . Thus from equation (6) can be written as $dV = (\frac{\partial V}{\partial \tau})_k d\tau + (\frac{\partial V}{\partial k})_\tau dk$.

3.2 Affinities of expansion

The rate of production of entropy is given as

$$\frac{dS}{dt} = \frac{\partial S}{\partial V}\frac{dV}{dt}. \tag{7}$$

Substituting $\frac{dV}{dt} = \frac{\partial V}{\partial \tau}_k \frac{d\tau}{dt} + \frac{\partial V}{\partial k}_\tau \frac{dk}{dt}$ in the above equation, we get

$$\frac{dS}{dt} = \frac{\partial S}{\partial V}\left[\frac{\partial V}{\partial \tau}_k \frac{d\tau}{dt} + \frac{\partial V}{\partial k}_\tau \frac{dk}{dt}\right]. \tag{8}$$

Solving further and using the mathematical definition of flux, we have equation (8) to be given as

$$\frac{dS}{dt} = \left(\frac{\partial S}{\partial \tau}\right)_k J_\tau + \left(\frac{\partial S}{\partial k}\right)_\tau J_k. \tag{9}$$

Thus from equation (7) and equation (9) we have the affinity due to volume expansion to be given as $(\frac{\partial S}{\partial \tau})_k = A_k$ and the affinity due to spatial expansion to be given as $(\frac{\partial S}{\partial k})_\tau = A_k$

Where the affinity due to volume expansion $(\frac{\partial S}{\partial \tau})_k = A_k$ is the generalized force responsible for the increase in the mean free path of the constituents due to the actual displacement of the constituents comprising the universe. The response to the affinity $J_\tau = \frac{d\tau}{dt}$ is the response to the affinity which the flux in the universe due to the actual movement of the particles.

The affinity due to spatial expansion $(\frac{\partial S}{\partial k})_\tau = A_k$ is the generalized force responsible for the increase of the space between the constituents of the universe by stretching the fabric of the space itself. The response to the affinity $J_k = \frac{dk}{dt}$ is the flux due to the expansion of the fabric of space itself.

4. Negative pressure and dark energy

From the first law of thermodynamics, we have for a quasi-static process $\delta W = \delta Q - dU$ where, δW is the work done, δQ is the heat exchanged, dU is the change in the internal energy of the system. We have $\delta W = -pdV$. In the above expression if we substitute dV with $dV = (\frac{\partial V}{\partial \tau})_k d\tau + (\frac{\partial V}{\partial k})_\tau dk$ we find,

$$\delta W = -p\left[\left(\frac{\partial V}{\partial \tau}\right)_k\right] d\tau - p\left[\left(\frac{\partial V}{\partial k}\right)_\tau dk\right]. \tag{10}$$

From equation (10) we have the first component $-p[(\frac{\partial V}{\partial \tau})_k]d\tau$ as the normal work done while the second component $-p[(\frac{\partial V}{\partial k})_\tau]dk$ is of some interest as it represents the work done to expand the fabric of the space. Or in other words it is the work done to expand the space between any two particles in an ensemble.

A comparison of the equation (10) with $\delta W = -pdV$ we have $-p[(\frac{\partial V}{\partial \tau})_k]$ is the generalized pressure due to the motion of the constituents while $-p[(\frac{\partial V}{\partial k})_\tau]$ is the generalized pressure due to the expansion of the space.

The work done to expand the space is stored in the fabric of the space. A similar analogy can be derived from the shearing of an iron rod. When one applies a force to expand an iron rod the work done by the force is stored between the molecules of the solid in the form of inter-molecular forces. a similar kind of process happens for the fabric of space. To expand the space fabric one has to do some work which is stored in the fabric of space just like in the case of the of iron rod.

5. Conclusion

The exponential factors present in equation (4) might refer to an inflationary process as the accelerated rate of expansion of the universe is proportional to an exponential factor [2]. But this doesn't refer to an inflationary process because the equation (1) is applicable only after the first elementary particles were formed i.e during the quark epoch. Referring to an era where the universe was filled with the quark gluon plasma as these are fermions and bosons and temperatures was high enough to safely assume them to be a gas of fermions and bosons i.e. the quarks and gluons couldn't have founded any bounded structures. Thus we can safely apply the Sackur-Tetrode equation of entropy for fermions and bosons respectively. Thus the total entropy will then be $S_{total} = S_{fermions} + S_{bosons}$, where S_{total} is the total entropy of the universe and $S_{fermions}$ is the entropy due to fermionic particles and S_{bosons} is the entropy due to bosonic particles. The form $S_{total} = S_{fermions} + S_{bosons}$ can be written as entropy is a extensive parameter. The Sackur-Tetrode equation for entropy thus is valid from the Quark epoch to all way through to the current state of the universe.

From the equation (4) one can predict that the active regions of the universe i.e. regions where the rate of change of entropy $\frac{dS}{dt}$ is very high those regions will have higher red shits compared to the regions where the $\frac{dS}{dt}$ is lower. Though the Hubble's law is not compromised rather along with that if the $(\frac{dS}{dt})$ is higher for a star system the faster will the system recede from us. Thus system like quasars and active galaxies have higher red shifts than the ones which have low $\frac{dS}{dt}$.

Considering the universe as a thermodynamic system under non-equilibrium conditions we see that there are two generalized forces that causes the expansion of the universe. One is a trivial force is the affinity due to volume expansion while the other, the non-trivial one is the affinity due to spatial expansion. This, affinity due to spatial expansion, is also a reason for the accelerated expansion of the universe if not the only.

Initial total energy released during the big bang was either converted into matter or was used to expand the space-time or for other various process. And this accounts for the missing energy or the dark energy as it is also characterized by a negative generalized pressure $-p[(\frac{\partial V}{\partial k})_\tau]$.

References

[1] A. G. Riess et al., Astron. J. **116**, 1009 (1998); S. Perlmutter et al., Astrophys. J. **517**, 565 (1999); P. Astier et al., Astron. Astrophys. **447**, 31 (2006); A. G. Riess et al., Astro. J. **659**, 98 (2007).

[2] A. H. Guth, Phys. Rev. D **23**, 347 (1981).

[3] J. A. S. Lima and S. H. Pereira Phys. Rev. D **78**, 083504 (2008).

[4] S. H. Pereira, arXiv:1002.4584v2.

[5] S. H. Pereira and J. A. S. Lima, Phys. Lett. B **669**, 266 (2008).

[6] E. J. Copeland, M. Sami and S. Tsujikawa, Int. J. Mod. Phys. D **15**, 1753 (2006); N. Straumann, Mod. Phys. Lett. A **21**, 1083 (2006).

[7] D. N. Spergel et al., Astrophys. J. Suppl. **148**, 175 (2003).

[8] A. G. Riess et al., Astrophys. J. **607**, 665 (2004); P. Astier et al., Astron. Astrophys. **447**, 31 (2006).

[9] A. D. Dolgov and M. Kawasaki, Phys. Lett. B **573**, 1 (2003).

[10] Kari Enqvist, arXiv:astro-ph/0709.2044v1.

[11] T. Padmanabhan, Phys. Rept. **380**, 235 (2003); P. J. E. Peebles and B. Ratra, Rev. Mod. Phys. **75**, 559 (2003); J. A. S. Lima, Braz. J. Phys. 34, **194** (2004).

[12] H. B. Callen, *Thermodynamics and an Introduction to Thermostatistics*, J. Wiley, (1985).

[13] H. C. Ottinger, *Beyond Equilibrium Thermodynamics*, J. Wiley,(2005).

[14] I. Prigogine, *Introduction to Thermodynamics of Irreversible Process*, J. Wiley, (1967).

[15] R. K. Pathria and P. D. Beale, *Statistical Mechanics*, Elsevier, (2011); P. B. Pal, *An Introductory Course of Statistical Mechanics*, Narosa Publishing House, (2011).

[16] S. Weinberg, *Cosmology*, Oxford University Press,(2008); P. Sharan, *Spacetime, Geometry and Gravitation*, Hindustan Book Agency,(2009); S. Weinberg, *Gravitation and Cosmology*, J. Wiley (2014).

Thermodynamic origin of the arrow of time in $f(R)$ gravity

M. M. Verma and B. K. Yadav

Department of Physics, University of Lucknow, Lucknow-226007, Uttar Pradesh, India

Presenter: M. M. Verma (*sunilmmv@yahoo.com*); COS.5, Oral, CICAHEP15.107.1

In this work, we determine a connection between the Ricci scalar R and the entropy of the universe in the $f(R)$ gravity models using metric formalism. Since the cosmological arrow of time is associated with entropy production, we show that this connection naturally leads to a time ordering of different phases of the universe. Further, using this approach we explain the dynamics of the universe and also investigate the arrow of time.

1. Introduction

Present universe is in the phase of accelerated expansion [1]. There are many observational evidences, which indicate the presence of hitherto unknown dark energy such as Supernovae Ia, Large-scale structure, Cosmic Microwave Background anisotropies, etc. [1, 2, 3, 4]. By all reckoning, the explanation of present accelerated expansion of the universe is a major challenge in cosmology. There are many approaches to explain its dynamics. The simplest candidate for dark energy is the cosmological constant [5]. However, there are two main problems associated with cosmological constant, viz., (i) the fine tuning problem and (ii) the coincidence problem. Besides cosmological constant, there exist two basic approaches to explain dark energy. The first approach is based on modified matter models. In this approach $T_{\mu\nu}$ in the Einstein equations includes an exotic matter component like quintessence, k-essence, Phantom etc. [6, 7, 8, 9]. The second approach is through modified gravity models wherin the late-time accelerated cosmic expansion is realized without using the explicit dark energy matter component in the universe. In these models, we have a spectrum of $f(R)$ gravity [10], scalar-tensor theories, Gauss-Bonnet dark energy model etc. [11, 12, 13]. Further, in $f(R)$ models, one modifies the laws of gravity by replacing Lagrangian density i.e. scalar curvature R of the Hilbert's action by an arbitrary function of R. At present, there is no specific functional form of R which may satisfy all the conditions of cosmological viability. To achieve this we use the stability conditions of respective eras and determine the corresponding forms of $f(R)$. By solving the field equations for different forms of $f(R)$ for the corresponding eras, the scale factor of expansion is determined. From here we find the scalar curvature R and compare them in different eras. This can lead to the determination of a time-ordering of various epochs, dominated by radiation, matter and dark energy, respectively, throughout the evolution of the universe.

2. Field equations, phase space dynamics and fixed points with radiation

The field equations of $f(R)$ gravity are

$$\begin{aligned} &F(R)R_{\mu\nu} - \frac{1}{2}f(R)g_{\mu\nu}, \\ &-\nabla_\mu \nabla \nu F(R) + g_{\mu\nu}\Box F(R) = \kappa^2 T_{\mu\nu}, \end{aligned} \tag{1}$$

where $F(R) \equiv \frac{\partial f}{\partial R}$ and $T_{\mu\nu}$ is the matter energy-momentum tensor. From these field equations we obtain the following equations:

$$3FH^2 = \kappa^2(\rho_m + \rho_r) + \frac{(FR - f)}{2} - 3H\dot{F}, \tag{2}$$

$$-2F\dot{H} = \kappa^2(\rho_m + \frac{4}{3}\rho_r) + \ddot{F} - H\dot{F}, \tag{3}$$

where ρ_m and ρ_r are energy densities of matter and radiation respectively. The effective equation of state is defined by $w_{eff} = -1 - \frac{2}{3}\frac{\dot{H}}{H^2} = -\frac{1}{3}(2x_3 - 1)$. There are four variables (dimensionless) defined as $x_1 \equiv -\frac{\dot{F}}{FH}$, $x_2 \equiv -\frac{f}{6FH^2}$, $x_3 \equiv \frac{R}{6H^2}$ and $x_4 \equiv \frac{\kappa^2\rho_r}{3FH^2}$

Next, we consider the radiation with other components of universe. In this case we have eight fixed points. Stability about the fixed points (x_1, x_2, x_3, x_4) is determined in the same way as in absence of radiation. Here we have 4×4 matrix of perturbations about each fixed point and four eigenvalues.

(1) Point P_1 corresponds to de-Sitter point. Here $w_{eff} = -1$ and eigenvalues corresponding to this point are

$$-4, \quad -3, \quad -\frac{3}{2} \pm \frac{\sqrt{25 - \frac{16}{m}}}{2}. \tag{4}$$

In the presence of radiation, we have an eigenvalue -4 in addition to those in the absence of radiation. Since this eigenvalue is negative, therefore the condition of stability is the same in both cases. P_1 is stable when $0 < m\ (q = -2) < 1$. This point may be taken as an acceleration point. The condition of stability for this point is same as in the case of without radiation because here we have only an extra eigenvalue -4, which is negative.

(2) Point P_2 is denoted by ϕ-matter-dominated (ϕ MDE) epoch. The eigenvalues corresponding to this point are given by

$$-2, \quad -1, \quad \frac{1}{2}\left[7 + \frac{1}{m} - \frac{m'}{m^2}q(1+q) \mp \sqrt{\left(7 + \frac{1}{m} - \frac{m'}{m^2}q(1+q)\right)^2 - 4\left(12 + \frac{3}{m} - \frac{m'}{m^2}q(3+4q)\right)}\,\right]. \tag{5}$$

P_2 is either saddle or stable point. In this case P_2 can not be a matter point because $\Omega_m = 2$ and $w_{eff} = \frac{1}{3}$.

(3) Point P_3 is known as kinetic point. The eigenvalues for the 4×4 matrix of perturbations about this point are

$$1, \quad 2, \quad \frac{1}{2}\left[9 + \frac{1}{m} - \frac{m'}{m^2}q(1+q) \mp \sqrt{\left(9 - \frac{1}{m} + \frac{m'}{m^2}q(1+q)\right)^2 - 4\left(20 - \frac{5}{m} - \frac{m'}{m^2}q(5+4q)\right)}\,\right]. \tag{6}$$

. If m is constant, the eigenvalues corresponding to this point are $2, 5, 4 - \frac{1}{m}$. In this case P_3 is unstable for $m < 0$ and $m > \frac{1}{4}$ and a saddle otherwise.

(4) Point P_4 has eigenvalues

$$-5, \quad -4, \quad -3, \quad 4(1 + \frac{1}{m}). \tag{7}$$

It is stable for $-1 < m < 0$ and saddle otherwise. This point can not be use as a radiation or a matter dominated point.

(5) Point P_5 can be regarded as a standard matter point in the limit $m \to 0$. Eigenvalues for point P_5 are given by

$$-1, \quad 3(1+m'), \quad \frac{-3m \pm \sqrt{m(256m^3 + 160m^2 - 31m - 16)}}{4m(m+1)}, \tag{8}$$

where m' is derivative of m w.r.t. q. For a cosmologically viable trajectory, we want a saddle matter point. The condition for a saddle matter epoch is given by $m(q \le -1) > 0, m'(q \le -1) > -1,$
$m(q = -1) = 0.$

(6) Point P_6 can also be an acceleration dominated point. The eigenvalues corresponding to this point are given by

$$-\frac{2(-1+2m+5m^2)}{m(1+2m)},\quad -4+\frac{1}{m},$$
$$\frac{2-3m-8m^2}{m(1+2m)},\quad -\frac{2(m^2-1)(1+m')}{m(1+2m)} \tag{9}$$

Stability of this point depends on both m and m'. Condition of acceleration $(w_{eff} < -\frac{1}{3})$ depends on the value of m.

(7) Point P_7 corresponds to a standard radiation point. The eigenvalues of P_7 for constant m are $4, 4, 1, -1$. Thus, P_7 is a saddle point.

(8) Point P_8 also is a radiation point. In this case dark energy is non-zero, therefore P_8 is acceptable as a radiation point. The eigenvalues of P_8 are given by

$$1,\quad 4(1+m'),\quad \frac{m-1\pm\sqrt{81m^2+30m-15}}{2(m+1)}. \tag{10}$$

Point P_8 is a saddle point in the limit $m \to 0$. The acceptable radiation dominated point P_8 lies at point $(0,-1)$ in the (m,q) plane.

3. Dynamics of radiation dominated phase

For radiation dominated era, phase space analysis shows that we can find a radiation point in the limit $m \to 0$ at point P_8. This point lies on the line $m = -q-1$ in the (m,q) plane. Hence, the necessary condition for this point to exist as an exact standard radiation point is given by $m\ (r=-1) \approx 0$. From definition of q and the above condition, the form of $f(R)$ for radiation dominated era is given by $f(R) = \alpha R$ where α is an integration constant. Standard radiation point is obtained by substitution of $m \approx 0$ in the radiation point of $m(q)$ curve. In this condition, the effective equation of state is $w_{eff} = \frac{1}{3}$. The Hubble parameter $H(t)$ is given by $H = \frac{1}{(2t-c_1)}$ where c_1 is an integration constant. The scale factor $a(t)$ for this era is given by

$$a(t) = c_2(2t-c_1)^{\frac{1}{2}}, \tag{11}$$

where c_2 is another integration constant.

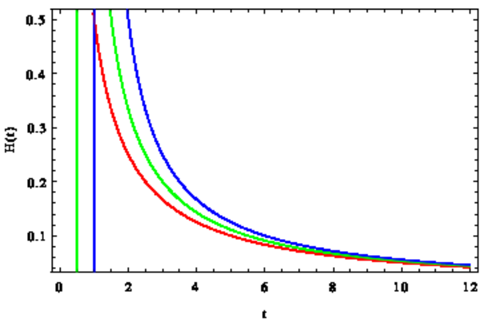

Figure 1. Plot for variation of Hubble parameter $H(t)$ with cosmic time t in radiation dominated phase.The red, green and blue curves correspond to $c_1 = 0, c_1 = 1, c_1 = 2$ respectively.

In radiation dominated phase we examine that the scale factor $a(t) \propto t^{\frac{1}{2}}$, which is same as in the case of standard model. Fig. (1) shows variation of Hubble parameter $H(t)$ with time t in radiation phase. The Ricci scalar R for radiation dominated era is given by $R = 0$.

4. Dynamics of matter dominated era

In phase space analysis of dynamical system, there is a point P_5 which represents a standard matter era in the limit $m \to 0$. In matter dominated phase of the Universe $m\ (q = -1) \approx 0$. Using the definition of q or m, the form of $f(R)$ is given by $f(R) = \beta R$, where β is a integration constant. Thus, in matter dominated phase the form of $f(R)$ is similar as in the case of radiation dominated phase. In matter dominated phase, we neglect the energy density of radiation i.e. $\rho_r = 0$. For $f(R) = \beta R$, $F = \beta$ and therefore $\dot{F} = 0$. The Hubble parameter is given as $H(t) = \frac{1}{(\frac{3}{2}t - c_3)}$, where c_3 is an integration constant. Scale factor in this phase is given by the expression $a(t) = c_4 \left(\frac{3}{2}t - c_3\right)^{\frac{2}{3}}$. The Ricci scalar in matter-dominated phase is given by $R = \frac{3}{(\frac{3}{2}t - c_3)^2}$. The variation of Hubble parameter $H(t)$, scale factor $a(t)$ and Ricci scalar R. Hubble parameter$H(t)$, scale factor $a(t)$ and Ricci scalar R in this phase can also be calculated by the same procedure as we followed in the radiation era. Expressions for these parameters are same in both approaches. For $m \approx 0$, the effective equation of state is given by

$$w_{eff} = 0. \tag{12}$$

These expressions of scale factor $a(t)$, Hubble parameter $H(t)$ and Ricci scalar R in matter dominated phase are similar to the expressions of standard (ΛCDM) model.

5. Arrow of time

We rewrite the action in the form:

$$\mathcal{A} = \int \sqrt{-g} \left(\frac{1}{2\kappa^2} FR - U \right) d^4x + \mathcal{A}_m, \tag{13}$$

where $U = \frac{FR - f}{2\kappa^2}$. It is possible to derive an action in the Einstein frame under the conformal transformation $\tilde{g}_{\mu\nu} = \Omega^2 g_{\mu\nu}$, where Ω^2 is the conformal factor and a tilde represents quantities in the Einstein frame. Relation between Ricci scalars in two frames is $R = \Omega^2(\tilde{R} + 6\tilde{\Box}\omega - 6\tilde{g}^{\mu\nu}\partial_\mu\omega\partial_\nu\omega)$, where $\omega \equiv \ln\Omega, \partial_\mu\omega \equiv \frac{\partial\omega}{\partial\tilde{x}^\mu}, \tilde{\Box}\omega \equiv \frac{1}{\sqrt{-\tilde{g}}}\partial_\mu(\sqrt{-\tilde{g}}\tilde{g}^{\mu\nu}\partial_\nu\omega)$. Now the action (13) is transformed as

$$\mathcal{A} = \int d^4x \sqrt{-\tilde{g}} \left[\frac{1}{2\kappa^2} F\Omega^{-2}(\tilde{R} + 6\tilde{\Box}\omega - 6\tilde{g}^{\mu\nu}\partial_\mu\omega\partial_\nu\omega) - \Omega^{-4}U \right] + \mathcal{A}_m. \tag{14}$$

We obtain the linear action in $\tilde{R}$ for the choice $\Omega^2 = F$. Let us consider a new scalar field ϕ defined by $\kappa\phi \equiv \sqrt{\frac{3}{2}}$. Now using these relations we get the action in Einstein frame is

$$\mathcal{A} = \int d^4x \sqrt{-\tilde{g}} \left[\frac{1}{2\kappa^2}\tilde{R} - \frac{1}{2}\tilde{g}^{\mu\nu}\partial_\mu\phi\partial_\nu\phi - V(\phi) \right] + \mathcal{A}_m, \tag{15}$$

where

$$V(\phi) = \frac{U}{F^2} = \frac{FR - f}{2\kappa^2 F^2}. \tag{16}$$

On varying the action (15) w.r.t. ϕ we get

$$\frac{d^2\phi}{d\tilde{t}^2} + 3\tilde{H}\frac{d\phi}{d\tilde{t}} + V_{,\phi} = 0. \tag{17}$$

The energy density and pressure of a homogeneous scalar field are respectively,

$$\rho = \frac{1}{2}\dot{\phi}^2 + V(\phi), \;\; p = \frac{1}{2}\dot{\phi}^2 - V(\phi) \tag{18}$$

and the scalar field equation of motion is given by equation (17).

Tolman described a cyclic universe with progressively larger cycles, assuming the presence of a viscous fluid with pressure $p = p_0 - 3\zeta H$, where p_0 is the equilibrium pressure and ζ is the coefficient of bulk viscosity. It is clear from this equation that $p < p_0$ during expansion $(H > 0)$ whereas $p > p_0$ during contraction. This asymmetry during the expanding and contracting phases results in the growth of both energy and entropy. This increase in entropy makes the amplitude of successive expansion cycles larger leading to a arrow of time.

The term $3\tilde{H}\frac{d\phi}{dt}$ in (17) behaves like friction and damps the motion of the scalar field when the universe $(H > 0)$. In a contracting universe $3\tilde{H}\frac{d\phi}{dt}$ behaves like anti-friction and accelerates the motion of the scalar field. A scalar field with the potential $V = m^2\phi^2$ gives $p \simeq -\rho$ when $(H > 0)$ and $p \simeq \rho$ when $(H < 0)$. These results are similar to that of the Tolman.

6. Conclusion

We conclude that the nature of the fixed points with radiation remains unaltered as that without radiation (except that with radiation we have the emergence of an extra eigenvalue for each point). The forms of $f(R)$ for different phases have been determined by using the conditions of phase space analysis for a cosmologically viable model. The Hubble parameter $H(t)$, Ricci scalar R have been determined for radiation-, matter- and acceleration-dominated phases of the universe, with a view that their time-ordering may explain an arrow of time throughout the cosmic evolution in a future study. These parameters are found to be consistent with Λ cold dark matter (ΛCDM) model. The time ordering in various phases defines an arrow of time and may be further investigated as an emergent phenomenon.

7. Acknowledgement

MMV thanks Edward Kolb at the Kavli Institute of Cosmological Physics, the University of Chicago, for hosting the visit and useful discussions.

References

[1] A. G. Riess et al., (Supernova Search Team Collaboration), Astron. J. **116**, 1009 (1998).
[2] B. Schmidt et al., Astrophys. J. **507**, 46 (1998).
[3] S. Perlmutter et al., Astrophys. J. **517**, 565 (1999).
[4] D. N. Spergel et al., Astrophys. J. Suppl. **148**, 97 (2003).
[5] T. Padmanabhan, Phys. Rept., **380**, 235 (2003).
[6] R. R. Caldwell, R. Dave, and P. J. Steinhardt, Phys. Rev. Lett. **80**, 1582 (1998).
[7] S. Capozziello, Int. J. Mod. Phys. D **11**, 483 (2002)
[8] T. Chiba, T. Okabe, and M. Yamaguchi, Phys. Rev. D **62**, 023511 (2000).
[9] R. R. Caldwell, Phys. Lett. B **545**, 23 (2002).
[10] A. A. Starobinski, Phys. Lett. B **91**, 99(1980).
[11] M. Kunz and D. Sapone, Phys. Rev. Lett. **98**, 121301 (2007).
[12] L. Amendola, R. Gannouji, D. Polarski and S. Tsujikawa, Phys. Rev. D **75**, 083504 (2007).
[13] V. Sahni and Y. Shantov, JCAP **0311**, 014 (2003).

Thermodynamics of interacting tachyonic scalar field

S. D. Pathak[a], M. M. Verma[b] and Shiyuan Li[a]

(a) School of Physics, Shandong University, Jinan-250100, China

(b) Department of Physics, University of Lucknow, Lucknow-226007, Uttar Pradesh, India

Presenter: M. M. Verma (*sunilmmv@yahoo.com*); COS.5, Poster, CICAHEP15.107.2

In this paper, we discuss the laws of thermodynamics for interacting tachyonic scalar field. The components of the tachyonic scalar field in the universe are taken to exist in the state of non-equilibrium initially, but due to interaction they undergo a transition towards the equilibrium state. We show that the zeroth law of thermodynamics demands interaction among the components of cosmic field. The second law of thermodynamics is governing dynamics in transfer of energy among the three components of the proposed field with local violation of conservation of energy for individual components.

1. Introduction

The accelerated expansion of the universe is revealed by a large number of cosmological observations [1] and can be understood by introduction of repulsive gravity, although the other alternatives [2] may also explain such expansion. The repulsive gravity demands some different types of entities which have negative pressure. Considering its repulsive character such type of entity is called dark energy.

A class of scalar fields is one of the promising candidates of dark energy. Among themselves tachyonic scalar field appearing in the context of string theory [3] is logically more appealing than its counterpart quintessence due to its relativistic Lagrangian as analogue of particles. Cosmological relevance of this field has been studied by several authors during last few decades [4]. Action and Lagrangian of the cosmological tachyonic scalar field is given by

$$\mathcal{A} = \int d^4x\sqrt{-g}\left(\frac{R}{16\pi G} - V(\phi)\sqrt{1-\partial^i\phi\partial_i\phi}\right) \tag{1}$$

with Lagrangian $L = -V(\phi)\sqrt{1-\partial_i\phi\partial^i\phi}$ and the equation of motion of the field is found by varying the action as

$$\frac{\ddot{\phi}}{\dot{\phi}} + \frac{(1-\dot{\phi}^2)V'(\phi)}{\dot{\phi}V(\phi)} + 3H(1-\dot{\phi}^2) = 0. \tag{2}$$

The stress energy tensor for this Lagrangian is

$$T^{ik} = \frac{\partial L}{\partial(\partial_i\phi)}\partial^k\phi - g^{ik}L. \tag{3}$$

This gives energy density and pressure respectively for spatially homogeneous field as

$$\rho = \frac{V(\phi)}{\sqrt{1-\dot{\phi}^2}}, \qquad P = -V(\phi)\sqrt{1-\dot{\phi}^2}. \tag{4}$$

2. Components of field

We assume that radiation with equation of state $w_r = 1/3$ also exists as one inherent component of same tachyonic scalar field. Due to some physical mechanism not known in detail at present to us, the cosmic tachyonic scalar field may be decomposed into several components with the assumption that the field is spatially homogeneous. we can write the expressions for energy density and pressure as

$$P = -\frac{V(\phi)}{\sqrt{1-\dot{\phi}^2}} + \frac{\dot{\phi}^2V(\phi)}{\sqrt{1-\dot{\phi}^2}} + 0, \tag{5}$$

$$\rho = \frac{V(\phi)}{\sqrt{1-\dot{\phi}^2}} + \frac{3\dot{\phi}^2 V(\phi)}{\sqrt{1-\dot{\phi}^2}} - \frac{3\dot{\phi}^2 V(\phi)}{\sqrt{1-\dot{\phi}^2}}. \tag{6}$$

From (5) and (6) it is seen that when we include radiation in tachyonic scalar field then one new exotic component also appears (say, exotic matter since its energy density is negative) with zero pressure. Thus, the tachyonic scalar field resolves into three components say a, b and c. The pressure and energy density of a is given as

$$P_a = -\frac{V(\phi)}{\sqrt{1-\dot{\phi}^2}}, \quad \rho_a = \frac{V(\phi)}{\sqrt{1-\dot{\phi}^2}} \Rightarrow w_a = -1 = w_\lambda.$$

This is nothing but the 'true' cosmological constant because of its equation of state being $w_\lambda = -1$. The second component with

$$P_b = \frac{\dot{\phi}^2 V(\phi)}{\sqrt{1-\dot{\phi}^2}}, \quad \rho_b = \frac{3\dot{\phi}^2 V(\phi)}{\sqrt{1-\dot{\phi}^2}} \Rightarrow w_b = 1/3$$

can be identified as radiation with $w_r = 1/3$. The last component is characterised by

$$P_c = 0, \quad \rho_c = -\frac{3\dot{\phi}^2 V(\phi)}{\sqrt{1-\dot{\phi}^2}} \Rightarrow w_c = 0.$$

This component mimics dust matter but has negative energy density. The exotic matter may include the Dirac fermions as well as the Majorana fermions whence the negative energy states turn into the positive energy states [5, 6]. In our earlier work [7] we allowed a small time dependent perturbation in the equation of state (EoS) of the cosmological constant with $\bar{w}_\lambda = -1 + \varepsilon\ (t)$. Thus, with the perturbed EoS, the true cosmological constant becomes a shifted cosmological parameter. This has a bearing upon the EoS of radiation and exotic matter, both. Therefore, these two entities turn into shifted radiation and shifted exotic matter respectively. With fixed energy density of field components, the expressions for the energy density and pressure of each component are given as below. For the shifted cosmological constant one has

$$\bar{\rho}_\lambda = \frac{V(\phi)}{\sqrt{1-\dot{\phi}^2}}, \qquad \bar{p}_\lambda = \frac{-V(\phi)}{\sqrt{1-\dot{\phi}^2}} + \frac{\varepsilon V(\phi)}{\sqrt{1-\dot{\phi}^2}} \tag{7}$$

and $\bar{w}_\lambda = -1 + \varepsilon\ (t)$. For shifted radiation, we have

$$\bar{\rho}_r = \frac{3\dot{\phi}^2 V(\phi)}{\sqrt{1-\dot{\phi}^2}}, \qquad \bar{p}_r = \frac{(1+3\varepsilon)\dot{\phi}^2 V(\phi)}{\sqrt{1-\dot{\phi}^2}}. \tag{8}$$

In presence of perturbation the zero pressure of exotic matter turns into negative non-zero pressure due to shifted exotic matter which would also accelerate the universe like dark energy. Thus, the energy density and pressure for shifted exotic matter are now, respectively, given as

$$\bar{\rho}_m = \frac{-3\dot{\phi}^2 V(\phi)}{\sqrt{1-\dot{\phi}^2}}, \qquad \bar{p}_m = p_\phi - \bar{p}_\lambda - \bar{p}_r = \frac{-\varepsilon(1+3\dot{\phi}^2)V(\phi)}{\sqrt{1-\dot{\phi}^2}} \tag{9}$$

with $\bar{w}_m = \frac{\varepsilon\ (1+3\dot{\phi}^2)}{3\dot{\phi}^2}$.

3. Thermodynamical laws for interacting components

Why must the components of cosmic field interact? This is one of the most interesting questions about interaction. Interaction might be justified by thermodynamical considerations [8]. As shown by obvious observations, the cosmic field must include at least three components representing matter, dark energy and radiation (many other components are also possible) and behave as an ensemble of three interacting thermodynamic systems. We apply the **Zeroth law of the thermodynamics** to these three systems called as shifted cosmological parameter (SCP), shifted radiation (SR) and shifted exotic matter (SEM) each. *If SCP is in equilibrium with SR and SR is in equilibrium with SEM then SEM should be also in equilibrium with SCP*. The zeroth law demands interaction among cosmic field components whenever equilibrium gets perturbed for any reasons. If equilibrium is disturbed and the components are in non-equilibrium (thermal, mechanical or else), then to re-attain the equilibrium the components must interact mutually. If the components are in equilibrium then due to interaction, perturbation in equilibrium state reacts trying to restore its state or achieve a new one (Le Châtelier-Braun principle) [9, 10]. If all components of tachyonic scalar field are in non-equilibrium, then, to achieve an equilibrium state they must fall into mutual interaction. This motivation provides one justification to study the interaction of these components. Here, we assuming that even though the total energy of the perturbed field (spatially homogeneous) is kept conserved **(First law of thermodynamics)** yet during interaction it can get reasonably violated for individual components. We consider the three components of cosmic tachyonic scalar field the components are shifted cosmological parameter (SCP), shifted radiation (SR) and shifted exotic matter (SEM). The individual equations of energy conservation for SCP, SR and SEM are respectively given as

$$\dot{\bar{\rho}}_\lambda + 3H(1+\bar{w}_\lambda)\bar{\rho}_\lambda = -Q_1, \tag{10}$$

$$\dot{\bar{\rho}}_r + 3H(1+\bar{w}_r)\bar{\rho}_r = Q_2, \tag{11}$$

$$\dot{\bar{\rho}}_m + 3H(1+\bar{w}_m)\bar{\rho}_m = Q_1 - Q_2, \tag{12}$$

where Q_1 and Q_2 are the interaction strengths and H is Hubble parameter. **Second Law of Thermodynamics** is the governing dynamics of interaction and sign of Q_1 and Q_2 shows the direction of flow of energy density during interaction among components. The positivity of the quantity $Q_1 - Q_2$ implies that Q_1 should be large and positive. For if Q_1 had been large and negative, then the second law of thermodynamics would have been violated and the SCP (as the dark energy candidate) would have dominated much earlier withholding the structure formation against the present observations. Also, Q_2 should be positive and small since if it is negative and large then conservation of energy of tachyonic field is violated.

4. Interaction among the components

The interacting dark energy models have been recently proposed by several authors [11]. We study the interaction of these three components assuming that even though the total energy of the perturbed field (spatially homogeneous) is kept conserved , yet during interaction it can get reasonably violated for individual components.

In the above expressions (10), (11) and (12) the following broad conditions must govern the dynamics:

Condition (I) $\mid Q_1 \mid > \mid Q_2 \mid$. This corresponds to the following cases:

(i) If $Q_1 > 0$, $Q_2 > 0$ then the right hand side of (10) is negative while (11) and (12) are positive, respectively. This means that there is energy transfer from shifted cosmological parameter to shifted radiation and shifted exotic matter, respectively. Thermodynamics allows this kind of transfer of energy.

(ii) $Q_1 < 0$, $Q_2 < 0$ implies that there is an energy transfer to shifted cosmological parameter from shifted radiation and shifted exotic matter.

Condition (II) $\mid Q_2 \mid > \mid Q_1 \mid$:

(i) $Q_2 > 0, Q_1 > 0$ would make the right hand side of (11) as positive and (10) and (12) as negative. This shows that there is an energy transfer to shifted radiation from shifted cosmological parameter and shifted exotic matter. Thermodynamics again does not allow this kind interaction.

(ii) $Q_1 < 0, Q_2 < 0$ makes way for the energy transfer from shifted radiation to shifted exotic matter and shifted cosmological parameter.

Condition (III) If $Q_2 = Q_1 = Q$, then we have the following possibility:

(i) $Q > 0$ leads to an energy transfer to shifted radiation from shifted cosmological parameter, while the shifted exotic matter remains free from interaction with its energy density held conserved. This type of interaction holds compatibility with the laws of thermodynamics.

(ii) If $Q < 0$, energy would flow from shifted radiation to shifted cosmological parameter, whereas the shifted exotic matter does not get involved in interaction mechanism. Thus, the conservation of energy for shifted exotic matter holds good.

(iii) As an alternative, $Q = 0$ would pull the components of tachyonic scalar field out of mutual interaction like the standard ΛCDM model.

The second case of condition (I) and condition (II) violates the laws of thermodynamics, therefore, we are not interested in these types of interactions. The interaction of type condition (III) has been discussed for two components of tachyonic scalar field in our earlier work [12]. Due to the lack of information regarding the exact nature of dark matter and dark energy (as the cosmological constant or else) we present the form of interaction term heuristically as function of time rate of change in energy densities as

$$Q_1 = \alpha\dot{\bar{\rho}}_\lambda, \quad Q_2 = \beta\dot{\bar{\rho}}_r, \tag{13}$$

where α, β are proportionality constant. While several authors have proposed different forms of Q [11].

From (10), (11) and (12), for the specific dynamical form of interaction strengths (13) one can found the functional form of energy density with redshift z as

$$\bar{\rho}_\lambda = \bar{\rho}_\lambda^0 x^{3\varepsilon/1+\alpha}, \tag{14}$$

where $\frac{a_0}{a} = 1 + z = x$

$$\bar{\rho}_r = \bar{\rho}_r^0 x^{4+3\varepsilon/1-\beta} \tag{15}$$

and

$$\bar{\rho}_m = \bar{\rho}_m^0 x^\eta + \left(\frac{3\varepsilon\alpha\bar{\rho}_\lambda^0}{3\varepsilon - \eta - \eta\alpha}\right)[x^{3\varepsilon/1+\alpha} - x^\eta] - \left(\frac{\beta\bar{\rho}_r^0(4+3\varepsilon)}{4+3\varepsilon-\eta+\eta\beta}\right)[x^{4+3\varepsilon/1-\beta} - x^\eta], \tag{16}$$

where η assuming constant (with $\dot{\phi}^2 \approx$ constant) is defined as

$$\eta = \frac{3\dot{\phi}^2(1+\varepsilon)+\varepsilon}{\dot{\phi}^2}. \tag{17}$$

Thus, the cosmic expansion history of the universe is given by Hubble parameter with interaction as

$$H^2 = \frac{\kappa^2}{3}[\bar{\rho}_\lambda + \bar{\rho}_r + \bar{\rho}_m], \tag{18}$$

where $\kappa^2 = 8\pi G$.

5. Conclusion

Having the motivation for the relativistic (tachyonic) scalar field, in contrast to quintessence, the single tachyonic scalar field which splits due to some unknown mechanism into three components (cosmological constant, radiation and dust matter). Due to consideration of radiation in this field the dust matter appears with negative energy. A small perturbation allowed in EoS of cosmological constant changes its status from a true cosmological constant to a shifted cosmological parameter (SCP). Similarly, status of radiation and dust matter changes to shifted radiation (SR) and shifted exotic matter (SEM). Thermodynamics laws (Zeroth, First and Second) might be responsible for interaction among components of single cosmic field. We consider the components of the field as thermodynamic systems and they interact to achieve a thermodynamical equilibrium. Particularly Zeroth Law invite interaction among components to maintain thermodynamical equilibrium or get new one, First Law demands the total energy of field stays conserved but the field components mutually interact with interaction strength parameter Q resulting in local violation of energy conservation and Second Law decide the direction of flow of energy during interaction. We conclude that the entire evolution of the universe arises from this process of interaction.

6. Acknowledgement

We thank the members of the theoretical physics group of Shandong University at Jinan, China for helpful discussions. MMV also thanks Edward Rocky Kolb for the kind hospitality at Kavli Institute of Cosmological Physics, the University of Chicago, USA.

References

[1] A. G. Riess et al. Astron. J. **116**, 1009 (1998); S. Perlmutter et al. Astrophys. J. **517**, 565 (1999); D. N. Spergel et al. Astrophys. J. Suppl. **148**, 175 (2003); E. Komatsu et al. ApJS **192**, 18 (2011); P. A. R. Ade et al. A & A **571**, A16 (2014).

[2] K. Tomita, Astrophys. J.**529**, 38 (2000); K. Tomita, Mon. Not. Roy. Astron. Soc. **326**, 287 (2001); M. N. Celerier, Astron. Astrophys **353**, 63 (2000); H. Iguchi, T. Nakamura and K. I. Nakao, Prog. Theor. Phys **108**, 809 (2002).

[3] A.Sen, JHEP **0204**, 048(2002); A.Sen, JHEP **0207**, 065 (2002); A. Sen, Mod. Phys. Lett. **A17**, 1797 (2002).

[4] G. W. Gibbons, Phys. Lett. B **537**, 1 (2002); T. Padmanabhan, Phys. Rev. D **66**, 021301 (2002); A. Frolov, L. Kofman and A. Starobinsky, Phys. Lett. B **545**, 8 (2002); Huiquan Li, JCAP **07**, 018 (2012); D. Choudhury, D. Ghoshal, D. P. Jatkar and S. Panda, Phys. Lett. B, **544**, 231 (2002); D. A. Steer and F. Vernizzi, Phys. Rev. D **70**, 043527 (2004); G. Shiu and I. Wasserman, Phys. Lett. B **541**, 6 (2002).

[5] E. S. Reich, NATURE **483**, 132 (2012).

[6] R. M. Lutchyn, J. D. Sau and S. D. Sarma, Phys. Rev. Lett. **105**, 077001 (2010).

[7] M. M. Verma and S. D. Pathak, Astrophys. Space Sci. **344**, 505(2013).

[8] S. D. Pathak and M. M. Verma, Journal of Physics: Conference Series **481**, 012015 (2014).

[9] H. B. Callen, *Equilibrium Thermodynamics*, Wiley. NY (1960).

[10] J. Keizer, *Statistical Thermodynamics of Non-equilibrium Processes*, Springer, NY (1987).

[11] M. S. Berger and H. Shojaei, Phys. Rev. D **77**, 123504 (2008); H. Farajollahi, A. Ravanpak and G. F. Fadakar, Phy. Let. B **711**, 225 (2012); S. Cao, N. Liang and Z. H. Zhu, Mon. Not. R. Astron. Soc. **416**, 1099 (2011); M. M. Verma and S. D. Pathak, Int. J. Mod. Phys. D **23 (9)**, 1450075 (2014); J. Valiviita, R. Maartens and E. Majerotto, Mon. Not. R. Astron. Soc. **402**, 2355 (2010); C. Feng, B. Wang, E. Abdalla and R. Su, Phys. Lett. B **665**, 111 (2008); M. Shahalam et al. Eur. Phys. J. C. **75**, 395 (2015); A. Aviles and J. L. C. Cota, Phys. Rev. D **84**, 083515 (2011); T. Clemson et al. Phys. Rev. D **85**, 043007 (2012); B. Wang et al. Nucl. Phys. B **778**, 69 (2007); H. Kodama and M. Sasaki, Prog. Theor. Phys. Suppl. **78**, 1 (1984); L. Amendola, C. Quercellini, D. T. Valentini and A. Pasqui, Astrophys. J. Lett. **583**, L53 (2003); V. Pettorino and C. Baccigalupi, Phys. Rev. D **77**, 103003 (2008).

[12] M. M. Verma and S. D. Pathak, Int. J. Theor. Phys., 10773 (2012).

Is there any possibility of doublet universe?

Tanmoy Chakraborty[a] and Pranavi Pachipula[b]

(a) Formerly Department of Mechanical Engineering, NITK Surathkal, Mangaluru-575025, Karnataka, India
(b) Formerly Department of ECE, Sri Venkateswara College of Engineering for Women, JNTUA, Tirupati-517507, Andhra Pradesh, India
Member of "Beyond Night Sky[a,b]"

Presenter: Tanmoy Chakraborty (*tanmoy.chakraborty19@gmail.com*); COS.9, Poster, CICAHEP15.108

Doublet universe can be formed by merging of source universe and sink universe within our visibility boundary range. The singularity points of the source-sink pair domain are nothing but act as black hole from which gravitational wave can travel within the visible boundary but nobody knows how far the energy of this traveling wave ends its dissipation. The similar effect can be seen in case of pond ripple after getting impacted by stone (or primordial atom) in two specific domains. Therefore, this paper reveals about the study of the pond ripple wave dynamics for understanding the possibility of doublet universe or the evidence of multiverse. Here, Buckingham pi theorem was used along with potential flow concept to model the impact between stone and pond surface. Further, a comparison was done with oscillating universe theory. The commercial softwares such as origin lab, Matlab was used to model the doublet universe.

1. Introduction:

According to potential flow theory [1], doublet flow formed when the separation distance between two source flow or two sink flow or source and sink flow tends to zero. As universe is the power set of all the properties which is happening at nature and the properties which are present in nature is the subset of that power set. Therefore doublet flow as an evidence one can find in nature when two stone thrown at same angle at zero separation distance on a liquid surface or pond surface due to which ripple generates. Similar things can also be possible in the universe when two quantized particle such as graviton [2] at zero separation distance fall on space time curvature which generates ripples which is termed as gravitational wave. This makes the importance of coining the term *Doublet Universe* over here. However, doublet flow or source flow or sink flow can be seen in case of pond ripples which are transverse wave that generates due to impact between stone and liquid surface. Since doublet universe means the association of two universes by capture theory [3]. Therefore here it makes the evidence to get the understanding regarding multiverse theory [4] as well as oscillating universe theory [5]. Though multiverse theory [6] is accepted by many cosmologists but the argument regarding the observational point beyond the horizon such as extrapolation upto 10^{100} times horizon distance or even more is very much alive [7]. However, oscillating universe theory depicts that universe exists between big bang and big crunch which is a cyclic event. Therefore to understand this two theory pond ripple wave generation with potential flow theory is the best idea that is available in nature. To understand the generation of ripple Buckingham pi theorem can be used that is a scheme for non dimensionalization and a key theorem of dimensional analysis which is the formalization of Rayleighs method of dimensional analysis [8, 9].

2. Model for strength of ripple wave generator

To establish a relation for finding the strength of ripple wave generator, Buckingham pi theorem [10] was used along with following assumptions to study an experimental situation (Fig. 1): (a) Temperature was taken as uniform and steady. Therefore, there will be no temperature term associated with pi terms. (b) Number of collisions of stone with medium particles was taken as 1 with respect to experiment facility. (c) Angle of impact of stone for experiment purpose was taken as 90^0 or (3.14/2) or 1.57 i.e. a constant pi term.
In Fig. 1, motion of stone from impact point for stone at specific height to impact point on liquid surface was studied by using Buckingham pi theorem. Therefore from Fig. 1, it can be written as

$$f(\xi, \theta, \delta, \tau, \eta_c, m, v, F, E, a, g, A) = 0 \tag{1}$$

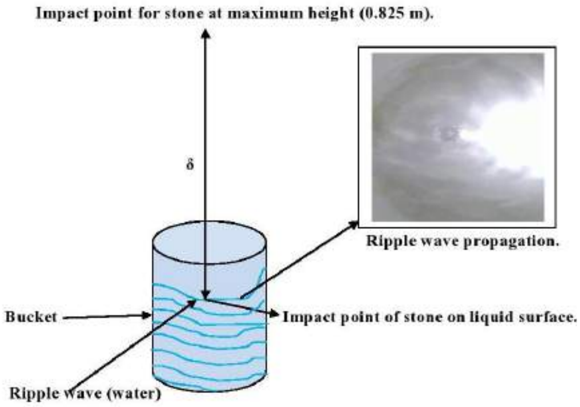

Figure 1. Schematic diagram of experimental setup and generated ripple wave propagation.

Where, ξ is the strength of ripple wave generator in cm^2/s, θ is the angle of impact of stone into liquid surface. Here it was taken as 1.57 for experiment, δ is the distance between impact point of stone and impact point on liquid surface in m., τ is the time required for stone to reach into the liquid surface in s., η_c is the total number of collisions in medium from impact point of stone into liquid surface impact point. Here it was assumed as 1, *m* is the mass of stone in kg., *v* is the velocity of stone in m/s., *F* is the impact force of stone in Newton, *E* is net energy (K.E. + P.E.) of stone for motion between impact point of stone to impact point of liquid surface in kW., *a* is the acceleration of stone in m/s^2., *g* is the acceleration due to gravity, which is 9.81 m/s^2 and *A* is the surface area of stone in m^2. Therefore, the governing equation for strength of ripple wave generator from the equation (1) is

$$\xi = \frac{1.57}{Ag}\frac{\delta^8}{\tau^7}\frac{m^2}{FE}\phi\left(\frac{\tau^3 av}{\delta^2}\right) \tag{2}$$

Experimental data show that the non dimensional term in equation (2) is approximately equal to 1 i.e.$\phi\ (\frac{\tau^3 av}{\delta^2}) \approx 1$.

3. Results and Discussion

To determine the strength of ripple wave generator an experiment was conducted to calculate the preliminary variables such as velocity of stone, acceleration of stone, impact force of stone, net energy of stone and ripple wave propagation velocity for understanding the ripple wave dynamics for different masses with respect to different heights such as 0.825 m, 0.725 m, 0.625 m and 0.525 m. Time of fall of stone from impact point to liquid surface was calculated by using stopwatch. The detailed information of the experiment are tabulated in Table 1 below. The

Table 1. Experimental details

Sl. No.	Equipments	Detailed information
1	Marbles (or stone)	Five marbles of different sizes: 0.023 m, 0.0205 m, 0.018 m, 0.0155 m, 0.015 m. Mass: 0.016 kg, 0.014 kg, 0.008 kg, 0.006 kg and 0.004 kg. Shape: Spherical
2	Vernier Calliper	Parco Company, 0 - 12.5 cm range.
3	Screw Gauge	Ajit Company, Range: 0 - 90 mm.
4	Buckets	Diameter of top most liquid surface in bucket - 0.2431 m, 0.2816 m
5	Tape	Libra Company, (0 - 1.5 m) range.

variation of impact force and net energy of stone with δ was studied to understand the mass variability, time of fall variability, velocity variability and acceleration of stone variability on impact of force and net energy results.

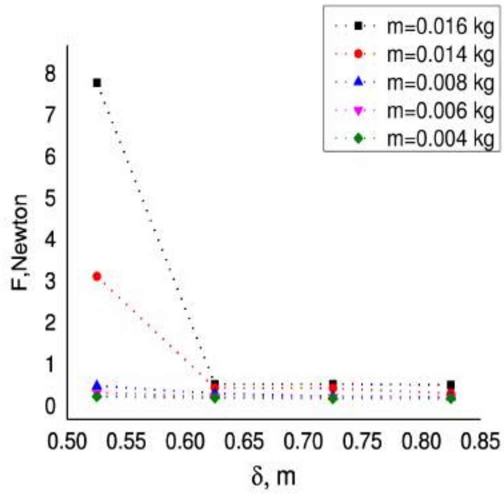

Figure 2. Impact force of stone of different masses on liquid surface variation with δ.

From Fig. 2, it can be noticed that impact force for higher mass stones such as 0.016 kg and 0.014 kg varies in the range of 0.1284 N - 7.6 N. But for lower mass stones it varies in the range 0.00724 N - 0.14 N. Also, it was seen that impact force of stone is more for low δ because at this distance stone has to suffer less collision or less resistance with media particles or medium.

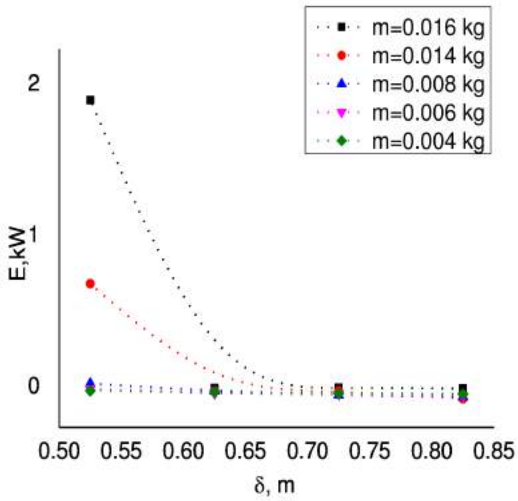

Figure 3. Required net energy for ripple generation of stone of different masses on liquid surface variation with δ.

From Fig. 3, it is seen that net energy varies - 0.00762 kW - 1.915 kW for higher mass stones whereas it varies - 0.00723 kW - 0.03944 kW for lower mass stones such as 0.008 kg, 0.006 kg and 0.004 kg. However, typically for lower mass stones motion due to gravity dominates kinetic motion which results negative net energy. To understand the behavior of ripple wave with bucket area variability, preliminary factor such as velocity of propagation of ripple wave (v_p) was studied. Propagation time was calculated by subtracting the time of fall for typical stone on the liquid surface from total time i.e. time of fall of stone plus required propagation time to standstill the liquid surface from undulation.

From Fig. 4 (a) and Fig. 4 (b) it can be observed that ripple wave propagation approximate velocity is more for

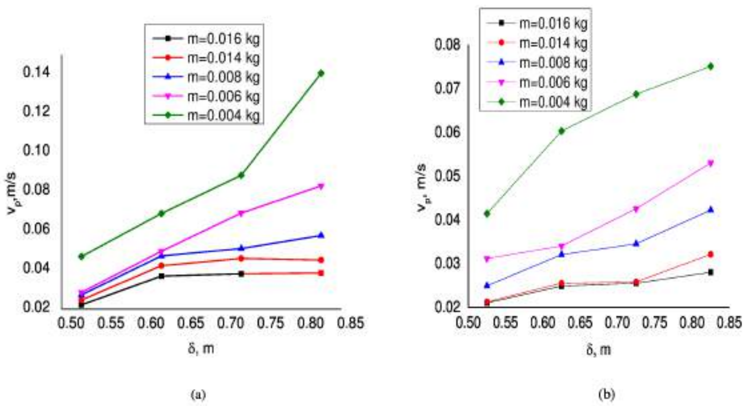

Figure 4. (a) Ripple wave propagation velocity variation with δ for bucket diameter 0.2431 m. (b) Ripple wave propagation velocity variation with δ for bucket diameter 0.2816 m.

lower mass stones compared to higher mass stones such as 0.016 kg and 0.014 kg. It is because during the impact with liquid surface higher mass stones lose net energy more compared to lower mass stones due to skin friction drag and shear resistance. This loss of energy is due to greater surface area. Therefore a simulation was done by using this results and universe size [11] which results if a particle dropped from - 2.02E27 m height on the space time curvature of the universe the propagation time it will take 8.574E28 second with propagation velocity 2.36E26 m/s. Now, equation (2) was recalled for strength of ripple wave generator calculation with the help of experimental data and then it was plotted as given below.

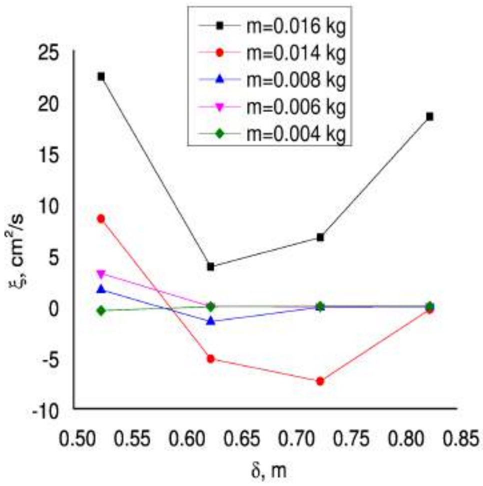

Figure 5. Variation of strength of ripple wave generator for different masses with δ.

From Fig. 5, it can be seen that strength of ripple wave generator fluctuates with height which is due to motion due to gravity and surface area of stone. However, in case of lower mass stones strength of ripple wave generator act as sink because of motion due to gravity dominates kinetic motion of stone in this case. The higher mass stones show almost similar variation of strength of ripple wave with height whereas lower mass stones show not much variation or fluctuation with height.

Fig. 6 was plotted using strength of the ripple wave generator and streamline function and velocity potential function [1]. The range of either side of the bucket was taken as (- 2, 2) cm in x and y direction.

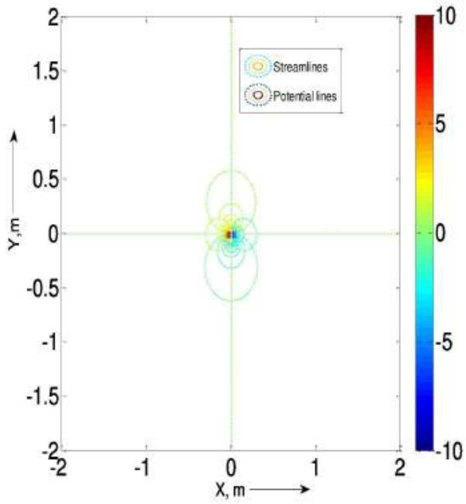

Figure 6. Matlab plot of streamlines and velocity potential lines of sink flow doublet universe of strength - 0.3 cm^2/s.

4. Conclusions

From above results and discussion it can be concluded that motion due to gravity dominates kinetic motion for lower mass stones that results negative net energy and sink flow. Above studies suggests that doublet universe can be possible for two merged source flow or two merged sink flow and merging of source- sink flow. Typically the study does not support oscillating universe theory fully because universe can also be possible due to two source/sink flow. So, the study partially supports oscillating universe theory as well as multiverse theory. Further studies can be done on this experiment for the possible evidence of parallel universe theory by varying the impact angle of stone and using LAB View analysis software for wave properties estimation.

5. Acknowledgement:

Authors likes to acknowledge Regional Science Center, Tirupati for their kind cooperation by providing space and required equipment during the experiment.

References

[1] E. L. Houghton et al, *Aerodynamics for Engineering Students*, Elsevier, pp:150-163, ISBN:978-0-08-096632-8 (2012).
[2] C. M. Will, Physical Rev. D **57(4)**, 2061 (1998) [arxiv:gr-qc/9709011].
[3] J.R. Dormand, M. M. Woolfson, MNRAS **151**, 307 (1971).
[4] Andrei Linde, arxiv:1512.01203[hep-th] (2015).
[5] D. Ruth, L. Joachim, arxiv:gr-qc/951004/v2 (1996).
[6] M. K. Munitz, Journal of the History of ideas **12(2)**, 231 (1959).
[7] Ellis et al, MNRAS **347(3)**, 921 (2004).
[8] E. Buckingham, Phys. Rev. **4(4)**, 345 (1914).
[9] E. Buckingham, Nature **96(2406)**, 396 (1915).
[10] E. Buckingham, Transactions of the American Society of Mechanical Engineers **37**, 263 (1915).
[11] P. Davies, *The Goldilocks Enigma*, First Mariner Books, pp:43ff, ISBN-978-0-618-59226-5 (2006).

Circular orbits for test particles around R-charged black hole spacetimes

Rashmi Uniyal[a], Anindya Biswas[b], H. Nandan[a] and K. D. Purohit[c]

(a) Department of Physics, Gurukula Kangri Vishwavidayalaya, Haridwar-249404, Uttarakhand, India
(b) Department of Physics, Ranaghat College, Ranaghat, West Bengal-741201, India
(c) Department of Physics, Hemwati Nandan Bahuguna Garhwal University, Srinagar Garhwal, Uttarakhand-246174, India

Presenter: Rashmi Uniyal (*rashmiuniyal001@gmail.com*); COS.7, Oral, CICAHEP15.143

We study the motion of massive as well as massless test particles in the background of a class of multiple charge black holes in gauged supergravity theories in D = 4. We have analysed the horizon structure along with the nature of the effective potentials for the case of four equal charges. The structure of circular orbits for incoming test particles is analysed specifically. The periods for one complete revolution and cone of avoidance for massless test particles are also investigated in greater detail.

1. Introduction

Over the last century, the *Einstein's theory of gravitation* i.e. General Relativity (GR) [1, 2, 3] has been extremely successful to understand various observational facts like gravitational redshift, the precession of Mercury's orbit, the bending of light etc. Though GR has enjoyed the great success, but it is still not a complete theory to understand the physics at sufficiently smaller length scale e.g. near the spacetime singularity which arises in case of gravitational collapse [3]. In the vicinity of the spacetime singularity, the quantum effects should be taken care of seriously and recently string theory has become a promising candidate for the same purpose which comprises gravity in the frame work of quantum theory [4, 5, 6]. In the continuing pursuit of the search for a viable quantum theory of gravity, the gauged supergravity [7, 8, 9] theories have also captured considerable attention in recent times. In such models of gravity, the maximally supersymmetric gauged supergravity is realized as truncation of string theory or $D = 11$ dimensional M theory compactified on a sphere where the gauge group is the isometry group of the sphere.

In the present work, we consider four dimensional charged black holes in $N = 8$[1], gauged supergravity upto four charges. The construction of these black holes have been explicitly performed in Ref. [10] and according to [11], such charged black hole congurations are termed as R-charged black holes. In gauged $N = 8$ supergravity models, the bosonic part of the complete Lagrangian has a negative cosmological constant Λ proportional to the square of the gauge coupling constant g [12] and the black hole solutions are asymptotically AdS.

In the next section, the horizon structure of R-charged black holes [10] with multiple charges is discussed briefly. In section 3, using the effective potential techniques, the motion of test particles and the structure of corresponding orbits are discussed. In section 4, the circular orbits are discussed for incoming massive as well as massless test particles. Finally, the results are summerised in the last section.

2. The spacetime with multiple charges

We consider the following spacetime metric of four electric charge black hole solution in $D = 4$, $N = 8$ gauged supergravity:

$$ds^2 = -\mathcal{H}^{-1/2} f dt^2 + \mathcal{H}^{1/2}(f^{-1}dr^2 + r^2 d\Omega^2_{2,k}) \,, \tag{1}$$

where

$$H_\alpha = 1 + \frac{\mu \sinh^2 \beta_\alpha}{kr}, \qquad f = k - \frac{\mu}{r} + 2g^2 r^2 \mathcal{H} \tag{2}$$

with $\mathcal{H} = H_1 H_2 H_3 H_4$. Here g is the gauge coupling constant and μ is the non-extremal parameter like mass term in pure Schwarzschild black hole, k can take three values i.e. 1, 0 and -1. The $\beta_\alpha(\alpha = 1......4)$ in eqs. (1) and

[1] N is the number of supermultiplates

(2) parametrizes the four electric charges. Here, we only consider the case of four equal charges i.e. $n = 4$ with $k = 1$. The lapse function f vanishes at the zeros of the following equation:

$$(kr)^n\,(kr-\mu)+2g^2r^3(kr+p)^n=0. \tag{3}$$

The real and positive zeroes of equation (3) are known as the horizons for the corresponding spacetime. Hence if a spacetime represents a black hole, f should vanish at some positive value of r. In presence of one and two equal charges one will always get a horizon for various values of β and g. In presence of three equal charges the constraint on parameters for the presence of horizon is given by,

$$2g^2\mu^2\mathrm{sinh}^6\beta<k^3. \tag{4}$$

In case of four equal charges present, the condition for the existence of at least one horizon is given by,

$$A+B-\frac{k^6}{256}<0, \tag{5}$$

where $A=\sinh^6\beta g^4\left(\sinh^2\beta+1\right)^3\mu^4$ and $B=\frac{1}{32}\,g^2k^3\mu^2\left(\sinh^8\beta+2\sinh^6\beta-\frac{7\mathrm{sinh}^4\beta}{2}-\frac{9\mathrm{sinh}^2\beta}{2}-\frac{27}{16}\right)$.

3. Nature of effective potential and classification of orbits

To understand the possible orbit structure of the test particles in the background of given spacetime geometry, one has to look for the nature of effective potential. The effective potential for massive test particles in the background of the R-charged black holes is given as,

$$V_{eff}=\frac{f}{2\mathcal{H}^{\frac{1}{2}}}\Big(\frac{L^2}{r^2\mathcal{H}^{\frac{1}{2}}}+1\Big). \tag{6}$$

For $r\to r_H$ (the horizon radius), $V_{eff}=0$ and for $r\to\infty$, $V_{eff}\to\frac{k}{2}+\frac{ng^2}{4k^2}\left(\frac{n}{2}-1\right)\mu^2\sinh^2(\beta)+\left(ng^2\mu^2\sinh^2(\beta)\right)\frac{r}{2k}+g^2r^2$, whereas for $r\to\infty$, $V_{eff}\to\frac{k}{2}$ (when $g=0$).

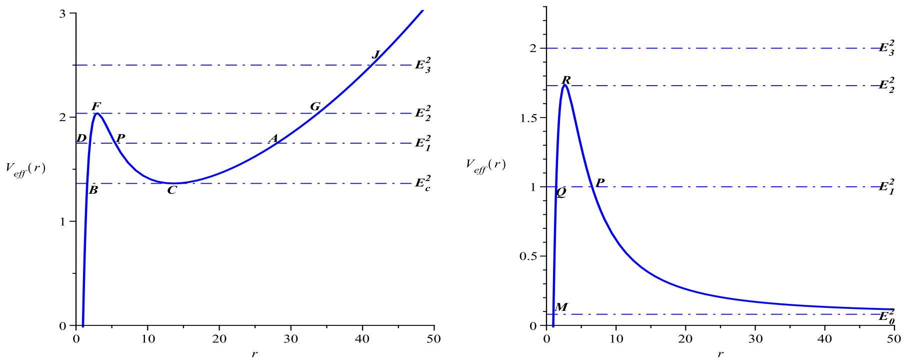

Figure 1. Effective potential for unit mass black hole (i. e. $\mu = 1$) in the presence of four equal charges with $L = 10$, β=1, $k = 1$, $g = 0.02$ for massive test particles (left panel) and for massless test particles (right panel).

The following orbits are allowed depending on the values of the energy of the incoming massive test particle:

(I) $\underline{E=E_c}$: (i) Here $V_{eff}={E_c}^2$ and $\dot{r}=0$ leading to a *stable circular orbit* at point C. (ii) A *terminating bound orbit* if test particle starts from the point B.

(II) $\underline{E=E_1}$: (i) A bounded *planetary orbit* between points A and P. (ii) A *terminating bound orbit* for the test particle starting from the point D.

(III) $\underline{E=E_2}$: The possible orbits are *unstable circular orbit* at point F. The particle starts from point F and then it can go either to point G or to the singularity after crossing the horizon.

(IV) $\underline{E=E_3}$: There exists *terminating bound orbit* for particle crossing point J. Hence there are no fly-by orbits possible for massive test particles. The effective potential for null geodesics (shown in the right panel of Fig.(1)) have no local minima. Hence the *stable circular orbits* are not present in this case.

4. Analysis of Circular Orbits

4.1 For Timelike Geodesics

The orbit equation can be obtained by using first integrals of the geodesic equations as,

$$\left(\frac{dr}{d\phi}\right)^2 = \frac{1}{L^2} P_n(r), \tag{7}$$

$$P_n(r) = \left(E^2 H^n - f H^{n/2} - \frac{L^2 f}{r^2}\right) r^4, \tag{8}$$

where $f = 1 - \frac{\mu}{r} + 2g^2 r^2 H^n$, $H = 1 + \frac{p}{r}$ and $p = \mu \sinh^2\beta$. The physically acceptable regions having positive values of $P_n(r)$ or equivalently $E^2 \geq V_{eff}$ for positive and real values of r, represents the allowed region of motion for test particles. Hence the number of positive real zeros of $P_n(r)$ uniquely determine the type of particles orbit in the background of these charged black holes. In case of *circular orbits*, $r = r_C =$ constant, where r_C is the distance of the circular orbit from the singularity and hence $\dot{r} = 0$. First integrals of the geodesic equations are used to calculate the time periods for circular orbits,

$$dt = \frac{E\mathcal{H}(r_C)}{Lf(r_C)}\, r_C^2\, d\phi\,. \tag{9}$$

The circular orbit condition $V'_{eff} = 0$ (where $\prime$ denotes differentiation w.r.t. r) can be used to express L in terms of r_C as,

$$L^2 = \frac{\mathcal{X}}{\mathcal{Y}}\,, \tag{10}$$

where $\mathcal{X} = \frac{\mu n p}{2k r_C^3} - \frac{1}{r_C^2}\left[\frac{np}{2} + \mu\left(1 + \frac{p}{k r_C}\right)\right] - 2g^2 \mathcal{H}(r_C)\left(\frac{-np}{2k} + \frac{2p}{k} + 2r_C\right)$,
$\mathcal{Y} = \mathcal{H}^{-1}(r_C)\left(-\frac{2k}{r_C^3} + \frac{3\mu}{r_C^4} + \frac{np}{r_c^4 H(r_C)} - \frac{\mu n p}{k r_c^5 H(r_C)}\right) + \frac{4g^2}{r_C H(r_C)}\left(1 - H(r_C) + \frac{p}{k r_C}\right)$,
$p = \mu \sinh^2(\beta)$, $H = 1 + \frac{p}{k r_C}$ and $\mathcal{H} = H^n$. As radial velocity $\dot{r}$ vanishes for circular orbit, it provides another condition for this orbit as $E^2 = V_{eff}(r_C)$. Substituting this in equation (9) with $\Delta t \equiv T_t$ and $\Delta\phi = 2\pi$ for one period then we obtain,

$$T_t = \left[\frac{\mu r_C}{2f(r_C)}\left(\frac{1}{r_C^2} + \frac{\mathcal{H}^{1/2}(r_C)}{L^2(r_C)}\right)\right]^{1/2} \left(\frac{k r_C}{k r_C + p}\right) T_{t,sch}\,, \tag{11}$$

where $T_{t,sch} = 2\pi\sqrt{\frac{2r_C^3}{\mu}}$. Similarly time period in proper time can also be obtained by integrating the first integral of the geodesic equation for ϕ as,

$$\begin{aligned} T_\tau &= \left[\frac{\mu r_C}{2f(r_C)}\left(\frac{1}{r_C^2} + \frac{\mathcal{H}^{1/2}(r_C)}{L^2(r_C)}\right)\left(\frac{2r_C}{\mu} - 3\right)\right]^{1/2} \left(\frac{k r_C}{k r_C + p}\right) 2\pi r_C^2 \\ &= r_C \left[\frac{\mu r_C}{2f(r_C)}\left(\frac{1}{r_C^2} + \frac{\mathcal{H}^{1/2}(r_C)}{L^2(r_C)}\right)\right]^{1/2} T_{\tau,sch}\,. \end{aligned} \tag{12}$$

The numerical values of the above time periods for a definite set of parameters are compared in the Table 1.

One can then easily notice the effect of charges on the time periods and also on the radius of circular orbits, which significantly differ from the corresponding values of the Schwarzschild black hole [2] in GR.

[2] for Schwarzschild black holes $r_C = 3$, $T_t = 2.5375$ and $T_\tau = 31.18\pi$, for $\mu = 1$, $k = 1$.

Table 1. Comparative view of the time periods for different number of charges for $\mu = 1$, $k = 1$, $g = 0.02$ and $\beta = 1$.

n	r_C	T_t	T_τ
0	3.7871	0.8640	41.6π
1	4.3042	1.0887	44.42π
2	4.8169	1.4322	51.20π
3	5.3145	1.9965	58.26π
4	5.7911	2.4851	65.43π

4.2 For Null Geodesics

Using the constraint for null geodesics (i.e. $u_\mu u^\mu$=0), the corresponding orbit equation reads as,

$$\left(\frac{dr}{d\phi}\right)^2 = \frac{1}{L^2} P_n{}^{null}(r), \tag{13}$$

here $P_n{}^{null}(r) = \left(E^2 H^n - L^2 f/r^2\right) r^4$ (f and H are similar as in the previous section). The circular orbit condition (i.e. V'_{eff}(r) = 0) for null geodesics reduces to,

$$2r^2 - (2p + 3\mu)r + \mu p = 0, \tag{14}$$

where $V_{eff} = f\, L^2/2r^2\mathcal{H}$ with n = 4, k = 1, p = $\mu \sinh^2 \beta$. Solution of equation (14) describes the radius of *unstable circular orbit* and is given as,

$$r_c = \frac{1}{4}\left[2p + 3\mu \pm \sqrt{(2p + 3\mu)^2 - 8\mu p}\,\right], \tag{15}$$

where $p = \mu \sinh^2 \beta$ and equation (14) has a real solution for $(2p + 3\mu)^2 \geq 8\mu p$. The larger root of equation (14) locates the position of unstable circular orbit, which again has the minimum value for the condition $(2p + 3\mu)^2 = 8\mu p$ as,

$$(r_c)_{min} = \frac{1}{4}\left(2p + 3\mu\right). \tag{16}$$

It is clear from equation (15) that radius of unstable circular orbit does not depend on the coupling constant g. In the absence of charges (i.e. $p \to 0$), equation (15) and equation (16) reduces to the Schwarzschild case. Hence due to the presence of charges, the radius of unstable circular orbits increases.

The Time Period: The time period for unstable circular orbits can be calculated in terms of proper time as well as coordinate time. The expression for time period in proper time can be obtained by integrating the first integral of the geodesic equation for ϕ as,

$$T_\tau = \frac{2\pi {r_C}^2}{L} H^{n/2}(r_C). \tag{17}$$

Time period in coordinate time can be obtained as,

$$T_t = 2\pi r_C \left(\frac{H^n(r_C)}{f(r_C)}\right)^{1/2}. \tag{18}$$

Cone of Avoidance: The cone of avoidance can be defined at any point [14, 15, 16] and the light rays included in the cone must necessarily cross the horizon and get trapped. If ψ denotes the half-angle of the cone directed towards the black hole at large distances, then

$$\cot\psi = +\frac{1}{\mathcal{R}}\frac{d\tilde{r}}{d\phi}, \tag{19}$$

where

$$d\tilde{r} = \frac{(r + p)}{r f^{1/2}} dr \tag{20}$$

Table 2. Comparison of the time periods for unstable circular orbits of massless test particles with different number of charges (i.e. n) for $\mu = 1$, $k = 1$, $g = 0.02$ and $\beta = 1$.

n	r_C	T_t	T_τ
0	1.5000	5.1822π	6.2366π
1	1.6477	7.0904π	7.3617π
2	1.8694	9.4472π	12.153π
3	2.1906	12.188π	19.982π
4	2.6174	15.179π	31.979π

and the radial function $\mathcal{R} = (r + p)$ for $n = 4$. Equation (20) describes the element of proper length along the generator of the cone. Hence,

$$\cot\psi = \frac{1}{rf^{1/2}}\frac{dr}{d\phi}. \tag{21}$$

Now using the equation (13), one can obtain,

$$\tan\psi = \left[\frac{L^2 f r^2}{E^2(r+p)^4 - L^2 f r^2}\right]^{1/2}. \tag{22}$$

From equation (22), it follows that,

$$\psi = \frac{\pi}{2} \quad for \quad r = r_c,$$

$$\psi = 0 \quad for \quad r = r_H,$$

$$\psi \approx \sqrt{\frac{1 + 6p^2 + 2g^2(4rp + r^2)}{\left(\frac{E^2}{L^2} - 2g^2\right)(6p^2 + 4rp + r^2)}} \quad for \quad r >> 1, \tag{23}$$

where r_c denotes the radius of circular orbit and r_H denotes the radius of event horizon.

5. Summary and Conclusions

In the work presented here, we have investigated the geodesic motion of massive as well as massless test particles around a particular class of R-charged black holes in $N = 8$, $D = 4$ gauged supergravity theory. Some of the important results of this work are summarised below:

(i) One horizon is always present for single and two charges, hence spacetime always represents a Black Hole in these two cases. As the number of charges increases more than two, it is possible to have multiple or no horizons in view of the behavior of lapse function of the spacetime.

(ii) Radius of the corresponding circular orbits for massive as well as massless test particles increases with the enhancement in the number of charges.

(iii) The radius of unstable circular orbit for a massless test particle is independent of the gauge coupling constant.

(iv) Cone of avoidance for a massless test particle depends on both the charge and gauge coupling constant at large distances.

6. Acknowledgement

One of the authors (HN) would like to thank Department of Science and Technology, New Delhi for financial support through grant no. SR/FTP/PS-31/2009. Authors are also thankful to the organisers in particular Dr. U. D. Goswami for warm hospitality during CICAHEP.

References

[1] A.Einstein, Sitzungderphysikalisch-mathematischenklasse **25**, 844 (1915).

[2] E.Poisson, *A Relativists Toolkit: The Mathematics of Black Hole Mechanics* (Cambridge University Press, Cambridge, 2004).
[3] P.S. Joshi, *Global Aspects in Gravitation and Cosmology* (Oxford University Press, Oxford, 1997).
[4] A. Sen, Curr. Sci. **88**, 2045 (2005).
[5] B. Zwiebach, *A First Course in String Theory* (Cambridge University Press, Cambridge, 2004).
[6] J. Polchinsk, *String Theory Vol. 1 and 2* (Cambridge University Press, Cambridge, 1998).
[7] B. de. Wit and H. Nicolai, Phys. Lett. **108B**, 285 (1982).
[8] B. de. Wit and H. Nicolai, Nucl. Phys. **B208**, 323 (1982).
[9] M.J. Duff, B.E.W. Nillson, and C.N. Pope, Phys. Rep. **130**, 1 (1986).
[10] M.J. Duff and J.T. Liu, Nucl. Phys. **B554**, 237 (1999).
[11] M. Cvetic and S.S. Gubser, J. High Energy Phys. 04 (1999) 024.
[12] M.J. Duff, Int. J. Mod. Phys. **A14**, 815 (1999).
[13] L.J. Romans, Nucl. Phys. **B383**, 395 (1992).
[14] S. Fernando, Phys. Rev. **D 85**, 024033 (2012).
[15] N. Cruz, M. Olivares, and J.R. Villanueva, Classical Quantum Gravity **22**, 1167 (2005).
[16] S. Chandrashekhar, *The Mathematical Theory of Black Holes* (Oxford University Press, Oxford, 1992), p. 646.

Cosmic ray production from large scale structure formation shocks

Reju Sam John^a, Surajit Paul^b and Harish Kumar^c

(a) Department of Physics, Pondicherry Engineering College and Visiting Scholar, IUCAA, Pune
(b) Department of Physics, University of Pune and Associate faculty IUCAA, Pune
(c) Department of Physics, Pondicherry Engineering College, Pondicherry

Presenter: Reju Sam John (*rejusamjohn@pec.edu*); COS.3, Oral, CICAHEP15.149

The galaxies in the Universe are not distributed randomly, rather they are embedded in cosmic web like structure. This cosmic web constitute galaxy clusters, filaments and voids, which are called large scale structure (LSS) in the universe. They grow by continuous accretion and mergers, which pumps up the energy of the particles present in the medium and fills the Intracluster Medium (ICM) with energetic cosmic rays. But, connection of evolution of cosmic ray (CR) fraction with the Cluster formation phases are not studied well. In order to study the evolution of cosmic ray fraction, we performed 10 sets of cosmological N-Body + Hydrodynamical simulations of cosmic structure formation using ENZO 2.2. We observed a very strong link between merging phases with the CR flux produced in the ICM. We also observed multiple flashing moments during the full (i.e. few Gyr) evolution period of Clusters. In this work, we also report a good correlation of Mass with the CR fraction while the clusters are relaxed, but a huge deviation is noticed during the mergers. Our finding has a far reaching effect, as, this will help us in understating the origin of cosmic rays and also can be used as a probe to determine the dynamical condition of the cluster by observing the fractional energy distribution in the ICM.

1. Introduction

Galaxy Clusters are formed through a process called hierarchical clustering, in which the larger structures are formed through the continuous merging of smaller structures. Galaxy Clusters are on the top of this hierarchy has gone through a cascade of dynamical events. Many studies had confirmed that the galaxy clusters formed out by the merger of smaller structures like stars, galaxies, groups of galaxies and the assertion of warm hot materials from the filaments [1]. So all the possible dynamical events in this universe like, star formation, supernova activity, AGN activity, galaxy formation, galaxy-galaxy group even galaxy cluster mergers and filamentary accretion etc. will result in the energetics of Galaxy Clusters [2, 3]. All these processes modify the energy balance of intracluster medium (ICM) through shock waves [4, 5, 6, 7]. The large-scale shocks fill the intracluster medium with energetic particles, or cosmic rays (CRs). Mpc scale (Giant Radio Structures) radio sources observed in the cluster centre or on the outskirts are the indirect evidence of the presence of non-thermal i.e. CR particles and magnetic fields (for review: [8]). These observations suggest the presence of relativistic electrons, protons, ions and magnetic field in the Cluster medium. But, connection of evolution of CR flux with the Cluster formation phases is not studied well. In this paper, we study the evolution of CRs in the Galaxy Clusters during different stages of its formation. In order to study the evolution of CR fraction, we performed 10 sets of cosmological N-Body + Hydrodynamical simulations of cosmic structure formation using ENZO 2.2.

2. Simulation of large scale structure formation

The large scale structure formation simulations were performed with the Adaptive Mesh Refinement (AMR), grid-based hybrid (N-body plus hydro-dynamical) code Enzo v. 2.2 [9]. The code uses adaptive refinement in space and time and introduces non-adaptive refinement in mass by multiple child grid insertions. A flat ΛCDM background cosmology with the parameters of the LCDM model, derived from WMAP (5-years data) combined with the distance measurements from the Type Ia supernovae (SN) and the Baryon Acoustic Oscillations (BAO) is used (see [10]). The simulations have been initialized at redshift $z = 60$ using the [11] transfer function, and evolved up to $z = 0$. An ideal equation of state was used for the gas, with $\gamma = 5/3$.

Hear our focus is on the production of CRs through Diffusive Shock Acceleration (DSA), which is a strong function of shock strength, shock detection has been done carefully. The shock compression can induce radiative cooling [12, 13]. Thus, the radiative cooling is implemented in this simulation from [14] for a fully ionized gas with a metallicity of 0.5 solar mass. We also implemented the a star formation feedback in the simulation.

Since the shocks are the vital component for our study, we have implemented a refinement criteria based on shocks. Where ever the Mack number of the shocks goes above 1.1, the cell is refined. With the introduction of 2 nested child grid and 4 levels of AMR at the central 32 Mpc^3 volume we achieved a resolution of 31.25 kpc at the highest level. The required physical parameters have been derived from the simulation using a powerful tool called 'yt' [15].

3. Robustness of our simulation

The relations between the mass, temperature and the virial radius of a virialized cluster is well defined. And these relations are $M_{vir} = r_{vir}^3$ and $T_{vir} = M_{vir}/r_{vir}$ or $r_{vir} \propto M_{vir}^{1/3} \propto T^{1/2}$ (e.g., [16]). We have plotted these parameters and fitted scalling laws (see Fig.1) to check the robustness of our simulations. The virialized clusters parameters in our simulation obey exactly the expected theoretical relations between temperature mass and radius.

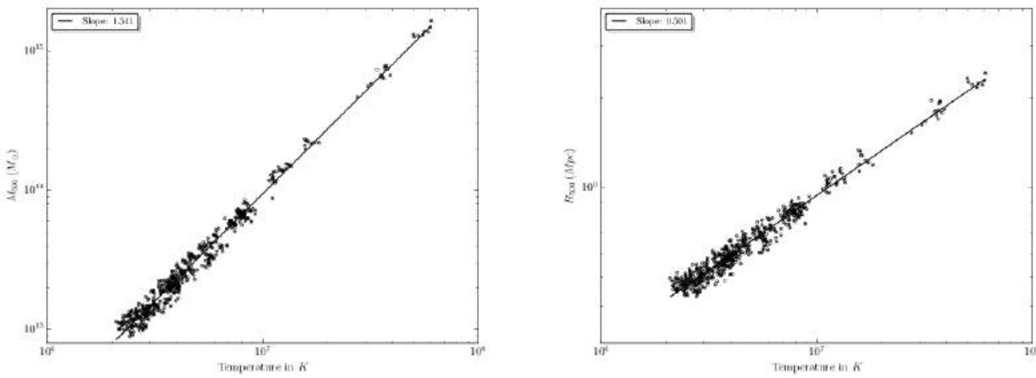

Figure 1: **Panel 1**: Total mass is plotted against the temperature. **Panel 2**: Virial radius is plotted against the temperature.

4. Cosmic ray production and evolution

In a simple model the CR acceleration in galaxy clusters can be assumed of injection of thermally energized particle at the shocks. A fraction of the shock kinetic energy will be transferred to the CRs. If the acceleration efficiency of the shocks is considered to be $\eta(\mathcal{M}_s)$, the CR energy flux at the shock can be quantified by

$$f_{CR} = \eta(\mathcal{M}_s) \times f_{kin}. \tag{1}$$

Where, f_{kin} is the kinetic energy flux and given by $f_{kin} = \frac{1}{2}\rho v^3$ for a density ρ and velocity dispersion v of the medium. The Mach number of the shock can be expressed as $\mathcal{M} = \frac{v}{c_s}$. So the kinetic energy flux can be written as a function of shock mach number $\mathcal{M}$. The CR flux then becomes a strong function of mach number only and can be expressed as

$$f_{CR} = \eta(\mathcal{M}) \times \frac{1}{2}\rho(\mathcal{M}c_s)^3. \tag{2}$$

Where CR acceleration fraction i.e. $\eta(\mathcal{M})$ can be obtained numerically from diffusive shock acceleration (DSA) simulations [17]:

$$\eta(\mathcal{M}) = \begin{cases} 1.025\delta_0, & \text{if } M \leq 1.5 \\ \displaystyle\sum_{n=0}^{4} a_n \frac{(M-1)^n}{M^4}, & \text{if } M > 1.5 \end{cases} \tag{3}$$

where a_0, a_1, ... are the fitted polynomial coefficients. Here δ_0 is the gas thermalization efficiency at shocks without CRs, which was calculated from the Rankine-Hugoniot jump condition:

$$\delta_0(M) = \frac{2}{\gamma(\gamma-1)M^2 R}\left[\frac{2\gamma M^2-(\gamma-1)}{(\gamma+1)} - R^{\gamma}\right], \qquad R \equiv \frac{\rho_2}{\rho_1} = \frac{\gamma+1}{\gamma-1+2/M^2}. \tag{4}$$

In the actual scenario, not only the thermally accelerated particles but there are also pre-existing energetic particles due to historical energetic events in the system.

5. Results

In the simulated clusters, the shock Mach numbers seen to be varying in the range 1 - 4 in the core region. And in some region from R_{500} to R_{200} it goes up to 7. Outside the virial radius (i.e. R_{200}) it goes beyond 10 (see Fig.2).

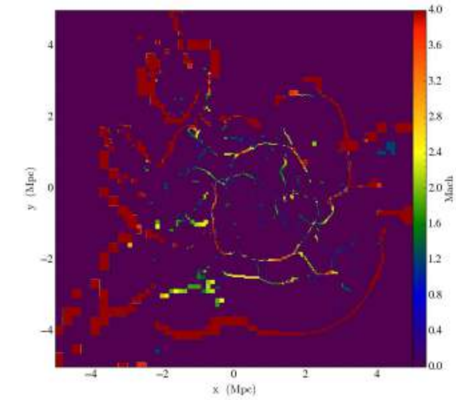

Figure 2: Slice plot of mach number of area of 10 Mpc h^{-1}.

In our simulations we found that the most cosmic ray acceleration is happening for the Mach number ranging 2 - 5 (mostly peaking at ~ 3) during the evolution of the cluster (see Fig.3), is consistent with the other such studies [18]. But, during mergers, the peak shifts towards higher mach numbers. This is due to the fact that the merger shocks, when moves towards the outskirts, Mach number and the occupying volume both increases. In this context, we have made a plot to see the correlation between total volume occupied by shocks in the range of Mach numbers above 2 at different stages of its evolution (see the Fig.3, Panel 2). This plot clearly shows that there are phases when shocked volume goes more than 10% (even upto 20%) of the total virial volume of the cluster, with a sharp contrast to the usual shocked volume of about a percent only in the relaxed condition. Another important observation is, at the low redshift, the shocked volume rapidly goes down by more than an order which may result in fall of total energy flux from the system. A crucial observation can also be made from this plot about the contribution for CR acceleration from the high mach number. In a relaxed system, Mach number beyond 10 is hardly existing, where as during mergers, strong shocks increases by more than 10^3 folds than that of a relaxed system and total volume occupying by such a strong shock becomes significant with almost about 1% of the total volume.

We also found that during the mergers, CR flux goes up by many times (Fig.4). There is a good correlation of merging phases and CR flux, this will definitely help us in explaining the merging galaxy clusters at different states.

6. Discussions and conclusions

- Large scale structure formation shocks are the most efficient particle acceleration agent, and responsible for production of the CR particle from the galaxy clusters.
- Mach number for internal shocks are in the range 1 - 4. While mach number for outer shocks can go beyond 10.
- The most CR acceleration is happening for the Mach number ranging 2 - 5 (mostly peaking at ~ 3)
- Main contribution in CR production is coming from the volume filling factor of shocks.
- We see a good correlation of merging phases and CR flux, this will definitely help us in explaining the merging galaxy clusters at different states.

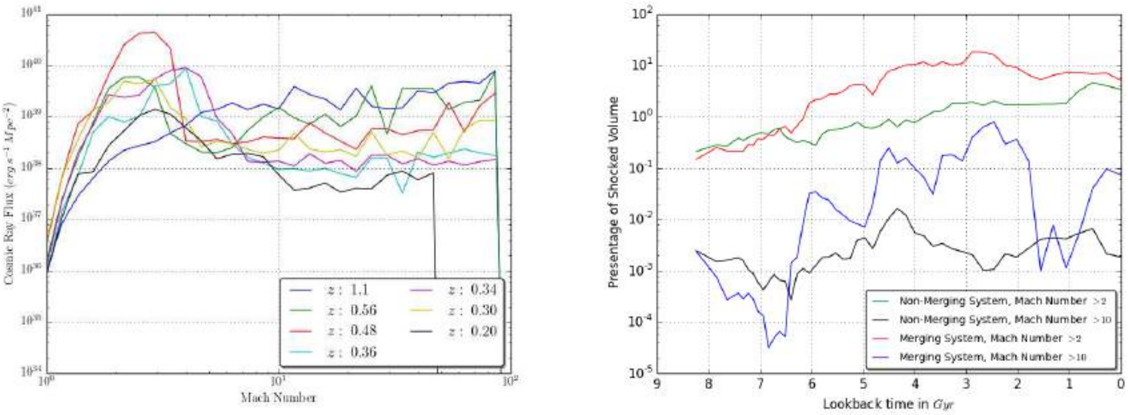

Figure 3: **Panel 1:** CR flux vs the Mach number (Log[f_{CR}] Vs Log[$\mathcal{M}$]). The most CR flux can be observed corresponding to mach number about 3. **Panel 2:** This shows a plot of fractional volume within a cluster that is shocked with Mach number more than 2 (red) and mach number $>$ 10 (blue). The same parameter for a cluster

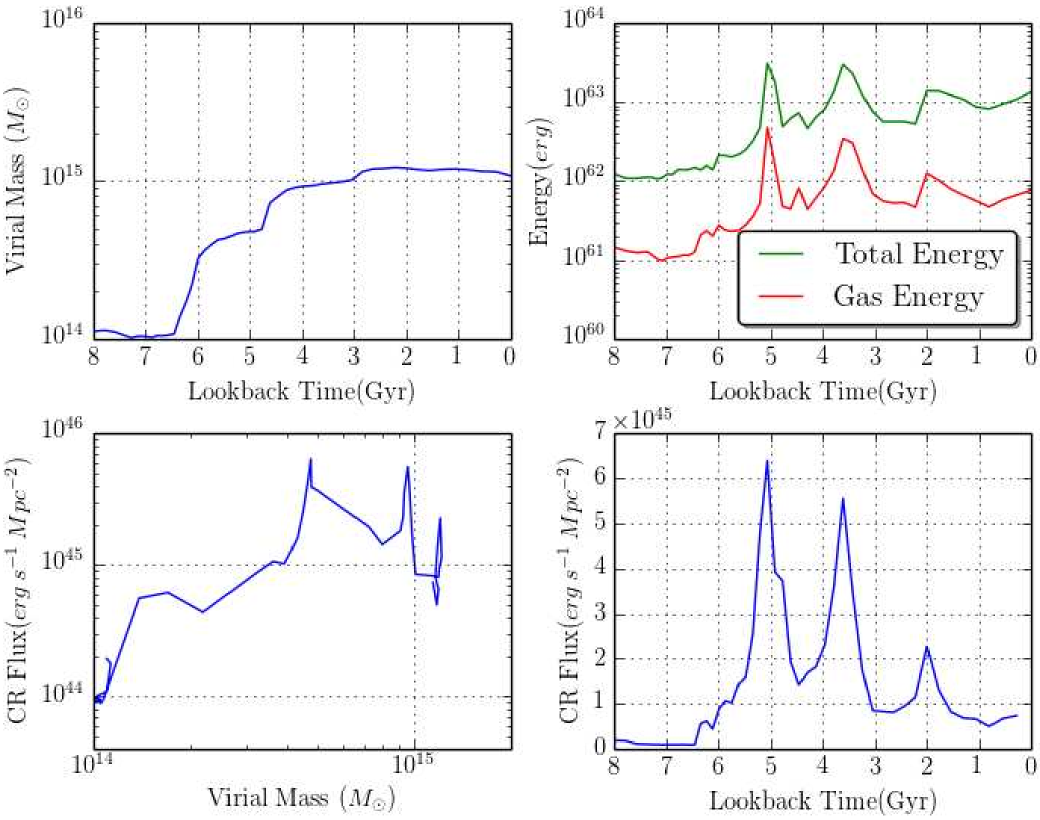

Figure 4: First 3 panels in clockwise direction shows the mass, energy, and CR flux evolution with look back time and 4^{th} one shows the evolution of CR flux with mass for a forming galaxy cluster.

7. Acknowledgment

We are very thankful to The Inter-University Centre for Astronomy and Astrophysics (IUCAA) for providing the HPC facility. RSJ and SP acknowledge DST-INSPIRE Faculty Scheme (IFA-12-PH-44) and also we acknowledge

DST-SERB Young Scientist Scheme (SR/FTP/PS-118/2011) for funding this project.

References

[1] A. M. Bykov, E. M. Churazov, C. Ferrari, W. R. Forman, J. S. Kaastra, U. Klein, M. Markevitch, de Plaa J., 2015, SSRv 188, 141.
[2] Berezinsky V. S., Blasi P., Ptuskin V. S., 1997a, ApJ, 487, 529
[3] Planck Collaboration Ade P. A. R., Aghanim N., Arnaud M., Ashdown M., Atrio-Barandela F., Aumont J., Baccigalupi C., Balbi A., Banday A. J., et al. 2013, A&A, 550, A134
[4] Kang H., Ryu D., Jones T. W., 1996, ApJ, 456, 422
[5] Miniati F., 2000, PhD thesis, University of Minnesota, USA
[6] Paul S., Iapichino L., Miniati F., Bagchi J., Mannheim K., 2011, ApJ, 726, 17
[7] Kang H., Ryu D., 2013, ApJ, 764, 95
[8] Kaastra J. S., Bykov A. M., Schindler S., Bleeker J. A. M., Borgani S., Diaferio A., Dolag K., Durret F., Nevalainen J., Ohashi T., Paerels F. B. S., Petrosian V., Rephaeli Y., Richter P., Schaye J., Werner N., 2008, SSR, 134, 1
[9] O'Shea B. W., Bryan G., Bordner J., Norman M. L., Abel T., Harkness R., Kritsuk A. , 2010, Enzo: AMR Cosmology Application
[10] Komatsu E., Dunkley J., Nolta M. R., Bennett C. L., Gold B., Hinshaw G., Jarosik N., Larson D., Limon M., Page L., Spergel D. N., Halpern M., Hill R. S., Kogut A., Meyer S. S., Tucker G. S., Weiland J. L., Wollack E., Wright E. L., 2009, ApJS, 180, 330
[11] Eisenstein D. J., Hu W., 1999, ApJ, 511, 5
[12] Akahori T., Yoshikawa K., 2012, PAJS, 64, 12
[13] Choi Y.-Y., Reynolds C. S., Heinz S., Rosenberg J. L., Perlman E. S., Yang J., 2004, ApJ, 606, 185
[14] Sarazin C. L., White III R. E., 1987, ApJ, 320, 32
[15] Turk M. J., Smith B. D., Oishi J. S., Skory S., Skillman S. W., Abel T., Norman M. L., 2011, ApJS, 192, 9
[16] Peebles P. J. E., 1980, The large-scale structure of the universe
[17] Kang H., Ryu D., Cen R., Ostriker J. P., 2007, ApJ, 669, 729
[18] Hong S. E., Ryu D., Kang H., Cen R., 2014, APJ, 785, 133

Horizon, homogeneity and flatness problems – do their resolutions really depend upon inflation?

Ashok K. Singal

Astronomy and Astrophysics Division, Physical Research Laboratory, Navrangpura, Ahmedabad-380 009, Gujarat, India

asingal@prl.res.in; COS3, Poster, CICAHEP15.169.1

In textbooks and review articles on modern cosmology [1, 2, 3, 4, 5, 6] one almost invariably comes across a section devoted to the subject of observed homogeneity and near-flatness of the universe, where it is argued that to explain these observations inflation is almost a must. In fact that was the prime motive of Guth [7] to propose inflation in the first place. We show that the arguments offered therein are not proper. The horizon problem, which leads to the causality arguments, arises only in the world models where homogeneity and isotropy (cosmological principle) is presumed to begin with. We do not know whether the horizon problem would still arise in non-homogeneous world models. Therefore as long as we are investigating consequences of the cosmological models based on Robertson-Walker line element, there is no homogeneity issue.

We also show that the flatness problem, as it is posed, is not even falsifiable. The usual argument used in literature is that the present density of the universe is very close (within an order of magnitude) to the critical density value. From this one infers that the universe must be flat since otherwise in past at 10^{-35} second (near the epoch of inflation) there will be extremely low departures of density from the critical density value (i.e., differing from unity by a fraction of order $\sim 10^{-53}$), requiring a sort of fine tuning. Actually we show that even if the present value of the density parameter (in terms of the critical density value) were very different, still at 10^{-35} second it would in any case differ from unity by a fraction of order $\sim 10^{-53}$. For instance, even if had an almost empty universe, with say, $\rho_o \sim 10^{-56}$ gm/cc or so (with density parameter $\Omega_o \sim 10^{-28}$, having a mass equivalent to that of Earth alone to fill the whole universe), we still get the same numbers for the density parameter at the epoch of inflation. So such a fine-tuning does not discriminate between various world models and a use of fine tuning argument amounts to *a priori* rejection of all models with $k \neq 0$, because inflation or no inflation, the density parameter in all Friedmann-Robertson-Walker (FRW) world models gets arbitrarily close to unity as we approach the epoch of the big bang. That way, without even bothering to measure the actual density, we could use any sufficiently early epoch and use "extreme fine-tuning" arguments to rule out all non-flat models. Thus without casting any whatsoever aspersions on the inflationary theories, we point out that one cannot use these type of arguments, viz. homogeneity and flatness, in support of inflation.

1. Horizon and homogeneity problem

Horizon in the cosmological context implies a maximum distance yonder which we as observers have not yet seen the universe due to a finite speed of light as well as a finite age of the universe. In other words these are the farthest regions of the universe (redshift $z \to \infty$) from which the light signals have just reached us. However when we look at the universe we find that distant regions in opposite directions seen by us have similar cosmic microwave background radiation (CMBR) temperatures. The object horizon problem in standard cosmological big bang model is that these different regions of the universe have not ever communicated with each other, but nevertheless they seem to have the same temperature, as shown by the CMBR which shows almost a uniform temperature (2.73° K) across the sky, irrespective of the direction. How can this be possible, considering that any exchange of information (say, through photons or any other means) can occur, at most, at the speed of light. How can such two causally disconnected regions have one and same temperature, unless one makes a somewhat "contrived" presumption that the universe was homogeneous and isotropic to begin with when it came into existence [1]?

One can illustrate the object horizon problem using a simple, though somewhat naive, argument in the following way. According to the big bang model the universe has only a finite age, say t_o. Then light (or information) from regions at a cosmological distance ct_o from us would have reached us just now, and could not have crossed over to similar distant regions on the other side of us. Then how two far-off regions on two opposite sides of us have managed to achieve the homogeneity so that we see them having same properties. Though the argument does contain an element of truth, but it could not be always true and its naive nature can be seen from the simplest of FRW models, namely empty universe of Milne ($\rho = 0, q_o = 0$), where even the most distant ($z \to \infty$) observable

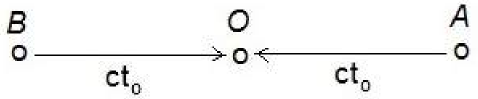

Figure 1. An observer at O (us) receiving signal from distant objects at A and B at time t_o, which is the time since big bang. Signal from A having just reached O could not have yet reached B and vice versa.

point in the infinite extent of the universe is within horizon for each and every point of the universe, let it be in any region in any direction from us in this infinite universe model. For instance, in this world-model B will receive signals from us (at O) and from A in same amount of time. In fact all regions in this universe at any time receive past signals from all other regions even though the universe is infinite. Thus horizon problem does not arise in this particular world-model. However, in more realistic cases of general relativistic cosmological models, say with finite density, almost invariably one comes across horizon problems.

From the observed CMBR, the universe appears to be very close to isotropic. At the same time Copernican principle states that earth does not have any eminent or privileged position in the universe and therefore an observer's choice of origin should have no bearing on the appearance of the distant universe. From this we infer that the cosmos should appear isotropic from any vantage point in the universe, which directly implies homogeneity. For this one uses Weyl's postulate of an infinite set of *equivalent fundamental observers* spread around the universe, who agree on a "global" time parameter, orthogonal to 3-d space-like hyper surfaces, and measured using some local observable like density, temperature, pressure etc. as a parameter [1, 3, 8]. Thus we are led to the cosmological principle that the universe on a sufficiently large scale should appear homogeneous and isotropic to all fundamental observers, and then one gets for such observers a metric for the universe known as Robertson-Walker metric.

Is there any other evidence in support of the cosmological principle? Optically the universe shows structures up to the scale of super clusters of galaxies and even beyond up hundreds of mega parsecs, but the conventional wisdom is that when observed on still larger scales the universe would appear homogeneous and isotropic. It is generally thought that radio galaxies and quasars, the most distant discrete objects (at distances of gig parsecs and farther) seen in the universe, should trace the distribution of matter in the universe at that large scale and should therefore appear isotropically distributed from any observing position in the universe.

But there is a caveat. In the 3CRR survey, the most reliable and most intensively studied complete sample of strong steep-spectrum radio sources, large anisotropies in the sky distributions of powerful extended quasars as well as some other sub-classes of radio galaxies are found [9]. If we include all the observed asymmetries in the sky distributions of quasars and radio galaxies in the 3CRR sample, the probability of their occurrence by a chance combination reduces to $\sim 2\times10^{-5}$. Such large anisotropies present in the sky distribution of some of the strongest and most distant discrete sources imply inhomogeneities in the universe at very large scales (covering a fraction of the universe).

Also using a large sample of radio sources from the NRAO VLA Sky Survey, which contains 1.8 million sources, a dipole anisotropy is seen [10] which is about 4 times larger than the CMBR dipole, presumably of a kinetic origin due to the solar motion with respect to the otherwise isotropic CMBR. These unexpected findings have recently been corroborated by two independent groups [11, 12]. The large difference in the inferred motion (as much as a factor of ~ 4) cannot be easily explained. A genuine discrepancy in the dipoles inferred with respect to two different cosmic reference frames would imply a large ($\sim 10^3$ km/sec) relative motion between these frames, not in accordance with the cosmological principle.

If we ignore these and some other similar threats to the cosmological principle and trust the assumption of homogeneity and isotropy *for the whole universe for all times*, then the line element can be expressed in the Robertson-Walker metric form [2, 3, 4, 8],

$$\mathrm{d}s^2 = c^2\mathrm{d}t^2 - R^2(t)\left[\frac{\mathrm{d}r^2}{(1-k\,r^2)^{1/2}} + r^2(\mathrm{d}\theta^2 + \sin^2\theta\,\mathrm{d}\phi^2)\right], \tag{1}$$

where the only time dependent function is the scale factor $R(t)$. The constant k is the curvature index that can take one of the three possible values $+1, 0$ or -1 and (r, θ, ϕ) are the time-independent comoving coordinates.

Using Einstein's field equations, one can express the curvature index k and the present values of the cosmic scale factor R_o in terms of the Hubble constant H_o, the matter energy density Ω_m and the vacuum energy (dark energy) density Ω_Λ as [2, 3, 4],

$$\frac{k\,c^2}{H_\mathrm{o}^2 R_\mathrm{o}^2} = \Omega_o - 1, \tag{2}$$

where $\Omega_o = \Omega_m + \Omega_\Lambda$. The space is flat ($k = 0$) if $\Omega_o = 1$.

In general it is not possible to express the comoving distance r in terms of the cosmological redshift z of the source in a close-form analytical expression and one may have to evaluate it numerically. For example, in the $\Omega_m + \Omega_\Lambda = 1, \Omega_\Lambda \neq 0$ world-models, r is given by [2],

$$r = \frac{c}{H_\mathrm{o} R_\mathrm{o}} \int_1^{1+z} \frac{\mathrm{d}z}{(\Omega_\Lambda + \Omega_m z^3)^{1/2}}. \tag{3}$$

For a given Ω_Λ, one can evaluate r from equation (3) by a numerical integration.

However for $\Omega_\Lambda = 0$ cosmologies, where the deceleration parameter $q_\mathrm{o} = \Omega_m/2$, it is possible to express the comoving (coordinate) distance r as an analytical function of redshift [13],

$$r = \frac{c}{H_\mathrm{o} R_\mathrm{o}} \frac{z}{(1+z)} \frac{\left[1 + z + \sqrt{1 + 2q_\mathrm{o} z}\right]}{\left[1 + q_\mathrm{o} z + \sqrt{1 + 2q_\mathrm{o} z}\right]}, \tag{4}$$

which for the empty Milne universe ($q_\mathrm{o} = 0$) of negative curvature ($k = -1$) yields,

$$r = \frac{c}{2H_\mathrm{o} R_\mathrm{o}} \left[1 + z - \frac{1}{1+z}\right], \tag{5}$$

while for the Einstein - de Sitter world-model ($q_\mathrm{o} = 1/2$) with zero curvature ($k = 0$) we get,

$$r = \frac{2c}{H_\mathrm{o} R_\mathrm{o}} \left[1 - \frac{1}{\sqrt{1+z}}\right]. \tag{6}$$

From equation (5) we see that in the Milne universe, corresponding to redshift $z \to \infty$, the comoving coordinate $r \to \infty$ too, thus there is no finite horizon limit in this case and the whole universe is visible to any observer at any time, consistent with our discussion above. On the other hand from equation (6) we notice in the flat universe redshift $z \to \infty$ yields for r a finite value. However in this world model the range of coordinate r goes up to infinity. Thus there is a certain finite object horizon $r_{oh} = 2c/(H_\mathrm{o} R_\mathrm{o})$ beyond which we are unable to see because there is only a finite amount of time since the big bang singularity (corresponding to $z \to \infty$), and thus only a finite distance that photons could have travelled within the age of the universe. It turns out that *all* non-trivial (that is with finite density) FRW world-models starting with a big bang necessarily have a object horizon [3].

Appearance of object horizon in a world model is generally interpreted as that different parts of the universe in that model did not get sufficient time to interact with each other and thus may have yet no causal relations and therefore could not have achieved uniformity everywhere. Therefore inflation is invoked in which an exponential expansion of space takes place at time $t \sim 10^{-35}$ sec by a factor of $\sim 10^{28}$ or larger and the space-points now far apart (and thus apparently not in touch with each other so they appear to be causally unrelated) were actually much nearer before $t \sim 10^{-35}$ sec or so and could have had time to interact with each other before inflation.

A most crucial point that somehow seems to have been missed (or ignored) in these deliberations is that the question of horizon problem arises only when we to begin with assume that the Universe was "always" homogeneous and isotropic, because only then we can make use of Robertson-Walker element where we separate the time co-ordinate from the 3-d space which may or may not be flat and has the time-dependence only through a single scale parameter $R(t)$. It is only there that horizon makes an appearance which in turn has given rise to the oft-discussed question of the uniformity and homogeneity of the space. However, as long as we make use of the Robertson-Walker metric we are taking for guarantee that the universe was *ever* homogeneous and isotropic, and that a single parameter $R(t)$

can describe the past and determine the future of the universe. There is no doubt about the presence of a horizon, which follows from the Robertson-Walker line element. However that in itself does not imply a nonexistence or lack of homogeneity as horizon itself exists only in models where to begin with homogeneity is presumed. All we find from calculations is that in a universe which is which is isotropic and homogeneous on a large enough scale and where one can assign a single common parameter to all fundamental observers to use as time, the light signals in a finite amount of time are not able to cover the whole available range of space coordinate r in the universe. In fact some of the world models even in an infinite time all r may not get covered by light signals emitted from a point ("event horizon"). Cause and effect seem to reverse their roles. It is not that because horizon exists so uniformity is not possible, ironically it is where a uniformity is present to begin with that we seem to end up with a horizon problem. In these models we assume not only a single parameter t, but all other parameters describing the universe having common values of scale factor $R(t)$, density $\rho(t)$, Hubble parameter H_o, deceleration parameter q_o etc. to be the same everywhere, at any given time t (even beyond object or event horizons wherever we encounter such horizons)). It is yet to be seen whether such horizons would still arise in models where one does not begin with the cosmological principle and one has to deal with a genuine non-uniformity problem.

Actually if we follow the standard arguments in the literature then inflation in one sense makes the application of cosmological principle worse than ever. Though it may alleviate the problem of object horizon, yet it gives rise to much more acute event horizon problems. After all even just before inflation began, there were object horizons which because of a rapid expansion of the universe due to inflation will become even more "remote" from each other ending up in growth of large number of event horizons, with all such regions of the universe never able to interact with each other. Thus such a universe will comprise huge number of large patches still isolated from each others. Then how can one still apply the cosmological principle to such a disjointed universe which would conflict with our starting assumption (Weyl's postulate!), where we cannot even get a single parameter to act as cosmic time, orthogonal to 3-d space-like hyper surfaces, which is purely based on the condition of universal homogeneity and isotropicity. We cannot then even use Robertson-Walker line element to describe the geometry and then all our conclusions about the cosmological models would have to be abandoned and we will then be back to square one.

Once again, the only saviour here is that, inflation or no inflation, these horizons are encountered only in the models where we have already assumed cosmological principle. However, if we do want to really examine the question of homogeneity or its absence then we need to abandon the standard model based on the Robertson-Walker metric and then with some new model, where possibility of anisotropy or inhomogeneity is assumed to begin with, one has to examine if in such models also we come across horizons and if so, then we may have a genuine problem to explain.

2. Flatness problem

In the so-called flatness problem, the current density of the universe is observed to be very close to the critical value, needed for a zero curvature ($k = 0$). Since the density departs rapidly from the critical value with time, the early universe must have had a density even closer to the critical density, so much so that if we extrapolate the density parameter to the epoch of inflation ($t \sim 10^{-35}$ sec) we find it to be within unity within an extremely small fraction of order $\sim 10^{-53}$. This leads to the question how the initial density came to be so closely fine-tuned to the critical value. Cosmic inflation was proposed to resolve this issue along with the horizon problem [7]. However, as we will show, the flatness problem, as it is posed, is not falsifiable.

A general form of equation (2) valid at any epoch is,

$$H^2R^2(\Omega - 1) = kc^2. \tag{7}$$

Making use of equation (2) we get,

$$H^2R^2(\Omega - 1) = H_o^2R_o^2(\Omega_o - 1), \tag{8}$$

which for the epoch of inflation ($t \sim 10^{-35}$ sec) can be simplified [1] to,

$$(\Omega - 1) \approx 10^{-53}(\Omega_o - 1). \tag{9}$$

The usual argument prevalent in literature is that the present density of the universe is very close (within an order of magnitude) to the critical density value, i.e., $0.1 < \Omega_o < 1$. From this one infers that the universe must be flat since otherwise in past at 10^{-35} second (near the epoch of inflation) there will be extremely low departures of density from the critical density value (i.e., differing from unity by a fraction of order $\sim 10^{-53}$), requiring a sort of fine tuning. However this argument could be applicable to almost any present value of the observed density of the Universe. What is implied here is that even in a hypothetical almost empty universe where the density of universe is say, $\rho_o \sim 10^{-56}$ gm/cc) or so (with density parameter $\Omega_o \sim 10^{-28}$, having only a mass equivalent to that of Earth alone to fill the whole universe), from equation (9) the density parameter at the epoch of inflation would differ from unity by the same fraction, of order $\sim 10^{-53}$. Thus without casting any whatsoever doubts on the inflationary theories, we merely point out that one cannot use these type of arguments to support inflation.

Is there really any substance in this type of arguments as even a mass equal to that of earth alone spread over the universe will lead to the same low departures from unity of 10^{-53}? In fact even the presence of a mere single observer would imply the same departures from unity of 10^{-53}. So a use of fine tuning argument amounts to *a priori* rejection of all models with $k \neq 0$, because inflation or no inflation, the density parameter in all Friedmann-Robertson-Walker (FRW) world models gets arbitrarily close to unity as we approach the epoch of the big bang. That is the property of all these FRW models. That way, irrespective of the actual density, we could use any sufficiently early epoch and use the "extreme fine-tuning" arguments to reject all non-flat models. But that is not what one could call a falsifiable theory. Thus without casting any whatsoever aspersions on the inflationary theories, we point out that one cannot use these type of arguments to support inflation.

In fact flatness and homogeneity problems seem to contradict each other. If we say that the universe is flat ($k = 0$) then we are assuming that the density is exactly equal to the critical value and does not depart from it to even by a smallest fraction. Or in words, each and every particle is essential and is thus accounted for and even a single particle is not extra or less in the whole cosmos, as excess of even a single particle more than that needed for the critical density will ultimately turn the universe from a flat to a curved one. Which means this much information we have about the whole universe. Then how can we say that we may have no information about some other parts of the universe due to the so-called horizon problem? While on one hand we guarantee that in $k = 0$ world models (flat space), each and every particle in the universe is accounted for (as otherwise even a single extra or missing particle more than the critical density would cause the universe to deviate from the flat universe (a runaway case!), but on the other hand we are saying that we (one part of the universe) have no communication or information about distant parts of the universe and know nothing about them i.e., about the density, temperature, pressure etc. there, so that uniformity or homogeneity could not have been enforced since the "birth" of the universe. Are we not contradicting ourselves?

By opting for a flat universe, the least probable out of three possible curvature values, we seem to be following the example of Copernicus epicycles on philosophical grounds. Further, the argument of flatness perhaps has a catch. Inflation might make the universe flatter (by bringing density parameter closer to unity) but it can make it flat (by making the density parameter exactly equal to unity). What we mean is that if we think that inflation has brought about only a near-flatness then we are essentially assuming that $k \neq 0$, because otherwise if $k = 0$, then inflation does not have a role to play here as it cannot flatten it further. And if $k \neq 0$ then inflation cannot make it $k = 0$, even though it might bring the density parameter closer to unity. In fact by assuming a flat model we are assuming the ultimate finest-ever tuning imaginable where even the least amount of perturbation on this unstable equilibrium model (in the form of an excess or deficiency of the smallest amount of matter from the critical density - a single particle or atom extra or missing!) can ultimately take the universe away from the flat-space model to a curved one.

References

[1] J. V. Narlikar, *Introduction to Cosmology*, Cambridge Univ. Press, Cambridge (1993).
[2] J. A. Peacock, *Cosmological Physics*, Cambridge Univ. Press, Cambridge (1999).
[3] W. Rindler, *Relativity - Special, General and Cosmological*, 2nd ed., Oxford Univ. Press, New York (2006).
[4] S. Weinberg, *Cosmology*, Oxford Univ. Press, New York (2008).
[5] T., Padmanabhan, & T. R. Seshadri, J. Astrophys. Astr. **8**, 275 (1987).
[6] M. J. Rees, J. Astrophys. Astr. **5**, 331 (1984).
[7] A. Guth, Phy. Review D **23**, 347 (1981).
[8] C. W. Misner, K. S. Thorne, J. A. Wheeler, *Gravitation*, Freeman, San Fransisco (1973).

[9] A. K. Singal, Astrphys. Sp. Sc. **357**, 152 (2015); DOI: 10.1007/s10509-015-2388-2.
[10] A. K. Singal, Astrophys. J. **742**, L23, (2011).
[11] M. Rubart, D. J. Schwarz, Astrophys. Astr. **555**, A117 (2013).
[12] P. Tiwari et al., Astropart. Phys. **61**, 1 (2015).
[13] J. Terrell, Am. J. Phys. **45**, 869 (1977).

Lorentzian wormholes without exotic matter in Eddington-inspired Born-Infeld gravity

Rajibul Shaikh

Centre for Theoretical Studies, Indian Institute of Technology Kharagpur, Kharagpur-721302, West Bengal, India.

rajibulshaikh@cts.iitkgp.ernet.in; COS.7, Oral, CICAHEP15.173

Within the framework of Eddington-inspired Born-Infeld (EiBI) gravity, we show that it is possible to construct a wide class of exact Lorentzian wormholes without violating the weak or null energy condition. The wormholes exist in a certain region of the parameter space spanned by the Eddington-Born-Infeld theory parameter and the parameters related to mass and energy density. Below the critical value of a parameter defined in our work, we have wormholes. Above the critical value, an event horizon is formed around the wormhole throat resulting in a regular black hole geometry. The traversability constraints on the wormholes, which restrict the tidal acceleration at the throat to values below one Earth gravity (g), lead to lower limits on the theory parameter and the throat radius. As a special case of our solution, we retrieve the wormhole supported by an electric field for a charge-to-mass ratio greater than the critical value 1.144.

1. Introduction

It is well known that the violation of energy conditions and hence the requirement of exotic matter are generic features of a wormhole in general relativity (GR) [1, 2]. However, this may not be true in modified or alternative gravity theories. A simple study on Raychaudhuri equation for a bundle of light rays passing through a wormhole, point out that, in general, the violation of the null convergence condition is a generic feature of a wormhole, not the violations of the energy conditions. In GR, the violation of null convergence condition is translated to the violation of null energy condition via Einstein field equation. This, in turn, leads to the violations of all other energy conditions (weak, strong, dominant, etc.). But, because of the modified field equations in some modified or alternative theories of gravity, a violation of null convergence condition may not lead to a violation of the energy conditions. Therefore, in such theories, we may have wormhole supported by non-exotic matter.

In this article, we review one such wormhole solution supported by non-exotic matter and obtained in [3] in the context of Eddington-inspired Born-Infeld gravity (EiBI) [4]. Born-Infeld type of gravitational action was first suggested by Deser and Gibbons [5], inspired by the earlier work of Eddington [6] and the nonlinear electrodynamics of Born and Infeld [7]. They considered metric formulation of the action. However, we shall focus on the Palatini formulation of the action with the matter coupling considered by Banados and Ferreira [4]. Banados and Ferreira's formulation of Born-Infeld gravity is commonly cited as Eddington-inspired Born-Infeld gravity (EiBI). Various aspects of EiBI gravity such as spherically symmetric solutions, cosmology, and astrophysical aspects, have been studied by many authors in the recent past [8, 9, 10, 11, 12]. Many authors have attempted to obtain wormhole solution in this theory. The matter supporting the wormhole solution obtained in [8] in three dimensional EiBI gravity, satisfies the energy condition for a negative cosmological constant. However, the energy conditions are violated for non-negative cosmological constant. The anisotropic fluid supporting the wormhole solution obtained in [9] in four dimension, has negative energy density and hence violates the energy conditions. The author in [10] obtained a wormhole solution supported by Maxwell electric field. However, we retrieve this wormhole solution as a special case of the general wormhole solution obtained in [3].

2. Wormholes, Raychaudhuri equations and energy conditions

The spacetime representing a static, spherically symmetric wormhole geometry is generically written as [1]

$$ds^2 = -e^{2\Phi(r)}dt^2 + \frac{dr^2}{1-\frac{b(r)}{r}} + r^2(d\theta^2 + \sin^2\theta d\phi^2), \tag{1}$$

where $\Phi(r)$ and $b(r)$ are, respectively, the redshift function and the wormhole shape function. The wormhole throat is at $r = r_0$ such that $b(r_0) = r_0$. One of the necessary conditions to construct a traversable wormhole is that $\Phi(r)$

must be finite everywhere (no horizon condition). The spatial shape of the wormhole is visualized by embedding the t =constant, $\theta = \pi/2$ spatial section of the wormhole spacetime in background cylindrical coordinates (z, r, ϕ) system using an embedding function $z(r)$. Therefore, the line element on the embedding surface can be written as

$$ds_2^2 = dz(r)^2 + dr^2 + r^2 d\phi^2 = \left[1 + \left(\frac{dz}{dr}\right)^2\right] dr^2 + r^2 d\phi^2.$$

Matching this with the t = constant, $\theta = \pi/2$ section of the metric in (1), one obtains the embedding equation $\frac{dz}{dr} = \pm\sqrt{\frac{b/r}{1-b/r}}$. The embedding diagram is obtained by taking the surface of revolution of the curve $z = z(r)$ by varying ϕ from 0 to 2π. The embedding diagram of a wormhole for a typical shape function $b(r)$ is shown in Fig. 1. The inverse embedding function $r = r(z)$ has a minimum at the throat. This is known as the minimality of the

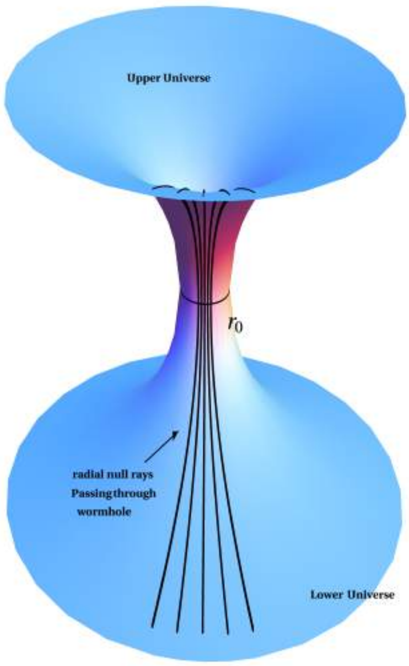

Figure 1. Embedding diagram of a wormhole.

wormhole throat. This leads to the well-known flare-out condition at the throat

$$\frac{d}{dz}\left(\frac{dr}{dz}\right) = \frac{b - b'r}{2b^2} > 0. \tag{2}$$

The minimality of the throat can be reinterpreted as divergent null rays passing through the throat. This requires the violation of the null convergence condition, from the Raychaudhuri equation. The Raychaudhuri equation for a bundle of light rays is given by

$$\frac{d\hat{\theta}}{d\lambda} + \frac{1}{2}\hat{\theta}^2 + \hat{\sigma}^2 - \hat{\omega}^2 + R_{\alpha\beta}\hat{u}^\alpha \hat{u}^\beta = 0,$$

where $\hat{\sigma}^2 = \hat{\sigma}_{\alpha\beta}\hat{\sigma}^{\alpha\beta}$, $\hat{\omega}^2 = \hat{\omega}_{\alpha\beta}\hat{\omega}^{\alpha\beta}$and $\hat{u}^\alpha$ is the four velocity of the light ray. There are also evolution equation for the shear ($\hat{\sigma}_{\alpha\beta}$) and rotation ($\hat{\omega}_{\alpha\beta}$) tensors [13]. For a radial null ray passing through the wormhole (see Fig. 1) in the equatorial plane ($\theta = \pi/2$), $\hat{u}^t = e^{-2\Phi(r)}$ and $\hat{u}^r = \pm e^{-\Phi(r)}\sqrt{1 - \frac{b(r)}{r}}$. Note that the family is ingoing at one side and outgoing at the other side of the throat. Therefore, the expansion for this family becomes $\hat{\theta} = \nabla_\alpha \hat{u}^\alpha = \pm\frac{2}{r}e^{-\Phi}\sqrt{1 - \frac{b(r)}{r}}$, where upper and lower signs are for outgoing and ingoing null rays, respectively. Note that the null expansion vanishes at the throat, i.e., $\hat{\theta}(r_0) = 0$. In the neighbourhood of the throat, the null expansion is positive at one side and negative at the other side of the throat. Along the radial null rays, null expansion goes from negative to zero at the throat and then becomes positive at the other side. Therefore, in the neighbourhood of the throat, $\frac{d\hat{\theta}}{d\lambda}$ is positive along this family. It can be shown that the rotation tensor $\hat{\omega}_{\alpha\beta} = (\partial_\beta \hat{u}_\alpha - \partial_\alpha \hat{u}_\beta)$ identically vanishes for this family. Also, $\hat{\sigma}^2 \geq 0$ since $\hat{\sigma}_{\alpha\beta}$ is spatial [13]. Therefore, in order to satisfy the Raychaudhuri equation for the family of radial null rays passing through the wormhole, we must have $R_{\alpha\beta}\hat{u}^\alpha \hat{u}^\beta < 0$. Note that, for a timelike velocity u^α, $R_{\alpha\beta}u^\alpha u^\beta \geq 0$ is known as timelike convergence condition. Therefore, **irrespective of the gravitational theory, the null convergence condition must be violated at the wormhole throat**.

In general relativity, after using the Einstein field equation $G_{\alpha\beta} = 8\pi T_{\alpha\beta}$, one can show that the violation of null convergence condition, i.e., $R_{\alpha\beta}\hat{u}^\alpha \hat{u}^\beta < 0$ implies violation of null energy condition, i.e., $T_{\alpha\beta}\hat{u}^\alpha \hat{u}^\beta < 0$ which, in turn, implies the violation of other energy conditions. The matter violating energy conditions are termed as exotic matter. Therefore, exotic matter is needed to support a wormhole in general relativity. It should be noted that the null convergence condition and null energy condition are same in general relativity. However, in some alternative or modified theory of gravity, these two conditions are different in general. This is because of the modified field equation in these theories. Therefore, in such theories, we may have violation of the null convergence condition without violating the energy condition, i.e., we may have wormholes without exotic matter. Therefore, **in general, the violation of the null convergence condition is a generic feature of a wormhole, not the violation of the energy conditions**. In the subsequent sections, we show that such a wormhole solution, without exotic matter, is possible in Eddington-inspired Born-Infeld (EiBI) gravity.

3. Eddington-inspired Born-Infeld (EiBI) gravity

The action in EiBI gravity is given by [4]

$$S_{BI}[g, \Gamma, \Psi] \quad = \quad \frac{c^4}{8\pi G\kappa} \int d^4x \left[\sqrt{-|g_{\mu\nu} + \kappa R_{\mu\nu}(\Gamma)|} - \lambda\sqrt{-g} \right] + S_M(g, \Psi),$$

where c is the speed of light, G is Newton's gravitational constant, $\lambda = 1 + \kappa\Lambda$, $R_{\mu\nu}(\Gamma)$ is the symmetric part of the Ricci tensor built with the connection Γ and $S_M(g, \Psi)$ is the action for the matter field. Λ is the cosmological constant. Variations of this action with respect to the metric tensor $g_{\mu\nu}$ and the connection Γ yield, respectively [4, 10, 11],

$$\sqrt{-q}q^{\mu\nu} = \lambda\sqrt{-g}g^{\mu\nu} - \bar{\kappa}\sqrt{-g}T^{\mu\nu}, \qquad \nabla^\Gamma_\alpha \left(\sqrt{-q}q^{\mu\nu} \right) = 0, \tag{3}$$

where $\bar{\kappa} = \frac{8\pi G\kappa}{c^4}$, ∇^Γ denotes the covariant derivative defined by the connection Γ and $q^{\mu\nu}$ is the inverse of the auxiliary metric $q_{\mu\nu}$ defined by $q_{\mu\nu} = g_{\mu\nu} + \kappa R_{\mu\nu}(\Gamma)$. To obtain these equations, it is assumed that both the connection Γ and the Ricci tensor $R_{\mu\nu}(\Gamma)$ are symmetric, i.e., $\Gamma^\mu_{\nu\rho} = \Gamma^\mu_{\rho\nu}$ and $R_{\mu\nu}(\Gamma) = R_{\nu\mu}(\Gamma)$. Equation (3) gives the metric compatibility equation which yields

$$\Gamma^\mu_{\nu\rho} = \frac{1}{2} q^{\mu\sigma} \left(q_{\nu\sigma,\rho} + q_{\rho\sigma,\nu} - q_{\nu\rho,\sigma} \right).$$

Therefore, the connection $\Gamma^\mu_{\nu\rho}$ is the Levi-Civita connection of the auxiliary metric $q_{\mu\nu}$.

4. Wormhole solution in EiBI gravity

To obtain wormhole solution, we consider following metric ansatze for the physical and auxiliary metric:

$$ds_g^2 = -\psi^2(r)f(r)dt^2 + \frac{dr^2}{f(r)} + r^2(d\theta^2 + \sin^2\theta d\phi^2), \tag{4}$$

$$ds_q^2 = -G^2(r)F(r)dt^2 + \frac{dr^2}{F(r)} + H^2(r)(d\theta^2 + \sin^2\theta d\phi^2). \tag{5}$$

For the matter part, we consider an anisotropic fluid having an energy-momentum tensor of the form,

$$T^\mu_\nu = diag(-\rho, p_r, p_\theta, p_\theta) = diag(-\rho, -\rho, \alpha\rho, \alpha\rho).$$

It has been shown that the above $T^{\mu\nu}$ can be obtained from non-linear electrodynamics having action of the form [14],

$$S_M = \frac{1}{8\pi}\int d^4x\sqrt{-g}\left(-\frac{1}{2}F_{\mu\nu}F^{\mu\nu}\right)^{\frac{1+\alpha}{2\alpha}}. \tag{6}$$

For $\alpha = 1$, it reduces to the Maxwell electrodynamics action. The energy conservation equation can be integrated to obtain $\rho = \frac{C_0}{r^{2(\alpha+1)}}$, where C_0 is an integration constant. To satisfy the energy conditions, we must have $C_0 > 0$ and $0 \le \alpha \le 1$. The full solution for the physical metric is given by [3]

$$\psi(r) = \left[1 \mp \frac{r_0^{2(\alpha+1)}}{r^{2(\alpha+1)}}\right]^{-\frac{1}{2}}, \tag{7}$$

$$f(r) = \frac{1 \mp \frac{r_0^{2(\alpha+1)}}{r^{2(\alpha+1)}}}{1 \pm \alpha\frac{r_0^{2(\alpha+1)}}{r^{2(\alpha+1)}}}\left[1 - \frac{r_0^{(2\alpha+1)}}{3|\kappa|r^{2\alpha}} - \frac{2}{r\sqrt{1 \mp \frac{r_0^{2(\alpha+1)}}{r^{2(\alpha+1)}}}}\left(\bar{M} + \frac{(\alpha+1)r_0^{2(\alpha+1)}}{3|\kappa|}I(r)\right)\right], \tag{8}$$

$$I(r) = \int \frac{dr}{r^{2\alpha}\sqrt{1 \mp \frac{r_0^{2(\alpha+1)}}{r^{2(\alpha+1)}}}} = \begin{cases} \frac{2}{3}\log\left[\left(\frac{r}{r_0}\right)^{\frac{3}{2}} + \sqrt{\left(\frac{r}{r_0}\right)^3 \mp 1}\right] & : \alpha = \frac{1}{2} \\ \frac{r^{1-2\alpha}}{1-2\alpha}\,{}_2F_1\left[\frac{1}{2}, \frac{2\alpha-1}{2\alpha+2}, \frac{4\alpha+1}{2\alpha+2}; \pm\left(\frac{r_0}{r}\right)^{2\alpha+2}\right] & : \alpha \neq \frac{1}{2}, \end{cases} \tag{9}$$

where $r_0 = (|\kappa|C_0)^{\frac{1}{2(\alpha+1)}}$ and $\bar{M} = \frac{GM}{c^2}$, M being related to the mass. Here, upper and lower signs are for $\kappa < 0$ and $\kappa > 0$, respectively. For radial null rays

$$\left|\hat{\theta}\right| = \frac{2}{r}\sqrt{1 \mp \frac{r_0^{2(\alpha+1)}}{r^{2(\alpha+1)}}}, \qquad R_{\alpha\beta}\hat{u}^\alpha\hat{u}^\beta = \mp 2(\alpha+1)\frac{r_0^{2(\alpha+1)}}{r^{2(\alpha+2)}}. \tag{10}$$

We have seen that $\hat{\theta} = 0$ and $R_{\alpha\beta}\hat{u}^\alpha\hat{u}^\beta < 0$ at the wormhole throat. Therefore, from the above expression, it is clear that we must have $\kappa < 0$ to have wormhole solution and $r = r_0$ represents the wormhole throat. The traversability and no-horizon conditions demand $e^{2\Phi(r)} = \psi^2(r)f(r)$ to be non-zero, positive, and finite, in the range $r_0 \le r < \infty$. But, for $\kappa < 0$, $\psi^2 f$ diverges as $r \to r_0$. However, this divergence can be removed by taking the following relation between κ, M and r_0 [3]:

$$\bar{M} = -\frac{(\alpha+1)r_0^{2(\alpha+1)}}{3|\kappa|}I(r_0) = \begin{cases} 0 & : \alpha = \frac{1}{2} \\ \frac{(\alpha+1)r_0^3}{3(2\alpha-1)|\kappa|}\,{}_2F_1\left[\frac{1}{2}, \frac{2\alpha-1}{2\alpha+2}, \frac{4\alpha+1}{2\alpha+2}; 1\right] & : \alpha \neq \frac{1}{2}. \end{cases} \tag{11}$$

It is clear that, we must have $\alpha \ge \frac{1}{2}$ to satisfy the above condition for non-negative mass M. It has been shown in [3] that the invariant scalars such as Ricci scalar and the Kretschmann scalar are finite at the throat. But, they diverge at the throat if the above condition is not satisfied. At the throat, we have

$$1 - \frac{b(r)}{r}\Big|_{r_0} = f(r)\big|_{r_0} = 0, \quad e^{2\phi(r)}\big|_{r_0} = \psi^2(r)f(r)\big|_{r_0} = \frac{1}{\alpha+1}(1-x)$$

$$\frac{b - b'r}{2b^2}\Big|_{r_0} = \frac{f'}{2(1-f)^2}\Big|_{r_0} = \frac{1}{r_0}(1-x), \qquad x = \frac{r_0^2}{|\kappa|}$$

Therefore, to satisfy the flare-out condition as well as $\psi^2 f > 0$ at the throat, we must have $x < 1$, i.e., $r_0 < |\kappa|^{1/2}$. Since, for $x < 1$, $f = 0$ and $f' > 0$ at the throat, f does not have any zeroes at $r > r_0$. But, for $x > 1$, it has zero (giving an event horizon) at $r = r_h > r_0$. Therefore, for $x > 1$, an event horizon is formed around the throat, thereby giving a regular black hole solution. The critical value $x_c = 1$ distinguishes the wormhole and black hole solutions. For $\alpha = 1$, we retrieve the electrically charged solution discussed in [10]. The energy density $\rho = \frac{1}{8\pi}\frac{Q^2}{r^4}$ gives $C_0 = \frac{Q^2}{8\pi}$, where Q is the charge. In this case, we obtain the critical charge-to-mass ratio $\left(\frac{Q}{M}\right)_c \approx 1.144$ from equation (11) and $x_c = 1$. Therefore, we have wormhole for $\frac{Q}{M} > \left(\frac{Q}{M}\right)_c$ and black hole for $\frac{Q}{M} < \left(\frac{Q}{M}\right)_c$, where we have taken $G = 1$ and $c = 1$. This is similar to the Reissner-Nordström metric where we have naked singularity for $\frac{Q}{M} > 1$ and black hole for $\frac{Q}{M} < 1$. For a traversable wormhole, the tidal acceleration between two parts of a traveller's body travelling through the wormhole must be within a tolerable limit. For the radial tidal acceleration to be below one Earth gravity g, the Eddington-Born-Infeld theory parameter κ and the wormhole throat must be greater than the minimum values $r_{0min} = \sqrt{\frac{c^2}{3g}} \simeq 8.64 R_E$ and $|\kappa|_{min} \simeq 3.0 \times 10^{15} m^2$ [3], where $R_E \simeq 6400$ km is the Earth radius. However, for the solar constraint $|\kappa| \lesssim 1.8 \times 10^{14} m^2$ obtained by Casanellas $et\ al.$ [15], the minimum radial acceleration is given by $17g$.

5. Conclusion

We have seen that, in general, the violation of the null convergence condition is a generic feature of a wormhole not the violations of the energy conditions. In GR, a violation of null convergence condition leads to a violation of the energy conditions, thereby requiring exotic matter to support a wormhole. But, this is not true in EiBI gravity, in general. In this gravity theory, we have obtained an exact wormhole solution supported by non-exotic matter. We have chosen a special relation between the mass M, wormhole throat radius r_0 and the theory parameter κ to remove the singularity appearing at the throat. We have also obtained the critical value $x_c = \left(\frac{r_0^2}{|\kappa|}\right)_c = 1$ that distinguishes between wormhole and black hole. As a special case, we retrieve the wormhole solution supported by electric field. For this special solution, we obtain the critical charge-to-mass ratio $\left(\frac{Q}{M}\right)_c \approx 1.144$. We have wormhole for $\frac{Q}{M} > \left(\frac{Q}{M}\right)_c$ and black hole for $\frac{Q}{M} < \left(\frac{Q}{M}\right)_c$.

6. Acknowledgement

The author acknowledges the Council of Scientific and Industrial Research, India, for providing support through a fellowship. He also acknowledges Indian Institute of Technology Kharagpur, India, for providing financial assistance to attend the conference CICAHEP-2015. He acknowledges the organizer of the conference for giving him an opportunity to present his work. He also acknowledges Sayan Kar for going through the manuscript.

References

[1] M. S. Morris and K. S. Thorne, Am. J. Phys. **56**, 395 (1988).
[2] M. Visser, *Lorentzian Wormholes: From Einstein to Hawking* (AIP,College Park, MD, 1995).
[3] R. Shaikh, Phys. Rev D **92**, 024015 (2015).
[4] M. Bañados and P. G. Ferreira, Phys. Rev. Lett. **105**, 011101 (2010).
[5] S. Deser and G. Gibbons, Classical Quantum Gravity **15**, L35 (1998).
[6] A. S. Eddington, *The Mathematical Theory of Relativity*, (Cambridge University Press, Cambridge, England, 1924).
[7] M. Born and L. Infeld, Proc. R. Soc. A **144**, 425 (1934).
[8] S. Jana and S. Kar, Phys. Rev. D **88**, 024013 (2013).
[9] T. Harko, F. S. N. Lobo, M. K. Mak, and S. V. Sushkov, Mod. Phys. Lett. A **30**, 1550190 (2015).
[10] G. J. Olmo, D. Rubiera-Garcia, and H. Sanchis-Alepuz, Eur. Phys. J. C **74**, 2804 (2014).
[11] I. Cho, H.-C. Kim, and T. Moon, Phys. Rev. D **86**, 084018 (2012).
[12] S. Jana and S. Kar, Phys. Rev. D **92**, 084004 (2015); P. Pani, V. Cardoso, and T. Delsate, Phys. Rev. Lett. **107**, 031101 (2011); P. Pani and T. P. Sotiriou, Phys. Rev. Lett. **109**, 251102 (2012); J. H. C. Scargill, M. Banados, and P. G. Ferreira, Phys. Rev. D **86**, 103533 (2012); T. Delsate and J. Steinhoff, Phys. Rev. Lett. **109**, 021101 (2012); S. W. Wei, K. Yang, and Y. X. Liu, Eur. Phys. J. C **75**, 253 (2015); H. Sotani and U. Miyamoto , Phys. Rev. D **90**, 124087 (2014); H. Sotani, U. Miyamoto, Phys. Rev. D **92**, 044052 (2015); P. P. Avelino, Phys. Rev. D **85**, 104053 (2012); P. P. Avelino and R. Z. Ferreira, Phys. Rev. D **86**, 041501(R) (2012); P. P. Avelino, arXiv:1511.03223; Y.-H. Sham, L.-M. Lin, and P. T. Leung, Phys. Rev. D **86**, 064015 (2012); K. Fernandes and A. Lahiri, Phys. Rev. D **91**, 044014 (2015); J. B. Jimenez, L. Heisenberg, G. J. Olmo, and Christophe Ringeval, J. Cosmol. Astropart. Phys. **11**, 046 (2015).
[13] R. M. Wald, *General Relativity*, (University of Chicago Press, Chicago, 1984).
[14] G. J. Olmo and D. Rubiera-Garcia, Universe **1**, 173 (2015).
[15] J. Casanellas, P. Pani, I. Lopes, and V. Cardoso, Astrophys. J. **745**, 15 (2012).

Deduction of equations to determine the age of the universe and its radius at primordial state

Ashit Kumar Chakraborty

Society for Cosmological Research, Kolkata-700026, West Bengal, India

ashitkumarchakraborty@gmail.com; COS.8, Oral, CICAHEP15.184.1

All astronomical bodies of the observable Universe are seen to be orbiting under the influence of gravitation. Notwithstanding the existence of CMB, extrapolation of the expansion of the Universe back in time indicates that astronomical bodies had been in orbital motion at all times. A table with values of orbital velocity (v) of a cosmic body orbiting at various times around the center of the Universe and the distance (d) between the center of the cosmic body and that of the Universe at such times shows that the velocity of the cosmic body orbiting the center of the primordial Universe $= C/$(Radius of the primordial Universe) $= K/C$, where K (Constant) $= v^2d$ and C a dimensional constant whose numerical value, regardless of the units of measurement, is 1. All orbital time periods of the astronomical body till date are aggregated. The total time of travel of that body till date or the age of the Universe $= 7.55274627K/V^3$, where V is the present orbital velocity of the body.

1. Introduction

The Sun, planets, satellites and most other visible astronomical bodies in our Galaxy are moving in orbital paths. In the observable Universe, the Galaxies too are moving [1]. With millions of glaring stars at millions of miles away, it is difficult to analyze the exact nature of their movements. Solar system orbits around the center of our Galaxy and takes about $225 - 250$ million years to complete one orbit [2]. Our Galaxy is also moving with a velocity measurable with respect to the CMB rest frame [3]. Observation of galaxies moving away from us does not necessarily mean that they are moving in straight lines. So it is likely that under the influence of gravitation, our Galaxy too orbits around an astronomical body of the Universe.

Extrapolation of the expansion of the Universe backwards in time using general relativity yields an infinite density and temperature at a finite time in the past [4]. Known laws of physics are valid till that point (hereafter referred to as the point of origin) and gravitation is believed to have been as strong as the other fundamental forces. The Big Bang model of cosmology predicted existence of background radiation and the discovery of CMB led to the present theories on Galactic evolution. Greatest emphasis has been laid on this prediction but the contribution of the huge energy released from Gamma Ray Bursts (GRB) towards the formation of CMB can not be ruled out either. The GRBs had occurred in galaxies that are one to eight billions of light years away and by studying all of the GRBs detected so far, it is possible to determine whether the GRBs throughout the Universe had happened for a specific period at regular intervals. Returning to our initial enquiry of the precise orbital motions of the visible satellites, planets, stars and galaxies, the extrapolation of the expansion back in time ostensibly leads to an inference that today's astronomical bodies had been in orbital motion from the point of origin to date. My submission here is based on this inference that from the point of origin, all astronomical bodies around the center of the Universe had expanded while moving in outwardly spiral paths while the astronomical body at the center of the Universe drifted in one direction as shown in Fig. 1. The extrapolation of the expansion back in time further shows that all astronomical bodies converge at the point of origin at the same time. So, all astronomical bodies must have moved out from the point of origin at the same time.

We have some universal relationships for orbital motions and we shall keep our calculations simple by adopting a view that the orbital paths of the astronomical bodies are circular. By Keplers 3rd law [5]:

$$D^3 = kT^2 \tag{1}$$

Other proven expressions used in planetary motion are:

$$T = 2\pi D/V, \tag{2}$$

$$g = V^2/D, \tag{3}$$

where D is the distance between the center of the Moon and that of the Earth, T the orbital time period of the

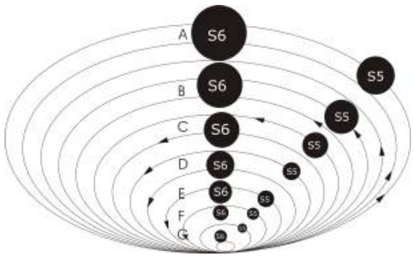

Figure 1. S6 expands while drifting from the point of origin to position A, and S5 expands while orbiting around S6.

Moon, V its orbital velocity, g its gravitational acceleration and k a constant. When the expansion of the Universe is extrapolated back in time, these relationships must be valid till the point of origin. We shall use these well-tested relationships applicable universally to all orbiting bodies to deduce a few equations for determination of the age of the Universe and its radius at primordial state.

2. The Laws of Creation

Combining equations (1) and (2), we find,

$$V^2 D = K, \tag{4}$$
$$T = 2\pi K / V^3. \tag{5}$$

Where $K = 4\pi^2 k$, a constant. Similarly combining equations (3) and (4), we may write,

$$gD^2 = K. \tag{6}$$

As shown in Fig. 1, S5 is an astronomical body orbiting directly around the astronomical body called S6 situated at the center of the Universe. S6 moves up from position G to A during expansion of the Universe. S5 spirals outward and moves up with S6. Let d be the distance between the center of S5 and that of S6 and v the orbital velocity of S5. By equation (4), $v^2 d = K_6 =$ a constant. In Table 1, magnitudes of d and v at various points of assent of S6 are listed.

Table 1. Magnitudes of d, V and $v^2 d$ at various points of assent of S6.

Position of S6	Magnitude of d	Magnitude of v	Magnitude of $v^2 d$ $(= K_6)$
A	100	1	100
B	25	2	100
C	4	5	100
D	1	10	100
E	0.25	20	100
F	0.04	50	100
G	0.01	100	100

At point G which can be said to be the point of origin, magnitude of $v = 1/$(magnitude of d) $=$ magnitude of$v^2 d$ $(= K_6)$ and S6 is in its minutest form. At that point, S5 orbits on the surface of S6 and hence $d =$ the radius R_6 of S6. If V_G be the orbital velocity of S5 at G, then

$$V_G = K_6 / C, \tag{7}$$
$$C / R_6 = K_6 / C. \tag{8}$$

Where C is a dimensional constant whose numerical value, regardless of the units of measurement, is 1 and $K_6 = V_G^2 R_6$. If the unit of R_6 is km and that of time is second, the unit of C is km^2/sec and the value of $C = 1$

km^2/sec. So, during the expansion of the Universe from the point of origin, $(V_G =)\ V_G^2 R_6/C$ is the initial orbital velocity of S5. Since the magnitude of $C = 1$, $V_G^2 R_6\ (= K6)$ is the magnitude of the initial orbital velocity of S5.

Therefore, if V be the orbital velocity of an astronomical body at a given time and D the distance between the center of the astronomical body and that of its orbital path at that time, $V^2 D$ of the astronomical body can be said to be the magnitude of its initial orbital velocity.

Referring to Fig. 1, the aggregate of all orbital time periods of S5 till date should be the present age of the Universe. Let in the present T_1 orbital time, S5 has an orbital velocity V_1, in the previous T_2 orbital time it had an orbital velocity $2V_1$, in T_3 orbital time it had an orbital velocity $3V_1$ and so on. By equation (5),

$$T_1 = 2\pi K_6/(V_1.1)^3$$

$$T_2 = 2\pi K_6/(V_1.2)^3$$

$$T_3 = 2\pi K_6/(V_1.3)^3$$

And so on. Or,

$$\sum_{Z=1}^{\infty} T_Z = (2\pi K_6/V_1^3) \times \sum_{n=1}^{\infty}(1/n^3).$$

Or, total of all orbital times $= t = (2\pi K_6/V_1^3) \times N$, where $N =$ Apery's constant, the approximate value of which is 1.202056903 and $\pi = 3.141592653$. Or, the present age of the Universe is

$$t = 7.55274627 K_6/V_1^3. \tag{9}$$

3. Results and Discussion

To have an indicative estimation of the radius and surface gravity of the primordial Universe, lets assume that the astronomical body at the center of our galaxy is directly orbiting around the center of the Universe. Its estimated velocity is 552 km/sec and the estimated age of the Universe is 13.8 billion years = 4.3549488 $\times$ 10^{17} seconds.

By Equation (9),

$K_6 = tV_1^3/7.55274627 = (4.3549488 \times 10^{17} \times 552^3)/7.55274627$ km^3/sec^2 $= 9.698295031 \times 10^{24}$ km^3/sec^2.

As defined, $C = 1$ km^2/sec. By Equation (8), R_6 or the radius of the primordial Universe = 1/(9.698295031 $\times$ $10^{24})$ km $= 10^{-7}$fm.

By Equation (6), surface gravity of the primordial Universe $\times$ $R_6^2 = K_6$. $R_6 = 10^{-7}$ fm $= 10^{-25}$ km, $K_6 = 9.698295031 \times 10^{24}$ km^3/sec^2. Surface gravity of the primordial Universe $= K_6/R_6^2 = (9.698295031 \times 10^{24})/(10^{-25})^2$ km/sec^2 $= 9.698295031 \times 10^{74}$ km/sec^2

4. Conclusion

The theoretical basis of this paper that the astronomical bodies around the center of the Universe had been in orbital motion at all times seems to be more reasonable than the present theories which depict a somewhat chaotic process of galactic evolution with the role of all important gravitation which had been very strong at the initial stages, kept in abeyance for a long period of evolutionary time. GRBs are presently not visible in our Galaxy and nearby Galaxies because the last spate of GRB throughout the Universe seemed to have happened more than one billion years back.

As indicated, the radius of the primordial Universe is much smaller than the classical electron or Lorentz radius of 2.8 fm. Its surface gravity of 9.7 $\times$ 10^{77} meter/sec^2 is enormous when we compare the same with the Earth's present surface gravity of 9.8 meter/sec^2. The indicative initial orbital velocity of the astronomical body at the center of our Galaxy is $K_6/C = 9.7 \times 10^{24}$ km/sec. $V^2 D\ (= K)$ of the solar planets is 1.3 $\times$ 10^{11} km^3/sec^2. Therefore, the initial orbital velocity of each planet is 1.3 $\times$ 10^{11} km/sec, much larger than the velocity of light. So, the orbital velocity of the Earth has decreased from the initial 130 billion km/sec to the present 30 km/sec.

References

[1] E. Hubble, Proceedings of the national academy of Sciences of the USA **15 (3)**, 168 (1929).
[2] S. Leong, *Period of the Sun's Orbit around the Galaxy (Cosmic Year)*, (ed) G. Elert (web: The Physics Factbook) (2002).
[3] A. Kogut et al, Astrophysical Journal **419**, 1 (1993).
[4] S. W. Hawking and G. F. R. Ellis, *The Large-Scale Structure of Space-Time* (London: Cambridge University Press) (1973).
[5] J. Kepler, *The Harmony of the World: Memoirs*, (eds) E. J. Aiton, A. M. Duncan and J. V. Field (Philadelphia: American Philosophical Society), Vol. 209 (1997).

Theoretical schematic of interacting forces of gravity to review the law of universal gravitation

Ashit Kumar Chakraborty

Society for Cosmological Research, Kolkata-700026, West Bengal, India

ashitkumarchakraborty@gmail.com; COS.7, Poster, CICAHEP15.184.2

Newton theorized that a force of a particle reaches out to another particle to cause attraction. Schematic of forces shows that a force of a particle reaches out to a force of another particle to cause attraction. These forces are spent to keep the particles bonded. For a spherical body, unspent forces of particles on its surface alone act to attract adjacent bodies, and in no way, the whole attracting force is issued from its center. Therefore, unlimited increase in mass of the larger lead ball in Cavendish experiment does not cause proportional increase in the force of attraction. $gD^2 = K$ (constant) drawn from equations of planetary motion shows that g of a free-falling body increases as the body travels from a distance (D) towards the center of Earth. It indicates existence of a unique formation at the center of Earth for creation of gravity. Hence, determination of G from a two-body interaction and its application in $F = Gm_1m_2/r^2$ to find the mass of a celestial body is an incorrect procedure as attraction of a body on Earth and gravity of a celestial body are two different phenomena in respect of the nature of their sources.

1. Introduction

Inverse square law distance dependence is well established in celestial mechanics, but is yet to be comprehensively proved in laboratories for two adjacent masses, particularly at submillimeter ranges. Report of inverse square law violation (ISLV) at distances of 4.5 cm – 29.9 cm was made by Daniel Long [1, 2] but was not supported by subsequent tests [3, 4, 5]. With several theories supporting the existence of other interfering forces that are weak and insensitive to present experimental setups, full-proof ISLV tests are yet to be accomplished and enquiries on ISLV continue to exist [6]. Besides whether unlimited increase in the mass of the larger test object causes proportional increase in the force of attraction is yet to be verified. Finally, the similarity between the source of attraction of an object towards another on Earth and that of a celestial body towards another is unverified though the equation $F = Gm_1m_2/r^2$ is used for both. Taking note of the unproven points, this paper analyzes the interaction between the particles in spherical objects from the schematic of their forces and draws inferences that contradict some of the theorems on spherical bodies and gravity in 'Principia' [7] and the equation of gravitation as well.

Newton's view of a spherical body consisting of numerous particles exerting equal forces in all directions [7] is accepted. Newton theorized that a force of a particle acts on another particle by covering the distance between them. In Fig. 1, the schematic of interacting forces of gravity shows that when a force of a particle meets a force of another particle around the mid-point of the distance between them, attraction between the particles takes place. It is something like a person extending his arms to pull the extended arms of two other persons standing on his two sides.

2. Definitive actions of forces in two-particle interaction

Pair of forces in Fig. 1 (a) act independently of each other in diametrically opposite directions like stretched arms of a person ready to pull two adjacent ones. In Fig. 1 (b), line XY joining the centers of particles X and Y, which lie adjacent to each other, is the shortest distance between them. Force XA of particle X and force YB of particle Y meet each other first as they act along XY. Upon conjunction of the forces, each particle exerts a single pull to the other, resulting in the convergence of the particles along XY by equal, tiny distances.

The convergence of the particles causes forces XC and XG of particle X to intersect with forces YD and YH of particle Y respectively. Assuming the magnitude of each of the forces of the particles to be F, the horizontal components of the forces XC, XG, YD and YH are $F\cos$ (CXY), $F\cos$ (GXY), $F\cos$ (DYX) and $F\cos$ (HYX) respectively, where $\angle$CXY = $\angle$GXY = $\angle$DYX = $\angle$HYX. The resultant of $F\cos$ (CXY) and $F\cos$ (GXY) acting simultaneously, is $2F\cos$ (CXY). Since $\angle$CXY is less than 60^o, $2F\cos$ (CXY) is greater than F. Similarly, $2F\cos$ (DYX) being the resultant of $F\cos$ (DYX) and $F\cos$ (HYX) to pull particle X, too is greater than F. So, particles

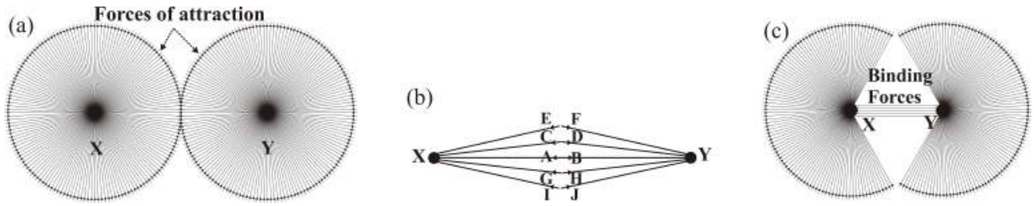

Figure 1. (a) Vertical cross-section of particles X and Y. (b) Intersection of forces of X and Y results in their convergence along the line XY. (c) Intersecting forces of X and Y transformed into binding forces.

X and Y converge by equal distances which are greater than those covered earlier by them due to the forces XA and YB. The convergence results in intersection of forces XE and XI of particle X with forces YF and YJ of particle Y respectively. As shown in Fig. 1 (c), the process continues till the resultant of a pair of horizontal components of forces (called binding forces hereafter) of each particle is so small that it fails to pull the other particle towards it. For example, when the angle between the horizontal component of a force and XY is more than 60^o, the cosine of that angle is less than $\frac{1}{2}$ and the magnitude of the resultant of the two horizontal components acting simultaneously is less than F. So, when the resultant force is less than F, it is unable to pull the other particle further.

3. Schematic of many-particle interactions

In a three-particle interaction as shown in Fig. 2 (a), the particle in the middle is attracted by the other two with equal and opposite forces that nullify each other while its forces acting upon the two bring them closer to it. In case of interaction between two balls having say, seven particles each as in Fig. 2 (b), the resultant of the binding forces of the particles closest to each other acts along the line joining the centers of the balls as they converge along that line, providing a wrong impression that the forces emanate from their centers.

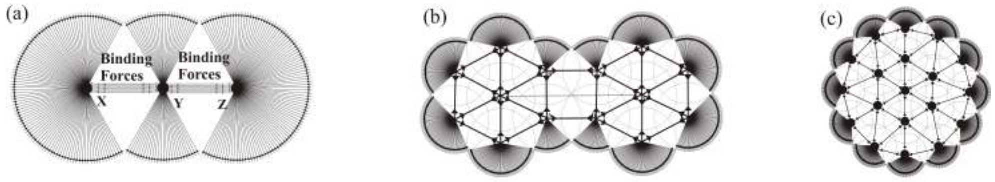

Figure 2. (a) Particle Y creates binding forces with particles X and Z and hence spends most of its forces of attraction. (b) For two interacting balls, particles closest to each other interact. (c) All forces of the particles under the surface of the ball are transformed into binding forces whereas unspent forces on the surface attract adjacent bodies.

With more particles interacting from all directions to form a larger cluster, the number of forces of the interacting particles diminishes due to their conversion into binding forces. As shown in Fig. 2 (c), the particles under the surface of a tiny ball spend all of their forces to create binding forces whereas those on the surface have unspent forces which act as forces of the ball to attract another ball adjacent to it.

4. Results and Discussion

The finding in Section 3 contradicts explanatory note to theorem 35, proposition 75, book I of 'Principia' [7], which says that the attraction of every particle of a sphere is the same as if the whole attracting force is issued from one single corpuscle placed in the centre of the sphere.

Like the forces of the particles under the surface of a ball, all forces of the particles under the surface of the Earth are transformed into binding forces. The particles on the surface of the Earth have unspent forces of attraction, which are feeble. These particles just under a persons feet and those of his feet, which are in contact, undergo a negligibly small mutual attraction between them. Hence the forces of the mass of the Earth can not be said to be its gravitational forces that extend beyond its Moon to attract celestial bodies. This inference contradicts theorem 7, proposition 7, book III of 'Principia' [7], which expresses that the Earth's gravitational force is proportional to its mass.

Experiments conducted in mine shafts and bore holes reportedly yielded values of G which are significantly higher than those in laboratory tests [8, 9] and it is necessary that the source of Earth's gravity is examined.

Kepler's 3rd law [10] for circular motion of an artificial satellite around the Earth is represented by: (1) $D^3 = kT^2$; other equations used in orbital motion are: (2) $T = 2\pi D/V$ and (3) $g = V^2/D$, where D is the distance between the center of the satellite and that of the Earth, T the orbital time period of the satellite, V its orbital velocity and k a constant. The equations give:

$$gD^2 = K, \tag{1}$$

where K (constant) $= 4\pi^2 k$.

The values of gD^2 for an object of any mass at rest on the Earth, for an artificial satellite and for the Earth's Moon are same. This also means that 'g' of a free falling body is zero at an infinite point above the Earth's surface but constantly increases as the body travels from the infinite point towards the center of the Earth. Hence, the value of G in mine shaft/borehole can be found to be higher than that on Earth. The deduction contradicts theorem 9, proposition 9, book III of 'Principia' [7], which states that 'g' of a body decreases as it goes down from the Earth's surface to its center. The Earth comprises of solid, liquid and air particles, all having mass and forces of attraction. There is no sensible reason why 'g' of a freefalling body, which increases during its passage through air, would abruptly change property by decreasing below the surface of the solid part of the Earth. The relationship $g \propto 1/d^2$ (equation (1)) shows that the gravity of the Earth is independent of its mass. It further indicates that a unique particle or formation of particles in the innermost core of the Earth exists, creating attraction towards all particles in and around the Earth.

It is also essential to examine how unlimited increase in the mass of a ball affects its magnitude of attraction towards a smaller ball.

In Fig. (3), vertical cross-section of lead balls P, Q and R having centers on the same line is drawn. R is the largest and P is the smallest of the balls that have identical, uniform densities. The cross-sections of Q and R touch each other at point M that lies on the line joining the centers of P, Q and R. BF || CG || MX where X is the center of P is drawn.

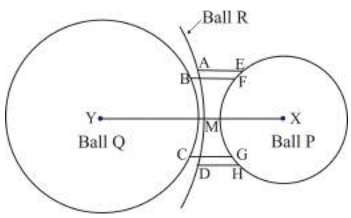

Figure 3. Particles on the surface of Q and R attract only those on the surface of the adjacent hemisphere of P.

Let's assume that in the absence of R, the forces of attraction of the particles in arc BMC intersect with those in arc FG resulting in mutual attraction between the cross-sections of Q and P. Arc AMD = arc BMC and AE || DH || MX are drawn so that in the absence of Q, the forces of attraction of the particles in arc AMD intersect with those in arc EH resulting in mutual attraction between the cross-sections of R and P. As drawn, arc AMD = arc BMC. Or, the number of the particles of lead in arc AMD = the number of the particles of lead in arc BMC. The particles in arc EH of P and those in arc AMD of R are mutually attracted while the particles in arc FG of P and those in arc BMC of Q are mutually attracted.

But arc EH $>$ arc FG. Or, the number of the particles of lead in arc EH $>$ the number of the particles of lead in arc FG. Therefore, the number of the particles in the cross-section of P that attract the particles in arc AMD of R $>$ the number of the particles in the cross-section of P that attract the particles in arc BMC of Q. Or, magnitude of the resultant force of P towards R $>$ magnitude of the resultant force of P towards Q.

So, the mutual attraction between two lead balls increases if the mass of the larger lead ball is increased but becomes constant once the particles on the surface of the larger lead ball manage to attract all particles on the surface of the nearer hemisphere of the smaller lead ball. This inference contradicts corollary 1 to theorem 29, proposition 69, book I of 'Principia' [7], which states that the force of gravity of a spherical body is directly proportional to its mass.

5. Conclusion

Theoretic observations in this paper do not support some of the theorems on spherical bodies and gravity in 'Principia' [7], particularly those related to force-mass proportionality. The findings further indicate that attraction between the bodies on the Earth and the gravity of the celestial bodies are two different phenomena in respect of the nature of their sources. Hence, determination of G from a two-body interaction on Earth and its application in $F = Gm_1m_2/r^2$ to find the mass of a celestial body is an incorrect procedure. Besides, if $g = GM/D^2$ drawn from Newton's law of universal gravitation is compared with $g = K/D^2$ of the equation (1), GM is seen to be equal to K which is an Earth-specific constant and is true even if hypothetically, a body under the surface of the Earth orbits around the Earth's center or for a body stationed under the Earths surface.

References

[1] D. R. Long, Nature (London) **260**, 417 (1976).
[2] D. R. Long, Nuovo Cim., B **55**, 252 (1980).
[3] V. I. Panov and V. N. Frontov, Sov. Phys. JETP **50**, 852 (1979).
[4] R. E. Spero, J. K. Hoskins, R. Newman, J. Pellam and J. Schultz, Phys. Rev. Lett. **46**, 1645 (1980).
[5] J. K. Hoskins, R. D. Newman, R. Spero, and J. Schultz, Phys. Rev. D **32**, 3084 (1985).
[6] R. D. Newman, E. C. Berg and P. E. Boynton, Space Sci. Rev. **148**, 175 (2009).
[7] I. Newton, *The Mathematical Principles of Natural Philosophy* edited by N. W. Chittenden (D Adee, New York, 1846).
[8] F. D. Stacey and G. J. Tuck, Nature (London) **292**, 230 (1981).
[9] S. C. Holding and G. J. Tuck, Nature (London) **307**, 714 (1984).
[10] J. Kepler, *The Harmony of the World: Memoirs Series* (American Philosophical Society, Philadelphia, 1997) Vol. **209**.

Part III
Astronomy and Astrophysics (PS2)

Resonant-bar detectors of gravitational wave as possible probe of the noncommutative structure of space

Anirban Saha and Sunandan Gangopadhyay

Department of Physics, West Bengal State University, Barasat, North 24 Paraganas, West Bengal, India

Presenter: Anirban Saha (*anirban@iucaa.ernet.in*); A&A.6, Oral, CICAHEP15.50.1

We report the plausibility of using quantum mechanical transitions, induced by the combined effect of Gravitational Wave (GW) and noncommutative (NC) structure of space, among the states of a 2-dimensional harmonic oscillator, to probe the spatial NC geometry. The phonon modes excited by the passing GW within the resonant bar-detector are formally identical to forced harmonic oscillator and they represent a length variation of roughly the same order of magnitude as the characteristic length-scale of spatial noncommutativity estimated from the phenomenological upper bound of the NC parameter. This motivates our present work. We employ various GW forms that are typically expected from possible astronomical sources. We find that the transition probabilities are quite sensitive to the nature of polarization of the GW. We also elaborate on the particular type of sources of GW, radiation from which can induce transitions that can be used as effective probe of the spatial noncommutative structure.

1. Introduction

The tantalizing news of the first direct detection of Gravitational Waves (GWs) [1] has opened a new window not only for astronomical observations but also for directly looking into the structure of space-time at a length-scale never probed before. GWs are small ripples in the fabric of space-time. The present day operational GW detectors are ground-based interferometers (LIGO, VIRGO, GEO, TAMA etc.) [2]. However, the search of GWs began with resonant-mass detectors, pioneered by Weber in the 60's [3]. In the decades that followed, the sensitivity of resonant-mass detectors have improved considerably [4]. Also, the study of resonant-bar detectors is fundamental since it focuses on how GW interacts with elastic matter causing vibrations with amplitudes many order smaller than the size of a nucleus. In a bar detector it is possible to detect these tiny vibrations corresponding to just a few tens of phonons [5], and variations ΔL of the bar-length $L \sim 1$ m, with $\frac{\Delta L}{L} \sim 10^{-19}$.

Interestingly, it has long been suggested in various Gedenken experiments that a sharp localization of events in space would induce an uncertainty in spatial coordinates [6, 7] at the quantum level. This uncertainty can be realized by imposing the NC Heisenberg algebra on the operators representing phase-space variables

$$[\hat{x}_i, \hat{p}_j] = i\hbar\delta_{ij} \ , \quad [\hat{x}_i, \hat{x}_j] = i\theta_{ij} = i\theta\epsilon_{ij} \ , \quad [\hat{p}_i, \hat{p}_j] = 0 \ , \tag{1}$$

where θ_{ij} is the constant antisymmetric tensor, which is written in terms of the constant NC parameter θ and the totally antisymmetric tensor ϵ_{ij}. Such granularity in spatial structure have been motivated by string theoretic [8] and quantum gravity [9] results also. A wide range of theories, dubbed the NC theories, have been constructed in this framework. This includes NC quantum mechanics (NCQM) [10], NC quantum field/gauge theories [11] and gravity [12, 13]. Certain possible phenomenological consequences [14] have also been predicted. Naturally, a part of the endeavour is spent in finding the order of the NC parameter and exploring its connection with observations [15, 16, 17, 18]. The stringent upperbound on the coordinate commutator $|\theta|$ found in [16] is $\lesssim (10 \text{ TeV})^{-2}$ which corresponds to 4×10^{-40} m^2 for $\hbar = c = 1$[1]. This upperbound correspond to the length scale $\sim 10^{-20}$ m which overlaps the length scale where the first GW has been detected [1]. Thus a good possibility of detecting the NC structure of space-time would be in the present GW detection experiments as it may as well pick up the NC signature of space-time as a noise source. So we need NCQM of GW-matter interaction that can anticiapte the NC effects in GW detection events.

With this motivation, we have studied the interaction of GWs with simple matter systems in a NCQM framework in [19, 20]. Our particular interest is in the NCQM of harmonic oscillator (HO) interacting with GW because the response of a bar-detector to GW can be cast as phonon mode excitations formally identical to forced HO [5]. Thus, NCQM of the HO interacting with GW is of fundamental importance. Therefore, we investigate the

[1] In a more general NC space-time structure [8] given by $[x^\mu, x^\nu] = i\theta^{\mu\nu}$ such upperbounds on time-space NC parameter is [17] $\theta^{0i} \lesssim 9.51 \times 10^{-18}$ m^2.

transition probabilities between the ground state and the excited states of this system in the present paper by treating the combined effect of GW and spatial noncommutativity as time-dependent perturbations. We employ a number of different GW forms that are typically expected from runaway astronomical events.

2. Formulation: constructing the NC Hamiltonian

To proceed we first obtain the classical Hamiltonian appropriate for the GW-HO interaction system. This can be simply done by noting that in the proper detector frame the geodesic deviation equation for a $2-$dimensional harmonic oscillator of mass m and frequency ϖ subject to linearized GW becomes [5]

$$m\ddot{x}^j = -mR^j{}_{0,k0}x^k - m\varpi^2 x^j, \tag{2}$$

where dot denotes derivative with respect to the coordinate time of the proper detector frame[2], x^j is the proper distance of the pendulum from the origin and $R^j{}_{0,k0}$ are the relevant components of the curvature tensor in terms of the metric perturbation $h_{\mu\nu}$ defined by[3] $g_{\mu\nu} = \eta_{\mu\nu} + h_{\mu\nu};\ |h_{\mu\nu}| << 1,$ on the flat Minkowski background $\eta_{\mu\nu}$.

The transverse-traceless (TT) gauge-choice $\left(h_{0\mu} = 0, h_{\mu\nu;}{}^{\mu} = 0, h^{\mu}_{\mu} = 0\right)$ removes all unphysical degrees of freedom (DOF) and only non-trivial components of the curvature tensor $R^j{}_{0,k0} = -\ddot{h}_{jk}/2$ appear in equation (2). Note that, equation (2) works as long as the spacial velocities are small and $|x^j|$ is much smaller than the reduced wavelength $\frac{\lambda}{2\pi}$ of GW. These conditions are collectively referred as the *small-velocity and long wavelength limit* and met by resonant bar-detectors and the Earth bound interferometric detectors, with the origin of the coordinate system centered at the detector. This also ensures that in a plane-wave expansion of GW, $h_{jk} = \int (A_{jk}e^{ikx} + A^*_{jk}e^{-ikx})d^3k/(2\pi)^3$, the spatial part $e^{i\vec{k}.\vec{x}} \approx 1$ all over the detector site. So only the time-dependent part of the GW is relevant.

The two physical DOF, referred as the $\times$ and $+$ polarizations of GW, are contained in A_{jk} and can be expressed in terms of the Pauli spin matrices as $h_{jk}(t) = 2f\left(\varepsilon_\times \sigma^1_{jk} + \varepsilon_+ \sigma^3_{jk}\right)$ if z is the propagation direction. Here $2f$ is the amplitude of the GW and $(\varepsilon_\times, \varepsilon_+)$ are the two possible polarization states of the GW satisfying the condition $\varepsilon^2_\times + \varepsilon^2_+ = 1$ for all t.

The Lagrangian for the system (2), can be written, upto a total derivative term as $\mathcal{L} = \frac{1}{2}m\dot{x}^2 - m\Gamma^j{}_{0k}\dot{x}_j x^k - \frac{1}{2}m\varpi^2(x_j)^2$, where $R^j{}_{0,k0} = -\frac{d\Gamma^j_{0k}}{dt} = -\ddot{h}_{jk}/2$. Computing the canonical momentum $p_j = m\dot{x}_j - m\Gamma^j_{0k}x^k$ we write the Hamitonian as

$$H = \frac{1}{2m}\left(p_j + m\Gamma^j_{0k}x^k\right)^2 + \frac{1}{2}m\varpi^2(x_j)^2\ . \tag{3}$$

Once we have the classical Hamiltonian we can have the NCQM description of the system[4] simply by elevating the phase-space variables $\left(x^j, p_j\right)$ to operators $\left(\hat{x}^j, \hat{p}_j\right)$ and imposing the NC Heisenberg algebra (1). But since this algebra can be mapped [19, 20] to the standard $(\theta = 0)$ Heisenberg algebra spanned by the operators X_i and P_j of the ordinary QM through the mapping $\hat{x}_i = X_i - \frac{1}{2\hbar}\theta\epsilon_{ij}P_j\ ,\ \ \hat{p}_i = P_i$ so that the NCQM Hamiltonian corresponding to equation (3) can be re-expressed as [5]

$$\hat{H} = \frac{{P_j}^2}{2m} + \frac{1}{2}m\varpi^2{X_j}^2 + \Gamma^j_{0k}X_jP_k - \frac{m\varpi^2}{2\hbar}\theta\epsilon_{jm}X^jP_m - \frac{\theta}{2\hbar}\epsilon_{jm}P_mP_k\Gamma^j_{0k} = \hat{H}_0 + \hat{H}_{\rm int}. \tag{4}$$

This Hamiltonian gives the commutative equivalent description of the noncommutative system (3) in terms of the operators X_i and P_j. Since they admit the standard Heisenberg algebra, the rules of ordinary QM applies to (4) . The first two terms in equation (4) represent the unperturbed HO Hamiltonian $\hat{H}_0$. Rest of the terms are small[6] compared to $\hat{H}_0$ and can be treated as perturbations $\hat{H}_{\rm int}$.

---

[2] It is the same as it's proper time to first order in the metric perturbation.

[3] As is usual, latin indices run from $1-3$. Also ; denotes covariant derivatives.

[4] Also note that it has been demonstrated in various formulations of NC general relativity [12, 13] that any NC correction in the gravity sector is second order in the NC parameter. Therefore, in a first order theory in NC space, the GW remains unaltered by NC effects.

[5] The traceless property of the GW is also required here.

[6] A term quadratic in Γ has been neglected in equation (4) since we deal with linearized gravity.

Defining raising and lowering operators $X_j = \sqrt{\frac{\hbar}{2m\varpi}}\left(a_j + a_j^\dagger\right)$ and $P_j = \sqrt{\frac{\hbar m\varpi}{2i}}\left(a_j - a_j^\dagger\right)$ in terms of the oscillator frequency ϖ, we write the time-dependent interaction part of the Hamiltonian (4) as[7]

$$\hat{H}'_{\text{int}}(t) = -\frac{i\hbar}{4}\dot{h}_{jk}(t)\left(a_j a_k - a_j^\dagger a_k^\dagger\right) + \frac{m\varpi\theta}{8}\epsilon_{jm}\dot{h}_{jk}(t)\left(a_m a_k - a_m a_k^\dagger + C.C\right). \tag{5}$$

3. Time-dependent perturbation

We now apply the time-dependent perturbation theory to compute the probability of transition between the ground state $|0,0\rangle$ and the excited states of the 2-d harmonic oscillator. To the lowest order the probability amplitude of transition from an initial state $|i\rangle$ to a final state $|f\rangle$, $(i \neq f)$, due to a perturbation $\hat{V}(t) = F_{jk}(t)\hat{Q}_{jk}$ is given by [21]

$$C_{i\to f}(t\to\infty) = -\frac{i}{\hbar}\int_{-\infty}^{t\to+\infty} dt' \left[F_{jk}(t')\, e^{\frac{i}{\hbar}(E_f - E_i)t'}\langle\Phi_f|\hat{Q}_{jk}|\Phi_i\rangle\right].$$

Using the above result, we find that the *probability of transition survives only between the ground state* $|0,0\rangle$ *and the second excited state* and it reads

$$C_{0\to2} = -\frac{i}{\hbar}\int_{-\infty}^{+\infty} dt \left[F_{jk}(t)\, e^{\frac{i}{\hbar}(E_2 - E_0)t}\left(\langle2,0|\hat{Q}_{jk}|0,0\rangle + \langle1,1|\hat{Q}_{jk}|0,0\rangle + \langle0,2|\hat{Q}_{jk}|0,0\rangle\right)\right], \tag{6}$$

where $F_{jk}(t) = \dot{h}_{jk}(t)$ contains the explicit time dependence of $\hat{H}'_{\text{int}}$ and $\hat{Q}_{jk} = -\frac{i\hbar}{4}\left(a_j a_k - a_j^\dagger a_k^\dagger\right) + \frac{m\varpi\theta}{8}\epsilon_{jm}\left(a_m a_k - a_m a_k^\dagger + C.C\right)$ contains the raising and lowering operators appearing in equation (5). Expanding out $\hat{Q}$ for $i,j = 1,2$, we obtain the transition amplitude between the ground state $|0,0\rangle$ and the second excited state to be

$$C_{0\to2} = -\frac{i}{\hbar}\int_{-\infty}^{+\infty} dt\, e^{2i\varpi t}\left(\frac{i\hbar}{2}\dot{h}_{12}(t) + \frac{m\varpi\theta}{4}\dot{h}_{11}(t)\right). \tag{7}$$

The above equation is the main working formula in this paper. Now using the general formula (7), we can compute the corresponding transition probabilities $P_{0\to2} = |C_{0\to2}|^2$ taking various template of GW forms that are likely to be generated in runaway Astronomical events.

4. Response to Templet GW signals from possible events

We start with the simple scenario of periodic GW with sinusoidally varying amplitude and a single frequency Ω $h_{jk}(t) = 2f_0\cos\Omega t\left(\varepsilon_\times\sigma^1_{jk} + \varepsilon_+\sigma^3_{jk}\right)$. In this limiting case of an exactly monochromatic wave, the temporal duration of the signal is infinite and we get for the transition probability

$$P_{0\to2} = (\pi f_0\Omega)^2\left({\varepsilon_\times}^2 + \Lambda^2{\varepsilon_+}^2\right)\left[\delta(2\varpi+\Omega) - \delta(2\varpi-\Omega)\right]^2, \tag{8}$$

where $\Lambda = \frac{m\varpi\theta}{2\hbar} = 1.888\left(\frac{m}{10^3\text{kg}}\right)\left(\frac{\omega}{1\text{kHz}}\right)$ is a dimensionless parameter carrying the NC signature. Here we have used the stringent upper-bound $|\theta| \approx 4\times10^{-40}\ \text{m}^2$ [16] for spatial noncommutativity and for reference mass and frequency used values appropriate for fundamental phonon modes of a bar detector [20] which are formally identical to the NC harmonic oscillator system considered here.

Consider periodic GW signal coming from a binary system (with quasi-circular orbit) being received by some earth-bound detector; if the orbit of the binary system is edge-on with respect to us, then we receive the + polarization of the radiation only [5] , i.e., $(\varepsilon_\times, \varepsilon_+) = (0,1)$, and in this case (8) shows that the transition probability will scale quadratically with the dimensionless parameter Λ characterized by spatial noncommutativity. Therefore such a transition will be driven by the combined perturbative effect of GW as well as spatial noncommutativity[8]

[7] C.C means complex conjugate.

[8] This corresponds to the last term in $\hat{H}_{\text{int}}$ in (5).

and will occur only if the space has a NC structure. In other words, *a quantum mechanical transition induced by the linearly polarized GW from a binary system with its orbital plane lying parallel to our line of sight can be an effective test of the noncommutative structure of space.* Note that the angular frequency Ω of the quadrupole radiation is twice the angular frequency of rotation of the source [5], thus (8) also tells us that *for transition to occur we need to have a harmonic oscillator with natural frequency ϖ that matches with that of the source.* Highly accurate X-ray/radio-astronomical measurement of the frequency of orbital rotation of binary Pulsars can be used to pin-point the natural frequency of the harmonic oscillator required here.

From another binary system similar to the one considered above, but with its orbital plane perpendicular to our line of sight, both the $+$ and $\times$ polarization of the radiation will reach the detector with equal amplitude and consequently we will have a source for circularly polarized GW signal that can be generically written as $h_{jk}(t) = 2f_0\left[\varepsilon_\times(t)\,\sigma^1_{jk} + \varepsilon_+(t)\,\sigma^3_{jk}\right]$ with $\varepsilon_+(t) = \cos\Omega t$ and $\varepsilon_\times(t) = \sin\Omega t$ and constant amplitude f_0. The transition probability in this case is[9]

$$P_{0\to 2} = (\pi f_0\Omega)^2\left[\{(1+\Lambda)\,\delta(2\omega+\Omega)\}^2 + \{(1-\Lambda)\,\delta(2\omega-\Omega)\}^2\right]. \tag{9}$$

Equation (9) shows a non-zero transition probability for $\Lambda = 0$, i.e. if our space has commutative structure. *Thus a transition induced by circularly polarized GW from a binary system cannot be used as a deterministic probe for spatial noncommutativity.* This feature lies with the earlier case of linearly polarized GW signals only.

In the last stable orbit of an inspiraling neutron star or black hole binary or during its merging and final ringdown, the system can liberate large amount of energy in GWs within a very short duration 10^{-3} sec $< \tau_{\rm g} < 1$ sec. Such signals are referred to as GW bursts. Supernova explosions and stellar gravitational collapse are other candidate generators. Since bursts originate from violent and explosive astrophysical phenomena, their waveform cannot be accurately predicted and only be crudely modeled as $h_{jk}(t) = 2f_0 g(t)\left(\varepsilon_\times\sigma^1_{jk} + \varepsilon_+\sigma^3_{jk}\right)$, where to be generic we have kept both components of the linear polarization. Here $g(t)$ is a smooth function which goes to zero rather fast for $|t| > \tau_{\rm g}$. A convenient choice is a function peaked at $t = 0$ with $g(0) = \mathcal{O}(1)$ so that $|h_{jk}(t)| \sim \mathcal{O}(f_0)$ near the peak. So we take a simple Gaussian $g(t) = e^{-t^2/\tau_g^2}$. Owing to its small temporal duration the burst have a continuum spectrum of frequency over a broad range upto $f_{\rm max} \sim 1/\tau_{\rm g}$ whereas the detector is sensitive only to a certain frequency window and blind beyond it. If the sensitive band-width is small compared to the typical variation scale of the signal in the frequency space, the crude choice here, instead of a precise waveform, is good enough. In terms of the Fourier decomposed modes the GW burst can thus be modeled as

$$h_{jk}(t) = \frac{f_0}{\pi}\left(\varepsilon_\times\sigma^1_{jk} + \varepsilon_+\sigma^3_{jk}\right)\int_{-\infty}^{+\infty}\tilde{g}(\Omega)\,e^{-i\Omega t}d\Omega, \tag{10}$$

where $\tilde{g}(\Omega) = \sqrt{\pi}\tau_g e^{-\left(\frac{\Omega\tau_g}{2}\right)^2}$ is the amplitude of the Fourier mode at frequency Ω. Using equation (10) in the general formula for transition amplitude (7) we find the probability for transition from the ground state to the second excited state induced by a GW burst is

$$P_{0\to 2} \;=\; \left(2\sqrt{\pi}f_0\varpi\tau_g\right)^2 e^{-2\varpi^2\tau_g^2}\left({\varepsilon_\times}^2 + \Lambda^2{\varepsilon_+}^2\right), \tag{11}$$

where the GW Fourier mode with twice the natural frequency of the harmonic oscillator (the detector in our consideration) gets picked up. Since the burst signal duration $\tau_g \sim 10^{-2} - 10^{-3}$ sec, the maximum frequency in the Fourier spectrum can be $\Omega_{\rm max}/2\pi \sim 0.1 - 1$ kHz which partially overlaps with the sensitive bandpass for the bar-detectors. From equation (11) we again see that the $+$ polarization of the GW burst can only induce a transition if the space has a NC structure. If the polarization state of a GW signal from a given source can be anticipated since it depends largely on the orientation of the source which can be determined by observing its electromagnetic radiation and the detector geometry. *So detecting a QM transition induced by a GW burst from an appropriate source can serve as a probe of the spatial noncommutativity.*

[9]Note that here the transition probability has terms both linear and quadratic in the dimensionless NC parameter Λ. However estimate for Λ shows that for phonon modes in a bar detector which are the realization of the NC HO system considered in this paper, Λ is of the order of unity , so we cannot drop the quadratic term even though we started with a theory to first order in the NC parameter.

5. Conclusion

In conclusion we would like to convey that the considerations in the present paper suggest that the joint operation of various resonant detector groups like ALLEGRO, AURIGA, EXPLORER, NAUTILUS and NIOBE around the world in IGEC (International Gravitational Event Collaboration) [23] may possess the potential to establish the possible existence of a granular structure of our space as a by-product in the event of a direct detection of GW and therefore must be continued.

6. Acknowledgement

AS acknowledges the financial support of DST SERB under Grant No. SR/FTP/PS-208/2012.

References

[1] B. P. Abbott *et al*, Phys. Rev. Lett **116** 061102 (2016).

[2] *Status of Gravitational Wave Detection*, A. Giazotto, in General Relativity and J. A. Wheeler, Ciufolini, R.A. Matzner (eds.), Astrophysics and Space Science Library 367, Springer, 2010.

[3] J. Weber, Phys. Rev. Lett., **22** (24) (1969)1320; V. Ferrari *et al*, Phys. Rev. **D 25** (1982) 2471; J. Weber in Gravitational Radiation and Relativity, Proceedings of the Sir Arthur Eddington Centenary Symposium, Nagpur, India, 1984, J. Weber and T. M. Karade (eds.) (World Scientific, Singapore, 1986), Vol. 3.

[4] *Search for Gravitational Waves with Resonant Detectors*, G. Pizzella, in General Relativity and J. A. Wheeler, Ciufolini, R. A. Matzner (eds.), Astrophysics and Space Science Library 367, Springer, 2010.

[5] Michele Maggiore, *Gravitational Wave, Vol I, Theory and Experiments* Oxford University Press, 2008.

[6] S. Doplicher*et al*, Phys. Lett. **B 331** 39 (1994); *ibid* Commun. Math. Phys. 172, 187 (1995).

[7] D. V. Ahluwalia, Phys. Lett. B 339, 301 (1994)

[8] N. Seiberg, E. Witten, [JHEP **09** (1999) 032]

[9] Craig. J.. Hogan, Phys. Rev. **D 77** (2008) 104031.

[10] B. Chakraborty *et al*, Phys. Rev. **D 70** (2004) 107707; F.G. Scholtz *et al*, Phys. Rev. **D 71** (2005) 085005; F.G. Scholtz *et al*, J. Phys. **A 38** (2005) 9849; S. Gangopadhyay, F.G. Scholtz, Phys. Rev. Lett. **102** (2009) 241602.

[11] R.J. Szabo, Phys. Rept. **378** (2003) 207 and the references therein.

[12] see for example R. J. Szabo, Class.Quant.Grav.**23** R199-R242, 2006 and the references therein.

[13] P. Mukherjee, A. Saha, Phys. Rev. **D 74** (2006) 027702 and the references therein; R.Banerjee *et al*, Phys. Rev. **D 75** :125020, 2007; R. Banerjee *et al*, Phys. Lett. B **686** (2010) 181.

[14] M. M. Sheikh-Jabbari, Phys. Lett. **B 455**, 129 (1999); *ibid.*Phys. Rev. Lett. **84**, 5625 (2000); M. M. Najafabadi, Phys. Rev. **D 74** 025021 (2006); S. A. Abel *et al*, JHEP **0601** (2006) 105; B. Melic *et al*, Phys. Rev. **D 72** 057502 (2005).

[15] I. Mocioiu *et al*, Phys. Lett. B **489**, 390 (2000); M. Chaichian *et al*, Phys. Rev. Lett. **86**, 2716 (2001).

[16] S.M. Carroll *et al*, Phys. Rev. Lett. **87** (2001). 141601.

[17] A. Saha, Eur. Phys. J.**C 51** 199 (2007); *ibid* Phys. Rev. **D 81** 125002 (2010); *ibid* Phys. Rev. **D 89**, 025010 (2014).

[18] A. Stern, Phys. Rev. Lett. **100** (2008) 061601.

[19] A. Saha, S. Gangopadhyay, Phys. Lett. **B 681**, 96 (2009).

[20] A. Saha *et al*, Phys. Rev. D 83 (2011) 025004; *ibid.* Mod. Phys. Lett. **A 28** (2013) 1350161; *ibid.* Gen.Rel.Grav. 47 (2015) 28.

[21] K. Gottfried, T.M. Yan, "Quantum Mechanics: Fundamentals", Springer-Verlag New York, 2003.

[22] *Introduction to Gravitational Waves*, R. Matzner in General Relativity and John Archibald Wheeler, Ciufolini and R.A. Matzner (eds.), Astrophysics and Space Science Library 367, Springer, 2010.

[23] P. Astone *et al*, Phys. Rev. **D 47** (2)(1993) 362; E. Mauceli *et al*, Phys. Rev. **D 54** (1996) 1264; D. G. Blair *et al*, Phys. Rev. Lett. **74** (1995) 1908; P. Astone *et al*, Astroparticle Physics **7** (1997) 231; M. Cerdonio *et al*, Class. Quant. Grav. **14** (1997) 1491.

Study of Optical, X-ray and Gamma-ray emission from blazar 3C 454.3 during the flaring activity observed in May-June 2014

K. K. Singh[a], Himali Bhatt[a,b], S. Bhattacharyya[a], N. Bhatt[a] and A. K. Tickoo[a]

(a) Astrophysical Sciences Division, Bhabha Atomic Research Centre, Mumbai-400085, Maharashtra, India
(b) Inspire Faculty, Department of Science and Technology, India

Presenter: K K Singh (*kksastro@barc.gov.in*); A&A.5, Oral, CICAHEP15.130

The blazar 3C 454.3 is a well known flat spectrum radio quasar at redshift $z = 0.859$. The object has attracted considerable attention due to its variable emission over the entire electromagnetic spectrum from radio to very high energy gamma-rays. In the present work, we study the flaring activity of 3C 454.3 observed by different instruments in the optical, X-ray and gamma-ray energy bands during May-June 2014. With the motivation of understanding the physical mechanism involved in the variable emission from the source during the outburst, we perform a detailed spectral and temporal analysis of the near simultaneous multi-wavelength data recorded over the period from May 1, 2014 (MJD 56778) to June 30, 2014 (MJD 56838). For this time period, we study the variability in UV-Optical, X-ray and gamma-ray regimes and possible correlation between flux levels observed in different energy bands. We also try to model the broad band spectral energy distribution of the source under the framework of leptonic synchrotron self Compton model for blazar emission.

1. Introduction

According to the unified scheme, blazars are defined as the subclass of active galactic nuclei (AGN) with their relativistic jets closely aligned to the line of sight of the observer at the Earth [1]. The broadband emission from the AGN over the entire electromagnetic spectrum from radio to γ–rays, is assumed to be originated from the outflow of accreted matter onto a supermassive black hole (SMBH) at the center of the galaxy. Blazars in particular are characterized by flat radio spectra, variable non-thermal emission with strong Doppler boosting and high optical polarization. The broadband continuum radiation from blazars is described by spectral energy distribution (SED) with two distinct humps [2]. Blazars are subdivided into BL Lacertae objects (BL Lacs: lower luminosity and lack of strong optical emission lines) and flat spectrum radio quasars (FSRQs: higher luminosity and broad optical emission lines). The first hump in the blazar SED at low energies peaks in optical through X-rays and is assumed to be dominated by the synchrotron radiation from relativistic leptons (electrons and positrons) within the jet. The origin of second hump peaking at high energy (HE, E$>$ 100 MeV) in γ–ray regime is attributed to the inverse Compton (IC) scattering of seed photons by the relativistic leptons emitting synchrotron radiation or by the ultrarelativistic hadrons from photo-pair production in the jet. The exact physical process for the high energy emission is still not clear with concerns over the origin of seed photons, however two fundamentally different approaches have been proposed, generally known as leptonic and hadronic models. In the leptonic context, the emission of energetic γ–rays is attributed to the IC scattering of the sychrotron (synchrotron self Compton, SSC) or external (external Compton, EC) photons by the same population of relativistic electrons and positrons [3]. The external seed photons may originate from the accretion disk, broad line region and dusty torus. The hadronic model attributes γ–ray emission to proton-synchrotron, neutral pion decay, synchrotron and IC emission from secondary decay products of charged pions and proton initiated cascades in a magnetic field dominated jet [4]. Study of broadband emission and correlated multi-wavelength variability of large sample of blazars provide a deep insight into the emission process and thus allows the way for addressing the geometry of the jet (size and structure) and location of the emission region in the jet.

In this paper, we study in multi-wavelength context the flaring activity of 3C 454.3 observed during May-June 2014 in HE γ–ray, X-ray and UV-Optical bands to understand the physical processes involved in the outburst. In Section 2, we summarize the results from previous observations of the source during flaring activity in brief. In Section 3, the multi-wavelength observations and data analysis are reported. We report our results with discussion in Section 4. Finally, we conclude our study in Section 5.

2. The blazar 3C 454.3

3C 454.3 (also cataloged as PKS 2251+158; $z = 0.859$ (3.6 Gpc)) belongs to the FSRQ class of blazars and is one of the brightest and highly variable source of electromagnetic radiation from radio to γ–rays. The γ–ray emission from this source was detected above 100 MeV by *EGRET* in 1999 with a flaring state flux of $\sim 5.0 \times 10^{-5}$ ph cm^{-2} s^{-1} [5]. A dramatic optical outburst was observed from 3C 454.3 during April-May 2005. Following this outburst, the source has been the target of several multi-wavelength campaigns and several flaring activities have been observed over the past decade from this object. In the first week of December 2009, the source reached a record γ–ray flux above 100 MeV for blazars with a daily flux of approximately 2.5$\times$10^{-5} ph cm^{-2} s^{-1} observed by *Fermi* and *AGILE* [6]. In November 2010, 3C 454.3 showed sustained flaring activity maintaining γ–ray flux above 100 MeV at 10^{-5} ph cm^{-2} s^{-1} observed by *Fermi* for several days. The source was also extensively monitored in X-ray, optical and radio bands during this period for multi-wavelength observation of the flaring activity [7].

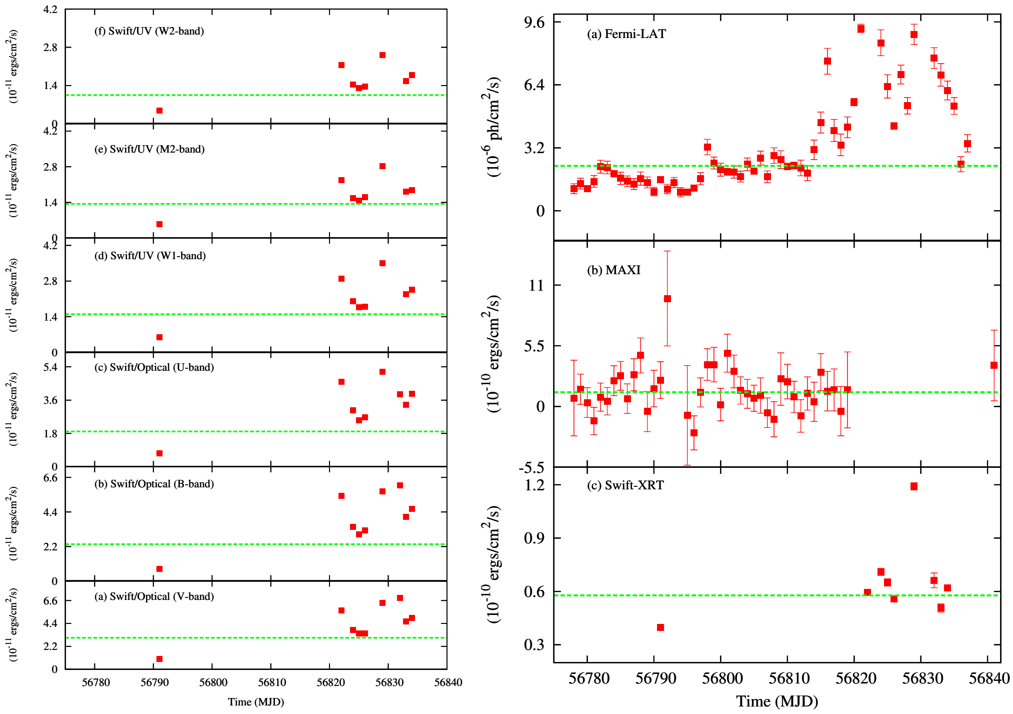

Figure 1. The UV-optical (left) and X-ray & γ–ray (right) light curves for 3C 454.3 during May 1, 2014 to June 30, 2014. The horizontal dotted lines represent the average emission in different energy bands during this period.

3. Multi-wavelength Observations and Data Analysis

We have used the multi-wavelength data from *Fermi* blazar observation program in our present study. The multi-wavelength data for 3C 454.3 recorded during May 1, 2014 to June 30, 2014 (MJD 56778-56838) are described below.

3.1 UV-Optical

The UV and optical observations of 3C 454.3 have been performed using *Swift*-UVOT covering the wavelength range of 180-600 nm [8]. We have analysed the data in six bands : V, B, U, UVW1, UVM2 and UVW2 (with central wavelengths $\lambda_c \sim$ 546.8, 439.2, 346.5, 260.0, 224.6 and 192.8 nm respectively) depending upon the availability of the data in the particular filter. A source region of 5 arcsec radius is selected around the source, while extracting the background from a circular region of 20 arcsec centered in a source-free region. The detection significance, magnitude and flux densities have been derived using the task *uvotsource*. The obtained fluxes are corrected for Galactic extinction of E(B-V) = 0.093 mag as given by [9]. We have derived the de-reddened flux densities in each UVOT filter using the relation given by [10] for AB system.

3.2 X-ray

We have analyzed the data from X-ray telescope (XRT) onboard *Swift* satellite [11] available during May 1, 2014 to June 30, 2014 in both Windowed Timing (WT) and Photon Counting (PC) modes. There are total nine observations available during the above period. The cleaned XRT event files have been generated using the task *xrtpipeline version 0.12.6* following the standard filtering criteria with recent calibration files (version 20140709). The source spectra are extracted from a circular region of radius of 40 arcsec about the source position for WT mode. For PC mode observations, an annular region with inner radius of 8 arcsec and outer radius of 40 arcsec is used. The inner region is excluded to avoid pileup of the source. The background has been estimated from an off-axis region of the same size for individual observation according to the source position in the detector. The ancillary response files (arfs) are extracted with the task *xrtmkarf*. The source spectra are rebinned to have atleast 20 counts per spectral bin with *grppha*.

The spectra are fitted with power-law model consisting of absorption due to a neutral hydrogen (PHABS $\times$ ZPOW) using XSPEC (ver 12.8.0) for z=0.859 in the energy band 0.3–10.0 keV. The line-of-sight absorption is fixed to a neutral hydrogen column density (N_H) of $6.63 \times 10^{20}\ \mathrm{cm}^{-2}$. The unabsorbed energy fluxes are calculated using *cflux* task in the energy band 0.3-10.0 keV and four sub-energy bands: 0.3-0.7 keV, 0.7-1.7 keV, 1.7-4.0 keV, 4.0-10.0 keV for a particular observation. We have also used archival X-ray data from the *MAXI*[1] telescope in the energy range 2-20 keV.

3.3 γ–ray

We have used HE γ–ray data from the large area telescope (LAT) onboard *Fermi* satellite [12] during the period May 1, 2014 to June 30, 2014 (MJD 56778-56838) from the publically available NASA data base[2]. We have performed an unbinned likelihood spectral analysis to produce the light curve using the standard analysis tool *gt-like*, provided in the *Fermi* ScienceTools software packages (version v9r27p1). A refined LAT response function P7_SOURCE_V6 reflecting the improved point-spread function and effective area with galactic and isotropic diffuse emission model files *gal_2yearp7v6_v0.fits* and *iso_p7v6source.txt* respectively have been used to generate the light curve of the source. We have included only photons located in a circular region of interest (ROI) with a 15° radius centered at the position of 3C 454.3 (RA = $22^h53^m57.7^s$, Dec = $16°8'53.5''$) in the present analysis. In addition, we have excluded the events arriving with zenith angles $> 100°$ to avoid the contamination from Earth limb γ–rays, and photons detected while the spacecraft rocking angle was $> 52°$. All the point sources from *Fermi* second LAT catalog (2FGL) [13] within 20° of 3C 454.3 have been considered in the source model file. Sources within ROI are fitted with power law model with spectral index and normalization as free parameters, while those beyond ROI have their model parameters fixed to the values as reported in 2FGL. We have produced the daily light curve in the energy range 0.1-100 GeV with minimum statistical significance accepted for each time bin as TS$\geq$ 16, where TS is the test statistic defined as twice the difference of the *log(likelihood)* with and without the source in the model file respectively ($\sqrt{TS}$ gives the statistical significance of the detection).

---

[1] http://maxi.riken.jp/top/index.php

[2] http://fermi.gsfc.nasa.gov/ssc/data/access

4. Results and Discussion

4.1 Light curve Analysis

The multi-wavelength light curves of 3C 454.3 in UV-Optical, X-ray and HE γ-ray bands during May 1, 2014 to June 30, 2014 (MJD 56778-56838) are shown in Fig.1. It is evident from Fig.1 that the source is observed in extreme flaring state on June 21, 2014 (MJD 56829) in all energy bands from UV (W1, M2 & W2), optical (V, B & U), X-ray (0.3-10 keV) and γ–ray (0.1-100 GeV). The average γ–ray flux is above 10^{-6} ph cm^{-2} s^{-1} which implies an active phase of the source during the above time period. In the highest flaring state on June 21, 2014, the γ–ray flux increases upto $\sim$ 10 times the average flux of the active phase. The HE γ–ray emission during May 1, 2014 to June 5, 2014 (MJD 56778-56813) is observed to be consistent with average or quiescent state emission. The X-ray activity observed with *Swift*/XRT in the energy range 0.3-10 keV also shows that the flux level during flaring state is approximately two times the average flux of the available observation during this period. In the UV-Optical band, a significant change in the source activity is observed during this period, with a peak on June 21, 2014. Therefore, a near simultaneous flaring episode in UV-Optical, X-ray and HE γ–ray is evident from the source.

To quantify the variability in different energy regimes, we have computed the fractional variability amplitude (F$_{var}$) and variability amplitude parameter (A$_{mp}$) as defined by [14] using daily light curves in each energy band. Both the parameters, F_{var} and A_{mp} are shown as a function of mean observational energy of different energy bands in Fig.2 using red squares and green circles respectively. We observe that F_{var} and A_{mp} show similar behaviour as a function of energy during the flaring activity of the 3C 454.3. From this figure, it is evident that the UV-Optical and X-ray emission from the source can be characterized by an average variability amplitude of $F_{var} \sim 50\%$ whereas it is observed to be $\sim 90\%$ in HE γ–ray regime. Similar variability amplitudes in low energy bands from UV to X-rays favour SSC process for their emission. The correlation study performed using *Pearson coefficient* suggests that the multi-wavelength emissions from the source are correlated with each other during the entire period. This provides evidence to support the one zone leptonic model for blazar emission.

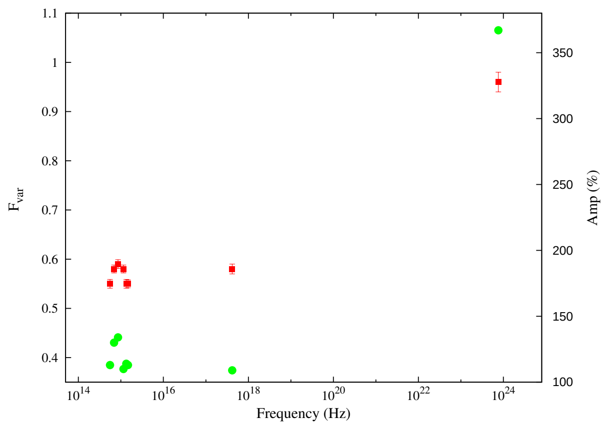

Figure 2. Variability amplitudes in different energy bands. The red squares represent fractional variability amplitude (F$_{var}$) and green circles denote variability amplitude parameter (A$_{mp}$).

4.2 Spectral Energy Distribution Modelling

We have used one zone blazar emission model to reproduce the SED of the source. In this model, we consider a spherical emission region filled with relativistic non-thermal electrons and moving with the bulk Lorentz factor Γ along the jet of the source. The size of emission region is constrained by variability time scale and light crossing effects. The relativistic electrons emit synchrotron radiation due to the presence of uniform magnetic field in the blob. The non-thermal electrons also emit high energy radiation by self synchrotron Compton process as well as by Comptonizing external soft photons from the accretion disk. The photon emissivities due to synchrotron, self synchrotron Compton and external Compton processes have been obtained from Finke et al. (2008) and Dermer et al. (2009) [15]. The broad band SED of the source in quiescent state is reproduced by assuming that the non-thermal spectrum of electrons is described by a broken power law with spectral indices of 1.5 before the break and 3.5 after the break. However, SED of the source during flaring activity is obtained by the non-thermal population of electrons following a power law spectrum with index ~ 2.5. The model SEDs of the source in the two states along with observed multi-wavelength flux points are shown in Fig.3. The best fit values of bulk Lorentz factor and magnetic field of the jet are found to be 200 and 0.06 G in the normal state while the same parameter values are obtained to be 700 and 0.01 G in flaring activity state. The parameters derived in our present study under the framework of synchrotron, SSC and EC models are consistent with the previous studies of the source.

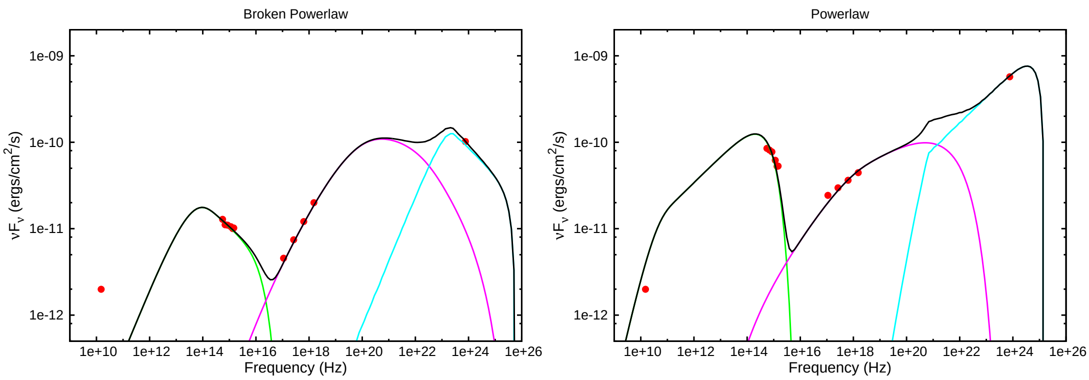

Figure 3. Spectral energy distribution of 3C 454.3 under the frame work of synchrotron external Compton (EC) model during quiescent state (left) on May 14, 2014 (MJD 56791) and flaring state (right) on June 21, 2014 (MJD 56829).

5. Conclusions

In this study, we focus on the analysis of multi-wavelength data recorded by *Swift* and *Fermi* satellites during the period May-June 2014 (MJD 56778-56838). We have obtained daily averaged light curves for the whole time span in the UV-optical, X-ray and HE γ–ray bands from these data sets. The source is observed to be in active state with a strong flaring activity on June 21, 2014 in the all energy bands. The activity of the source is characterized by two variability parameters namely F_{var} and A_{mp}. The highest variability of the source is observed in high energy regime with a comparatively less variability in lower energy bands (UV-optical and X-rays). The multi-wavelength emission during the active phase of the source (including flaring activity) is very well correlated. This exceptional multi-wavelength flaring activity of FSRQ 3C 454.3 allows us for day scale spectral analysis with good quality data and gives unique opportunity for modelling the SED of the source. Therefore, we have performed spectral analysis for some selected time period involving the flaring activity to study the simultaneous broadband SED of 3C 454.3 using one zone leptonic model with synchrotron, SSC and EC processes. The model parameters obtained in the two states of source activity suggest that the jet is magnetically dominated during normal state while the jet energy is contained in particles during flaring activity.

6. Acknowledgement

We acknowledge the use of public data obtained through *Fermi* Science Support Center (FSSC) provided by NASA. This work made use of data supplied by the UK *Swift* Science Data Centre at the University of Leicester. This research has made use of the MAXI data, provided by RIKEN, JAXA and the MAXI team. KKS would like to thank Dibrugarh University for providing partial financial support to attend the conference.

References

[1] R. D. Blandford & M. J. Rees, MNRAS **169**, 395 (1974).
[2] G. Fossati et l., MNRAS **299**, 433 (1998).

[3] G. Ghisellini et al., MNRAS **301**, 451 (1998); M. Sikora et al., ApJ **421**, 153 (1994).
[4] F. Aharonian et al., New Astronomy **5**, 377 (2000).
[5] R. C. Hartman et al., ApJS **123**, 79 (1999).
[6] M. Ackermann et al., ApJ **721**, 1383 (2010); E. Striani et al., ApJ **718**, 455 (2010).
[7] S. G. Jorstad et al., ApJ **773**, 147 (2013); A. Abdo et al., ApJ **733**, 26 (2011).
[8] P. W. A. Roming et al., SSRv **120**, 95 (2005).
[9] D. J. Schlegel et al., ApJ 500, **525** (1998).
[10] J. Kataoka et al., ApJ **685**, 839 (2008).
[11] D. N. Burrows et al., SSRv **120**, 165 (2005).
[12] W. B. Atwood et al., ApJ **697**, 1071 (2009).
[13] P. L. Nolan et al., ApJS **199**, 31 (2012).
[14] R. Edelson et al., ApJ **568**, 610 (2002); J. Heidt et al., A&A **305**, 42 (1996).
[15] J. D. Finke et al., ApJ **686**, 181 (2008); C. D. Dermer et al., ApJ **692**, 32 (2009).

Generalised Pseudo-Newtonian potential for Kerr Black Holes

Tamal Sarkar[a,b], Arunava Bhadra [b] and Shubrangshu Ghosh[c]

(a) University Science Instrumentation Centre, University of North Bengal, Siliguri-734013, India
(b) High Energy and Cosmic Ray Research Centre, University of North Bengal, Siliguri-734013, India
(c) Centre for Astroparticle Physics and Space Science, Bose Institute, Block EN , Sector V, Salt Lake-700091, Kolkata, India

Presenter: Tamal Sarkar (*ta.sa.nbu@hotmail.com*); A&A.5, Oral, CICAHEP15.158

We have formulated a generalized Pseudo-Newtonian potential (PNP) based on the conserved Hamiltonian for a test particle motion around a spinning black hole described by Kerr Spacetime. The formulated potential reproduces most of the general relativistic effects for a test particle motion around the Kerr black hole with resonable accuracy within Newtonian framework. Unlike the other prevailing PNPs for Kerr spacetime, the present PNP contains the explicit information of frame dragging effect. The general relativistic effects like perihelion advancement and bending of light also can be evaluated with high accuracy from the derived potential. The formulated Pseudo-Newtonian potential should be quite useful to study complex accretion plasma dynamics within Newtonian framework.

1. Introduction

The Kerr spacetime in the Boyer-Lindquist coordinate system is given by

$$ds^2 = -\left(1 - \frac{2\,r_s\,r}{\Sigma}\right)c^2dt^2 - \frac{4ar_s\,r\sin^2\theta}{\Sigma}cdtd\phi + \frac{\Sigma}{\Delta}dr^2$$
$$+\Sigma d\theta^2 + \left(r^2 + a^2 + \frac{2r_s\,ra^2\sin^2\theta}{\Sigma}\right)\sin^2\theta\, d\phi^2\,, \tag{1}$$

where $\Delta = r^2 + a^2 - 2r_s r$, $\Sigma = r^2 + a^2\cos^2\theta$ and $a = \frac{J}{Mc}$ named as Kerr parameter. $r_s = GM/c^2$. The Lagrangian density of the particle of mass m in the Kerr spacetime is then given by

$$2\mathcal{L} = -\left(1 - \frac{2r_s\,r}{\Sigma}\right)c^2\left(\frac{dt}{d\tau}\right)^2 - \frac{4ar_s\,r\sin^2\theta\,c}{\Sigma}\frac{dt}{d\tau}\frac{d\phi}{d\tau} + \frac{\Sigma}{\Delta}\left(\frac{dr}{d\tau}\right)^2$$
$$+\Sigma\left(\frac{d\theta}{d\tau}\right)^2 + \left(r^2 + a^2 + \frac{2r_s\,ra^2\sin^2\theta}{\Sigma}\right)\sin^2\theta\left(\frac{d\phi}{d\tau}\right)^2. \tag{2}$$

From the symmetries, we obtain two constants of motion corresponding to two ignorable coordinates t and ϕ, given by

$$\mathcal{P}_t = \frac{\partial\mathcal{L}}{\partial\tilde{t}} = -\left(1 - \frac{2r_s\,r}{\Sigma}\right)c^2\frac{dt}{d\tau} - \frac{2ar_s\,r\sin^2\theta}{\Sigma}c\frac{d\phi}{d\tau}$$
$$= \text{constant} = -\epsilon \tag{3}$$

and

$$\mathcal{P}_\phi = \frac{\partial\mathcal{L}}{\partial\tilde{\phi}} = -\frac{2ar_s\,r\sin^2\theta}{\Sigma}c\frac{dt}{d\tau} + \left(r^2 + a^2 + \frac{2r_s\,ra^2\sin^2\theta}{\Sigma}\right)\sin^2\theta\frac{d\phi}{d\tau}$$
$$= \text{constant} = \lambda\,, \tag{4}$$

where ϵ and λ are specific energy and specific angular momentum of the orbiting particle, respectively. Here, $\tilde{t}$ and $\tilde{\phi}$ represent the derivatives of 't' and 'ϕ' with respect to proper time τ. For particle motion in the equatorial plane $(\theta = \pi/2)$, by solving the above two equations we obtain

$$\frac{dt}{d\tau} = \frac{\frac{\epsilon}{c^2}\left(r^3 + a^2r + 2r_sa^2\right) - \frac{2ar_s\lambda}{c}}{r\Delta}\,, \tag{5}$$

$$\frac{d\phi}{d\tau} = \frac{\frac{\epsilon}{c}2ar_s + (r-2r_s)\lambda}{r\Delta}\,. \tag{6}$$

Using $\mathcal{L} = -\frac{1}{2}m^2c^2$ and substituting (5) and (6) in (2) we obtain

$$\frac{\epsilon^2 - c^4}{2c^2}\left(1 + \frac{a^2}{r^2}\right) = \frac{1}{2}\dot{r}^2\left(\frac{dt}{d\tau}\right)^2 - \frac{r_s a^2}{r^3}\frac{\epsilon^2}{c^2} + \frac{2ar_s\lambda}{r^3}\frac{\epsilon}{c}$$
$$-\frac{GM}{r} + \frac{1}{2}\frac{\lambda^2}{r^2}\left(1 - \frac{2r_s}{r}\right)\,. \tag{7}$$

Using (5) and (6) we find

$$\frac{dt}{d\tau} = \frac{\epsilon}{c^2}\frac{r}{\left[(r-2r_s) + \frac{2ar_s}{c}\dot{\phi}\right]}\,. \tag{8}$$

2. Formulation of the generalized potential

The basis of our potential formulation is the low energy limit of the test particle motion [1, 2, 3] , which is $\epsilon/c^2 \sim 1$. We write $E = \frac{\epsilon^2 - c^4}{2c^2}$ considering a locally inertial frame for test particle motion which will reduce to the total mechanical energy ($\equiv$ Hamiltonian) in Newtonian mechanics in nonrelativistic limit with $a = 0$. Second term in the above definition of E is the rest mass energy of the particle which is subtracted from relativistic energy owing to the low energy limit, in analogy to Newtonian Hamiltonian. Computing λ from (6) and substituting in (7) and using (8), we finally obtain the generalized Hamiltonian ($E_{\rm GK}$) of test particle around Kerr spacetime in low energy limit as

$$E_{\rm GK} = -\frac{GM}{r} + \left(\frac{1}{2}\dot{r}^2\frac{r-2r_s}{\Delta} + \frac{\Delta}{2r}\dot{\phi}^2\right)\frac{r^3}{\left[(r-2r_s) + \frac{2ar_s}{c}\dot{\phi}\right]^2}\,, \tag{9}$$

where overdots represent the derivative with respect to coordinate time t. With $a = 0$, $E_{\rm GK}$ reduces to that of Schwarzschild geometry. The generalized Hamiltonian $E_{\rm GK}$ in the low energy limit should be equivalent to the Hamiltonian in the Newtonian framework. The effective Hamiltonian in the Newtonian regime with the generalized potential in the equatorial plane will then be equivalent to $E_{\rm GK}$ in (9). Thus

$$E_{\rm GK} \equiv \frac{1}{2}\left(\dot{r}^2 + r^2\dot{\phi}^2\right) + V_{\rm GK} - \dot{r}\frac{\partial V_{\rm GK}}{\partial \dot{r}} - \dot{\phi}\frac{\partial V_{\rm GK}}{\partial \dot{\phi}}\,, \tag{10}$$

where $T = \frac{1}{2}(\dot{r}^2 + r^2\dot{\phi}^2)$ is the nonrelativistic specific kinetic energy of the test particle. $V_{\rm GK}$ is the most generalized form of the potential in Newtonian analogue of Kerr spacetime in the spherical geometry with test particle motion in the equatorial plane, which contains the entire information of the source. The potential $V_{\rm GK}$ is then given by

$$V_{\rm GK} = -\frac{GM}{r}(1 - \omega\dot{\phi}) - \frac{\left(\mathcal{G}_1\dot{r}^2 + \mathcal{G}_2 r^2\dot{\phi}^2\right)}{2\left(1 + \omega\dot{\phi}\right)} + \frac{\dot{r}^2 + r^2\dot{\phi}^2}{2}\,, \tag{11}$$

where

$$\mathcal{G}_1 = \frac{r^3}{(r-2r_s)\Delta},\;\; \mathcal{G}_2 = \frac{\Delta}{(r-2r_s)^2}\,. \tag{12}$$

Note that all the dynamical quantities expressed are specific quantities. In the Newtonian limit $\mathcal{G}_1 = \mathcal{G}_2 = 1$. $\omega = 2ar_s/c(r-2r_s)$. $\omega\dot{\phi}$ in the potential in (11) arises due to the effect of frame dragging. Potential $V_{\rm GK}(\equiv V_{\rm KN})$ is a modified potential deviating from exact Newtonian (spherical symmetric part). 'KN' symbolizes 'Kerr-Newtonian'.

3. Discussion about the utility of formulated pseudo-Newtonian potential

The potential is an explicit velocity dependent potential containing all gravitational effects of Kerr spacetime for a stationary observer. Thus, the potential in (11) contains the explicit information of gravitomagnetic and frame dragging effects which has been obtained directly from the Kerr metric by solving geodesic equations of motion. Putting $a = 0$, the potential reduces to that in Schwarzschild geometry. Unlike most other PNPs which are either derived or prescribed for particle motion in circular orbit, the potential in (11) is applicable for generalized orbital dynamics. It is to be noted that we have restricted ourselves in deriving a Kerr-Newtonian potential corresponding to a particle motion in the equatorial plane. Formulation of a more generalized Kerr-Newtonian potential for off-equatorial particle orbits is immensely complicated within our present approach, where the necessary use of Carter constant seems to be a prerequisite (see GM07). Such a study would be pursued in the near future.

Although the Kerr-Newtonian potential, in principle, should precisely reproduce all orbits in exact Kerr geometry, the form of the potential in (11) gets diverge at $r = 2r_s = 2GM/c^2$. This is precisely happening owing to the presence of the $\left[(r-2r_s)+\frac{2ar_s}{c}\dot{\phi}\right]^2$ in the denominator of Hamiltonian $E_{\rm GK}$ in (9), which has been obtained while replacing the conserved specific angular momentum λ by $\dot{\phi}$. Thus, the potential in the form given in (11) would not be useful within the range $r \lesssim 2r_s$. Note that for Kerr BH, the horizon $r_H = r_s$ for maximal spin. However, such a radial zone of range $r \lesssim 2\,r_s$ is in the extreme vicinity of the rotating BH, which either lies within the ergosphere for a certain range of a or having a direct ergospheric effect. Moreover, at $r \lesssim 2\,r_s$, the notion of potential indeed becomes insignificant and exact GR equations become relevant, where ergospheric effects would dominate. The accretion powered phenomena which we would be more interested in are more relevant at much outer radii, as most of the observed phenomena related to BH accretion occur at radii much beyond $\sim 2\,r_s$. Also, it is to be noted that for lesser BH spin, r_H is much greater than r_s for which the inner accretion edge is way beyond $\sim 2\,r_s$.

In Fig.1 we show the variation of the Kerr-Newtonian potential with r for both prograde and retrograde circular orbits and compare them with Schwarzschild and Newtonian cases. It is being seen that for co-rotating case (Fig.1a), the magnitude of the corresponding Kerr-Newtonian potential is less than that with respect to Schwarschild spacetime in the inner regions of the central BH, and decreases with the increase in Kerr parameter a. This occurs exactly due to the effect of frame dragging. With the increase in a, the effect of frame dragging increases which tends to diminish the radial effect of Kerr-Newtonian potential. This property of Kerr spacetime has a direct consequence on the accreting plasma in the vicinity of rotating BHs, by providing an additional boost to propel matter and radiation out of the accretion flow. On the contrary, for counterrotating particle orbits, the magnitude of Kerr-Newtonian potential is much higher as compared to that in Schwarzschild geometry, which increases with the increase in a (Fig.1b)

The Lagrangian of the particle in the presence of this Kerr-Newtonian potential is given by

$$\mathcal{L}_{\rm KN} = \frac{GM}{r}(1-\omega\dot{\phi}) + \frac{\left(\mathcal{G}_1\dot{r}^2 + \mathcal{G}_2 r^2\dot{\phi}^2\right)}{2\left(1+\omega\dot{\phi}\right)}\,, \tag{13}$$

which exactly reduces to that in Schwarzschild geometry with $a = 0$. Specific angular momentum which is a constant of motion corresponding to Kerr-Newtonian potential is then given by

$$\lambda_{\rm KN} = \frac{\partial\mathcal{L}_{\rm KN}}{\partial\dot{\phi}} = -\frac{GM\omega}{r} + \frac{\mathcal{G}_2 r^2\dot{\phi}\left(2+\omega\dot{\phi}\right)}{2\left(1+\omega\dot{\phi}\right)^2} - \frac{\mathcal{G}_1\dot{r}^2\omega}{2\left(1+\omega\dot{\phi}\right)^2}\,. \tag{14}$$

Obtaining the specific Hamiltonian from (13), the radial motion of the particle in the presence of this potential is

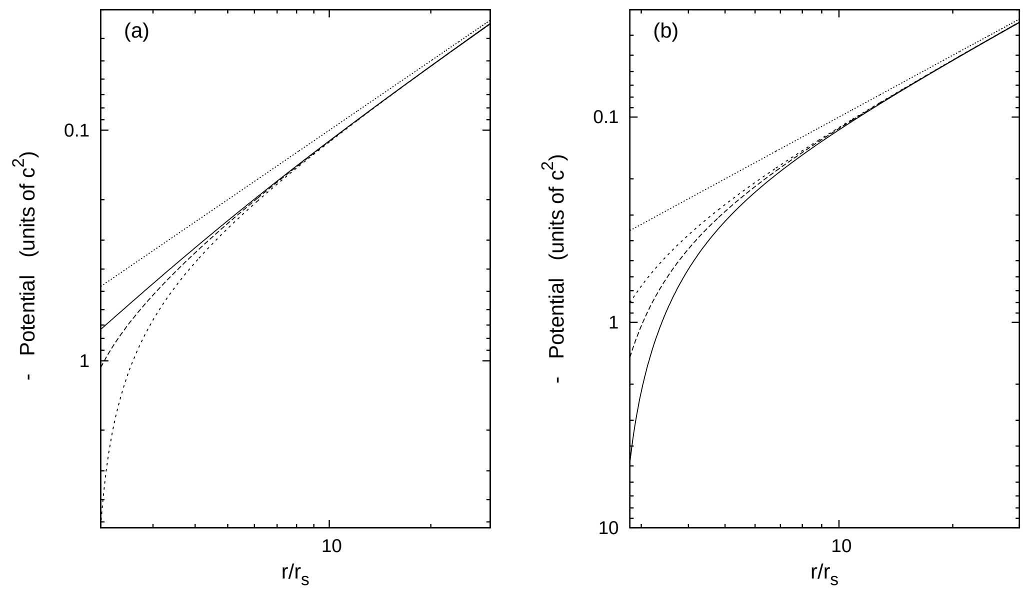

Figure 1. Variation of potential with radial distance r. Solid, long-dashed, short-dashed and dotted curves in (a) are for Kerr-Newtonian potential with Kerr parameter $a = 1$, $a = 0.5$, Schwarzschild-Newtonian potential ($a = 0$) and Newtonian potential respectively. Similarly Solid, long-dashed, short-dashed and dotted curves in (b) are for Kerr parameter $a = -1$, $a = -0.5$, Schwarzschild case and Newtonian case respectively. Potential in y-axis has negative values expressed in units of c^2. r and a are expressed in units of r_s. Both x-axis and y-axis are in logarithmic scale.

then given by

$$\dot{r}^2 = \frac{2}{\mathcal{G}_1}\left(E_{\rm KN} + \frac{GM}{r}\right)\left(1+\omega\dot{\phi}\right)^2 - \frac{\mathcal{G}_2}{\mathcal{G}_1} r^2 \dot{\phi}^2 \,. \tag{15}$$

$E_{\rm KN}$ is the conserved specific Hamiltonian of the particle motion in Kerr-Newtonian which is equivalent to $E_{\rm GK}$. $\dot{r}$ is identical to the expression in exact Kerr geometry in low energy limit. Next we compute the equations of motion of test particle using the Kerr-Newtonian potential. For r coordinate we obtain

$$\begin{aligned} \left(1 - \frac{\mathcal{A}_3}{\mathcal{B}_1}\mathcal{B}_5 \dot{r}^2\right)\ddot{r} + \left[\mathcal{A}_1 + \frac{\mathcal{A}_3}{\mathcal{B}_1}\left(\mathcal{B}_2 + \mathcal{B}_3 + \mathcal{B}_4\right)\right]\dot{r}^2 \\ -\mathcal{A}_2\dot{\phi}^2 + \mathcal{A}_4 + \frac{\mathcal{A}_3}{\mathcal{B}_1}\mathcal{B}_6 \dot{r}^4 \;=\; 0\,. \end{aligned} \tag{16}$$

Similarly for ϕ coordinate we have

$$\begin{aligned} \left(1 - \frac{\mathcal{A}_3}{\mathcal{B}_1}\mathcal{B}_5 \dot{r}^2\right)\ddot{\phi} + \left[\frac{1}{\mathcal{B}_1}\left(\mathcal{B}_2 + \mathcal{B}_3 + \mathcal{B}_4 + \mathcal{A}_4\mathcal{B}_5\right)\right]\dot{r} \\ -\frac{\mathcal{A}_2\mathcal{B}_5}{\mathcal{B}_1}\dot{r}\dot{\phi}^2 + \frac{1}{\mathcal{B}_1}\left(\mathcal{B}_6 + \mathcal{A}_1\mathcal{B}_5\right)\dot{r}^3 \;=\; 0\,. \end{aligned} \tag{17}$$

Here,

$$\mathcal{A}_1 = \frac{1}{2(r-2r_s)}\left[\frac{2a^2(r-3r_s) - 4rr_s(r-2r_s)}{r\Delta} + \frac{\omega\dot{\phi}}{1+\omega\dot{\phi}}\right],$$

$$\mathcal{A}_2 = \frac{\mathcal{G}_2}{2r}\left[2(r-3r_s)(r-2r_s) - 4\frac{r_s}{r}a^2 \;+\; \Delta\frac{\omega\dot{\phi}}{1+\omega\dot{\phi}}\right],$$

$$\mathcal{A}_3 = \frac{\omega}{1+\omega\dot{\phi}},\; \mathcal{A}_4 = \frac{GM}{r^2\mathcal{G}_1}\left[1 - \frac{4ar_s}{c}\frac{r-r_s}{(r-2r_s)^2}\dot{\phi}\right],$$

$$\mathcal{B}_1 = \left(\mathcal{G}_2 r^2 + \mathcal{G}_1 \omega^2 \dot{r}^2\right),\ \mathcal{B}_2 = \frac{r^2\dot{\phi}}{2(r-2r_s)}\mathcal{G}_2\,\omega\dot{\phi}\left(3+\omega\dot{\phi}\right)$$

$$\mathcal{B}_3 = \frac{r^2\dot{\phi}\left(1+\omega\dot{\phi}\right)}{2(r-2r_s)}\left[\frac{2(r-3r_s)(r-2r_s)-4\frac{r_s}{r}a^2}{(r-2r_s)^2}\left(2+\omega\dot{\phi}\right)\right],$$

$$\mathcal{B}_4 = \frac{4GMr_s a(r-r_s)\left(1+\omega\dot{\phi}\right)^3}{cr^2(r-2r_s)^2},\ \mathcal{B}_5 = \omega\mathcal{G}_1\left(1+\omega\dot{\phi}\right),$$

and

$$\mathcal{B}_6 = \frac{\omega}{2}\left[\frac{\mathcal{G}_1\left(1-\omega\dot{\phi}\right)}{r-2r_s} - \frac{2a^2r^2(r-3r_s)-4r^3r_s(r-2r_s)}{(r-2r_s)^2\frac{\Delta^2}{\left(1+\omega\dot{\phi}\right)}}\right].$$

The equations (14), (15), (16) and (17) will provide a complete particle dynamics around Kerr BHs in Kerr-Newtonian framework. They reduce to the expressions corresponding to Schwarzschild case, with $a = 0$.

Acknowledgments

The authors would like to thank Emilo Tejada & their group, Dibrugarh University as well as University Library of University of North Bengal .

References

[1] E. Tejeda, S. Rosswog, MNRAS **433**, 1930 (2013).
[2] T. Sarkar, S. Ghosh, A. Bhadra, PhRvD **90**, 063008 (2014).
[3] S. Ghosh, T. Sarkar, MNRAS **445**, 4460 (2014).

The pitch angle paradox and radiative life times in a synchrotron source

Ashok K. Singal

Astronomy and Astrophysics Division, Physical Research Laboratory, Navrangpura, Ahmedabad-380009, Gujarat, India

asingal@prl.res.in; A&A.7, Oral, CICAHEP15.169.2

In synchrotron radiation there is a paradox whether or not the pitch angle of a radiating charge varies. The conventional wisdom is that the pitch angle does not change during the radiation process. The argument is based on Larmor's radiation formula, where in a synchrotron case the radiation power is along the instantaneous direction of motion of the charge. Then the momentum loss will also be parallel to that direction and therefore the pitch angle of the charge would remain unaffected. The accordingly derived formulas for energy losses of synchrotron electrons in radio galaxies are the standard text-book material for the last 50 years. However, if we use the momentum transformation laws from special relativity, then we find that the pitch angle of a radiating charge varies. While the velocity component parallel to the magnetic field remains unaffected, the perpendicular component does reduce in magnitude due to radiative losses, implying a change in the pitch angle. This apparent paradox is resolved when effects on the charge motion are calculated not from Larmor's formula but from Lorentz's radiation reaction formula. We derive the exact formulation by taking into account the change of the pitch angle due to radiative losses. From this we first time derive the characteristic decay time of synchrotron electrons over which they turn from highly relativistic into mildly relativistic ones.

1. Introduction

Synchrotron radiation is of extreme importance in many relativistic plasma and is widely prevalent in extragalactic radio sources, supernovae remnants, the Galaxy, and many other astrophysical phenomena. A power-law spectrum is the main characteristic of this radiation process. As electrons emit radiation and thereby lose energy, the radiation spectrum steepens. This steepening of the spectrum causes even a break in the spectrum slope. This break is a direct indication of the radiative life-time of electrons and tells us about the age of the source of synchrotron radiation. Therefore it is important to understand these radiation losses in detail.

Formulas for synchrotron radiative losses were derived more than about 50 years back and have been in use ever since for calculating radiative losses in a variety of radio sources. In these formulas, it has always been assumed that the pitch angle of the radiating charged particle remains constant and the dynamics and the life-time of radiating electrons are accordingly derived [1]. This formulation is now a standard text-book material [2, 3]. However, it turns out that this formulation is not relativistically covariant. It will be shown here that in the case of synchrotron losses, the pitch angle in general changes. We shall derive the exact formulation for radiative losses, taking into account the pitch angle changes.

2. Synchrotron power loss

We use Gaussian (cgs) system of units throughout. A relativistic charged particle, say, an electron of charge - e, rest mass m_0, having a velocity $\boldsymbol{\beta} = \mathbf{V}/c$ and energy $\mathcal{E} = m_0c^2\gamma$ (with Lorentz factor $\gamma = 1/\sqrt{(1-\beta^2)}$), moves in a magnetic field B in a helical path with θ as the pitch angle, defined as the angle that the velocity vector makes with the magnetic field direction. We assume the magnetic field to be uniform, say, along the z-axis (Fig.(1)). As there is no force component due to the magnetic field parallel to itself, a charge with a velocity component $\beta_\parallel$ only along the z-axis keeps on moving unaffected by the field.

The charge spiraling in a magnetic field radiates in the forward direction of its instantaneous motion. For a highly relativistic motion of the charge, like in a synchrotron case, all the radiated power, as calculated from Larmor's formula (or rather from Liénard's formula), is confined to a narrow cone of angle $1/\gamma$ around the instantaneous direction of motion of the charge. Therefore the momentum carried by the radiation will be along the direction of motion of the charge. From the conservation of momentum it can then be construed that the radiation should cause only a decrease in the magnitude of the velocity vector without affecting its direction. As a result it is expected that the pitch angle θ of the motion should not change due to radiative losses [1]. Thus the ratio $V_\perp/V_\parallel = \beta_\perp/\beta_\parallel = \tan\theta$, will not change.

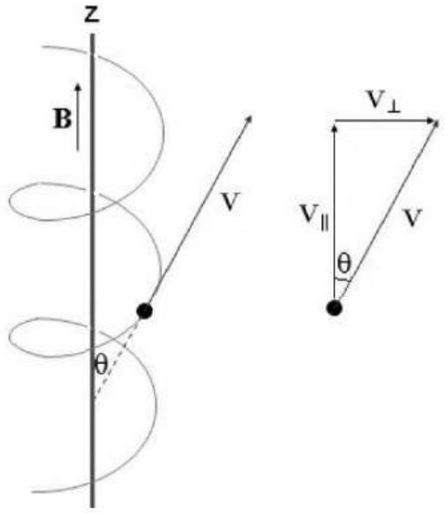

Figure 1. Helical motion of the electron moving with a velocity $\mathbf{V}$ along pitch angle θ in a uniform magnetic field $\mathbf{B}$. $\mathbf{V}_{\parallel}$ is the velocity component parallel to $\mathbf{B}$ while $\mathbf{V}_{\perp}$ is the perpendicular velocity component.

With the pitch angle as a constant of motion, half life-times of radiating electrons have been calculated, using an approximate power loss formula [1, 2, 3],

$$\frac{\mathrm{d}\mathcal{E}}{\mathrm{d}t} = -\zeta \sin^2\theta\, \mathcal{E}^2 \,, \tag{1}$$

where $\zeta = 2e^4 B^2/(3m_o^4 c^7) = 2.37 \times 10^{-3} B^2 \mathrm{erg}^{-1}\mathrm{s}^{-1}$. Let $\mathcal{E}_0$ be the initial energy at $t = 0$, then from equation (1) the energy of the radiating charge at $t = \tau$ is calculated to be,

$$\mathcal{E} = \frac{\mathcal{E}_0}{1 + \zeta \sin^2\theta\, \tau\, \mathcal{E}_0} \,. \tag{2}$$

From equation (2) it follows that the electron loses half of its energy in a time $\tau_{1/2} = 1/(\zeta \sin^2\theta\, \mathcal{E}_\mathrm{o})$.

One thing we note from equation (2) is that it can be true only for a highly relativistic charge ($\gamma = \mathcal{E}/(m_0 c^2) \gg 1$) and that it is not a general equation. This can be seen immediately from $\tau \to \infty$, where $\mathcal{E} \to 0$ implying $\gamma \to 0$, while we know that $\gamma \geq 1$ always. Actually an approximation $\beta \approx 1$ has been used right from the beginning and instead of equation (1), the exact equation for the energy loss rate is [4, 5, 6],

$$\frac{\mathrm{d}\mathcal{E}}{\mathrm{d}t} = -\zeta\beta^2 \sin^2\theta\, \mathcal{E}^2. \tag{3}$$

We can rewrite the power loss rate in terms of the Lorentz factor γ ($= \mathcal{E}/(m_0 c^2)$, which implies expressing energy in units of the rest mass energy), to write,

$$\frac{\mathrm{d}\gamma}{\mathrm{d}t} = -\eta\beta^2 \sin^2\theta\, \gamma^2. \tag{4}$$

Here $\eta = 2e^4 B^2/(3m_\mathrm{o}^3 c^5) = 1.94 \times 10^{-9} B^2\ \mathrm{s}^{-1}$.

3. The pitch angle paradox

Consider a charge particle in its gyrocenter (GC) frame $\mathcal{K}'$, which is moving with a velocity $\beta_{\parallel}$ with respect to the lab frame $\mathcal{K}$. In $\mathcal{K}'$ therefore the charge has no component of velocity parallel to the magnetic field and has only a circular motion in a plane perpendicular to the magnetic field (with a pitch angle $\theta = \pi/2$). In this frame, due to radiative losses by the charge, there will be a decrease in the velocity which is solely in a plane perpendicular to the magnetic field, and the charge will never ever attain a velocity component parallel to the magnetic field.

Now we look at this particle from the lab frame $\mathcal{K}$, in which the charge has (at least to begin with) a motion, $\beta_{\|}$ along the magnetic field. Since in the inertial frame $\mathcal{K}'$, the charge never gets a velocity component parallel to the magnetic field and the two inertial frames ($\mathcal{K}$ and $\mathcal{K}'$) continue to move with reference to each other with a constant $\beta_{\|}$, the parallel component of velocity of the charge should remain unchanged even in $\mathcal{K}$. However, magnitude of the perpendicular component of velocity is continuously decreasing because of radiative losses, therefore the pitch angle of the charge, $\theta = \tan^{-1}(\beta_{\perp}/\beta_{\|})$, should decrease continuously with time and the velocity vector of the charge should increasingly align with the magnetic field vector.

Thus we have a paradox here. While conservation of momentum argument led us to the conclusion that the pitch angle of the charge is a constant, the second argument from relativistic transformation considerations showed that the pitch angle will be progressively reducing as the charge radiates with time. Which of the two is true then? It turns out that the second argument is correct and we shall show that the pitch angles of the radiating charges decrease continuously and due to that their angular distribution in the momentum space changes with time. Even if to begin with there were an isotropic energy distribution of electrons in a synchrotron source, electrons radiating synchrotron radiation develop a pitch angle anisotropy because of $\sin^2\theta$ dependence of the radiated power (equation (4)). Then there is the additional fact that the pitch angle of radiating electrons monotonically decreases with time, and as we shall show the rate of change of the pitch angle depends upon the value of the pitch angle itself.

Instead of calculating the effects of radiation on charge energy from Larmor's formula (or its relativistic generalization Liénard's formula) if we use the Lorentz's radiation reaction formula and apply it in frame $\mathcal{K}'$, we get a force along $\ddot{\boldsymbol{\beta}}'$, which is in a direction opposite to the velocity vector in $\mathcal{K}'$, and the charge accordingly would have a deceleration vector only in a plane perpendicular to the magnetic field. It should be noted that in all reference frames gyro acceleration $\dot{\boldsymbol{\beta}}$ always lies in the plane perpendicular to the magnetic field and so is the vector $\ddot{\boldsymbol{\beta}}$ therefore. And a relativistic transformation of acceleration due to radiation losses, between frames $\mathcal{K}$ to $\mathcal{K}'$, gives a non-zero vector only along the direction perpendicular to the magnetic field and a nil acceleration along the parallel direction [9], consistent with conclusions reached based on the theory of relativity.

There is another way of arriving at the paradox. Larmor's formula says that a charge moving with non-relativistic speeds radiates energy at a rate $\propto \dot{\beta}^2$. However, the radiation pattern of such a charge has a $\sin^2\phi$ dependence [4, 7, 8], about the direction of acceleration. Due to this azimuthal symmetry the net momentum carried by the radiation is nil. Therefore the charge too cannot be losing momentum. Thus we have the paradox of a radiating charge losing its kinetic energy but without a corresponding change in its momentum.

4. Synchrotron losses and the radiative life times

We first calculate the power losses in the GC frame $\mathcal{K}'$, where pitch angle is a constant ($\theta = \pi/2$) and thus the standard formulation should be applicable, and then using special relativistic transformations, convert them to the lab frame $\mathcal{K}$.

In the GC frame $\mathcal{K}'$, there is no motion along the z direction and the charge moves in a circle in the x-y plane. The velocity β' of the charge as well as the force F' due to radiation losses are perpendicular to the z'-axis in frame $\mathcal{K}'$ and there is hardly any ambiguity about that. From the 4-force transformation [9, 10] to the lab frame $\mathcal{K}$, with respect to which the GC frame $\mathcal{K}'$ is moving along the z direction with a velocity $\beta_{\|}$, we get,

$$F_{\|} = F'\gamma_{\|}\beta_{\|}\beta_{\perp} \ , \tag{5}$$

$$F_{\perp} = \frac{F'}{\gamma_{\|}} \ . \tag{6}$$

There is of course no acceleration component $\dot{\beta}_{\|}$ along the z-axis, even though a finite parallel force component $F_{\|}$ exists. From a relativistic transformation of acceleration [9] we can verify that there is no parallel component of acceleration in frame $\mathcal{K}$ if it is zero in frame $\mathcal{K}'$ (i.e., $\dot{\beta}_{\|} = 0$ if $\dot{\beta}'_{\|} = 0$). Actually in frame $\mathcal{K}$, a force component along z direction shows up solely because of a rate of change of γ due to $\dot{\beta}_{\perp}$, even though $\dot{\beta}_{\|} = 0$. It can be recalled that in special relativity, force and acceleration vectors are not always parallel, e.g., in a case where force is not parallel to the velocity vector, the acceleration need not be along the direction of the force. When the applied force is either parallel to or perpendicular to the velocity vector, it is only then that the acceleration is along the direction of force [9]. It has to be further kept in mind that the acceleration we are talking about here is not that due to the force by the magnetic field on the moving charge (which is perpendicular to the instantaneously velocity of the charge), but the acceleration (or rather a deceleration) caused on the charge due to the radiation reaction force. An alternative derivation of radiation losses and the pitch angle changes based on radiation reaction force is available in Singal [11].

In equation (4) $\sin\theta$ is a variable, but we can write this equation for the GC frame $\mathcal{K}'$, where pitch angle is always a constant ($\theta' = \pi/2$). Then we have,

$$\frac{\mathrm{d}\gamma'}{\mathrm{d}t'} = -\eta\beta'^2\gamma'^2 = -\eta(\gamma'^2 - 1)\ . \tag{7}$$

Equation (7) has a solution,

$$\tanh^{-1}\frac{1}{\gamma'} = \eta t' + a\ . \tag{8}$$

Let γ'_o be the initial energy at $t' = 0$ in frame $\mathcal{K}'$, then $1/\gamma'_\mathrm{o} = \tanh(a)$ and at time $t' = \tau'$ we have,

$$\tanh^{-1}\frac{1}{\gamma'} = \tanh^{-1}\frac{1}{\gamma'_\mathrm{o}} + \eta\tau'\ . \tag{9}$$

which complies with the expectations that as $\tau' \rightarrow \infty$, $\gamma' \rightarrow 1$.

Now a transformation between $\mathcal{K}'$ and $\mathcal{K}$ gives $\gamma'\gamma_{\|} = \gamma$ and $\gamma'\beta' = \gamma\beta_\perp$ or $\beta' = \gamma_{\|}\beta_\perp$ [5]. Also we have $\mathrm{d}t/\mathrm{d}t' = \gamma_{\|}$ or $\tau = \tau'\gamma_{\|}$. For the transformation of acceleration we then get $\dot\beta' = \gamma_{\|}^2\dot\beta_\perp$ with $\dot\beta_{\|} = \dot\beta'_{\|}/\gamma_{\|}^3 = 0$.

Equation (9) can then be transformed in terms of quantities expresses in the lab frame $\mathcal{K}$,

$$\tanh^{-1}\frac{\gamma_{\|}}{\gamma} = \tanh^{-1}\frac{\gamma_{\|}}{\gamma_\mathrm{o}} + \frac{\eta\tau}{\gamma_{\|}}\ . \tag{10}$$

This is a general solution for all values of γ. We can rewrite it as,

$$\gamma = \gamma_{\|}\ \frac{\gamma_\mathrm{o} + \gamma_{\|}\tanh(\eta\tau/\gamma_{\|})}{\gamma_\mathrm{o}\tanh(\eta\tau/\gamma_{\|}) + \gamma_{\|}}\ . \tag{11}$$

For an initially ultra relativistic charge ($\gamma_0 \gg 1, \beta_0 \approx 1$), we have $1/\gamma_{\|} = \surd(1 - \beta_0^2\cos^2\theta_0) \approx \sin\theta_0$. That also implies that (except for initially small pitch angle cases) $\sin\theta_0 \gg 1/\gamma_0$ or $\gamma_{\|}/\gamma_0 \ll 1$, and from equation (10) we could write,

$$\tanh^{-1}\frac{1}{\gamma\sin\theta_0} = \eta\tau\sin\theta_0\ . \tag{12}$$

This implies that for $\tau = \gamma_{\|}/\eta \approx 1/(\eta\sin\theta_0)$, we have $\gamma \approx 1.3/\sin\theta_0$. Thus even if an electron had started with an almost infinite energy, it loses most of its kinetic energy in a time interval of the order of $1/\eta$, reducing to perhaps a mildly relativistic status (for not too small an initial pitch angle). For instance let us consider $\gamma_0 = 10^3$ and $\theta_0 = \pi/4$, then $\gamma_{\|} \approx 1/\sin\theta_0 = \surd 2$, then from equation (10) or equation (12) we get for $\tau = 1/\eta$, $\gamma = 2.3$. In another example, taking $\gamma_0 = 10^4$ and $\theta_0 = \pi/3$, for $\tau = 1/\eta$ we get $\gamma_{\|} \approx 1/\sin\theta_0 = 2/\surd 3$ and $\gamma = 1.7$. Thus $1/\eta$ represents the characteristic decay time of synchrotron electrons over which they turn from ultra relativistic into mildly relativistic ones.

5. Reduction in the pitch angle

Equation (7) can be also written as,

$$\gamma'^3\dot\beta'\beta' = -\eta\beta'^2\gamma'^2, \tag{13}$$

or

$$\frac{\dot\beta'}{\beta'} = \frac{-\eta}{\gamma'}\ . \tag{14}$$

Then transforming to the lab frame $\mathcal{K}$ we have,

$$\frac{\dot{\beta}_\perp}{\beta_\perp} = \frac{-\eta}{\gamma} \,, \tag{15}$$

Both β and θ in $\beta_\perp = \beta \sin\theta$ are functions of time. Therefore we can rewrite equation (15) as,

$$\beta \cos\theta \frac{\mathrm{d}\theta}{\mathrm{d}t} + \dot{\beta} \sin\theta = \frac{-\eta\beta\sin\theta}{\gamma} \,. \tag{16}$$

Also from $\dot{\beta}_\| = 0$ we get,

$$\beta \sin\theta \frac{\mathrm{d}\theta}{\mathrm{d}t} = \dot{\beta}\cos\theta \,. \tag{17}$$

Eliminating $\dot{\beta}$ from equations (16) and (17), we get,

$$\frac{\mathrm{d}\theta}{\mathrm{d}t} = \frac{-\eta \sin\theta\cos\theta}{\gamma} = \frac{-\eta\sin 2\theta}{2\gamma} \,. \tag{18}$$

This is the relation for the rate of change of the pitch angle of a charge undergoing synchrotron radiative losses. The negative sign implies that the pitch angle decreases with time and the velocity vector gets increasingly aligned with the magnetic field. The rate of alignment is very slow for low pitch angles ($\theta \approx 0$) as well as for high pitch angles ($\theta \approx \pi/2$), and the highest rate of change of the pitch angle is for $\theta = \pi/4$.

With the help of equation (10), we can integrate equation (18),

$$\int_{\theta_0}^{\theta} \frac{\mathrm{d}\theta}{\sin\theta\cos\theta} = -\int_0^{\tau} \frac{\eta \mathrm{d}t}{\gamma_\|} \tanh\left(\frac{\eta t}{\gamma_\|} + a\right) \,, \tag{19}$$

where $a = \tanh^{-1}(\gamma_\|/\gamma_\mathrm{o})$. This gives us,

$$\ln\frac{\tan\theta}{\tan\theta_0} = \ln\frac{\cosh(a)}{\cosh\left(\frac{\eta\tau}{\gamma_\|} + a\right)} \,. \tag{20}$$

or

$$\tan\theta = \frac{\tan\theta_0}{\cosh\left(\frac{\eta\tau}{\gamma_\|}\right) + \frac{\gamma_\|}{\gamma_\mathrm{o}}\sinh\left(\frac{\eta\tau}{\gamma_\|}\right)} \,. \tag{21}$$

In equation (21), $\theta < \theta_0$, because pitch angle always reduces with time. There are many notable points. If $\theta_0 = \pi/2$, then $\theta = \pi/2$ also, which is because if the pitch angle is $\pi/2$, then the radiating electron always moves in a circular path in the plane perpendicular to the magnetic field. And if $\theta_0 = 0$, then $\theta = 0$ too as there is no more reduction in the pitch angle. For any $0 < \theta_0 < \pi/2$, $\theta \to 0$ as $\tau \to \infty$. For large γ_0 values,

$$\tan\theta = \frac{\tan\theta_0}{\cosh\left(\eta\tau\sin\theta_0\right)} \,, \tag{22}$$

which can be used to estimate change in pitch angle with time. For example for say, $\theta_0 = \pi/3$, and $\theta = \pi/6$, $\cosh(\eta\tau\sin\theta_0) = 3$, which gives $\tau \approx 2/\eta$ for this change in the pitch angle. Thus there are appreciable pitch angle changes in time $\tau \sim 1/\eta$ (except for in the vicinity of very small pitch angles).

All charges of a given energy and pitch angles, directed towards the observer in a narrow angle $1/\gamma$ around the line of sight not only lose energy but will also get shifted outside the angle $1/\gamma$ around the line of sight towards the observer, in a time $\tau \sim 1/\eta$. Thus in a mono-energetic and a narrow pitch angle distribution, the pitch angle changes might be quite relevant. But it may be of less importance when there is a wide angular (isotropic!) distribution of pitch angles.

References

[1] N. S. Kardashev, Sov. Astr. - AJ **6**, 317 (1962).
[2] A. G. Pacholczyk, *Radio astrophysics*, Freeman, San Francisco (1970).
[3] G. B. Rybicki & A. P. Lightman, *Radiative processes in astrophysics*, Wiley, New York (1979).
[4] J. D. Jackson, *Classical electrodynamics*, 2nd ed., Wiley, New York (1975).
[5] D. B. Melrose, ApL **8**, 35 (1971).
[6] M. S. Longair, *High energy astrophysics*, Cambridge Univ. Press, Cambridge (2011).
[7] W. K. H. Panofsky, M. Phillips, *Classical electricity and magnetism*, 2nd ed., Addison-Wesley, Massachusetts (1962).
[8] D. J. Griffiths, *Introduction to electrodynamics*, 3rd ed., Prentice, New Jersey (1999).
[9] R. C. Tolman, *Relativity thermodynamics and cosmology*, Clarendon, Oxford (1934).
[10] R. A. Mould, *Basic relativity*, Springer, New York (1994).
[11] A. K. Singal, MNRAS., DOI: 10.1093/mnras/stw349, in press (2016) arxiv: 1507.08580v3.

2MASS analytical study of galactic star cluster Teutsch 40

D. Bisht[a], R. K. S. Yadav[b] and A. K. Durgapal[a]

(a) Department of Physics, DSB Campus, Kumaun University, Nainital-263002, Uttarakhand, India
(b) Aryabhatta Research Institute of Observational Sciences, Manora peak, Nainital-263002, Uttarakhand, India

Presenter: Devendra Bisht (*devendrabisht297@gmail.com*); A&A.2, Oral, CICAHEP15.183

The astrophysical parameters of poorly studied open star cluster Teutsch 40 are estimated using the *2MASS JHK*s data. The stellar density distribution, colour-magnitude and colour-colour diagram are used to estimate the geometrical structure parameters (cluster center, cluster radius, core radius, the distance from the Sun, galactocentric distance and the distance from the galactic plane).

1. Introduction

Open clusters (OCs) are gravitationally bound group of stars situated at the same distance from the Sun and have same age. They are very important tools to study the star formation and evolution in the Galactic disk. Fundamental parameters of the clusters, e.g. distance, reddening, age and metallicity are very essential to study the Galactic disk. Ref. [1] provided statistically significant samples of star clusters of known distance, age and metallicity.

In the present study, we aim to estimate the basic parameters of open cluster Teutsch 40 using near-IR photometric data taken from Two Micron All Sky Survey (*2MASS*). Teutsch 40 ($\alpha_{2000} = 19^h\ 29^m\ 17^s$ (292°.31), $\delta_{2000} = 23°\ 18'\ 18''$ (23°.35); $l = 57°.85$, $b = 2°.64$) is an old age open star cluster. This cluster is located in first galactic quadrant and towards anticentre direction. In the literature this cluster is not well studied.

This paper is organized as follows. Section 2 presents the description of data used. Section 3 described the derivation of fundamental parameters of the cluster. Finally, the conclusion are drawn in Section 4.

2. Data used

The astrophysical parameters of the cluster Teutsch 40 are estimated using the *2MASS* Point Source catalouge [2]. The *2MASS* [3] uses two highly-automated 1.3m telescope (one at Mt. Hopkins, Arizona (AZ), USA and other at CTIO, Chile) with a 3-channel camera (256 × 256 array of HgCdTe detectors in each channel). This *2MASS* photometric catalouge provides J $(1.25\ \mu m)$, H $(1.65\ \mu m)$ and Ks $(2.17\ \mu m)$ band photometry for millions of galaxies and nearly a half-billion stars [4]. The sensitivity of *2MASS* catalouge is 15.8 mag for J, 15.1 mag for H and 14.3 mag for Ks band at S/N=10. The photometric data are taken with in the radius 20 arcmin from the cluster center.

The errors given in *2MASS* catalouge for J, H and Ks band are plotted against J magnitudes in Fig. 1. This figure shows that the mean error in J, H and Ks band is $\leq$ 0.04 at $J \sim$ 13.0 mag. The errors become $\sim$ 0.08 at $J \sim$ 15 mag.

3. Derivation of fundamental parameters

3.1 Center estimation

The centre of any cluster can be roughly estimated by eye, but to determine the centre coordinates more precisely, we applied the star count method to the whole area of cluster. To estimate the cluster centre, we plotted the histogram in Right ascension (RA) and declination (DEC) for cluster Teutsch 40 as shown in Fig. 2. The purpose of this counting process is to determine the maximum central density of the cluster. The Gaussian curve-fitting is applied to the profiles of star counts in RA and DEC respectively. The cluster centre is assumed as the location of the maximum stellar density in the clusters area. In this way we found the coordinates of center as $\alpha = 292.32 \pm 0.01$ deg and $\delta = 23.27 \pm 0.01$ deg. These coordinates are very close to the value given in the literature for the cluster Teutsch 40.

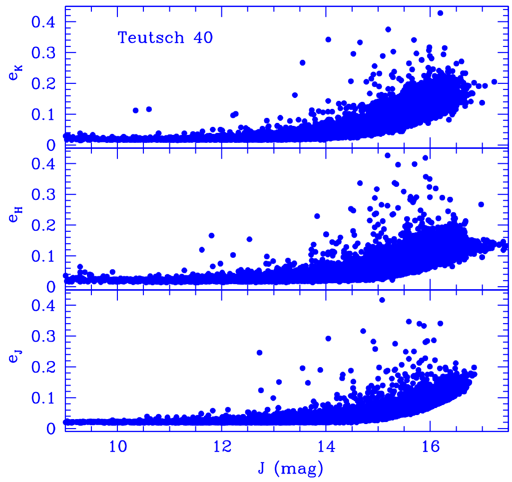

Figure 1. Photometric errors in J, H and K magnitudes against J magnitude.

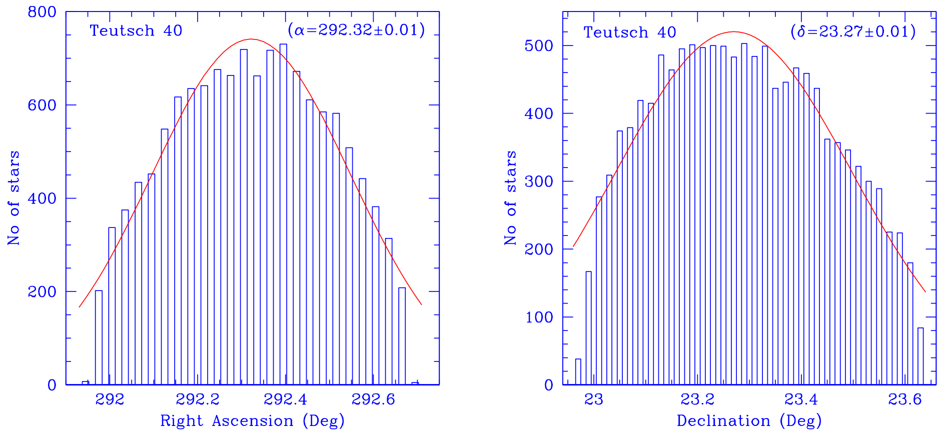

Figure 2. Profiles of stellar counts across the cluster Teutsch 40. The Gaussian fits have been applied. The center of symmetry about the peaks of Right Ascension and Declination is taken to be the position of the cluster center.

3.2 Radial density profile

To estimate the cluster extent, we established the radial density profile for cluster Teutsch 40. The observed area of this cluster is divided into many concentric circles. We have used cluster center which is estimated by us in the previous section. The number density, R_i, in the i^{th} zone is calculated by using the formula R_i = $\frac{N_i}{A_i}$. Where N_i is the number of stars and A_i is the area of the i^{th} zone. Fig. 3 represents RDP for the cluster Teutsch 40. The background density level with errors is also shown with dotted lines. RDP flattens at $r \sim 2.0$ arcmin and begin to merge with the background stellar density as seen in Fig. 3. Therefor we consider 2.0 arcmin as cluster extent. A smooth continuous line represents fitted [5] profile:

$$f(r) = f_b + \frac{f_0}{1 + (r/r_c)^2},$$

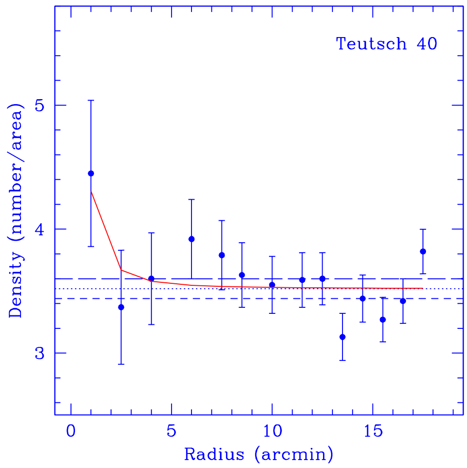

Figure 3. Surface density distribution of the cluster Teutsch 40. Errors are determined from sampling statistics ($=\frac{1}{\sqrt{N}}$, where N is the number of stars used in the density estimation at that point). The smooth line represent the fitted profile whereas dotted line shows the background density level. Long and short dash lines represent the errors in background density.

where f_0 is the central density, r_c is core radius and f_b is the background density. By fitting the King model to the cluster density profile, we estimated the peak stellar density (f_0), core-radius (r_c) and background density (f_b) as 7.74 ± 0.8 stars/arcmin^2, 0.5 ± 0.1 arcmin and 3.52 ± 0.08 stars/arcmin^2.

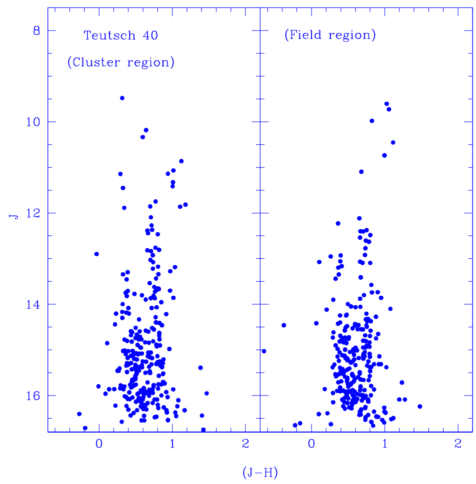

Figure 4. The $J, (J - H)$ colour-magnitude diagram for the cluster Teutsch 40 using stars with in cluster radius. Stars outside the cluster radius are also plotted as field region stars.

3.3 Colour-magnitude diagram

Colour-magnitude diagram plays most important role for the estimation of age and distance of open star clusters. The $J, (J - H)$ CMDs of the cluster and field region for the cluster Teutsch 40 is shown in Fig. 4. Stars falling with in the cluster radius is considered as cluster region stars while those outside the radius are assumed as field region stars. To get the clear sequence in the CMD, we consider the stars within cluster radius. The area of the

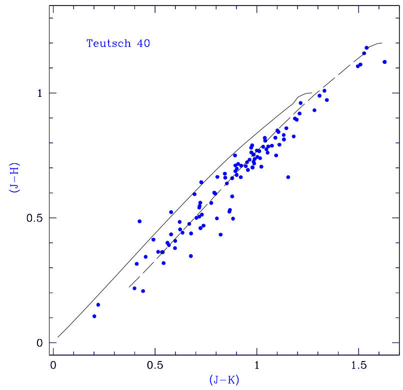

Figure 5. The plot of $(J-H)$ versus $(J-K)$ colour-colour diagram of the cluster Teutsch 40 using stars within the cluster radius. The solid line is the ZAMS taken from [6]. The dotted lines is the ZAMS shifted by the values given in the text.

field region was kept equal to area of the cluster region. The CMDs shown in Fig. 4 exhibits a poor main-sequence (MS) extending from $J \sim 13.8$ mag, where the turn off point is located down to $J \sim 15.5$ mag. The main sequence fainter than ~ 15.5 mag is more scattered and heavily contaminated by field stars. CMD of the cluster Teutsch 40 shows a poorly populated old age open star cluster.

3.4 Colour-colour diagram

Reddening is one of the very useful parameter for the reliable estimation of distance and age of the cluster. To estimate the reddening of the cluster Teutsch 40 we have plotted $(J-H)$ versus $(J-K)$ colour-colour diagram as shown in Fig. 5. Stars plotted in this figure are taken within the cluster radius. The Zero age main sequence (ZAMS) shown by the solid line is taken from [6]. The same ZAMS is shifted by $E(J-H) = 0.20 \pm 0.02$ mag & $E(J-K) = 0.37 \pm 0.04$ mag for Teutsch 40 and shown by dotted line. The ratio $E(J-H)/E(J-K) \sim 0.54 \pm 0.02$ for this cluster is in good agreement with the normal interstellar extinction value of 0.55 suggested by [7]. However, scattering is larger due to error in JHK data.

3.5 Age and distance estimation

In Fig. 6, we show the fitting of isochrones to $J/(J-H)$ and $J/(J-K)$ CMDs. The isochrones of different age (log (age) = 8.90, 9.00 and 9.10) and $Z = 0.019$ have been superimposed on the CMDs. The overall fit is good for log (age) = 9.00 (middle isochrone). The best fitted isochrone provides an age of 1 ± 0.2 Gyr. The distance modulus $m - M_k = 13.85$ mag provide a heliocentric distance 4.4 ± 0.5 kpc. The galactocentric distance is 11.72 kpc, which is determined by assuming 8.5 kpc as the distance of the Sun to the Galactic center. The Galactocentric coordinates are estimated as $X_\odot = 0.08$ kpc, $Y_\odot = 11.20$ kpc and $Z_\odot = 0.180$ kpc. The value of Z indicates that this object is above ~ 180 pc from the Galactic plane in the Galactic disc.

4. Conclusion

In the present work, we have studied the cluster Teutsch 40 using *2MASS JHK*s data. This cluster is very useful for studying the disc subsystem. The main findings of our analysis are given below:

- We estimated radius of the cluster Teutsch 40 as 2 arcmin, by using radial density profile.
- From the two colour $(J-H)$ versus $(J-K)$ diagram, we estimated $E(J-H) = 0.20 \pm 0.02$ mag and $E(J-K) = 0.37 \pm 0.04$ mag.

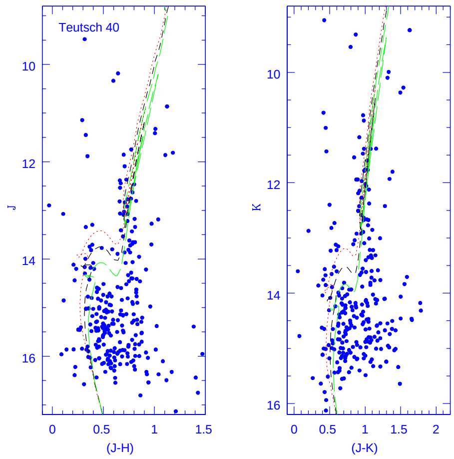

Figure 6. The J, $(J-H)$ and K, $(J-K)$ color-magnitude diagrams of the cluster Teutsch 40 using stars within cluster radius. The different lines are the different age isochrones taken from [8]. Three isochrones of different age (log (age) = 8.90, 9.00 and 9.10) of metallicity $Z = 0.019$ are shown in this figure.

- Distance and age to the cluster is determined as 4.4 ± 0.5 Kpc and 1 ± 0.2 Gyr respectively. These values are estimated by comparing the isochrones of $Z = 0.019$ given by [8].
- The value of Z indicates that cluster Teutsch 40 is above $\sim$ 180 pc from the Galactic plane in the Galactic disc.

5. Acknowledgment

This publication made use of data products from the Two Micron All Sky Survey (2MASS), a joint project of the University of Massachusetts and the Infrared Processing and Analysis Center/California Institute of Technology, funded by the National Aeronautics and Space Administration and the National Science Foundation.

References

[1] Gaburov E., Gieles. M, MNRAS, 391(1), 190-196, 2008.
[2] Cutri, R., et al. 2003, 2MASS All-Sky Catalogue of Point Sources, CDS/ADC Electronic Catalogues 2246.
[3] Skrutskie, M., Cutri, R., Stiening, R., et al. 2006, AJ, 131, 1163.
[4] Carpenter, J. M. 2001, AJ, 121, 2851.
[5] King, I, 1962, AJ, 67, 471.
[6] Caldwell, J, A. R., Cousins, A. W. J., Ahlers, C. C., Van Wamelen, P., Maritz, E. J., 1993, South African Astron. Observatory, Circ. No. 15.
[7] Cardelli, J. A., Clayton, G. C., Mathis, J. S., 1989, ApJ, 345, 245.
[8] Girardi L., Bressan A., Bertlli G., Chiosi C., 2000, A&AS, 141, 371.

Part IV
High Energy Physics (PS3)

Some observable parameters of Cherenkov photons in Extensive Air Showers of different primaries at various zenith angles

G. S. Das, P. Hazarika and U. D. Goswami
Department of Physics, Dibrugarh University, Dibrugarh-786004, Assam, India

Presenter: G. S. Das (*goureesdas@gmail.com*); HEP.6, Oral, CICAHEP15.40

We have studied the density and angular distributions of Cherenkov photons in extensive air showers initiated by γ-ray and proton primaries at different energies and at different zenith angles. The study of this kind is important to distinguish the γ-ray initiated showers from hadronic showers by understanding the nature of γ-ray and hadronic showers. In this work, we used CORSIKA 6.990 simulation package. For the high energy hadronic interaction part, QGSJET-II and EPOS hadronic interaction models are used whereas for low energy interaction FLUKA model is used. Here we are going to report the result of this work.

1. Introduction

For ground based detection of γ-rays in the range of few hundred GeV to few TeV, the Atmospheric Cherenkov Technique (ACT) is the most extensively used technique which is based on detection of Cherenkov photons emitted in the Extensive Air Showers (EASs) created during the process of interaction between the primary γ-rays and earths atmosphere [1]. It should be noted that, the sources which emit γ-rays also emit Cosmic Rays (CRs). As the CRs are mostly charged particles they got deflected by the intergalactic magnetic fields and hence they loose their directional property, whereas γ-rays being neutral, retain their direction of origin. So the detection of γ-rays can lead to the estimation of the locations of such astrophysical objects.

ACT, being an indirect process of γ-ray detection and due to the presence of huge CR background, a detailed Monte Carlo simulation studies of atmospheric Cherenkov photons have to be carried out for detection and proper estimation of their energy from the observational data of experiments based on ACT. Although both γ-ray and CR can generate EAS, the nature of two are different as the former is purely electromagnetic in nature whereas the later is a mixture of electromagnetic and hadronic cascades. Many studies have already been carried out on the density, arrival time and angular distributions of Cherenkov photons in EASs using available detailed simulation techniques [2, 3, 4, 5, 6, 7], however not many studies have been done on model dependent behaviour of density and angular distributions of Cherenkov photons initiated by γ-ray and hadronic particles incident at various zenith angles, particularly at high altitude observation levels. Consequently, in this work we have studied the angular and density distributions of Cherenkov photons at different energies and at different zenith angles on a high altitude observation level, using two different high energy hadronic interaction models, viz., QGSTJETII and EPOS with FLUKA low energy hadronic interaction model available in the CORSIKA simulation package [8].

CORSIKA is a detailed Monte Carlo simulation package to study the evolution and properties of extensive air showers in the atmosphere. This allows to simulate interactions and decays of nuclei, hadrons, muons, electrons and photons in the atmosphere up to energies of some 10^{20}eV. For the simulation of hadronic interactions, presently CORSIKA has the option of seven high energy hadronic interaction models and three low energy hadronic interaction models. It uses EGS4 code [9] for the simulation of electromagnetic component of the air shower [8]. This paper is organized as follows. In the section 2, we discuss briefly about the simulation process. The section 3 contains the analysis and results of the simulated data. The summary of the work with conclusion is put in the section 4.

2. Simulation of the Extensive Air Showers

The simulation of the Cherenkov photons in EASs is carried out by using the CORSIKA 6.990 simulation package. As mentioned earlier, we have used two high energy hadronic interaction models, viz., QGSJETII.3 and EPOS 1.99 with the low energy hadronic interaction model FLUKA to generate EASs for the monoenergetic γ-ray and proton primaries incident vertically as well as inclined at zenith angle 10^o, 20^o and 30^o. The QGSJETII and EPOS high energy hadronic interaction models are preferred because QGSJETII is the improved version of the model

QGSJET01 and EPOS is based on quantum mechanical multiple scattering approach based on partons and strings, which performed better compared to RHIC data [10]. By using QGSJETII-FLUKA and EPOS-FLUKA model combinations, the following numbers of showers were generated at different energies and at different zenith angles for the γ-ray and proton primaries as given in Table 1.

Table 1. Number of showers generated at different energies and at different zenith angles for different primaries using QGSJETII-FLUKA and EPOS-FLUKA model combinations.

Primary particle	Energy	Number of Showers
γ-ray	100 GeV	10000
	250 GeV	7000
	500 GeV	5000
	1 TeV	2000
	2 TeV	1000
Proton	250 GeV	10000
	500 GeV	8000
	1 TeV	5000
	2 TeV	2000
	5 TeV	800

The energies of the primaries selected for this work are the typical ACT energy range of respective primaries in terms of the equivalent number of Cherenkov photons yield. The altitude of HAGAR experiment at Hanle (longitude: 78^o $57'$ $51''$ E, latitude: 32^o $46'$ $46''$ N, altitude: 4270 m) is used as the observational level in the generation of these showers. The cores of the EASs is considered to be at the centre of the detector array. The detector geometry is set as a horizontal flat detector array, where there are 25 telescopes in each of the E–W direction and the N–S direction with a separation of 25 m in between two telescopes. The mirror area of each telescope is taken as 9 m^2. Details of the simulation parameters can be obtained in our earlier work in [7].

3. Analysis and results

The density of the Cherenkov photon is obtained by counting the numbers of photons incident on each detector for each of the shower, while the angular distribution of Cherenkov photons is obtained by counting the number of photons produced per angular bin with respect to the shower axis. For angular distribution the numbers of photons are then normalized to one photon ($\frac{1}{N}\frac{dN}{d\theta}$ (degree^{-1})) with averaged over azimuth. The analysis has been done on the ROOT software [11] platform by using C++ programs developed by us. The results of this work are discussed in the following subsections:

3.1 Cherenkov photon density

Fig. 1 shows the variation of average Cherenkov photon density ρ_{ch} as a function of core distance r (in meter) in the EASs initiated by the γ and proton primaries of various energies incident at zenith angles 0^o and 30^0. The hadronic interaction model combination used here is the EPOS-FLUKA. In Fig. 2 the density distributions for γ-ray and proton primaries have been plotted for fixed energies but for different zenith angles. It is seen that the density distribution has an exponential fall with increasing core distance for both the primaries at all energies [7] and at all zenith angles. It is clear that with increasing zenith angle, the ρ_{ch} decreases sufficiently upto a certain core distance depending upon the primary particle type and energy. This effect of zenith angle decreases with increasing energy of primary particle. For γ-ray primaries at energy 100 GeV, the characteristic hump is visible at a core distance of about 100 m.

3.2 Angular distribution

Fig. 3 shows the angular distributions of Cherenkov photons for γ-ray and proton primaries at different energies and incident at zenith angles 0^o and 30^o. It can be seen that for both γ-ray and proton primaries, the Cherenkov

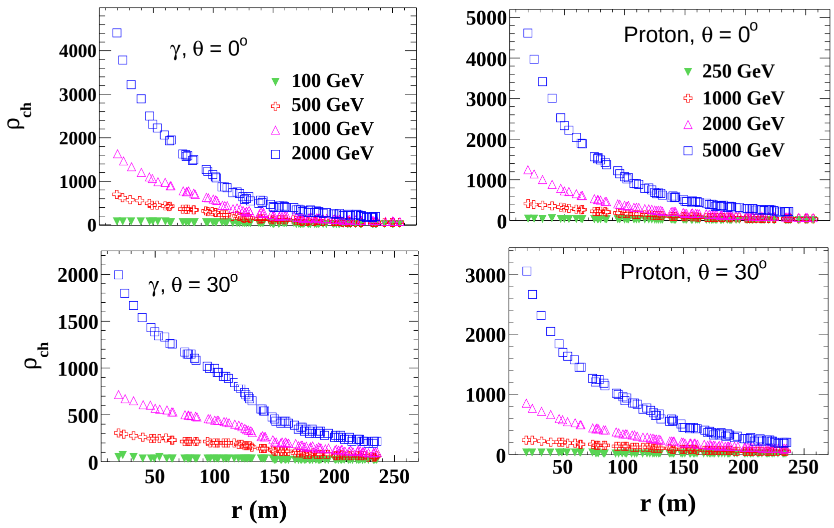

Figure 1. Density distributions of Cherenkov photons in EASs of γ-ray and proton primaries at different energies and incident at angles 0^o and 30^o.

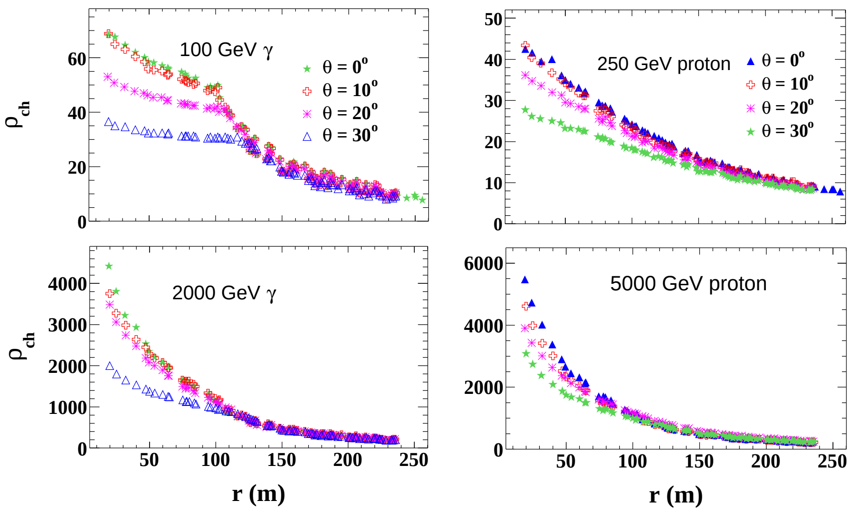

Figure 2. Density distributions of Cherenkov photons in EASs of γ-ray and proton primaries at two different energies incident at angles 0^o, 10^o, 20^o and 30^o.

photons are distributed on average within 1^0 to $30^o/40^o$ from the shower axis. Most of the photons are scattered within 1^o to 2^o from the shower axis after which there is a rapid fall in the number of particles scattered at larger angles. For each of the angle of incidence, the pattern has become flatter with increase in energy of the incident primary. Further, for larger value of the angle of incidence the distribution profile has become steeper as well as symmetric for all values of energy. For proton primaries, the distribution follows a rather linear fall than in comparison to the exponential fall for the γ-ray. Moreover, the distributions for the γ-ray at higher zenith angles are more symmetric than that for the proton primary.

3.3 Dependence on hadronic interaction model

Fig. 4 and 5 show the angular distributions of Cherenkov photons initiated by γ-ray of energy 100 GeV and 1000 GeV and proton primaries of energy 250 GeV and 2000 GeV respectively as obtained by using two hadronic

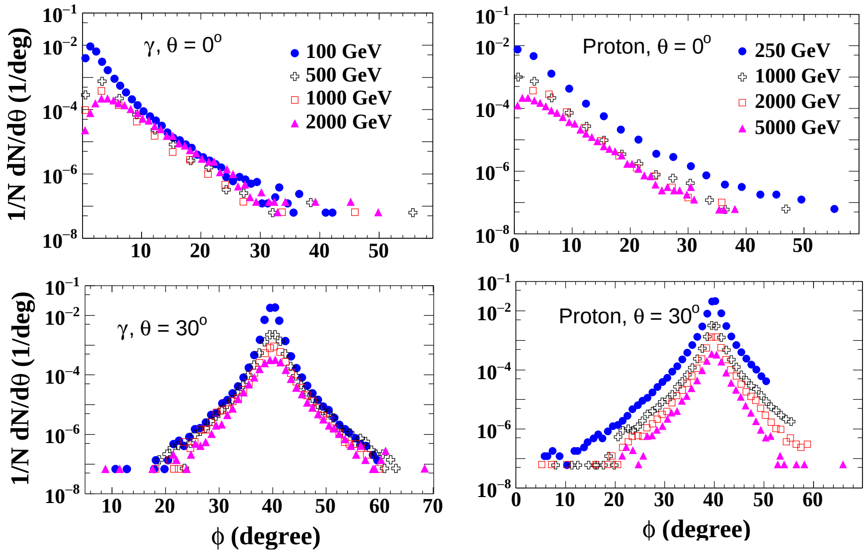

Figure 3. Angular distributions of Cherenkov photons in EASs of γ-ray and proton primaries at different energies incident at zenith angles 0^o and 30^o.

interaction model combinations viz. EPOS-FLUKA and QGSJETII-FLUKA for four different zenith angles under consideration. It is seen from the distributions that both the model combinations produce similar results except for the 250 GeV proton where the EPOS-FLUKA combination seems to have generated slightly higher numbers of Cherenkov photons than the QGSJETII-FLUKA model combinations.

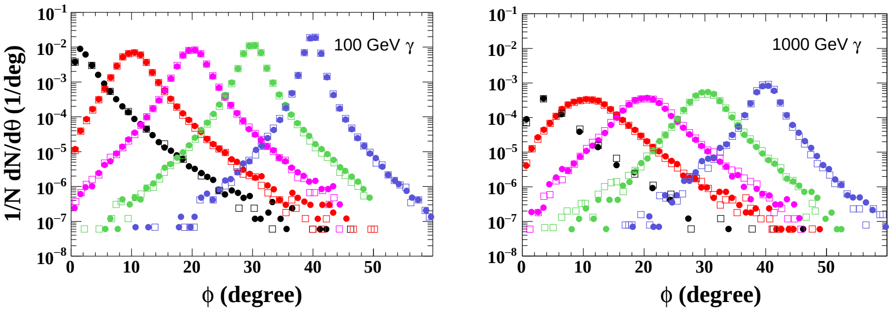

Figure 4. Angular distribution of Cherenkov photons initiated by γ-rays of energy 100 GeV and 1000 GeV incident at various zenith angles obtained by using EPOS-FLUKA and QGSJETII-FLUKA model combinations. In the respective plots, different coloured ● and □ indicate the EPOS-FLUKA and QGSJETII-FLUKA model combinations respectively. Plots with peaks from left to right represent the showers with zenith angles from 0^o to 30^o respectively.

4. Summary and conclusion

Considering the importance of effective gamma-hadron separation techniques and the lack of sufficient studies in this context, we have studied the density and the angular distributions of Cherenkov photons in EASs produced by γ-ray and proton primaries at different energies and at different zenith angles using the CORSIKA 6.990 simulation package [8]. The density of Cherenkov photons in EASs of both primaries is the increasing function of energy of primary particle, but the decreasing functions the zenith angle and the distance from the shower core. The decreasing effect of the zenith angles decreases with increasing energy of primary particle. Most of the Cherenkov photos are scattered within 1^o to 2^o with respect to the shower axis. Angular distributions of Cherenkov photons for γ-ray and proton primaries have slightly different patterns. A detail study on the difference in the patterns of

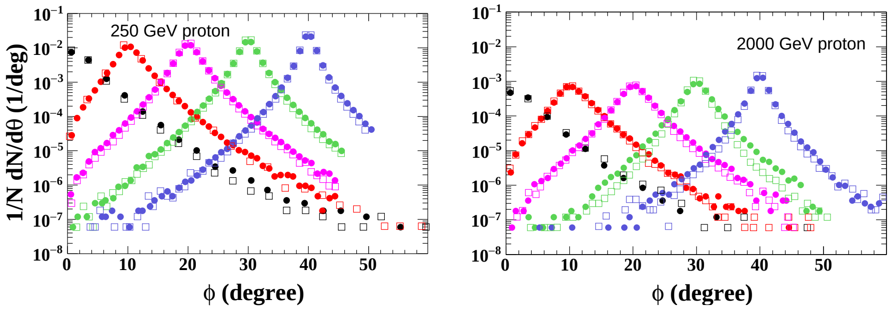

Figure 5. Angular distribution of Cherenkov photons initiated by proton primaries of energy 250 GeV and 2000 GeV incident at various zenith angles obtained by using EPOS-FLUKA and QGSJETII-FLUKA model combinations. In the respective plots, different coloured ● and □ indicate the EPOS-FLUKA and QGSJETII-FLUKA model combinations respectively. Plots with peaks from left to right represent the showers with zenith angles from 0^o to 30^o respectively.

distributions of Cherenkov photons obtained from EASs of γ-ray and proton primaries may be useful for distinguishing the γ-rays from the CR background. The angular distributions of Cherenkov photons are found to be model independent for both γ-ray and proton primaries in the range of 100 GeV to 100 TeV.

References

[1] René A. Ong, Phys. Reports **305**, 93 (1998); C. M. Hoffman and C. Sinnis, Rev. Mod. Phys. **71**, 897 (1999); T. C. Weekes, astroph/0811.1197v1 (2009); P. N. Bhat, Bull. Astr. Soc. India **30**, 135 (2002); B. S. Acharya, 29th ICRC, **10**, 271 (2005).

[2] H. M. Bardan, T. C. Weekes, Astropart. Phys. **7**, 307 (1997); Herve Cabot et al., Astropart. Phys. **9**, 269 (1998).

[3] V. R. Chitnis, P. N. Bhatt, Astropart. Phys. **12**, 45 (1999).

[4] A. M. Hillas, J. Phys. G: Nucl. Phys.**8**, 1461 (1982).

[5] S. Lafebre, R. Engel, H. Flacke, J. Horandel, T. Huege, J. Kuijpers, R. Ulrich, Astropart. Phys.**31**, 243 (2009).

[6] F. Nerling, J. Blumer, R. Engel, M. Risse, Astropart. Phys. **24**, 421 (2006).

[7] P. Hazarika, U. D. Goswami, V. R. Chitnis, B. S. Acharya, G. S. Das, B. B. Singh, R. Britto, Astropar. Phys. **68**, 16 (2015) [arXiv:1404.2068].

[8] J. Knapp, D. Heck, EAS Simulation with CORSIKA V 6990: A User's Guide (1998); D. Heck et al., Report **FZKA 6019** (1998), Forschungszentrum Karlsruhe; http://wwwik.fzk.de/corsika/physicsdescription/corsika phys.html

[9] W. R. Nelson, H. Hirayamal, D. W. O. Rogers, The EGS4 Code System, SLAC Report 265 (1985).

[10] T. Pierog, K. Werner, Nucl. Phys. Proc. Suppl. **196**, 102 (2009) [arXiv:0905.1198].

[11] http://root.cern.ch

A singularity free self-similar model of proton at small *x* and analysis of quarks and gluons momentum fraction

Baishali Saikia[a] and D. K. Choudhury[a,b]

(a) Department of Physics, Gauhati University, Guwahati-781014, Assam, India
(b) Physics Academy of North-East, Guwahati-781014, Assam, India

Presenter: Baishali Saikia (*baishalipiks@gmail.com*); HEP.3, Poster, CICAHEP15.47

In this paper we make reanalysis of a self-similarity based model of the proton structure function at small Bjorken *x* pursued in recent years. The additional assumption is that it should be singularity free in the entire kinematic range $0 < x < 1$. Our analysis indicates that the model is valid in a more restrictive range of Q^2. We also report an analysis of momentum fractions carried by quarks and gluons in the model.

1. Introduction

The idea of self-similarity in the structure of proton received attention in 2002 when Lastovicka [1] proposed a relevant formalism and a functional form of the structure function $F_2(x, Q^2)$ at small *x*. One of the limitations of the phenomenological analysis of Ref [1] is that it has a singularity at $x \sim 0.019$ which is well within the kinematical range of validity $0 < x < 1$. In the present report, we therefore make a reanalysis of the model [1], demanding it to be singularity free in the entire *x*-range of $0 < x < 1$. To that end we will use the more recently compiled HERA data [2]. We also use momentum sum rule [3] to compute the fractions of momentum carried by quarks and gluons in such a model.

2. Formalism

2.1 Proton Structure Function based on self-similarity

The self-similarity based model of the proton structure function of Ref. [1] is based on Transverse Momentum Dependent (TMD) Parton Distribution Function (PDF) $f_i(x, k_t^2)$. Here k_t^2 is the parton transverse momentum squared. Choosing the magnification factors $\left(\frac{1}{x}\right)$ and $\left(1 + \frac{k_t^2}{k_{0t}^2}\right)$, it can be written as [1, 12]

$$\log[M^2 . f_i(x, k_t^2)] = D_1 . \log\frac{1}{x} . \log\left(1 + \frac{k_t^2}{k_{0t}^2}\right) + D_2 . \log\frac{1}{x} + D_3 . \log\left(1 + \frac{k_t^2}{k_{0t}^2}\right) + D_0^i, \tag{1}$$

where *i* denotes a quark flavor. Here $D_1,\ D_2,\ D_3$ are the three flavor independent model parameters, while D_0^i is the only flavor dependent normalization constant. M^2 (= 1 GeV^2) is introduced to make PDF $q_i(x, Q^2)$as defined below [in equation (2)] dimensionless. The integrated quark densities then defined as

$$q_i(x, Q^2) = \int_0^{Q^2} f_i(x, k_t^2) dk_t^2. \tag{2}$$

As a result, the following analytical parametrization of a quark density is obtained by using equation (2) [8]:

$$q_i(x, Q^2) = e^{D_0^i} f(x, Q^2), \tag{3}$$

where

$$f(x, Q^2) = \frac{Q_0^2\, x^{-D_2}}{M^2\left(1 + D_3 + D_1 \log\left(\frac{1}{x}\right)\right)} \left(\left(\frac{1}{x}\right)^{D_1 \log\left(1 + \frac{Q^2}{Q_0^2}\right)} \left(1 + \frac{Q^2}{Q_0^2}\right)^{D_3 + 1} - 1\right) \tag{4}$$

is flavor independent. Using equation (3) in the usual definition of the structure function $F_2(x, Q^2)$, one can get

$$F_2(x, Q^2) = x \sum_i e_i^2 \left(q_i(x, Q^2) + \bar{q}_i(x, Q^2)\right) \tag{5}$$

or it can be written as

$$F_2(x,Q^2) = e^{D_0} x f(x,Q^2), \tag{6}$$

where

$$e^{D_0} = \sum_{i=1}^{n_f} e_i^2 \left(e^{D_0^i} + e^{\bar{D}_0^i}\right) \tag{7}$$

involves both quarks and anti-quarks. From HERA data [4, 5], equation (6) was fitted in Ref. [1] with

$$\begin{aligned} D_0 &= 0.339 \pm 0.145, \\ D_1 &= 0.073 \pm 0.001, \\ D_2 &= 1.013 \pm 0.01, \\ D_3 &= -1.287 \pm 0.01, \\ Q_0^2 &= 0.062 \pm 0.01 \text{ GeV}^2 \end{aligned} \tag{8}$$

in the kinematical region,

$$\begin{aligned} 6.2 \times 10^{-7} \leq x \leq 10^{-2}, \\ 0.045 \leq Q^2 \leq 120 \text{ GeV}^2. \end{aligned} \tag{9}$$

3. Limitations of Lastovicka Model

The above phenomenological analysis has been two inherent limitations:

First, the parameter D_3 is negative contrary to the expectation of positivity of fractal dimension [6]. Secondly, due to its negative value, equation (5) develops a singularity at $x \sim 0.019$ as it satisfies the condition $1 + D_3 + D_1 \log \frac{1}{x} = 0$ contrary to the physically viable form of structure function.

To overcome these limitations we make the model singularity free under the condition that D_1, D_2 and D_3 must be positive. Redefining the model parameters D_js by D_j's of equation (4) in the present phenomenological analysis we get the structure function as

$$F_2'(x,Q^2) = \frac{e^{D_0'}\, Q_0'^2\, x^{-D_2'+1}}{M^2\left(1 + D_3' + D_1' \log \frac{1}{x}\right)} \left(\left(\frac{1}{x}\right)^{D_1' \log\left(1+\frac{Q^2}{Q_0'^2}\right)} \left(1 + \frac{Q^2}{Q_0'^2}\right)^{D_3'+1} - 1 \right). \tag{10}$$

4. Results

4.1 Analysis of singularity free model

To determine the model parameters $\left(D_0', D_1', D_2', D_3', Q_0'^2\right)$ we have used recently compiled HERA data [2] instead of earlier data [4, 5] used in Ref. [1]. Following this procedure of Ref. [1], we make χ^2 analysis of the data and obtained the more restrictive range of Q^2 and x : $0.85 \leq Q^2 \leq 10$ GeV^2 and $2 \times 10^{-5} \leq x \leq 0.02$ receptively with the fitted parameters given below:

$$\begin{aligned} D_0' &= -2.971 \pm 0.409, \\ D_1' &= 0.065 \pm 0.0003, \\ D_2' &= 1.021 \pm 0.004, \\ D_3' &= 0.0003 \pm 0.0001, \\ Q_0'^2 &= 0.20 \pm 0.0008 \text{ GeV}^2. \end{aligned} \tag{11}$$

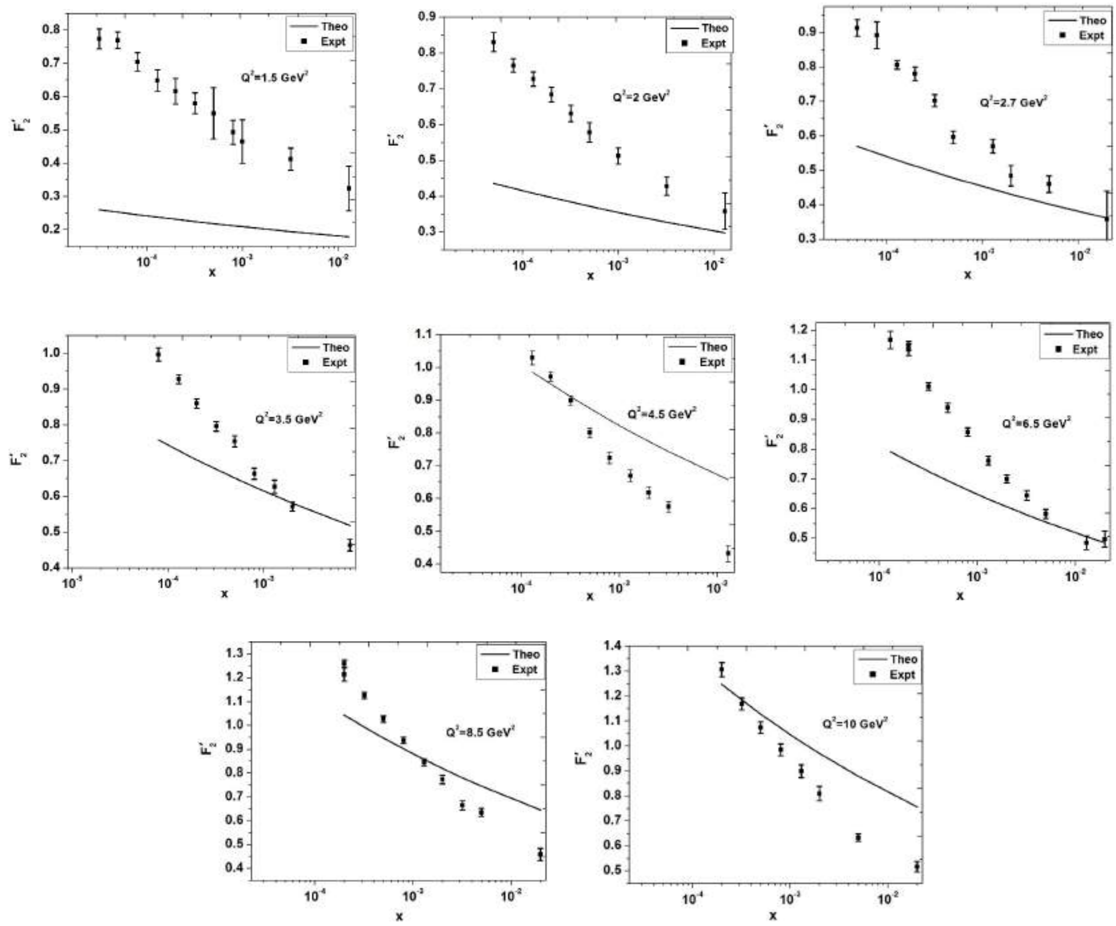

Figure 1: Comparison of the present model of structure function F_2' as a function of x in bins of Q^2 with measured data of F_2 from recently compiled HERA data [2].

5. Momentum sum rule

The momentum sum rule [3, 7, 8] is given as

$$\int_0^1 x \sum \left(q_i(x,Q^2) + \bar{q}_i(x,Q^2)\right) dx + \int_0^1 G(x,Q^2)\, dx = 1, \tag{12}$$

where

$$G(x,Q^2) = xg(x,Q^2) \tag{13}$$

and $g(x,Q^2)$ is the gluon number density. It can be converted [8] into an inequality if the information about quarks and gluons is available only in a limited range of x, say $x_a \leq x \leq x_b$ i.e.

$$\int_{x_a}^{x_b} x \sum \left(q_i(x,Q^2) + \bar{q}_i(x,Q^2)\right) dx + \int_{x_a}^{x_b} G(x,Q^2)\, dx \ \leq 1. \tag{14}$$

This yields the respective information when the momentum fractions carried by small x quarks and gluons in $x_a < x < x_b$ to be

$$\langle \hat{x} \rangle_q = \int_{x_a}^{x_b} x \sum \left(q_i(x,Q^2) + \bar{q}_i(x,Q^2)\right) dx \tag{15}$$

and

$$\langle \hat{x} \rangle_g = \int_{x_a}^{x_b} G(x,Q^2)\, dx \ \leq 1 - \langle \hat{x} \rangle_q. \tag{16}$$

Note that equation (16) yields only the upper limit of the fractional momentum carried by the gluons in the regime $x_a < x < x_b$. Equations (12)-(16) show that the momentum fraction needs information about the parton distribution of the proton within the model. In terms of structure function the momentum sum rule inequality is

$$\int_{x_a}^{x_b} \left\{aF_2(x,Q^2) + G(x,Q^2)\right\} dx \;\leq 1. \tag{17}$$

So, we can express the momentum fraction carried by quarks by taking the structure function of equation (10) in a limited range of $x_a \leq x \leq x_b$ as

$$\langle \hat{x} \rangle_q = \int_{x_a}^{x_b} aF_2(x,Q^2)dx, \tag{18}$$

where $a = \frac{e^{\bar{D}_0}}{e^{D_0}}$ is Q^2-independent parameter determined from data [9], $a = 3.1418$, using the fractionally charged quarks.

6. Numerical Results

In Table 2 we record the numerical values of $\langle \hat{x} \rangle_q$ of equation (18) for a few representative values of Q^2 which are well within the kinematical range. For completeness we have taken a few points beyond its validity upto Q^2 = 120 GeV^2 which was earlier cut off of Ref. [1]. We have not taken the analytical approach of calculating $\langle \hat{x} \rangle_q$ of Ref. [8] because our recent analysis [10] has shown that results are not convergent, rather oscillating. Therefore we use equation (18) directly to calculate the momentum fraction numerically.

Table 1: Numerical values of $\langle \hat{x} \rangle_q$ for different Q^2

.

Q^2(GeV^2)	$\langle \hat{x} \rangle_q$
0.85	3.5335×10^{-4}
2	9.0482×10^{-3}
4	1.9533×10^{-2}
5	2.5008×10^{-2}
8	4.2632×10^{-2}
10	5.4901×10^{-2}
20	1.2105×10^{-1}
60	4.2078×10^{-1}
80	5.8450×10^{-1}
120	9.3236×10^{-1}

7. Conclusion

In the present report we have made a reanalysis of the structure function $F_2(x,Q^2)$ based on self-similarity using the more recently compiled HERA data [2]. The present study is based on the notion that a physically viable model of proton should be finite in the x-range $0 < x < 1$, hence singularity free. It also conforms to the expectation that "fractal dimension" associated with self-similarity are invariably positive definite. However our analysis indicates that the range of validity of the present version of the model becomes lower in Q^2, $0.85 < Q^2 < 10$ GeV^2 instead of $0.045 < Q^2 < 120$ GeV^2 of Ref. [1]. It indicates that the present version of singularity free model of proton can explain the data only for low Q^2 and low x. From Table 1 we see as Q^2 increases the fraction of momentum carried by quarks increases. To illustrate that point we have taken a few representative values of Q^2 = 20, 60, 80, 120 GeV^2 . It implies that the present pattern does not conform to the usual expectation of QCD [11] which states that $\langle x \rangle_q$ (rather than $\langle \hat{x} \rangle_q$) decreases as Q^2 increases.

Let us now conclude with the comment regarding the limitations of the present model. It is basically a parametrization based on self-similarity for Transverse Momentum Dependent Parton Distribution Function (TMDPDF) equation (1) that is related to PDF [equation (3)]. So the proper choice of TMD and hence the magnification factors are very essential in such study [12, 13]. Further work is necessary to improve the present method of self-similarity based parametrization of TMD and PDF such that the models can accommodate a large range of x and Q^2 and possibly conforms to QCD expectations. Such work is currently under progress.

The model can be further improved by changing the magnification factor $\frac{1}{x}$ to $\left(\frac{1}{x}-1\right)$ accommodate large x behavior as in suggested in Ref. [12]. We will then be able to compare the self-similarity based PDF with the standard PDF [14]. Such possibility is also currently under study.

8. Acknowledgement

Baishali Saikia acknowledges the UGC-RFSMS for financial support. One of the authors (DKC) acknowledges the Rudolf Peirels, Center of Theoretical Physics, University of Oxford. He thanks Professor Subir Sarkar and Professor Amanda Cooper-Sarkar for healthful discussions where the final version of the work is completed.

References

[1] T. Lastovicka, Euro. Phys. J. **C24**, 529 (2002) [hep-ph/0203260].
[2] H1 and ZEUS collaborations JHEP **01**, 109 (2010).
[3] F. E. Close, *An introduction to quarks and partons* (Academic Press 1979), pp 233.
[4] H1:C Adloff et. al, Euro. Phys. J. **C21**, 33 (2001) [hep-ex/0012053].
[5] ZEUS: J Breitweg et. al, Phys. Lett. **B 487**, 53 (2000) [hep-ex/0005018].
[6] D. K. Choudhury and Rupjyoti Gogoi, hep-ph/0310260, hep-ph/0503047.
[7] A. Jahan and D. K. Choudhury, Mod. Phys. Lett. **A27**, 1250193 (2012) [hep-ph/1304.6882].
[8] A. Jahan and D. K. Choudhury, Mod. Phys. Lett. A28 1350056 (2013) [hep-ph/1306.1891].
[9] T. Sloan, G. Smadja and R. Voss, Phys. Rep. **162**, 45 (1988).
[10] B. Saikia and D. K. Choudhury, *An improved analysis of momentum fraction carried by quarks and gluons in a self-similar model* (under communication).
[11] D. J. Gross and F. Wilczek, Phys. Rev. **D9**, 980 (1974); X. Ji, J. Tang and P. Hoodbho, hep-ph/9510304.
[12] D. K. Choudhury and A. Jahan, Int. J. M. Phys. **A28**, 1350079 (2013) [hep-ph/1305.6180].
[13] A. Jahan and D.K. Choudhury, Phys. Rev. **D89**, 014014 (2014) [hep-ph/1401.4327].
[14] Martin A. D. et.al., Phys. Lett. **B 604 (1-2)**, 61 (2004); Strump D. et.al., JHEP **10** (2003), 046 (1-35); Gluck M. et.al., Euro. Phys. J. **C3**, 461 (1998).

Observations of blazars 1ES 1426+428, 1ES 1218+304 and 3C 454.3 by HAGAR telescope

P. Hazarika[a], B. B. Singh[b], V. R. Chitnis[b], B. S. Acharya[b] and U. D. Goswami[a]

(a) Department of Physics, Dibrugarh University, Dibrugarh-786004, Assam, India

(b) Department of High Energy Physics, Tata Institute of fundamental Research, Homi Bhabha Road, Mumbai-400005, India

Presenter: P. Hazarika (*poppyhazarika1@gmail.com*); HEP.6, Oral, CICAHEP15.48

We have observed three blazers, viz., 1ES 1426+428, 1ES 1218+304 and 3C 454.3 using the High Altitude Gamma Ray (HAGAR) telescope array. The HAGAR array is a wavefront sampling array of 7 telescopes, set-up at Hanle, at 4270 amsl, in Ladakh region of the Himalayas (Northern India). These three sources 1ES 1426+428, 1ES 1218+304 and 3C 454.3 are observed for 28, 56 and 10 hrs respectively. Our observation span is about 6 year period from 2009 to 2015. From the preliminary data analysis of above mentioned sources we do not find any evidence for a statistically significant γ-ray signal. The results of these analysis will be discussed in this paper.

1. Introduction

High Altitude GAmma Ray (HAGAR) telescope system is an array of 7 telescopes which is based on the nonimaging atmospheric Cherenkov technique. It is designed to detect very high energy γ-rays from various astronomical sources. In the nonimaging atmospheric Cherenkov technique, the arrival time of Cherenkov shower front at various locations in the Cherenkov light pool is measured, from which the direction of shower axis is estimated to enable rejection of off-axis cosmic ray showers [14]. HAGAR set-up at Hanle (longitude: 78^o $57'$ $51''$ E, latitude: 32^o $46'$ $46''$, altitude: 4270 m) is the first array of atmospheric Cherenkov telescopes established at a so high altitude. Because of the high altitude, even with a modest mirror area of 31 m^2, this experiment achieves a comparatively low energy threshold of 208 GeV. Since September 2008 regular source observations have been going on with the complete set up of seven telescopes. In this article we present details of HAGAR data analysis done to obtain the γ-ray flux from three blazars, viz., 1ES 1426+428, 1ES 1218+304 and 3C 454.3.

2. The HAGAR experiment details

Out of the seven telescopes of the HAGAR array, six are deployed at the vertices of a hexagon and the seventh one is placed at the center of the hexagon (see Fig. 1) [2]. Each telescope consists of seven front coated mirrors of parabolic shape with $\frac{f}{d}$ equal to 1 and each of diameter 0.9 m. The mirrors are fabricated from 10 mm thick float glass sheets. All the seven mirrors of each telescope are mounted para-axially on a single platform while the telescopes themselves are mounted alt-azimuthally. A fast Photonis UV sensitive PMT XP 2268B is placed at the focus of each mirror. The diameter of PMT photo cathode defines the field of view to be 3^o at FWHM. Coaxial cables of length 85 m and of types LMR-ultraflex-400 (of length 30 m) and RG 213 (of length 55 m) are used to bring pulses from the photo-tubes to control room situated below the central telescope. The telescope movement is maneuvered by a control software written on Linux platform. High voltages fed to photo tubes are controlled and monitored using C.A.E.N controller (model SY1527). PMT pulses are given to CAMAC based

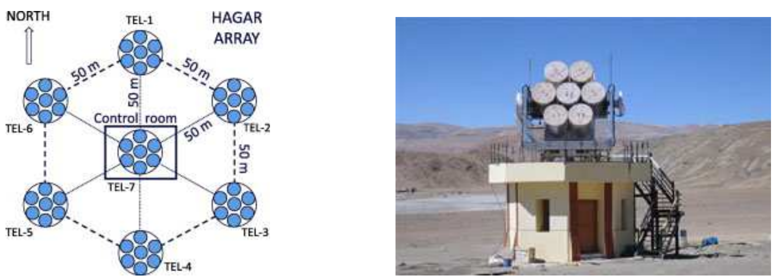

Figure 1. Schematic layout of HAGAR array (left) and one of the telescope of the array (right).

interrupt driven system in control room which acquires and records the data. For trigger generation, the 7 pulses of PMTs of a given telescope are linearly added to form telescope pulse, called royal sum pulse. A coincidence of any 4 telescope pulses above a preset threshold out of 7 royal sum pulses with in a resolving time of 150 to 300 ns generates a trigger pulse [3]. RS discriminator biases are adjusted to keep the RS rates within 25 to 35 kHz to maintain a chance coincidence rate within a few percent of the trigger rate. Data recorded on event interrupt includes relative arrival time of a shower front recorded by the TDCs accurate to 0.25 ns. 12 bit QDCs are used to record the Cherenkov photon density at each telescope, given the total charge in PMT pulses. An absolute arrival time of an event accurate to μs is given by a Real Time Clock (RTC) module synchronized with GPS. Various other information, such as the triggered telescopes in an event, are also recorded.

3. Signal extraction procedure

The HAGAR data analysis is based on the arrival angle estimation of the incident atmospheric shower w.r.t. the source direction. This angle called space angle i.e the angle between the direction of arrival of the shower and the direction of the source, is obtained for each event by measuring relative arrival times of the showers at each telescope. An accurate pointing of telescopes as well as precise time calibration of the optoelectronic chain is then required [2]. The later part is achieved first by computing TDC differences between pairs of telescopes from fix angle runs. Fix angle runs are used to compute the theoretical time-offsets, using information on the pointing direction, coordinates of telescopes, and on the transit time of each channel through the electronic chain. The TDC differences between pairs of telescopes from fix angle runs yield the calculation of *T_0's* (read as *tzeros*). T_0's are the relative time offsets for all telescopes to be used in the analysis to ensure a valid estimation of the relative timing differences in the arrival of the Cherenkov signal on the telescopes. Plane front approximation is then used to fit the arriving spherical Cherenkov wavefront in order to compute the space angle. For each event, the value of the χ^2 of the fit and other fit parameters are taken, and the number of telescopes with valid TDC information, i.e. participating in the trigger, is written. Thus four types of events, based on the Number of Triggered Telescopes (NTT), viz. events with NTT = 4, NTT = 5, NTT = 6 and NTT = 7 are defined. Atmospheric conditions change during observation time, reflected by variations on the trigger rate readings. This add systematics in our analysis. In order to remove isotropic emission due to cosmic rays, source observation region (ON) is compared with OFF-source region at same local coordinates on the sky, but at a different time (before or after tracking the source region for about 30 to 50 min). Normalisation of background events of both the ON and OFF source data sets is done by comparing number of events at large space angles, where no γ-ray signal is expected. This yield a ratio, called normalisation constant, which allows to calculate the ON-OFF excess below one specific cut on the space angle distribution [3].

4. Data selection criteria

In order to reduce systematics as much as possible data selection is done using some parameters which characterize good quality data. First, only those runs are selected for which trigger rate is stable. Runs with high value of the trigger rate are data that were taken under different conditions and hence are kept aside for future analysis. Then, the stability of the trigger rate of each run is quantified using one variable, called R_{stab}, defined as the RMS of the rate on the square root of its mean. For perfect Poissonnian fluctuations, this variable is expected to be equal to 1. Difference of R_{stab} ($R_{stab(ON)} - R_{stab(OFF)}$) of a given ON-OFF pair, gives relative rate stability of that run pair. A Gaussian fit to distribution of $R_{stab(ON)} - R_{stab(OFF)}$ and events within 3σ (standard deviation) limit define the range of R_{stab} cut for selection of pairs. Pair selection is then done imposing constraints on several other parameters. The relative difference of the coincidence window rate between ON and OFF source runs is imposed to be less than 10%, otherwise the pair is rejected. This parameter is related to the night sky background rate. Difference between the mean trigger rates of an ON and an OFF run is restricted to less than 2 Hz. Also, to prevent additional systematics during space angle computing, where some events are rejected, we impose difference between mean trigger rates to be less than 1 Hz after this analysis processing. During the pair processing, ratio of events for each telescope are computed and constrained to be between 0.8 and 1.2. Events with $\chi^2 \geq$ (mean + 1σ) are rejected, where χ^2 is the parameter of plane front fit. Further events with space angle greater than 7^o are rejected, as these are mostly due to bad fits [3]. Additional cuts viz., position error (Pos_{err}) cut of reproduced source position from TDC events relative to source position in sky is also applied. Position error is calculated separately for RA and DEC directions. A Gaussian fit to distribution of relative Pos_{err} in between ON-OFF pairs and events within 3σ (standard deviation) limit define the range of position error cut for selection of pairs [5]. At the last step of the selection, value of the normalization constant between ON and OFF events is computed and is constrained to be between 0.85 and 1.15.

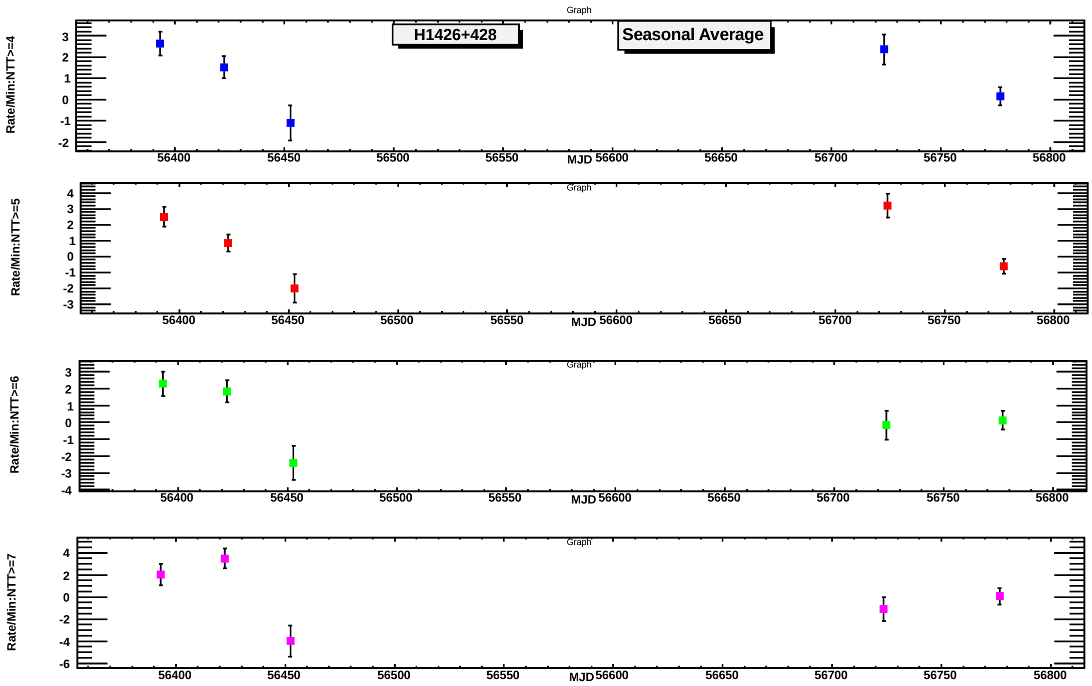

Figure 2. Light curve of 1ES 1426+428 averaged over each observation season.

5. Observed sources

3C454.3 is a powerful flat-spectrum radio quasar located at a redshift z = 0.859. Its RA is 22:53:57.7 and DEC is 16:08:54. It is one of the brightest gamma ray sources in the sky. In 2005 it underwent a very active phase in optical and X-ray bands, triggering intensive observations in the radio, optical and X-ray (Swift, Chandra, INTEGRAL) bands [6, 7, 8].

1ES 1228+304 is a HBL object. It has a redshift of z = 0.182 and it is one of the more distant VHE blazars detected to date. Its RA is 12:21:26.3 and DEC is 30:11:29. It was first detected at VHE by MAGIC [9] and confirmed by VERITAS [10].

1ES 1426+428 (z = 0.129) is classified as a BL Lac object. Its RA is 14:28:32.6 and DEC is 42:40:21. H 1426 + 428 is classified as an *extreme*. The source was first detected at TeV energies by the Whipple collaboration [11] and later confirmed using other ground-based imaging atmospheric Cherenkov telescopes [12].

6. Results

The HAGAR has observed these three sources 1ES 1426+428, 1ES 1218+304 and 3C 454.3 for 28, 56 and 10 hours respectively over an observation span of about 6 year period from September, 2009 to May, 2015. After imposing different analysis cuts, out of 39, 79 and 16 total run pairs, we had 23, 16 and 50 good ON-OFF pairs for the 1ES 1426+428, 1ES 1218+304 and 3C 454.3 that corresponds to 16.4, 9.8 and 35.9 hours of data respectively. The light curve of the three sources 1ES 1426+428, 1ES 1218+304 and 3C 454.3, for different telescope trigger conditions are shown in the Fig. 2, Fig. 3 and Fig. 4 respectively. Rate excess from the pair analysis is now

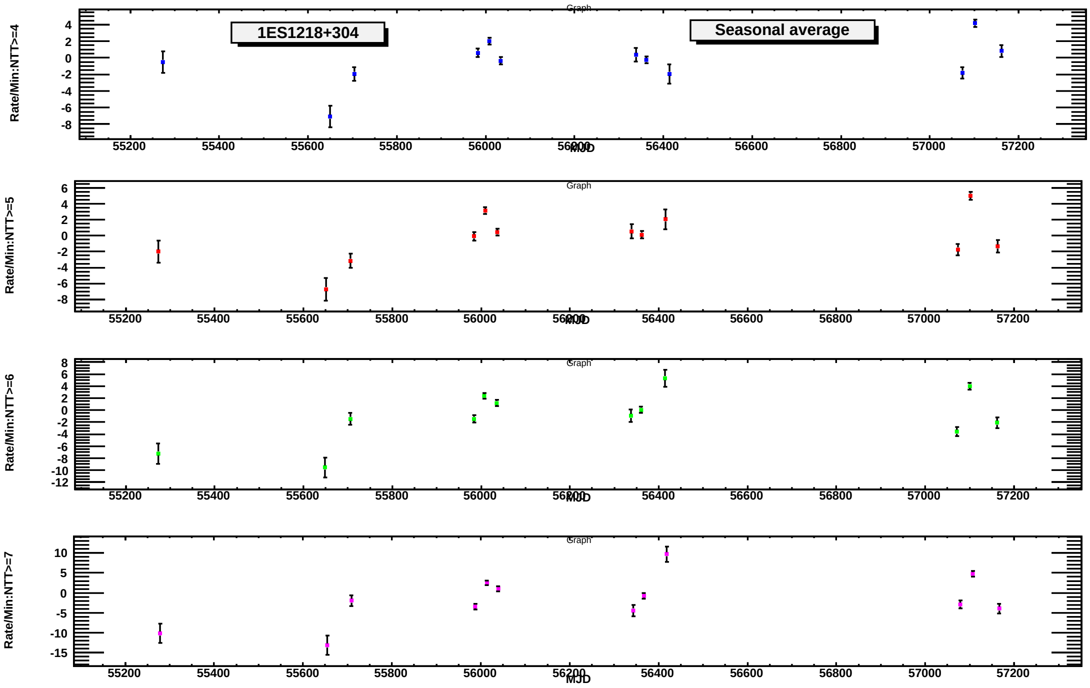

Figure 3. Light curve of 1ES 1218+304 averaged over each observation season.

represented for each selected pair as a number of counts per minute, expected to contain a significant fraction of γ-rays. The estimated γ-ray rates from these three sources for different triggering criteria are given in Table 1, Table 2 and Table 3 respectively.

Considering the facts that the sources 1ES 1426+428, 1ES 1218+304 and 3C 454.3 are situated farther in distance and the sensitivity of HAGAR, very long duration observations are required to detect significant excess from these three sources. Therefore we have estimated flux upperlimit for these three sources from our observations. Thus we have obtained 3σ upperlimit on VHE γ-ray flux as 2.43x10^{-6} photons $m^{-2}s^{-1}$, 6.57x10^{-6} photons $m^{-2}s^{-1}$ and 1.63x10^{-6} photons $m^{-2}s^{-1}$ at the energy threshold of about 182 GeV for NTT $\geq$ 4-fold for these sources respectively.

Table 1. Results of the 1ES 1426+428 for NTT $\geq$ 4-fold, 5-fold, 6-fold and 7-fold.

NTT	Rate/min.	RMS/min.	σ	T(hours)	Runs	σ/T
NTT $\geq$ 4	- 6.67	1.44	- 4.64	7.91	12	- 1.65
NTT $\geq$ 5	- 3.18	1.18	- 2.70	7.91	12	- 0.96
NTT $\geq$ 6	- 2.19	0.95	- 2.31	7.91	12	- 0.82
NTT$\geq$7	- 0.70	0.70	- 1.00	7.91	12	- 0.36

7. Summary

In summary, we have presented data analysis from HAGAR observations of the three blazers 1ES 1426+428, 1ES 1218+304 and 3C 454.3. We had a total of 28, 56 and 10 hrs of data for these three sources respectively, over an observation span of about 6 year period from 2009 to 2015. We have not detected a signal from either of these

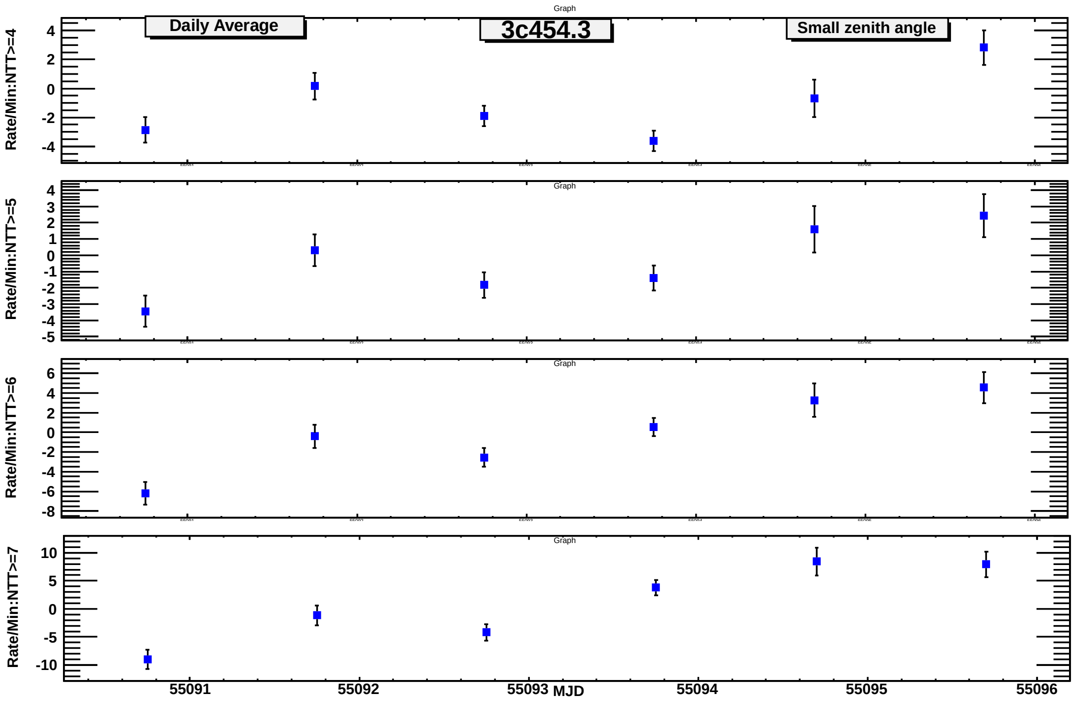

Figure 4. Light curve of 3C 454.3 averaged over a day (zenith $< 30^o$).

Table 2. Results of the 1ES 1218+304 for NTT $\geq$ 4-fold, 5-fold, 6-fold and 7-fold.

NTT	Rate/min.	RMS/min.	σ	T(hours)	Runs	σ/T
NTT ≥ 4	2.02	0.68	2.96	35.99	50	0.49
NTT ≥ 5	2.22	0.54	4.10	35.99	50	0.68
NTT ≥ 6	0.21	0.41	0.52	35.99	50	0.09
NTT ≥ 7	-0.48	0.27	-1.83	35.99	50	-0.30

Table 3. Results of the 1ES 3c454.3 for NTT$\geq$ 4-fold, 5-fold, 6-fold and 7-fold (zenith $< 30^o$).

NTT	Rate/min.	RMS/min.	σ	T(hours)	Runs	σ/T
NTT ≥ 4	- 6.67	1.44	- 4.64	7.91	12	- 1.65
NTT ≥ 5	- 3.18	1.18	- 2.70	7.91	12	- 0.96
NTT ≥ 6	- 2.19	0.95	- 2.31	7.91	12	- 0.82
NTT ≥ 7	- 0.70	0.70	- 1.00	7.91	12	- 0.36

sources and have set upper limits on their γ-ray flux levels. The source 3c454.3 is a quasar with a very high redshift (z = 0.859). The flux of very high energy γ-rays from this source is likely to be affected by absorption due to extragalactic background radiation during their propagation in the inter galactic medium and get attenuated. As a result this source is not detected by the any of the VHE experiments so far. Further, since HAGAR sensitivity is very less compared to other ground based VHE γ-ray telescopes, so for a significant detection of 1ES 1426+428 and 1ES 1218+304 number of hours of observation must be increased.

References

[1] L. Saha et al., Astropart. Phys. **42**, 33 (2013).
[2] V. R. Chitnis et al., in proc. of 31st ICRC, Lodz (2009).
[3] R. J. Britto et al., in proc. of the 31st ICRC, Lodz (2009).
[4] R. J. Britto et al., Astrophys. Space Sci. Trans. **7**, 501 (2011).
[5] B. B. Singh, *A Report on the Status of HAGAR Data Analysis Method and Results*, TIFR, Mumbai.
[6] M. Villata, C. M. Raiteri, T. J. Balonek et al., A&A **453**, 817 (2006).
[7] P. Giommi, A. J. Blustin, M. Capalbi et al., A&A **456**, 911 (2006).
[8] E. Pian, L. Foschini, V. Beckmann et al., A&A **449**, L21 (2006).
[9] J. Albert et al., ApJL **642**, 119 (2006).
[10] V.A. Acciari et al., ApJL **684**, L73 (2008).
[11] D. Horan et al., ApJ **571**, 753 (2002).
[12] F. Aharonian, A&A **384**, L23 (2002).
[13] D. Bose, Ph D thesis from T.I.F.R, Mumbai (2007).
[14] L. Saha, Ph D thesis from S.I.N.P, Kolkata (2014).

Masses of heavy flavored mesons in an improved QCD potential model

Tapashi Das[a] and Dilip Kumar Choudhury[a,b]

(a) Department of Physics, Gauhati University, Guwahati-781014, Assam, India
(b) Physics Academy of North-East, Guwahati-781014, Assam, India

Presenter: Tapashi Das (*t4tapashi@gmail.com*); HEP.3, Poster, CICAHEP15.52

The QCD potential $V(r) = -\frac{4\alpha_s}{3r} + br + c$, which is also known as Cornell potential is not analytically solvable. We use the Dalgarno's method of perturbation to solve Schrodinger's equation and obtain the corresponding meson wave function. We first demonstrate that the Dalgarno's method of perturbation theory is compatible with the quantum mechanical expectation: that the scale factor 'c' even if it is present in the potential should not appear in the wave function of the system, a feature overlooked in the previous applications. Using this improved formalism we calculate the masses of various heavy flavored mesons. The obtained results are then compared with the experimental values.

1. Introduction

Quantum Chromodynamics, familiarly called QCD is the sector of the Standard Model (SM) where heavy hadron spectroscopy played a major role. The motivation of the present work is to find the masses of the heavy flavored mesons in a QCD potential model. The present work takes into account the idea of quantum mechanics that a scale factor 'c' in a potential should not effect the wave function of the meson while using perturbation theory like Dalgarno's method [1]. The methodology involves the construction of the wave functions out of the Schrodinger equation. In Section 2, we outline the formalism, while Section 3 summarizes the results. Section 4 contains the conclusion.

2. Formalism

2.1 QCD potentials and corresponding wave functions

QCD potential between a quark and an anti-quark has been one of the first important ingredient of phenomenological models to be studied in quantum physics. We calculate the total wave function using Dalgarno's method of perturbation using Cornell potential [2]

$$V(r) = -\frac{4\alpha_s}{3r} + br + c, \tag{1}$$

where - $\frac{4}{3}$ is due to the color factor, α_s is the strong coupling constant, r is the inter quark distance, b is the confinement parameter (phenomenologically, $b = 0.183$ GeV^2) and 'c' is a constant scale factor. The Schrodinger equation describing the quark-anti quark bound state is

$$-\frac{\hbar^2}{2m}\nabla^2\psi(r) + [E - V]\psi(r) = 0 \tag{2}$$

The potential is defined as the function $V(r)$. To apply the perturbation, the choice of parent child is very important. For the potential as defined in equation (1), we can make four choices with the constant term 'c':

(i) - $\frac{4\alpha_s}{3r}$ as parent and $br + c$ as perturbation, (ii) br as parent and - $\frac{4\alpha_s}{3r} + c$ as perturbation, (iii) - $\frac{4\alpha_s}{3r} + c$ as parent and br as perturbation, and (iv) $br + c$ as parent and - $\frac{4\alpha_s}{3r}$ as perturbation.

The wave function for choice (i) is calculated in Ref. [3] using Dalgarno's method of perturbation, which is

$$\psi_I^{total}(r) = \frac{N_1}{\sqrt{\pi a_0^3}}\left[1 + cA_0\sqrt{\pi a_0^3} - \frac{1}{2}\mu b a_0 r^2\right]\left(\frac{r}{a_0}\right)^{-\epsilon} e^{-\frac{r}{a_0}}, \tag{3}$$

where

$$a_0 = \left(\frac{4}{3}\mu\alpha_s\right)^{-1}, \tag{4}$$

$$\mu = \frac{m_1 m_2}{m_1 + m_2}, \tag{5}$$

m_1 and m_2 are the masses of quark and anti quark respectively and μ is the reduced mass of the mesons and

$$\epsilon = 1 - \sqrt{1 - \left(\frac{4}{3}\alpha_s\right)^2} \tag{6}$$

the relativistic effect due to Dirac modification factor and A_0 is the undetermined co-efficient appearing in the series solution of Schrodinger equation and N_1 is the normalization constant.

Again the wave function for choice (ii) of the Hamiltonian is calculated in Ref. [4] which is

$$\psi_{II}^{total}(r) = \frac{N_2}{r}\left[1 + A_1(r)r + A_2(r)r^2 + A_3(r)r^3 + A_4(r)r^4\right] A_i[\rho_1 r + \rho_0]\left(\frac{r}{a_0}\right)^{-\epsilon}, \tag{7}$$

where $A_i(r)$ is the Airy function and N_2 is the normalization constant. The co-efficients are:

$$A_0 = 0 \tag{8}$$

$$A_1 = \frac{-2\mu\frac{4\alpha_s}{3}}{2\rho_1 k_1 + \rho_1^2 k_2} \tag{9}$$

$$A_2 = \frac{-2\mu(W^1 - c)}{2 + 4\rho_1 k_1 + \rho_1^2 k_2} \tag{10}$$

$$A_3 = \frac{-2\mu W^0 A_1}{6 + 6\rho_1 k_1 + \rho_1^2 k_2} \tag{11}$$

$$A_4 = \frac{-2\mu W^0 A_2 + 2\mu b A_1}{12 + 8\rho_1 k_1 + \rho_1^2 k_2} \tag{12}$$

The parameters are:

$$\rho_1 = (2\mu b)^{\frac{1}{3}} \tag{13}$$

$$\rho_0 = -\left[\frac{3\pi(4n-1)}{8}\right]^{\frac{2}{3}} \tag{14}$$

In our case ($n = 1$ for ground state)

$$k_1 = 1 + \frac{k}{r} \tag{15}$$

$$k = \frac{0.3550281 - (0.2588194)\rho_0}{(0.2588194)\rho_1} \tag{16}$$

$$k_2 = \frac{k^2}{r^2} \tag{17}$$

Similarly, we have calculated the wave function for choice (iii) which is

$$\psi_{III}^{total}(r) = \frac{N_3}{\sqrt{\pi a_0^3}} \left[1 - \frac{1}{2}\mu b a_0 r^2 - \frac{1}{20}\mu^2 bca_0 r^4\right] \left(\frac{r}{a_0}\right)^{-\epsilon} e^{-\frac{r}{a_0}}, \tag{18}$$

where N_3 is the normalization constant. Finally, the wave function for choice (iv) including relativistic effect considering upto O(r^4) is

$$\psi_{IV}^{total}(r) = \frac{N_4}{r} \left[1 + A_1(r)r + A_2(r)r^2 + A_3(r)r^3 + A_4(r)r^4\right] A_i[\rho_1 r + \rho_0] \left(\frac{r}{a_0}\right)^{-\epsilon}, \tag{19}$$

where N_4 is the normalization constant. The co-efficients are

$$A_0 = 0 \tag{20}$$

$$A_1 = \frac{-2\mu\frac{4\alpha_s}{3}}{2\rho_1 k_1 + \rho_1^2 k_2} \tag{21}$$

$$A_2 = \frac{-2\mu W^1}{2 + 4\rho_1 k_1 + \rho_1^2 k_2} \tag{22}$$

$$A_3 = \frac{-2\mu(W^0 - c)A_1}{6 + 6\rho_1 k_1 + \rho_1^2 k_2} \tag{23}$$

$$A_4 = \frac{-2\mu(W^0 - c)A_2 + 2\mu b A_1}{12 + 8\rho_1 k_1 + \rho_1^2 k_2} \tag{24}$$

The equations (3), (7), (18) and (19) showed that the effect of 'c' in the total wave function will be present in all the cases. Thus Dalgarno's method conflicts with the quantum mechanical idea that the scale factor 'c' should not have an observable effect except the energy shift.

For the validation of the quantum mechanical expectation, we therefore consider $c = 0$ in the potential (1). In such situation choice (i) & (iii) and (ii) & (iv) are identical.

However the inter-quark separation 'r' can be roughly divided into short distance (r^S) and long distance (r^L) effectively, one of the potential will dominate over the other. In such situation confinement parameter (b) and the strong coupling parameter (α_s) can be considered as effective and appropriate small perturtbative parameters. To find the cut offs (r^S and r^L) we use the following two perturbation conditions:

Case-I: For coulomb as parent and linear as perturbation:

$$-\frac{4\alpha_s}{3r} > r \tag{25}$$

Case-II: For linear as parent and coulomb as perturbation:

$$br > -\frac{4\alpha_s}{3r} \tag{26}$$

From (25) and (26) we can find the bounds on r up to which case-I and II are valid. Case-I gives the cut off on the short distance $r_{max}^S < \sqrt{\frac{4\alpha_s}{3b}}$ and case-II gives the cut off on the long distance $r_{min}^L > \sqrt{\frac{4\alpha_s}{3b}}$. Now using this improved perturbative approach we calculate the masses of various heavy flavored mesons.

2.2 Definition of masses of mesons

Masses of heavy flavored mesons in a specific potential model in the ground state can be obtained as:

$$M = m_q + m_{\bar{q}} + \langle H \rangle, \tag{27}$$

where M is the mass of pseudoscalar meson and m_q and $m_{\bar{q}}$ are the masses of quark and anti-quark of the meson respectively. The above expression shows that to calculate the masses of mesons one needs to find $\langle H \rangle$:

$$\langle H \rangle = \langle \frac{p^2}{2\mu} \rangle + \langle V(r) \rangle$$

$$= 4\pi \int_0^\infty r^2 \psi^*(r) H \psi(r) dr$$

$$= 4\pi \int_0^\infty r^2 \psi^*(r) \left(\frac{p^2}{2\mu} + V(r) \right) \psi(r) dr \tag{28}$$

To take into account both the coulomb and linear part of the potential we improve the above equation to

$$\langle H \rangle = 4\pi \left[\int_0^{r^{short}} r^2 \psi^*(r) \left(\frac{p^2}{2\mu} + V(r) \right) \psi(r) dr + \int_{r^{long}}^{r_0} r^2 \psi^*(r) \left(\frac{p^2}{2\mu} + V(r) \right) \psi(r) dr \right]. \tag{29}$$

3. Results and discussion:

Considering $c = 0$, we calculate the masses of various heavy light mesons using equation (27) and results are compared with the previous work [6] with $c = 0$ as shown in the Table 1. The input parameters in the numerical calculations used are $m_u = 0.336$ GeV, $m_s = 0.483$ GeV, $m_c = 1.55$ GeV and $m_b = 4.95$ GeV, $b = 0.183$ GeV^2.

Table 1. Masses of heavy light mesons.

α_s	Meson	$r^S = r^L$(fm)	Mass (GeV)	Mass (in Ref. [6] with $c = 0$)	Experimental Mass (GeV)
0.39	D($c\bar{u}/cd$)	0.3320	1.886	2.35	1.869± 0.0016
	$D_s(c\bar{s})$		2.033	2.35	1.968± 0.0033
0.22	$B_c(bc)$	0.2494	6.500	7.04	6.277± 0.006

Again, the application of Airy function as meson wave function needs suitable cut off to make the analysis normalizable and convergent. We therefore set the cut off (r_0) in the range 1 fm (5.076 GeV^{-1}) [5] for our calculations.

The results above are improvement over the earlier analysis [6]. To obtain the results as given in the 5th column of Table 1, we impose the condition $c = 0$ instead of $cA_0 = 1$ GeV as in Ref. [6].

4. Conclusion:

Thus the analysis shows that our calculated values of masses of mesons are found to be in better agreement with the experimental values. Therefore the improved perturbative approach is suitable to find masses of various heavy flavored mesons. The modification of the model with a non-zero scaling factor is currently under study.

Acknowledgement:

Tapashi Das acknowledges the support of University Grants Commission in terms of fellowship under BSR scheme to pursue research work at Gauhati University, Department of Physics. Tapashi Das is also thankful to Dr. K. K. Pathak of Arya Vidyapeeth College, Guwahati for various helpful suggestions.

References

[1] A. K. Ghatak and S. Lokanathan, *Quantum Mechanics*, McGraw Hill (1997), pp 291.
[2] E. Eichten et al., Phys. Rev. **D21**, 203 (1980).
[3] N. S. Bordoloi, D. K. Choudhury, Mod. Pys. Lett. A **24 (6)**, 443 (2009).
[4] S. Roy, D. K. Choudhury, MPLA **27**, 1250110 (2012).
[5] G. S. Bali, arXiv:hep-ph/0010032v1.
[6] K. K. Pathak, D. K. Choudhury, Pramana **79 (6)**, 1385 (2012).
[7] T. Das, D. K. Choudhury and K. K. Pathak, arXiv:1505.05634 [hep-ph].

A DGLAP based second order *x* evolution equation of quarks and gluon distribution at small *x* and their solutions

Luxmi Machahari[a], D. K. Choudhury[a] and P. K. Sahariah[b]

(a) Department of Physics, Gauhati University, Guwahati-781014, Assam, India

(b) Department of Physics, Cotton College, Guwahati-781001, Assam, India

Presenter: Luxmi Machahari (*luxmimachahari@gmail.com*); HEP.3, Oral, CICAHEP15.57

The coupled DGLAP equations at small *x* is Taylor approximated upto the second order O(x^2) and are solved analytically. Assuming a plausible relation between quark and gluon distribution we demonstrate that the two different sets of quark and gluon distributions are possible from the two coupled equations not reported earlier. Using the proper matching condition, we then obtain the range of (x, Q^2) where they will be identical.

1. Introduction

This paper reports the solution of Taylor approximated $O(x^2)$ DGLAP [1, 2, 3, 4] equations at small x using the Method of separation of Variables [5]. We demonstrate that such DGLAP equations are of elliptic nature under plausible assumptions relating quark and gluon distributions and the coupled version of them have got two alternate solutions for quark and gluon distributions a feature not noticed earlier[6]. It gives a very restrictive range of x and Q^2 for this validity, which we study numerically as well. Taylor approximated upto $O(x^2)$ form of the coupled DGLAP equations [7] are:

$$t\frac{\partial}{\partial t}q(x,t) = \frac{\alpha_s(t)}{2\pi}[J_1(x) + J_4(x)C(t)]q(x,t) + \frac{\alpha_s(t)}{2\pi}x[J_2(x) + J_5(x)C(t)]\frac{\partial}{\partial x}q(x,t) + \frac{\alpha_s(t)}{2\pi}x^2[J_3(x) + J_6(x)C(t)]\frac{\partial^2}{\partial x^2}q(x,t), \quad (1)$$

$$t\frac{\partial}{\partial t}(C(t)q(x,t)) = \frac{\alpha_s(t)}{2\pi}[J_7(x) + J_{10}(x)C(t)]q(x,t) + \frac{\alpha_s(t)}{2\pi}x[J_8(x) + J_{11}(x)C(t)]\frac{\partial}{\partial x}q(x,t) + \frac{\alpha_s(t)}{2\pi}x^2[J_9(x) + J_{12}(x)C(t)]\frac{\partial^2}{\partial x^2}q(x,t). \quad (2)$$

Where J_i's (i = 1, 2, ...12) are explicit calculable functions of x. We assumed the relation between quark and gluon distribution [8, 9] given by,

$$xg(x,t) = C(t)x\sum_i \{q_i(x,t) + \overline{q_i}(x,t)\}. \quad (3)$$

Neglecting the flavor and antiquark degrees of freedom equation (3) is can be simplified to

$$xg(x,t) = C(t)xq(x,t), \quad (4)$$

where $C(t)$ is a 't' dependent function.

1.1 Solution $q^I(x,t)$ from quark distribution equation

In standard QCD quark and gluon distributions, are in general not factorizable in x and t. To fecilitate our solution analytically, we however use the method of separation of variables[5]. We assume the solution of equation (1) to be $q^I(x,t) = X(x)T(t)$. Substituting this in equation(1) we get the solution for $T(t)$ as:

$$T(t) = \exp[-k^2 \log t + D], \quad (5)$$

where $-k^2$ is separation constant and D is an integration constant. To obtain the solution for $X(x)$ we define,

$$\begin{aligned} A(x,t) &= \frac{\alpha_s(t)}{2\pi}x^2[J_3(x)+J_6(x)C(t)], \\ B(x,t) &= \frac{\alpha_s(t)}{2\pi}x[J_2(x)+J_5(x)C(t)], \\ C(x,t) &= \frac{\alpha_s(t)}{2\pi}[J_1(x)+J_4(x)C(t)]+k^2. \end{aligned} \tag{6}$$

Assuming them to be nearly x and t independent such that, $A(x,t) \simeq A,\ B(x,t) \simeq B,\ C(x,t) \simeq C$. One gets the solution for three separate cases depending on the sign of the discriminant (B^2-4AC). To that end we also need to define: $m_1 = \frac{-B+\sqrt{B^2-4.A.C}}{2.A},\ \ m_2 = \frac{-B-\sqrt{B^2-4.A.C}}{2.A}$.

CASE I: $B^2-4AC>0$ (Hyperbolic equation): If m_1 and m_2 are real and unequal i.e $m_1 \neq m_2$, then the solution $q^I(x,t)$ for quark distribution of equation (1) is

$$q^I(x,t) = \exp[-k^2\log t + D].\,[c_1 e^{m_1.x} + c_2 e^{m_2.x}]\,, \tag{7}$$

where c_1 and c_2 are arbitrary constants.

CASE II: $B^2-4AC=0$ (Parabolic equation): Here m_1 and m_2 are equal ($\sim m$), then the quark distribution solution $q^I(x,t)$ for equation (1) is

$$q^I(x,t) = \exp[-k^2\log t + D].\,[c_1 e^{m.x} + c_2 x e^{m.x}]\,. \tag{8}$$

CASE III: $B^2-4AC<0$ (Elliptic equation): If $m_1 = \alpha + i\beta$, and $m_2 = \alpha - i\beta$ are complex numbers, where α and β are respectively $\frac{-B}{2A}$ and $\frac{\sqrt{4AC-B^2}}{2A}$, then the solution $q^I(x,t)$ of equation (1) would be

$$q^I(x,t) = \exp[-k^2\log t + D].\,[e^{\alpha x}(c_1\cos\beta x + c_2\sin\beta x)]\,. \tag{9}$$

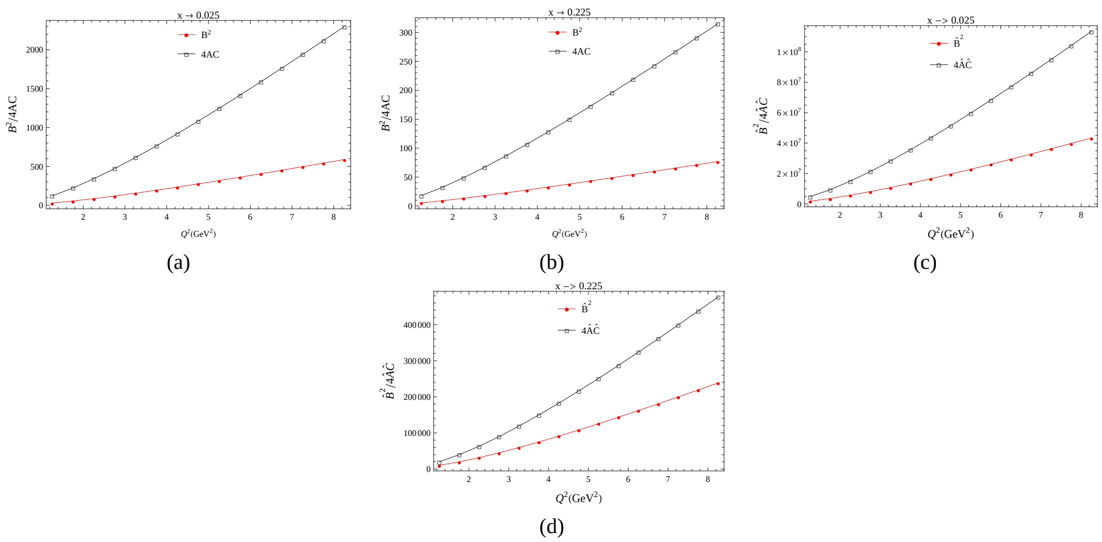

Figure 1: Plots (a), (b) are for $B^2/4AC$ versus Q^2 and (c), (d) are for $\hat{B}^2/4\hat{A}\hat{C}$ versus Q^2 at different fixed x.

1.2 Solution $q^{II}(x,t)$ from gluon distribution equation

For equation (2) we write the solution as $q^{II}(x,t)) = \hat{X}(x)\hat{T}(t)$. The analysis yields again three plausible solutions as follows:

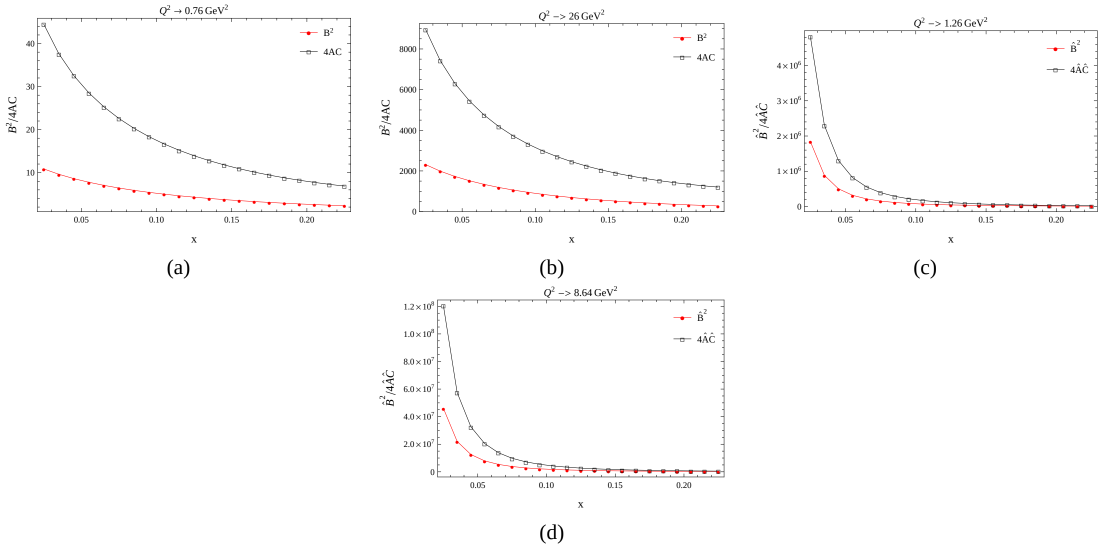

Figure 2: Plots (a), (b) are for $B^2/4AC$ versus x and (c), (d) are for $\hat{B}^2/4\hat{A}\hat{C}$ versus x at different fixed Q^2.

CASE I: $\hat{B}^2 - 4\hat{A}\hat{C} > 0$ (Hyperbolic equation):

$$q^{II}(x,t) = \exp\left[\int\left(\frac{-\hat{k}^2}{tC(t)} - \frac{1}{C(t)}\frac{\partial C(t)}{\partial t}\right)dt + F\right].\left[\hat{c}_1 e^{\frac{-\hat{B}+\sqrt{\hat{B}^2-4\hat{A}\hat{C}}}{2\hat{A}}.x} + \hat{c}_2 e^{\frac{-\hat{B}-\sqrt{\hat{B}^2-4\hat{A}\hat{C}}}{2\hat{A}}.x}\right], \tag{10}$$

where, $\hat{A}, \hat{B}, \hat{C}$ are the corresponding parameters similar to equation (6). $-\hat{k}^2$ is separation constant and $\hat{c}_1$, $\hat{c}_2$ are arbitrary constants.

CASE II: $\hat{B}^2 - 4\hat{A}\hat{C} = 0$ (Parabolic equation):

$$q^{II}(x,t) = \exp\left[\int\left(\frac{-\hat{k}^2}{tC(t)} - \frac{1}{C(t)}\frac{\partial C(t)}{\partial t}\right)dt + F\right].[\hat{c}_1 e^{m.x} + \hat{c}_2 x e^{m.x}]. \tag{11}$$

CASE III: $\hat{B}^2 - 4\hat{A}\hat{C} < 0$ (Elliptic equation):

$$q^{II}(x,t) = \exp\left[\int\left(\frac{-\hat{k}^2}{tC(t)} - \frac{1}{C(t)}\frac{\partial C(t)}{\partial t}\right)dt + F\right].\left[e^{\hat{\alpha}x}(\hat{c}_1\cos\hat{\beta}x + \hat{c}_2\sin\hat{\beta}x)\right]. \tag{12}$$

From equations (7), (8), (9) and equations (10), (11), (12) we establish that $q^I(x,t) \neq q^{II}(x,t)$. For completeness we also record the solution of DGLAP equations taking only O(x) terms from equation (1) and (2). Here too we obtain two non unique solutions $q^I(x,t)$ and $q^{II}(x,t)$ using the same method as follows:

$$q^I(x,t) = \exp[-k^2\log t + D].\exp[\frac{-C}{B}x + c_1], \tag{13}$$

$$q^{II}(x,t) = \exp\left[\int\left(\frac{-\hat{k}^2}{tC(t)} - \frac{1}{C(t)}\frac{\partial C(t)}{\partial t}\right)dt + F\right].\exp[\frac{-\hat{C}}{\hat{B}}x + \hat{c}_1], \tag{14}$$

where $B, C, \hat{B}, \hat{C}$ are the counterterms as in $O(x^2)$ and c_1, $\hat{c}_1$ are constants of integration.

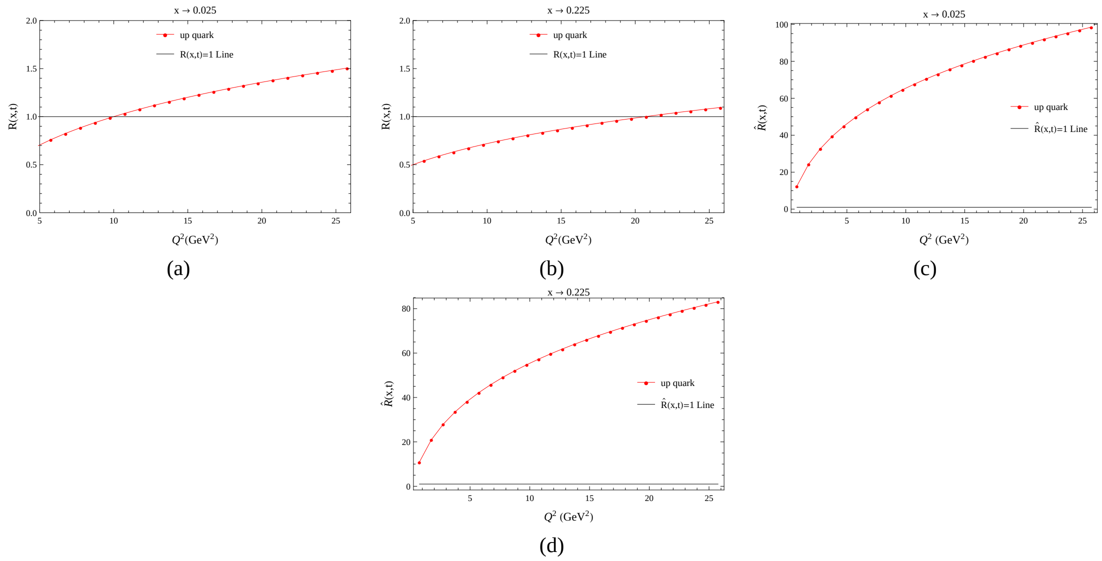

Figure 3: Plots (a), (b) are for $R(x,t)$ versus Q^2 and (c), (d) are for $\hat{R}(x,t)$ versus Q^2 at certain fixed x.

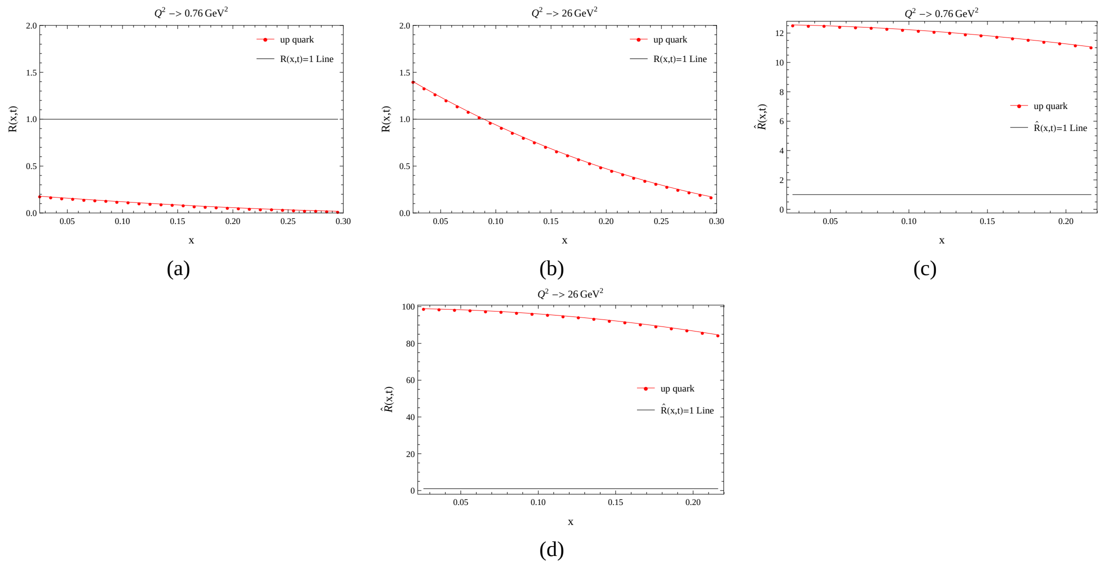

Figure 4: Plots (a), (b) are for $R(x,t)$ versus x and (c), (d) are for $\hat{R}(x,t)$ versus x at certain fixed Q^2.

2. Results

2.1 Nature of the equation

To ascertain the nature of the above equations, we numerically determine $(B^2 - 4AC)$ and $(\hat{B}^2 - 4\hat{A}\hat{C})$ by taking $\frac{\alpha_s(t)}{2\pi} = \frac{6}{(33-2N_f)}\frac{1}{t}$, $N_f = 1$, $C(t) = \log(\frac{Q^2}{\Lambda^2})^\sigma, \sigma = 2.5$ [10], $\Lambda = 220$ MeV [11] and approximating $k^2 = \hat{k}^2 = 0$. Then we see graphically in which class they belong. Fig. 1and Fig. 2 show $B^2 < 4AC$ and $\hat{B}^2 < 4\hat{A}\hat{C}$ indicating elliptic nature. Fig. 1 shows that such nature is always true for any Q^2, while Fig. 2 indicates that for large x, it might have a tendency to transform into a parabolic nature.For graphical representation of $q^I(x,t) \neq q^{II}(x,t)$ we approximate $D = 0, c_1 + c_2 = U$ (say) for equation (9) and $F = 0, \hat{c_1} + \hat{c_2} = \hat{U}$ (say) for equation (12). U and $\hat{U}$ are found to be 7.9×10 and 4597 respectively, taking the input of MSTW2008 LO [12] for up quarks with the value of $Q^2 = 2$ GeV^2 and $x = 0.005$ and $q(x,t) = 78.44$ [12]. We obtain the ratio $R(x,t) = \frac{q^I(x,t)}{q^{II}(x,t)}$ numerically. Correspondingly we obtain the counterterm $\hat{R}(x,t) = \frac{q^I(x,t)}{q^{II}(x,t)}$ numerically as well, taking similar approximations as in O(x^2) for $O(x)$ and assuming $c_1 = 0$ and $\hat{c}_1 = 0$. We show it graphically $R(x,t)$ and $\hat{R}(x,t)$ as in Fig. 3 and Fig. 4 for a certain range of (x, Q^2) i.e, $0.025 \leq x \leq 0.225$ and $0.76 \leq Q^2 \leq 26$ GeV^2. From both the figures we observe that for various x and Q^2, the two quark distributions are identical only at certain x and Q^2. However it is not obvious that one will obtain such intersecting point for any value of x and Q^2. Fig. 3 and Fig. 4 illustrate that there is no allowed range of x and Q^2 that will coincide.

3. Conclusion

We highlight the Elliptic nature of leading order $O(x^2)$ DGLAP equations at small *x* neglecting the flavor and antiquark degrees of freedom.The incorporation of flavor as well as antiquark degrees of freedom and testing with data are currently in progress.

Acknowledgment

One of the authors (LM) acknowledges the Rajiv Gandhi National Fellowship, New Delhi for financial support.

References

[1] V. N. Gribov and L. N. Lipatov, Sov. J. Nucl. Phys. **15**, 438 (1972).
[2] L. N. Lipatov, Sov. J. Nucl. Phys. **20**, 94 (1975).
[3] Yu. L. Dokshitzer, Sov. Phys. JETP **46**, 641 (1977).
[4] G. Altarelli and G. Parisi, Nucl. Phys. B **126**, 298 (1977).
[5] A. B. Gupta, *Fundamentals of Mathematical Physics*, Books and Allied (P) LTD, Kolkata (2004), pp 381.
[6] J. K. Sarma, D. K. Choudhury and G. K. Medhi, Phys. Lett. B **403**, 139 (1997).
[7] R. K. Ellis, W. J Stirling and B.R.Webber, *QCD and collider Physics*.
[8] C. Lopez and F. J. Yndurain, Nucl. Phys. B **171**, 231 (1980).
[9] A. Jahan and D. K. Choudhury, Commun. Theor. Phys. **61**, 654 (2014).
[10] D. K. Choudhury and Neelakshi N. K. Borah, arXiv:1508.06041v2[hep-ph] (2015).
[11] A. D. Martin , R. G. Roberts , W. J. Stirling and R. S. Thorne, arXiv:hep-ph/0201127v1 (2002).
[12] *Parton Distribution Functions from HEPDATA: The DURHAM HEP DATA bases*, http://hepdata.cedar.ac.uk/pdf/pdf3.html
[13] D.K. Choudhury, Journal of Physics: Conference series **481**, 012001 (2014).
[14] Neelakshi N. K. Borah, D.K. Choudhury and P. K. Sahariah, Advances in High Energy Physics, 829803 (2013).

Evaluation of mass of Z' boson from $B_d \to \tau^+\tau^-$ decay

Debika Banerjee and Sukadev Sahoo

Department of Physics, National Institute of Technology, Durgapur-713209, West Bengal, India

Presenter: Debika Banerjee (*rumidebika@gmail.com*); HEP.3, Oral, CICAHEP15.58

Rare B decays induced by flavor-changing neutral current (FCNC) transitions provide promising approaches to probe the flavor sector of the standard model (SM) and provides important constraints on models of new physics (NP). In the SM they can only occur through loop level processes and are generally suppressed. However, these processes can be significantly enhanced in the model which goes beyond the SM. In recent scenario, $B_d \to \tau^+\tau^-$ rare decay has been the subject of many theoretical as well as experimental studies. There are strong predictions of the existence of Z' boson in theories beyond the SM. But its exact mass is still unknown as it has not yet been discovered experimentally. Considering the effect of such Z'-mediated FCNCs on the $B_d \to \tau^+\tau^-$ decay we calculate the branching ratio. Here, using the experimental value of branching ratio and recent values of the parameters we estimate the mass of Z' boson.

1. Introduction

The rare B meson decays with leptons in the final states $B_d \to l^+l^-$ $(l = e, \mu, \tau)$ induced by FCNCs are very important to probe the flavour sector of the SM as well as provide a new window to search new physics (NP) beyond the SM [$1-9$]. The rate of FCNC processes are generally suppressed by small electroweak gauge couplings, off-diagonal Cabibbo-Kobayashi-Maskawa (CKM) matrix elements and the loop factors in the SM. However, these suppression can be lifted in theories beyond SM such as minimal supersymmetric standard model (MSSM), littlest Higgs model, flavor-changing Z' models etc. [10-12]. In this paper, we study $B_d \to \tau^+\tau^-$ decay considering the effect of both Z and Z' mediated FCNCs. The $B_d \to \tau^+\tau^-$ decay involves $b \to d$ transitions which are highly suppressed in the SM of the particle physics. But, these decays can be significantly enhanced in many scenarios beyond the SM [13]. Existence of Z' bosons are predicted in the theories beyond the SM [14], such as grand unified theories (GUTs), superstring theories and theories with large extra dimensions [15]. The Z' sector gives a good platform for understanding the new physics beyond the SM [16]. The right-handed quarks d_R , s_R and b_R have different $U'(1)$ quantum numbers than exotic q_R. Their mixing induces Z' mediated flavor-changing neutral current (FCNC) [17, 18] among the ordinary down quark types. The tree level FCNC transitions can also be mediated through an additional Z' boson on the up-type quark sector [19]. In the Z' model [20], the FCNC coupling is related to the flavor-diagonal couplings qqZ' in a predictive way, which can be used to get the upper limits on the leptonic llZ' couplings. Therefore, it is possible to evaluate the branching ratio for $B_d \to \tau^+\tau^-$ decay.

This paper is organized as follows: in Section 2, we briefly discuss the model and explain why it implies FCNC at the tree level. In Section 3, we evaluate the effective Hamiltonian for $B_d \to \tau^+\tau^-$ decay considering the contribution coming from Z and Z' bosons. Then corresponding branching ratio is also evaluated using the recent experimental data. In Section 4, we estimate the mass of Z' boson using the recent experimental value of branching ratio for $B_d \to \tau^+\tau^-$ decay and discuss our result.

2. The Model

In extended quark sector model [10, 21], including the three standard generations of the quarks, there is another $SU(2)_L$ singlet of charge $-\frac{1}{3}$. This model allows Z-mediated FCNCs. The up quark sector interaction eigenstates are identified with mass eigenstates but down quark sector interaction eigenstates are related to the mass eigenstates by a 4×4 unitary matrix which is denoted by K. The charged-current interactions are described by

$$L^W_{int} = \frac{g}{\sqrt{2}}(W^-_\mu J^{\mu^+} + W^+_\mu J^{\mu^-}), \tag{1}$$

$$J^{\mu^-} = V_{ij}\overline{u}_{iL}\gamma^\mu d_{jL}. \tag{2}$$

The charged-current mixing matrix V is a 3×4 submatrix of K

$$V_{ij} = K_{ij}; \text{for } i = 1, 2, 3; j = 1, 2, 3, 4. \tag{3}$$

Here, V is parameterized by six real angles and three phases, instead of three angles and one phase in the original CKM matrix.

The neutral-current interactions are described by

$$L^Z_{int} = \frac{g}{\cos\theta_W} Z_\mu (J^{\mu 3} - \sin^2\theta_W J^\mu_{em}). \tag{4}$$

$$J^{\mu 3} = -\frac{1}{2} U_{pq} \overline{d}_{pL} \gamma^\mu d_{qL} + \frac{1}{2} \delta_{ij} \overline{u}_{iL} \gamma^\mu u_{jL}. \tag{5}$$

In neutral-current mixing, the matrix for the down sector is $U = V^\dagger V$. Since in this case V is not unitary, $U \neq 1$. Its nondiagonal elements do not vanish:

$$U_{pq} = -K^*_{4p} K_{4q} for p \neq q. \tag{6}$$

Since the various U_{pq} are non-vanishing, they allow FCNC and would be signal for new physics (NP).

3. $B_d \to \tau^+\tau^-$ decay process in Z' model

Let us consider the $B_d \to l^+l^-$, $(l = \tau)$ decay process, which involves $b \to d$ transitions. The effective Hamiltonian describing this process can be written as [7, 22]:

$$H_{eff} = \frac{G_F \alpha}{\sqrt{2}\pi} \lambda_t [C_9^{eff} (\bar{d}\gamma^\mu P_L b)(\bar{l}\gamma^\mu l) + C_{10}(\bar{d}\gamma^\mu P_L b)(\bar{l}\gamma^\mu \gamma_5 l) + \frac{2C_7 m_b}{p^2} (\bar{d}\mathbf{p}\gamma^\mu P_R b)(\bar{l}\gamma^\mu \gamma_5 l)], \tag{7}$$

where G_F is the Fermi coupling constant, $\lambda_t = V_{tb}V^*_{td}$, $P_{R,L} = \frac{1}{2}(1 \pm \gamma^5)$, $p = P_+ + P_-$ the sum of the momentum of l^+ and l^-, and C_7, C_9^{eff} and C_{10} are Wilson coefficients [23] evaluated at the b quark mass scale.

We use the Vacuum Insertion Method (VIM) [24] for the evaluation of matrix elements and write the transition amplitude for this process as

$$M(B_d \to l^+l^-) = i\frac{G_F \alpha}{\sqrt{2}\pi} \lambda_t f_{B_d} C_{10} m_l (\bar{l}\gamma_5 l) \tag{8}$$

and the corresponding branching ratio [16,17] is given by

$$B(B_d \to l^+l^-) = \frac{G_F^2 \tau_{B_d}}{16\pi^3} \alpha^2 f^2_{B_d} m_{B_d} m_l^2 |V_{tb}V^*_{td}|^2 C^2_{10} \sqrt{1 - \frac{4m_l^2}{m^2_{B_d}}}. \tag{9}$$

From equation (8), it is clear that the amplitude for the decay of $B_d \to l^+l^-$ is proportional to m_l and thus the decay rates are suppressed by $(m_l/m_{B_d})^2$. The suppression is smallest for $B_d \to \tau^+\tau^-$ due to the large τ lepton mass. The value of branching ratio in the standard model is predicted as $B(B_d \to \tau^+\tau^-) = (2.22 \pm 0.04) \times 10^{-8}$ [5]. In 2006, BABAR [25] has placed the limit on $\tau^+\tau^-$ channel as: $B(B_d \to \tau^+\tau^-) < 4.1 \times 10^{-3}$ $(90\%\ C.L.)$. The difference in the observed branching ratio with respect to the SM prediction would provide a direction in which the SM should be extended.

Now considering the $B_d \to l^+l^-$, $(l = \tau)$ decay process in the presence of Z-mediated FCNC [10, 11, 21] at tree level , one can write the effective Hamiltonian [7, 22] as

$$H_{eff}(Z) = \frac{G_F}{\sqrt{2}} U_{db} [\bar{d}\gamma^\mu (1 - \gamma_5) b][\bar{l}(C^l_V \gamma_\mu - C^l_A \gamma_\mu \gamma_5) l], \tag{10}$$

where C^l_V and C^l_A are the vector and axial vector Zl^+l^- couplings and are given as

$$C^l_V = -\frac{1}{2} + 2\sin^2\theta_W, C^l_A = -\frac{1}{2}. \tag{11}$$

The transition amplitude is given as

$$M(B_d \to l^+l^-) = -i\frac{G_F}{\sqrt{2}}U_{db}f_{B_d}C_A^l 2m_l(\bar{l}\gamma_5 l) \tag{12}$$

and the corresponding branching ratio is given as

$$B(B_d \to l^+l^-)|_Z = \frac{G_F^2\tau_{B_d}}{4\pi}|U_{db}|^2 f_{B_d}^2 m_{B_d} m_l^2 |C_A^l|^2 \sqrt{1-\frac{4m_l^2}{m_{B_d}^2}}. \tag{13}$$

The same idea can be applied to Z' boson i.e., mixing among particles which have different Z' quantum numbers will induce FCNCs due to Z' exchange [6, 11] and surprisingly these effects can be just as large as Z-mediated FCNCs. The Z'-mediated coupling $U_{pq}^{Z'}$ can be generated via mixing of particles with same weak isospin and so suffer new suppression. Even though Z'-mediated interactions are suppressed relative to Z, these are compensated by $U_{pq}^{Z'}/U_{pq}^{Z} \sim M_2/M_1$. Thus the effect of Z'-mediated FCNCs are comparable to that of Z-mediated FCNCs. Since Z' doesnt couple to charged leptons in the leptophobic model, we can write the $H_{eff}(Z')$, with same coupling as that of $Z(g = g')$, as

$$H_{eff}(Z') = \frac{G_F}{\sqrt{2}}U_{db}[\bar{d}\gamma^\mu(1-\gamma_5)b][\bar{l}(C_V^l\gamma_\mu - C_A^l\gamma_\mu\gamma_5)l]\frac{M_Z^2}{M_{Z'}^2}. \tag{14}$$

Hence the net effective Hamiltonian can be written as $H_{eff} = H_{eff}(Z) + H_{eff}(Z')$ and

$$H_{eff} = \frac{G_F}{\sqrt{2}}U_{db}\left[\bar{d}\gamma^\mu(1-\gamma_5)b\right]\left[\bar{l}(C_V^l\gamma_\mu - C_A^l\gamma_\mu\gamma_5)l\right]\left(1+\frac{M_Z^2}{M_{Z'}^2}\right) \tag{15}$$

and the corresponding branching ratio is given as

$$B(B_d \to l^+l^-)|_{Z+Z'} = \frac{G_F^2\tau_{B_d}}{4\pi}|U_{db}|^2 f_{B_d}^2 m_{B_d} m_l^2 |C_A^l|^2 \sqrt{1-\frac{4m_l^2}{m_{B_d}^2}}(1+\frac{M_Z^2}{M_{Z'}^2}). \tag{16}$$

4. Results and discussion

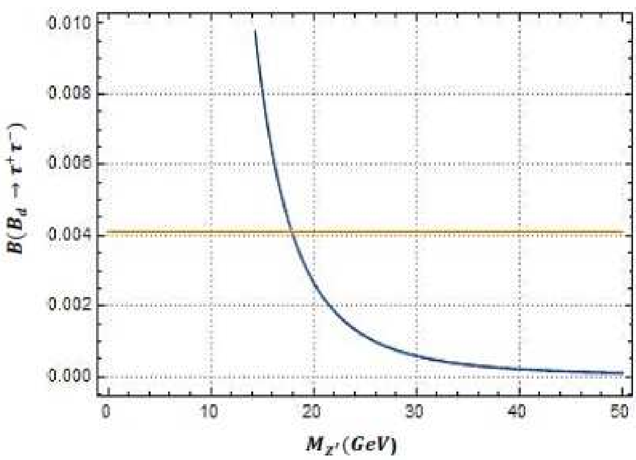

Figure 1. Blue line represents the variation of branching ratio $B(B_d \to \tau^+\tau^-)$ with $M_{Z'}$ and yellow line represents its experimental upper limit.

In this section, we estimate the mass of Z' boson using the upper bound of the experimental value $B(B_d \to \tau^+\tau^-) < 4.1 \times 10^{-3}$ [25]. For this purpose we use all the recent data from Particle Data Group 2014 [26]:

$m_\tau = 1776.99MeV$, $m_{B_d} = (5279.4 \pm 0.5)MeV$, average B_d lifetime $\tau_{B_d} = (1.536 \pm 0.014) \times 10^{-12}s$, decay constant $f_{B_d} = 190MeV$, $M_Z = 91.1876GeV$, $G_F = 1.16639 \times 10^{-5}GeV^{-2}$ and $\sin^2\theta_W = 0.23$. With these values, we observe that the value of branching ratio in Z' model is consistent with the value of $M_{Z'} \geq 18GeV$. The variation of branching ratio $B(B_d \to \tau^+\tau^-)$ with $M_{Z'}$ is shown in Fig. 1. The existence of light Z' boson could have important implications in dark matter (DM) phenomenology. Recently [27] it is shown that the genesis of DM is possible with a light Z' boson. They have studied the genesis of DM by a Z' portal for a spectrum of Z' mass in the range 1 GeV – 1 TeV. In [28] it is depicted that the strong first order electroweak phase transition (EWPT) can be realized in the light of Z' boson region, $M_{Z'} < 220GeV$. Furthermore, it is claimed that in our model [29] for a light Z' boson $M_{Z'} \sim 16GeV$, the D0 result for the same-sign dimuon charge asymmetry can be produced. Since long back from 1970s experimental particle physicists have been testing the accuracy of the SM with more precession of data. Many physicists think that failure of the SM will account for phenomena such as gravity and dark matter. It may be an approximation of another description beneath. This is clearly something that must be studied in more detail. We are looking forward to get more data and analysis of these decays as well as some more similar decays at the LHC Run-2 or any of the future colliders. Furthermore, the improved theory accuracy is also essential for interpreting the experimental findings in terms of the SM or new physics.

5. Acknowledgement

S. Sahoo acknowledges the financial support of NIT Durgapur through 'Research Initiation Grant' office order No. NITD/Regis/OR/25 dated 31st March, 2014. D. Banerjee gratefully acknowledges the Department of Science and Technology (DST), Govt. of India for providing INSPIRE Fellowship (IF140258) for her research.

References

[1] T. Blake, T. Gershon and G. Hiller, DOI:10.1146/annurev-nucl-102014-022231, Annu. Rev. Nucl. Part. Sci. (2015).
[2] T. Aaltonen et al. (CDF Collab.), Phys. Rev. D **87**, 072003 (2013).
[3] The CMS and LHCb Collaborations, Nature **522**, 68 (2015).
[4] R. Aaij et al. (LHCb Collab.), Phys. Rev. Lett. **110**, 021801 (2013).
[5] C. Bobeth et al., Phys. Rev. Lett. **112**, 101801 (2014).
[6] D. London, arXiv:1207.4672 [hep-ph] (2012).
[7] R. Mohanta, Phys. Rev. D **71**, 114013 (2005).
[8] S. Sahoo, D. Banerjee, M. Kumar and S. Mohanty, Int. J. Mod. Phys. A **27**, 1250184 (2012).
[9] G. Buchalla and A. J. Buras, Nucl. Phys. B **548**, 309 (1999).
[10] Y. Nir and D. Silverman, Phys. Rev. D **42**, 1477 (1990).
[11] M. Gronau and D. London, Phys. Rev. D **55**, 2845 (1997).
[12] A. J. Buras and J. Girrbach, Acta Phys. Pol. B **43**, 1427 (2012).
[13] S. Choudhury and N. Gaur, Phys. Lett. B **451**, 86 (1999); K. S. Babu and C. Kolda, Phys. Rev. Lett. **84**, 228 (2000); T. Blask et al., Phys. Lett. B **589**, 39 (2004).
[14] P. Langacker, Rev. Mod. Phys. **81**, 1199 (2008).
[15] A. Leike, Phys. Rev. **317**, 143 (1999).
[16] S. Sahoo, L. Maharana, S. Acharya and A. Roul, Int. J. Mod. Phys. A **20**, 2625 (2005); X.-G. He, G. Valencia, Phys. Rev. D **74**, 013011 (2006); D. Feldman, Z. Liu and P. Nath, Phys. Rev. Lett. **97**, 021801 (2006).
[17] K. S. Babu, C. Kolda and J. March-Russell, Phys. Rev. D **54**, 4635 (1996).
[18] S. Sahoo and L. Maharana, Phys. Rev. D **69**, 115012 (2004); V. Berger, C.-W. Chiang, P. Langacker and H.-S. Lee, Phys. Lett. B **580**, 186 (2004).
[19] A. Arhrib, K. Chung, C.-W. Chiang and T.- C. Yuan, Phys. Rev. D **73**, 075015 (2006).
[20] K. Cheung, C.- W. Chiang, N. G. Deshpande and J. Jiang, Phys. Lett. B **652**, 285 (2007).
[21] D. Silverman, Phys. Rev. D **45**, 1800 (1992); V. Barger, M. S. Berger, and R. J. N. Phillips, Phys. Rev. D **52**, 166 (1995).
[22] A. K. Giri and R. Mohanta, Phys. Rev. D **68**, 014020 (2003).
[23] A. J. Buras, M. Jamin and M. E. Lautenbacher, Nucl. Phys. B **408**, 209 (1993); G. Buchalla, A. J. Buras and M. E. Lautenbacher, Rev. Mod. Phys. **68**, 1125 (1996)

[24] M. K. Gaillard and B. W. Lee, Phys. Rev. D **10**, 897 (1974).
[25] B. Aubert et al., (BABAR Collaboration), Phys. Rev. Lett. **96**, 241802 (2006).
[26] K. A. Olive et al. [Particle Data Group], Chin. Phys. C **38**, 090001 (2014).
[27] X. Chu et al., JCAP **01**, 034 (2014)
[28] E. Senaha, Phys. Rev. D **88**, 055014 (2013).
[29] S. Sahoo, M. Kumar and D. Banerjee, Int. J. Mod. Phys. A **28**, 1350060 (2013).

Compact extra dimension and mass of mesons in a QCD potential model

Jugal Lahkar[a] and D. K. Choudhury[a,b]

(a) Department of Physics, Gauhati University, Guwahati-781014, Assam, India
(b) Physics Academy of North-East, Guwahati-781014, Assam, India

Presenter: Jugal Lahkar (*neetju77@gmail.com*); HEP.1, Oral, CICAHEP15.63

We consider a simple QCD potential model in compact extra dimension and find the wave function of mesons in higher dimensions (3 non compact + others compact) solving Schrodinger equation. Then we report the dimensional dependence of mass of heavy flavoured mesons considering only the Coulomb potential with a plausibly generalization to compact extra dimension, without taking into account the confinement effect, which is yet to be known in compact extra dimensions. Our analysis suggests that if the gluon effect, due to the Coulomb term can spread even to the compact extra dimension of size 1 fm - 10^{-4} fm, it can effectively account for the expected confinement effect, presumably indicating confinement-compact extra dimension duality. The above estimated range of compact extra dimension is not inconsistent with the corresponding bounds obtained from various experiments.

1. Introduction

According to current level of thought, notion of extra dimension is very important. Splitting one of the spatial dimension from the rest made it apparent that the structure of electromagnetism is contained in General theory of Relativity. Different theories such as Kaluza-Klein [1], ADD model [2], RS model [3] etc support this fact. If fields propagate on such extra dimension, mass of the standard model particles will change [1, 2]. The earlier analysis [4, 5] with assumption that all the extra-dimensions are of infinite extent do not correspond to current level of thought. In this work, we therefore confine to finite extra-dimension and apply to QCD potential model.

In the present work, we solve D-dimensional Schrodinger equation with modified Coulomb term in the potential. Specifically, we consider one finite extra-dimension and obtain proper wavefunction and normalization. We calculate mass of some heavy flavoured mesons, and show their variation with size of compact extra-dimension. We confine to heavy flavoured mesons [14, 15], because non-relativistic potential approach is more successful in such mesons. Our analysis suggests that if the gluon effect, due to the Coulomb term can spread even to the compact extra dimension of size 1 fm - 10^{-4} fm, it can effectively account for the expected confinement effect, presumably indicating confinement-compact extra dimension duality. The above estimated range of compact extra dimension is not inconsistent with the corresponding bounds obtained from various experiments. The last section includes summary of this work and future outlook.

2. Formalism:

2.1 Potential model in finite extra-dimension

We consider the general 3 dimensions to be 0 to α and the extra dimension to be compact within the range 0 to L [2, 3]. Thus

$$r_d^2 = r^2 + y^2, \tag{1}$$

where $r^2 = r_1^2 + r_2^2 + r_3^2$, y is the size of compact extra dimension. Hence,

$$r_d \simeq r + \frac{y^2}{2r}. \tag{2}$$

Now, we consider the Coulomb potential in d-dimension:

$$V(r_d) = -\frac{A}{r_d}, \tag{3}$$

where $A = \frac{4\alpha_s}{3}$ at $d = 3$ and with finite extra-dimension it is generalized to

$$\frac{4\alpha_s}{3} \longrightarrow \frac{4\alpha_s}{3} e^{-\mu_L y} = \frac{4\alpha_s}{3}(1 - \mu_L y) \tag{4}$$

for $\mu y \ll 1$. At $d = 3,\ y = 0$, and we get back the standard 3-dimensional QCD coupling constant. We assume that mass parameter (μ_L) occurred in equation (4) is identical to the mass of the heavy flavoured mesons.

2.2 Wave function (D-dimensional with only Coulomb term in compact extra dimension)

The D-dimensional Schrodinger equation is [17, 18]

$$\left[\frac{d^2}{dr^2} + \frac{d-1}{r_d}\frac{d}{dr} - \frac{l(l+d-2)}{r_d^2} + \frac{2\mu_L}{\hbar^2}(E - V_0)\right] R(r_d) = 0. \tag{5}$$

For ground state $(n = 0)$ we get the unperturbed wave function as

$$\psi(r_d) = N_d(r^2 + y^2)^{\frac{\sigma(d-3)}{2}} e^{-\mu_L A(r+\frac{y^2}{2r})}. \tag{6}$$

Now at $d = 3,\ y = 0$ we get from above equation (6) that

$$\psi(r) = Ne^{-\mu_L Ar}, \tag{7}$$

which is consistent with standard H-atom wave function [20] at $d = 3$ with $A = \frac{1}{\mu\alpha}$. Also, for consistency of the wave function with H-atom wave function μ_L corresponds to reduced mass μ of H-atom.

2.3 Normalization: with 3 non-compact and one compact extra dimension

The normalization condition [21] is

$$\int_0^{\alpha}\int_0^{l} dC_d(r^2 + y^2)^{\frac{\sigma(d-3)}{2}} |\psi(r, y)|^2 drdy = 1, \tag{8}$$

where $C_d = \frac{(\pi)^{\frac{d}{2}}}{\Gamma(\frac{d}{2}+1)}$. The normalization constant obtained from the above equation has got singularity at $d = 3$, but for $d = 3,\ L = 0$ it is free of singularity. At $d = 3$, in analogy with H-atom, N_H=$(\frac{\mu^3\alpha^3}{\pi})^{\frac{1}{2}}$, standard QCD normalization constant is

$$N_s = [\frac{(\mu\frac{4}{3}\alpha_s)^3}{\pi}]^{\frac{1}{2}}. \tag{9}$$

Now putting equation (6) in equation (8) we get (neglecting higher orders of L):

$$N_d = [\frac{(2\mu A)^{(2\sigma+\frac{3}{2})}}{dC_d(\frac{\pi}{\mu A})^{0.5}\Gamma(2\sigma + \frac{3}{2})}]^{\frac{1}{2}}. \tag{10}$$

For $d = 3$ and $A = \frac{4\alpha_s}{3}$, we find

$$N_d = [\frac{2^{2\sigma+1.5}}{4\pi^2\Gamma(2\sigma + \frac{3}{2})}][(\frac{4}{3}\alpha_s\mu)^{2\sigma+2}]^{\frac{1}{2}}. \tag{11}$$

Now, equating this with equation (9) for $\alpha_s = 0.39$ and $\mu = 0.27$ at c-scale, we get, $\sigma_f \approx \frac{\pi}{9}$ (by graphical method and using mathematica). The similar value of σ_f at b-scale for $\alpha_s = 0.22$ and $\mu = 0.173$ is $\frac{\pi}{16}$. Hence, the correct wave function in compact extra dimension with only Coulomb term in the potential is

$$\psi(r_d) = N_d(r_d)^{\frac{\sigma_f(d-3)}{2}} e^{-\mu A(r+\frac{y^2}{2r})}. \tag{12}$$

This is an improvement over the earlier result [4, 19], where σ_f is assumed to be 1.

2.4 Mass calculation : With only Coulomb term in compact extra dimension

Pseudoscalar meson mass can be computed from the following relation [15, 22]:

$$M_p = m_Q + m_{\overline{Q}} + \Delta E \tag{13}$$

where, $\Delta E = \langle H \rangle$. In D-spatial dimension, the Hamiltonian operator H has the form[18]:

$$H = -\frac{\nabla_d^2}{2\mu} + V(r_d) \tag{14}$$

where, $\mu = \frac{(m_Q)(m_{\overline{Q}})}{m_Q + m_{\overline{Q}}}$ is the reduced mass of the meson with m_Q and $m_{\overline{Q}}$ are the quark and anti-quark masses; $V(r_d)$ is the inter-quark potential given in equation (3), and ∇_d^2 is the Laplace's operator in D-dimension [18], which at $l = 0$ is given by

$$\nabla_d^2 \equiv \frac{d^2}{dr^2} + \frac{d-1}{r}\frac{d}{dr}. \tag{15}$$

Now, $\langle H \rangle$ can be expressed as (with only Coulomb term in the potential in compact extra dimension),

$$\langle H \rangle = \langle -\frac{\nabla_d^2}{2\mu} \rangle + \langle \frac{-A}{r_d} \rangle. \tag{16}$$

The correct D-dimensional wave function (3 non compact and other compact) is

$$\psi(r_d) = N_d (r^2 + y^2)^{\frac{\sigma(d-3)}{2}} e^{-\mu A (r + \frac{y^2}{2r})} \tag{17}$$

where, $\sigma = \frac{\pi}{9}$ and $A = \frac{4}{3}\alpha_s$ at $d = 3$. We consider,

$$\frac{4}{3}\alpha_s \longrightarrow \frac{4}{3}\alpha_s e^{-\mu L} \simeq \frac{4}{3}\alpha_s (1 - \mu L) \tag{18}$$

at $d = 3,\ L = 0$ and we get back to the standard 3-dimensional result. Since, $H = -\frac{\nabla_d^2}{2\mu} + V(r_d)$, so we get,

$$\langle H \rangle = \langle -\frac{\nabla_d^2}{2\mu} \rangle + \langle -\frac{1}{2\mu}\frac{\delta^2}{\delta y^2} \rangle + \langle -\frac{A}{r_d} \rangle = \langle H_1 \rangle + \langle H_2 \rangle + \langle H_3 \rangle. \tag{19}$$

Again, $\langle -\frac{\nabla_d^2}{2\mu} \rangle = \frac{9}{32\mu}\frac{\mu\pi}{12}^2$ [4], so

$$\langle H_1 \rangle = \langle -\frac{\nabla_d^2}{2\mu} \rangle = \frac{9}{32\mu}(\frac{\mu\pi}{12})^2. \tag{20}$$

For the only compact extra dimension, $\psi = N_d e^{-\mu A y}$ and with it we get,

$$\langle H_2 \rangle = \langle -\frac{1}{2\mu}\frac{\delta^2}{\delta y^2} \rangle = \frac{N_d^2 A}{4}(1 + 2\mu A L). \tag{21}$$

With only Coulomb term in the potential and considering the fact that $\frac{4}{3}\alpha_s \longrightarrow \frac{4}{3}\alpha_s(1 - \mu L)$, we get

$$\langle H_3 \rangle = \langle -\frac{A}{r_d} \rangle = N_d^2 A d C_d \left[\frac{1}{2}\frac{\sqrt{\pi}}{\sqrt{\mu A}} \frac{\Gamma(5\sigma + \frac{1}{2})}{(2\mu A)^{(5\sigma + \frac{1}{2})}} + \frac{1}{2}\sqrt{\pi} L \frac{\Gamma(5\sigma)}{(2\mu A)^{5\sigma}} \right] \tag{22}$$

neglecting higher orders of L as L is very small. Then we get the final result,

$$\langle H \rangle = \langle H_1 \rangle + \langle H_2 \rangle + \langle H_3 \rangle = \frac{9}{32\mu}(\frac{\mu\pi}{12})^2 + \frac{N_d^2 A}{4}(1 + 2\mu A L) + N_d^2 A d C_d \left[\frac{1}{2}\frac{\sqrt{\pi}}{\sqrt{\mu A}} \frac{\Gamma(5\sigma + \frac{1}{2})}{(2\mu A)^{(5\sigma + \frac{1}{2})}} + \frac{1}{2}\sqrt{\pi} L \frac{\Gamma(5\sigma)}{(2\mu A)^{5\sigma}} \right]. \tag{23}$$

3. Result

With the expression obtained for $\langle H \rangle$, for only Coulomb term in the potential in compact extra dimension we calculate the mass of heavy flavoured meson [4], [15] $B(\bar{b}c)$. We take the value of 'L' from Ref. [24]. Table 1 shows that as size of extra-dimension increases, mass also increases. Further, for $L = 0$ at$d = 3$, the theoretical mass is above the experimental value. That means, confinement effect reduces mass in 3D. We therefore raise the question if such reduction of mass due to the confinement effect can be generated equivalently through the assumption that gluon effect propagates to extra-dimension, which is shown in Table 2. In Table 2 we generalize the effect of confinement through the extra dimension with only coulomb potential for $B(\bar{b}c)$ at $\alpha_s = 0.39$. The expected mass can be generated with these assumption that if there is some unobservable extra-dimension. We show that for L $\sim$ 0.009 fm, exact experimental mass of $B(\bar{b}c)$ meson can be achieved at c-scale without confinement. This value of L is well within the experimental limit [24].

Table 1. Variation of mass of $B(\bar{b}c)$ with size of extra dimension.

Size (L in fm)	bare mass	$\langle H_1 \rangle + \langle H_2 \rangle$	$\langle -\frac{A}{r_d} \rangle$	M$_P$ (gev)
0.01	5.97	0.0.46439	0.44212	6.4343
0.02	5.97	0.47741	0.45512	6.4474
0.03	5.97	0.48784	0.4656	6.4578
0.04	5.97	0.49985	0.4776	6.469
0.05	5.97	0.51211	0.48986	6.4821

Table 2. Generation of mass of $B(\bar{b}c)$ without confinement.

L (fm)	QUARK mass of $q\bar{q}$	A	$\langle -\frac{A}{r_d} \rangle$	M$_P$ (Gev)	Exp. mass (Gev)
0.005	5.97	0.5175	0.266	6.24	
0.006	5.97	0.5170	0.269	6.247	
0.007	5.97	0.5163	0.271	6.25	
0.008	5.97	0.5157	0.272	6.26	
0.009	5.97	0.5152	0.2744	6.27	6.27

4. Discussion and Conclusion

We have developed a wave-function for mesons in D-dimension(3 non compact and other compact) considering only Coulomb term in the potential and find the correct normalization constant. Also we check whether our results agrees with well known 3-dimensional results [20], when dimension is reduced to 3.Our analysis indicates that if the gluon effect, due to the Coulomb term can spread [24] even to the compact extra dimension of size 1 fm - 10^{-4} fm, it can effectively account for the expected confinement effect, presumably indicating confinement-compact extra dimension duality. The above estimated range of compact extra dimension is not inconsistent with the corresponding bounds obtained from various experiments and theories suggested in different papers [2,3, 24]. Also,we have checked that above values of μ and L always satisfy $\mu_L y << 1$.

5. Acknowledgement

We thank Dr. Bhaskar jyoti Hazarika for helpful discussions, Dr. Sabyasachi Roy of Karimganj College for collaboration at the initial stage of the work . One of the authors (Jugal Lahkar) acknowledges CSIR for financial support.

References

[1] T. Kaluza, Sitzungsber. Preuss. Akad. Wiss. Berlin (Math. Phys.) **K1**, 966 (1921); O. Klein, Z. Phys. **37**, 895 (1926).
[2] N. Arkani Hamed, S. Dimopolous, G. Dvali, Phys. Lett. B **429**, 263 (1998).
[3] L. Randall, R. Sundrum, PRL. **83**, 17 (1999).
[4] S. Roy and D. K. Choudhury, Arxiv:1308.1757 [hep-ph].
[5] S. Roy and D. K. Choudhury, Phys. scr. **87**, 065101 (2013).
[6] C. Gang, Chinese Phys. **14**, 1075 (2005).
[7] S. H. Dong et al., Found. Phys. lett. **12**, 465 (1999).
[8] S. H. Dong, Phys. Scr. **64**, 273 (2001).
[9] S. H. Dong, *Wave equation in higher dimension*, Springer,pp 81 (2011), ISBN-978-94-007-1916-3.
[10] M. Bures and P. Seigl, Annals of Phy., **354**, 316 (2015).
[11] N. Isgur and M. B. Wise, Phy Lett.B **232**, 113 (1989).
[12] S. Roy, D. K. Choudhury., Phys. Scr., **86**, 045101 (2012).
[13] A. Delgarno and J. T. Lewis, Proc. R. Soc. Lond. **A23370** (1955).
[14] M. Neubart, Phy. Rept. **245**, 259 (1994)
[15] A. K. Rai, B. Patel and P. C. Vinodkumar, Phys. Rev. C **78**, 055202 (2008).
[16] M. Luscher and P. Weisz, JHEP. **07**, 049 (2002).
[17] S. Roy and D. K. Choudhury, Canadian J. Phy. **91**, 34 (2013).
[18] S. Roy, *Mesons in quantum chromodynamics and string inspired potential model* (2013).
[19] A. Beiser, *Concepts of Modern Physics*, pp 234 [ISBN:978-0-07-015155-0](2006).
[20] M. Eduarda and D. G. Henderson, *Experiencing Geometry: On plane and sphere*, Prentice Hall (1996).
[21] K. K. Pathak and D. K. Choudhury, Pramana J. Phys. **79 (6)**, 1385 (2012)
[22] F. Halzen and A. D. Martin, *Quarks and Leptons*, Wiley (1984).
[23] Limits on the size of extra dimension, Particle physics and cosmology: second tropical workshop, cp540, AIP, I-56396-965-3/00.
[24] J. J. Sakurai, *Advanced Quantum Mechanics*, Wiley (1986).
[25] E. Eichten et al., Phys. Rev. D **21**, 203 (1980).
[26] E. Eichten, Talk given at the Third International Conference at Vanderbilt University on New Results in High Energy Physics, Nashville, Tennesee, March 6-8 (1978).

Studying the Left-Right Symmetric Model through charged Higgs production at the LHC

Deepanjali Goswami, Poulose Poulose and Debasish Borah

Department of Physics, Indian Institute of Technology, Guwahati-781039, Assam, India

Presenter: Deepanjali Goswami (*goswamideepanjali@gmail.com*); HEP.4, Oral, CICAHEP15.72

We investigate the single production of doubly and singly charged Higgs bosons in the Minimal Left Right Symmetric Model (MLRSM), in association with gauge bosons and neutral scalars. In order to accommodate the present experimental constraints, the $SU(2)_R$ breaking scale is considered to be about 8 TeV and the vacuum expectation value of one of the Higgs doublets is set close to zero, while that of the other doublet is kept as the same as EW symmetry breaking scale. We have found that the cross-section for two particle productions involving doubly charged scalars is not significant enough at 14 TeV LHC. On the other hand, three particle productions like $H_L^{++}W^-H_3^0$ / $H_L^{++}W^-W^-$ / $H_L^{++}W^-A_2^0$ / $H_L^{++}W^-H_1^-$ are found to be significant with cross-section in the 1-10 pb range. Right handed doubly charged scalar (H_R^{++}) does not have enough production cross-section even in the three body production modes. We analyze the above processes considering the subsequent decays into SM final state particles. We also carry out the background analysis and establish the significant parameter space regions that could be probed at the LHC.

1. Introduction

The Standard Model (SM) successfully explains almost all the experimental results so far, including the measurements related to the recently discovered Higgs boson at LHC. Yet, there are many unanswered questions related to the hierarchy problem, dark matter, the number of families in the quark and lepton sector, neutrino mass problem, etc., requiring to go beyond the SM to find explanations. The Left-Right Symmetric Model (LRSM) is one of the simplest models beyond the SM, which has the potential to offer answers to some of the above issues. The gauge group of the LRSM is a very simple extension of the SM, with an additional $SU(2)_R$ symmetry under which the right-handed fermions transform as doublets, while the left-handed ones are invariant. This leads to three heavy gauge bosons $W_R^{\pm}$ and Z_R along with SM gauge bosons in EW scale.The presence of additional right-handed neutrinos give rise to Majorana Masses, resulting in naturally small neutrino masses through. This minimal version of the model, MLRSM incorporates a Higgs bi-doublet and two Higgs triplets. The Left -Right Symmetric gauge theory keep the fermionic content of the SM intact, also incorporate the full quark-lepton symmetry of the weak interactions and give rise the U(1) generator of the electroweak symmetry group a definite meaning in terms of the $B-L$ quantum number. The triplet representations of the Higgs fields are chosen such that they can couple to lepton-lepton channels, thereby leading to the generartion of Seesaw Mechanism.

The MLRSM is elaborately explained in [1, 2, 3, 4], to which we refer the reader for the details, while the next section introuduces the model in a concise manner, especially focusing on what is relevant to this report. Following this, in section 3, we discuss the process being considered, and the results obtained. In section 4 we summarise the study and present the conclusions.

2. The Model

The full Lagrangian of the MLRSM, with the gauge symmetry of $SU(3)_c \times SU(2)_L \times SU(2)_R \times U(1)_{B-L}$ is discussed in Ref. [1]. In order to be brief, we shall present the scalar potential of the model, which is relevant to the phenomenology of the Higgs sector at the LHC. The bi-doublet (ϕ), and the left- and right-triplet scalar fields transform under the $SU(3)_c$, $SU(2)_L$, $SU(2)_R$ and $U(1)_{B-L}$ gauge groups as denoted in the brackets along side the fields below:

$$\phi(1,2,2,0),\ \Delta_L(1,3,1,2),\ \Delta_R(1,1,3,2). \tag{1}$$

The $B-L$ quantum number in Δ_R field has been chosen to realise the seesaw mechanism to explain small neutrino masses. A convenient representation of the field is given by the 2×2 matrices:

$$\phi = \begin{pmatrix} \phi_1^0 & \phi_1^+ \\ \phi_2^- & \phi_2^0 \end{pmatrix}, \quad \Delta_{L,R} = \begin{pmatrix} \delta_{L,R}^+/\sqrt{2} & \delta_{L,R}^{++} \\ \delta_{L,R}^0 & -\delta_{L,R}^+/\sqrt{2} \end{pmatrix}. \tag{2}$$

The most general scalar field potential of the model can be written as [5]

$$\begin{aligned}
V(\phi,\Delta_L,\Delta_R) &= -\mu_1^2(Tr[\phi^\dagger\phi]) - \mu_2^2(Tr[\tilde{\phi}\phi^\dagger] + (Tr[\tilde{\phi}^\dagger\phi])) - \mu_3^2(Tr[\Delta_L\Delta_L^\dagger] + Tr[\Delta_R\Delta_R^\dagger]) \\
&+\lambda_1((Tr[\phi\phi^\dagger])^2) + \lambda_2(Tr[\tilde{\phi}\phi^\dagger]^2 + Tr[(\tilde{\phi}^\dagger\phi])]^2) + \lambda_3(Tr[\tilde{\phi}\phi^\dagger]Tr[\tilde{\phi}^\dagger\phi]) \\
&+\lambda_4(Tr[\phi\phi^\dagger](Tr[\tilde{\phi\phi}] + Tr[\tilde{\phi}^\dagger\phi])) + \rho_1((Tr[\Delta_L\Delta_L^\dagger])^2 + (Tr[\Delta_R\Delta_R^\dagger])^2) \\
&+\rho_2(Tr[\Delta_L\Delta_L]Tr[\Delta_L^\dagger\Delta_L^\dagger] + Tr[\Delta_R\Delta_R]Tr[\Delta_R^\dagger\Delta_R^\dagger]) + \rho_3(Tr[\Delta_L\Delta_L^\dagger]Tr[\Delta_R\Delta_R^\dagger]) + \\
&+\rho_4(Tr[\Delta_L\Delta_L]Tr[\Delta_R^\dagger\Delta_R^\dagger]) + \alpha_1(Tr[\phi\phi^\dagger](Tr[\Delta_L\Delta_L^\dagger] + Tr[\Delta_R\Delta_R^\dagger])) + \alpha_2(Tr[\phi\tilde{\phi}^\dagger]Tr[\Delta_R\Delta_R^\dagger] \\
&+Tr[\phi^\dagger\tilde{\phi}]Tr[\Delta_L\Delta_L^\dagger]) + \alpha_2^\star(Tr[\phi\tilde{\phi}^\dagger]Tr[\Delta_R\Delta_R^\dagger] + Tr[\phi^\dagger\tilde{\phi}]Tr[\Delta_L\Delta_L^\dagger]) \\
&+\alpha_3(Tr[\phi\phi^\dagger\Delta_L\Delta_L^\dagger] + Tr[\phi^\dagger\phi\Delta_R\Delta_R^\dagger]) + \beta_1(Tr[\phi\Delta_R\phi^\dagger\Delta_L^\dagger] + Tr[\phi\Delta_L\phi\Delta_R^\dagger]) + \\
&\beta_2(Tr[\tilde{\phi}\Delta_R\phi^\dagger\Delta_L^\dagger] + Tr[\tilde{\phi}^\dagger\Delta_L\phi\Delta_R^\dagger]) + \beta_3(Tr[\phi\Delta_R\tilde{\phi}^\dagger\Delta_L^\dagger] + Tr[\phi^\dagger\Delta_L\phi\Delta_R^\dagger]).
\end{aligned} \tag{3}$$

Because of the non-zero quantum number $B-L$ of the Δ_R and Δ_L triplets, these always appear in quadratic combinations. Here, $\tilde{\phi} \equiv \tau_2\phi^\star\tau_2$, and the LR symmetry implies that the Lagrangian is symmetric under

$$\Delta_R \leftrightarrow \Delta_L, \phi \leftrightarrow \phi^\dagger. \tag{4}$$

The $SU(2)_R$ symmetry is broken spontaneously with the neutral Higgs fields δ_R^0 acquiring VEV of υ_R, leading to massive W_R and Z_R, and also generating masses to the right-handed neutrinos. The VEV's of the higgs bidoublet field κ_1 and κ_2 with the relation of SM VEV $v = \sqrt{k_1^2 \pm k_2^2}$ have double action of breaking the remaining symmetry $SU(2)_L \times U(1)_{B-L}$ down to the usual $U(1)_{EM}$ and setting the mass scale for the W_L and Z boson along with quark and lepton Dirac masses. The VEV of the left-triplet, $<\delta_L^0> = \upsilon_L$, if present, will affect the precision electroweak observable, ρ parameter, and therefore requires to be very small (less than 3.5 GeV) [6]. The VEV υ_R must be larger than κ_1 and κ_2 such that the mass of W_R and Z_R are significantly heavier than W_L and Z. After the symmetry breaking of the potential, we will have three extra heavy gauge bosons $W_R^\pm$ and Z_R; four neutral Higgs scalars H_0^0, H_1^0, H_2^0 and H_3^0; two neutral pseudo scalars A_1^0, A_2^0 and four charged Higgs scalars $H_1^\pm, H_2^\pm, H_L^{\pm\pm}, H_R^{\pm\pm}$. The parameters and mass relations of scalars and gauge bosons of MLRSM can be found in Ref. [7].

The recent LHC analysis limits the W_R mass to be above 2.8 TeV [8, 9]. For the left-right symmetry of the model, we considered $g_L = g_R$. Z_R is related to the W_R mass, $M_{Z_2} \simeq 1.7M_{W_2}$. The heavy gauge boson masses restrict the $SU(2)_R$ breaking scale to be $\upsilon_R > 5$ TeV, which dictates the mixing between the left and right sectors to be negligibly small, due to the relation, $\tan 2\xi = -\frac{2k_1k_2}{\upsilon_R^2}$. Experimental limits on $W_L - W_R$ mixing constrains $\xi \leq 0.05$ [6]. We have also taken in to account the bounds on neutral Higgs bosons obtained from FCNC constraints assuming $M_{A_1^0}, M_{H_1^0} > 15$ TeV by requiring $\alpha_3 = 7.1$. Assuming a 100% same-sign di-lepton decay, the LHC direct searches limit the doubly charged Higgs boson mass to be $M_{H^{++}} \geq 445$ GeV (409 GeV) for CMS (ATLAS) [10, 11].

3. Results

We consider the production of one doubly charged Higgs boson in association with other Higgses, as well as the gauge bosons at the 13 TeV LHC. Compatible with the constrained described above, we consider the following Benchmark Points (BP).

Input parameters:

υ_R = 8 TeV, υ_L = 0, v = 246 GeV, k_1 = 246 GeV, k_2 = 0

ρ_1 = 0.239764, ρ_2 = 2.36 $\times 10^{-4}$, ρ_3 = 0.48, α_3 = 4.69, λ = 0.13

Derived masses (in GeV):

$W_R^{\pm}$ = 3676.9 , Z_R = 6150.7, H_0^0 = 125, H_1^0 = 15073, H_2^0 = 5539.84, H_3^0 = 122.9

H_1^+ = 350, H_2^+ = 15076.7, A_1^0 = 15073, A_2^0 = 122.9, H_L^{++} = 479.5, H_R^{++} = 495

We have calculated the production cross-section of different channels containing $H_{L/R}^{++}$ in association with scalars and gauge bosons with BP mentioned above at 13 TeV LHC as shown in Table 1. It is seen that the cross-section for production of $H_L^{++}H_1^-$ is sizable at 13 TeV LHC.

Table 1. List of production cross-section of $H_{L/R}^{\pm}$ in association with gauge boson and scalars with the BP at 13 TeV LHC.

Production of H_R^{++} at LHC	σ in fb	Production of H_L^{++} at LHC	σ in fb
$H_R^{++}W^-$	0	$H_L^{++}W^-$	0
$A_2^0H_3^0$	0.4	$H_L^{++}H_1^-$	4.2
$H_R^{++}W_2^-$	0.02	$H_L^{++}W^-H_3^0$	2.0
$H_R^{++}W^-H_1^-$	0	$H_L^{++}W^-A_2^0$	2.0
$H_R^{++}ZH_1^-$	0	$H_L^{++}W^-H_1^-$	1.8
$H_R^{++}W^-A_2^0/H_3^0$	0	$H_L^{++}ZH_1^-$	0.02
$H_R^{++}H_1^-H_1^-$	0.007	$H_L^{++}W^-W^-$	0
$H_R^{++}W_2^-W_2^-$	$6.39.10^{-9}$	$H_L^{++}W^-\gamma$	0

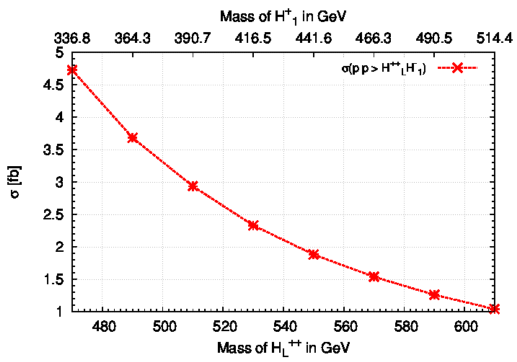

Figure 1. Variation of production cross-section of $H_L^{++}H_1^-$ with different mass of H_L^{++} at 13 TeV LHC.

The variation of cross-section for $H_L^{++}H_1^-$ produced at LHC with different mass of H_L^{++}/H_1^+ is depicted in Fig. 1, which decreases with increasing mass of H_L^{++}/H_1^+. The channel we considered for our preliminary study at LHC is $H_L^{++}W^-H_3^0/A_2^0$, which constitutes most of $H_L^{++}H_1^-$, with subsequent decay of $H_1^- \rightarrow W^-H_3^0/A_2^0$. Below we list out all possible tri-linear and quartic couplings, which contribute to the above process:

$H_1^-W^-H_L^{++}$: i $\cos\xi\; g_W$, $\qquad$ $W^+H^-H_3^0(W^+H^-A_2^0)$: i $\cos\xi\; g_W/\sqrt{2}\,(\cos\xi g_W/\sqrt{2})$

$W^-H_3^0W^-H_L^{++}$: -i $\cos\xi^2\; g_w^2\sqrt{2}$, $\qquad$ $H_R^{++}H_3^0H_L^{++}$: -2i $\rho_4\upsilon_R$

$H_2^-H_1^-H_L^{++}$: $\frac{i\alpha_3 k_1 k_2}{v\sqrt{1+0.5(k_1^2-k_2^2)^2/v^2\upsilon_R^2}}$, $\qquad$ $H_1^-H_3^0H_2^-$: $\frac{-i\alpha_3 k_1 k_2}{v\sqrt{2}\sqrt{1+0.5(k_1^2-k_2^2)^2/v^2\upsilon_R^2}}$

In Table 2 we present the cross sections, at two different chosen values of $\upsilon_R = 8$, and 10 TeV at 13 TeV LHC. The BR of $H_L^{++} \rightarrow W^+H_1^+$ is 99% and corresponding BR of $H_1^+ \rightarrow W^+H_3^0$ is 50 %. The cross-section of the major SM background is also listed in Table 2. The Transverse Momentum (PT) of W boson and the Missing Transverse Energy (MET) for the intermediate state $W^+W^-W^+\nu_\ell\nu_\ell\nu_\ell\nu_\ell$ for signal with two different υ_R value of 8 TeV and 10 TeV are showed in red and blue respectively and in green, PT of W boson and MET for SM

Table 2. Final state cross-section with different υ_R value along with SM background at LHC.

Signal	cross-section in fb
$pp \to H_L^{++}W^-H_3^0 \to W^+W^-W^+\nu_\ell\nu_\ell\nu_\ell\nu_\ell$	σ_{13TeV} = 0.94 fb (υ_R = 8 TeV) σ_{13TeV} = 2.6 fb (υ_R = 10 TeV)
SM background $pp \to W^+W^-W^+\nu_\ell\tilde{\nu}_\ell$	σ_{13TeV} = 0.08 fb

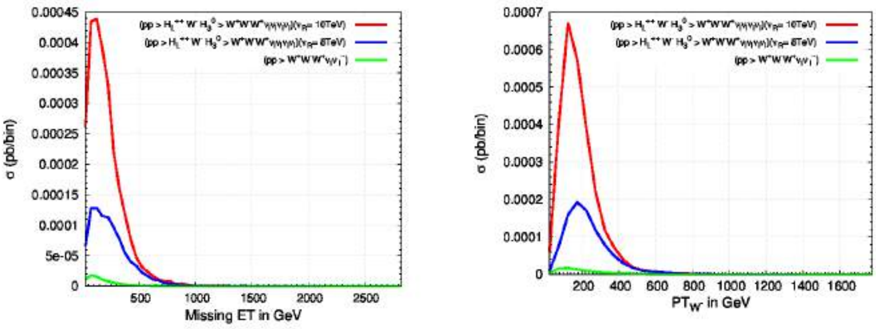

Figure 2. Kinematic distribution of W boson for the final state $W^+W^-W^+\upsilon_\ell\upsilon_\ell\upsilon_\ell\upsilon_\ell$ of the process $pp \to H_L^{++}W^-H_3^0$ with different υ_R at 13 TeV LHC.

background are shown in Fig. 2. In this preliminary study, we have found that MLRSM signal with a chosen BP can be found over SM background at 13 TeV LHC.

4. Summary and outlook

The Minimal Left Right Symmetric Model (MLRSM) has the potential to address the issues of dark matter as well as the neutrino mass problems. The Higgs sector of this model is much richer and non-standard with triplet and bidoublet scalar fields present, leading to doubly charged Higgs boson in the physical spectrum, apart from singly charged and more than one neutral Higgs bosons. In the project being discussed, we consider the signatures of the doubly charged Higgs bosons at the LHC. In the preliminary analysis, we have found that distinct scenarios (with different Benchmark Points in the parameter space) where cross section for single production of H_L^{++} along with H_1^- is significant . Detailed of the study will be carried out with the analyses of detector level final states, to establish methods to identify the signature of the doubly charged Higgs bosons for the selected Benchmark Points.

5. Acknowledgement

One of the authors (DG) is specialy thankful to the orgnizers of the CICAHEP-2015 for their dearly hospitality at Dibrugarh University. Same author also wants to acknowledge the co-authors of this research work for their discussion and help to carry out the study.

References

[1] G. Senjanovic and R. N. Mohapatra, Phys. Rev. D **12**,1502 (1975); R. N. Mohapatra, F. E. Paige and D.P. Sidhu, ibid. **17**, 2462 (1978); R. N. Mohapatra and G. Senjanovic, Phys. Rev. Lett. **44**, 912 (1980); Phys. Rev. D **23**, 165 (1981).
[2] C. S. Lim and T. Inami, Prog. Theor. Phys. **67**, 1569 (1982); doi:10.1143/PTP.67.1569.
[3] J. F. Gunion, J. Grifols, A. Mendez, B. Kayser and F. I. Olness, Phys. Rev. D **40**, 1546 (1989); doi:10.1103/PhysRevD.40.1546.
[4] N. G. Deshpande, J. F. Gunion, B. Kayser and F. I. Olness, Phys. Rev. D **44**, 837 (1991); doi:10.1103/PhysRevD.44.837.

[5] P. Duka, J. Gluza and M. Zralek, Annals Phys. **280**, 336 (2000); doi:10.1006/aphy.1999.5988 [hep-ph/9910279].
[6] J. Beringer *et al.* [Particle Data Group Collaboration], Phys. Rev. D **86**, 010001 (2012); doi:10.1103/PhysRevD.86.010001.
[7] A. Roitgrund, G. Eilam and S. Bar-Shalom, arXiv:1401.3345 [hep-ph].
[8] CMS Collaboration [CMS Collaboration], CMS-PAS-EXO-12-017.
[9] C. Vuosalo [CMS Collaboration], PoS DIS **2013**, 122 (2013) [arXiv:1307.2168].
[10] CMS Collaboration [CMS Collaboration], CMS-PAS-HIG-12-005.
[11] G. Aad *et al.* [ATLAS Collaboration], Eur. Phys. J. C **72**, 2244 (2012); doi:10.1140/epjc/s10052-012-2244-2 [arXiv:1210.5070 [hep-ex]].

Medium screening effects on the different bottomonia states

Palak Bhatt, Smruti Patel, P. C. Vinodkumar
Department of Physics, Sardar Patel University, Vallabh Vidyanagar, Gujarat-388120, India

Presenter: Smruti Patel (*fixizsmruti@gmail.com*); HEP.3, poster, CICAHEP15.92

We have studied the stability of bottomonia states in QGP by incorporating color screening effects and vacuum screening effects. We have particularly looked into the medium effects on the ground state and excited states of bottomonia. The dependence of energy eigenvalues on screening parameter μ and the strength of the quark-antiquark potential have been studied. It is observed that with increase in the potential strength, color screening radii r_D increases, while vacuum screening parameter μ_{vs} decreases with increase in potential strength.

1. Introduction

The relativistically heavy ion collision experiments at the RHIC at Brookhaven National Laboratory and LHC at CERN, characterize the properties of the matter at high temperature with high density. This leads to the deconfined state of hadronic matter because of the screening effects between quarks and glouns. As the hadron moves through the medium, the higher excited states with smaller binding energy and higher radii breakup to open quark-antiquark. There are menay attempts to understand the dissociation phenomenon of quarkonia $Q\bar{Q}$ states in a deconfined medium using theories like QCD sum rules, lattice calculation, effective field theories and effective potential models. The study of a deconfined medium has been attempted by solving the schrödinger equation with a non-relativistic Hamiltonian given by

$$H = M + \frac{p^2}{2m} + V(r,T) \tag{1}$$

where, $M = m_1$+m_2 and $m = \frac{m_1 m_2}{m_1+m_2}$. Here, $m_{1/2}$ corresponds, to the mass of the quark/antiquark constituting the quarkonia states. For the bottomonium, the bottom quark mass is taken as $m_b = 4.746$ GeV/c^2 [3]. The medium dependent quark-antiquark potential [4] is considered as

$$V(r,\mu(T)) = \frac{-\alpha}{r} exp[-\mu(T)r] + \frac{\sigma}{\mu(T)}(1 - exp[-\mu(T)r^{\nu}]) \tag{2}$$

where, $\alpha = 0.471$ [5] and σ has been determined by taking the corresponding spin average mass of bottomonia (1s, 2s and 1p-states) without considering the medium effects ($\mu \rightarrow$0). The parameter σ for different choices of ν thus are obtained are plotted in the Fig. 1. It is found that for $\nu = 1$ the value of σ remains almost same for the different $b\bar{b}$ states.

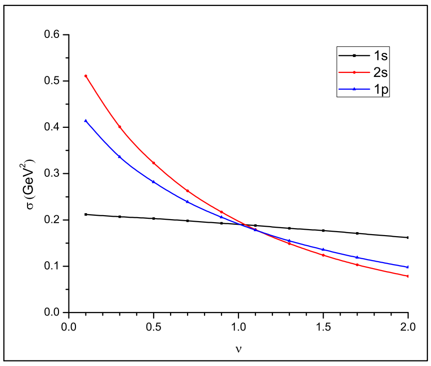

Figure 1. String tension σ at different choices of power index ν for bottomonia.

Table 1. Screening parameters of the $b\bar{b}$ (1s) state for $\mu = \mu_c$ for the different choices of ν.

ν	σ	μ_c	r	M	r_D
	$GeV^{\nu+1}$	GeV	fm	GeV	fm
0.1	0.212	1.3640	0.39804	9.6474	0.14467
0.3	0.207	1.3374	0.39389	9.6468	0.14755
0.5	0.203	1.3155	0.38960	9.6463	0.15000
0.7	0.198	1.2969	0.38611	9.6447	0.15215
0.9	0.193	1.2823	0.38369	9.6426	0.15389
1.0	0.192	1.2776	0.38253	9.6423	0.15445
1.1	0.188	1.2712	0.38228	9.6399	0.15523
1.3	0.1821	1.2619	0.38184	9.6363	0.15637
1.5	0.177	1.2552	0.38180	9.6330	0.15721
1.7	0.171	1.2490	0.38231	9.6289	0.15799
2.0	0.162	1.2408	0.38343	9.6226	0.15904

Table 2. Screening parameters of the $b\bar{b}$ (2s) state for $\mu = \mu_c$ for the different choices of ν.

ν	σ	μ_c	r	M	r_D
	$GeV^{\nu+1}$	GeV	fm	GeV	fm
0.1	0.511	1.0600	0.71679	9.9740	0.18616
0.3	0.401	0.9472	0.79303	9.9153	0.20833
0.5	0.323	0.8359	0.86467	9.8784	0.23607
0.7	0.263	0.7255	0.93271	9.5453	0.27202
0.9	0.217	0.6228	0.99571	9.8404	0.31685
1.0	0.192	0.5726	1.03308	9.8273	0.34465
1.1	0.179	0.5340	1.06148	9.8272	0.36955
1.3	0.149	0.4646	1.14111	9.8127	0.42475
1.5	0.124	0.4128	1.23972	9.7924	0.47805
1.7	0.103	0.3761	1.34601	9.7657	0.52470
2.0	0.0784	0.3436	1.47302	9.7202	0.57433

2. Colour screening effects

The Schrödinger equation

$$\left[\frac{1}{2\mu}\left(\frac{-d^2}{dr^2} + \frac{l(l+1)}{r^2}\right) + V(r)\right]\Phi_{n,l}(r) = E_{n,l}(r)\Phi_{n,l}(r) \tag{3}$$

with the potential defined by equation (2) is solved to get the energy eigenvalue $E^{n,l}(\mu)$ as a function of the medium parameter μ. We now define an effective binding energy expressed as [3, 6]

$$E_{cs}^{n,l}(\mu) \equiv 2m + \frac{\sigma}{\mu} - E_{n,l}(\mu). \tag{4}$$

$E_{cs}^{n,l}(\mu)$ described by equation (4) provides a positive value for the bound state and as μ increases, it decreases. For a particular value of $\mu = \mu_c$ at which

$$E_{cs}^{n,l}(\mu = \mu_c) = 0 \tag{5}$$

defines a critical value for the screening mass μ_c, beyond which no more binding is possible and it just dissociates.

Table 1 to 3 contains the screening parameters of 1s, 2s, and 1p-state of the $b\bar{b}$ and the Fig. 2 shows the change in binding energy with respect to screening parameter μ for different choices of potential exponent ν. The value of μ_c is extracted from the condition given by equation (5). It is observed that the critical value for the screening mass μ_c decreases with increase in the choice of potential exponent ν. Also with increase of ν, the color screening radii r_D ($r_D = 1/\mu_c$) and the r.m.s value (r) at $\mu = \mu_c$ show a increasing trend (see Fig. 3).

Table 3. Screening parameters of the $b\bar{b}$ (1p) state for $\mu = \mu_c$ for the different choices of ν.

ν	σ	μ_c	r	M	r_D
	$GeV^{\nu+1}$	GeV	fm	GeV	fm
0.1	0.414	1.0717	0.69182	9.8783	0.18412
0.3	0.336	0.9430	0.75084	9.8484	0.20925
0.5	0.282	0.8238	0.80592	9.8343	0.23954
0.7	0.239	0.7115	0.85072	9.8279	0.27735
0.9	0.206	0.6143	0.87292	9.8273	0.32122
1.0	0.192	0.5725	0.87716	9.8273	0.34469
1.1	0.178	0.5349	0.88272	9.8248	0.36892
1.3	0.155	0.4731	0.90015	9.8196	0.41712
1.5	0.136	0.4249	0.93709	9.8121	0.46443
1.7	0.119	0.3857	0.99319	9.8005	0.51163
2.0	0.098	0.3407	1.10460	9.7793	0.57913

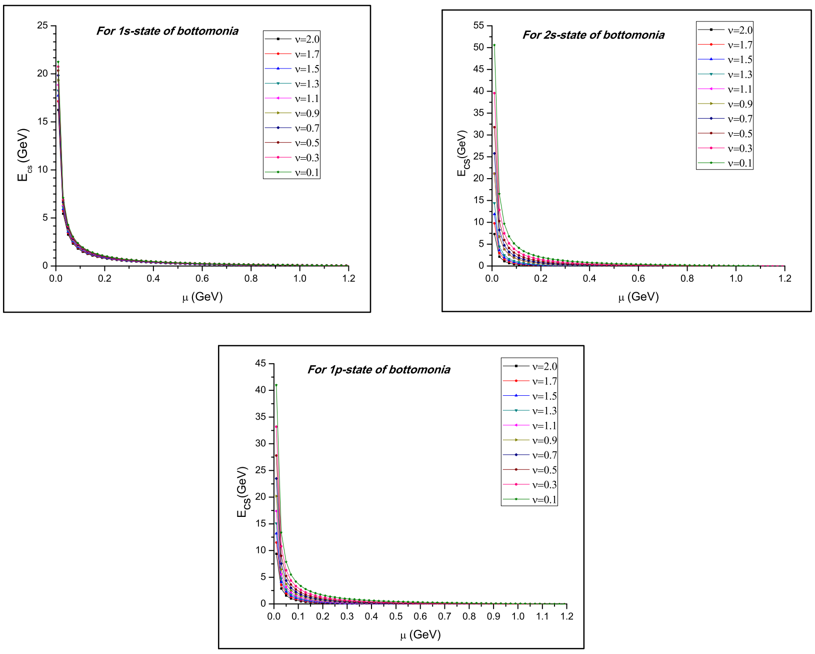

Figure 2. Colour Screening energy $E_{cs}^{n,l}(\mu)$ of the bound states of bottomonium for the different values of ν.

3. Vacuum screening effects

At $T = 0$, the absence of light quarks indicates the screening parameter $\mu = 0$ while the presence of light quark-antiquark from vacuum correspond to $\mu \neq 0$. As the separation between $Q - \bar{Q}$ increases the gluonic flux that binds Q and $\bar{Q}$ breaks and the light quark and antiquark pairs are produced out of vacuum. This breaking of string is attributed to the creation of $q\bar{Q}$ and $\bar{q}Q$ but not exactly due to colour screening. Energy is required to bring out the virtual $q\bar{q}$ pair from vacuum and hence, $\mu \neq 0$. Considering the vacuum screening, the effective binding energy can be represented as [3]

$$E_{vs}(T = 0) = 2m_{b\bar{q}} - M_{b\bar{b}}. \tag{6}$$

Comparing equation (6) with equation (4) the vacuum screening parameter, calculated for the different choices of power exponent ν and we get the vacuum screening parameters which are tabulated in the Table 4.

The effect of medium on the binding energy of the $b\bar{b}$ states are studied by introducing a medium dependent

Table 4. Vacuum screening parameter μ_{vs} for bottomonia states.

ν	μ_{vs}(GeV)		
	Υ	$\Upsilon^{'}$	χ_b
0.1	0.1712	0.3093	0.2534
0.2	0.1708	0.3004	0.2486
0.3	0.1704	0.2915	0.2438
0.5	0.1698	0.2779	0.2356
0.7	0.1690	0.2613	0.2260
0.9	0.1682	0.2453	0.2164
1.0	0.1676	0.2283	0.2085
1.1	0.1671	0.2195	0.2033
1.3	0.1663	0.2022	0.1930
1.5	0.1654	0.1856	0.1827
1.7	0.1645	0.1695	0.1725
1.9	0.1637	0.1543	0.1624
2.1	0.1628	0.1416	0.1528
2.3	0.1619	0.1288	0.1433
2.5	0.1610	0.1174	0.1342
2.7	0.1601	0.0927	0.1218
3.0	0.1587	0.0752	0.1081

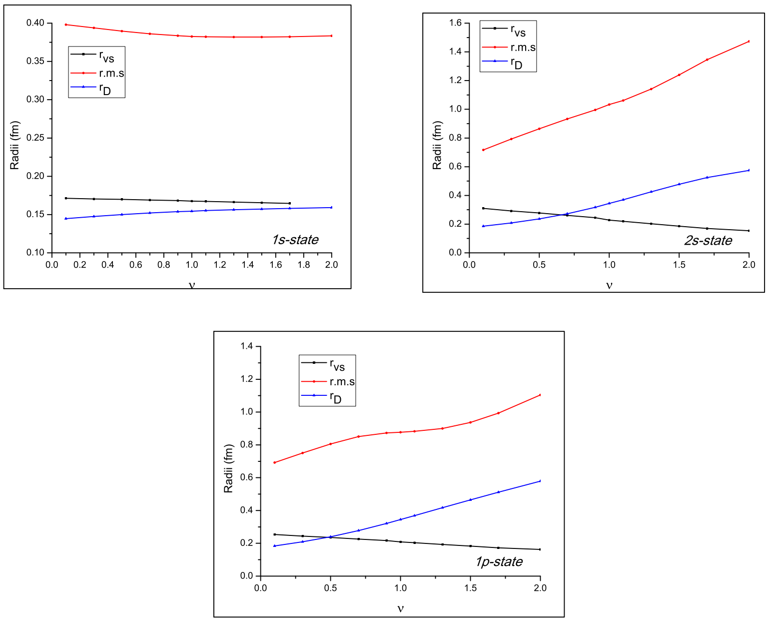

Figure 3. Screening effects on the different states of bottomonia.

screening mass parameter μ. For the different choices of μ we have calculated the effective binding energy and the bound state radii by solving the Schrödinger equation. Here, we defined an colour screening effective binding energy ($E_{cs}^{n,l}$) which is found to vanish for a particular value of $\mu = \mu_c$. This value μ_c is then defined as critical screening mass parameter of the quarkonia state above which bound state will not be possible. And corresponding to this μ_c we obtained the screening parameter $r_D = 1/\mu_c$ and the r is radius of last binding of bottomonia states for each choices of ν.

References

[1] T. Matsui and H. Satz, Phys. Lett. B **178**, 416 (1986).
[2] B. K. Patra, V. Agotiya, V. Chandra, Eur. phys. J. C **61**, 705 (2009).
[3] F. Karsch, M. T. Mehr, H. Satz, Z.Phys. C - Particles and Fields **37**, 617 (1988).
[4] Arpit Parmar, Bhavin Patel, P. C. Vinodkumar, Nuclear Physics A **848**, 299 (2010).
[5] S. Jacobs, M. G. Olsson, C. Suchyta, Phys. Rev. D **33**, 3338 (1986).
[6] W. Lucha, F. Schorberl, Int. J.Mod. Phys. C **10**, 607 (1999), arXiv:hepph/9811453v2.

Performance of PANDA barrel TOF detector : A simulation study

K. Dutta and K. Kalita

Department of Physics, Gauhati University, Guwahati-781014, Assam, India

Presenter: K. Dutta (*kamalpdutta@gmail.com*); HEP.3, Poster, CICAHEP15.106

The barrel time-of-flight (TOF) detector for PANDA experiment at GSI, Germany is proposed to be a Scintillator tile hodoscope (SciTil) using about 6000 small scintillator tiles readout by silicon photomultiplier (SiPM). Each of the scintillator tiles has the dimension of $3 \times 3 \times 0.5$ cm^3 . This thin scintillator hodoscope provides π/K separation for particle momentum below 700 MeV/c with the time resolution of 100 ps. We perform a simulation work to study the performance of this detector sub-system. Some of the preliminary results are presented in this paper.

1. Introduction

PANDA (anti**P**roton **AN**nihilation at **DA**rmstdt) is one of the major projects at FAIR, GSI, Germany [1]. The main objective of this experiment is to study the fundamental questions of hadron physics and QCD in $p\bar{p}$ annihilation using high intensity cooled anti-proton beams with momenta between 1.5 GeV/c and 15 GeV/c. To achieve high momentum resolution and full solid angle coverage, the PANDA detector is split in to two parts: target spectrometer and forward spectrometer (see Fig. 1). The target spectrometer is a complex detector consisting of several sub-systems surrounding the interaction point. It is surrounded by a 2T superconducting solenoid magnet. A Micro Vertex Detector (MVD), close to interaction point, detects secondary vertices of D and Hyperon decays. The Straw Tube Tracker (STT) is the central tracking system around the MVD. A cherenkov counter named DIRC (Detection of Internally Reflected Cherenkov light), provides π/K separation for particle momenta up to 3.5 GeV/c. The barrel Time-of-Flight (TOF) detector, consists of plastic scintillator tiles with a time resolution of 100 ps. It is used to identify particles of momentum below cherenkov threshold. Following the TOF detector, an electromagnetic calorimeter (EMC) is placed to detect e^-, e^+ and γ particles. The Muon detector is the outermost part of the PANDA target spectrometer. The complete description and technical details of the PANDA detector can be found elsewhere [2].

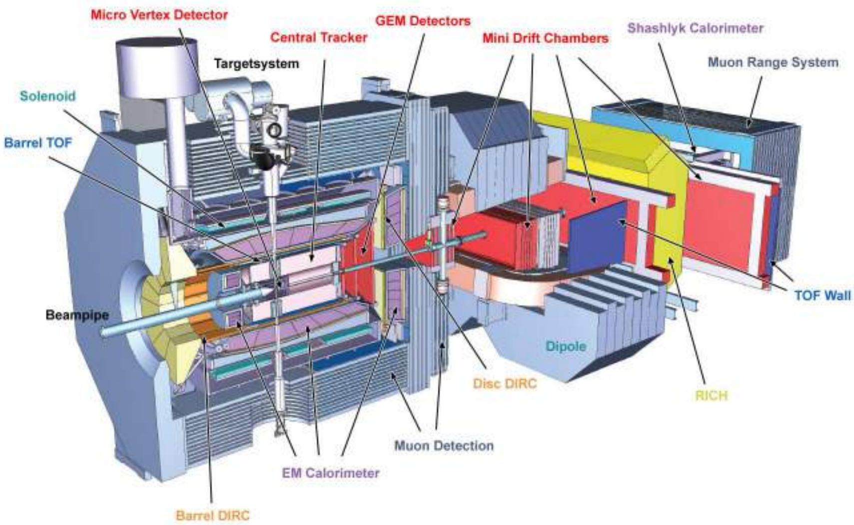

Figure 1. The PANDA detector. The beam enters from the left and interacts in the target spectrometer.

2. The barrel time-of-flight detector

The barrel time-of-flight (TOF) detector is motivated by physics as well as technical benefits [3]. It provides particle identification for charged particles below the momentum threshold of barrel DIRC detector below 700 MeV/c. In addition to the particle identification, it also provides timing information to construct event building algorithm to avoid an event-mixing at high collision rates. The PANDA detector does not have a start timing detector. Nevertheless based on the relative time-of-flight algorithm, the event start time can be calculated by using the timing information of barrel TOF. Plastic scintillators are insensitive to photons, but highly sensitive to charged particles. This helps to detect the preshowers in PANDA barrel spectrometer by using barrel TOF information. The barrel TOF detector has a minimum material budget below 2% of a radiation length and less than 2 cm radial thickness, including the readout electronics and mechanics and provide a large angular acceptance of $22^0 \leq \theta \leq 140^0$. For the reasons given above a good time resolution $\sigma < 100$ ps and a fast readout and signal processing is mandatory.

3. Study of preshower in the PANDA Target Spectrometer

The presence of other detectors in front of the electromagnetic calorimeter with a high material budget leads to the possibility for a high energetic photon to start the electromagnetic shower in front of the EMC. An electromagnetic shower started in front of the EMC is called preshower. In the PANDA detector, the material budget in front of the EMC is mostly contributed by the DIRC detector material [4]. Therefore, this study is concentrated on preshowers in the DIRC detector. A study for the BaBar experiment [5] show, that detecting the preshower in the DIRC, the energy resolution of π^0 could be improved by about 5%. The BaBar DIRC detector itself was used to detect the preshower and 50% of converted photons were recovered. However, unlike the BaBar detector, the PANDA target spectrometer is facilitated with the TOF detector between DIRC and EMC. This thin detector system is capable of detecting preshowers in the DIRC with a high efficiency and may help in the reconstruction of photon showers in the EMC.

4. Simulation in PandaRoot

We use PandaRoot [6] to study the preshowers. Single photon MC events of energy 1 GeV are generated using box generator. The radial part of the starting point of an electromagnetic (EM) shower can be obtained from the simulation output. A shower is identified as preshower if the starting point falls between the inner radius and outer radius of the DIRC detector. The variation of the gamma conversion probability with polar angle (θ) is shown in Fig. 2. A comparison of the reconstructed photon energies for preshower and non preshower events is

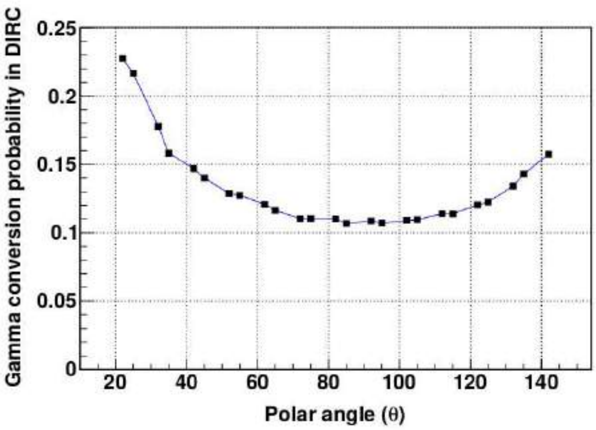

Figure 2. Gamma conversion probability in DIRC as a fuction of polar angle (θ) for 1 GeV photons.

shown in Fig. 3. It has been observed that the energy distribution for non preshower events (black histogram)

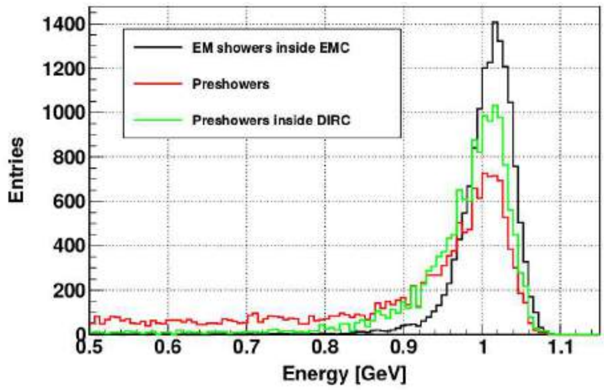

Figure 3. Reconstructed energy of 1 GeV photons for preshower and non preshower events.

can be well described by a Gaussian function. The preshower events (red and green) add a low-end tail part to the energy distribution. However, there is no remarkable deterioration in photon energy resolution due to DIRC preshowers is observed in our simulation. Previous beam-test [7] showed, that for energies above 1 GeV a preshower improves the energy resolution, while for energies below 1 GeV a preshower deteriorates the energy and position reconstruction. The TOF detector can help to identify these cases and may help to improve the situation.

5. Conclusion

Simulation studies are in progress for better understanding of DIRC preshowers in the PANDA target spectrometer. It is also planned to recover the converted photons in the DIRC using barrel TOF detector with high efficiency.

6. Acknowledgement

We acknowledge the help and support of Dr. K. Suzuki and D. Steinschaden, PANDA barrel TOF group, Stefan Meyer Institute for Subatomic Physics, Austrian Academy of Sciences, Boltzmanngasse 3, 1090 Vienna, Austria. We also gratefully acknowledge DST, INDIA for the financial support to carry out this work.

References

[1] W.F. Henning, *FAIR and its experimental programm*, J. Phys. G **34**, S551 (2007).
[2] Erni. W. et al., *Physics performance report for PANDA: Strong interaction studies with antiprotons*, arXiv preprint arXiv:0903.3905 (2009).
[3] K. Goetzen et al., *Proposal for a Scintillator Tile Hodoscope for PANDA, PANDA Note*, Version 1.1 (2011).
[4] PANDA Collaboration, *TDR for PANDA Electromagnetic Calorimeter (EMC)*, arXiv:0810.1216.
[5] A. Adametz, *Preshower Measurement with the Cherenkov Detector of the BaBar Experiment*, Diploma Thesis, Heidelberg University, January 2005.
[6] S. Stefano (PANDA Collaboration), *The PandaRoot framework for simulation, reconstruction and analysis*, JOP: Conference Series **331(3)**, IOP Publishing (2011).
[7] S. Diehl, German physical society meeting, Frankfurt, 2014

Susceptibility calculation under one loop correction in the mean field potential

S. Somorendro Singh

Department of Physics & Astronomy, University of Delhi, Delhi-110007, India

sssingh@physics.du.ac.in; HEP.3, Oral, CICAHEP15.144

We calculate quark susceptibility and velocity of sound incorporating one loop correction in mean field potential. The calculation shows continuous increasing susceptibility and velocity of sound up to the temperature $T = 0.4$ GeV. Then the susceptibility and sound velocity approach to the behaviour of lattice result for higher value of temperature. The result indicates that the calculated values of the model fit well to reach the ideal gas pattern with the one loop correction in the mean field potential.

1. Introduction

Strong interactions predicts quark-hadron phase transition under the condition of extreme high energy nuclear density and high temperature. In this process of transition [1, 2] phenomena a deconfined phase of free quarks, gluons at very large temperature and a confined phase of bound quarks at lower temperature, lived for a short period. During this short time, the formation of the deconfined phase known as quark-gluon plasma (QGP) is still a theoretical conjecture. So the system is still considered to be a complicated phenomena from the beginning of early universe. Due to this complicated nature it has facilitated a lot of interest in this topics and a lot of affords has been taken care in working out to investigate this transformation of quark-hadron phases. To investigate and search this nature of the universe there are a number of experimental facilities set up around the globe like relativistic heavy-ion collision (RHIC) at BNL and large hadron collider (LHC) at CERN. Besides these experiments set up, there are another experimental facilities like FAIR at Darmstadt and NICA at Dubna, where the study have focused on dense baryonic matter and the baryonic matter at Nuclotron (BM@N) experiments with ion beams extracted from modernized Nuclotron. These facilities are trying to provide the information about the existence of the early universe phase transition, formation of QGP and chromodynamics (QCD) phase structure [3, 4, 5, 6]. So, the study of quark-gluon plasma (QGP) in Ultra Relativistic Heavy-Ion Collisions has become an exciting field in the present day of heavy ion collider physics [7, 8]. In this brief article, we focus on the calculation of quark susceptibility and velocity of sound through the free energy evolution of QGP with one loop correction in mean field potential. To evaluate the susceptibility and velocity, we need to understand the thermodynamic partition function which correlate the Gibb's free energy of the system. To incorporate one loop correction in the mean field potential we modify the free energy incorporating the loop correction with quark and gluon flow parameters. Due to the correction factor in the mean field potential, there are changes in the free energy expansion of QGP fireball, and it also impacts in the stability of droplet formation with the variation of dynamical quark and gluon flow parameters [9, 10, 11]. So the flow parameter takes the role of stability in forming droplet size with changing temperature. In brief, we review free energy evolution through the density of state which is modified by one loop correction with quark and gluon flow parameters. The loop correction is introduced in the coupling parameter and hence modified the density of state constructed through the coupling value. Then we calculate quark susceptibility, entropy and specific heat with the relevant flow parameters of stability droplets. We further calculate velocity of sound also through these two above thermodynamic entities, entropy and specific heat. In conclusion, we give the details of evolution of QGP fireball with different flow parametrization values and show the results of susceptibility, entropy, specific heat and velocity of sound.

2. Free energy evolution

The free energy of quarks and gluons can be obtained through a simple model modifying density of state with the inclusion of one loop correction factor [12, 13, 14, 15] as given by,

$$F_i = \pm T g_i \int \rho_{q,g}(p) \ln[1 \mp e^{-(\sqrt{m_i^2+p^2}-\mu)/T}]dp \, , \tag{1}$$

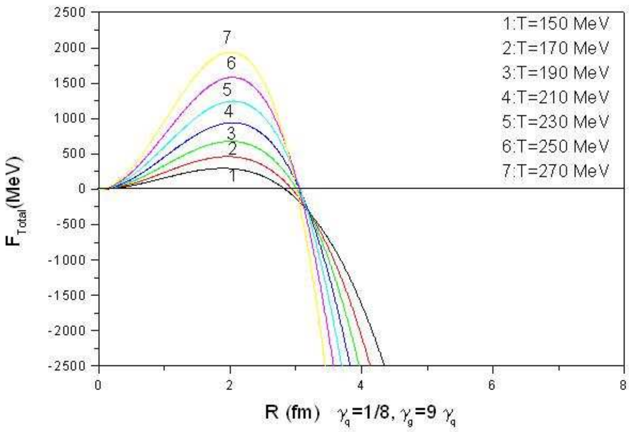

Figure 1. Free energy evolution versus QGP droplet size at this particular quark and gluon flow parameter.

where minus sign if for the bosonic particle and plus sign is for fermionic particles. g_i is color and particle-antiparticle degeneracy for quarks and gluons. $\rho_{q,g}$ is the density of states in phase space under the inclusion of one loop correction in the interacting potential. It is reviewed through our earlier paper [16]:

$$\rho_{q,g}(p) = \frac{\nu}{\pi^2}[\frac{\gamma_{q,g}^3 T^2}{2}]^3 g^6(p)A, \tag{2}$$

where

$$A = \{1 + \frac{\alpha_s(p)a_1}{\pi}\}^2[\frac{(1+\alpha_s(p)a_1/\pi)}{p^4} + \frac{2(1+2\alpha_s(p)a_1/\pi)}{p^2(p^2+\Lambda^2)\ln(1+\frac{p^2}{\Lambda^2})}], \tag{3}$$

where $\gamma_{q,g}$ is quark and gluon parametrization factors taken as $\gamma_q = 1/8$ and $\gamma_g = (8-10)\ \gamma_q$. These factors determine the dynamics of QGP flow and enhance the transformation to hadrons. ν is the volume occupied by the QGP. $g^2(p) = 4\pi\alpha_s(p)$. The coefficient a_1 used in the above expression is due to one loop correction obtained in their interactions and contribute in the modification of density of state. In addition to these free energies, there is an inter-facial energy which takes care of the hydrodynamic effects in the system and the Bag energy constant. It is:

$$F_{interface} = \frac{\gamma T R^2}{4}\int p^2\delta(p-T)dp, \tag{4}$$

in which γ is root mean square value of quark γ_q and gluon flow parameter γ_g. R is size of QGP droplet. The hadronic contribution of free energy with the corresponding degeneracy factor of g is [17]

$$F_h = (gT/2\pi^2)\nu\int_0^\infty p^2\ln[1-e^{-(\sqrt{m_h^2+p^2}-\mu/T)}]dp. \tag{5}$$

Where, m_h is considered to be the corresponding mass of hadronic particles. We can thus compute the total modified free energy F_{total} as,

$$F_{total} = \sum_i F_i\ +\ F_{interface}\ +\ F_h, \tag{6}$$

where i stands for u, d and s quark and gluon.

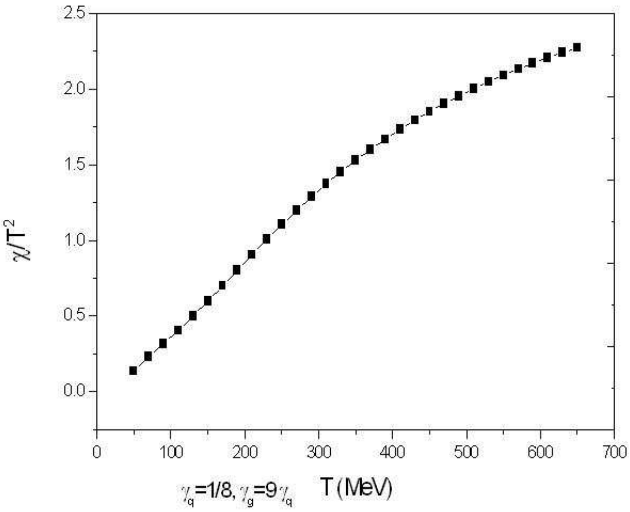

Figure 2. Quark susceptibility versus temperature at this particular quark and gluon flow parameter.

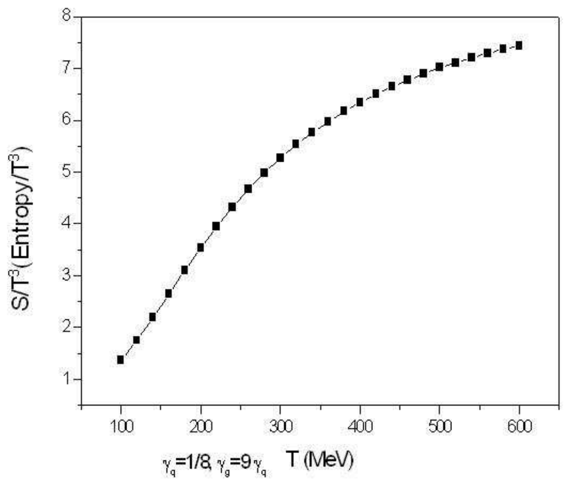

Figure 3. Entropy versus temperature at this particular quark and gluon flow parameter.

3. Quark susceptibility, entropy, specific heat and velocity of sound:

The quark susceptibility, entropy, specific heat and velocity of sound are calculated from the total free energy. The susceptibility is calculated by the following relations [18, 19, 20],

$$\chi = (\frac{\partial^2 F}{\partial \mu_i^2})_{\mu_i=0}. \tag{7}$$

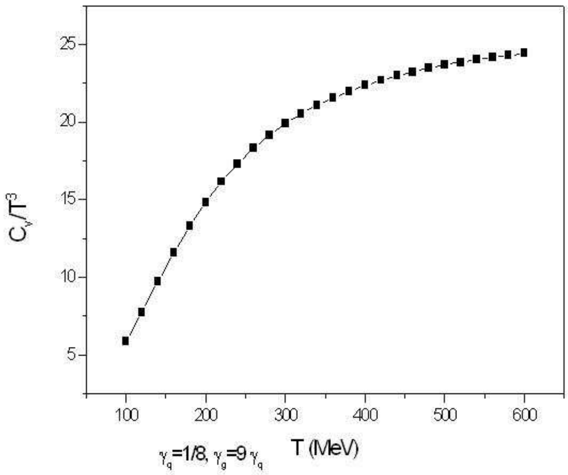

Figure 4. Specific heat versus temperature at this particular quark and gluon flow parameter.

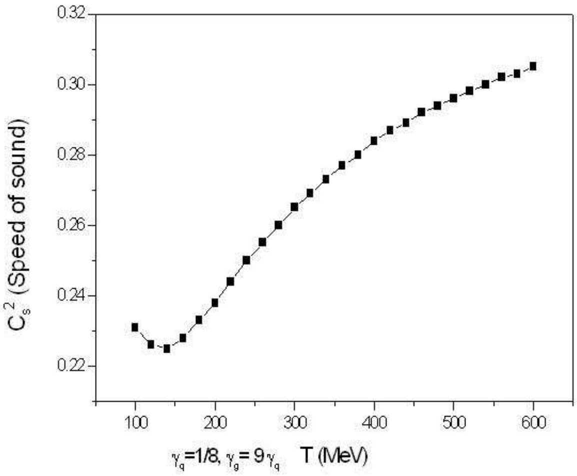

Figure 5. Velocity of sound versus temperature at this particular quark and gluon flow parameter.

The susceptibility value can be observed from the figure with the variation of temperature. We look the calculation of entropy and specific heat from the free energy. The entropy and specific are defined as,

$$s = (-\frac{\partial F}{\partial T})_v, \tag{8}$$

$$C_v = (T\frac{\partial s}{\partial T})_v. \tag{9}$$

Then, we look the velocity of sound with this model of one loop correction in the coupling value. The speed of sound is ratio of the thermodynamic property entropy to specific heat, which are calculated through the free energy, and it is given as [21, 22],

$$C_s^2 = \frac{S/T^3}{C_v/T^3} \tag{10}$$

The value of sound velocity is also shown in the following figure with the corresponding temperature.

4. Results:

Analytical calculation of free energy of QGP-hadron fireball evolution with one loop correction factor in the interacting mean-field potential is reviewed for looking into quark susceptibility, entropy, specific heat and velocity of sound . The stability droplets are found in quark and gluon parametrization factor $\gamma_q = 1/8$ and $10\gamma_q \leq \gamma_g \geq 8\gamma_q$. At these particular ranges we numerically calculate quark susceptibility entropy, specific heat and velocity of sound for one particular flow parameter out of the above ranges. The choice of this particular flow value is because of highly stable in the QGP droplet. In Fig.1 we show the free energy evolution for one particular stable droplet of the system with the change in temperature. The free energy spectrum is almost showing at this $\gamma_q = 1/8$ and $\gamma_g = 9\gamma_q$. It shows very nice evolution with the stable droplet size of 3.2 fm. In Fig.2 again we plot the quark susceptibility with the variation of temperature. The figure shows that the system with the modification of one loop correction in the mean field potential agree with many other works [21, 22, 23]. This indicates that the choice of parameter during the time of QGP formation play very important and significant role. It's value is probably a kind of Reynold number of this dense nuclear fluid. Again in Figs.3 and 4 we look the entropy and specific heat. These results follow almost same pattern with the lattice and ideal gas behaviour. Again from these two thermodynamic entities we obtained velocity of sound. It is shown in Fig.5 and the value is found to be $1/3$ around the temperature range of $T = 0.4$ GeV to $T = 0.6$ GeV and also matches with the recent data of velocity of sound for the whole range of temperature.

5. Conclusion:

We can conclude from these results that due to the presence of loop correction in the mean field potential, the stability of droplets increases while its size decreases in comparison with the result of uncorrected potential. So, we can further study velocity of sound on the basis of these smaller droplets through the thermodynamic properties like entropy and specific heat of QGP. In our further work, we plan to compare the results with available data on fireball radius and possible experimental tests.

6. Acknowledgment

We thank R. Ramanathan for useful discussions in preparing manuscript and critical reading of the manuscript. Author thanks the University for providing research and development grants.

References

[1] A. Ali Khan *et al.*, CP-PACS Collab: Phys. Rev. D **63**, 034502 (2001).
[2] E. Karsch, A. Peikert and E. Laermann, Nucl. Phys. B **605**, 579 (2001).
[3] I. Arsene *et al.*, BRAHMS Collab: Nucl. Phys. A **757**, 1 (2005).
[4] B. B. Back *et al.*, PHOBOS Collab: Nucl. Phys A **757**, 28 (2005).
[5] J. Adams *et al.*, STAR Collab: Nucl. Phys. A **757**, 102 (2005).
[6] K. Adcox *et al.*, PHENIX Collab: Nucl. Phys. A **757**, 184 (2005).
[7] F. Karsch, E. Laermann, A. Peikert, Ch. Schmidt and S. Stickan, Nucl. Phys. B **94**, 411 (2001).
[8] F. Karsch and H. Satz, Nucl. Phys. A **702**, 373 (2002).
[9] S. S. Singh and R. Ramanathan, Prog. Theo. Expt. Phys. **103D02**, (2014).
[10] R. Ramanathan, Y. K. Mathur, K. K. Gupta and A. K. Jha, Phys. Rev. C **70**, 027903 (2004).
[11] R. Ramanathan, K. K. Gupta, A. K. Jha and S. S. Singh, Pram. J. Phys. **68**, 757 (2007).

[12] G. Neergaad and J. Madsen, Phys. Rev. D **60**, 05404 (1999).
[13] M. B. Christiansen and J. Madsen, J. Phys. G **23**, 2039 (1997).
[14] H. T. Elze and W. Greiner, Phys. Lett. B **179**, 385 (1986).
[15] S. S. Singh, D. S. Gosain, Y. Kumar and A. K. Jha, Pram. J. Phys. **74**, 27 (2010).
[16] S. S. Singh, K. K. Gupta and A. K. Jha, Int. J. Mod. Phys. A **29**, 1550092 (2014); S. S. Singh and R. Ramanathan, ArXiv: 1308.3757.
[17] R. Balian and C. Block, Ann. Phys. (NY) **60**, 401 (1970).
[18] Y. Aoki, G. Endrödi, Z Fodor, S. D. Katz and K. K. Szabó, Nature **443**, 675 (2006).
[19] C. Sasaki, B. Friman and K. Redlich, Phys. Rev. D **75**, 074013 (2007).
[20] A. Vuorinen, Phys. Rev. D **67**, 074032 (2003).
[21] R. V. Gavai, S. Gupta and S. Mukherjee, Pram. J. Phys. **71**, 487 (2008).
[22] S. Borsányi, Nucl. Phys. A, **904**, 270c (2013).
[23] Th. Graf, J. S. Bielich and E. S. Fraga, hep-ph, arXiv:1507.08941v1.

PS3 :: National Conference on CICAHEP, Dibrugarh (2015), **01**, 199 – 203

Neutrino mass models with one vanishing minor under Z_8 cyclic group symmetry

Priyanka Kumar and Mahadev Patgiri

Department of Physics, Cotton College, Guwahati-781001, Assam, India

Presenter: Priyanka Kumar (*prianca.kumar@gmail.com*); HEP.4, Oral, CICAHEP15.178

Some Type-I seesaw mass models [1] are revisited with the motivation to study their textures under Z_8 cyclic symmetry. These neutrino mass models are based on both diagonal charged lepton mass matrices and Dirac neutrino mass matrices with the non-diagonal right handed Majorana neutrino mass matrices M_R. We observe that the one zero texture of M_R propagate to the left-handed neutrino mass matrices M_ν as their vanishing minors and the symmetry of the textures corresponds to Z_8 cyclic group symmetry. It is done by extending the SM to include two or three Higgs doublet and some SU(2) singlet scalar.

1. Introduction

The series of neutrino experiments have confirmed without any doubt that the neutrinos are massive. To achieve massive neutrinos in theory, one has to move beyond the SM of particle physics which can accommodate massless neutrinos only. The basic SM extensions include the existence of right-handed Majorana neutrino. These RH Majorana neutrinos are often used to explain neutrino masses via the type-I seesaw mechanism.

In the Type-I seesaw mechanism, the effective neutrino mass matrix M_ν is given by

$$M_\nu = -M_D M_R^{-1} M_D^T, \tag{1}$$

where M_D and M_R are respectively the Dirac neutrino mass matrix and right-handed Majorana mass matrix. Zero textures [2, 3, 4], vanishing minors [5] and hybrid textures [6] are some of the interesting proposals that are being studied extensively so as to restrict the form of the neutrino mass matrix and thus reduce the number of free parameters. Zero textures in M_ν have been extensively studied because of their implications for the possible existence of family symmetries which require certain entries of the matrix, which are extremely small compared to the other elements of the matrix, to vanish. Since according to equation (1), M_ν is a combination of the Dirac mass matrix M_D and the heavy right-handed Majorana neutrino mass matrix M_R, so the zeros of M_D and M_R, propagate as zeros in M_ν. Thus the study of zero texture of M_D and M_R is more basic than the study of M_ν [7]. The zeros in M_D and M_R apart from propagating as zeros in M_ν may also reflect as vanishing minors in M_ν, provided M_D is diagonal. Zeros in any arbitrary entries of the mass matrices can be enforced effectively with the help of certain cyclic group symmetry [8]. In our paper, we have made use of the Z_8 cyclic group symmetry to enforce zeros in the mass matrices.

The paper is organised as follows: in section 2, we have presented a general form of texture zero and vanishing minor in the neutrino mass matrices. In section 3, we have studied the one zero textures of the symmetric RH Majorana mass matrix of the bimaximally mixed neutrino mass matrices [1], where M_D and M_l are chosen to be diagonal, also vanishing minors were observed in each case. We present symmetry realization of the mass matrices using an Abelian cyclic group Z_8 with suitable scalar singlets and Higg's doublets in section 4. And finally end up with conclusion in section 5.

2. General form of one zero textures of M_R and vanishing minors in M_ν

We work in the basis where the charged lepton mass matrix M_l is diagonal, and the Dirac mass matrix M_D [1] and the general form of the symmetric RH Majorana mass matrix respectively takes the form:

$$M_D = \tan\beta \begin{pmatrix} \lambda^m & 0 & 0 \\ 0 & \lambda^n & 0 \\ 0 & 0 & 1 \end{pmatrix} m_\tau, \quad M_R = \begin{pmatrix} a & b & c \\ b & d & e \\ c & e & f \end{pmatrix}, \tag{2}$$

where $\lambda = 0.22$ is the Wolfenstein parameter, $m = 6, n = 2$ and $\tan\beta m_\tau = C(say)$ is a constant. The effective neutrino mass matrix, in the context of Type-I seesaw mechanism becomes,

$$M_\nu = \frac{1}{|M_R|}\begin{pmatrix} (df-e^2)\lambda^{2m} & (bf-ce)\lambda^{m+n} & (be-cd)\lambda^m \\ (bf-ce)\lambda^{m+n} & (af-c^2)\lambda^{2n} & (ae-bc)\lambda^n \\ (be-cd)\lambda^m & (ae-bc)\lambda^n & (ad-b^2) \end{pmatrix} R_1, \tag{3}$$

where R_1 is a constant and $|M_R| = (adf - ae^2 - b^2 f + 2bce - c^2 d)$. All the possible one zero texture of the symmetric RH Majorana mass matrix are shown in the table below:

Table 1: All possible one zero texture of M_R.

A	B	C
$\begin{pmatrix} 0 & b & c \\ b & d & e \\ c & e & f \end{pmatrix}$	$\begin{pmatrix} a & 0 & c \\ 0 & d & e \\ c & e & f \end{pmatrix}$	$\begin{pmatrix} a & b & 0 \\ b & d & e \\ 0 & e & f \end{pmatrix}$
D	E	F
$\begin{pmatrix} a & b & c \\ b & 0 & e \\ c & e & f \end{pmatrix}$	$\begin{pmatrix} a & b & c \\ b & d & 0 \\ c & 0 & f \end{pmatrix}$	$\begin{pmatrix} a & b & c \\ b & d & e \\ c & e & 0 \end{pmatrix}$

Here we have distinguished the different structures of texture zero in different classes. For example, class A: gives the mass matrix where the zero corresponds to the position 'a' of the matrix; class B: mass matrix where the zero corresponds to the position 'b' of the matrix and so on. As our M_D is diagonal, the zeros of M_R will show as a vanishing minor in M_ν. In the context of type-I seesaw, the effective neutrino mass matrix M_ν with M_D as diagonal and one zero texture of M_R (class A) becomes,

$$M_\nu = \frac{1}{|M_R|}\begin{pmatrix} (df-e^2)\lambda^{2m} & (bf-ce)\lambda^{m+n} & (be-cd)\lambda^m \\ (bf-ce)\lambda^{m+n} & -c^2\lambda^{2n} & -bc\lambda^n \\ (be-cd)\lambda^m & -bc\lambda^n & -b^2 \end{pmatrix}, \tag{4}$$

where $|M_R| = (-b^2 f + 2bce - c^2 d)$. Thereby giving rise to a vanishing minor in M_ν for a zero corresponding to class A in M_R. Similarly, for each class of M_R, a vanishing minor is obtained in M_ν with M_D as diagonal.

3. One zero texture of the RH Majorana mass matrix

When M_l = diag(m_e, m_μ, m_τ) and M_D = diag(λ^6, λ^2, 1) C (C being a constant) the neutrino mass matrix arises solely due to M_R. It is found that the texture study of the right handed Majorana mass matrices in each case, that is, normal, degenerate and inverted heirarchy from Ref. [1], gives different texture structure.

3.1 Normal heirarchy

I(A): The right-handed Majorana mass matrices [1] of the form,

$$M_R = \begin{pmatrix} \lambda^{11} & \lambda^7 & \lambda^5 \\ \lambda^7 & \lambda^6 & 0 \\ \lambda^5 & 0 & 1 \end{pmatrix} v_R \tag{5}$$

with $v_R \approx 10^{14}$ gives rise to a structure with $e = 0$ (class E), thereby leading to the following form of effective neutrino mass matrix through seesaw mechanism:

$$M_\nu = \frac{1}{|M_R|}\begin{pmatrix} df\lambda^{12} & bf\lambda^8 & -cd\lambda^6 \\ bf\lambda^8 & (af-c^2)\lambda^4 & -bc\lambda^2 \\ -cd\lambda^6 & -bc\lambda^2 & (ad-b^2) \end{pmatrix} R_1, \tag{6}$$

where R_1 is a constant and $|M_R| = (adf - b^2 f - c^2 d)$. Thus a vanishing minor is obtained in M_ν for $e = 0$ in M_R.

3.2 Degenerate case

I(B): The right-handed Majorana mass matrix [1] is of the form,

$$M_R = \begin{pmatrix} (1+2\delta_1+2\delta_2)\lambda^{12} & \delta_1\lambda^8 & \delta_1\lambda^6 \\ \delta_1\lambda^8 & (1+\delta_2)\lambda^4 & \delta_2\lambda^2 \\ \delta_1\lambda^6 & \delta_2\lambda^2 & (1+\delta_2) \end{pmatrix} v_R, \tag{7}$$

where $\delta_1 = 3.6\times 10^{-5}, \delta_2 = 3.9\times 10^{-3}, v_R \approx 10^{13}$ GeV, enforcing $(\delta_1+\delta_2)\lambda^{12} = 0, \delta_1\lambda^8 = 0$, M_R reduces to the following structure:

$$M_R = \begin{pmatrix} a & 0 & c \\ 0 & d & e \\ c & e & f \end{pmatrix} (\text{class B}). \tag{8}$$

3.3 Inverted hierarchy

II(A): With $a = 0.5, \epsilon = 0.002, \eta = 0.0001, v_R \approx 10^{12}$ in

$$M_R = \begin{pmatrix} 2a\eta(1+2\epsilon)\lambda^{12} & \eta\epsilon\lambda^8 & \eta\epsilon\lambda^6 \\ \eta\epsilon\lambda^8 & a\lambda^4 & -(a-\eta)\lambda^2 \\ \eta\epsilon\lambda^6 & -(a-\eta)\lambda^2 & a \end{pmatrix} \frac{v_R}{2a\eta} \tag{9}$$

the terms $a\eta\epsilon\lambda^{12}$ and $\eta\epsilon\lambda^8$ can be effectively forced to zero.Thereby reducing M_R to the following form,

$$M_R = \begin{pmatrix} a & 0 & c \\ 0 & d & e \\ c & e & f \end{pmatrix} (\text{class B}). \tag{10}$$

Thus the structure of M_ν (I(B), II(A) with $b = 0$) becomes,

$$M_\nu = \frac{1}{|M_R|} \begin{pmatrix} (df-e^2)\lambda^{12} & -ce\lambda^8 & -cd\lambda^6 \\ -ce\lambda^8 & (af-c^2)\lambda^4 & ae\lambda^2 \\ -cd\lambda^6 & ae\lambda^2 & ad \end{pmatrix} m_0, \tag{11}$$

where m_0 is a constant and $|M_R| = (adf - ae^2 - c^2 d)$. In each case a vanishing minor is obtained in M_ν for a corresponding zero in M_R. Similarly when a texture study is made on all the other models I(B), I(A), I(C), II(B) from Ref. [1] they reveals different texture structure as shown in the Table below:

Table 2: Texture structure of the mass models.

Mass Models ($M_R's$)		Zero Texture in M_R
I(B) (Normal)	$\begin{pmatrix} -\lambda^{10} & \lambda^6 & \lambda^4 \\ \lambda^6 & \lambda^6 & \lambda \\ \lambda^4 & \lambda & 1 \end{pmatrix} v_R$, where $v_R \approx 10^{13}$ GeV	$M_{R_{11}} = 0$ Class A
I(A) (Degenerate)	$\begin{pmatrix} -2\delta_2\lambda^{2m} & (\frac{1}{\sqrt{2}}+\delta_1)\lambda^{m+n} & (\frac{1}{\sqrt{2}}+\delta_1)\lambda^m \\ \frac{1}{\sqrt{2}}+\delta_1)\lambda^{m+n} & (\frac{1}{2}+\delta_1-\delta_2)\lambda^{2n} & (-\frac{1}{2}+\delta_1-\delta_2)\lambda^n \\ (\frac{1}{\sqrt{2}}+\delta_1)\lambda^m & (-\frac{1}{2}+\delta_1-\delta_2)\lambda^n & (\frac{1}{2}+\delta_1-\delta_2) \end{pmatrix} v_R$, where $\delta_1 = 6.18\times 10^{-3}$,$\delta_2 = 3.06\times 10^{-3}$,$v_R \approx 10^{13}$ GeV	$M_{R_{11}} = 0$ Class A
I(C) (Degenerate)	$\begin{pmatrix} (1+2\delta_1+2\delta_2)\lambda^{2m} & \delta_1\lambda^{m+n} & \delta_1\lambda^m \\ \delta_1\lambda^{m+n} & \delta_2\lambda^{2n} & (1+\delta_2)\lambda^n \\ \delta_1\lambda^m & (1+\delta_2)\lambda^n & \delta_2 \end{pmatrix} v_R$, where $\delta_1 = 3.6\times 10^{-5}$, $\delta_2 = 3.9\times 10^{-3}$, $v_R \approx 10^{13}$ GeV	$M_{R_{12}} = 0$ Class B
II(B) (Inverted)	$\begin{pmatrix} -\lambda^{15} & \lambda^8 & \lambda^6 \\ \lambda^8 & \lambda & \lambda^{-1} \\ \lambda^6 & \lambda^{-1} & \lambda^{-3} \end{pmatrix} v_R$, where $v_R \approx 10^{12}$ GeV	$M_{R_{11}} = 0$ Class A

4. Symmetry Realization

Texture zeros can be enforced in any arbitrary entries of the mass matrices with an extended scalar sector and Higg's doublet by means of Abelian symmetries. For symmetry realization of different textures of M_R we consider the Z_8 cyclic group symmetry. The leptonic field transformations are different for different texture mass matrices. Let the fields transform under Z_8 as

$\bar{D}_{e_L} \to \omega \bar{D}_{e_L}, e_R \to \omega^6 e_R, \nu_{e_R} \to \nu_{e_R},$
$\bar{D}_{\mu_L} \to \omega^4 \bar{D}_{\mu_L}, \mu_R \to \omega^5 \mu_R, \nu_{\mu_R} \to \omega^4 \nu_{\mu_R},$
$\bar{D}_{\tau_L} \to \omega^6 \bar{D}_{\tau_L}, \tau_R \to \omega^2 \tau_R, \nu_{\tau_R} \to \omega \nu_{\tau_R},$

where $\omega = e^{i2\pi/8}$ is the generator of Z_8, $\bar{D}_{jL}(j = e, \mu, \tau)$ denotes $SU(2)_L$ doublets, $l_R(l = e, \mu, \tau)$ denotes the RH $SU(2)_L$ singlets and $\nu_{k_R}(k = e, \mu, \tau)$, the RH neutrino singlets.

The bilinears $\bar{D}_{j_L}\nu_{k_R}, \bar{D}_{j_L} l_R, \bar{\nu}^T_{k_R} C^{-1}\nu_{j_R}$ relevant for M_D ,M_l and M_R respectively transforms as

$$\bar{D}_{k_L}\nu_{j_R} = \begin{pmatrix} \omega & \omega^5 & \omega^2 \\ \omega^4 & 1 & \omega^5 \\ \omega^6 & \omega^2 & \omega^7 \end{pmatrix}, \;\; \bar{D}_{k_L} e_{j_R} = \begin{pmatrix} \omega^7 & \omega^6 & \omega^3 \\ \omega^2 & \omega & \omega^6 \\ \omega^4 & \omega^3 & 1 \end{pmatrix}, \;\; \bar{\nu}^T_{k_R} C^{-1}\nu_{j_R} = \begin{pmatrix} 1 & \omega^4 & \omega \\ \omega^4 & 1 & \omega^5 \\ \omega & \omega^5 & \omega^2 \end{pmatrix} \tag{12}$$

We introduce three $SU(2)_L$ doublet Higg's (ϕ_1, ϕ_2, ϕ_3) transforming under Z_8 as

$$\phi_1 \to \phi_1, \;\; \phi_2 \to \omega\phi_2, \;\; \phi_3 \to \omega^7\phi_3. \tag{13}$$

For the case i(a)(class E texture)we consider three scalar singlets $(\chi_{12}, \chi_{13}, \chi_{33})$ transforming under Z_8 as

$$\chi_{12} \to \omega^4\chi_{12}, \;\; \chi_{13} \to \omega^7\chi_{13}, \;\; \chi_{33} \to \omega^6\chi_{33}. \tag{14}$$

thereby leading to the following form of M_D, M_l and M_R:

$$M_D = \begin{pmatrix} X & 0 & 0 \\ 0 & X & 0 \\ 0 & 0 & X \end{pmatrix}, \; M_l = \begin{pmatrix} X & 0 & 0 \\ 0 & X & 0 \\ 0 & 0 & X \end{pmatrix}, \; M_R = \begin{pmatrix} X & X & X \\ X & X & 0 \\ X & 0 & X \end{pmatrix}. \tag{15}$$

The Z_8 invariant Yukawa Lagrangian becomes,

$$\begin{aligned} -\mathcal{L} = Y^l_{11}\bar{D}_{e_L}\Phi_2 e_R + Y^l_{22}\bar{D}_{\mu_L}\Phi_3\mu_R + Y^l_{33}\bar{D}_{\tau_L}\Phi_1\tau_R + Y^D_{11}\bar{D}_{e_L}\tilde{\Phi}_3\nu_{e_R} + Y^D_{22}\bar{D}_{\mu_L}\tilde{\Phi}_1\nu_{\mu_R} \\ +Y^D_{33}\bar{D}_{\tau_L}\tilde{\Phi}_2\nu_{\tau_R} + \frac{M^M_{11}}{2}\bar{\nu}^T_{e_R}C^{-1}\nu_{e_R} + \frac{Y^M_{12}}{2}\bar{\nu}^T_{e_R}C^{-1}\nu_{\mu_R}\chi_{12} + \frac{Y^M_{13}}{2}\bar{\nu}^T_{e_R}C^{-1}\nu_{\tau_R}\chi_{13} \\ +\frac{M^M_{22}}{2}\bar{\nu}^T_{\mu_R}C^{-1}\nu_{\mu_R} + \frac{Y^M_{33}}{2}\bar{\nu}^T_{\tau_R}C^{-1}\nu_{\tau_R}\chi_{33} + h.c, \end{aligned} \tag{16}$$

where $\tilde{\phi} = i\tau_2\phi*$. Similarly for the case I(B) (class B texture), we consider three scalar singlets:

$$\chi_{13} \to \omega^7\chi_{13}, \;\; \chi_{23} \to \omega^3\chi_{23}, \;\; \chi_{33} \to \omega^6\chi_{33}.$$

reducing M_R to the form,

$$M_R = \begin{pmatrix} X & 0 & X \\ 0 & X & X \\ X & X & X \end{pmatrix}. \tag{17}$$

The Z_8 invariant Yukawa Lagrangian becomes,

$$\begin{aligned} -\mathcal{L} = Y^l_{11}\bar{D}_{e_L}\Phi_2 e_R + Y^l_{22}\bar{D}_{\mu_L}\Phi_3\mu_R + Y^l_{33}\bar{D}_{\tau_L}\Phi_1\tau_R + Y^D_{11}\bar{D}_{e_L}\tilde{\Phi}_3\nu_{e_R} + Y^D_{22}\bar{D}_{\mu_L}\tilde{\Phi}_1\nu_{\mu_R} \\ +Y^D_{33}\bar{D}_{\tau_L}\tilde{\Phi}_2\nu_{\tau_R} + \frac{M^M_{11}}{2}\bar{\nu}^T_{e_R}C^{-1}\nu_{e_R} + \frac{Y^M_{13}}{2}\bar{\nu}^T_{e_R}C^{-1}\nu_{\tau_R}\chi_{13} + \frac{M^M_{22}}{2}\bar{\nu}^T_{\mu_R}C^{-1}\nu_{\mu_R} \\ +\frac{Y^M_{23}}{2}\bar{\nu}^T_{\mu_R}C^{-1}\nu_{\tau_R}\chi_{23} + \frac{Y^M_{33}}{2}\bar{\nu}^T_{\tau_R}C^{-1}\nu_{\tau_R}\chi_{33} + h.c. \end{aligned} \tag{18}$$

Here M_R contains two types of mass terms viz. the terms arising from Yukawa coupling to the scalar singlets

$\chi's$ and bare mass terms. The scale of the former depends upon the scale of the Abelian Group Z_8 breaking. The bare mass terms are the mass terms that arises without the involvement of the extra scalar singlets which were incorporated in our extended form of the SM. So there is no restriction on the scale of the bare mass terms, and hence can have a higher mass scale. Thus a large effective neutrino mass can arise in such a model.
For the case II(A), the texture structure and symmetry realization is same as I(B). The symmetry realization of all the other models are illustrated in the table below:

Table 3: Transformation properties of leptons and scalar fields under Z_8 cyclic group.

Models	$\bar{D}_{e_L}, \bar{D}_{\mu_L}, \bar{D}_{\tau_L}$	e_R, μ_R, τ_R	$\nu_{e_R}, \nu_{\mu_R}, \nu_{\tau_R}$	ϕ's	χ's
I(B), I(A), II(B)	$\omega^7, \omega^5, \omega^4$	$\omega^5, \omega^3, \omega^4$	$\omega, \omega^3, 1$	$1, \omega^4$	$\omega^4, \omega^7, \omega^2, \omega^5$
I(C)	$\omega, \omega^4, \omega^6$	$\omega^6, \omega^5, \omega^2$	$1, \omega^4, \omega$	$\omega, 1, \omega^7$	$\omega^7, \omega^3, \omega^6$

5. Conclusion

We have explored one zero texture of the bimaximally mixed neutrino mass models [1] and achieved the symmetry realization of these textures under Z_8 abelian group. It is an interesting observation that the location of one zero of symmetric M_R determines the possible schemes of neutrino mass spectrum in certain cases. The $a = 0$ texture (class A) of M_R allows all the three schemes, viz., normal, degenerate and inverted schemes. The $b = 0$ texture (class B) favours the degenerate and inverted schemes, while the $e = 0$ texture (class E) allows only the normal hierarchical scheme. The $c = 0$ (class C), $d = 0$ (class D) and $f = 0$ (class F) textures of M_R have not been found to favour any models under consideration. For the a=0 texture models, two Higgs doublet and four scalar singlets need to be included to extend SM while for the $b = 0$ and $e = 0$ texture models, three Higg's doublet and three scalar singlets are required to extend the SM. It is the inherent problem of symmetry realization of one zero texture of neutrino mass matrices which requires a couple of Higg's doublets and scalar singlets.

References

[1] N. Nimai Singh, Mahadev Patgiri, Int. J. Mod. Phys. A **17**, 3629 (2002); hep-ph/0111319; N. Nimai Singh, Mahadev Patgiri, Indian. J. Mod. Phys. A **76**, 423 (2002); hep-ph/0204021.
[2] Zhi-Zhong Xing, Phys. Lett. B **530**, 159 (2002); hep-ph/0201151.
[3] Alexander Merle and Werner Rodejohann, Phys. Rev. D **73**, 073012 (2006); hep-ph/0603111.
[4] S. Dev, Sanjeev Kumar, Surender Verma amd Shivani Gupta, Nucl. Phys. B **784**, 117 (2007); hep-ph/0611313; S.Dev, Sanjeev Kumar, Surender Verma and Shivani Gupta, Phys. Rev. D **76**, 013002 (2007); hep-ph/0612102.
[5] S. Dev, Surender Verma, Shivani Gupta and R. R. Gautam, Phys. Rev. D **81**, 053010 (2010); arXiv:1003.1006[hep-ph]; S. Dev, Shivani Gupta and Radha Raman Gautam, Mod. Phys. Lett. A **26**, 501 (2011); arXiv:1011.5587[hep-ph].
[6] S. Dev, Surender Verma and Shivani Gupta, Phys. Lett. B 687, 53 (2010); arXiv:0909.3182[hep-ph]; S. Dev, Shivani Gupta and Radha Raman Gautam, Phys. Rev. D **82**, 073015 (2010); arXiv:1009.5501[hep-ph].
[7] E. Ma, Phys.Rev. D **71**, 111301 (2005).
[8] Walter Grimus, Anjan S. Joshipura, Luis Lavoura, Morimitsu Tanimoto, arXiv:hep-ph/0405016; Walter Grimus, arXiv:hep-ph/0511078; Radha Raman Gautam, Madan Singh, Manmohan Gupta, hep-ph/1506.04868; E. I. Lashin, N Chamoun, hep-ph/1108.4010.

Parametrization of lepton mixing matrix in terms of deviations from bi-maximal and tri-bimaximl mixing

Chandan Duarah[a], K. Sashikanta Singh[b] and N. Nimai Singh[c]

(a) Department of Physics, Dibrugarh University, Dibrugarh-786004, Assam, India
(b) Department of Physics, Gauhati University, Guwahati-781014, Assam, India
(c) Department of Physics, Manipur University, Canchipur, Imphal-795003, Manipur, India

Presenter: Chandan Duarah (*chandan.duarah@gmail.com*); HEP.3, Oral, CICAHEP15.186

We parametrize lepton mixing matrix, known as PMNS matrix, in terms of three parameters which account deviations of three mixing angles from their bi-maximal or tri-bimaximal values. On the basis of this parametrization we can determine corresponding charged lepton mixing matrix in terms of those three parameters which can deviate bi-maximal or tri-bimaximal mixing. We find that the charged lepton mixing matrices which can deviate bi-maximal mixing matrix and tri-bimaximal mixing matrix exhibit similar structures. Numerical analysis shows that these charged lepton mixing matrices are close to CKM matrix of quark sector.

1. Introduction

Over the last three years contributions from reactor [1, 2, 3], accelerator [4, 5] and solar [6] neutrino experiments have provided precise values of three mixing angles and two mass squared differences under a three-neutrino mixing scenario. Global analysis[7, 8, 9] of 3ν oscillation data available from various experiments provides us an overall view on mixing parameters.

As neutrino experiments have been trying for more and more precision measurements of neutrino mixing parameters, meanwhile theorists have been trying to realize the flavour mixing pattern of leptons. Bimaximal mixing (BM) [10] and Tri-bimaximal mixing (TBM) [11] have been playing an attractive role in the search of flavour mixing pattern over a decade. Both these mixing schemes are $\mu - \tau$ symmetric [12] and predict maximal atmospheric mixing and zero reactor angle. They differ in their predictions of solar angle in such that BM mixing predicts maximal value of solar angle while TBM mixing leads to a value which equals $\arcsin(\frac{1}{\sqrt{3}})$. Out of these two mixing schemes predictions of TBM mixing are more closer to global data [7, 8, 9] compared to the other. With the confirmation of non zero θ_{13}, the deviation of lepton mixing from exact BM or TBM pattern is clear. It is therefore useful to study the deviations of lepton mixing from exact BM or TBM pattern. Deviations from BM or TBM mixing is in fact a natural idea frequently discussed in the literature [13, 14, 15].

In this paper, we introduce three parameters which account for deviations of the three mixing angles, namely solar, atmospheric and reactor angle from their exact BM or TBM values. We then parametrize the lepton mixing matrix in terms of these three deviation parameters. Parametrization of lepton mixing matrix in terms of deviation parameters is also discussed in Ref. [16]. Our parametrization set up is however different from that. We mainly implicate the parametrization set up in predicting possible structure of charged lepton mixing matrix which in turn can generate the lepton mixing matrix from BM or TBM neutrino mixing via charged lepton correction. Charged lepton correction [17, 18] is a very common tool to deviate special mixing schemes like BM or TBM mixing. Corrections to special mixing schemes can also be accounted in mass matrix formalism. We also analyse numerically the charged lepton mixing matrices with an interest to compare them with the CKM matrix [19] of quark sector. In Grand Unified Theory (GUT) based models [20] CKM like charged lepton corrections to special mixing schemes are naturally considered. Such models also incorporates Quark-Lepton Complementarity (QLC) [21].

Rest of the paper is organized as follows : in Section 2 we discuss the parametrization of the lepton mixing matrix in terms of deviation parameters. In Section 3 we discuss an implication of our model in charged lepton correction scenario. Finally Section 4 is devoted to summary and discussion.

2. Parametrization of lepton mixing matrix

In general, lepton mixing matrix, known as PMNS matrix, is parametrized in terms of three mixing angles, namely θ_{12}, θ_{23} and θ_{13} which are commonly known as solar, atmospheric and reactor angle; and three CP violating phases: one Dirac CP phase δ and two Majorana phases α and β. In the standard Particle Data Group (PDG) parametrization it looks like

$$U_{PMNS} = \begin{pmatrix} c_{12}c_{13} & s_{12}c_{13} & s_{13}e^{-i\delta} \\ -s_{12}c_{23} - c_{12}s_{23}s_{13}e^{i\delta} & c_{12}c_{23} - s_{12}s_{23}s_{13}e^{i\delta} & s_{23}c_{13} \\ s_{12}s_{23} - c_{12}c_{23}s_{13}e^{i\delta} & -c_{12}s_{23} - s_{12}c_{23}s_{13}e^{i\delta} & c_{23}c_{13} \end{pmatrix} .P, \tag{1}$$

where $c_{ij} = \cos\theta_{ij}$, $s_{ij} = \sin\theta_{ij}$ $(i, j = 1, 2)$ and $P = diag(1, e^{i\alpha}, e^{i\beta})$ contains the Majorana CP phases. In the present work, we however, drop Majorana phase matrix P assuming that neutrinos obey Dirac nature.

Both BM and TBM matrices predict $\theta_{13}^{bm/tb} = 0$ and $\theta_{23}^{bm/tb} = 45°$ (suffices bm and tb represent BM and TBM respectively). However their predictions for solar angle are different and are given by $\theta_{12}^{bm} = 45°$ and $\theta_{12}^{tb} = \arcsin(\frac{1}{\sqrt{3}})$. Putting these predictions in equation (1), BM and TBM matrices can be obtained as

$$U_{BM} = \begin{pmatrix} \frac{1}{\sqrt{2}} & \frac{1}{\sqrt{2}} & 0 \\ -\frac{1}{2} & \frac{1}{2} & \frac{1}{\sqrt{2}} \\ \frac{1}{2} & -\frac{1}{2} & \frac{1}{\sqrt{2}} \end{pmatrix}, \tag{2}$$

$$U_{TBM} = \begin{pmatrix} \sqrt{\frac{2}{3}} & \frac{1}{\sqrt{3}} & 0 \\ -\sqrt{\frac{1}{6}} & \frac{1}{\sqrt{3}} & \frac{1}{\sqrt{2}} \\ \sqrt{\frac{1}{6}} & -\frac{1}{\sqrt{3}} & \frac{1}{\sqrt{2}} \end{pmatrix}. \tag{3}$$

We now introduce three parameters which account for the deviations of three mixing angles from their corresponding BM or TBM values as follows :

$$\left.\begin{array}{rcl} \theta_{12} & = & \theta_{12}^{bm/tb} + \delta\theta_{12}^{bm/tb}, \\ \theta_{23} & = & \theta_{23}^{bm/tb} + \delta\theta_{23}^{bm/tb}, \\ \theta_{13} & = & \theta_{13}^{bm/tb} + \delta\theta_{13}^{bm/tb}, \end{array}\right\} \tag{4}$$

where the deviation parameters $\delta\theta_{12}^{bm/tb}$ and $\delta\theta_{23}^{bm/tb}$ can take positive as well as negative values, whereas $\delta\theta_{13}^{bm/tb}$ takes only positive values. We present the best fit and 3σ values of mixing angles and Dirac CP phase in Table 1 [9]. Based on these global data we calculate the values of deviation parameters and are presented in Table 2.

Table 1. Best fit and 3σ values of mixing angles and Dirac CP phase for normal and inverted hierarchy (NH and IH) from global data [9].

Model	Parameter	Best Fit	$3\ \sigma$
NH	θ_{12}	34.6°	31.8° - 37.8°
	θ_{23}	48.9°	38.8° - 53.3°
	θ_{13}	8.6°	7.9° - 9.3°
	δ	254°	0° - 360°
IH	θ_{12}	34.6°	31.8° - 37.8°
	θ_{23}	49.2°	39.4° - 53.1°
	θ_{13}	8.7°	8.0° - 9.4°
	δ	266°	0° - 360°

For BM mixing we have from equation (4)

$$\left.\begin{array}{rcl} \theta_{12} & = & 45° + \delta\theta_{12}^{bm}, \\ \theta_{23} & = & 45° + \delta\theta_{23}^{bm}, \\ \theta_{13} & = & \delta\theta_{13}^{bm}. \end{array}\right\} \tag{5}$$

Table 2. Calculated values of deviation parameters from global data.

Mixing Scheme	Model	Parameter	Best Fit	3 σ
BM	NH	$\delta\theta_{12}$	$-10.4°$	$13.2°$ - $(-7.2°)$
		$\delta\theta_{23}$	$3.9°$	$-6.2°$ - $8.3°$
		$\delta\theta_{13}$	$8.6°$	$7.9°$ - $9.3°$
	IH	$\delta\theta_{12}$	$-10.4°$	$13.2°$ - $(-7.2°)$
		$\delta\theta_{23}$	$4.2°$	$-5.6°$ - $8.1°$
		$\delta\theta_{13}$	$8.7°$	$8.0°$ - $9.4°$
TBM	NH	$\delta\theta_{12}$	$-0.66°$	$-3.46°$ - $2.53°$
		$\delta\theta_{23}$	$3.9°$	$-6.2°$ - $8.3°$
		$\delta\theta_{13}$	$8.6°$	$7.9°$ - $9.3°$
	IH	$\delta\theta_{12}$	$-0.66°$	$-3.46°$ - $2.53°$
		$\delta\theta_{23}$	$4.2°$	$-5.6°$ - $8.1°$
		$\delta\theta_{13}$	$8.7°$	$8.0°$ - $9.4°$

Substituting these values in equation (1) we have PMNS matrix as

$$U_{PMNS} = \begin{pmatrix} \frac{1}{\sqrt{2}}p\tilde{r} & \frac{1}{\sqrt{2}}\tilde{p}\tilde{r} & re^{-i\delta} \\ -\frac{1}{2}\left(\tilde{p}\tilde{q} + pqre^{i\delta}\right) & \frac{1}{2}\left(p\tilde{q} - \tilde{p}qre^{i\delta}\right) & \frac{1}{\sqrt{2}}q\tilde{r} \\ \frac{1}{2}\left(\tilde{p}q - p\tilde{q}re^{i\delta}\right) & -\frac{1}{2}\left(pq + \tilde{p}\tilde{q}re^{i\delta}\right) & \frac{1}{\sqrt{2}}\tilde{q}\tilde{r} \end{pmatrix}, \tag{6}$$

where

$$\left.\begin{array}{rcl} p &=& \cos\delta\theta_{12}^{bm} - \sin\delta\theta_{12}^{bm}, \\ \tilde{p} &=& \cos\delta\theta_{12}^{bm} + \sin\delta\theta_{12}^{bm}, \\ q &=& \cos\delta\theta_{23}^{bm} + \sin\delta\theta_{23}^{bm}, \\ \tilde{q} &=& \cos\delta\theta_{23}^{bm} - \sin\delta\theta_{23}^{bm}, \\ r &=& \sin\delta\theta_{13}^{bm}, \\ \tilde{r} &=& \cos\delta\theta_{13}^{bm}. \end{array}\right\} \tag{7}$$

For TBM mixing we have from equation (4)

$$\left.\begin{array}{rcl} \theta_{12} &=& 35.26° + \delta\theta_{12}^{tb}, \\ \theta_{23} &=& 45° + \delta\theta_{23}^{tb}, \\ \theta_{13} &=& \delta\theta_{13}^{tb}. \end{array}\right\} \tag{8}$$

Substituting these values in equation (1) we have PMNS matrix as

$$U_{PMNS} = \begin{pmatrix} \frac{\sqrt{2}}{\sqrt{3}}p'\tilde{r}' & \frac{1}{\sqrt{3}}\tilde{p}'\tilde{r}' & r'e^{-i\delta} \\ -\frac{1}{\sqrt{6}}\left(\tilde{p}'\tilde{q}' + \sqrt{2}p'q'r'e^{i\delta}\right) & \frac{1}{\sqrt{3}}\left(p'\tilde{q}' - \frac{1}{\sqrt{2}}\tilde{p}'q'r'e^{i\delta}\right) & \frac{1}{\sqrt{2}}q'\tilde{r}' \\ \frac{1}{\sqrt{6}}\left(\tilde{p}'q' - \sqrt{2}p'\tilde{q}'r'e^{i\delta}\right) & -\frac{1}{\sqrt{3}}\left(p'q' + \frac{1}{\sqrt{2}}\tilde{p}'\tilde{q}'r'e^{i\delta}\right) & \frac{1}{\sqrt{2}}\tilde{q}'\tilde{r}' \end{pmatrix}, \tag{9}$$

where

$$\left.\begin{array}{rcl} p' &=& \cos\delta\theta_{12}^{tb} - \frac{1}{\sqrt{2}}\sin\delta\theta_{12}^{tb}, \\ \tilde{p}' &=& \cos\delta\theta_{12}^{tb} + \sqrt{2}\sin\delta\theta_{12}^{tb}, \\ q' &=& \cos\delta\theta_{23}^{tb} + \sin\delta\theta_{23}^{tb}, \\ \tilde{q}' &=& \cos\delta\theta_{23}^{tb} - \sin\delta\theta_{23}^{tb}, \\ r' &=& \sin\delta\theta_{13}^{tb}, \\ \tilde{r}' &=& \cos\delta\theta_{13}^{tb}. \end{array}\right\} \tag{10}$$

We want to emphasize that parametrization of lepton mixing matrix in terms of deviation parameters has also been discussed by King [16]. There also exists some interest in parametrizing the lepton mixing matrix in terms of Wolfenstein parameter λ [22], where λ accounts for the deviations of mixing angles from their values predicted by special mixing schemes.

3. An implication of the model : charged lepton mixing matrix

Deviations from BM or TBM mixing can be accounted in terms of charged lepton corrections [17, 18]. In the basis where both charged lepton mass matrix (m_l) and left handed Majorana mass matrix (m_ν) are non diagonal, lepton mixing matrix is given by the product of two mixing matrices as

$$U_{PMNS} = U_{lL}^{\dagger} U_{\nu}, \tag{11}$$

where U_{lL} diagonalizes m_l and U_ν corresponds to the diagonalization of m_ν. In the basis in which charged lepton mass matrix is itself diagonal PMNS matrix is directly given by U_ν, U_{lL} being identity matrix. The general idea of charged lepton correction is to work in the basis where both m_l and m_ν are non diagonal and then considering U_ν be a special mixing matrix like BM or TBM a small perturbation to it is accounted from U_{lL} leading to the desired PMNS matrix. Following this set up charged lepton corrections to special mixing patterns like BM, TBM, Hexagonal mixing etc. are done. For example charged lepton corrections to BM mixing are found in Refs. [23, 24] and those to TBM mixing are discussed in Refs. [24, 25]. With the same idea, in our work, we first find out U_{lL} which can deviate BM neutrino mixing matrix and yield the lepton mixing matrix in equation (6). In that case U_ν in equation (11) is given by U_{BM} and corresponding U_{lL} is then given by

$$U_{lL}^{bm} = \begin{pmatrix} a & -\frac{1}{\sqrt{2}}(b+z_1) & \frac{1}{\sqrt{2}}(c-z_2) \\ \frac{1}{\sqrt{2}}(d+z_3) & \frac{1}{2}(e+z_4) & \frac{1}{2}(f-z_5) \\ -\frac{1}{\sqrt{2}}(d-z_3) & \frac{1}{2}(e-z_4) & \frac{1}{2}(f+z_5) \end{pmatrix}, \tag{12}$$

where

$$\left.\begin{array}{rcl} a &=& \cos\delta\theta_{12}^{bm}\tilde{r}, \\ b &=& \sin\delta\theta_{12}^{bm}\tilde{q}, \\ c &=& \sin\delta\theta_{12}^{bm}q, \\ d &=& \sin\delta\theta_{12}^{bm}\tilde{r}, \\ e &=& q\tilde{r}, \\ f &=& \tilde{q}\tilde{r}, \\ z_1 &=& \cos\delta\theta_{12}^{bm}qre^{-i\delta}, \\ z_2 &=& \cos\delta\theta_{12}^{bm}\tilde{q}re^{-i\delta}, \\ z_3 &=& re^{i\delta}, \\ z_4 &=& \cos\delta\theta_{12}^{bm}\tilde{q} - \sin\delta\theta_{12}^{bm}qre^{-i\delta}, \\ z_5 &=& \cos\delta\theta_{12}^{bm}q - \sin\delta\theta_{12}^{bm}\tilde{q}re^{-i\delta}. \end{array}\right\} \tag{13}$$

The parameters a-f and z_1-z_5 are used to express the matrix in equation (12) in convenient way.

For TBM mixing case U_ν in equation (11) is given by U_{TBM} and corresponding U_{lL} is then given by

$$U_{lL}^{tb} = \begin{pmatrix} a' & -\frac{1}{\sqrt{2}}(b'+z_1') & \frac{1}{\sqrt{2}}(c'-z_2') \\ \frac{1}{\sqrt{2}}(d'+z_3') & \frac{1}{2}(e'+z_4') & \frac{1}{2}(f'-z_5') \\ -\frac{1}{\sqrt{2}}(d'-z_3') & \frac{1}{2}(e'-z_4') & \frac{1}{2}(f'+z_5') \end{pmatrix}, \tag{14}$$

where the parameters a'-f' and z_1'-z_5' are given by equation (13) with the substitutions of $\delta\theta_{12}^{bm}$, q, $\tilde{q}$, r and $\tilde{r}$ by $\delta\theta_{12}^{tb}$, q', $\tilde{q}'$, r' and $\tilde{r}'$ respectively.

We note that both charged lepton mixing matrices U_{lL}^{bm} and U_{lL}^{tb} have similar structure due to $\mu-\tau$ symmetry of BM and TBM mixing matrices. We estimate the numerical values (in modulus) of the elements of these mixing matrices for best fit values of deviation parameters and are presented in equations (15) and (16) as

$$U_{lL}^{bm} = \begin{pmatrix} 0.972512 & 0.183349 & 0.143535 \\ 0.185651 & 0.980189 & 0.062209 \\ 0.140544 & 0.074912 & 0.980319 \end{pmatrix}, \tag{15}$$

$$U_{lL}^{tb} = \begin{pmatrix} 0.988657 & 0.114991 & 0.096260 \\ 0.108234 & 0.991394 & 0.072972 \\ 0.103806 & 0.062329 & 0.992184 \end{pmatrix}. \tag{16}$$

Naturally there exists naive interest in searching connection between quark sector and lepton sector. GUTs generally provide the framework for quark-lepton unification. Quark-lepton-complementarity (QLC), which signifies interesting phenomenological relations between the lepton and quark mixing angles supports the idea of grand unification. Derivation of QLC relations assumes the deviation of lepton mixing from exact BM pattern to be described by quark mixing matrix. In GUT based models [14, 25, 20] charged lepton corrections to special neutrino mixing schemes are considered as CKM like. From such points of view we make comparison of the charged lepton mixing matrices in equations (15) and (16) with the CKM matrix. For convenience, we present the best fit values (in modulus) of the elements of CKM matrix in equation (17) [26]:

$$V_{CKM} = \begin{pmatrix} 0.97428 & 0.2253 & 0.00347 \\ 0.2252 & 0.97345 & 0.0410 \\ 0.00862 & 0.0403 & 0.999152 \end{pmatrix}. \tag{17}$$

Wee see that both the mixing matrices are close to CKM matrix. Like CKM matrix the diagonal elements in these mixing matrices are close to unity and non diagonal elements exhibit an approximate symmetric nature. One significant point, we note, is that the corner elements, namely $(U_{lL})_{13}$ and $(U_{lL})_{31}$ in both the mixing matrices are relatively larger compared to those of V_{CKM} matrix.

4. Summary and Discussion

BM and TBM are two special neutrino mixing schemes. To accommodate non zero θ_{13} and deviations of solar mixing and atmospheric mixing from maximality these special mixing schemes should be modified. We have three parameters, viz. $\delta\theta_{12}^{bm/tb}$, $\delta\theta_{23}^{bm/tb}$ and $\delta\theta_{13}^{bm/tb}$, which account the deviations of lepton mixing angles from their BM or TBM values. Numerical values of these deviation parameters can be obtained from global 3ν oscillation data. We then parametrize PMNS matrix in terms of these parameters. Such parametrization of lepton mixing matrix may help authors in phenomenological works which incorporate deviation of special mixing schemes. We implicate our parametrization set up in predicting possible structure of charged lepton mixing matrices which can generate the desired lepton mixing matrix from BM or TBM mixing matrices. We have found that charged lepton mixing matrices U_{lL}'s in both cases (BM and TBM) exhibit similar structures. Numerical analysis shows that these mixing matrices (U_{lL}^{bm} and U_{lL}^{tbm}), necessary to deviate BM mixing and TBM mixing in obtaining mixing parameters consistent with global data, are close to the CKM matrix of quark sector. This result is in agreement with the assumption, generally made in GUT based model, that charged lepton correction to neutrino mixing can be considered as CKM like.

References

[1] F P An *et al.* [DAYA-BAY Collaboration], *Phys. Rev. Lett.* **108**, 171803 (2012) [arXiv:1203.1669 [hep-ex]]; *Phys. Rev. Lett.* **112**, 061801 (2014).
[2] J K Ahn *et al.* [RENO Collaboration], *Phys. Rev. Lett.* **108**, 191802 (2012) [arXiv:1204.0626 [hep-ex]].
[3] Y Abe *et al.* 2012 [DOUBLE-CHOOZ Collaboration], *Phys. Rev. Lett.* **108**, 131801 [arXiv:1112.6353 [hep-ex]].
[4] P. Adamson *et al.* [MINOS Collaboration], *Phys. Rev. Lett.* **110**, 251801 (2013), *Phys. Rev. Lett.* **110**, 171801 (2013).
[5] K Abe *et al.* [T2K Collaboration], *Phys. Rev. Lett.* **112**, 061802 (2014), *Phys. Rev. Lett.* **112**, 181801 (2014).
[6] A Renshaw *et al.* [SK Collabortion], *Physics Procedia* **00**, (2014) 110.
[7] G Fogli, E Lisi, D Montanino, A Palazzo and A Rotunno, *Phys. Rev. D* **86**, 013012 (2012).
[8] D Forero, M Tortola and J Valle, *Phys. Rev. D* **86**, 073012 (2012).
[9] D Forero, M Tortola and J Valle, arXiv:1405.7540v3 [hep-ph].
[10] V. D. Barger, S. Pakvasa, T. J. Weiler and K. Whisnant, *Phys. Lett. B* **437**, 107 (1998).
[11] P F Harrison, D H Perkins and W G Scott 2002 *Phys. Lett. B* **530**, 167 [arXiv:hep-ph/0202074]; P F Harrison and W G Scott, *Phys. Lett. B* **535**, 163 (2002) [arXiv:hep-ph/0203209].
[12] C S Lam, *Phys. Lett. B* **507**, 214 (2001); P F Harrison and W G Scott, *Phys. Lett. B* **547**, 219 (2002); C S Lam, *Phys. Rev. D* **71**, 093001 (2005).

[13] M. Jezabek and Y. Sumino, *Phys. Lett. B* **457**, 139 (1999); Z. Z. Xing, *Phys. Rev. D* **64**, 093013 (2001), *Phys. Lett. B* **533**, 85 (2002) [arXiv:hep-ph/0204049v1].

[14] C. Giunti and M. Tanimoto, *Phys. Rev. D* **66**, 053013 (2002).

[15] S. K. Kang and C. S. Kim, *Phys. Rev. D* **90**, 7, 077301 (2014); S. T. Petcov, *Nucl. Phys. B* **892**, 400 (2015); J. Barry and W, Rodejohann, *Phys. Rev. D* **81**, 093002 (2010); X. G. He and A. Zee, *Phys. Rev. D* **84**, 053004 (2011); S. Morisi, K M Patel and E Peinado, *Phys. Rev. D* **84**, 053002 (2011) [arXiv:1107.0696v2[hep-ph]]; D. A. Sierra, I. M. Varzielas and E. Houet, *Phys. Rev. D* **87**, no. 9, 093009 (2013) [arXiv:1302.6499 [hep-ph]]; D. A. Sierra, I. M. Varzielas *J. High Energy Phys.* **1407**, 042 (2014), [arXiv:1404.2529 [hep-ph]].

[16] S. F. King, *Phys. Lett. B* **659**, 244 (2008) [arXiv:0710.0530v3 [hep-ph]].

[17] S. Antusch and S. F. King, *Phys. Lett. B* **631**, 42 (2005) [arXiv:hep-ph/0508044v2]; A. Romanino *Phys. Rev. D* **70**, 013003 (2004); K. A. Hochmuth, S. T. Petcov and W. Rodejohann, *Phys. Lett. B* **654**, 177 (2007) [arXiv:0706.2975v2 [hep-ph]]; S. Boudjemaa and S. F. King, *Phys. Rev. D* **79**, 033001 (2009).

[18] D Marzocca, S. T. Petcov, A Romanino and M. C. Sevilla *J. High Energy Phys.* **1305**, 073 (2013); D. Marzocca, A. Romanino *J. High Energy Phys.* **1411**, 159 (2014); S. Dev, R. R. Gautam and L. Singh *Phys. Rev. D* **89**, 1,013006 (2014); S. Roy and N. N. Singh *Indian J. Phys.* **88**, 5, 513 (2014); K. Siyeon [arXiv:1208.2645[hep-ph]]; J. A. Acosta, A. Aranda, M. A. Buen-Abad, A. D. Rojas *Phys. Lett. B* **718**, 1413 (2013); A Rashed *Nucl. Phys. B* **874**, 679 (2013).

[19] N. Cabibbo, *Phys. Rev. Lett.* **10**, 531 (1963); M. Kobayashi and T. Maskawa *Prog. Theor. Phys.* **49**, 652 (1973).

[20] T. Ohlsson *Phys. Lett. B* **622**, 159 (2005); D. Marzocca, S. T. Petcov, A. Romanino, M. Spinrath arXiv:1108.0614v2 [hep-ph]; S. Antusch and V. Maurer, *Phys. Rev. D* **84**, 117301 (2011) [arXiv:1107.3728v2[hep-ph]]; S. Antusch, C. Gross, V. Maurer and C. Sluka arXiv:1205.1051v2[hep-ph].

[21] M. Raidal, *Phys. Rev. Lett.* **93**, 161801 (2004); H. Minakata and A. Y. Smirnov, *Phys. Rev. D* **70**, 073009 (2004); S. Antusch, S. F. King and R. N. Mohapatra, *Phys. Lett. B* **618**, 150 (2005); Y. Zheng *Phys. Rev. D* **81**, 073009 (2010).

[22] S. F. King, *Phys. Lett. B* **718** 136 (2012) [arXiv:1205.0506v2 [hep-ph]]; B. Hu *Phys. Rev. D* **87** (2013) 5, 053011; S. Roy, S. Morisi, N. N. Singh and J. W. F. Valle arXiv:1410.3658v1 [hep-ph].

[23] P. H. Frampton, S. T. Petcov and W. Rodejohann, *Nucl. Phys. B* **687**, 31 (2004) [arXiv:hep-ph/0401206v2].

[24] F. Bazzocchi and L. Merlo, arXiv:1205.5135v1[hep-ph]; C. Duarah, A. Das and N. N. Singh *Phys. Lett. B* **718** 147 (2012) [arXiv:1207.5225[hep-ph]].

[25] C. Duarah, A. Das, N. N. Singh, *Indin J. Phys.*, **87**(12), 1269 (2013).

[26] K Nakamura *et. al.* (Particle Data Group) *J. Phys. G: Nucl. Part. Phys.* **37**, 075021 (2010).

Mass spectra of four quark states in the charm and strange sector

Smruti Patel and P. C. Vinodkumar
Department of Physics, Sardar Patel University, Vallabh Vidyanagar-388120, Gujarat, India

Presenter: Smruti Patel (*fizix.smriti@gmail.com*); HEP.3, Poster, CICAHEP15.194

We have developed a non-relativistic approach to study exotic heavy hadron spectroscopy, where the four body system is considered as three subsequent two-body systems. We have solved numerically the Schrödinger equation using an effective Cornell-like potential to model the two-body interaction in each step of the tetraquark calculation. We have studied four body systems consisting of diquark-antidiquark in the charm and strange sector and determined the mass spectra of ground and excited tetraquark states by incorporating the spin hyperfine, spin-orbit and tensor components of the one gluon exchange interaction. Here, the tetraquark model consists of a diquark-antidiquark system ($Qq - \bar{Q}\bar{q}$), in which the diquarks interact through the exchange of colored objects and the attraction force can be intense. We have been able to assign the J^{PC} values for many of the recently observed exotic states according to their structure. Our results are in good agreement with experiment and other available theoretical results.

1. Introduction

In last few years many charmonium and charmonium-like states were discovered at B-factories [1] which cannot be simply accommodated in the quark-antiquark ($c\bar{c}$ and $q\bar{s}$) picture. These states and especially the charged charmonium-like ones can be considered as indications of the possible existence of exotic multiquark states. Whereas some of these are good charmonium candidates, as predicted in different models, many states have exotic properties, which may indicate that exotic states, such as multi-quark, molecule, hybrid or hadron-quarkonium have been observed [2]. Understanding the nature of the exotic XYZ resonances is one of the open problems in hadronic spectroscopy. Despite the experimental efforts, the structure of these particles still lacks of an accepted theoretical framework. The most popular models proposed to describe the internal structure of these particles are the compact diquark-antidiquark [3, 4, 5], the loosely bound meson molecule [6, 7, 8, 9, 10], the so-called hadro-charmonium [11] and the gluonic hybrid [12]. None of these models have been generally accepted as the right one yet. In our earlier work [5], we have calculated masses of the hidden heavy-flavor tetraquarks and light tetraquarks in the framework of the non-relativistic quark model using the Cornell like potential in Quantum Chromo Dynamics(QCD). Here we extend this analysis to the consideration of heavy tetraquark states with open charm and strange. This study could help in revealing the nature of the anomalous charmed-strange tetraquarks.

The paper is organized as follows. In Section 2, we describe the phenomenological quark-antiquark interaction potential and extract the parameters that describe the ground state masses of four quark system. We also compute the low lying orbital excited states of these systems. In Section 3 we present and analyze our results to draw important conclusions.

2. The phenomenology and extraction of the spectroscopic parameters

There are many methods to estimate the mass of a hadron, among which phenomenological potential model is a fairly reliable one, specially for heavy hadrons. In this paper we shall take a different path and investigate different ways in which the experimental data can be reproduced. Non-relativistic interaction potential we have used here is the Cornell potential consists of a central term $V(r)$ which is being just a sum of the Coulomb (vector) and linear confining (scalar) parts given by

$$V(r) = V_V + V_S = k_s \frac{\alpha_s}{r} + \sigma r, \tag{1}$$

where

$$\begin{aligned} k_s &= -4/3 \;\; for \;\; q\bar{q}, \\ &= -2/3 \;\; for \;\; qq \;\; or \;\; \bar{q}\bar{q}. \end{aligned} \tag{2}$$

The value of the α_s running coupling constant is determined through the model, namely

$$\alpha_s(\mu^2) = \frac{4\pi}{(11 - \frac{2}{3}n_f)(\ln \frac{\mu^2}{\Lambda^2})}, \tag{3}$$

where μ is the renormalization scale related to the constituent quark mass, $\Lambda = 0.413$ GeV and n_f is number of flavours. The model parameters we have used in the present study are same as in Refs. [13, 14]. The constituent quark masses employed here are taken from Particle Data Group [15]. Different degenerate n$^{2S+1}L_J$ low-lying tetraquark states are calculated by including spin dependent part of the usual one gluon exchange potential [16, 17, 18, 19]. The potential description extended to spin dependent interactions results in three types of potential terms such as the spin-spin, the spin-orbit and the tensor part that are to be added to the spin independent potential as given by equation (1). Accordingly, the spin-dependent part V_{SD} is given by

$$\begin{aligned} V_{SD} \quad = \quad & V_{SS}\left[\frac{1}{2}(S(S+1)-\frac{3}{2}))\right] \\ & +V_{LS}\left[\frac{1}{2}(J(J+1)-S(S+1)-L(L+1))\right] \\ & +V_T\left[12\left(\frac{(S_1.r)(S_2.r)}{r^2}-\frac{1}{3}(S_1.S_2)\right)\right]. \end{aligned} \tag{4}$$

The spin-orbit term containing V_{LS} and tensor term containing V_T describe the fine structure of the states, while the spin-spin term containing V_{SS} proportional to $2S_1.S_2$ gives the hyperfine splitting. The co-efficient of these spin-dependent terms of equation (4) can be written in terms of the vector and scalar parts of static potential $V(r)$ as

$$V_{LS}^{ij}(r) = \frac{1}{2M_iM_jr}\left[3\frac{dV_V}{dr} - \frac{dV_S}{dr}\right], \tag{5}$$

$$V_T^{ij}(r) = \frac{1}{6M_iM_j}\left[3\frac{d^2V_V}{dr^2} - \frac{1}{r}\frac{dV_S}{dr}\right], \tag{6}$$

$$V_{SS}^{ij}(r) = \frac{1}{3M_iM_j}\nabla^2 V_V = \frac{16\pi\alpha_s}{9M_iM_j}\delta^3(r). \tag{7}$$

Where M_i, M_j corresponds to the masses and r is relative co-ordinate of the two body system under consideration.

Our main aim is to interpret the four quark state structure in the different scheme i.e. clusters of diquark-antidiquark like structure. In this picture, we have treated the four particle system as two-two body systems interacting through effective potential of the same form of the two body interaction potential discussed above. The Schrödinger equation with the potential given by equation (1) is numerically solved using the Mathematica notebook of the Runge-Kutta method [20] to obtain the energy eigen values and the corresponding wave functions.

2.1 The four quark state as Qq, $\bar{Q}\bar{q}$ clusters

In this section, we calculate the mass spectra of tetraquarks with hidden charm as the bound states of two clusters (Qq and $\bar{Q}\bar{q}$), ($Q = c$; $q = u, d$). We think of the diquarks as two correlated quark with no internal spatial excitation. Because a pair of quarks can't be a color singlet, the diquark can only be found confined into the hadrons and used as effective degree of freedom. Heavy light diquarks can be the building blocks of a rich spectrum of exotic states which can not be fitted in the conventional charmonium assignment. Maiani et al [3] in the framework of the phenomenological constituent quark model considered the masses of hidden/open charm diquark-antidiquark states in terms of the constituent diquark masses with their spin-spin interactions included.

We discuss the spectra in the framework of a non-relativistic Hamiltonian including chromo-magnetic spin-spin

Table 1. The mass spectra of $Qq - \bar{Q}\bar{q}$ states for quark content $cs\bar{c}\bar{s}$ (in GeV).

Diquark content	S	L	J	Mass	V_{ss}	V_{LS}	V_T	M_J
$S\bar{S}$	0	0	0	4.069	0.0	0.0	0.0	4.069
	0	1	1	4.530	0.0	0.0	0.0	4.530
						0.0		
$S\bar{A}$	1	0	1	4.089	0.0	0.0	0.0	4.089
	1	1	0	4.550	0.0	-0.029	-0.133	4.388
			1		0.0	-0.0145	0.033	4.569
			2		0.0	0.0145	-0.033	4.532
$A\bar{A}$	0	0	0	4.110	-0.140	0.0	0.0	3.969
	1	0	1		-0.070	0.0	0.0	4.039
	2	0	2		0.070	0.0	0.0	4.189
	0	1	1	4.571	-0.013	0.0	-0.11	4.469
	1	1	0	4.571	-0.0069	-0.029	-0.220	4.314
			1		-0.0069	-0.014	-0.055	4.494
			2		-0.0069	14	-0.121	4.457
	2	1	1	4.571	0.0069	-0.043	-0.340	4.192
			2		0.0069	-0.014	0.121	4.685
			3		0.0069	0.029	-0.176	4.430

Table 2. The mass spectra of $Qq - \bar{Q}\bar{q}$ states for quark content $cs\bar{s}\bar{s}$ (in GeV).

Diquark content	S	L	J	M_{cw}	V_{SS}	V_{LS}	V_T	M_T
$S\bar{A}$	1	0	1	3.991	0.0	0.0	0.0	3.991
	1	1	0	4.449	0.0	-0.0272	-0.132	4.289
			1		0.0	-0.013	0.033	4.469
			2		0.0	0.013	-0.033	4.429
$A\bar{A}$	0	0	0	4.015	-0.131	0.0	0.0	3.884
	1	0	1		-0.065	0.0	0.0	3.950
	2	0	2		0.065	0.0	0.0	4.081
	0	1	1	4.474	-0.0123	0.0	-0.110	4.351
	1	1	0	4.474	-0.0061	-0.027	-0.220	4.220
			1		-0.0061	-0.0135	-0.055	4.399
			2		-0.0061	0.0135	-0.121	4.360
	2	1	1	4.474	0.0061	-0.040	-0.341	4.098
			2		0.0061	-0.013	0.121	4.588
			3		0.0061	0.027	-0.176	4.331

interactions between the quarks (antiquarks) within a diquark (antidiquark). Masses of diquark (antidiquark) states are obtained by numerically solving the Schrödinger equation with the respective two body potential given by equation (1) and incorporating the respective spin interactions described by equation (4) perturbatively. In the diquark-antidiquark structure, the masses of the diquark/diantiquark system are given by

$$m_d = m_Q + m_q + E_d + \langle V_{SD} \rangle_{Qq}, \tag{8}$$

Table 3. Comparison of the masses of diquark antidiquark states with other theoretical predictions for quark content $cs\bar{c}\bar{s}$ (left to the table) and $cs\bar{s}\bar{s}$ (right to the table) (in GeV).

J^{PC}	Present $[cs\bar{c}\bar{s}]$	[13]	[4]	Present $[cs\bar{s}\bar{s}]$	[14]
0^{++}	4.069	4.051		3.241	3.025
1^{++}	4.089	4.113			
0^{++}	3.969	4.110		3.136	3.003
1^{++}	4.039	4.113		3.200	3.051
2^{++}	4.189	4.209		3.326	3.135
1^{--}	4.469	4.466	4.330 ± 0.070		

Table 4. Comparison of some predicted states with experimental results (in GeV).

State	Mass	J^{PC}	Exp
Y(4360)	4.360	1^{--}	4.361 ± 0.013 [21]
Y(4274)	4.289	0^{-+}	$4.274^{+0.0084}_{-0.0067}$ [22]
Y(3943)	3.950	1^{+-}	3.943 ± 0.017 [23]
X(4350)	4.360	2^{++}	$4.350^{+0.0046}_{-0.0051}$[24]

$$m_{\bar{d}} = m_{\bar{Q}} + m_{\bar{q}} + E_{\bar{d}} + \langle V_{SD} \rangle_{\bar{Q}\bar{q}}. \tag{9}$$

Further, the same procedure is adopted to compute the binding energy of the diquark-antidiquark bound system as

$$M_{d-\bar{d}} = m_d + m_{\bar{d}} + E_{d\bar{d}} + \langle V_{SD} \rangle_{d\bar{d}}. \tag{10}$$

Where Q and q represents the heavy quark and light quark respectively. In the present paper, d and $\bar{d}$ represents diquark and antidiquark respectively. While E_d, $E_{\bar{d}}$, $E_{d\bar{d}}$ are the energy eigen values of the diquark, antidiquark and diquark-antidiquark system respectively. The spin-dependent potential (V_{SD}) part of the Hamiltonian described by equation (4) has been treated perturbatively.

3. Results and Discussions

The masses of the low lying hidden charm and strange four quark states as diquark−diantiquark ($Qq - \bar{Q}\bar{q}$) states have been computed. Various combinations of the orbital and spin excitations have been considered. The results obtained are listed in Tables 1 and 2. We have compared the present results for $[cs\bar{c}\bar{s}]$ and $[cs\bar{s}\bar{s}]$ quark content with other available theoretical data and these results are listed in Table 3. The authors of Refs. [4, 13] have considered only diquark−diantiquark spin interactions and thus they have not considered spin-orbit interactions between diquarks and antidiquarks. This ignorance of the spin-orbit interactions have contributed to the differences between the present results and those of the Refs. [4, 13]. We have predicted some of the states with its parity quantum number which are listed in Table 4 and they are in good agreement with the experimental results. Finally, we believe that future high luminosity experiments will be able to shed more light in the understanding of the these exotic states.

References

[1] A. J. Bevan et al. [BaBar and Belle Collaborations], *The Physics of the B Factories*, Eur. Phys. J. C **74**, 3026 (2014).

[2] For a recent review, see N. Brambilla et al., *Heavy quarkonium: progress, puzzles, and opportunities*, Eur. Phys. J. C **71**, 1534 (2011).

[3] L. Maiani, F. Piccinini, A. Polosa and V. Riquer, Phys. Rev. D **71**, 014028 (2005) hep-ph/0412098; L. Maiani, V. Riquer, R. Faccini, F. Piccinini, A. Pilloni and A. D. Polosa, Phys. Rev. D **87**, 111102 (2013) [arXiv:1303.6857].
[4] L. Maiani, F. Piccinini, A. Polosa and V. Riquer, Phys. Rev. D **89**, 114010 (2014) arXiv:1405.1551; A. Ali, L. Maiani, A. D. Polosa and V. Riquer, Phys. Rev. D **91**, 017502 (2015) arXiv:1412.2049.
[5] S. Patel et. al. , Eur. Phys. J. A. **50**, 131(2014).
[6] E. Braaten and M. Kusunoki, Phys. Rev. D **69**, 074005 (2004).
[7] A. K. Rai et al., Nuclear Physics A **782**, 406 (2007).
[8] A. K. Rai and D. P. Rathaud, Eur. Phys. J. C **75**, 462 (2015).
[9] Smruti Patel et. al., Proceedings of Science (PoS) (Hadron 2013) **189** (2013).
[10] M. Cleven, F. K. Guo, C. Hanhart and U.G. Meiyner, Eur. Phys. J. A **47**, 120 (2011); Q. Wang and Q. Zhao, Phys. Lett. B **725**, 127-133 (2013) [arXiv:1306.3096].
[11] S. Dubynskiy and M. Voloshin, Phys. Lett. B **666**, 344 (2008) [arXiv:0803.2224].
[12] L. Liu et al. [Hadron Spectrum Collaboration], JHEP **1207**, 126 (2012); P. Guo, A. P. Szczepaniak, G. Galata, A. Vassallo and E. Santopinto, Phys. Rev. D **78**, 056003 (2008).
[13] D. Ebert, R.N. Faustov, V.O. Galkin, Eur. Phys. J. C **58**,399405 (2008) .
[14] D. Ebert, R.N. Faustov, V.O. Galkin, Phys. Lett. B **634**, 214219 (2006).
[15] K. A. Olive et al (Particle Data Group), Chinese Physics C **38**, No. 9, 090001(2014).
[16] T. Barnes, S. Godfrey, E.S. Swanson, Phys. Rev. D **72**, 054026(2005).
[17] Olga Lakhina, Eric S. Swanson, Phys. Rev D **74**, 014012 (2006)[arXiv:hep-ph/0603164].
[18] M. B. Voloshin, Prog. Part. Nucl. Phys. **61**, 455 (2008) [arXiv:0711.4556 [hep-ph]].
[19] E. Eichten, S. Godfrey, H. Mahlke, J.L. Rosner, Rev. Mod. Phys. **80**, 1161(2008).
[20] W. Lucha, F. Shoberl, Int. J. Mod. Phys. C **10** (1999) [arXiv:hep-ph/9811453].
[21] B Aubert et.al., [BABAR Collaboration], Phys. Rev. Lett. **98**, 212001(2007).
[22] T. Aaltonen et.al., [CDF Collaboration], arXiv:1101.6058 [hep-ex].
[23] S. K. Choi, et al. [Belle Collaboration], Phys. Rev. Lett. **94**, 182002(2005).
[24] C. P. Shen et.al., [BELLE Collaboration], Phys. Rev. Lett. **104**, 112004(2010).

Comparison of analytical solutions of the coupled DGLAP equations for F_2^P at small *x*

Neelakshi Niti Kachari Borah[a] and Dilip Kumar Choudhury [a,b]

(a) Department of Physics, Gauhati University, Guwahati-781014, Assam, India.
(b) Physics Academy of North-East, Guwahati-781014, Assam, India.

Presenter: Neelakshi Niti Kachari Borah (*nishi_indr@yahoo.co.in*); HEP.3, Poster, CICAHEP15.204

Coupled DGLAP equations involving singlet quark and gluon distributions are explored by a Taylor expansion at small *x* as two first order partial differential equations in two variables: Bjorken *x* and *t* ($t = ln\frac{Q^2}{\Lambda^2}$). The system of equations are then solved by the Lagrange's method and Method of Characteristics. We obtain the proton structure function F_2^P by combining the corresponding non-singlet and singlet structure functions by both the methods. Analytical solutions for F_2^P thus obtained are compared with the data available and their compatibility is checked. Data favours the analytical solution by Lagrange's method.

1. Introduction

Solutions of DGLAP [1, 2, 3, 4] evolution equations give quark and gluon structure functions which produce ultimately proton, neutron and deuteron structure functions. The standard program to study the x dependence of quark and gluon PDFs is to compare the numerical solutions of the DGLAP equations with the data and so to fit the parameters of the x profiles of the PDFs at some initial factorization scale Q_0^2 and the asymptotic scale parameter Λ. However, for analyzing exclusively the small-x region, there exists alternative simpler analysis, some of which are the existing analytical solutions of the DGLAP equations in the small-x limit with considerable phenomenological success [5, 6, 7, 8, 9]. In this work, we make an extensive comparative study on the applicability of two analytical methods: Lagrange's method [10] and method of characteristics [11, 12, 13] in context of the unpolarized proton structure function F_2^P. This suggests utility of such approaches in understanding the dynamics of evolution of quarks and gluons at small *x*.

In Section 2 we describe the formalism, Section 3 is devoted to testing our prediction's comparison with the data, while in Section 4, we give our conclusion.

2. Formalism

2.1 Singlet coupled DGLAP equations in Taylor approximated form

In order to get the F_2^P we need both singlet and non-singlet structure functions. In our earlier work [5] we reported our analytical solutions by the two analytical methods . Hence we discuss only the solution for the quark singlet part here. The coupled DGLAP equations for quark singlet ($\Sigma(x, Q^2)$) and gluon ($G(x, Q^2)$) densities are [1, 2, 3, 4],

$$\frac{\partial}{\partial \ln Q^2}\begin{pmatrix} \Sigma\left(x, Q^2\right) \\ G\left(x, Q^2\right) \end{pmatrix} = \frac{\alpha_s\left(Q^2\right)}{2\pi}\begin{pmatrix} P_{qq} & P_{qg} \\ P_{gq} & P_{gg} \end{pmatrix} \otimes \begin{pmatrix} \Sigma\left(x, Q^2\right) \\ G\left(x, Q^2\right) \end{pmatrix}. \tag{1}$$

Introducing the variable $t = \ln\frac{Q^2}{\Lambda^2}$ and using the explicit forms of the splitting functions $P_{i,j}(i, j = q, g)$, the evolution equation for singlet distribution in LO can be written as

$$\frac{\partial F_2^S(x,t)}{\partial t} - \frac{A_f}{t}\left[\{3 + 4\ln(1-x)\}F_2^S(x,t) + 2\int_x^1 \frac{dz}{(1-z)}\left\{(1+z^2)F_2^S\left(\frac{x}{z}, t\right)\right.\right.$$
$$\left.\left. -2F_2^S(x,t)\right\} + \tfrac{3}{2}n_f\int_x^1 dz\left(z^2 + (1-z)^2\right)G\left(\tfrac{x}{z}, t\right)\right] = 0. \tag{2}$$

Here $A_f = \frac{4}{3\beta_0}$, $\beta_0 = 11 - \frac{2}{3}n_f$ and $\alpha_s(t) = \frac{4\pi}{\beta_0 t}$. $F_2^S(x,t)$ is the singlet structure functions of the proton. Introducing a variable u defined as $u = 1 - z$ and doing Taylor approximation we can express equation (2) in a more precise form as

$$\frac{\partial F_2^S(x,t)}{\partial t} - \frac{A_f}{t}\left[3 + 4\ln(1-x)F_2^S(x,t) + (2x-3)F_2^S(x,t) + \left(x + 2x\ln\frac{1}{x}\right)\frac{\partial F_2^S(x,t)}{\partial x}\right]$$
$$-\frac{A_f}{t}\left[n_f\left(1-\frac{3}{2}x\right)G(x,t) - \frac{n_f}{2}\left(5x - 3x\ln\frac{1}{x}\right)\frac{\partial G(x,t)}{\partial x}\right] = 0. \quad (3)$$

The exact relation between the gluon distribution function $G(x,t) = xg(x,t)$ and quark distribution function $F_2^S(x,t) = x\sum_i e_i^2 \{q_i(x,t) + \bar{q}_i(x,t)\}$ is not derivable in QCD even in LO. However, simple forms of such relation are available in literature to facilitate the analytical solution of coupled DGLAP equations [14, 15]. A more rigorous analysis was done by Lopez and Yundurain [16] and they investigated the behaviour of the singlet $F_2^S(x,Q^2)$ and gluon $G(x,Q^2)$ as $x \to 0$. They observed that,

$$F_2^S(x,Q^2)_{x\to 0} = B_s(Q^2)x^{-\lambda_s}, \quad (4)$$

$$G(x,Q^2)_{x\to 0} = B_G(Q^2)x^{-\lambda_s}, \quad (5)$$

where B_s and B_G are Q^2 dependent and λ_s is strictly positive. Thus,

$$\frac{G(x,Q^2)}{F(x,Q^2)}_{x\to 0} \simeq f(Q^2). \quad (6)$$

It suggests a more general form [17],

$$G(x,Q^2) = k(Q^2)F_2^S(x,Q^2). \quad (7)$$

Using above relation given by equation (7), we express equation (3) as

$$\frac{\partial F_2^S(x,t)}{\partial t} - \frac{A_f}{t}\left[\{3 + 4\ln(1-x) + (2x-3)\}F_2^S(x,t) + n_f\left(1-\frac{3}{2}x\right)K(Q^2)F_2^S(x,t)\right]$$
$$-\frac{A_f}{t}\left[x + 2x\ln\frac{1}{x} - \frac{n_f}{2}\left(5x - 3x\ln\frac{1}{x}\right)K(Q^2)\right]\frac{\partial F_2^S(x,t)}{\partial x} = 0. \quad (8)$$

Which is a partial differential equation for the singlet structure function $F_2^S(x,t)$ with respect to the variables x and t. We solve this PDE equation (8) with the two formalisms described here, the Lagrange's method and Method of Characteristics. In order to do that we express equation (8) as

$$t\frac{\partial F_2^S(x,t)}{\partial t} = \omega_1\frac{\partial F_2^S(x,t)}{\partial x} + \omega_2 F_2^S, \quad (9)$$

where

$$\omega_1 = \frac{4}{3\beta_0}\{x + 2x\ln\frac{1}{x} - \frac{n_f}{2}\left(5x - 3x\ln\frac{1}{x}\right)K(Q^2), \quad (10)$$

$$\omega_2 = \frac{4}{3\beta_0}\{3 + 4\ln(1-x) + (2x-3) + n_f\left(1-\frac{3}{2}x\right)K(Q^2). \quad (11)$$

2.2 Solution by the Lagrange's Auxiliary Method

To solve the equation (9) by the Lagrange's Auxiliary method [10], we write the equation in the form,

$$Q(x,t)\frac{\partial F_2^S(x,t)}{\partial t} + P(x,t)\frac{\partial F_2^S(x,t)}{\partial x} = R(x,t,F_2^S(x,t)), \quad (12)$$

where

$$Q(x,t) = t, \quad (13)$$

$$P(x,t) = -\omega_1, \quad (14)$$

and

$$R(x,t,F_2^S(x,t)) = R'(x)F_2^S(x,t) \tag{15}$$

with

$$R'(x) = \omega_2. \tag{16}$$

If $u(x,t,F_2^S) = C_1$ and $v(x,t,F_2^S) = C_2$ are the two independent solutions of equation (12), then in general, the solution of equation (12) is

$$F(u,v) = 0, \tag{17}$$

where F is an arbitrary function of u and v. Using the physically plausible boundary conditions and solving the auxiliary system for u and v, we obtain the solution for equation (12) as

$$F_2^S(x,t) = F_2^S(x,t_0)\left(\frac{t}{t_0}\right)\frac{[X^S(x) - X^S(1)]}{[X^S(x) - (\frac{t}{t_0})X^S(1)]} \tag{18}$$

with the explicit analytical form of $X^S(x)$ in the leading $(\frac{1}{x})$ approximation are,

$$X^S(x) = \exp\left[-\frac{6\beta_0}{4(4+3n_f K(Q^2)}\log[\log x]\right], \tag{19}$$

leading to

$$X^S(1) = 0 \tag{20}$$

which yields,

$$F_2^S(x,t) = F_2^S(x,t_0)\left(\frac{t}{t_0}\right). \tag{21}$$

Equation (21) gives the t evolutions of singlet structure function at LO.

2.3 Solution by the method of characteristics

To solve the PDE equation (9) by the method of characteristics, we express it in terms of a new set of coordinates (s,τ), such that equation (9) becomes an ODE w.r.t. one of the new variables. The characteristic equations of equation (9) are given by,

$$\frac{dt}{ds} = t, \tag{22}$$

$$\frac{dx}{ds} = -\omega_1. \tag{23}$$

The left hand side of equation (9) can be expressed as an ordinary derivative with respect to t and the equation becomes an ordinary differential equation:

$$\frac{dF_2^S(s,\tau)}{dt} + c^S(s,\tau)\,F_2^S(s,\tau) = 0, \quad \text{where} \quad c^S(s,\tau) = \omega_2. \tag{24}$$

Integrating equation (24) over t from t_0 to t along the characteristic curve, the solution of the equation for characteristic equations leads us to the solution for $F_2^S(x,t)$ as

$$F_2^S(x,t) = F_2^S(x,t_0)(\frac{t}{t_0})^{n(x,t)} \tag{25}$$

where,

$$n(x,t) = \frac{1}{\log(\frac{t}{t_0})}\log\left(\frac{F_2^S(\tau)}{F_2^S(x,t_0)}\right) + \frac{(-\frac{4}{3\beta_0}\xi_1)}{\log\frac{t}{t_0}}, \tag{26}$$

$$\xi_1 = 4\log\left(1-\tau\exp\left[-(\frac{t}{t_0})^{\frac{1}{\alpha_1}}\right]\right) + 2\tau\exp\left[-(\frac{t}{t_0})^{\frac{1}{\alpha_1}}\right] + n_f\left(1-\frac{3}{2}\tau\exp\left[-(\frac{t}{t_0})^{\frac{1}{\alpha_1}}\right]\right)K(Q^2), \tag{27}$$

$$\tau = x\exp\left[(\frac{t}{t_0})^{\frac{1}{\alpha_1}}\right], \tag{28}$$

$$\alpha_1 = \frac{3\beta_0}{4}\{2+K(Q^2)\frac{9}{2}\}. \tag{29}$$

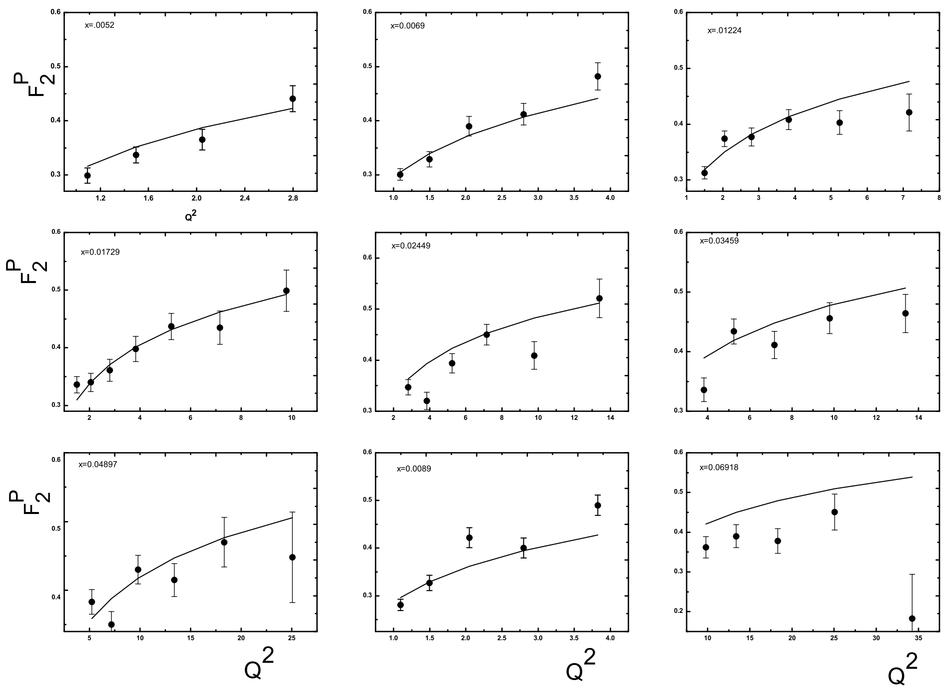

Figure 1. Proton structure function $F_2^P(x,t)$ as function of Q^2 at different x values using Lagrange's method. Data are taken from E665 [19].

2.4 The function $K(Q^2)$

Traditional determination of quark and gluon distribution function includes simultaneous fitting of experimental data (mainly at small x) of the proton structure function $F_2^P(x,Q^2)$ measured in deep inelastic scattering, with a large number of values of x and Q^2. The most appropriate QCD inspired functional form for the function $K(Q^2)$ has to be of the logarithmic form and we consider it to be,

$$K(Q^2) = (\log\frac{Q^2}{\Lambda^2})^{\sigma}, \tag{30}$$

where σ is a parameter to be determined. To determine the 'best-fit' value for σ, we consider the input PDFs at entire x region. Our analysis yields that the best-fit value of σ lies in between 2 and 3 for $Q^2 = 2$ GeV^2. For our further calculations we take the average and fix $\sigma = 2.5$.

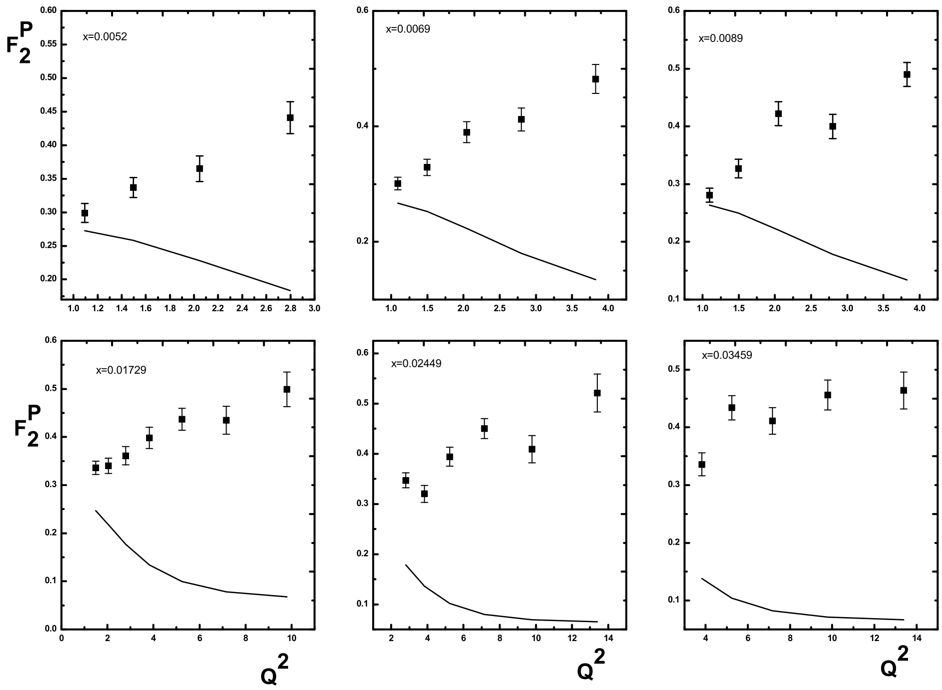

Figure 2. Proton structure function$F_2^P(x,t)$ as function of Q^2 at different x values using Method of characteristics. Data are taken from E665 [19].

2.5 Results and Discussion

We check the compatibility of the analytical methods in terms of proton structure function F_2^P, which we derive combining our analytical solutions for both non-singlet [5] and singlet structure functions to calculate the proton structure function. We use the MSTW 2008 [18] input for evolution and the range of data considered for comparison are $0.0052 \leq x \leq 0.18$ and 1.094 GeV^2 $\leq Q^2 \leq 34.27$ GeV^2 for E665 [19]. Figs. 1 and 2 show comparison of our analytical results for F_2^P obtained by Lagrange's method and method of characteristics respectively, with E665 experimental data within small x and low Q^2 range $0.0052 \leq x \leq 0.04897$ and 1.093 GeV^2 $\leq Q^2 \leq 25$ GeV^2. Though the evolution of analytical result by Lagrange's method conforms well with data, that of method of characteristics decreases with increasing Q^2, which is against the general expectations of pQCD. The Q^2 dependence of the function $K(Q^2)$, given by equation (7) is playing an important role in our analytical solutions. For hence it shows in the solution by equation (25) by method of characteristics, though in case of the solution by Lagrange's method, equation (21), it does not have any visible effect, due to the consideration of $\frac{1}{x}$ limit.

3. Conclusion

This work is an extension of the comparative study of the two important analytical methods, Lagrange's and Method of Characteristics for proton structure function F_2^P, derived from corresponding analytical solutions for F_2^{NS} and F_2^S. For this part we pursue a general form as given by equation (7), relating $F_2^S(x,Q^2)$ and $G(x,Q^2)$ for comparison with theoretical analysis of [16]. The solution by Method of Characteristics has exclusive dependence on the relation. However, data analysed in the range $0.0052 \leq x \leq 0.04897$ and 1.093 GeV^2 $\leq Q^2 \leq 25$ GeV^2 is found to favour the former (Lagrange's method) and not the later (Method of Characteristics).

References

[1] Yu. L. Dokshitzer, *Calculation of the structure functions for deep inelastic scattering and e+ e- annihilation by perturbation theory in quantum chromodynamics (in Russian)*, Sov. Phys. JETP **46**, 641 (1977).
[2] V. N. Gribov and L. N. Lipatov, *Deep inelastic ep scattering in perturbation theory*, Sov. J. Nucl. Phys. **15**, 438 (1972).
[3] L. N. Lipatov, *The parton model and perturbation theory*, Sov. J. Nucl. Phys. **20**, 94 (1975).
[4] G. Altarelli and G. Parisi, *Asymptotic freedom in parton language*, Nucl. Phys. B **126**, 298 (1977).
[5] N. N. K. Borah, D. K. Choudhury and P. K. Sahariah, Advances in High Energy Physics, vol. 2013, Article ID **829803**, 2013.
[6] Mayuri Devee, R. Baishya and J. K. Sarma, *Evolution of singlet structure functions from DGLAP equation at next-to-next-to-leading order at small-x* Euro. Phys. J. C **72**, 2036 (2012).
[7] G. R. Boroun, Commun. Theor.Phys. **43**, 283 (2005).
[8] N. Ghahramany, G.R. Boroun, *Phys. Lett.* B **528**, 239 (2002).
[9] G. R. Boroun, Lithuanian J. of Phys. **48**, 121 (2008).
[10] I. Sneddon, *Elements of Partial Differential Equations*, M.Graw Hill, NewYork (1957) p131.
[11] S. J. Farlow, *Partial Differential Equations for Scientists and Engineers*, John Willey (1982).
[12] W. E. Williams, *Partial Differential Equations*, Clarendon Press, Oxford (1980).
[13] E. C. Zachmanoglou and D. W. Thoe, *Introduction to Partial Differential Equations with Applications*, Williams and Wilkins (1976).
[14] D. K. Choudhury, A. Siakia, Pramana J. Phys. **33**, 359 (1989).
[15] J. K. Sarma, D. K. Choudhury, and G. K. Medhi, *x-distribution of deuteron structure function at low x*, Phys. Lett. B **403**, 139 (1997).
[16] C. Lopez and F. J. Yndurain, *Behaviour of Deep inelastic Structure Functions Near Physical Region End-points From QCD.* Nucl. Phys. B **171**, 231 (1980).
[17] A. Jahan, D. K. choudhury, Comm. Theo. Phys. **61**, 5 (2014).
[18] A. D. Martin, W. S. Stirling, R. S. Thorne and G Watt. hep-ph/0901.0002v3.
[19] M. R. Adams et al. (E665), Phys. Rev. D **54**, 3006 (1996).

Field decomposition formulation for QCD and confinement potential – A non-perturbative approach

Garima Punetha and H. C. Chandola

Centre of Advanced Study, Department of Physics, D.S.B. Campus, Kumaun University, Nainital-263001, India

Presenter: Garima Punetha (*garimapunetha@gmail.com*); HEP.1, Oral, CICAHEP15.214.1

A gauge independent field decomposition formulation for $\mathrm{SU}(3)_c$ QCD, has been constructed in terms of dual gauge potentials which takes into account the local as well as the topological structure of the color gauge group into its dynamics. The topological magnetic charges associated with resulting monopoles have been shown to evolve through the second homotopy of the gauge group. The dynamical configuration of the resulting dual QCD vacuum and its flux tube configuration have been investigated for analyzing the non-perturbative features of QCD. Using color reflection invariance, the correct physical spectrum of resulting dual QCD in the dynamically broken phase of magnetic symmetry has been computed which has been shown to include two magnetic glueballs appearing as the collective excitations of the magnetically condensed dual QCD vacuum. Evaluating the associated non-perturbative dual gluon propagator, the inter-quark static potential has been derived and analyzed for its color confining properties.

1. Introduction

Quark confinement is one of the most important non-perturbative phenomena in Quantum Chromodynamics (QCD), the proper understanding of which continues to be a challenge for the physics of elementary particles. One of the most [1] popular mechanism of quark confinement has been propagated using the dual version of the superconductivity, in which the QCD vacuum state behaves like a magnetic superconductor and the monopole degrees of freedom play the most prominent role to describe confinement. The existence of chromomagnetic monopole has been studied explicitly through lattice formulation of gauge theories [2] using a gauge condition [3, 4, 5, 6]. However, such gauge condition is centered around fixing to one particular gauge which leads to the problem of the color symmetry breaking in view of the Schlider's theorem. The present paper, therefore, deals to present a gauge independent field decomposition formalism for $\mathrm{SU}(3)_c$ QCD in which the QCD potential splits into the non-topological abelian part and the topological monopole part [7, 8, 9, 10] to establish the magnetic confinement and to construct the heavy quark-antiquark confining potential leading to a viable topological basis for the confinement.

2. Monopole condensation and quark confinement potential in SU(3) dual QCD

The mathematical foundation for the field decomposition formulation for QCD evolves from the fact that the non-abelian gauge symmetry always allows an internal symmetry called magnetic symmetry which imposes a strong constraint on the connections and the associated gauge covariant magnetic symmetry condition may be expressed in the following form [7, 8, 10, 11, 12],

$$D_\mu \hat{m} = 0\,,\ i.e.\ (\,\partial_\mu + g\,\mathbf{W}_\mu \times\,)\,\hat{m} = 0\,, \tag{1}$$

where $\hat{m}$ is the magnetic killing vector which forms an adjoint representation of the gauge group G. The killing vector $\hat{m}$ automatically selects another $\hat{m}^{'}$ by the symmetric product of $\hat{m}$,

$$\hat{m}^{'} = \sqrt{3}\hat{m} * \hat{m},\ \ D_\mu \hat{m}^{'} = 0, \tag{2}$$

where $*$ denotes the symmetric product. For a complete description of the monopole solutions two killing vectors [8] $\hat{m}$ and $\hat{m}^{'}$ are necessary and sufficient and one may choose the fundamental symmetry $\hat{m}$ to be always λ_3-like, in which the product symmetry $\hat{m}^{'}$ automatically becomes λ_8-like.

The most general gauge potential in SU(3) QCD which satisfies the constraints (1) and (2) can then be expressed as,

$$\mathbf{W}_\mu = A_\mu\,\hat{m} + A^{'}_\mu\,\hat{m}^{'} - g^{-1}\,(\,\hat{m} \times \partial_\mu\,\hat{m}) - g^{-1}\,(\,\hat{m}^{'} \times \partial_\mu\,\hat{m}^{'}), \tag{3}$$

where, A_μ and A'_μ are the abelian (color electric) component of $\mathbf{W}_\mu$ along $\hat{m}$ and $\hat{m}'$ respectively and are unrestricted by the constraint while the second part, determined completely by the magnetic symmetry are of topological in origin and are of dual nature. The associated generalized field strength may then be written as,

$$\mathbf{G}_{\mu\nu} = (\,F_{\mu\nu} + B^{(d)}_{\mu\nu}\,)\,\hat{m} + (\,F'_{\mu\nu} + B'^{(d)}_{\mu\nu}\,)\,\hat{m}', \tag{4}$$

where,

$$F_{\mu\nu} = \partial_\mu A_\nu - \partial_\nu A_\mu,\ F'_{\mu\nu} = \partial_\mu A'_\nu - \partial_\nu A'_\mu,$$
$$B^{(d)}_{\mu\nu} = \partial_\mu B_\nu - \partial_\nu B_\mu = g^{-1}\,(\,\hat{m}\times\partial_\mu\,\hat{m}),\ B'^{(d)}_{\mu\nu} = \partial_\mu B'^{(d)}_\nu - \partial_\nu B'^{(d)}_\mu = g^{-1}\,(\,\hat{m}'\times\partial_\mu\,\hat{m}'). \tag{5}$$

The effective gauge strength takes the separate contributions from both parts, one unrestricted and the other completely determined by the magnetic symmetry. Thus the topological structure may be brought into dynamics in a dual symmetric way by imposing magnetic symmetry and the λ_3-like multiplet $\hat{m}$ may be viewed to define the mapping,

$$S^2_R \rightarrow SU(3)/U(1)\otimes U'(1)\ \ with\ \ \Pi_2(SU(3)/U(1)\otimes U'(1)) \simeq \Pi_1(U(1)\otimes U'(1)),$$

where $U(1)$ and $U'(1)$ are the two abelian subgroups generated by λ_3 and λ_8. Rotating the magnetic vector $\hat{m}$ to a fix time independent direction using the following parametrization [8],

$$U = exp\left[-\beta'(-\frac{1}{2}t_3 + \frac{1}{2}\sqrt{3}t_8)\right] \times e^{-\alpha t_n} exp\left[-(\beta - \frac{1}{2}\beta')t_3 e^{-\alpha t_2}\right], (\beta = n\varphi, \beta' = n'\varphi), \tag{6}$$

leads to the value of gauge potential in the following form,

$$\mathbf{W}_\mu \xrightarrow{U} g^{-1}\left[\left((\partial_\mu\beta - \frac{1}{2}\partial_\mu\beta')cos\alpha\right)\hat{\xi}_3 + \frac{1}{2}\sqrt{3}(\partial_\mu\beta' cos\alpha)\hat{\xi}_8\right]. \tag{7}$$

Thus, the dual QCD Lagrangian density in the magnetic gauge with complex scalar fields $\phi(x)$ and $\phi'(x)$ for the monopole is expressed in the following form,

$$\begin{aligned}
\pounds = &-\frac{1}{4}F^2_{\mu\nu} - \frac{1}{4}F'^2_{\mu\nu} - \frac{1}{4}B^2_{\mu\nu} - \frac{1}{4}B'^2_{\mu\nu} + \bar{\psi}_r\gamma^\mu[i\partial_\mu + \frac{1}{2}g(A^{(d)}_\mu + B_\mu) + \frac{1}{2\sqrt{3}}g(A'^{(d)}_\mu + B'_\mu)]\psi_r \\
&+\bar{\psi}_b\gamma^\mu[i\partial_\mu + \frac{1}{2}g(A^{(d)}_\mu + B_\mu) + \frac{1}{2\sqrt{3}}g(A'^{(d)}_\mu + B'_\mu)]\psi_b + \bar{\psi}_g\gamma^\mu[i\partial_\mu - \frac{1}{\sqrt{3}}g(A'^{(d)}_\mu + B'_\mu)]\psi_g + \\
&|(\partial_\mu + i\frac{4\pi}{g}(A_\mu + B^{(d)}_\mu)\phi|^2 + |(\partial_\mu + i\frac{4\pi\sqrt{(3)}}{g}(A'_\mu + B'^{(d)}_\mu)\phi'|^2 - m_0(\bar{\psi}_r\psi_r + \bar{\psi}_b\psi_b + \bar{\psi}_g\psi_g),
\end{aligned} \tag{8}$$

where the red, blue and green quarks are denoted by ψ_r, ψ_b and ψ_g and $A^{(d)}_\mu$ and $A'^{(d)}_\mu$ are the dual singular potentials introduced to describe the dual interaction between the quarks and the monopoles. Further, in absence of color electric sources the Lagrangian density may be reduced in the following form,

$$\pounds = -\frac{1}{4}B^2_{\mu\nu} - \frac{1}{4}B'^2_{\mu\nu} + |(\partial_\mu + i\frac{4\pi}{g}B^{(d)}_\mu)\phi|^2 + |(\partial_\mu + i\frac{4\pi\sqrt{(3)}}{g}B'^{(d)}_\mu)\phi'|^2 - V. \tag{9}$$

The above Lagrangian has a manifest $U(1)\otimes U'(1)$ magnetic gauge invariance and is known to generate the dynamical breaking of magnetic symmetry through an effective potential given by,

$$V = \frac{48\pi^2}{g^4}\lambda(\phi^*\phi - \phi_0^2)^2 + \frac{432\pi^2}{g^4}\lambda'(\phi^*\phi' - \phi_0'^2)^2, \tag{10}$$

and induces the magnetic condensation of QCD vacuum which, in turn, leads to a definite flux tube structure to the dual QCD vacuum. It is, therefore, naturally desired to analyze the flux tube structure and the nature of the magnetically condensed vacuum. The field equations associated with the λ_3 and λ_8 -component using Lagrangian (9) may be derived in the following form,

$$B_{\mu\nu,}{}^{\nu} + i\frac{4\pi}{g}(\phi^*\overset{\leftrightarrow}{\partial}_\mu\,\phi) - \frac{32\pi^2}{g^2}B^{(d)}_\mu\,\phi\,\phi^* = 0\,, \tag{11a}$$

$$(\partial^\mu - i\frac{4\pi}{g}B_\mu^{(d)})(\partial_\mu + i\frac{4\pi}{g}B_\mu^{(d)})\phi + \frac{96\lambda\pi^2}{g^4}(\phi^*\phi - \phi_0^2)\phi = 0, \tag{11b}$$

$$(\partial^\mu - i\frac{4\pi\sqrt{3}}{g}B_\mu^{'(d)})(\partial_\mu + i\frac{4\pi\sqrt{3}}{g}B_\mu^{'(d)})\phi^{'} + \frac{864\pi^2}{g^4}\lambda^{'}(\phi^{'*}\phi^{'} - \phi_0^{'2})\phi^{'} = 0, \tag{11c}$$

$$B_{\mu\nu,}^{'\ \nu} + i\frac{4\pi\sqrt{3}}{g}(\phi^{'*}\overleftrightarrow{\partial}_\mu\phi^{'}) - \frac{96\pi^2}{g^2}B_\mu^{'(d)}\phi^{'}\phi^{'*} = 0\,. \tag{11d}$$

Using the cylindrical symmetry with the co-ordinates $(\rho,\ \varphi, z)$ the dual gauge field and the monopole field for the λ_3 and λ_8 -component can be expressed as,

$$B_\mu^{(d)} \;=\; g^{-1}cos\alpha(\partial_\mu\beta)\hat{m},\;\; B_\mu^{'(d)} \;=\; \frac{\sqrt{3}}{2g}\,cos\,\alpha\,(\partial_\mu\,\beta^{'})\,\hat{m}^{'}, \tag{12}$$

$$\phi(x) \;=\; exp\,(i\,n\,\varphi)\,\chi(\rho),\;\; \phi^{'}(x) \;=\; exp\,(i\,n^{'}\,\varphi)\,\chi^{'}(\rho). \tag{13}$$

Using the field ansatz given by, (12) and (13), the field equations (11a), (11b), (11c) and (11d) in the static limit may be expressed as given below,

$$\frac{d}{d\rho}\left[\rho^{-1}\,\frac{d}{d\rho}\Big(\rho B(\rho)\Big)\right] \,-\, (16\pi\alpha_s^{-1})^{1/2}\Big(\frac{n}{\rho} \,+\, (4\pi\alpha_s^{-1})^{1/2}B(\rho)\Big)\,\chi^2\,(\rho) \;=\; 0, \tag{14a}$$

$$\frac{1}{\rho}\,\frac{d}{d\rho}\Big(\rho\,\frac{d\chi(\rho)}{d\rho}\Big) \,-\, \left[\Big(\frac{n}{\rho} \,+\, (4\pi\alpha_s^{-1})^{1/2}B(\rho)\Big)^2 \,+\, 6\lambda\alpha_s^{-2}\Big(\chi^2-\phi_0^2\Big)\right]\chi(\rho) = 0, \tag{14b}$$

$$\frac{d}{d\rho}\left[\rho^{-1}\,\frac{d}{d\rho}\Big(\rho B^{'}(\rho)\Big)\right] \,-\, (48\pi\alpha_s^{-1})^{1/2}\Big(\frac{n^{'}}{\rho} \,+\, (12\pi\alpha_s^{-1})^{1/2}B^{'}(\rho)\Big)\,\chi^{'2}\,(\rho) \;=\; 0, \tag{14c}$$

$$\frac{1}{\rho}\,\frac{d}{d\rho}\Big(\rho\,\frac{d\chi^{'}}{d\rho}\Big) \,-\, \left[\Big(\frac{n^{'}}{\rho} \,+\, (12\pi\alpha_s^{-1})^{1/2}B^{'}(\rho^{'})\Big)^2 \,+\, 54\lambda^{'}\alpha_s^{-2}\Big(\chi^{'2}-\phi_0^{'2}\Big)\right]\chi^{'}(\rho) = 0. \tag{14d}$$

Imposing the asymptotic boundary condition appropriate for the large-scale behavior of QCD as, $B(\rho) \overset{\rho\to\infty}{\longrightarrow} -\frac{ng}{4\pi\rho}$, $B^{'}(\rho) \overset{\rho\to\infty}{\longrightarrow} -\frac{n^{'}g}{4\sqrt{3}\pi\rho}$ and $\phi \overset{\rho\to\infty}{\longrightarrow} \phi_0$, $\phi^{'} \overset{\rho\to\infty}{\longrightarrow} \phi_0^{'}$ leads to the asymptotic solution for as $B(\rho) = -\frac{ng}{4\pi\rho}[1 + F(\rho)]$, $B^{'}(\rho) = -\frac{n^{'}g}{4\sqrt{3}\pi\rho}[1 + G(\rho)]$, where the function $F(\rho)$ and $G(\rho)$, in asymptotic limit are obtained as,

$$\begin{aligned} F(\rho) &\overset{\rho\to\infty}{\longrightarrow}\; -n \,+\, C\sqrt{\rho}\,exp\,(-m_B\,\rho), \\ G(\rho) &\overset{\rho\to\infty}{\longrightarrow}\; -n^{'} \,+\, C^{'}\sqrt{\rho}\,exp\Big(-m_B^{'}\rho\Big), \end{aligned} \tag{15}$$

where C and $C^{'}$ are constant and $m_B = (8\pi\alpha_s^{-1})^{\frac{1}{2}}\phi_0$, $m_B^{'} = (24\pi\alpha_s^{-1})^{\frac{1}{2}}\phi_0^{'}$ are the vector glueball masses generated after the dynamical breaking of magnetic symmetry. The corresponding string tension of the resulting flux tube configuration then takes the following form,

$$\begin{aligned} k_{(n,n^{'})} \;=\; 2\pi\int_0^\infty \rho\,d\rho\Bigg[&\left\{\frac{n^2g^2}{32\pi^2\rho^2}\left(\frac{dF}{d\rho}\right)^2 \,+\, \frac{n^2}{\rho^2}\,F^2(\rho)\chi^2(\rho) + \left(\frac{d\chi}{d\rho}\right)^2 + 3\lambda\alpha_s^{-2}(\chi^2-\phi_0^2)^2\right\} \\ &+\left\{\frac{n^{'2}g^2}{96\pi^2\rho^2}\left(\frac{dG}{d\rho}\right)^2 \,+\, \frac{n^{'2}}{\rho^2}\,G^2(\rho)\chi^{'2}(\rho) + \left(\frac{d\chi^{'}}{d\rho}\right)^2 + 27\lambda^{'}\alpha_s^{-2}(\chi^{'2}-\phi_0^{'2})^2\right\}\Bigg]. \end{aligned} \tag{16}$$

The masses of the magnetic glueballs may be estimated by evaluating the string tension $k_{(n,n^{'})}$ of the resulting flux tube which can be written as, $k_{(n,n^{'})} = \frac{1}{2\pi\alpha^{'}} = \gamma_{(n,n^{'})}\phi_0^2 = \frac{\alpha_s}{8\pi}\gamma_{(n,n^{'})}m_B^2$, where $\gamma_{(n,n^{'})} = \gamma_n + \left(\frac{\phi_0^{'}}{\phi_0}\right)^2\gamma_{n^{'}}$ is a dimensionless parameter which can be calculated from the string solution of the quark pair and $\alpha^{'} = 0.93$ GeV^{-2} as the Regge slope parameter of the meson trajectories. Using the numerical computation of equation (16) for $\gamma_{(n,n^{'})}$ and incorporating color reflection invariance, we obtain the vector and scalar glueball masses for some

Table 1. Vector and scalar glueball masses in dual QCD.

λ	γ	α_s	$\bar{m}_B$ (GeV)	$\bar{m}_\phi$ (GeV)
$\frac{1}{4}$	5.617	0.25	1.75	1.20
$\frac{1}{2}$	6.828	0.24	1.62	1.69
1	8.093	0.23	1.52	2.17
2	9.833	0.22	1.41	2.90

typical values of strong coupling in infrared sector of QCD and are given in the Table 1 [13]. The color reflection invariance is incorporated by insisting $\bar{m}_\phi = m_\phi = m_\phi^{'}$ and $\bar{m}_B = m_B = m_B^{'}$, or equivalently

$$\phi_0^{'} = \frac{1}{\sqrt{3}}\phi_0, \;\; \lambda^{'} = \frac{1}{3}\lambda. \tag{17}$$

Furthermore, in order to investigate the heavy quark-antiquark confining potential let us start from the Lagrangian density (8) and apply Zwanziger formalism [14] to eliminate the singular behavior of potentials. In addition, using the assertion for the coupling of quark fields with the color electric potential and that of the monopole field with the dual magnetic potential, using the effective potential given by equation (10) and carrying out the monopole field expansion under mean-field approximation, the Lagrangian density reduces to the following form,

$$\begin{aligned}\mathcal{L} = &-\frac{1}{2n^2}[n.(\partial\wedge\mathbf{A})]^\nu[n.(\partial\wedge\mathbf{B}^{(d)})^d]_\nu + \frac{1}{2n^2}[n.(\partial\wedge\mathbf{B}^{(d)})]^\nu[n.(\partial\wedge\mathbf{A})^d]_\nu - \frac{1}{2n^2}[n.(\partial\wedge\mathbf{A})]^2 - \frac{1}{2n^2}[n.(\partial\wedge\mathbf{B}^{(d)})]^2 \\ &-\frac{1}{2n^2}[n.(\partial\wedge\mathbf{A}^{'})]^\nu[n.(\partial\wedge\mathbf{B}^{'(d)})^d]_\nu + \frac{1}{2n^2}[n.(\partial\wedge\mathbf{B}^{'(d)})]^\nu[n.(\partial\wedge\mathbf{A}^{'})^d]_\nu - \frac{1}{2n^2}[n.(\partial\wedge\mathbf{A}^{'})]^2 - \frac{1}{2n^2}[n.(\partial\wedge\mathbf{B}^{'(d)})]^2 + \\ &\bar{\psi}(i\gamma_\mu\partial^\mu - g\gamma_\mu\mathbf{A}^\mu.\lambda_3 - m)\psi + \bar{\psi}(i\gamma_\mu\partial^\mu - g\gamma_\mu\mathbf{A}^{'\mu}.\lambda_8 - m)\psi + \frac{1}{2}m_B^2 B_\mu^{(d)2} + \frac{1}{2}m_B^{'2} B_\mu^{'(d)2}.\end{aligned} \tag{18}$$

Within quenched approximation, integrating out A_μ and B_μ, the effective Lagrangian including external source j to represent heavy quark is given as follows,

$$\mathcal{L}_q = -\frac{1}{2}(j_\mu^3 D^{\mu\nu} j_\nu^3 + j_\mu^8 D^{'\mu\nu} j_\nu^8), \tag{19}$$

where $D^{\mu\nu}$ and $D^{'\mu\nu}$ are the propagator of the diagonal gluons,

$$D^{\mu\nu} = -\frac{1}{2}\frac{g^{\mu\nu}}{\partial^2 + m_B^2} - \frac{1}{2}\frac{n^2}{(n.\partial)^2}\left(\frac{m_B^2}{\partial^2 + m_B^2}\right)\left(g^{\mu\nu} - \frac{n^\mu n^\nu}{n^2}\right), \tag{20}$$

$$D^{'\mu\nu} = -\frac{1}{2}\frac{g^{\mu\nu}}{\partial^2 + m_B^{'2}} - \frac{1}{2}\frac{n^2}{(n.\partial)^2}\left(\frac{m_B^{'2}}{\partial^2 + m_B^{'2}}\right)\left(g^{\mu\nu} - \frac{n^\mu n^\nu}{n^2}\right). \tag{21}$$

The action is obtained in the following form,

$$\begin{aligned}S_j = \int \mathcal{L}_j d^4x = \int d^4x \Bigg[& j_\mu^3\left(-\frac{1}{2}\frac{g^{\mu\nu}}{\partial^2 + m_B^2} - \frac{1}{2}\frac{n^2}{(n.\partial)^2}\left(\frac{m_B^2}{\partial^2 + m_B^2}\right)\left(g^{\mu\nu} - \frac{n^\mu n^\nu}{n^2}\right)\right)j_\nu^3 \\ & + j_\mu^8\left(-\frac{1}{2}\frac{g^{\mu\nu}}{\partial^2 + m_B^{'2}} - \frac{1}{2}\frac{n^2}{(n.\partial)^2}\left(\frac{m_B^{'2}}{\partial^2 + m_B^{'2}}\right)\left(g^{\mu\nu} - \frac{n^\mu n^\nu}{n^2}\right)\right)j_\nu^8\Bigg].\end{aligned} \tag{22}$$

The quark currents for static system of a heavy quark and antiquark pair with opposite color charge located at $\mathbf{a}$ and $\mathbf{b}$, respectively are given by

$$j_\mu^3(k) = Q_3 g_{\mu 0} 2\pi\delta(k_0)(e^{-i\mathbf{k}.\mathbf{b}} - e^{-i\mathbf{k}.\mathbf{a}}), \;\; j_\mu^8(k) = Q_8 g_{\mu 0} 2\pi\delta(k_0)(e^{-i\mathbf{k}.\mathbf{b}} - e^{-i\mathbf{k}.\mathbf{a}}),$$

where Q_3 and Q_8 are the color electric charge of the static quark and the action reduces to the following form,

$$S_j = -Q_3^2 \int dt \int \frac{d^3k}{(2\pi)^3}\frac{1}{2}(1 - e^{i\mathbf{k}.\mathbf{r}})(1 - e^{-i\mathbf{k}.\mathbf{r}})\left[\frac{1}{\mathbf{k^2} + m_B^2} + \frac{m_B^2}{\mathbf{k^2} + m_B^2}\frac{1}{(\mathbf{n}.\mathbf{k})^2}\right]$$

$$-Q_8^2 \int dt \int \frac{d^3k}{(2\pi)^3} \frac{1}{2}(1 - e^{i\mathbf{k}.\mathbf{r}})(1 - e^{-i\mathbf{k}.\mathbf{r}}) \left[\frac{1}{\mathbf{k^2} + m_B^{'2}} + \frac{m_B^{'2}}{\mathbf{k^2} + m_B^{'2}} \frac{1}{(\mathbf{n}.\mathbf{k})^2} \right], \tag{23}$$

where, $\mathbf{n}$ is a unit vector and $\mathbf{r} = \mathbf{b} - \mathbf{a}$ is a vector which connects the quark to the antiquark. The static quark-antiquark potential obtained from the action (23) may be expressed as,

$$U(r) = -\frac{Q_3^2}{4\pi}\frac{e^{-m_B r}}{r} - \frac{Q_8^2}{4\pi}\frac{e^{-m_B' r}}{r} + \frac{Q_3^2 m_B^2}{8\pi} r ln \frac{m_B^2 + m_\phi^2}{m_B^2} + \frac{Q_8^2 m_B^{'2}}{8\pi} r ln \frac{m_B^{'2} + m_\phi^{'2}}{m_B^{'2}}. \tag{24}$$

Using color reflection invariance the expression reduces to the following form,

$$U(r) = -\frac{\mathbf{Q^2}}{4\pi}\frac{e^{-\bar{m}_B r}}{r} + \frac{\mathbf{Q}^2 \bar{m}_B^2}{8\pi} r ln(1 + \kappa_{QCD}^2), \tag{25}$$

where $\mathbf{Q}^2 = Q_3^2 + Q_8^2$ and the $\kappa_{QCD} = \bar{m}_\phi/\bar{m}_B$ is the GL-parameter for the dual QCD.. The first one in the expression (25) is a Yukawa-like term and the second one describes, a linear potential in the inter-quarks separation. The corresponding plot for the case of static quark (25) has been shown in figure 1 for $\alpha_s = 0.25$ and $\alpha_s = 0.24$

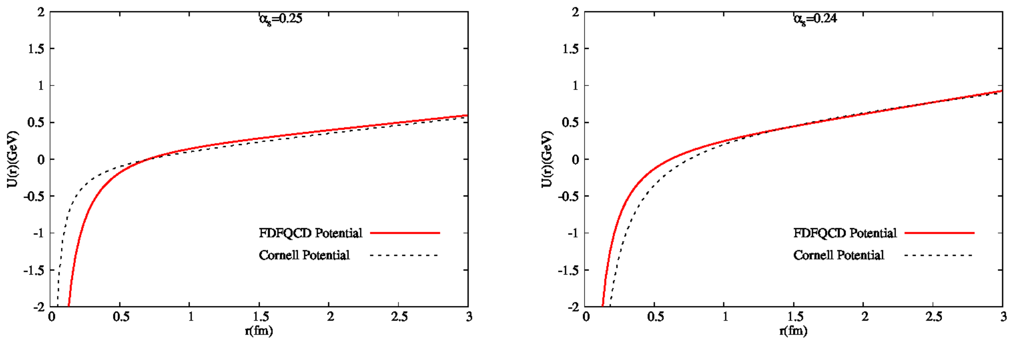

Figure 1. The quark-antiquark static potential for $\alpha_s = 0.25$ and $\alpha_s = 0.24$.

coupling in infrared sector of QCD. For $\alpha_s = 0.25$ the plot is well in agreement with the phenomenological Cornell potential [15]. However $\alpha_s = 0.24$ needs an correction factor of 0.45 GeV in order to fit it with the Cornell potential. The graphical representation clearly shows that the Yukawa term dominates the short-range physics and the linear term dominates the physics at large distances responsible for quark confinement.

3. Acknowledgements

The authors are thankful to the organizers of CICAHEP-2015 for their hospitality during the conference and University Grants Commission (UGC), New Delhi, India, for the financial assistance under the UGC-RFSMS research fellowship during the course of the study.

References

[1] Y. Nambu, Phys. Rev. D **10**, 4262 (1974), G. 't Hooft, Nucl. Phys. B **153**, 141 (1979), S. Mandelstam, Phys. Rept. **23**, 245 (1976).
[2] Y. M. Cho, Phys. Rev. D **62**, 074009 (2000).
[3] A. Kronfeld, M. Laursen, G. Schierholz, U.-J. Wiese, Phys. Lett. B **198 (4)**, 516 (1987).
[4] T. Suzuki, I. Yotsuyanagi, Phys. Rev. D **42**, 4257 (1990).
[5] J. D. Stack, S. D. Neiman, R. J. Wensley, Phys. Rev. D **50**, 3399 (1994).
[6] H. Shiba, T. Suzuki, Phys. Lett. B **351**, 519 (1995).
[7] Y. M. Cho, Phys. Rev. D **21**, 1080 (1980); Phys. Rev. D **23**, 2415 (1981).

[8] Y. M. Cho, Phys. Rev. Lett. **44**, 1115 (1980).
[9] Y. M. Cho, F. H. Cho, J. H. Yoon, Phys. Rev. D **87**, 085025 (2013).
[10] H. C. Pandey and H. C. Chandola, Phys. Lett. B **476**, 193 (2000).
[11] H. C. Chandola, D. Yadav, H. C. Pandey and H. Dehnen, Int. Jour. Mod. Phys. A **20**, 2743 (2005).
[12] H. C. Chandola, Garima Punetha, H. Dehnen, Nucl. Phys. A **945**, 226 (2016).
[13] Y. M. Cho, Phys. Rev. Lett. **46**, 302 (1981).
[14] D. Zwanziger, Phys. Rev. D **3**, 880 (1971).
[15] E. Eichten et al. Phys. Rev. Lett. **34**, 369 (1975); ibid **36**, 500 (1976); Phys. Rev. D **17**, 3090 (1978); ibid D **21**, 203 (1980).

QCD at large scales and phase transition at finite temperature*

Garima Punetha and H. C. Chandola

Centre of Advanced Study, Department of Physics, D.S.B. Campus, Kumaun University, Nainital-263001, India

Presenter: Garima Punetha (*garimapunetha@gmail.com*); HEP.1, Poster, CICAHEP15.214.2

Based on the topological structure of non-abelian gauge theories, a dual QCD gauge formulation has been developed in terms of magnetic symmetry, which manifest the topological structure of the symmetry group in a non-trivial way. The dynamical breaking of the magnetic symmetry has been shown to impart the dual superconducting properties to the magnetically condensed QCD vacuum, which ultimately leads to a unique flux tube configuration in QCD vacuum responsible for enforcing the color confinement. For the study of phase structure of QCD, the deconfinement phase transition in QCD has been investigated at finite temperatures. Utilizing the path-integral formalism, dual QCD has also been extended to the thermal domain by undertaking the mean field approach. The effective potential at finite temperature has been derived to compute the critical temperature for phase transition which has been shown to be in good agreement with the lattice results. A large reduction of color monopole condensate and glueball masses near the critical point has been shown to lead to a first order deconfinement phase transition in QCD. The evaporation of color monopole condensate and the release of the magnetic degrees of freedom in high temperature domain in QCD vacuum has been shown to lead the restoration of magnetic symmetry, which has its intimate connection with the quark-gluon plasma phase of QCD.

1. Introduction

After the advent of Quantum Chromodynamics (QCD) [1, 2, 3] as a viable theory of strong interactions and in particular asymptotic freedom [1, 4], the attention focused on the ideas of Quark Gluon Plasma (QGP), a typical phase of QCD in which the quarks and gluons degrees of freedom are supposed to be defrozen. It is believed, that such a deconfined matter has a deep relevance and implications on cosmology, astrophysics and in the phenomenology of heavy-ions collisions which provide a unique opportunity to study such typical QCD phase transition from HG to QGP [6]. At present, the best available tool to study the non-perturbative properties of QCD matter at zero chemical potential [7, 8, 9, 10, 11] is the numerical simulation on the lattice. However, the lattice methods still lack a reliability to describe the properties of matter possessing a finite density of baryons [12]. In view of these facts, it is therefore very much desired to perform a detailed analytical study to understand many new features of QCD phase structure, under the extreme conditions of temperature and density. The present paper deals mainly with the analysis of the large scale structure of QCD, its thermal response and the study of the QCD phase transition. In section 2, the dual QCD formulation based on magnetic symmetry has been analyzed and its resulting flux tube structure has been investigated for the mechanism of color confinement. In section 3, utilizing the path integral formalism, dual QCD has been extended to the thermal domain by undertaking the mean field approach in order to the compute the critical parameters of phase transition. In section 4, the numerical results and conclusions of the work have been presented.

2. Dual QCD with magnetic symmetry

The topological structure expressed in the form of magnetic symmetry plays a crucial role to establish the duality which exists in non-abelian gauge theory to provide the magnetically condensed vacuum important for the analysis of non-perturbative phenomenon of QCD vacuum. In this context, it is important to note that a gauge symmetry can be viewed as an n-dimensional isometry which leads to P as a principal fibre bundle $P(M, G)$ with a canonical projection $\Pi : P \to M$. Since, a connection on $P(M, G)$ admits a left isometry, the magnetic symmetry may be introduced as an internal isometry H (with Killing vector fields as $\hat{m}_a$) which is Cartan's subgroup of G and commutes with it. The associated Killing condition, $\mathcal{L}_{m_a} g_{AB} = 0$, then leads to a gauge covariant magnetic symmetry conditions as given by [13, 14, 15, 16, 17],

$$D_\mu \hat{m} = 0 \, , \; i.e. \; (\partial_\mu + g \, \mathbf{W}_\mu \times) \, \hat{m} = 0 \, , \tag{1}$$

*Best poster presentation in the High Energy Physics section.

where $\mathbf{W}_\mu$, is the gauge potential and $\hat{m}$ is the killing vector which automatically selects another $\hat{m}^{'}$ obtained by the symmetric product of $\hat{m}$,

$$\hat{m}^{'} = \sqrt{3}\hat{m} * \hat{m} \text{ such that, } D_\mu \hat{m}^{'} = 0, \tag{2}$$

where $*$ denotes the symmetric product and the self-consistency requirement comes from the following identities,

$$D_\mu(\hat{m}_1 \times \hat{m}_2) = (D_\mu \hat{m}_1) \times \hat{m}_2 + \hat{m}_1 \times (D_\mu \hat{m}_2),$$
$$D_\mu(\hat{m}_1 * \hat{m}_2) = (D_\mu \hat{m}_1) * \hat{m}_2 + \hat{m}_1 * (D_\mu \hat{m}_2). \tag{3}$$

For a complete description of the monopole solutions two killing vectors [13] $\hat{m}$ and $\hat{m}^{'}$ are necessary and sufficient and one may choose the fundamental symmetry $\hat{m}$ to be always λ_3-like, in which the product symmetry $\hat{m}^{'}$ automatically becomes λ_8-like.

The most general gauge potential in SU(3) QCD which satisfies the constraints (1) and (2) can easily be expressed as,

$$\mathbf{W}_\mu = A_\mu \hat{m} + A_\mu^{'} \hat{m}^{'} - g^{-1} (\hat{m} \times \partial_\mu \hat{m}) - g^{-1} (\hat{m}^{'} \times \partial_\mu \hat{m}^{'}), \tag{4}$$

where

$$A_\mu = \hat{m}.\mathbf{W}_\mu, \quad A_\mu^{'} = \hat{m}^{'}.\mathbf{W}_\mu, \tag{5}$$

are the abelian component unrestricted by the magnetic symmetry. On the other hand, the second part which is determined completely by the magnetic symmetry, is of topological origin since the multiplet $\hat{m}$ may be viewed to define the homotopy of the mapping $S_R^2 \rightarrow SU(3)/U(1) \otimes U^{'}(1)$, $\Pi_2(SU(3)/U(1) \otimes U^{'}(1)) \simeq \Pi_1(U(1) \otimes U^{'}(1))$, where $U(1)$ and $U^{'}(1)$ are two abelian subgroups generated by λ_3 and λ_8, so that the monopoles must be classified by two integers. The topological structure of the theory may be then brought into dynamics explicitly by performing the separation of gauge fields in the magnetic gauge obtained by rotating $\hat{m}$ to a prefixed direction in isospace using a gauge transformation (U) [14] such that $\hat{m}$ exhibits the homotopy class which consists of n windings of the i-spin subgroups followed by $n^{'}$ windings of the u-spin subgroup of SU(3), and thus may be explicitly expressed as,

$$\hat{m} = \begin{pmatrix} \sin\alpha \ \cos\frac{\alpha}{2} \ \cos[(\beta - \beta^{'})] \\ \sin\alpha \ \cos\frac{\alpha}{2} \ \sin[(\beta - \beta^{'})] \\ \frac{1}{4}\cos\alpha(3 + \cos\alpha) \\ \sin\alpha \ \sin\frac{\alpha}{2} \ \cos\beta \\ \sin\alpha \ \sin\frac{\alpha}{2} \ \sin\beta \\ -\frac{1}{2}\sin\alpha \ \cos\alpha \ \cos\beta^{'} \\ -\frac{1}{2}\sin\alpha \ \cos\alpha \ \sin\beta^{'} \\ \frac{1}{4}\sqrt{3}\cos\alpha(1 - \cos\alpha) \end{pmatrix}. \tag{6}$$

This leads to the value of gauge potential and corresponding gauge field strength in the magnetic gauge as,

$$\mathbf{W}_\mu \xrightarrow{U} g^{-1}\Big[\Big((\partial_\mu\beta - \frac{1}{2}\partial_\mu\beta^{'})\cos\alpha\Big)\hat{\xi}_3 + \frac{1}{2}\sqrt{3}(\partial_\mu\beta^{'}\cos\alpha)\hat{\xi}_8], \tag{7}$$

$$\mathbf{G}_{\mu\nu} \xrightarrow{U} -g^{-1}\Big[\sin\alpha\Big((\partial_\mu\alpha\partial_\nu\beta - \partial_\nu\alpha\partial_\mu\beta) - \frac{1}{2}(\partial_\mu\alpha\partial_\nu\beta^{'} - \partial_\nu\alpha\partial_\mu\beta^{'})\Big)\hat{m} + \frac{1}{2}\sqrt{3}\sin\alpha(\partial_\mu\alpha\partial_\nu\beta^{'} - \partial_\nu\alpha\partial_\mu\beta^{'})\hat{m}^{'}\Big]. \tag{8}$$

For a field-theoretic description of the resulting dual QCD we use the regular dual magnetic potential ($B_\mu^{(d)}$ and $B_\mu^{'(d)}$) associated with the monopoles and introduce complex scalar fields $\phi(x)$ and $\phi^{'}(x)$ for the monopole and with these consideration the Lagrangian in absence of color electric sources quenched approximation may be expressed in the following form,

$$\pounds = -\frac{1}{4}B_{\mu\nu}^2 - \frac{1}{4}B_{\mu\nu}^{'2} + |(\partial_\mu + i\frac{4\pi}{g}B_\mu^{(d)})\phi|^2 + |(\partial_\mu + i\frac{4\pi\sqrt{(3)}}{g}B_\mu^{'(d)})\phi^{'}|^2 - V, \tag{9}$$

where

$$V = \frac{48\pi^2}{g^4}\lambda(\phi^*\phi - \phi_0^2)^2 + \frac{432\pi^2}{g^4}\lambda^{'}(\phi^*\phi^{'} - \phi_0^{'2})^2 \tag{10}$$

is the proper quadratic effective potential which enforces the magnetic symmetry breaking and the resulting magnetic condensation in QCD vacuum and leads to a definite flux tube structure in the dual QCD vacuum. With such potential, using the cylindrical symmetry with the co-ordinates $(\rho,\, \varphi, z)$ the dual gauge field and the monopole field for the λ_3 and λ_8 -component can be expressed as,

$$B_\mu^{(d)} \;=\; g^{-1}\cos\alpha(\partial_\mu\beta)\hat{m},\;\; B_\mu^{'(d)} \;=\; \frac{\sqrt{3}}{2g}\,\cos\,\alpha\,(\partial_\mu\,\beta^{'})\,\hat{m}^{'}, \tag{11}$$

$$\phi(x) \;=\; exp\,(i\,n\,\varphi)\,\chi(\rho),\;\; \phi^{'}(x) \;=\; exp\,(i\,n^{'}\,\varphi)\,\chi^{'}(\rho), \tag{12}$$

and the field equation associated with the Lagrangian in static limit may be derived in the following form,

$$\frac{d}{d\rho}\left[\rho^{-1}\,\frac{d}{d\rho}\Big(\rho B(\rho)\Big)\right] \,-\, (16\pi\alpha_s^{-1})^{1/2}\Big(\frac{n}{\rho} \,+\, (4\pi\alpha_s^{-1})^{1/2}B(\rho)\Big)\,\chi^2\,(\rho) \;=\; 0, \tag{13a}$$

$$\frac{1}{\rho}\,\frac{d}{d\rho}\Big(\rho\,\frac{d\chi(\rho)}{d\rho}\Big) \,-\, \left[\Big(\frac{n}{\rho} \,+\, (4\pi\alpha_s^{-1})^{1/2}B(\rho)\Big)^2 \,+\, 6\lambda\alpha_s^{-2}\Big(\chi^2 - \phi_0^2\Big)\right]\chi(\rho) = 0, \tag{13b}$$

$$\frac{d}{d\rho}\left[\rho^{-1}\,\frac{d}{d\rho}\Big(\rho B^{'}(\rho)\Big)\right] \,-\, (48\pi\alpha_s^{-1})^{1/2}\Big(\frac{n^{'}}{\rho} \,+\, (12\pi\alpha_s^{-1})^{1/2}B^{'}(\rho)\Big)\,\chi^{'2}\,(\rho) \;=\; 0, \tag{13c}$$

$$\frac{1}{\rho}\,\frac{d}{d\rho}\Big(\rho\,\frac{d\chi^{'}}{d\rho}\Big) \,-\, \left[\Big(\frac{n^{'}}{\rho} \,+\, (12\pi\alpha_s^{-1})^{1/2}B^{'}(\rho^{'})\Big)^2 \,+\, 54\lambda^{'}\alpha_s^{-2}\Big(\chi^{'2} - \phi_0^{'2}\Big)\right]\chi^{'}(\rho) = 0. \tag{13d}$$

Utilizing the asymptotic solutions of the associated dual QCD fields, $B(\rho) \;=\; -\frac{ng}{4\pi\rho}[1 \,+\, F(\rho)]$, $B^{'}(\rho) \;=\; -\frac{n^{'}g}{4\sqrt{3}\pi\rho}[1 + G(\rho)]$, the energy per unit length of the resulting flux tube configuration may be given as,

$$k_{(n,n^{'})} \;=\; 2\pi\,\int_0^\infty\,\rho\,d\rho\Bigg[\Bigg\{\frac{n^2g^2}{32\pi^2\rho^2}\bigg(\frac{dF}{d\rho}\bigg)^2 \,+\, \frac{n^2}{\rho^2}\,F^2(\rho)\chi^2(\rho) + \bigg(\frac{d\chi}{d\rho}\bigg)^2 + 3\lambda\alpha_s^{-2}(\chi^2 - \phi_0^2)^2\Bigg\}$$
$$+\Bigg\{\frac{n^{'2}g^2}{96\pi^2\rho^2}\bigg(\frac{dG}{d\rho}\bigg)^2 \,+\, \frac{n^{'2}}{\rho^2}\,G^2(\rho)\chi^{'2}(\rho) + \bigg(\frac{d\chi^{'}}{d\rho}\bigg)^2 + 27\lambda^{'}\alpha_s^{-2}(\chi^{'2} - \phi_0^{'2})^2\Bigg\}\Bigg]. \tag{14}$$

The masses of the magnetic glueballs can be estimated by evaluating the string tension $k_{(n,n^{'})}$ of the resulting flux tube which can be expressed as, $k_{(n,n^{'})} = \frac{1}{2\pi\alpha^{'}} = \gamma_{(n,n^{'})}\phi_0^2 = \frac{\alpha_s}{8\pi}\gamma_{(n,n^{'})}m_B^2$, where $\gamma_{(n,n^{'})} = \gamma_n + \Big(\frac{\phi_0^{'}}{\phi_0}\Big)^2\gamma_{n^{'}}$ is a dimensionless parameter. In view of the relationship of k with Regge slope parameter and $\alpha^{'} = 0.9GeV^{-2}$, using the numerical computation of equation (14) for γ and incorporating color reflection invariance, we obtain the masses $\bar{m}_\phi$ and $\bar{m}_B$ of the 0^{++} and 1^{++} magnetic glueballs for some typical values of strong coupling in full infrared sector of QCD at zero temperature and are presented in table 1 [18]. The color reflection invariance is incorporated by insisting $\bar{m}_\phi = m_\phi = m_\phi^{'}$ and $\bar{m}_B = m_B = m_B^{'}$, or equivalently $\phi_0^{'} = \frac{1}{\sqrt{3}}\phi_0,\;\; \lambda^{'} = \frac{1}{3}\lambda$, which tells us that the two modes m_ϕ and $m_\phi^{'}$ (also m_B and $m_B^{'}$) should actually describe one and the same mode $\bar{m}_\phi$ (and $\bar{m}_B$, respectively).

Table 1. The masses of vector and scalar glueball as functions of α_s.

λ	α_s	$\bar{m}_\phi$ (GeV)	$\bar{m}_B$ (GeV)	$\lambda_{QCD}^{(d)}$ (fm)	$\xi_{QCD}^{(d)}$ (fm)	κ_{QCD}
$\frac{1}{4}$	0.25	1.20	1.75	0.57	0.83	0.69
$\frac{1}{2}$	0.24	1.69	1.62	0.61	0.59	0.99
1	0.23	2.17	1.52	0.65	0.46	1.42
2	0.22	2.90	1.41	0.70	0.34	2.05

These two scales are basically related to the penetration depth $(\lambda_{QCD}^{(d)})$ and coherence length $(\xi_{QCD}^{(d)})$ in the following manner, $\bar{m}_B = (\lambda_{QCD}^{(d)})^{-1}$ and $\bar{m}_\phi = (\xi_{QCD}^{(d)})^{-1}$. With these set of dual QCD parameters, we may identify the nature of the dual QCD vacuum in infrared sector by defining the Ginzburg-Landau parameter κ_{QCD}, which is basically the ratio of the characteristic length scales given by, $\kappa = \frac{\lambda^{(d)}_{QCD}}{\xi^{(d)}_{QCD}}$. The transition from type-I to type-II behaviour of dual QCD vacuum is evident from the table-1 around the strong coupling value 0.23. Using these parameters as the initial (zero temperature) parameters and to understand the behavior of QCD at finite temperatures alongwith its phase structure, let us use the partition function approach alongwith the mean-field treatment for the QCD monopole field to evaluate the thermal contributions to the effective potential in dual QCD. The parameters associated with the dual QCD vacuum are extremely useful for understanding the nature of phase transition in infrared sector of QCD.

3. Effective potential formalism at finite temperature in dual QCD

In order to deal with the non-perturbative aspects of QCD at finite temperature, let us start with the partition functional, for the dual QCD in thermal equilibrium at a constant temperature T, which is expressed in the following form,

$$Z[J] = \int D[\phi]D[B^{(d)}_\mu]D[\phi^{'}]D[B^{'(d)}_\mu]exp(-S^{(d)}), \tag{15}$$

where, $S^{(d)}$ is the dual QCD action and is given by [19],

$$S^{(d)} = -i\int d^4x(\mathcal{L}^{(m)}_d - J|\phi|^2 - J^{'}|\phi^{'}|^2). \tag{16}$$

Using the mean-field treatment and separating the fluctuation part of the QCD-monopole field from its mean value as [20],

$$\phi \rightarrow (\phi + \tilde{\phi})exp(i\xi),\ \phi^{'} \rightarrow (\phi^{'} + \tilde{\phi}^{'})exp(i\xi^{'}), \tag{17}$$

so that the intregrand in action (16) may be expressed as,

$$\begin{aligned}\mathcal{L}^{(m)}_d - J|\phi|^2 - J^{'}|\phi^{'}|^2 &= -3\lambda\alpha_s^{-2}(\phi^2-\phi_0^2)^2 - J\phi^2 - \frac{1}{4}B^2_{\mu\nu} + \frac{1}{2}m_B^2(B^{(d)}_\mu)^2 + [(\partial_\mu\tilde{\phi})^2 - (m_\phi\tilde{\phi})^2]\\
&+\Big[4\pi\alpha_s^{-1}(B^{(d)2}_\mu)(2\phi\tilde{\phi}+\tilde{\phi}^2) - 3\lambda\alpha_s^{-2}(\tilde{\phi}^4+4\phi\tilde{\phi}^3)\Big] - \big[12\lambda\alpha_s^{-2}(\phi^2-\phi_0^2)\phi + 2J\phi\big]\tilde{\phi} - 27\lambda^{'}\alpha_s^{-2}(\phi^{'2}-\phi_0^{'2})^2\\
&-J^{'}\phi^{'2} - \frac{1}{4}B^{'2}_{\mu\nu} + \frac{1}{2}m_B^{'2}(B^{'(d)}_\mu)^2 + [(\partial_\mu\tilde{\phi}^{'2}) - (m^{'}_\phi\tilde{\phi}^{'})^2] + [12\pi\alpha_s^{-1}(B^{'(d)}_\mu)^2(2\phi^{'}\tilde{\phi}^{'}+\tilde{\phi}^{'2}) - 27\lambda^{'}\alpha_s^{-2}(\tilde{\phi}^{'4}+4\phi^{'}\tilde{\phi}^{'3})]\\
&-[108\lambda^{'}\alpha_s^{-2}(\phi^{'2}-\phi_0^{'2})\phi^{'} + 2J^{'}\phi^{'}]\tilde{\phi}^{'},\end{aligned} \tag{18}$$

where $J = -6\lambda\alpha_s^{-2}(\phi^2 - \phi_0^2)$ and $J^{'} = -54\lambda^{'}\alpha_s^{-2}(\phi^{'2} - \phi_0^{'2})$. The corresponding partition function may be written as,

$$\begin{aligned}Z[J] &= exp[i\int d^4x(-3\lambda\alpha_s^{-2}(\phi^2-\phi_0^2)^2 - J\phi^2 - 27\lambda^{'}\alpha_s^{-2}(\phi^{'2} - J^{'}\phi^{'2})]\\
&\times[Det(iD_{\mu\nu})^{-1}(\mathbf{B},\mathbf{k})]^{-1}[Det(i\triangle^{-1}(\phi,k))]^{-1/2} \times [Det(iD_{\mu\nu})^{-1}(\mathbf{B}^{'},\mathbf{k})]^{-1}[Det(i\triangle^{-1}(\phi^{'},k))]^{-1/2}.\end{aligned} \tag{19}$$

The effective action leads to the following form,

$$\begin{aligned}S_{eff} &= \int d^4x\{-3\lambda\alpha_s^{-2}(\phi^2-\phi_0^2)^2 - 27\lambda^{'}\alpha_s^{-2}(\phi^{'2}-\phi_0^{'2})^2\} + ilnDet(iD^{-1}_{\mu\nu}(\mathbf{B},\mathbf{k}))\\
&+\frac{i}{2}lnDet(i\triangle^{-1}(\phi,k)) + ilnDet(iD^{-1}_{\mu\nu}(\mathbf{B}^{'},\mathbf{k})) + \frac{i}{2}lnDet(i\triangle^{-1}(\phi^{'},k)).\end{aligned} \tag{20}$$

The effective potential, which corresponds to the thermodynamical potential at finite temperature is obtained as [21],

$$\begin{aligned}V_{eff}(\phi) &= -\frac{S_{eff}}{\int d^4x} = 3\lambda\alpha_s^{-2}(\phi^2-\phi_0^2)^2 + 27\lambda^{'}\alpha_s^{-2}(\phi^{'2}-\phi_0^{'2})^2 + 3\frac{T}{\pi^2}\int_0^\infty dkk^2ln(1-e^{-\sqrt{k^2+m_B^2}/T})\\
&+\frac{3T}{2\pi^2}\int_0^\infty dkk^2ln(1-e^{-\sqrt{k^2+m_\phi^2}/T}) + 3\frac{T}{\pi^2}\int_0^\infty dkk^2ln(1-e^{-\sqrt{k^2+m_B^{'2}}/T})\end{aligned}$$

$$+\frac{3T}{2\pi^2}\int_0^\infty dkk^2 ln(1-e^{-\sqrt{k^2+m_\phi'^2}/T}). \tag{21}$$

Minimization of the thermodynamical potential alongwith the requirement of color reflection invariance then leads to the thermal values of the VEV of the monopole field and the vector glueball masses as,

$$<\phi>_0^{(T)}=\sqrt{\phi_0^2-\left(\frac{4\pi\alpha_s+\lambda}{\lambda}\right)\frac{T^2}{8}},\ m_B^{(T)}=\sqrt{8\pi\alpha_s^{-1}}\sqrt{\phi_0^2-\left(\frac{4\pi\alpha+\lambda}{\lambda}\right)\frac{T^2}{8}}. \tag{22}$$

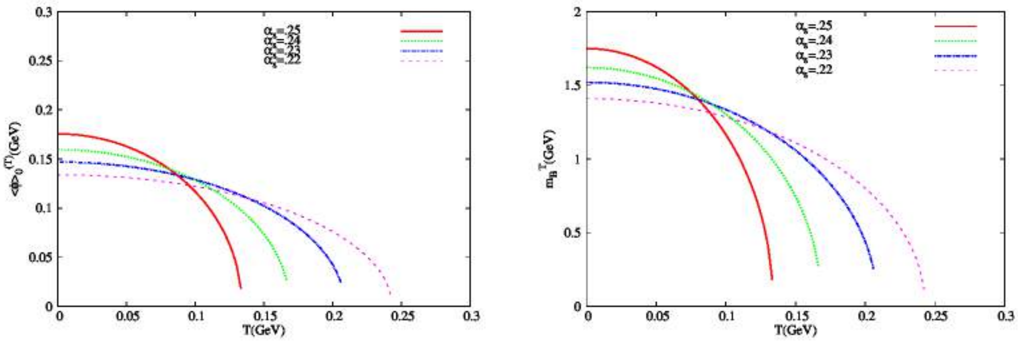

Figure 1. Thermal response of monopole condensate and vector glueball masses in dual QCD.

4. Results and Conclusions

For the analysis of the vital phase transition parameters of QCD, the vacuum expectation value of ϕ field at finite temperature has been obtained by minimization condition on effective potential (22). The variation of vacuum expectation value $<\phi>_0^{(T)}$ with temperature for different coupling has been shown in figure 1. The $<\phi>_0^{(T)}$ value in high temperature region, ultimately vanishes at some typical characteristic value of temperature, called the critical temperature (T_c) of phase transition, which is obtained as 0.241GeV, 0.206 GeV, 0.166 GeV and 0.133 GeV for the coupling values of 0.22, 0.23, 0.24 and 0.25 respectively. The disappearance of the QCD monopole condensate at sufficiently high temperature indicates the restoration of the magnetic symmetry and evaporation into thermal monopoles. The vacuum expectation value leads to temperature dependent scalar and vector glueball masses and has been depicted in Fig. 1. These plots demonstrate a decrease in monopole condenstate and glueball masses with temperature which is an indicative of a first-order deconfinement phase transition in dual QCD.

Acknowledgements

The authors are thankful to the organizers of CICAHEP-2015 for their hospitality during the conference and University Grants Commission (UGC), New Delhi, India, for the financial assistance under the UGC-RFSMS research fellowship during the course of the study.

References

[1] D. J. Gross and F. Wilczek, Phys. Rev. Lett. **30**, 1343 (1973).
[2] H. Hinchliffe, Phys. Rev. D **50**, 1177 (1994).
[3] K. Abbe et al., Phys. Rev. D **51**, 962 (1995).
[4] H. D. Politzer, Phys. Rev. Lett. **30**, 1346 (1973).
[5] M. Creutz, L. Jacobs and C. Rebbi, Phys. Rev. D **20**, 1915 (1979).

[6] L. McLerran, Rev. Mod. Phys. **58**, 1021 (1986).
[7] P. Huovinen and P. Petreczky, Nucl. Phys. A **837**, 26 (2010); J. Phys. Conf. Ser. **230**, 012012 (2010).
[8] C. Ratti et al., Nucl. Phys. A 855, **253** (2011).
[9] S. Plumari, W. M. Alberico, V. Greco and C. Ratti, Phys. Rev. D **84**, 094004 (2011).
[10] S. Borsanyi et al., JHEP **01**, 138 (2012); J. Phys. G **38**, 124060 (2011).
[11] M. Cheng et al., Phys. Rev. D **81**, 054504 (2010).
[12] K. Splittorff and J. J. M. Verbaarschot, Phys. Rev. Lett. **98**, 031601 (2007).
[13] Y. M. Cho, Phys. Rev. D **21**, 1080(1980); Phys. Rev. D **23**, 2415 (1981).
[14] Y. M. Cho. Phys. Rev. Lett. **44**, 1115 (1980).
[15] H. C. Pandey and H. C. Chandola, Phys. Lett. B **476**, 193 (2000).
[16] H. C. Chandola, D. Yadav, H. C. Pandey and H. Dehnen, Int. Jour. Mod. Phys. A **20**, 2743 (2005).
[17] H. C. Chandola, Garima Punetha, H. Dehnen, Nucl. Phys. A **945**, 226 (2016).
[18] Y. M. Cho, Phys. Rev. Lett. **46**, 302 (1981).
[19] P. Ring, P. Schuck, *The Nuclear Many-Body-Problem*, Springer-Verlag, New York, 1980.
[20] L. Dolan, R. Jackiw, Phys. Rev. D **9**, 3320 (1974).
[21] T. P. Cheng, L. F. Li, *Gauge Theory of Elementary Particle Physics*, Clarendon Press, Oxford, 1984.


National Conference
CURRENT ISSUES IN COSMOLOGY, ASTROPHYSICS AND HIGH ENERGY PHYSICS
2 - 5, 2015
INDIA
DAE-BRNS


AND HIGH ENERGY
(CICAHEP)
2 - 5, 2015
OF PHYSICS
ASSAM, INDIA

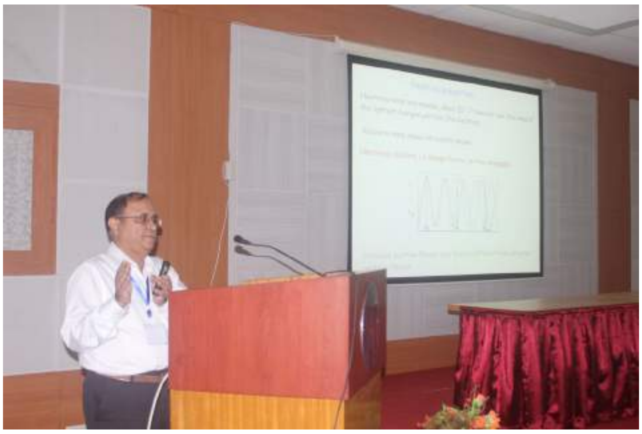

Conference website: http://www.cicahep.org/